

nature

TURNING BACK TIME

Reprogramming retinal cells can reverse age-related vision loss

Coronavirus
Could delirium in COVID lead to long-term cognitive decline?

Sea change
Securing a sustainable future for the world's oceans

Setting standards
A highly accurate measurement of the fine-structure constant

Vol. 586 No. 7821
www.nature.com

Nature

[Fri, 04 Dec 2020]

- [Donation](#)
- [This Week](#)
- [News in Focus](#)
- [Books & Arts](#)
- [Opinion](#)
- [Work](#)
- [Research](#)
- [Amendments & Corrections](#)

Donation

- -> [**打赏 - Donation**](#)

打赏 - JUST FOR FUN

一杯咖啡钱, 打赏金额随意, 感谢大家~ :)

支付宝	微信
 <p>支付就用支付宝  打开支付宝[扫一扫] 免费寄送收钱码: 拨打95188-6 https://blog.csdn.net/bboyfelyu</p>	 <p>推荐使用微信支付  Mr.SIMPLE (**辉)  微信支付</p>

资源来自: www.github.com/hehonghui

This article was downloaded by **calibre** from <http://economist.cool/donate.html>

This Week

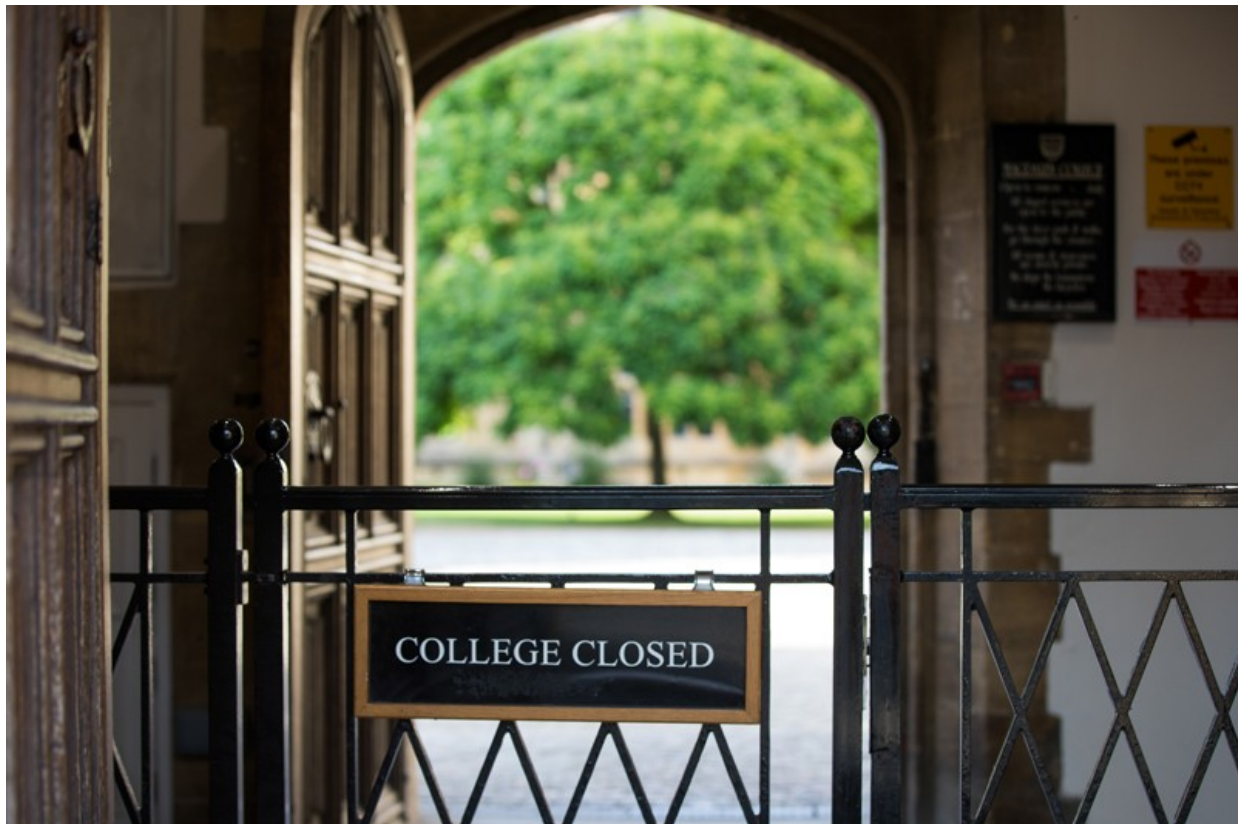
- **[Postdocs need urgent financial support amid COVID conditions](#)** [01 December 2020]
Editorial • Most funders have no plans to provide postdoctoral researchers with additional pandemic funding. Society will pay a high price if this neglect continues.
- **[Even Earth's largest-ever sharks needed nurseries for their babies](#)** [25 November 2020]
Research Highlight • Ancient teeth hint that a handful of sites served as sheltered sanctuaries for immature megalodon sharks.
- **[The crystalline armour that protects ants in battle](#)** [24 November 2020]
Research Highlight • A species of leaf-cutter ant is the first known example of an insect with mineralized armour, which shields them during combat.
- **[How mud volcanoes are born under the sea](#)** [26 November 2020]
Research Highlight • Trapped gas causes buried sediments to flow like water, rising and erupting dangerously at the sea floor.

EDITORIAL

01 December 2020

Postdocs need urgent financial support amid COVID conditions

Most funders have no plans to provide postdoctoral researchers with additional pandemic funding. Society will pay a high price if this neglect continues.



University closures and delays to research projects are stretching the finances of postdocs, *Nature*'s survey has found. Credit: Chris Ratcliffe/Bloomberg/Getty

The first ever *Nature* survey to focus on postdoctoral researchers at universities [paints a gloomy picture](#). As we [reported in September](#), half of

respondents revealed that they had recently considered leaving academic research, in part because of concerns for their mental health.

This week, we report on [other aspects of postdoc life covered by the survey](#). It revealed a generation of researchers who are worried about projects being shut down, having insufficient funding to support themselves for the duration of the pandemic, and the steep drop in job vacancies.



Uncertain prospects for postdoctoral researchers

In the wake of these findings, we approached around ten funding agencies and postdoctoral support organizations in the United States and Europe — home to the overwhelming majority of the survey's self-selecting group of 7,670 respondents. We asked what they are doing to address these concerns. Those we contacted included the European Commission, the Howard Hughes Medical Institute, UK Research and Innovation (UKRI), the US National Institutes of Health and the US National Science Foundation.

Earlier in the year, many funders agreed to extend deadlines for research projects halted or delayed by the pandemic — but fewer offered extra

funding to cover this period. Worryingly, most of the funders we approached still have no concrete plans to provide such additional financial support to postdocs. Many postdocs are not eligible for the government salary subsidies, or furlough schemes, that have been made available to many workers during the pandemic. Expanding access to such schemes is arguably the one intervention that could do the most to ease pressures at this time.

Financial struggles and insecurities are contributing to postdocs' anxiety and distress, *Nature*'s survey reveals. Postdocs are almost always employed on short-term contracts, and the survey's comments section featured many accounts of day-to-day struggles. Postdocs say that they are barely managing, but the urgency of their plight doesn't seem to be getting through to decision makers.



Postdoc survey reveals disenchantment with working life

It's not that nothing is happening. In addition to agreeing to extend project deadlines, some funders have said that they are looking at other ways to support postdocs and their career development.

The European Commission's funding body for postdocs told *Nature* that it is providing grantees with access to careers advice — including advice on non-academic careers — a crucial service at a time of widespread layoffs and hiring freezes at universities. The commission says that it is also trying to find ways to make it easier for postdocs to obtain funding from other EU sources.

The United Kingdom's main research funding body, UKRI, has previously said that it is providing some grantees, including some postdocs, with funding extensions during the pandemic. However, it was unable to respond to our request for an update on its policy by the time *Nature* went to press.

The United Kingdom's research system is powered by its 45,000 postdocs — for comparison, the United States has around 80,000, but the country's population is five times larger. UKRI is also a signatory to the 2019 Concordat to Support the Career Development of Researchers, an agreement that sets out ways to support career development and improve research culture.



Postdocs under pressure: ‘Can I even do this any more?’

The Howard Hughes Medical Institute, a philanthropic organization based in Chevy Chase, Maryland, told *Nature* that it will continue to pay postdocs even if labs remain shut during the pandemic. The organization has given postdocs extra time to complete projects, and has provided extra paid leave when necessary. The funder has also increased the minimum annual salary for postdocs from US\$50,000 in 2019 to \$51,000 in 2020 as part of an annual review.

Worldwide, the approach taken by this institution is the exception, not the rule. And although at the start of the pandemic some public funders and universities did urge governments to allow researchers to be compensated as part of furlough schemes, those calls went unheeded.

As a consequence, the research world is facing a situation where the futures of many of those in its most precarious community are hanging by a thread. As one survey respondent, a physicist in Denmark, told us: “The lack of stability in a postdoc position is a huge source of anxiety and depression.”

Governments and research funders must recognize that this urgent situation demands an urgent response. Postdocs are the future of science, and the lifeblood of the research workforce. If they don’t receive some extra financial help soon, research — and society as a whole — will bear the consequences of denying a lifeline to the next generation of researchers, inventors and innovators.

Nature **588**, 8 (2020)

doi: <https://doi.org/10.1038/d41586-020-03377-z>

Jobs from Nature Careers

- - - [All jobs](#)
 -
 - [Gene Therapy Lab & Research Manager](#)

University of Hawai'i at Manoa (UH Mānoa)

Honolulu, United States

JOB POST

▪ **RN Case Manager**

Oklahoma Medical Research Foundation (OMRF)

Oklahoma City, United States

JOB POST

▪ **Research Associate**

The University of British Columbia (UBC)

Vancouver, Canada

JOB POST

▪ **Postdoctoral Fellows in Quantum Mathematics**

University of Southern Denmark (SDU)

Odense M, Denmark

JOB POST

This article was downloaded by **calibre** from <https://www.nature.com/articles/d41586-020-03377-z>



Young megalodon sharks (artist's impression) spent time in sheltered coastal areas while they grew to their gigantic adult proportions. Credit: Humberto Ferrón

Palaeontology

25 November 2020

Even Earth's largest-ever sharks needed nurseries for their babies

Ancient teeth hint that a handful of sites served as sheltered sanctuaries for immature megalodon sharks.

The prehistoric shark *Otodus megalodon* was an awe-inspiring beast, measuring up to three times the length of the modern great white shark. But even the mightiest of predators were babies once.

Carlos Martínez-Pérez at the University of Valencia in Spain, Humberto Ferrón at the University of Bristol, UK, and their colleagues compared megalodon teeth recently collected at two quarries in northeastern Spain with records of teeth found at eight other sites around the world. A disproportionate number of teeth gathered at five of the nine global locations were from young sharks, suggesting that those sites represent megalodon ‘nurseries’.

Nurseries are protected areas with shallow waters and abundant prey where young sharks can develop in relative safety. Big, slow-growing species of shark persist only when the survival rate of juveniles is high, and nurseries can make this possible. But the researchers note that there’s a downside, too: species can become dependent on the availability of suitable nursery sites, which can be disrupted by sea-level changes.

[Biol. Lett. \(2020\)](#)

- [Palaeontology](#)

This article was downloaded by **calibre** from <https://www.nature.com/articles/d41586-020-03304-2>

| [Section menu](#) | [Main menu](#) |



A soldier ant of the species *Attala cephalotes* (right) extends its mandibles towards an *Acromyrmex echinatior* worker ant. Mineralized body armour protects some *A. echinatior* workers from attack. Credit: Caitlin M. Carlson

Biomaterials

24 November 2020

The crystalline armour that protects ants in battle

A species of leaf-cutter ant is the first known example of an insect with mineralized armour, which shields them during combat.

Just as superheroes don armour to fight villains, so some ants make their own close-fitting protective shield to fend off attackers and parasites.

Pupa Gilbert and Cameron Currie at the University of Wisconsin–Madison and their colleagues discovered that in workers of one species of leaf-cutter ant (*Acromyrmex echinatior*), almost the entire body is covered in a magnesium-rich layer containing a bone-like mineral called calcite. The armour, which is made up of tiny crystals that form a curved surface, develops as the ants mature and seems to be produced by the underlying waxy outer coating of the body of mature workers.

In fights with soldiers of another ant species, worker *A. echinatior* ants equipped with the calcite armour lost fewer body parts and were more likely to survive than were those without the protective covering. The armour also helped to protect the insects against infection with a disease-causing microorganism.

Calcite armour is common in lobsters and other marine animals but has never before been observed in insects. The findings suggest that this type of covering might be more widespread than previously thought, the researchers say.

[Nature Commun. \(2020\)](#)

- [Biomaterials](#)

This article was downloaded by **calibre** from <https://www.nature.com/articles/d41586-020-03280-7>



A mud volcano in Shirvan National Park, Azerbaijan. Researchers have investigated how similar mud volcanoes could form under water. Credit: Alamy

Geology

26 November 2020

How mud volcanoes are born under the sea

Trapped gas causes buried sediments to flow like water, rising and erupting dangerously at the sea floor.

Mud volcanoes are an unpredictable and dangerous phenomenon — but now scientists have a better understanding of how some of them form and evolve.

More than 1,000 mud volcanoes have been identified around the world, both on land and under water. The most famous eruption, known as Lusi, began in Indonesia in 2006 and buried nearby villages in thick mud.

Arthur Blouin at the French Research Institute for the Exploitation of the Sea in Plouzané and his colleagues studied a mud volcano in the Caspian Sea, a centre of oil and gas exploration, which has the densest distribution of such volcanoes anywhere in the world.

The researchers simulated how methane becoming trapped in the sediments at the site could trigger changes in pore pressure, causing mud to form some 3.5 kilometres beneath the sea floor and begin rising. They calculate that it takes around 100 years for the mud to reach the sea floor and erupt.

Understanding what causes the mud to form, and how long it takes to get to the surface, could help researchers to improve predictions of future eruptions, the authors say.

[J. Geophys. Res. \(2020\)](#)

- [Geology](#)

This article was downloaded by **calibre** from <https://www.nature.com/articles/d41586-020-03346-6>

News in Focus

- **[China Moon mission and a scholar on death row](#)** [02 December 2020]
News Round-Up • The latest science news, in brief.
- **[Coronaviruses closely related to the pandemic virus discovered in Japan and Cambodia](#)** [23 November 2020]
News • The viruses, both found in bats stored in laboratory freezers, are the first SARS-CoV-2 relatives to be found outside China.
- **[Why Oxford's positive COVID vaccine results are puzzling scientists](#)** [23 November 2020]
News • Preliminary data suggest that the immunization was more effective in trial participants who received a lower dose.
- **[Why emergency COVID-vaccine approvals pose a dilemma for scientists](#)** [23 November 2020]
News • Immunizations are speeding towards approval before clinical trials end, but scientists say this could complicate efforts to study long-term effects.
- **[Nature journals reveal terms of landmark open-access option](#)** [24 November 2020]
News • The journals will charge authors up to €9,500 to make research papers free to read, in a long-awaited alternative to subscription-only publishing.
- **[Hints of twisted light offer clues to dark energy's nature](#)** [24 November 2020]
News • Cosmologists suggest that an exotic substance called quintessence could be accelerating the Universe's expansion — but the evidence is still tentative.
- **[Could COVID delirium bring on dementia?](#)** [02 December 2020]
News Feature • Delirium is very common on COVID wards. Researchers are testing whether these temporary bouts of confusion could bring on permanent cognitive decline.

NEWS ROUND-UP

02 December 2020

China Moon mission and a scholar on death row

The latest science news, in brief.



A Long March-5 rocket carrying Chang'e-5 lifts off. Credit: Mark Schiefelbein/AP/Shutterstock

China probe on way to Moon

A Chinese spacecraft is on its way to the Moon after launching off the coast of Hainan Island in southern China at 4.30 a.m. local time on 24 November.

Chang'e-5's mission is to [retrieve rocks from the Moon](#) and return them to Earth. If successful, the craft will be the first to collect lunar material in 44 years — and the mission will be a first for China, ushering in the next phase of its increasingly complex lunar-exploration programme. Several Chang'e spacecraft, which are named after a Chinese Moon goddess, have reached and touched down on the Moon.

Chang'e-5 blasted off from Wenchang Satellite Launch Center aboard the Chinese Long March-5 rocket. Its 800,000-kilometre round trip to the Moon will take about three weeks.

“This will greatly encourage people, especially the younger generation, to study and explore the worlds beyond our Earth,” says Xiao Long, a planetary geologist at the China University of Geosciences in Wuhan.

If the mission achieves its goals, it will mark the beginning of a new era of robotic sample returns from the Moon, which will undoubtedly change scientists' understanding of the planetary body, says Clive Neal, a geoscientist at the University of Notre Dame in Indiana. “Now we wait for the samples to be collected and returned.”



Ahmadreza Djalali has been sentenced to death in Iran. Credit: Belga via ZUMA Press

Execution looms for Iran scholar on death row

A medical researcher sentenced to death in Iran three years ago on a charge of spying — which he denies — is [under threat of imminent execution](#), *Nature* has been told.

As *Nature* went to press, Ahmadreza Djalali, a scholar in disaster medicine who has dual Iranian–Swedish nationality, was nearing the end of a week of solitary confinement at Evin prison in Tehran, where he has been held since 2016. He is expected to be transferred to Rajai Shahr prison, west of Tehran, where the execution could be carried out, according to a letter dated 24 November that carries the name of Mohammad Barae, understood to be a judge in Iran's legal system.

Vida Mehrannia, Djalali's wife, told *Nature* she had received a telephone call from him on 25 November in which he said he was being moved to solitary confinement, and then to a different prison to be executed.

"This letter looks to be a court order from a judge declaring that the death sentence is to be carried out," says Ziba Mir-Hosseini, a scholar of Iran's legal system who is based at SOAS University of London.

Human-rights organizations, researchers and Sweden's foreign ministry are urging Iranian head of state Ali Khamenei to show clemency.



Spain's science minister, astronaut Pedro Duque, hopes to keep raising the research budget in the coming years.Credit: E. Parra/Europa Press via Getty

Spanish scientists celebrate huge budget boost

Scientists in Spain have welcomed a [boost to their research budget](#), which they hope could help to reverse damage done by a decade of cuts. The Spanish government's draft budget for 2021 increases the science ministry's funds by nearly 60% compared with 2020. If approved, the boost would raise the ministry's budget to €3.2 billion (US\$3.8 billion) — the most ever earmarked for science in Spain.

“My eyes almost popped out,” says Amaya Moro-Martín, a researcher at the Space Telescope Science Institute in Baltimore, Maryland, who is from Spain and in 2012 co-led a protest of scientists against the country’s austerity measures.

Much of the increase comes from a European Commission programme for member states hit hardest by the COVID-19 pandemic. Spain will receive €140 billion from the European Union over six years. For 2021, the government has devoted €1.1 billion of EU money to the science ministry, and added €2.1 billion from its own coffers.

Many researchers hope that the cash will help institutes to renew their facilities and hire more staff.

The budget must now pass through Parliament. Science minister Pedro Duque told *Nature* he was confident it would do so.

Nature **588**, 13 (2020)

doi: <https://doi.org/10.1038/d41586-020-03349-3>

[**Jobs from Nature Careers**](#)

- - - [All jobs](#)
 - - [**Gene Therapy Lab & Research Manager**](#)

[University of Hawai'i at Manoa \(UH Mānoa\)](#)

[Honolulu, United States](#)

[JOB POST](#)

▪ [**RN Case Manager**](#)

[Oklahoma Medical Research Foundation \(OMRF\)](#)

[Oklahoma City, United States](#)

[JOB POST](#)

▪ [**Research Associate**](#)

[The University of British Columbia \(UBC\)](#)

[Vancouver, Canada](#)

[JOB POST](#)

▪ [**Postdoctoral Fellows in Quantum Mathematics**](#)

[University of Southern Denmark \(SDU\)](#)

[Odense M, Denmark](#)

[JOB POST](#)

This article was downloaded by **calibre** from <https://www.nature.com/articles/d41586-020-03349-3>

NEWS

23 November 2020

- Correction [29 November 2020](#)

Coronaviruses closely related to the pandemic virus discovered in Japan and Cambodia

The viruses, both found in bats stored in laboratory freezers, are the first SARS-CoV-2 relatives to be found outside China.

Smriti Mallapaty

Search for this author in:

- [Pub Med](#)
- [Nature.com](#)
- [Google Scholar](#)

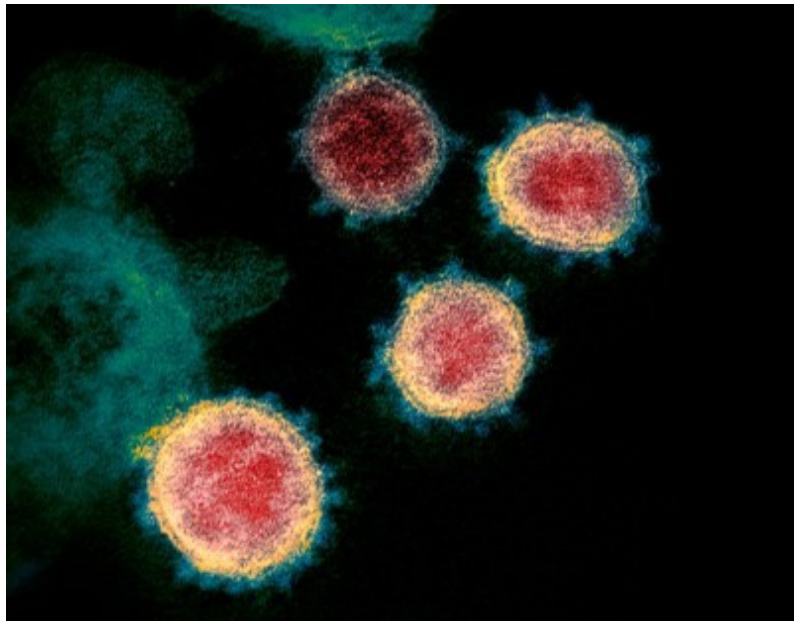


A coronavirus related to SARS-CoV-2 has been found in Shamel's horseshoe bats captured in Cambodia in 2010. Credit: Merlin D. Tuttle/SPL

Two lab freezers in Asia have yielded surprising discoveries. Researchers have told *Nature* they have found a coronavirus that is closely related to SARS-CoV-2, the virus responsible for the pandemic, in horseshoe bats stored in a freezer in Cambodia. Meanwhile, a team in Japan has reported the discovery of another closely related coronavirus — also found in frozen bat droppings.

The viruses are the first known relatives of SARS-CoV-2 to be found outside China, which supports the World Health Organization's [search across Asia](#) for the pandemic's animal origin. Strong evidence suggests that SARS-CoV-2 originated in horseshoe bats, but whether it passed directly from bats to people, or through an intermediate host, remains a mystery.

The virus in Cambodia was found in two Shamel's horseshoe bats (*Rhinolophus shamelii*) captured in the country's north in 2010. The virus's genome has not yet been fully sequenced — nor its discovery published — making its full significance to the pandemic hard to ascertain.



Coronavirus and COVID-19: Keep up to date

If the virus is very closely related to — or even an ancestor of — the pandemic virus, it could provide crucial information about how SARS-CoV-2 passed from bats to people, and inform the search for the pandemic's origin, says Veasna Duong, a virologist at the Pasteur Institute in Cambodia in Phnom Penh, who led the search of the old samples in Cambodia and alerted *Nature* to the discovery in early November. To provide such insights, the virus would have to share more than 97% of its genome with SARS-CoV-2, which is more than its closest known relative, say researchers.

But the new virus might be more distantly related, in which case, studying it will help scientists to learn more about the diversity in this virus family, says Etienne Simon-Loriere, a virologist at the Pasteur Institute in Paris, who plans to sequence the virus, after which it will be shared publicly.

That is the case with the other virus, called Rc-o319, identified in a little Japanese horseshoe bat (*Rhinolophus cornutus*) captured in 2013. That virus shares 81% of its genome with SARS-CoV-2, according to a paper¹ published on 2 November — which makes it too distant to provide insights into the pandemic's origin, says Edward Holmes, a virologist at the University of Sydney in Australia.

No matter what the Cambodian team finds, both discoveries are exciting because they confirm that viruses closely related to SARS-CoV-2 are relatively common in *Rhinolophus* bats, and even in bats found outside China, says Alice Latinne, an evolutionary biologist at the Wildlife Conservation Society Vietnam in Hanoi, who has seen some of the Cambodian team's analysis but was not involved in the investigation.

“This is what we were looking for, and we found it,” says Duong. “It was exciting and surprising at the same time.”

Pandemic origins

The findings also suggest that other as-yet undiscovered SARS-CoV-2 relatives could be stored in lab freezers, says Aaron Irving, an infectious-diseases researcher at Zhejiang University in Haining, China, who also plans to test stored samples of bats and other mammals for antibodies against SARS-CoV-2.

“I did not expect to find a relative of SARS-CoV-2,” says virologist Shin Murakami at the University of Tokyo, who was part of the team that decided to retest frozen animal samples for viruses in the wake of the pandemic.

Only a handful of known coronaviruses are closely related to SARS-CoV-2, including its closest known relative, RaTG13. That was discovered in intermediate horseshoe bats (*Rhinolophus affinis*) in the Chinese province of Yunnan in 2013, and was published² only earlier this year. There are also several other coronaviruses, found in other *Rhinolophus* bats and pangolins captured between 2015 and 2019, that scientists now know to be closely related to SARS-CoV-2.

“SARS-CoV-2 probably wasn’t a brand new virus that popped up all of a sudden. Viruses in this group existed before we became aware of them in 2019,” says Tracey Goldstein, associate director of the One Health Institute at the University of California, Davis, who is involved with the Cambodian team.

Latinne says the discoveries confirm that *Rhinolophus* bats are the reservoir of these viruses.

Virus in Cambodia

Duong’s team captured the Shamel’s horseshoe bats in Cambodia as part of the US-government-funded PREDICT project, which surveyed wildlife worldwide for viruses with pandemic potential for decades and ended earlier this year. In April, the US Agency for International Development gave the programme an additional US\$3 million and a 6-month extension to look for evidence of SARS-CoV-2 in animal samples — mostly bats, as well as pangolins and other animals — that were sitting in laboratory freezers in Laos, Malaysia, Nepal, Thailand, Vietnam, and Cambodia. A full report of these investigations is expected in the coming weeks.

Duong says preliminary genome sequencing of a short fragment of the new bat virus — 324 base pairs long — showed that it was similar to the same region in SARS-CoV-2 and RaTG-13, suggesting that the three are closely related. That region is highly conserved in coronaviruses, says Latinne, and is often used to quickly identify whether a virus is new or known. But it’s not yet clear whether RaTG-13 or the new virus is more closely related to SARS-CoV-2.

It is difficult to say with such a small fragment, says Vibol Hul, a virologist also at the Institute Pasteur in Cambodia, who trapped the Shamel’s horseshoe bats at the entrance to a cave in 2010. The genomes of most known coronaviruses contain about [30,000 base pairs](#).

In a separate analysis, the Cambodia team sequenced some 70% of the new virus’s genome using the technology available locally, says Erik Karlsson, a virologist at the Pasteur Institute in Cambodia, who helped to analyse the

bats. Missing from that sequence were the instructions for crucial parts of the virus, such as the genes that encode the spike protein that coronaviruses typically use to enter cells. Sequencing that section will indicate whether this virus can infect human cells, says Duong.

The new virus would have to be at least 99% similar to SARS-CoV-2 to be an immediate ancestor of the current pandemic virus, says Irving. The genomes of RaTG13 and SARS-CoV-2 differ by only 4%, but that divergence represents between 40 and 70 years of evolution since they shared a common ancestor. Although decades apart, the viruses are similar enough to use the same receptor to enter cells. Cell studies suggest that RaTG13 could infect people³.

Another close relative

Of the known coronaviruses related to SARS-CoV-2, the newly discovered Rc-o319 seems to be the most distantly related, says Duong.

In cell studies, the Japan team found that the virus can not bind to the receptor that SARS-CoV-2 uses to enter human cells, suggesting that it could not easily infect people.

Shin says his colleagues captured more bats in Japan earlier this year, and plan to test them for coronaviruses. And in October, Hul returned to the cave in northern Cambodia to catch more bats.

More SARS-CoV-2-related coronaviruses probably exist in *Rhinolophus* bat populations, which live across the region, says Holmes. “Hopefully, one or more of these will be so closely related to SARS-CoV-2 that we can regard it as the true ancestor.”

Nature 588, 15-16 (2020)

doi: <https://doi.org/10.1038/d41586-020-03217-0>

Updates & Corrections

- **Correction 29 November 2020:** This story now refers to the correct location of Zhenjiang University.

References

1. 1.

Murakami, S. *et al. Emerg. Infect. Dis.*
<https://doi.org/10.3201/eid2612.203386> (2020).

2. 2.

Zhou, P. *Nature* **579**, 270–273 (2020).

3. 3.

Shang, J. *et al. Nature* **581**, 221–224 (2020).

Jobs from Nature Careers

- - - [All jobs](#)
 - - [Gene Therapy Lab & Research Manager](#)
[University of Hawai'i at Manoa \(UH Mānoa\)](#)
[Honolulu, United States](#)
[JOB POST](#)
 - [RN Case Manager](#)
[Oklahoma Medical Research Foundation \(OMRF\)](#)
[Oklahoma City, United States](#)

JOB POST

▪ **Research Associate**

The University of British Columbia (UBC)

Vancouver, Canada

JOB POST

▪ **Postdoctoral Fellows in Quantum Mathematics**

University of Southern Denmark (SDU)

Odense M, Denmark

JOB POST

This article was downloaded by **calibre** from <https://www.nature.com/articles/d41586-020-03217-0>

| [Section menu](#) | [Main menu](#) |

NEWS

23 November 2020

Why Oxford's positive COVID vaccine results are puzzling scientists

Preliminary data suggest that the immunization was more effective in trial participants who received a lower dose.

Ewen Callaway

Search for this author in:

- [Pub Med](#)
- [Nature.com](#)
- [Google Scholar](#)



The vaccine results from Oxford and AstraZeneca are based on data collected in Brazil and the United Kingdom.Credit: Felix Dlangamandla/Beeld/Gallo Images/Getty

A highly anticipated COVID-19 vaccine has delivered some encouraging — but head-scratching — results. The vaccine developed by the University of Oxford, UK, and pharmaceutical giant AstraZeneca was found to be, on average, 70% effective in a preliminary analysis of phase III trial data, the developers announced in a press release on 23 November.

But the analysis found a striking difference in efficacy depending on the amount of vaccine delivered to a participant. A regimen consisting of 2 full doses given a month apart seemed to be just 62% effective. But, surprisingly, participants who received a lower amount of the vaccine in the first dose and then the full amount in the second dose were 90% less likely to develop COVID-19 than were participants in the placebo arm.

Earlier this month, drug companies Pfizer and BioNTech [reported that their RNA-based vaccine was around 90% effective](#) after the trial reached its

primary endpoint, and an interim analysis of an RNA vaccine by biotechnology firm [Moderna showed it worked roughly as well](#).



What Pfizer's landmark COVID vaccine results mean for the pandemic

Researchers caution against making head-to-head comparisons of vaccines on the basis of incomplete data. The disparity in the latest results means there will be considerable uncertainty over precisely how well the Oxford vaccine protects against COVID-19 until ongoing efficacy trials report more data, say scientists. “We’re slightly in danger of rushing to compare apples and oranges,” says Daniel Altmann, an immunologist at Imperial College London. “There’s a long, long way to go before these data settle down and get reported and published in full.”

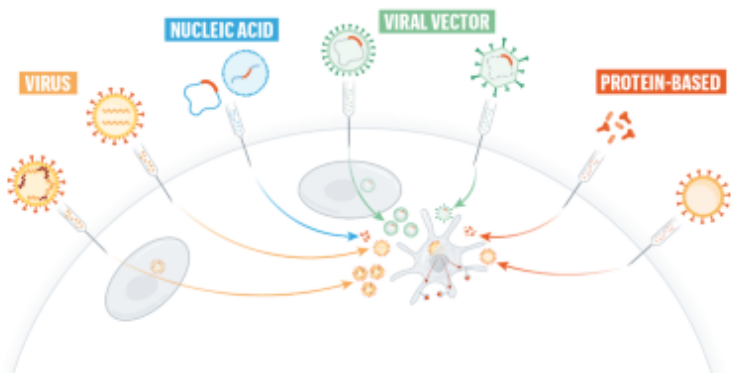
Viral vector

The Oxford–AstraZeneca vaccine is made from a cold-causing adenovirus that was isolated from the stool of chimpanzees and modified so that it no longer replicates in cells. When injected, the vaccine instructs human cells to

produce the SARS-CoV-2 spike protein — the immune system's main target in coronaviruses. The vaccine entered phase III efficacy trials before other front runners, including Pfizer and Moderna, and trials are continuing in countries including the United States, South Africa, Japan and Russia. The 23 November analysis is based on 131 COVID-19 cases among more than 11,000 trial participants in the United Kingdom and Brazil, up to 4 November.

Overall, the developers found that the 2-dose vaccine had an efficacy of 70%, when measured 2 weeks after participants received their second dose. But that figure is an average of the 62% and 90% efficacy from the two dosing regimens. “90% is pretty good, but the 62% for the second tested regimen are not that impressive,” said Florian Krammer, a virologist at Icahn School of Medicine at Mount Sinai in New York City, [on Twitter](#).

A top priority for researchers is understanding why the vaccine seems to have performed so much better with a lower first dose. One explanation could lie in the data: the trial might not have been big enough to gauge the differences between the two regimens, in which case the differences might vanish once more cases of COVID-19 are detected, says Luk Vandenberghe, a virologist at the Massachusetts Eye and Ear institute and Harvard Medical School in Boston. The more effective ‘half-dose, full dose’ results were based on 2,741 trial participants, whereas the less efficacious arm included 8,895 volunteers. The press release did not specify in which group cases occurred.



The race for coronavirus vaccines: a graphical guide

On the basis of the data, Stephen Evans, a statistical epidemiologist at the London School of Hygiene & Tropical Medicine, estimates that the ‘half-dose, full dose’ regimen could have an efficacy as low as 66%.

Dosing theories

But, if the differences are real, researchers are eager to understand why. “I don’t think it’s an anomaly,” says Katie Ewer, an immunologist at Oxford’s Jenner Institute who is working on the vaccine. “I’m keen to get into the lab and start thinking about how we address that question.” She has two leading theories for why a lower first dose might have led to better protection against COVID-19. It’s possible that lower doses of vaccine do a better job at stimulating the subset of immune cells called T cells that support the production of antibodies, she says.

Another potential explanation is the immune system’s response to the chimpanzee virus. The vaccine triggers a reaction not only to the SARS-CoV-2 spike protein, but also to components of the viral vector. It’s possible that the full first dose blunted this reaction, says Ewer. She plans to look at antibody responses to the chimpanzee virus to help address this question.

“This is a plausible explanation,” says James Wilson, a virologist at the University of Pennsylvania in Philadelphia who pioneered the use of adenoviruses for vaccines in the 1990s. By giving a half-dose first, “it is possible that AstraZeneca threaded the needle with their dosing”, he adds.



COVID vaccine excitement builds as Moderna reports third positive result

Hildegund Ertl, a viral immunologist at the Wistar Institute in Philadelphia, says the results make sense in the light of some of her work on adenovirus vaccines in mice. She, too, has found that for a two-dose vaccine, a low first dose can lead to better protection than a high first dose. She thinks this is because a lower first dose leads more quickly to the establishment of ‘memory’ immune cells that are triggered by a second-dose boost. Waiting longer between the two doses could achieve the same effect.

AstraZeneca hopes to gather more data on the dosing regimen. The company has so far given the vaccine to around 10,000 participants in a US arm of the efficacy trial, which was paused for more than a month starting in September, while researchers investigated a neurological condition in a UK trial participant.

The company plans to ask regulators whether it can modify the trial to include the more efficacious dosing regimen, said Mene Pangalos, vice-

president of biopharmaceuticals research at AstraZeneca, which is based in Cambridge, UK, at a press briefing.

“It would be madness to use more vaccine than you needed to get less efficacy,” says Ewer. “I think we will see a move towards roll-out of the ‘low dose, standard dose’ regime.”

Hints of optimism

While Oxford and AstraZeneca make sense of their trial data and gather more, there is reason for optimism in other facets of the vaccine’s performance, say scientists. No participants who received the vaccine were hospitalized or developed severe COVID-19, suggesting the vaccine might do a good job at preventing severe disease.



Russia announces positive COVID-vaccine results from controversial trial

There were also hints that the vaccine might prevent infected people from transmitting the virus, even if they aren't showing symptoms. In the trial's UK arm, some participants routinely swabbed themselves for SARS-CoV-2 testing, even if they weren't showing symptoms. Differences in infection rates between people who received the placebo and those who got the Oxford vaccine suggest the vaccine blocks transmission, says Ewer. (The Pfizer and Moderna trials tested only people who showed symptoms.)

Even with a question mark hanging over its efficacy, the Oxford–AstraZeneca vaccine could see wider roll-out than some other COVID-19 immunizations. The vaccine is stable at refrigerator temperatures, in contrast to the Pfizer and BioNTech vaccine, which must be stored at -70°C until hours before vaccination.

And more of the vaccine could be available sooner, relative to other jabs. AstraZeneca estimates that it will have 200 million doses ready worldwide by the end of 2020, and capacity to produce 100 million to 200 million doses per month once production is ramped up, according to Pam Cheng, vice-president for operations and information technology at AstraZeneca.

"The battle really between all these vaccines is going to be really a logistical one," says Vandenberghe. "We will be able to use every dose that becomes available."

Nature **588**, 16–18 (2020)

doi: <https://doi.org/10.1038/d41586-020-03326-w>

Jobs from Nature Careers

- - - [All jobs](#)
 - - [Gene Therapy Lab & Research Manager](#)

[University of Hawai'i at Manoa \(UH Mānoa\)](#)

[Honolulu, United States](#)

[JOB POST](#)

▪ [**RN Case Manager**](#)

[Oklahoma Medical Research Foundation \(OMRF\)](#)

[Oklahoma City, United States](#)

[JOB POST](#)

▪ [**Research Associate**](#)

[The University of British Columbia \(UBC\)](#)

[Vancouver, Canada](#)

[JOB POST](#)

▪ [**Postdoctoral Fellows in Quantum Mathematics**](#)

[University of Southern Denmark \(SDU\)](#)

[Odense M, Denmark](#)

[JOB POST](#)

This article was downloaded by **calibre** from <https://www.nature.com/articles/d41586-020-03326-w>

NEWS

23 November 2020

Why emergency COVID-vaccine approvals pose a dilemma for scientists

Immunizations are speeding towards approval before clinical trials end, but scientists say this could complicate efforts to study long-term effects.

David Cyranoski

David Cyranoski reports for *Nature* from Shanghai, China.

Search for this author in:

- [Pub Med](#)
- [Nature.com](#)
- [Google Scholar](#)



Trials of the Pfizer–BioNTech vaccine suggest that it is highly effective at preventing COVID-19. Credit: Dogukan Keskinkilic/Anadolu Agency/Getty

After a flurry of positive results from clinical trials of COVID-19 vaccines, developers are now seeking ‘emergency use’ approvals, which could see these immunizations deployed in potentially tens of millions of people. But scientists are concerned that this kind of early deployment could compromise the ongoing clinical trials that seek to show conclusively how well the vaccines work.

Following the release of early data from [phase III trials on 9 November](#), vaccine makers Pfizer and BioNTech have sought regulatory permission to deploy their vaccine under emergency-use rules. The developer of [another leading vaccine, Moderna](#), is expected to do the same within weeks.

Once a vaccine is granted emergency approval, there is pressure on developers to offer the immunization to trial participants who received a

placebo. But if too many people cross over to the vaccine group, the companies might not have enough data to establish long-term outcomes, such as safety, how long vaccine protection lasts and whether the jab prevents infection or just the disease.

“It’s a real vaccine-development dilemma,” says Klaus Stöhr, who formerly headed vaccine design at the pharmaceutical company Novartis in Cambridge, Massachusetts, and is now retired. Still, Stöhr thinks that the vaccine should be granted emergency-use authorization, because its effectiveness has been established and there is a dire need.

Vaccine dilemma

Such competition between a clinical trial for a vaccine and emergency use of it is new for vaccine development. Only this month, the World Health Organization approved the first-ever emergency use for an immunization still being tested, against a type of poliovirus that is spreading in the Southern Hemisphere. But phase III trials for that jab have not yet begun.

Pfizer, based in New York, and BioNTech, based in Mainz, Germany, submitted an application on 20 November for an Emergency Use Authorization (EUA) from the US Food and Drug Administration (FDA). Under the FDA’s rules for COVID-19 vaccines, companies can apply for an EUA when half the trial participants (half of 43,000 people in Pfizer’s case) have been followed for two months after their last dose. Pfizer–BioNTech has already hit that mark; Moderna, based in Cambridge, Massachusetts, says it expects to meet this milestone for its trial of 30,000 participants soon, and that it will apply for an EUA in the coming weeks.

The FDA announced that its vaccine advisory committee will meet on 10 December. The committee will assess the companies’ data and decide whether the vaccines are safe and effective enough for restricted use.

Many researchers expect that the authorizations will be granted. Once a vaccine is approved, a committee of the US Centers for Disease Control and Prevention in Atlanta, Georgia, will determine which groups should be the first in line for vaccination. The panel is considering high-risk groups, such

as elderly people, those with diseases such as diabetes that make them more susceptible to COVID-19, and health-care workers.

Early use of the vaccines in high-risk groups will almost certainly save lives, says Jerome Kim, director-general of the International Vaccine Institute in Seoul. The vaccines have been tested for only a couple months, however, so it is too early to know how long they will be effective for, he says.

Ethical crossover

Trial participants are typically ‘blinded’ as to whether they received the vaccine or a placebo. But once a vaccine has been shown to work, it becomes harder to ask participants to remain in the placebo arm unprotected, says Paul Offit, a vaccine researcher at the Children’s Hospital of Philadelphia in Pennsylvania. “It is a question of ethics,” he says.

On 10 November, Pfizer sent a letter to participants, seen by *Nature*, which states that the company is exploring ways to allow interested participants in the placebo group who meet eligibility criteria for emergency access to cross over into the trial’s vaccine arm. A spokesperson told *Nature* that the company would have “an ethical responsibility to inform all study participants about the availability of an Emergency Authorized Vaccine.”

Nature heard from around a dozen participants in the Pfizer–BioNTech or Moderna trials, most of whom said that if they learnt they had received a placebo, they would take the vaccine if offered. “One reason I participated was my understanding that the standard for blinded studies is to unblind the study if the vaccine is highly effective, and offer all groups the vaccine,” says Moderna trial participant Emma Bernay, from Cincinnati, Ohio.

But if too many people cross over, the trials might not have sufficiently large control groups to gather statistically significant results for some long-term goals, says Stöhr. These include ruling out any long-term safety issues, and conclusively establishing whether the vaccine prevents people getting infected with SARS-CoV-2, or whether it simply protects infected people from getting the disease. There’s also the risk of people in trials other than the Pfizer–BioNTech and Moderna ones dropping out to get vaccinated

under emergency-use provisions, says Larry Corey, a vaccinologist at the Fred Hutchinson Research Center in Seattle, Washington.

The Pfizer spokesperson says that the company will discuss with the FDA how it will gather data to comprehensively measure safety and efficacy if participants cross over. The company's clinical-trial plan says it intends to monitor participants for two years after their final vaccine dose.

Other COVID-19 vaccine developers are also grappling with these issues. Eduardo Spitzer, the scientific director of the Elea Phoenix Laboratory in Buenos Aires, which is running trials in Argentina of a Chinese vaccine from Sinopharm in Beijing, is sure that the country will start an emergency-use vaccination programme. If that happens, doctors, nurses and other essential workers, many of whom have been enrolled in the trial, might be given mandatory vaccinations and therefore no longer qualify for participation in the trial. Other participants in the placebo group might drop out to get a shot they know is the vaccine. "I am 200% sure that an EUA will affect the trial," says Spitzer.

Managing trial disruption

There are ways of managing such disruptions without jeopardizing the trial outcome, says Kathleen Neuzil, director of the Center for Vaccine Development and Global Health at the University of Maryland in Baltimore. She is also co-chair of the US National Institutes of Health's COVID-19 Prevention Trials Network, which arranges clinical trials for companies including Pfizer and Moderna. Participants who initially received a placebo but crossed over to get the vaccine could be monitored as a separate group, and a comparison of the vaccine's long-term efficacy and safety could be made between those groups, she says. Neuzil used a similar set-up to determine the length of protection offered by the first shingles vaccine.

Before unblinding the trials, companies could also ask volunteers to remain in the study and receive the vaccination as soon as the trial is over, says Corey.

Christian Smerz from Houston, Texas, a participant in the Pfizer trial, told *Nature* that he understands the importance of the placebo group for further testing and would consider staying in the trial.

Companies and regulators can also gather safety and efficacy data on people in the high-risk groups who purchase the vaccines, says Eng Eong Ooi, an infectious-disease researcher at Duke–NUS Medical School in Singapore.

But such data can be biased because they cannot be compared with data from a control group, says Ooi. However, they can still provide useful insights into safety and efficacy, he says. “We cannot have the best of both worlds. The world is in need of what we have now,” he says.

Nevertheless, once a COVID-19 vaccine receives emergency authorization, trials of subsequent vaccines will become more complicated, says Ooi, who is developing a vaccine that is in early trials. Companies starting new trials will have to show that their vaccines are better than those granted emergency approval, making trials more expensive. “Any vaccine approved, even if only for emergency use, will change the landscape of how vaccines get into the market,” he says.

Nature **588**, 18–19 (2020)

doi: <https://doi.org/10.1038/d41586-020-03219-y>.

Additional reporting by Smriti Mallapaty.

Jobs from Nature Careers

- - - [All jobs](#)
 -
 - [Gene Therapy Lab & Research Manager](#)
 - [University of Hawai'i at Manoa \(UH Mānoa\)](#)

[Honolulu, United States](#)

[JOB POST](#)

▪ [**RN Case Manager**](#)

[Oklahoma Medical Research Foundation \(OMRF\)](#)

[Oklahoma City, United States](#)

[JOB POST](#)

▪ [**Research Associate**](#)

[The University of British Columbia \(UBC\)](#)

[Vancouver, Canada](#)

[JOB POST](#)

▪ [**Postdoctoral Fellows in Quantum Mathematics**](#)

[University of Southern Denmark \(SDU\)](#)

[Odense M, Denmark](#)

[JOB POST](#)

This article was downloaded by **calibre** from <https://www.nature.com/articles/d41586-020-03219-y>

NEWS

24 November 2020

Nature journals reveal terms of landmark open-access option

The journals will charge authors up to €9,500 to make research papers free to read, in a long-awaited alternative to subscription-only publishing.

Holly Else

Search for this author in:

- [Pub Med](#)
- [Nature.com](#)
- [Google Scholar](#)



Nature and 32 other subscription titles in the Nature family will offer open-access publishing from 2021. Credit: *Nature*

Publisher Springer Nature has announced how scientists can make their papers in its most selective titles free to read as soon as they are published — part of a long-awaited move to offer open-access publishing in the Nature family of journals.

From 2021, the publisher will charge €9,500, US\$11,390 or £8,290 to make a paper open access (OA) in *Nature* and 32 other journals that currently keep most of their articles behind paywalls and are financed by subscriptions. It is also trialling a scheme that would halve that price for some journals, under a common-review system that might guide papers to a number of titles.

OA advocates are pleased that the publisher has found ways to offer open access to all authors, which it first committed to [in April](#). But they are concerned about the price. The development is a “very significant” moment in the movement to make scientific articles free for all to read, but “it looks very expensive”, says Stephen Curry, a structural biologist at Imperial College London.

The change was spurred by the [‘Plan S’ movement](#), in which funders are mandating that their grant recipients must make their work OA as soon as it is published; the funders will generally cover researchers’ costs for this in journals that meet their requirements. Last month, Springer Nature [signed a deal](#) that allowed some German scientists to publish openly in Nature-branded journals for free, with a €9,500-per-article price baked into their institutions’ subscription fees. But today’s announcement reveals the options for any author who wants to publish OA. (*Nature* is editorially independent of its publisher.)

Publishers of extremely selective journals, such as *Nature* and *Science*, have been trying to work out how to switch from subscriptions to OA since Plan S was announced. A large proportion of their production costs come from evaluating manuscripts that are ultimately rejected; when revenue can be collected only from the few articles that get published, the fee per article is high.

High price

No other journals charge as much as €9,500 per OA paper: [the highest fees elsewhere](#) are less than \$6,000 (about €5,000). Some OA advocates criticize Springer Nature's fee as too high. Peter Suber, director of the Harvard Office for Scholarly Communication in Cambridge, Massachusetts, says it is a "prestige tax", because it will pay for the journals' high rejection rates, but will not, in his opinion, guarantee higher quality or discoverability. "I think it would be absurd for any funder, university or author to pay it," he says. But Lisa Hinchliffe, a librarian at the University of Illinois at Urbana–Champaign, says that the fees are not necessarily too high for authors. "I think many authors will find this to be an acceptable price for value," she says.

Juan Pablo Alperin, a communications scholar at Simon Fraser University in Vancouver, Canada, says that although the announcement "signals that universal open access is inevitable", the costs are out of reach for researchers in poorer countries.

A Springer Nature spokesperson responds that costs are higher than at other titles because Nature-branded journals review many more papers than are published, and because they employ in-house editors and press officers, whose work is of "huge value" to researchers. "Making comparisons is difficult, as no other highly selective journal portfolio is offering OA on this scale," they say. Authors who don't choose OA can continue to freely publish their research behind a paywall, the spokesperson notes: these papers are available to subscribers, and authors can make their accepted manuscripts available online after a delay; for *Nature*, that is six months after publication.

The group of funders backing Plan S, called cOAlition S, says publishers should provide data to break down how publishing fees relate to the services provided. "Once this information is available, the research community will be better placed to decide whether the fees levied by publishers are fair and reasonable," says coalition coordinator Robert Kiley, who is also head of open research at the biomedical-research funder Wellcome in London.

‘Guided’ OA pilot

Springer Nature is also introducing a scheme that would roughly halve OA fees for some journals, which it is trialling with *Nature Physics*, *Nature Genetics* and *Nature Methods*. Under the scheme, called guided OA, authors submit manuscripts and — if they pass a suitability screen — pay a non-refundable fee of €2,190 to cover an editorial assessment and the peer-review process. In return, they get a review document, which the publisher says includes more detailed editorial evaluation than typical review reports, and they are told which Springer Nature title their work is recommended for.

Authors who submit to *Nature Physics*, for instance, might be accepted at that journal or told what revisions they need to make to reach it; they might be guided to the less-selective journals *Nature Communications* or *Communications Physics*; or their manuscript might be rejected. They can then walk away with their report or, if accepted, can pay a top-up fee of €2,600 to publish in *Nature Physics* or *Nature Communications*. The total fee of €4,790 is half the standard OA fee for *Nature Physics*, and a slight increase on the price of publishing in *Nature Communications*, the only Nature-branded title that is already fully OA. The top-up fee is €800 for *Communications Physics*, again making the total cost a slight increase on the current price in that OA journal; the increase is to cover the extra editorial work involved in the guided OA route compared with direct submissions to these journals, the publisher says.

This mechanism “shares the cost more evenly over multiple authors” and will save time by avoiding multiple rounds of review in different journals, says James Butcher, vice-president of journals at the Nature Portfolio and BMC, an imprint owned by Springer Nature. Hinchliffe sees it as “a creative experiment for authors and publisher to manage financial risk”.

The scheme could be tempting to researchers hoping to publish in a Nature-branded journal, says Alperin. Compared with the full-price OA option, it “offers a lower initial barrier of entry with a higher threshold of success”, he says. But peer reviewers who have appraised the manuscript under this scheme might feel that Nature titles are “essentially selling their free labour to authors” if a reviewed paper is not eventually published, says Curry.

Test run

Kiley will watch the idea with interest. “Ultimately, we believe that publishing costs need to be split so that they reflect the different services publishers provide, and this experiment by [Springer Nature] will help inform this approach,” he says.

Journals in the Nature family have committed to increasing their OA content over time, so most Plan S funders have said they will pay their OA fees, despite a general reluctance to support hybrid journals (which keep some papers behind a paywall and make others open). But some, including the European Commission and the Dutch Research Council (NWO), have not yet agreed to this.

Other publishers of highly-selective journals haven’t yet announced policies in response to Plan S. Cell Press (owned by Elsevier in Amsterdam) says that the journal *Cell* is finalizing its approach: it currently offers OA publishing at \$5,900, but only to authors whose funding agency “has an appropriate agreement” with the journal. That policy doesn’t suit Plan S, Kiley says.

The publisher of Science-branded journals, the American Association for the Advancement of Science in Washington DC, says it is still thinking about how to adjust to Plan S. Since 2013, it has allowed authors to post an accepted version of their article in an online repository when their paper is published. But that doesn’t satisfy Plan S funders, who ask that manuscripts be shared under an open licence that allows anyone else to redistribute or adapt the work. *Science*’s policy does not currently permit this.

Nature 588, 19-20 (2020)

doi: <https://doi.org/10.1038/d41586-020-03324-y>

Jobs from Nature Careers

- - - [All jobs](#)

o

- **Gene Therapy Lab & Research Manager**

University of Hawai'i at Manoa (UH Mānoa)

Honolulu, United States

JOB POST

- **RN Case Manager**

Oklahoma Medical Research Foundation (OMRF)

Oklahoma City, United States

JOB POST

- **Research Associate**

The University of British Columbia (UBC)

Vancouver, Canada

JOB POST

- **Postdoctoral Fellows in Quantum Mathematics**

University of Southern Denmark (SDU)

Odense M, Denmark

JOB POST

NEWS

24 November 2020

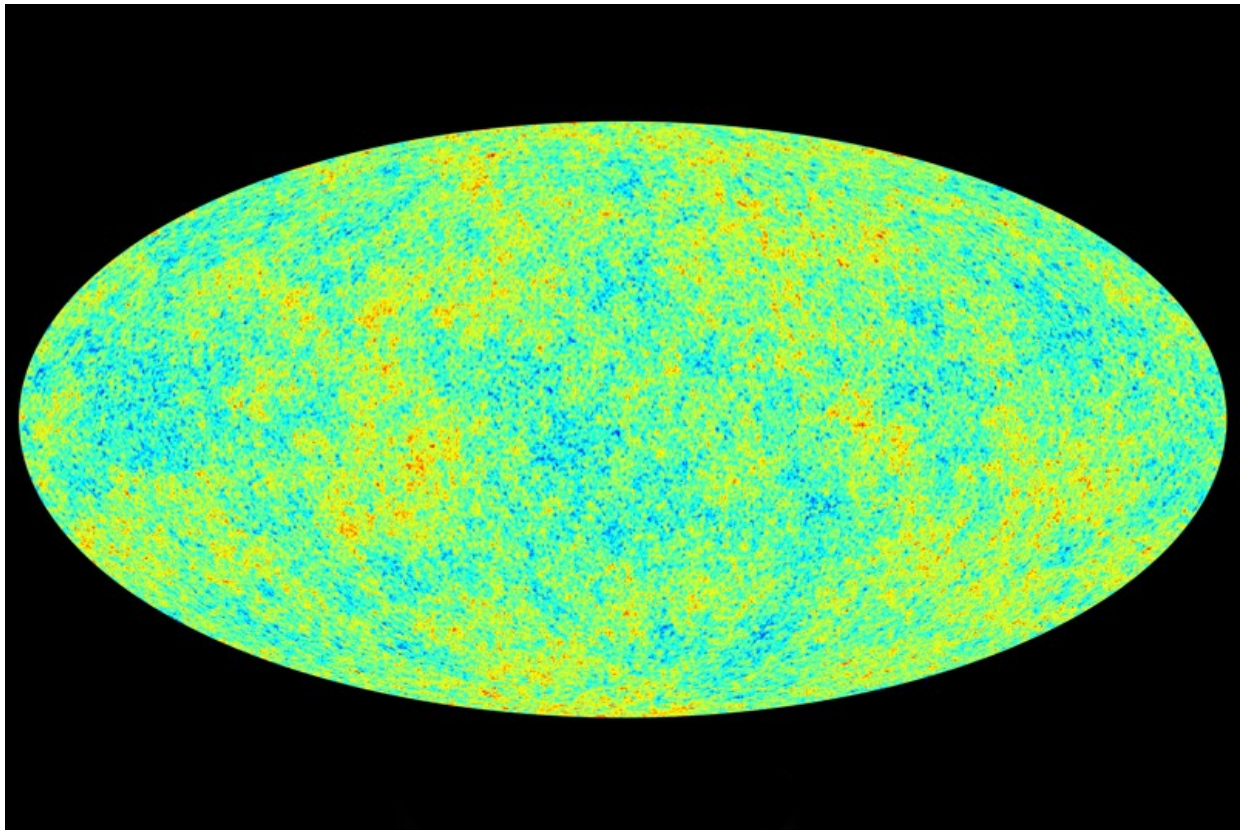
Hints of twisted light offer clues to dark energy's nature

Cosmologists suggest that an exotic substance called quintessence could be accelerating the Universe's expansion — but the evidence is still tentative.

Davide Castelvecchi

Search for this author in:

- [Pub Med](#)
- [Nature.com](#)
- [Google Scholar](#)



A map of the Universe's cosmic microwave background radiation, measured by the Planck space observatory.Credit: ESA

Cosmologists say that they have uncovered hints of an intriguing twisting in the way that ancient light moves across the Universe, which could offer clues about the nature of dark energy — the mysterious force that seems to be pushing the cosmos to expand ever-faster.

They suggest that the twisting of light, which they identified in data on the cosmic microwave background (CMB) collected by the Planck space telescope, and the acceleration of the Universe could be produced by a cosmic ‘quintessence’, an exotic substance that pervades the cosmos. Such a discovery would require a major revision of current theories, and physicists warn that the evidence is tentative — it does not meet the ‘5 sigma’ threshold used to determine whether a signal is a discovery. But it underscores the fact that modern cosmology still has an incomplete picture of the Universe’s contents.

If dark energy is a quintessence, its push on the expansion could slowly wither or disappear, or could even reverse to become an attractive force, causing the Universe to collapse into a ‘big crunch’, says Sean Carroll, a theoretical physicist at the California Institute of Technology in Pasadena. “We’re back to a situation where we have zero idea about how the Universe is going to end.” The work was reported on 23 November in *Physical Review Letters*¹.

The fifth element

The first direct evidence that an unknown force was pushing cosmic expansion to accelerate emerged in 1998, from [two separate surveys of supernovae](#). A host of other studies have since confirmed the presence of this force, dubbed dark energy, but have provided precious little information about its nature.

Researchers’ first guess — which remains the leading theory — was that dark energy is an intrinsic property of space, which would mean that the amount of dark energy per unit volume of space is fixed as a ‘cosmological constant’. But some cosmologists theorized that dark energy is made of something else entirely. They call this a quintessence field, after the fifth element, or aether — the name that ancient Greek philosophers gave to an invisible material thought to fill all the empty space in the Universe.

Unlike the cosmological constant, quintessence “is a tangible medium and it has fluctuations of its own”, says Robert Caldwell, a cosmologist at Dartmouth College in Hanover, New Hampshire, who was one of the first researchers to propose the material’s existence². Quintessence could have properties that are intermediate between those of matter and of a cosmological constant, Caldwell adds. As the Universe expands, a cosmological constant would maintain a constant density, whereas the density of quintessence would decrease — although not as fast as the density of matter, which drops as galaxies spread out.

In 1998, Carroll proposed an experimental test for quintessence³, based on the prediction that it alters how light propagates in space. A group led by the theoretical physicist Marc Kamionkowski, now at Johns Hopkins University

in Baltimore, Maryland, then calculated⁴ how this effect could be measured in the CMB, the primordial radiation often described as the afterglow of the Big Bang. The researchers suggested that it would be possible to detect signs of quintessence by looking at maps of polarized light across the CMB. Light is polarized when its electric field ‘wiggles’ in a particular direction, rather than in a random one. The theory says that quintessence twists the direction in which the polarization points, in a way that could be detected by looking at polarization across the whole sky.

Now, two cosmologists — Yuto Minami at the High Energy Accelerator Research Organization (KEK) in Tsukuba, Japan, and Eiichiro Komatsu at the Max Planck Institute for Astrophysics in Garching, Germany — have identified that CMB signature in data from the European Space Agency’s Planck mission, [which concluded in 2013](#).

Planck’s main purpose was to [map tiny variations in the CMB’s temperature](#) across the sky, but the mission also measured the radiation’s polarization. Minami and Komatsu were able to detect signs of quintessence using a new technique that they reported last year⁵. Their results differ from those of other groups, which have looked at CMB polarization maps — including Planck’s — and found no twist, says physicist Suzanne Staggs at Princeton University in New Jersey, whose team measures CMB radiation using the [Atacama Cosmology Telescope](#) (ACT) in Chile. Staggs’s team plans to try out Minami and Komatsu’s technique on ACT data. “We are interested in exploring it,” she says.

Big implications

The paper is “quite a nice analysis”, but noise in the Planck signals could be a complicating factor, says George Efstathiou, a leading Planck cosmologist at the University of Cambridge, UK.

Theoreticians are responding with caution, too. “If it were real, it’s big,” says Carroll. But he notes that the statistical significance — only 2.5 sigma — of the result is weak, and says that such results often fade away on further scrutiny.

Kamionkowski agrees. “I think we’ll probably want to be going through all that very carefully before getting too worked up,” he says. He adds that the existence of quintessence would have implications not only for cosmology but also for fundamental physics: the standard model of particle physics does not predict any kind of quintessence.

Other efforts are in the works to map the CMB polarization with greater accuracy than ever before, and will put a stringent test on quintessence. These projects include the Simons Observatory, another CMB experiment now being set up in the Atacama Desert, and a future Japanese-led space probe called LiteBIRD.

If quintessence does pan out as an explanation, it will have cascading effects on the best estimates of the Universe’s features, including its age, which could be a bit younger than the 13.8 billion years cosmologists have calculated on the basis of Planck data. It could also help to explain why CMB data predict that the Universe should be expanding at a slower pace than currently observed. “The rock that they’re standing on is the cosmological constant. If you change that rock, that could have an effect on everything else,” says Caldwell.

Nature **588**, 21 (2020)

doi: <https://doi.org/10.1038/d41586-020-03201-8>

References

1. 1.

Minami, Y. & Komatsu, E. *Phys. Rev. Lett.* **125**, 221301 (2020).

2. 2.

Caldwell, R. R., Dave, R. & Steinhardt, P. J. *Phys. Rev. Lett.* **80**, 1582–1585 (1998).

3. 3.

Carroll, S. M. *Phys. Rev. Lett.* **81**, 3067–3070 (1998).

4. 4.

Lue, A., Wang, L. & Kamionkowski, M. *Phys. Rev. Lett.* **83**, 1506–1509 (1999).

5. 5.

Minami, Y. *et al. Prog. Theor. Exp. Phys.* **2019**, 083E02 (2019).

Jobs from Nature Careers

- - - [All jobs](#)
 - - **[Gene Therapy Lab & Research Manager](#)**
[University of Hawai'i at Manoa \(UH Mānoa\)](#)
[Honolulu, United States](#)
[JOB POST](#)
 - **[RN Case Manager](#)**
[Oklahoma Medical Research Foundation \(OMRF\)](#)
[Oklahoma City, United States](#)
[JOB POST](#)
 - **[Research Associate](#)**
[The University of British Columbia \(UBC\)](#)

Vancouver, Canada

JOB POST

▪ **Postdoctoral Fellows in Quantum Mathematics**

University of Southern Denmark (SDU)

Odense M, Denmark

JOB POST

This article was downloaded by **calibre** from <https://www.nature.com/articles/d41586-020-03201-8>

| [Section menu](#) | [Main menu](#) |

NEWS FEATURE
02 December 2020

Could COVID delirium bring on dementia?

Delirium is very common on COVID wards. Researchers are testing whether these temporary bouts of confusion could bring on permanent cognitive decline.

Carrie Arnold

Carrie Arnold is an independent public-health reporter based in Virginia.

Search for this author in:

- [Pub Med](#)
- [Nature.com](#)
- [Google Scholar](#)



Illustration by Fatinha Ramos

In her job as a physician at the Boston Medical Center in Massachusetts, Sondra Crosby treated some of the first people in her region to get COVID-19. So when she began feeling sick in April, Crosby wasn't surprised to learn that she, too, had been infected. At first, her symptoms felt like those of a bad cold, but by the next day, she was too sick to get out of bed. She struggled to eat and depended on her husband to bring her sports drinks and fever-reducing medicine. Then she lost track of time completely.

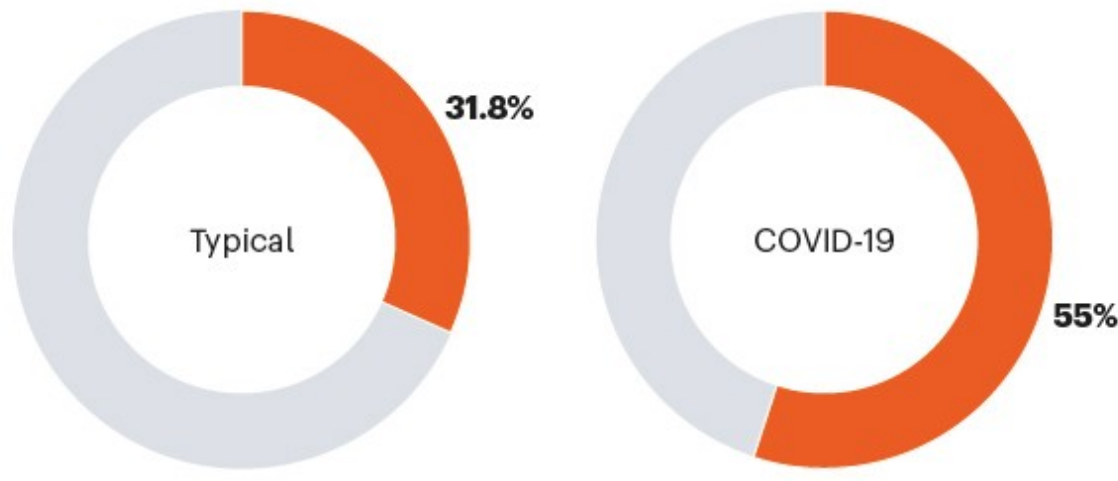
For five days, Crosby lay in a confused haze, unable to remember the simplest things, such as how to turn on her phone or what her address was. She began hallucinating, seeing lizards on her walls and smelling a repugnant reptilian odour. Only later did Crosby realize that she had had delirium, the formal medical term for her abrupt, severe disorientation.

“I didn’t really start processing it until later when I started to come out of it,” she says. “I didn’t have the presence of mind to think that I was anything more than just sick and dehydrated.”

Physicians treating people hospitalized with COVID-19 report that a large number experience delirium, and that the condition disproportionately affects older adults. An April 2020 study in Strasbourg, France, found that 65% of people who were severely ill with coronavirus had acute confusion — a symptom of delirium¹. Data presented last month at the annual meeting of the American College of Chest Physicians by scientists at the Vanderbilt University Medical Center in Nashville, Tennessee, showed that 55% of the 2,000 people they tracked who were treated for COVID-19 in intensive-care units (ICUs) around the world had developed delirium. These numbers are much higher than doctors are used to: usually, about one-third of people who are critically ill develop delirium, according to a 2015 meta-analysis² (see ‘How common is delirium?’).

HOW COMMON IS DELIRIUM?

Typically, almost one-third of people who are critically ill will have an episode of delirium; for COVID-19, the proportion rises to more than half.



©nature

Source: Ref. 2

Delirium is so common in COVID-19 that some researchers have proposed making the condition one of the disease's diagnostic criteria. The pandemic has sparked physicians' interest in the condition, says Sharon Inouye, a geriatrician at the Marcus Institute for Aging and Harvard Medical School in Boston, who has studied delirium for more than 30 years.

As clinicians face the immediate realities of confusion and agitation on their wards, Inouye and other researchers are concerned about the future. In the past decade, long-term studies have revealed that a single episode of delirium can increase the risk of developing dementia years later³, and accelerate rates of cognitive decline in those who already have the condition⁴. The reverse is also true: having dementia makes someone more likely to develop delirium³. A set of simple steps, such as ensuring a family member is present to help people orient themselves, can reduce the incidence of delirium by 40%, but doctors struggle to follow that advice on COVID-19 wards.

How COVID-19 can damage the brain

But the links between delirium and dementia have been difficult to untangle: researchers need to follow patients for years to get results. The surge in people with delirium produced by the pandemic has focused attention on the condition and provided scientists with a unique opportunity to follow patients and determine if and how delirium might affect long-term cognition. Researchers have launched several studies to explore the long-term neurocognitive impacts of COVID-19, including dementia, and Inouye and others hope that this work will allow researchers to explore the links between the two conditions in real time.

If the pandemic can be said to have a silver lining, says Inouye, it has been to spur interest in how delirium can lead to dementia — and vice versa. What's more, says Catherine Price, a neuropsychologist at the University of Florida in Gainesville, the spread of COVID-19 "has highlighted the blurring of the lines between delirium and dementia, especially with more older adults in our populace".

Neglected condition

Inouye's interest in delirium began when she landed her first job as an internal-medicine physician at a Veterans Administration hospital in Connecticut in 1985. In her first month there, she treated more than 40 people for a variety of conditions. Six of them developed delirium during their stay; none seemed to return to their previous level of physical and mental health. To Inouye, the connection between her patients' delirium and their poor prognosis was obvious. When she confessed her suspicions to her bosses, however, they just shrugged. Their attitude, Inouye says, was that delirium was just one of those things that happened.

"Why is it okay for older adults to come in the hospital and lose their minds?" Inouye asked. Answering this question, she says, would be "an uphill battle my entire career".



Visits from relatives are a source of comfort for people with delirium, a common symptom of COVID-19, but many hospitals have strict no-visitor policies. Credit: Morteza Nikoubazl/NurPhoto/Getty

Shortly after, she began a two-year fellowship to study the condition in depth. Her work showed that delirium occurs when several stressors converge. Pre-existing vulnerabilities such as chronic disease or cognitive impairment can combine with precipitating factors including surgery, anaesthesia or overwhelming infection to cause a sudden onset of confusion, disorientation and attention difficulties, especially in older adults⁵.

“Delirium easily occurs when the brain is unable to compensate for a stressful situation,” explains Tino Emanuele Poloni, a neurologist at the Golgi Cenci Foundation outside Milan, Italy. Researchers think that the underlying biological causes are inflammation and an imbalance in neurotransmitters — chemical messengers such as dopamine and acetylcholine.

Inouye's mounting clinical experience has taught her that regardless of what precipitates delirium, around 70% of those with symptoms eventually recover completely. In the 30% who don't, however, an episode of delirium predicts a downward spiral over a period of months that leads to profound cognitive impairment, even to symptoms of dementia.

More-formal studies have reinforced the link, to varying degrees. Inouye investigated a group of 560 people aged 70 or older who had undergone surgery, and saw that cognitive decline over the subsequent 36 months was three times faster in those who developed delirium than in those who did not have the condition⁶. A 2020 meta-analysis of 23 studies showed that delirium during a hospital stay was associated with 2.3 times greater odds of developing dementia⁷. And work⁸ by a team of Brazilian scientists showed that, in a group of 309 people with an average age of 78 years, 32% of those who developed delirium in hospital progressed to having dementia, compared with just 16% of those who did not become delirious (see 'Delirium and cognitive decline').

DELIRIUM AND COGNITIVE DECLINE

People who experience delirium during hospitalization are at increased risk of cognitive decline after discharge, according to a study of 309 patients in Brazil.

Dementia after no delirium

16%

Dementia after delirium

32%

©nature

Source: Ref. 8

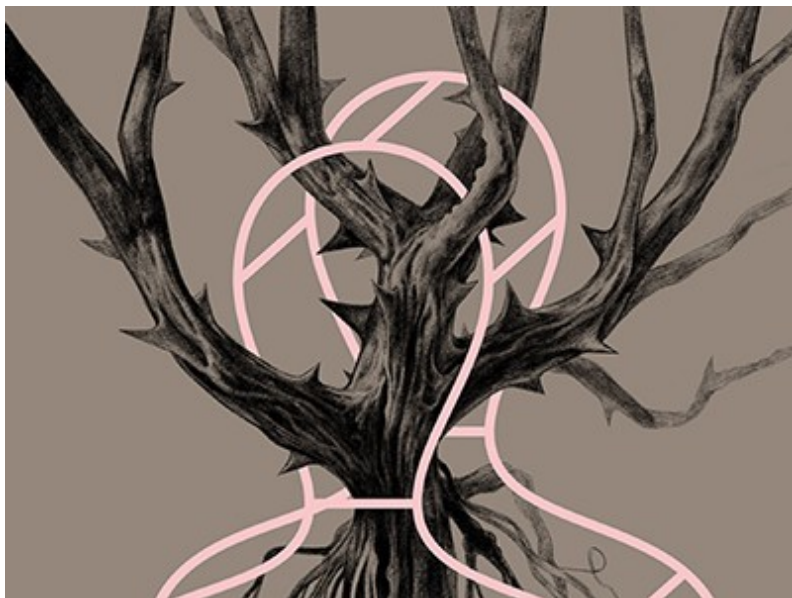
What's more, the longer a person is delirious, the greater their risk of subsequent cognitive impairment, according to a 2013 study by psychologist James Jackson at Vanderbilt University, and his colleagues⁹. Work by Inouye, Jackson, and other researchers found that the reverse was also true:

even after controlling for age, existing dementia symptoms increased the chances of developing delirium³.

Causing confusion

Scientists still don't agree whether the link between delirium and dementia is strong only in those who would have developed dementia anyway, or whether delirium increases the risk of cognitive decline even in individuals who are not predisposed to it. Nor can they say precisely what it is about delirium that could provoke dementia. If researchers could identify these connections, then perhaps they could prevent delirium from escalating into dementia.

"We don't understand the mechanisms of delirium at all — we really don't. And there is no successful management of delirium from a pharmaceutical standpoint," Price says.



The hidden links between mental disorders

Scientists have developed three hypotheses to explain how delirium might provoke dementia. One line of thinking holds that an accumulation of toxic cellular trash in the brain could cause short-term delirium and lead to longer-term damage. The body usually clears this molecular rubbish by way of the bloodstream and the glymphatic system, which is a network of channels filled with cerebrospinal fluid. Damage to vessels from an acute episode of delirium could persist and trigger dementia, or a brain that experiences delirium could become more prone to vascular problems in future.

The second suspect is inflammation, which often troubles people who are hospitalized for infections, respiratory distress or cardiovascular disease. Surgery and severe infections can cause a build-up of cellular detritus in the brain, which triggers more inflammation. This short-term, all-hands-on-deck reaction safeguards the brain because it clears the harmful debris and the inflammation ultimately dies down. That is not the case for those who develop delirium, Inouye says. Persistent inflammation can trigger an acute episode of delirium, and cause neurons and associated cells, such as astrocytes and microglia, to deteriorate, leading to cognitive damage.

The third idea is what's known as the threshold hypothesis. Someone with dementia (even in the earliest stages) has fewer connections between neurons, and can show damage to the insulation that wraps them and helps convey signals — known as white matter. This loss strips the neurological reserves that help the person to cope with inflammation or infection, throwing them over the edge not just into delirium but into a more advanced dementia.

The lasting misery of coronavirus long-haulers

Even though the genesis of delirium and its molecular connections to dementia remain unknown, Inouye has managed to find a way to cut rates of delirium in hospital. She created a programme of simple strategies known as HELP (Hospital Elder Life Programme), which focus on reducing sedation,

even during mechanical ventilation, paying close attention to nutrition and hydration, and ensuring the presence of family members to help reassure and orient patients. A 2015 meta-analysis¹⁰ showed that these steps reduced delirium by around 40%. Hospitals around the United States began instituting these simple protocols. Then COVID-19 struck and made this all but impossible.

Dementia surge

As Crosby endured coronavirus-induced delirium in her Boston bedroom, Poloni was treating delirious people with COVID-19 in Lombardy — Italy’s ground zero for the coronavirus. Many of Poloni’s patients already had dementia and, like many physicians, he was watching for common symptoms of respiratory infections such as fever, cough and difficulty breathing. But some of his patients didn’t show those signs at all. Instead, they mostly became “dull and sleepy”, Poloni said. Others became restless and agitated — all signs of delirium. It was so prominent that Poloni argued that delirium should be added to the virus’s diagnostic criteria. Inouye has made that argument, too, and it is supported by a study she published last month showing that 28% of older adults with COVID-19 have delirium when they present to the emergency department¹¹.

The high numbers of people who developed delirium immediately made Inouye, Price and other researchers worry that the pandemic could lead to a surge in dementia cases in the coming decades, on top of the increase in cases as a result of ageing populations (see ‘The cost of delirium’). “Is there going to be an increase in dementia from people who had COVID-19 during adulthood or midlife?” asks Natalie Tronson, a neuropsychologist at the University of Michigan in Ann Arbor. “What happens over the next decades, as the population ages more?”

THE COST OF DELIRIUM

In the United States, the annual health-care costs for delirium are higher than those for many other conditions common in older adults.

Cardiovascular disease

US\$258 billion

Delirium

\$152 billion

Diabetes

\$92 billion

Non-fatal falls

\$19 billion

Hip fractures

\$7 billion

©nature

Source: D. L. Leslie *et al. J. Am. Geriatr. Soc.* **59**, S241–S243 (2011)

To begin to find answers, institutes around the world have funded a variety of studies into the long-term cognitive effects of COVID-19, some of which will look at delirium. Already under way in the United States is a study tracking people who have been treated in hospital for COVID-19, many of whom developed delirium during their stay. This study will measure cognitive and psychiatric function in people participating in a trial to assess the safety and efficacy of hydroxychloroquine to treat coronavirus. An [international study is planned](#) to measure the prevalence of delirium in people with COVID-19 in ICUs, as well as identifying factors that predict long-term outcomes. A separate study in Germany and the United Kingdom is also tracking neurocognitive outcomes in people with COVID-19 to determine how delirium affects brain function months later. Another research project led by a team at Vanderbilt University is looking for an alternative to commonly-used sedatives such as benzodiazepines, which are known to increase delirium. The researchers are testing a sedative called

dexmedetomidine to see whether it is a safer option for people hospitalized with COVID-19.

Inouye and Tronson hope that the funding of these long-term studies will lead to ongoing scientific interest in the delirium–dementia connection, and provide some insight.

“It’s going to be, I think, a little bit frightening and a little bit enlightening, both about how illness affects dementia risk, but also what other lifestyle and genetic protective factors can influence risk as well,” Tronson says. “We’re learning quickly, but there’s still a lot of black boxes.”

Nature **588**, 22-24 (2020)

doi: <https://doi.org/10.1038/d41586-020-03360-8>

References

1. 1.
Helms, J. *et al.* *N. Engl. J. Med.* **382**, 2268–2270 (2020).
2. 2.
Salluh, J. I. F. *et al.* *Br. Med. J.* **350**, h2538 (2015).
3. 3.
Fong, T. G. *et al.* *Lancet Neurol.* **14**, 823–832 (2015).
4. 4.
Fong, T. G. *et al.* *Neurology* **72**, 1570–1575 (2009).
5. 5.
Fong, T. G., Tulbaev, S. R. & Inouye, S. K. *Nature Rev. Neurol.* **5**, 210–220 (2009).

6. 6.

Inouye, S. K. *et al.* *Alzheimer's Dementia* **12**, 766–775 (2016).

7. 7.

Goldberg, T. E. *et al.* *JAMA Neurol.* **77**, 1373–1381 (2020).

8. 8.

Garcez, F. B. *et al.* *Age Ageing* **48**, 845–851 (2019).

9. 9.

Pandharipande, P. P. *et al.* *N. Engl. J. Med.* **369**, 1306–1316 (2013).

10. 10.

Hshieh, T. T. *et al.* *JAMA Intern. Med.* **175**, 512–520 (2015).

11. 11.

Kennedy, M. *et al.* *JAMA Netw. Open.* **3**, e2029540 (2020).

Jobs from Nature Careers

- - - [All jobs](#)
 - - [Gene Therapy Lab & Research Manager](#)
[University of Hawai'i at Manoa \(UH Mānoa\)](#)
[Honolulu, United States](#)
[JOB POST](#)

- **RN Case Manager**

Oklahoma Medical Research Foundation (OMRF)

Oklahoma City, United States

JOB POST

- **Research Associate**

The University of British Columbia (UBC)

Vancouver, Canada

JOB POST

- **Postdoctoral Fellows in Quantum Mathematics**

University of Southern Denmark (SDU)

Odense M, Denmark

JOB POST

This article was downloaded by **calibre** from <https://www.nature.com/articles/d41586-020-03360-8>

Books & Arts

- **[Wood — the vein that runs through human history](#)** [01
December 2020]
Book Review • Why do stone, bronze, iron, oil and data get all the attention?
- **[The demons and devils that haunt scientists' imaginations](#)**
[30 November 2020]
Book Review • Strange beasts stalk a history of thought experiments.

BOOK REVIEW
01 December 2020

Wood — the vein that runs through human history

Why do stone, bronze, iron, oil and data get all the attention?

Josie Glausiusz

Josie Glausiusz is a science journalist in Israel. Twitter: [@josiegz](#)

Search for this author in:

- [Pub Med](#)
- [Nature.com](#)
- [Google Scholar](#)



A late-seventeenth-century carving at Petworth House, UK. Credit: The National Trust Photolibrary/Alamy

The Age of Wood: Our Most Useful Material and the Construction of Civilization Roland Ennos Scribner (2020)

Wood runs like a vein throughout human history. It is integral to everything from early copper and iron smelting to wheels, windmills, Viking longships, Celtic barrels, Renaissance crumhorns and Stradivarius violins. It was even the subject of the first book published by a nascent Royal Society troubled

by the rapacious demands of a seafaring empire (see [G. Hemery *Nature* 507, 166–167; 2014](#)).

All this and more is dovetailed in *The Age of Wood*, a lively history of biology, mechanics and culture that stretches back 60 million years, from the evolution of small, tree-dwelling, bush babies, with which humans share a common ancestor. It ends in our more sobering modern times, as megafires, propelled by climate change, incinerate millions of hectares in Australia and the United States, and thousands of square kilometres of Brazilian rainforest are razed to make way for mining and cattle ranching.

For much of human history, our impact on forests has been much more benign, argues biologist Roland Ennos. Even while using wood to make spears, tools, axe handles, huts and boats, our forebears found ways to protect the source of this most versatile material. Superior skills with wood had an outsize role in our evolution, from an ability to sharpen digging sticks with teeth or stones — a skill ascribed to semi-arboreal early hominins — to the control of fire, which enabled our ancestors to cook meat, allowing them to absorb more energy from it than from raw flesh, and so maintain a larger brain.

The forgotten age

A specialist in the mechanics of wood, Ennos has a fierce love for his topic. Archaeologists and anthropologists, he writes, tend to focus all their attention on stone, bronze and iron tools — to the extent that nineteenth-century Danish antiquarian Christian Thomsen classified the “ages of man”, according to these materials. The “Age of Wood” has been effaced, along with its fragile, rapidly decaying remnants.



Voices from the greenwood

The earliest evidence for woodworking comes from a 1.5-million-year-old *Homo erectus* site called Peninj in Tanzania. Here, researchers found residues of acacia wood clinging to stone hand axes. Most likely used to carve spears, these axes “may not seem much of an advance”, Ennos writes, but “it involved a step change in the human imagination”. Wood was handy for hunting: the earliest recorded wooden tool, the yew-hewn Clacton Spear, is 400,000 years old. Discovered near a UK coastal town, it might have been a weapon, a snow probe or a lance. Aboriginal Australians invented boomerangs at least 20,000 years ago, as evidenced by rock art.

It was during the Neolithic period, beginning about 12,000 years ago, that humans first made a major impact on the environment. As the climate warmed and forests advanced northwards, humans hafted small flint blades onto wooden handles to craft ‘tranchet’ axes to cut down trees, clearing land for agriculture and leading to the rise of a new material culture. They also began coppicing — cutting trees such as oak, ash, and chestnut down to ground level every two decades or so to stimulate rapid re-sprouting from dormant buds low in their trunks. In California, the Wintu and Cahuilla peoples developed “balanoculture”, caring for oak forests and living on foods made from acorn flour.

Production paradox

Paradoxically, as Ennos explains, the smelting of metals such as copper made people even more reliant on wood. A key element in these processes is burning charcoal, generated by heating wood to high temperatures. And metals such as copper and bronze make better axes for chopping down trees.

Having depleted their own forests, emerging empires looked elsewhere. Ennos describes the arms race that developed in the late seventeenth century between France and Britain. As the nations competed to build their navies, they needed trees tall enough to craft masts up to 36 metres long. For France, the wilds of the Pyrenees mountains yielded huge fir trees; in Britain, tree cover had been slashed to less than 10%. The country turned to its American colonies, “where the old-growth forests of New England contained huge, straight-trunked white pine trees in seemingly limitless numbers”. Growing up to 70 metres tall, they became the British Navy’s “tree of choice”.



In retrospect: Sylva

Before European colonists arrived, what is now the United States had about 400 million hectares of forests, covering half the total land area. Settlers cleared about 116 million hectares, roughly the size of Colombia. In

Barbados — which was apparently named after the bearded fig tree (*Ficus citrifolia*), by Portuguese explorer Pedro a Campos — 95% of the original forest cover was cleared to make way for sugar cane. Cultivated and cut by enslaved African people, it was a source of monstrous wealth for British plantation owners.

It's hard to maintain a sense of optimism in the face of continuing forest decimation, yet Ennos makes valiant efforts. He points to mass-tree-planting projects in Ethiopia (almost 354 million trees planted in one July day in 2019); and rewilding on the Knepp Estate in West Sussex, UK. Allowing vast areas of abandoned farmland and grassland in Europe, New England and New Zealand to revert to forest, he argues, could absorb billions of tonnes of heat-trapping carbon dioxide. It's an appealing counterpoint to the sense of doom many feel in these apocalyptic times.

Reading about rewilding, I think back to a beloved picture that hung in my grandparents' house: a reproduction of John Constable's 1821 masterpiece, *The Hay Wain*. In the sleepy scene, black poplar trees tower over the waters of England's River Stour in which the eponymous wain stands, spoke-deep. It was once common practice, I learn from Ennos, for farmers to leave their carts in shallow pools to keep the wooden wheels swollen and the joints taut. Sad to say, the poplars Constable conjured with splodgy strokes were cut down to make carts, house frames and farm equipment, as well as rifle butts for the First World War. One can't help longing for the return of that lush, woody world.

Nature 588, 26-27 (2020)

doi: <https://doi.org/10.1038/d41586-020-03378-y>

Jobs from Nature Careers

- - - [All jobs](#)
 - - [Gene Therapy Lab & Research Manager](#)

University of Hawai'i at Manoa (UH Mānoa)

Honolulu, United States

JOB POST

- **RN Case Manager**

Oklahoma Medical Research Foundation (OMRF)

Oklahoma City, United States

JOB POST

- **Research Associate**

The University of British Columbia (UBC)

Vancouver, Canada

JOB POST

- **Postdoctoral Fellows in Quantum Mathematics**

University of Southern Denmark (SDU)

Odense M, Denmark

JOB POST

This article was downloaded by **calibre** from <https://www.nature.com/articles/d41586-020-03378-y>

BOOK REVIEW
30 November 2020

The demons and devils that haunt scientists' imaginations

Strange beasts stalk a history of thought experiments.

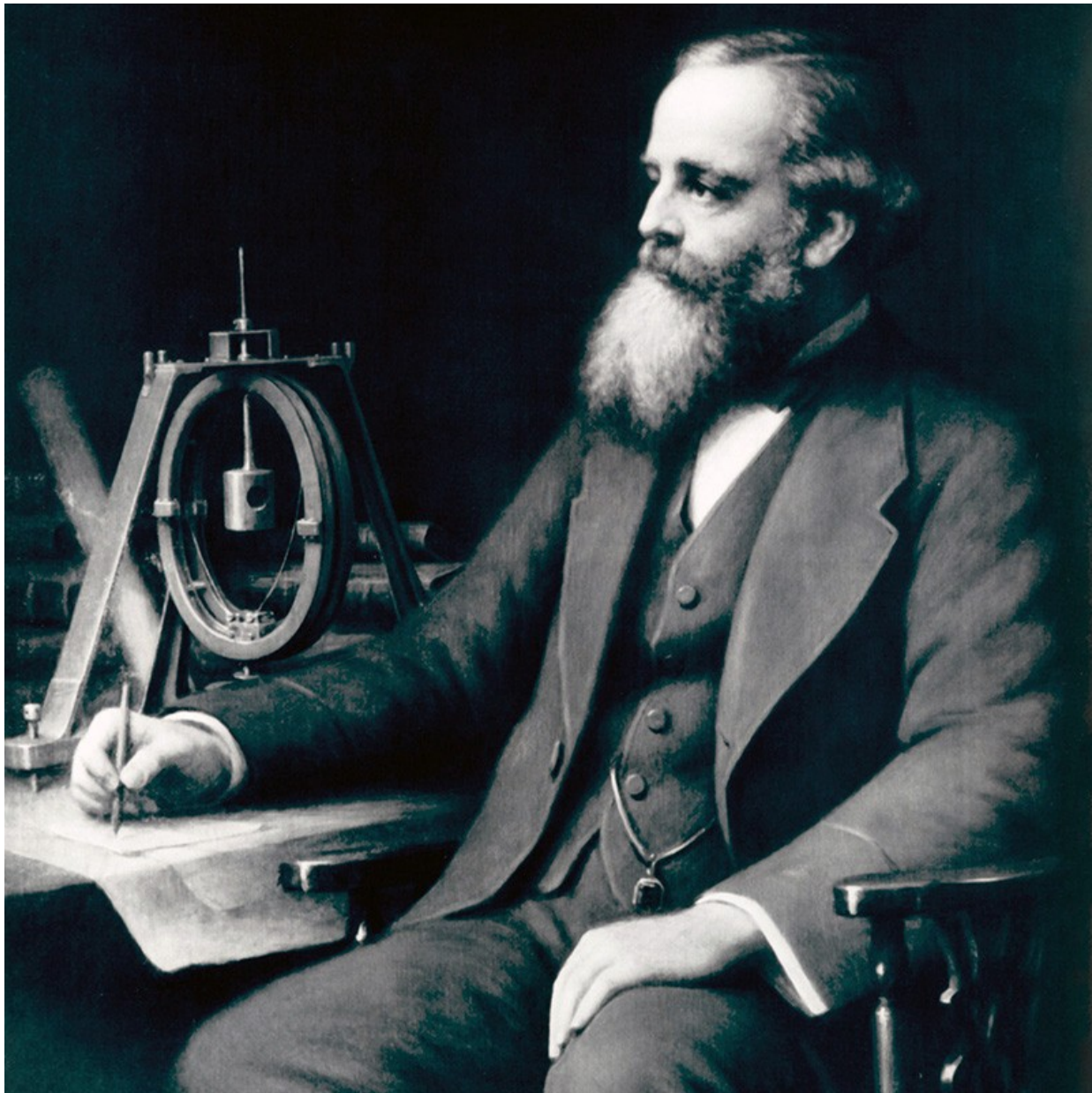
Ramin Skibba

Ramin Skibba is an astrophysicist turned science writer based in San Diego, California.

[Contact](#)

Search for this author in:

- [Pub Med](#)
- [Nature.com](#)
- [Google Scholar](#)



Physicist James Clerk Maxwell envisaged a demon that could reverse entropy. Credit: Science History Images/Alamy

Bedeveled: A Shadow History of Demons in Science *Jimena Canales*
Princeton Univ. Press (2020)

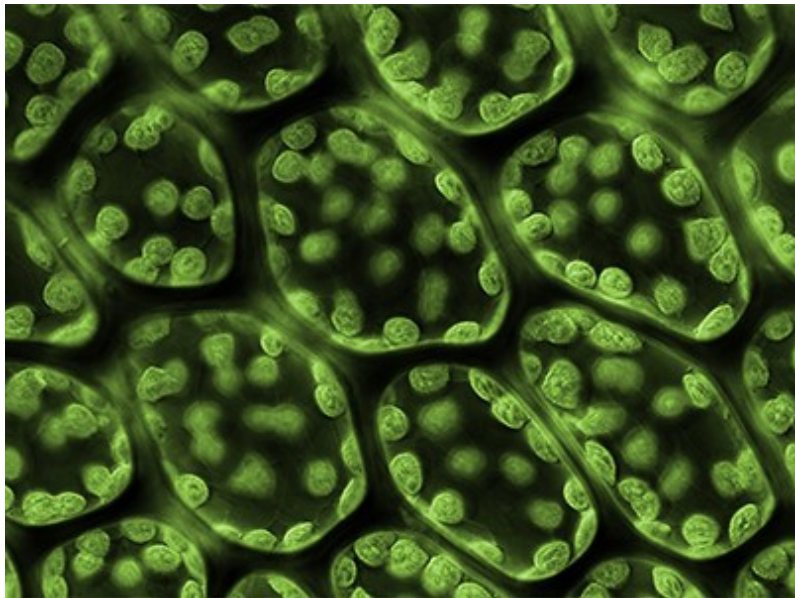
The workings of powerful computers, the processes of evolution, the market forces that drive the global economy. To conceptualize such unseen forces, researchers have long invoked thought experiments involving demons, devils, golems or genies.

These strange beasts aren't creatures of superstition and pseudoscience. They are useful ideas that have had an important role in the advancement of science, argues historian of science Jimena Canales. Her latest book, *Bedeaviled*, sizes up imagined imps over the centuries and follows their impacts.

The seventeenth-century French philosopher René Descartes conceived of the disturbing possibility that some devious spirit could hijack our sense of reality. This 'malicious demon' would affect what we think we see, hear, smell and touch — presaging how virtual reality challenges us today. Descartes's idea caused him to question his senses, and even his existence. He found his way back to reality by asserting that *cogito ergo sum* — he thought, therefore he was. A reasoning human being foiled the deceptive demon.

The spectres of physics

In the early nineteenth century, scientists built on the physics of Isaac Newton to understand the forces of nature, making it possible to calculate with precision the motions of atoms and planets or the forces of a steam engine. Taking those ideas to their logical conclusion, French mathematician Pierre-Simon Laplace proposed that some demonic intellect would be able to calculate the past and future of anything if it knew the precise location and trajectory of all particles and all forces acting on it. British mathematician Ada Lovelace was aware of Laplace's work, and in 1842 she was arguably the first to speculate about whether computing programs could be considered thinking beings. Laplace's demon thus seeded a debate that continues 180 years later.



Maxwell's demon and the hunt for alien life

In 1867, Scottish physicist James Clerk Maxwell summoned an even more powerful demon while trying to understand the statistical behaviour of gas particles. Maxwell's tiny demon operates a door between compartments in a gas-filled vessel, choosing when to allow molecules to pass from one side to the other. The demon can open the door for faster-moving molecules but leave the slower ones on the other side, thus heating up one compartment and cooling the other — decreasing entropy and thwarting the second law of thermodynamics. To some, Maxwell's ideas suggested the possibility of a perpetual-motion machine, or even of reversing time.

In practice, Maxwell's research informed improvements in the efficiency of engines and refrigerators. His demon also demonstrates the surprises that can arise from probabilities, because every once in a while, the rarest events do occur — such as only fast gas molecules spontaneously slipping through a hole.

Canales also surveys thought experiments on the uncertainties in quantum mechanics. Unlike in classical physics, for example, particles in the quantum

world can seem to go through two doors at once. But German mathematician Grete Hermann and, later, US physicist David Bohm suggested that such paradoxes could be resolved if “hidden variables” or unknown mechanisms determine whether a particle travels through one door or another. A few physicists dubbed this “Bohm’s demon”.

Nanoscale demons

Canales explores so many fields and societal implications of scientific debates, from atomic bombs to stock-market fluctuations, that she seems to weave in nearly every demon reference of the past four centuries, however tangential. Some meandering historical asides stray from her solid survey of seminal demonic invocations.



Reimagining of Schrödinger's cat breaks quantum mechanics — and stumps physicists

Today’s demons dwell in genetics, economics and artificial intelligence (AI). Searle’s demon is named after the US philosopher John Searle, who in the 1980s pointed out that a powerful nanobot — or some nanoscale demon — could control which neurons in a person’s brain get stimulated and which don’t, thus making the brain’s base operations similar to a computer

program. If such a demon were possible, then one could imagine AI mechanisms almost indistinguishable from human intelligence. Taking this debate about consciousness versus machine learning further, Searle criticized the idea of “strong AI” — that machines could think as well as or better than humans, operating not merely as tools but as minds of their own. (The University of California, Berkeley, stripped Searle of emeritus status in 2019 after finding that he had violated its sexual-harassment policies.)

Canales highlights some women, including Marie Curie, who envisaged quantum-level demons acting on radiation, and mentions others in passing, such as Rosalind Franklin and Lise Meitner, who did groundbreaking work on DNA and nuclear fission, respectively. But she mostly takes in demons imagined by male scientists in Europe since the Renaissance. Her history would have benefited from an exploration of the disputes between astrology and science in the medieval period, such as those between figures such as Abu Rayhan al-Biruni and Ibn Sina (Avicenna) in Persia. These scholars, too, probed the limits of theory, observation and experiment, and their demarcation from pseudoscience.

In his classic 1995 book *The Demon-Haunted World*, astronomer Carl Sagan wrote that because scientists frequently use their imagination in their work, they don’t know what to expect as they push against the boundaries of knowledge. Canales has given us a glimpse into this haunted realm.

Nature **588**, 27-28 (2020)

doi: <https://doi.org/10.1038/d41586-020-03379-x>

Jobs from Nature Careers

- - - [All jobs](#)
 -
 - [**Gene Therapy Lab & Research Manager**](#)

[University of Hawai'i at Manoa \(UH Mānoa\)](#)

[Honolulu, United States](#)

[JOB POST](#)

▪ [**RN Case Manager**](#)

[Oklahoma Medical Research Foundation \(OMRF\)](#)

[Oklahoma City, United States](#)

[JOB POST](#)

▪ [**Research Associate**](#)

[The University of British Columbia \(UBC\)](#)

[Vancouver, Canada](#)

[JOB POST](#)

▪ [**Postdoctoral Fellows in Quantum Mathematics**](#)

[University of Southern Denmark \(SDU\)](#)

[Odense M, Denmark](#)

[JOB POST](#)

This article was downloaded by **calibre** from <https://www.nature.com/articles/d41586-020-03379-x>

Opinion

- **[Arthur Ashkin \(1922–2020\)](#)** [30 November 2020]
Obituary • Physicist who won Nobel for optical tweezers that trap atoms and proteins.
- **[Five priorities for a sustainable ocean economy](#)** [02 December 2020]
Comment • Unleash the ocean's potential to boost economies sustainably while addressing climate change, food security and biodiversity.

OBITUARY

30 November 2020

Arthur Ashkin (1922–2020)

Physicist who won Nobel for optical tweezers that trap atoms and proteins.

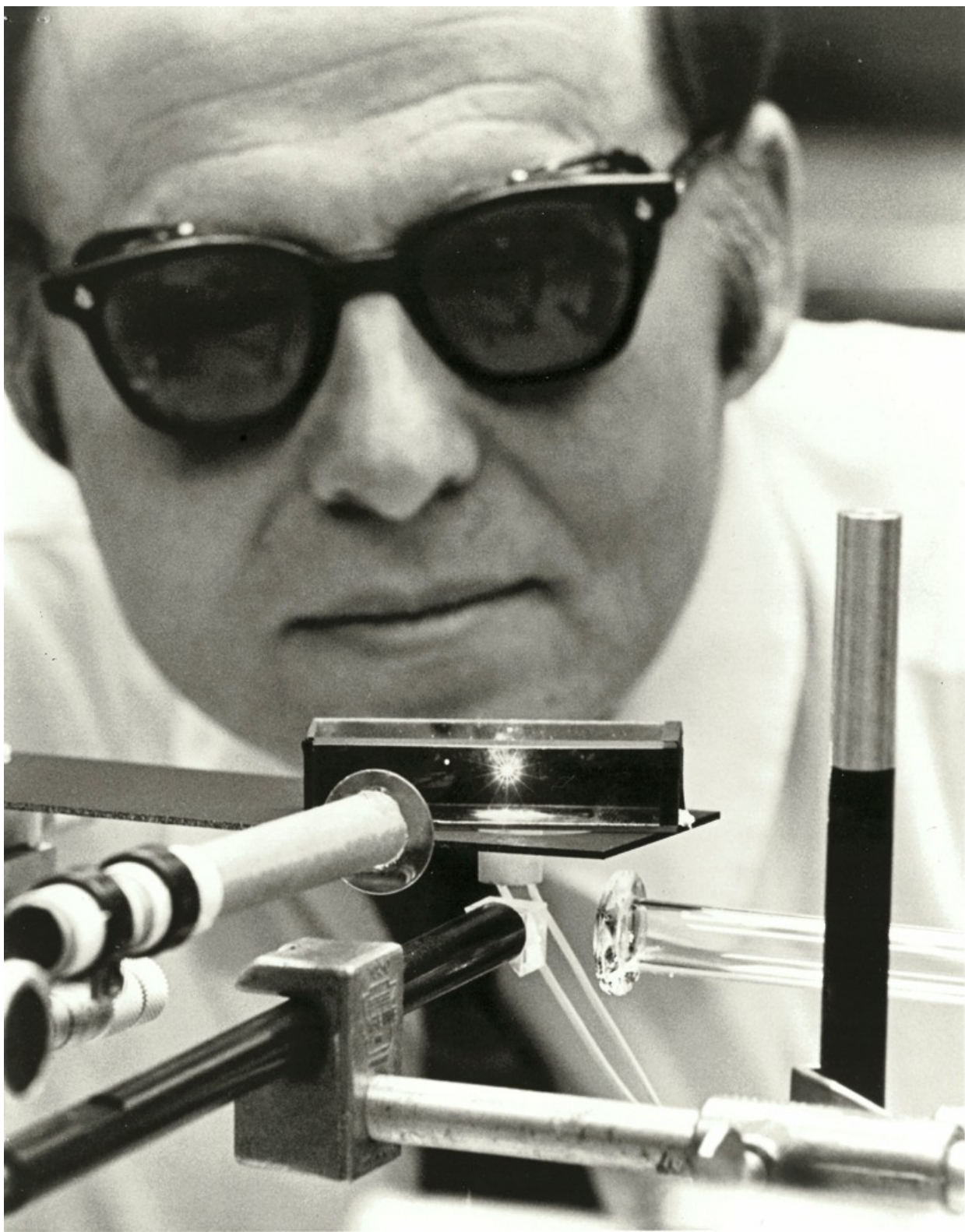
Steven Chu

Steven Chu is the William R. Keenan Jr professor of physics and professor of molecular and cellular physiology at Stanford University, California. He was a fellow department head with Ashkin at Bell Labs from 1983 to 1987. In 1997, he received a share of the Nobel Prize in Physics for laser cooling and atom trapping.

[Contact](#)

Search for this author in:

- [Pub Med](#)
- [Nature.com](#)
- [Google Scholar](#)



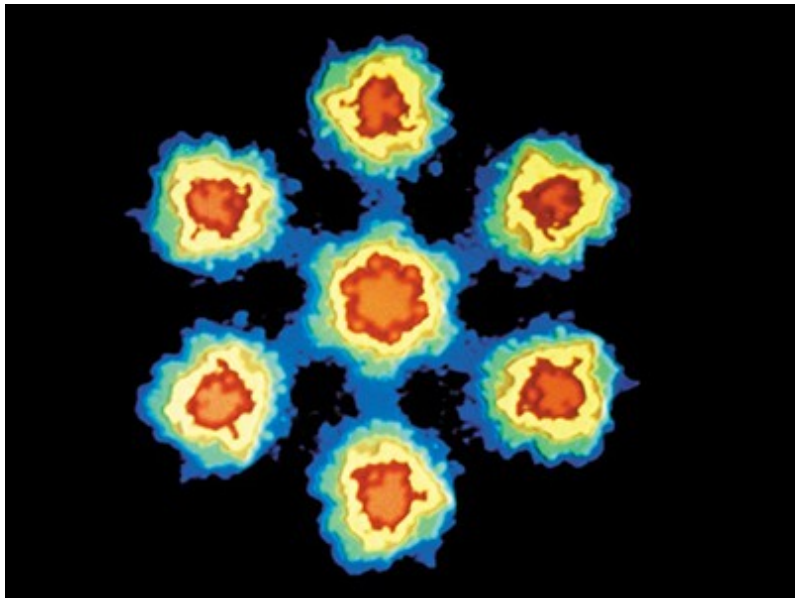
Credit: Nokia Bell Labs

Arthur Ashkin was the father of optical trapping. Using focused laser beams, he manipulated particles ranging in size from atoms to cells and their components. In 2018, aged 96, he shared the Nobel Prize in Physics for “optical tweezers and their application to biological systems”. He also made pioneering discoveries about the forces that light exerts. Ashkin — ‘Art’ to most of us— died on 21 September, aged 98.

Today, optical tweezers are indispensable to biology. They can measure movement with a precision equal to the diameter of an atom, or the force generated by using the chemical energy of a single molecule of the energy-carrying molecule ATP.

Ashkin was born in Brooklyn, New York, to immigrant parents from what is now part of Ukraine. He and his older brother Julius taught themselves physics and calculus, and cobbled together financial contributions from their extended family to go to Columbia University in New York. When the United States entered the Second World War in his second year, Ashkin’s mentor Sidney Millman convinced the army to let him stay at Columbia to work on radar technology.

For his PhD at Cornell University in Ithaca, New York, Ashkin measured the angular dependence of electron–electron and electron–positron scattering accurately enough to verify the full quantum electrodynamic (relativistic) theory. Then, invited by Millman, he went to Bell Laboratories in Holmdel, New Jersey, where he stayed until his retirement in 1992. At first, he worked on microwave physics. After Theodore Maiman demonstrated the laser in 1960, Ashkin worked in this new field and, with Gary Boyd, made important advances in non-linear optical devices.



Fire up the atom forge

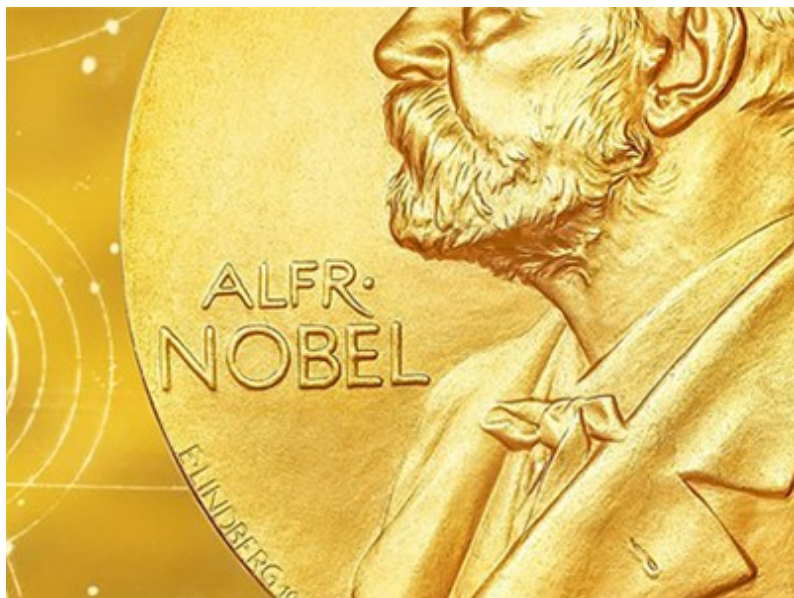
Since childhood, Ashkin had been fascinated by the forces due to light. In the mid-1960s, he heard Eric Rawson at the University of Toronto in Canada describe how tiny dust particles were trapped in a light beam inside a helium–neon laser cavity. Later, Rawson showed the effect is due to the radiometric force. This is the force that causes the black and white vanes in a Crookes radiometer, encased in a partially evacuated glass bulb, to rotate, as the result of the thermal interactions with the residual gas molecules, but in the opposite direction to the scattering force due to photons recoiling from the vanes.

Intrigued, Ashkin focused a laser beam onto latex spheres micrometres in diameter immersed in water. The water cooled the spheres, eliminating the thermal radiometric force, but the particles were still drawn into the high-intensity beam. Ashkin showed that the particle acts as a tiny lens that alters the momentum of the light. This rate of change of momentum creates an equal but opposite force on the particle that attracts it to higher light intensity.

Ashkin also investigated the optical forces on atoms. He demonstrated the atomic version of lensing — the ‘dipole force’ — with John Bjorkholm and

Richard Freeman. In 1978, he proposed that a combination of the scattering and dipole forces could trap atoms. He highlighted an atom trap made of two opposing laser beams, but also proposed “the conceptually simplest trap” of one focused laser beam.

By 1980, the experimental work on atom trapping had stopped, but Art remained steadfast. He piqued my interest after I moved to Bell Labs at Holmdel in 1983. In 1985, my research team, with Art and Bjorkholm, showed that light could cool atoms to less than a thousandth of a degree above absolute zero by using an ‘optical molasses’ created by three counter-propagating sets of laser beams. The basic idea had been proposed a decade earlier by Theodor Hänsch and Arthur Schawlow.



Nobel Prize in Physics 2018

We showed that optical molasses slowed atoms enough for optical forces to trap them. Art, Bjorkholm and I tried, but failed for several months, to demonstrate a large-volume trap proposed by Art. We rejected the single focused beam because the tiny trapping volume would contain, at most, a few atoms in a cloud of millions. But we eventually realized that thousands of atoms near the trap would rapidly diffuse into the focal region and remain cold and trapped.

Holding atoms cooled to just above absolute zero in a single beam was analogous to trapping micrometre-sized polystyrene spheres in water at room temperature. Once he realized this, Art quickly showed that 0.025–10- μm diameter polystyrene particles in water could be trapped in the one beam. A few months later, we trapped atoms. Ironically, all the ingredients for the optical-tweezers trap were established by Art in 1970.

In 1987, Art came into my lab with eyes sparkling and declared, “Steve, you’re not going to believe this, but I discovered LIFE!” He had found that bacteria growing in his experimental set-up could be optically manoeuvred. When the light was turned off the bacteria swam away, but by steering the focal spot of the laser they could be recaptured. By 1990, several researchers were using optical tweezers to trap particles, atoms, single cells, organelles, and individual biomolecules by attaching them to polystyrene spheres.

The elegance and creativity of Ashkin’s ideas were extraordinary. He remained indefatigably enthusiastic about science, working in his home basement into his nineties. He happily taught many biophysicists how to duplicate the optical-tweezers trap. His infectious passion for exploring optical forces changed the course of many scientific careers, mine included.

Nature 588, 29 (2020)

doi: <https://doi.org/10.1038/d41586-020-03380-4>

Jobs from Nature Careers

- - - [All jobs](#)
 -
 - [Gene Therapy Lab & Research Manager](#)
 - [University of Hawai'i at Manoa \(UH Mānoa\)](#)
 - [Honolulu, United States](#)

JOB POST

- **RN Case Manager**

Oklahoma Medical Research Foundation (OMRF)

Oklahoma City, United States

JOB POST

- **Research Associate**

The University of British Columbia (UBC)

Vancouver, Canada

JOB POST

- **Postdoctoral Fellows in Quantum Mathematics**

University of Southern Denmark (SDU)

Odense M, Denmark

JOB POST

This article was downloaded by **calibre** from <https://www.nature.com/articles/d41586-020-03380-4>

COMMENT

02 December 2020

Five priorities for a sustainable ocean economy

Unleash the ocean's potential to boost economies sustainably while addressing climate change, food security and biodiversity.

Jane Lubchenco,

Jane Lubchenco is distinguished university professor in the Department of Integrative Biology, Oregon State University, Corvallis, Oregon, USA.

[Contact](#)

Search for this author in:

- [Pub Med](#)
- [Nature.com](#)
- [Google Scholar](#)

Peter M. Haugan &

Peter M. Haugan is programme director at the Institute of Marine Research, Bergen, Norway.

Search for this author in:

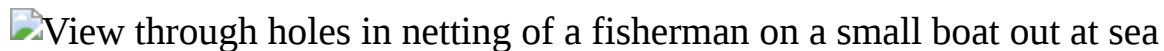
- [Pub Med](#)
- [Nature.com](#)
- [Google Scholar](#)

Mari Elka Pangestu

Mari Elka Pangestu is managing director of Development Policy and Partnerships at the World Bank, Washington DC, USA.

Search for this author in:

- [Pub Med](#)
- [Nature.com](#)
- [Google Scholar](#)



A fisher in Mauritius adds bait to a wire fish trap. Credit: Tommy Trenchard/Panos

Ocean ecosystems are under threat. They also hold solutions. Climate change is increasing sea levels and making the ocean warmer, more acidic and depleted in oxygen. The ocean has absorbed [around 90% of the excess heat](#) trapped by greenhouse-gas emissions and one-third of the carbon dioxide emitted by human activities since the 1980s¹.

Excessive and destructive fishing [threaten ocean habitats and biodiversity](#), from coastal margins to open waters and the deep sea². Unsustainable development along coastlines is destroying coral reefs, seagrass beds, saltmarshes and mangrove forests. These house biodiversity, sequester carbon, provide nurseries for fish and buffer coasts against storm surges (go.nature.com/3m4trjd). Plastics and nutrients washed from the land are also killing wildlife (go.nature.com/3t4ffpa). All of these threats erode the capacity of the ocean to provide nutritious food, jobs, medicines and pharmaceuticals as well as regulate the climate. Women, poor people, Indigenous communities and young people are most affected.

For much too long, the ocean has been out of sight, out of mind and out of luck. Attention has been scant — from governments, funding agencies, financial institutions, food-security organizations and the climate-mitigation community. Nations usually manage their waters sector by sector, or issue by issue. The resulting hodgepodge of policies fails to consider collective impacts.

Countries are agreed on what needs to happen — use marine resources responsibly and equitably and manage them sustainably, avoiding overfishing, pollution and habitat destruction. Our knowledge about the ocean is deep. But political action to deliver a healthy ocean has been lacking. Until now.



The ocean in humanity's future

In September 2018, 14 nations, led by Norway and Palau, commissioned a major science-based review of ocean threats and opportunities as a baseline for resetting policies. Today, this High Level Panel for a Sustainable Ocean Economy (the Ocean Panel) [publishes its conclusions³](#) and [commitments⁴](#).

The reports highlight what stands to be gained by 2050 by taking a holistic approach to the ocean, by asking what it can deliver, and for whom. They find that a healthy ocean could, with 30% of it protected effectively, deliver the following: 20% of the carbon emission reductions needed to achieve the Paris climate agreement's warming limit of 1.5 °C above pre-industrial levels; 40 times more renewable energy than was generated in 2018 (see go.nature.com/3767y3b); 6 times more sustainable seafood⁵; 12 million jobs; and US\$15.5 trillion in net economic benefits (go.nature.com/366fnf2).

These outcomes are not guaranteed. They require new policies, practices and collaborations.

As co-chairs of the expert group of scientists convened by the Ocean Panel, here we highlight five priority areas for policy action.

Hidden crisis

The Ocean Panel is an ad hoc group focused on the seas that is made up of serving world leaders with direct authority to trigger, amplify and accelerate action worldwide. Co-chaired by Norway and Palau, the panel comprises Australia, Canada, Chile, Fiji, Ghana, Indonesia, Jamaica, Japan, Kenya, Mexico, Namibia and Portugal, with support from the United Nations Secretary-General's Special Envoy for the Ocean. Collectively, these leaders manage nearly 40% of the world's coastlines and nearly 30% of its exclusive economic zones, 20% of the world's fisheries and 20% of the world's shipping fleets.

At the panel's invitation, we chaired an expert group (go.nature.com/2vdsutz) of more than 75 scientists chosen for their knowledge, experience and diversity of perspectives. We also worked with a larger group of scientists and policy or legal experts, totalling more than 250 people from 48 countries or regions, to produce syntheses of knowledge and options for action on topics identified by the Ocean Panel (go.nature.com/3nnowty and go.nature.com/2j8c51b). The 19 syntheses ranged from food⁵, energy and mineral production (go.nature.com/3m9jdod), genetic resources⁶ and conservation⁶ (go.nature.com/376dapp) to climate change (go.nature.com/3m52poz), technology⁷, equity (go.nature.com/378hjjy), illegal fishing⁸, crime⁹ and ocean accounting¹⁰ (go.nature.com/39gpims).

A parallel group of more than 135 organizations, called the Advisory Network (go.nature.com/39dsz8v), included representatives from industry, financial institutions and civil society. Participants coalesced as Action Coalitions around areas of shared interest — for example, renewable ocean energy, sustainable seafood or ocean accounting.



A reef in the Maldives displays a wealth of biodiversity.Credit: Giordano Cipriani/Getty

Five priorities

Investing in the following five areas, the reports found, would address global challenges, create jobs and boost economies, while protecting people and the planet.

Manage seafood production sustainably. Currently, fish, crustaceans and molluscs provide only 17% of edible meat⁵. More protein and essential nutrients will be needed to feed the world's rising population, expected to reach almost 10 billion by 2050.

Land-based agriculture is hard to expand, because doing so would exacerbate climate change, biodiversity loss and water scarcity. Sustainable fisheries and mariculture together, however, might deliver 36–74% higher yields by 2050, meeting 12–25% of the extra meat needed⁵.

Aquaculture has greatest potential for expansion, notably un-fed seafoods such as molluscs, including oysters, clams and mussels, which obtain their food by filter feeding. Currently, most mariculture (around 75%) requires feed, typically fishmeal and fish oil. Such production of fed bony fish could be increased somewhat⁵. But there are ecological limits to how much fish and feed could be caught without depleting stocks.



World leaders are waking up to the ocean's role in a healthy planet

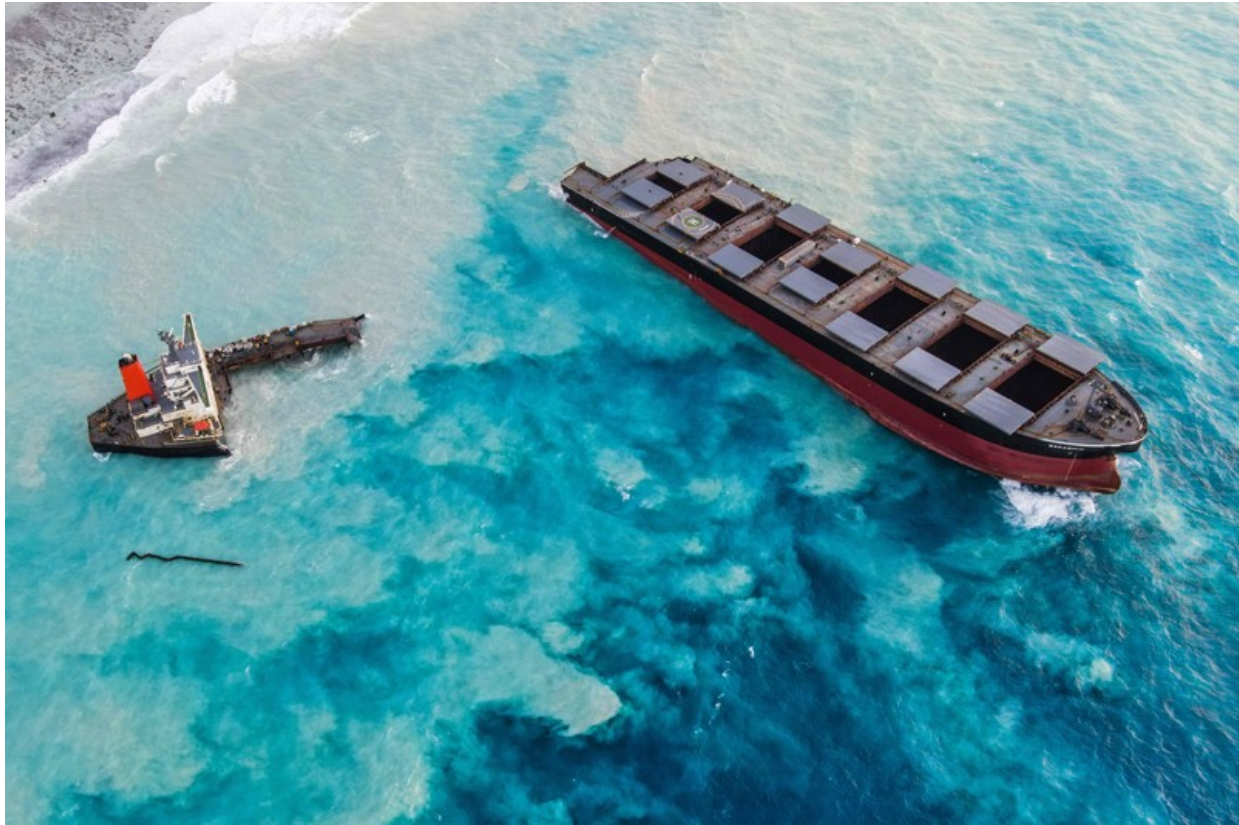
Policy reforms are needed¹¹. And Ocean Panel leaders commit to restoring wild fish stocks, catching them at sustainable levels and expanding sustainable mariculture by 2030. They pledge to eliminate illegal, unreported and unregulated fishing and prohibit harmful fisheries subsidies. They will implement science-based plans to rebuild depleted stocks, develop climate-ready fisheries (go.nature.com/3m52poz) and strengthen international Regional Fisheries Management Organizations. Policies to minimize environmental impacts and accelerate sustainable practices will be introduced for mariculture. Seafood businesses in the Advisory Network are highly supportive.

Mitigate climate change. Around the world, climate change is wreaking havoc on weather patterns, producing more powerful hurricanes, floods and storm surges. Warmer waters are eating away at the bases of Antarctic glaciers and killing coral reefs¹. Greenhouse-gas emissions need to be reduced sharply. But most mitigation options focus on the land — clean wind and solar energy, for example, or increasing the efficiency of transportation, buildings and appliances. More consideration needs to be given to the ocean.

The panel's reports suggest that ocean-based options might deliver as much as one-fifth of the total emissions reductions needed to limit warming to the Paris goal of 1.5°C by 2050 (11.8 gigatonnes of CO₂ equivalents (GtCO₂e) annually). The numbers are tentative and based on maximum contributions from five sectors: renewable energy (5.4 GtCO₂e), transport (1.8 GtCO₂e), coastal and marine ecosystems (1.4 GtCO₂e), food (1.2 GtCO₂e) and carbon storage in the seabed (2 GtCO₂e) (go.nature.com/3767y3b; see also ref. 12). Although carbon storage needs further study, three other opportunities warrant immediate action.

Ocean-based renewables offer varied options for power generation — wind, wave, tidal, current, thermal and solar — suitable for different places. Ocean Panel leaders pledge to invest in research, development and demonstration projects to make these technologies cost-competitive, accessible to all and environmentally sustainable. They will work with industry to address environmental impacts and market impediments to deployment.

Decarbonizing shipping is sorely needed. More than 90% of global goods move across the seas. But ships use heavy fuel oils that release soot and sulfur as well as CO₂ — amounting to 18% of some air pollutants and 3% of greenhouse-gas emissions. Panel leaders agree to set national targets and strategies to decarbonize vessels and develop and adopt technologies for producing and storing new zero-emission fuels. They will incentivize low-carbon ports to support clean shipping, and strengthen regulations within the International Maritime Organization. These include minimizing the transfer of aquatic invasive species by ships, reducing engine noise and banning the use of heavy fuel oil in the Arctic.



A cargo ship ran aground near Mauritius in late July, spilling oil as it broke up near the Blue Bay Marine Park in August. Credit: AFP/Getty

‘Blue carbon’ ecosystems of mangroves, seagrass beds and salt marshes store carbon at up to ten times the rate of terrestrial ecosystems. Much of that ends up in the atmosphere if these ecosystems are damaged or destroyed. Although they cover only 1.5% of the area of land forests, degraded blue-carbon ecosystems release 8% of the total emissions from these and terrestrial deforestation combined. Between 20% and 50% of these ecosystems have already been lost. Ocean Panel leaders pledge to halt that decline and improve the extent and condition of these ecosystems.

Successful restoration of 3,000 hectares of seagrass beds in Virginia lagoons along the US eastern seaboard has resulted in sequestration of about 3,000 tonnes of carbon per year, for example¹³.

Stem biodiversity loss. The diversity of plants, animals and microbes that inhabit ocean ecosystems, from the deep sea to estuaries and from the tropics to the poles, is the main reason the ocean delivers so many benefits. That

biodiversity is being lost. In 2019, an international assessment of biodiversity² identified overharvesting as the biggest single threat.



Norway's Prime Minister: Ocean science can boost jobs and wellbeing

Effective marine protected areas (MPAs) are the most powerful tool to stop this loss. Fishing and other damaging activities are banned within them (go.nature.com/3ma76rf). But they take time to implement. They require planning, design, funding, compliance and enforcement. Only 2.6% of the global ocean is in fully or highly protected classes of MPAs (<https://mpatlas.org>). Many scientific analyses have concluded that at least 30% of the ocean globally should be covered to protect biodiversity (see, for example, ref. 14). The Ocean Panel supports that goal by 2030.

Seize opportunity for economic recovery. Ocean workers and sectors have been largely absent from economic stimulus packages in response to the COVID-19 pandemic. Yet a ‘blue recovery’ effort holds great potential for jump-starting economies.

The Ocean Panel highlights five opportune areas for economic investment (go.nature.com/3otqsdp). First, restore coastal and marine ecosystems to create jobs and enhance tourism, fisheries and carbon sequestration. After the 2008–09 crisis, for instance, every \$1 million invested in coastal restoration in the United States created an average of 17 jobs, or more than twice those created per dollar spent on road construction and fossil-fuel exploration and extraction combined¹⁵.

Second, extend sewage and wastewater infrastructure to create jobs and improve health, tourism and water quality. Over the past 30 years, wastewater and sewage run-off has cost the global economy \$200 billion to \$800 billion per year (go.nature.com/2kjdhtr).



Protect the Antarctic Peninsula — before it's too late

Third, invest in sustainable, community-led, non-fed mariculture such as shellfish, especially in developing and emerging economies. This would enhance local livelihoods and diversify economies while producing food and other products.

Fourth, catalyse incentives to encourage zero-emission marine transport. This would create jobs, accelerate a transition to lower carbon emissions, promote efficiency gains and help to minimize stranded assets in the maritime shipping sector, such as existing ships that burn dirty fuels. Decarbonizing shipping could yield a benefit of between \$1 trillion and \$9 trillion over 30 years¹⁶.

Fifth, investing in ocean-based renewable energy could deliver climate benefits, reduce local and global pollution, and build energy security. Projections suggest that this could be a \$1-trillion industry that has the potential to deliver up to one million full-time jobs by 2050 (go.nature.com/3otqsdp).

Manage the ocean holistically. Patchy management cuts across all areas mentioned. For example, plans for a new port or tidal energy project might not consider the destruction of blue-carbon ecosystems or the impacts of shipping on fish.

Tools for ecosystem-based management and integrated ocean management exist¹⁷. These consider a suite of current or anticipated activities, how they might coexist successfully and what combination can operate without serious harm. It is a major undertaking: all stakeholders must be involved (go.nature.com/378hjjy), data and maps must be assembled, probable impacts identified and interactions considered. Success requires clear goals, funding and an inclusive process.

Achieving the three main goals of the Ocean Panel — to protect effectively, produce sustainably and prosper equitably — will require being smarter about ocean uses, seeking greater efficiencies, using leapfrogging technologies⁷ and seeking ongoing scientific guidance (<https://en.unesco.org/ocean-decade>). It also requires heeding lessons from other transitions¹⁸, acting with precaution (for example, in deep-sea mining¹⁹) and paying closer attention to the welfare of all people (go.nature.com/3nukkzf) and to the health of ecosystems.

Ultimately, the High Level Panel for a Sustainable Ocean Economy commits member nations to manage all of their ocean area sustainably by 2025. Other coastal and ocean states should join this effort, so that by 2030, all waters

under national jurisdiction are sustainably managed. If guided by science and mindful of equity, sustainable management of national waters could be a boon for people, nature and the economy²⁰.

Nature **588**, 30-32 (2020)

doi: <https://doi.org/10.1038/d41586-020-03303-3>

References

1. 1.
Intergovernmental Panel on Climate Change. *Special Report on the Ocean and Cryosphere in a Changing Climate* (IPCC, 2019).
2. 2.
Intergovernmental Science-Policy Platform on Biodiversity and Ecosystem Services. *Summary for Policymakers of the Global Assessment Report on Biodiversity and Ecosystem Services* (IPBES, 2019).
3. 3.
Stuchtey, M. R. et al. *Ocean Solutions that Benefit People, Nature and the Economy. Report* (World Resources Institute, 2020).
4. 4.
The High Level Panel for a Sustainable Ocean Economy. *Transformations for a Sustainable Ocean Economy: A Vision for Protection, Production and Prosperity. Report* (World Resources Institute, 2020).
5. 5.
Costello, C. et al. *Nature* <https://doi.org/10.1038/s41586-020-2616-y> (2020).

6. 6.

Blasiak, R. *et al. Nature Sustain.* **3**, 588–596 (2020).

7. 7.

Brett, A. *et al. Nature* **582**, 181–183 (2020).

8. 8.

Long, T., Widjaja, S., Wirajuda, H. & Juwana, S. *Nature Food* **1**, 389–391 (2020).

9. 9.

Witbooi, E. *et al. Nature* <https://doi.org/10.1038/s41586-020-2913-5> (2020).

10. 10.

Fenichel, E. P. *et al. Nature Sustain.* **3**, 889–895 (2020).

11. 11.

Lubchenco, J., Cerny-Chipman, E. B., Reimer, J. N. & Levin, S. A. *Proc. Natl Acad. Sci. USA* **113**, 14507–14514 (2016).

12. 12.

Gattuso, J. P. *et al. Front. Mar. Sci.* **5**, 337 (2018).

13. 13.

Orth, R. J. *et al. Sci. Adv.* **6**, eabc6434 (2020).

14. 14.

Roberts, C. M. *et al. Proc. Natl Acad. Sci. USA* **114**, 6167–6175 (2017).

15. 15.

Edwards, P., Sutton-Grier, A. & Coyle, G. *Mar. Policy* **38**, 65–71 (2013).

16. 16.

Konar, M. & Ding, H. *A Sustainable Ocean Economy for 2050: Approximating Its Benefits and Costs* (World Resources Institute, 2020).

17. 17.

Winther, J.-G. *et al. Nature Ecol. Evol.* **4**, 1451–1458 (2020).

18. 18.

Brodie Rudolph, T. *et al. Nature Commun.* **11**, 3600 (2020).

19. 19.

Levin, L. A., Amon, D. J. & Lily, H. *Nature Sustain.* **3**, 784–794 (2020).

20. 20.

Lubchenco, J. & Gaines, S. D. *Science* **364**, 911 (2019).

Competing Financial Interests

J.L. received some salary compensation from the Ocean Panel Secretariat at the World Resources Institute to serve as co-chair of the Expert Group for the High Level Panel for a Sustainable Ocean Economy.

Jobs from Nature Careers

- - - [All jobs](#)
 -

- **Gene Therapy Lab & Research Manager**

University of Hawai'i at Manoa (UH Mānoa)

Honolulu, United States

JOB POST

- **RN Case Manager**

Oklahoma Medical Research Foundation (OMRF)

Oklahoma City, United States

JOB POST

- **Research Associate**

The University of British Columbia (UBC)

Vancouver, Canada

JOB POST

- **Postdoctoral Fellows in Quantum Mathematics**

University of Southern Denmark (SDU)

Odense M, Denmark

JOB POST

Work

- **Uncertain prospects for postdoctoral researchers** [01 December 2020]
Career Feature • Nature's first-ever survey of this key segment of the scientific workforce uncovers anxiety and doubt about their professional pathway.
- **Why scientists are turning to Rust** [01 December 2020]
Technology Feature • Despite having a steep learning curve, the programming language offers speed and safety.
- **Watching the sentinels** [30 November 2020]
Where I Work • Immunologist Federica Benvenuti investigates the guard dogs of the immune system while training young scientists from developing nations.

CAREER FEATURE

01 December 2020

Uncertain prospects for postdoctoral researchers

Nature's first-ever survey of this key segment of the scientific workforce uncovers anxiety and doubt about their professional pathway.

Chris Woolston

Chris Woolston is a freelance writer in Billings, Montana.

Search for this author in:

- [Pub Med](#)
- [Nature.com](#)
- [Google Scholar](#)

[Find a new job](#)



Credit: Miguel Monk

As she considers her future, Meihui Wu is committed to staying in science. “I don’t want my skills to go to waste,” says Wu, a postdoctoral researcher in cancer immunology at the Singapore Eye Research Institute. She’s equally sure that she doesn’t want to take another postdoctoral position. She’s already on her second short-term contract as a postdoc, and wants to avoid yet another period of ‘training’ with no end in sight. “I’ve seen friends who get stuck in multiple postdoc positions,” she says.

Wu now faces a question familiar to postdocs worldwide: what’s next? *Nature*’s first survey of postdoctoral researchers, which drew responses from more than 7,600 respondents in 93 countries, included a series of questions about job prospects, a topic that has long been a source of anxiety and uncertainty for researchers at this stage in their careers.

Highly trained and highly educated, postdoctoral researchers often struggle to turn their temporary positions into full-time, stable careers — a struggle that is now made even more daunting by the COVID-19 pandemic.

Although many despair about the dwindling number of academic positions, others find optimism in a world that increasingly depends on scientific expertise. (Previous articles on the survey offered an [overview of postdocs around the world](#), an examination of the many [impacts of COVID-19](#) and a look at [postdocs' quality of life](#); see ‘*Nature*’s postdoc survey’.)

Despite the many challenges, postdocs from all scientific fields have some reason to be hopeful, says Rachel Coulthard-Graf, career-development adviser at the European Molecular Biology Laboratory (EMBL) in Heidelberg, Germany. “They have very strong job prospects,” she says. “Academia has clearly become competitive, and they may worry about exploring other sectors that they don’t know so well, but it’s entirely doable”, she says.

Nature’s postdoc survey

In September, *Nature* reported survey results about [how COVID-19 has affected postdocs](#) and their views of the future. The second article in the series offers an [overview of their circumstances worldwide](#). The third explores [postdocs' quality of life](#), including mental health and experiences of discrimination and harassment. The final article examines respondents’ sense of their career prospects, a crucial issue for postdocs as they look ahead. The survey, created together with Shift Learning, a market-research company in London, was advertised on nature.com, in Springer Nature digital products and through e-mail campaigns. It was offered in English, Mandarin Chinese, Spanish, French and Portuguese. The full survey data sets are available at go.nature.com/3tmckuq.

Cloudy prospects

As a group, postdocs are worried about their futures. Little more than one-quarter (28%) of respondents had a positive view of their career prospects; twice as many (56%) had a negative view, including 17% whose outlook

was “extremely negative”. Pessimism about job prospects was slightly higher for female respondents (58%) than for male respondents (53%). Coulthard-Graf notes that the majority of postdocs who seek out career services at EMBL are female, suggesting that many women are turning their worries into action.



Rachel Coulthard-Graf, career development adviser at the European Molecular Biology Laboratory in Heidelberg, Germany, says postdocs often aren't aware of the options available to them outside academia. Credit: Kinga Lubowiecka/EMBL

Pessimism is especially common in astronomy and planetary science, where 27% had extremely negative career outlooks, as well as in ecology and evolution (23%). Biomedical researchers, who accounted for a slight majority of all respondents, also disclosed apprehension: more than half (55%) had a negative view of their job prospects, and just 28% felt optimistic. Eleven per cent of researchers in computer science and mathematics said they felt “extremely positive” about job prospects, the highest proportion of any field.

Most respondents feel that they picked a bad time to pursue science. Three-quarters said that their job prospects were worse than those of previous generations of scientists, with 37% saying they were “much worse” (see ‘Academic ambitions’). Just 7% said their job outlook was somewhat better than earlier scientists’, and just 1% felt their prospects were much better. Notably, 23% of respondents in Africa said their prospects were better than those of previous generations, a sign of growing optimism on that continent (see [*Nature* 572, 143–145; 2019](#)).

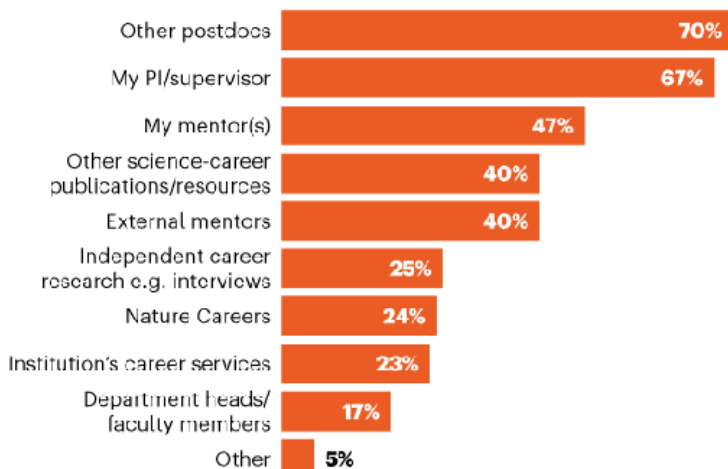
ACADEMIC AMBITIONS

Despite hiring freezes and layoffs at universities around the world, most respondents aspire to a career in academia. And although they turn to peers and principal investigators (PIs) for career advice, they still have a negative view of their prospects. A large majority feel that previous generations of postdocs had it better.

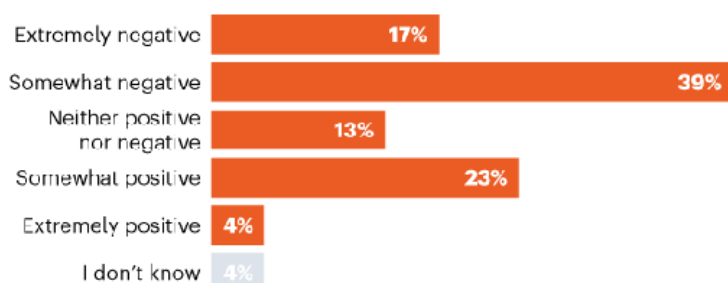
Do you hope to pursue a career in academia?



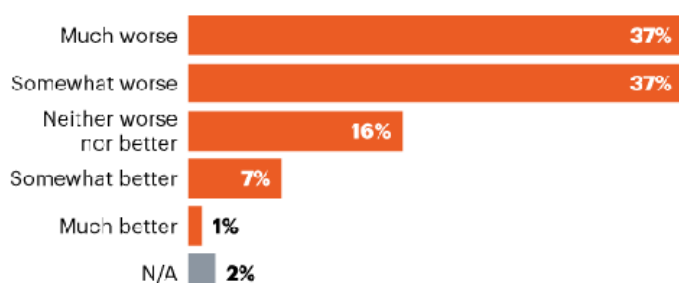
Which sources do you use to seek career advice?



How do you feel about your job prospects?



Do you see your job prospects as better or worse than those of previous postdoc generations?

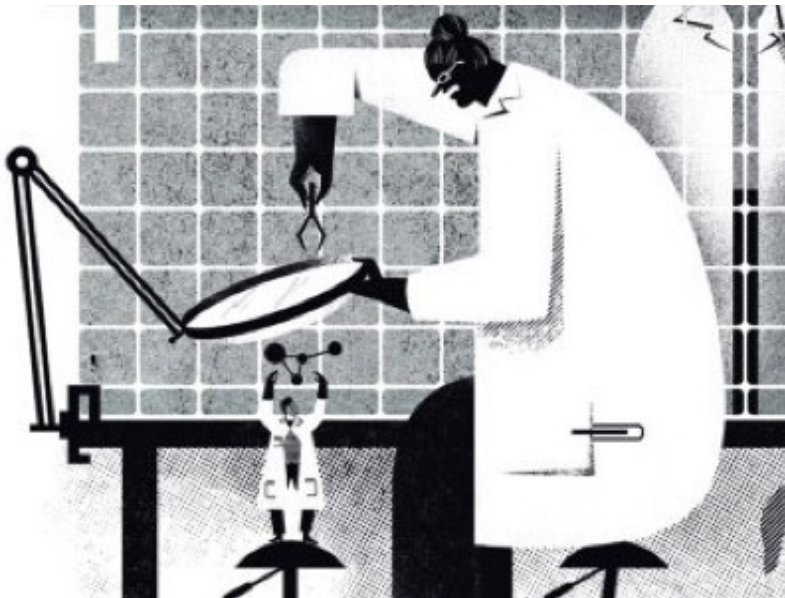


Many respondents have reasons for pessimism. Asked to list the biggest challenges to personal career progression, nearly two-thirds (64%) named a lack of funding in their field, almost half (45%) blamed a lack of jobs and 40% pointed to the impacts of the pandemic. One-quarter said that they are held back at least partly by their desire to stay in academia.

Postdocs who can't find permanent work often end up taking another postdoc position. As previously reported (see [*Nature* 587, 505-508; 2020](#)), more than 30% of respondents had already had at least two such placements, and a few reported completing up to six. Clearly, a stint that had originally been conceived as a 'training' period has instead become a holding pattern for many.

Academic ambitions

Although the chances of landing an academic research position are becoming ever slimmer, particularly in light of the pandemic, nearly two-thirds (63%) of respondents hope to pursue a career in academia. One-quarter (26%) aren't sure of their plans. Men (68%) were more likely than women (59%) to aspire to academic careers. Natalie Sirisaengtaksin, a postdoctoral cancer researcher at the University of Texas Health Sciences Center in Houston, says that her thinking vacillates between pursuing a job in academia and looking elsewhere. "It's a really hard decision," she says. "It's difficult to give up on that dream. I love mentoring students and thinking about big ideas." However, she's not sure she has the laboratory skills to be competitive, and she worries that running her own lab would take over her life. "If I got it, there's a big question about whether I'd be happy," she says.



Career resources for postdoctoral researchers

Chrystal Starbird, a structural biologist at Yale School of Medicine in New Haven, Connecticut, has a much clearer vision for her future. “I’m applying for faculty positions,” she says. Starbird, who worked at the pharmaceutical company Pfizer before she started her PhD programme, says that universities encouraged her to apply for faculty positions immediately after she got her degree. She decided to complete a postdoc to build skills and establish credentials, but never lost sight of her ultimate goal of running her own university lab. “If I think an idea is worth pursuing, I want to be driving that idea forward,” she says.

Data on postdoctoral success rates in academia are sketchy, partly because postdocs are a poorly defined and undercounted group. According to a 2018 report, roughly 15% of postdocs in the United States could expect to go on to tenure-track faculty positions ([S. C. McConnell *et al.* *eLife* 7, e40189; 2018](#)).

Rory Duncan, based in Edinburgh and director of talent and skills at UK Research and Innovation, the leading funder of UK research, says the

numbers are stacked against researchers who want permanent academic jobs in his part of the world. “We support roughly 40,000 postdocs in our universities, and there aren’t that many faculty positions available,” he says. “We are trying to help develop really talented people with broad, high-level skills that are sought after in the research and innovation ecosystem. Some will work in academia, but most will go on to work in some other sector.”



Chrystal Starbird, a postdoc in structural biology at Yale School of Medicine in New Haven, Connecticut, has always wanted to run her own laboratory, and is now applying for faculty positions. Credit: Courtney Smith

Coulthard-Graf estimates that roughly 30% of postdocs at EMBL secure faculty positions, a rate that almost certainly exceeds global averages. She says that about twice that number would list academia as their preferred destination, which means that a significant proportion of postdocs will have to turn to plan B.

University hiring freezes and layoffs during the pandemic have further dimmed the prospects of those hoping to land in academia (see ‘It is difficult to see why anybody would embark on a career in academia’), although the [full impact is still unclear](#). An analysis of academic job postings in October 2020 suggested that faculty openings in the United States had dropped by 70% compared with the same period in 2019 (see go.nature.com/3pvjnk).

‘It is difficult to see why anybody would embark on a career in academia’

Free-text comments in *Nature*’s survey of postdoctoral researchers worldwide detailed the fear and apprehension that respondents feel concerning their career prospects. Comments have been lightly edited for length and clarity, and, where necessary, translated into English.

- The biggest problem that researchers face in my country is the enormous job uncertainty. My contract ends at the end of this year, and I don’t know if I’m going to go unemployed or get another one that will allow me at least to work in science for another year. I’m always thinking about the possibility of having to abandon science. *Physicist, Spain.*
- Every year of postdoc work clearly makes me less and less attractive to employers outside of academia. *Chemist, Ireland.*
- Postdocs in India don’t receive support from their mentors in terms of their careers. They never get recommendations on how to move ahead. *Biomedical researcher, India.*
- I wish it was less scary and isolating to do something I really love and that I am very good at. The lack of job prospects in academia is daunting. *Biomedical researcher, Canada.*

- Looking at career prospects objectively, it is difficult to see why anybody would really embark upon a career in academia. The entire system needs to change if we are to really see any improvement at the postdoc level.

Biomedical researcher, United Kingdom.

- Universities are quick to close the doors to hiring full-time staff at absolutely any opportunity. But they remain happy to exploit many workers on terrible short-term contracts. After dedicating a significant amount of your life to education and earning a PhD, you are rewarded with the prospects of short, fixed-term contracts with no guarantee of anything stable appearing. *Psychologist, United States.*

- I feel postdocs are trapped in their positions and are not being given the tools they need to progress in their careers. Progress is not about hard work; it's about being lucky enough to be there for an important discovery or knowing the right person to get the next position. *Chemist, United States.*

- Career prospects have shrunk instead of expanded. I earn less in my third postdoc than in my first one even though I have much more experience.

Biomedical researcher, Canada.

- China's massive investment in basic sciences allows postdoctoral fellows to have a positive view of their future career prospects if they are willing to return to work in China. There are abundant job opportunities in my home country, including postdoctorate or faculty positions. This makes me feel at ease, and I'm optimistic about the future. *Astronomer, South Korea.*

- The number of faculty positions is much smaller than the number of postdoctoral students, leading to fierce competition. Female postdocs who want to get a teaching position dare not give birth or take vacations.

Biomedical researcher, United States.

- My lab has enough funding for the next two years, which is perfect for me to finish up and then search for a new job — maybe in academia, maybe in industry. I am open to both. I am optimistic that I will find a job in the future. *Biomedical researcher, United States.*

Looking for guidance

With such uncertain prospects, many postdocs could benefit from career advice, but help isn't always nearby. When asked to identify their sources of guidance, more respondents gave credit to other postdocs (70%) than to their supervisors (67%). Postdocs are so valuable to the scientific enterprise that some supervisors might be reluctant to help them progress in their careers, Duncan says. "It's in the interest of supervisors to keep the best people they have as long as they can," he says. "There is some deep soul-searching required to ensure that the person who is in the transitional role receives the type of development that they ought to be receiving."

Career development and guidance are top priorities at EMBL, Coulthard-Graf says. She notes that the institute now has two career advisers who provide training and advice to its 500 or so PhD students and postdocs. When she encounters postdocs who are intent on an academic career, she suggests specific steps that will increase their chances of success. "I try to never actively discourage it," she says. And when postdocs say that they might be open to other possibilities, she has much to offer. "We discuss alternatives," she says. "They haven't always been exposed to other options."



How failure benefits science

Coulthard-Graf has found that many postdocs are driven above all by curiosity, and so can be drawn to other career paths — such as industry, journal editing and government regulatory affairs — when these are pointed out to them. “People who leave the academic track find ways to satisfy that curiosity,” she says. “I wish they would view these goals equally.”

Amar Parvate turned a two-year postdoc in virology at the La Jolla Institute for Immunology in California into a springboard for his new job. Since August, he’s been a microscopist and biochemist at the Pacific Northwest National Laboratory (PNNL), a US government research lab in Richland, Washington. Unlike many of his peers, Parvate never really longed for academia. “The odds would have been stacked against me,” he says.

Alternative paths

Parvate had already applied for virology jobs at a few biotech and pharmaceutical companies without success when the position at the PNNL opened up. “It was more chance than thought,” he says. A national research laboratory wasn’t part of his long-term plans, but it turned out to be a great fit. He is one of just a few researchers who have access to a top-of-the-range cryo-electron microscope. “It’s one of the most amazing pieces of equipment you can get your hands on,” he says. Eventually, he plans to become a ‘super user’ in charge of all applications of the microscope, from sample preparation to data analysis. For him, it’s a high-tech path to job security. “I plan to be here for quite a while,” he says.



Brian Groendyke, who took the survey while he was a medicinal-chemistry postdoc at Harvard University in Cambridge, Massachusetts, is now about to join a biotech company.Credit: Brian Groendyke

Brian Groendyke was a postdoc in medicinal chemistry at Harvard University in Cambridge, Massachusetts, when he took the survey. A couple of months later, he received an offer from a biotech company in nearby Boston, and he is now about to start a career in industry. “The job opportunities are good here, and I won’t have to relocate.”

Like many other scientists, he went into his postdoc with a vision of running his own university lab some day, but gradually warmed to the idea of focusing on science without worrying about teaching or other academic obligations. He says that his postdoc left him well prepared for his career path. “I’ve gained a lot of skills that I would not have had coming straight out of graduate school.”

Not everyone feels that they have the right tools to move forwards. Asked to list their weak areas, 48% pointed to computational skills, 47% wished they

were better at specific experimental techniques and 37% lamented their lack of proficiency with statistics (see ‘What’s next?’).

WHAT'S NEXT? Postdocs surveyed by Nature voiced widespread concern about their career progression.

Still, postdocs would often be surprised to find where their skills could take them if they keep an open mind, says Coulthard-Graf. “A lot of postdocs haven’t really looked beyond research,” she says. “What’s on their radar is academia or pharmaceuticals and biotech.” Many possibilities exist, she says, and postdocs sometimes have to look past long-standing stigmas against non-research careers to consider potentially rewarding, high-paying jobs. “There are a lot of sales positions related to pharma, biotech or medical devices,” she says. “If you even mention that, a lot of postdocs will automatically say, ‘Oh, no, that’s not for me’ — without even considering it.”

After much thought, Wu plans to stay where she is. She says that she never really saw herself running her own lab, and her few applications for industry jobs led nowhere. Now she hopes to stay in her current lab as a staff scientist. “My supervisor needs someone to help support her lab,” she says. “I could be here for a long time.”

Wu wants to encourage other postdocs to keep their heads up even if employment prospects look bleak in the short term. “Don’t be too negative if things aren’t going well,” she says. “The world needs us.”

Nature **588**, 181-184 (2020)

doi: <https://doi.org/10.1038/d41586-020-03381-3>

Jobs from Nature Careers

- - - [All jobs](#)
 -

- **Gene Therapy Lab & Research Manager**

University of Hawai'i at Manoa (UH Mānoa)

Honolulu, United States

JOB POST

- **RN Case Manager**

Oklahoma Medical Research Foundation (OMRF)

Oklahoma City, United States

JOB POST

- **Research Associate**

The University of British Columbia (UBC)

Vancouver, Canada

JOB POST

- **Postdoctoral Fellows in Quantum Mathematics**

University of Southern Denmark (SDU)

Odense M, Denmark

JOB POST

TECHNOLOGY FEATURE

01 December 2020

- Correction [02 December 2020](#)

Why scientists are turning to Rust

Despite having a steep learning curve, the programming language offers speed and safety.

Jeffrey M. Perkel

Search for this author in:

- [Pub Med](#)
- [Nature.com](#)
- [Google Scholar](#)

Cartoon of a person in a safety helmet travelling fast whilst sitting in front of a laptop made up of symbols of code. Illustration by The Project Twins

In 2015, bioinformatician Johannes Köster was what he called “kind of a full-time Python guy”. He had already written one popular tool — the workflow manager Snakemake — in the programming language. Now he was contemplating a project that required a level of computational performance that Python simply couldn’t deliver. So he began casting about for something new.

Köster, now at the University of Duisburg-Essen in Germany, was looking for a language that offered the “expressiveness” of Python but the speed of languages such as C and C++. In other words, “a high-performance language that is still, let’s say, ergonomic to use”, he explains. What he found was Rust.

First created in 2006 by Graydon Hoare as a side project while working at browser-developer Mozilla, headquartered in Mountain View, California, Rust blends the performance of languages such as C++ with friendlier syntax, a focus on code safety and a well-engineered set of tools that simplify development. Portions of Mozilla’s Firefox browser are written in Rust, and developers at Microsoft are reportedly using it to recode parts of the Windows operating system. The annual Stack Overflow Developer Survey, which this year polled nearly 65,000 programmers, has ranked Rust as the “most loved” programming language for 5 years running. The code-sharing site GitHub says Rust was the second-fastest-growing language on the platform in 2019, up 235% from the previous year.

Scientists, too, are turning to Rust. Köster, for instance, used it to create an application, called Varlociraptor, that compares millions of sequence reads against billions of genetic bases to identify genomic variants. “This is huge data,” he says. “So that needs to be as fast as possible.” But that power comes at a cost: the Rust learning curve is steep.

“It does take some up-front time,” says Carol Nichols, a member of the Rust core team and founder of the consultancy firm Integer 32 in Pittsburgh, Pennsylvania. “But it has enabled me to do things that I wouldn’t otherwise be able to do. I see that time as well spent.”

Caution: no guide rails

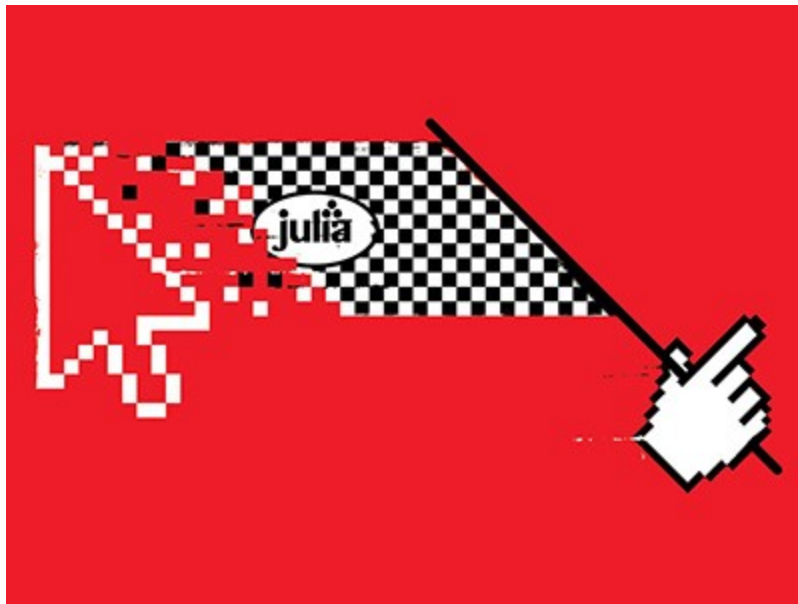
Workflows for analysing scientific data tend to use languages such as Python, R and Matlab. These interpret lines of code one by one and then execute them, a style of programming that is good for exploring data, but not at speed.

C and C++ are fast, but they have “no guide rails”, says Ashley Hauck, a Rust programmer (or ‘Rustacean’, as community members are known) in Stockholm. For instance, there are no controls that stop a C or C++ programmer from inappropriately accessing memory that has already been released back to the operating system, or to prevent the program from releasing the same piece twice. In the best-case scenario, this would cause the program to crash. But it can also return meaningless data or expose

security vulnerabilities. According to researchers at Microsoft, 70% of the bugs that the company fixes each year relate to memory safety.

Memory rules

Rust's model uses rules to assign each piece of memory to a single owner and enforce who can access it. Code that violates those rules never gets the chance to crash — it won't compile. "They have a memory-management system that is based on this concept of lifetimes that lets the compiler track at compile-time when memory is allocated, when it's freed, who owns it, who can access it," explains Rob Patro, a computational biologist at the University of Maryland, College Park. "There's an entire large class of correctness errors that go away simply by virtue of the way the language is designed."



Julia: come for the syntax, stay for the speed

The same guarantees help to ensure that parallelized code — software written to run on multiple processors — can run safely, for instance by

eliminating the possibility that multiple computational threads will access the same data at the same time.

The result is a language that is easier to maintain and debug, but harder to learn. “No other mainstream languages really have these concepts, and they’re really core to understanding a lot of how you have to write code in Rust,” Nichols says. Stephan Hügel, who studies the visualization of geographical data at Trinity College Dublin, estimates that he spent two or three months porting a Python algorithm for converting geospatial coordinates from one reference system into another into Rust, achieving fourfold faster execution. Richard Apodaca, founder of the cheminformatic-software company Metamolecular in La Jolla, California, says it took him about six months to become proficient in the language.

Focus on usability

To compensate, Rust’s developers have optimized the user experience, says Manish Goregaokar, who leads the Rust developer-tooling team and is based in Berkeley, California. For instance, the compiler produces particularly informative error messages, even highlighting offending code and suggesting how to fix it. “If your language is going to introduce a novel concept, it had better be pleasant to work with,” Goregaokar explains.

The Rust community also provides extensive documentation and online help, including a popular online reference called the [Book](#) and a [‘Cookbook’](#) of recipes for solving common problems. Users praise the Rust toolchain — the applications that programmers use to turn code into applications (see ‘Let’s get oxidizing’). “The tooling and infrastructure around Rust is really phenomenal,” Patro says. Unlike the many compilers and ancillary utilities that programmers use to build C code, Rustaceans can use a single tool, called Cargo, to compile Rust code, run tests, auto-generate documentation, upload a package to a repository and more. It also downloads and installs third-party packages automatically. A third-party Cargo plug-in called Clippy flags common errors and ‘non-idiomatic’ Rust code, a feature that Patro calls “absolutely phenomenal”.

Let’s get oxidizing

Here's how to create a GenBank file reader so you can explore some of the features of Rust.

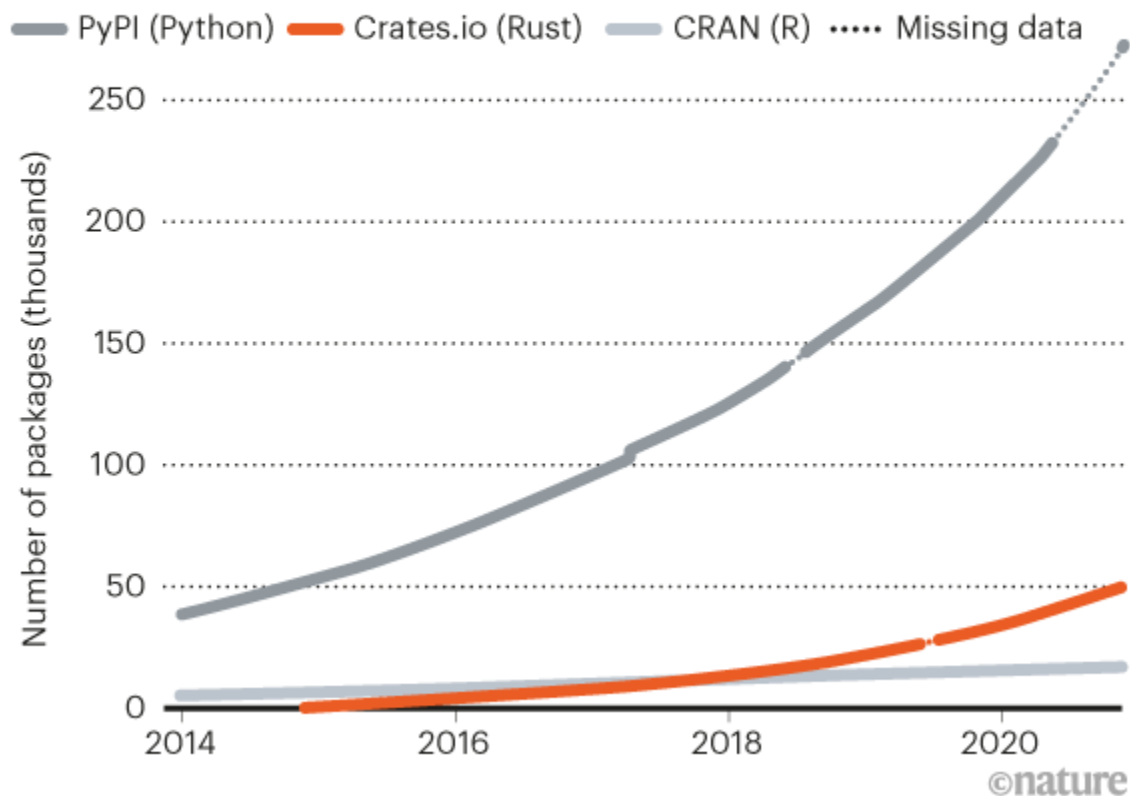
- Install Rust at www.rust-lang.org/learn/get-started
- Clone the GitHub repository at https://github.com/jperkel/gb_read
- Execute 'cargo run' from the command line to download external dependencies and build the application. By default, the application parses the GenBank file 'nc_005816.gb' in the GitHub repository, but you can specify an alternative input file with 'cargo run <filename>'
- Execute the included tests using 'cargo test'.
- Create and view documentation with 'cargo doc --open'.

There are Rust plug-ins for popular development environments, such as Microsoft's [Visual Studio Code](#) and JetBrains' IntelliJ, as well as a [Rust playground](#) that provides a live, online Rust environment for code experimentation. And David Lattimore, a software developer in Sydney, Australia, created a 'kernel' for using Rust in Jupyter computational notebooks, as well as a Python-style interactive environment called a REPL (read-evaluate-print loop).

Aiding development is Rust's ecosystem of third-party packages, or 'crates', currently numbering nearly 50,000 (see 'Rust rising'). These encapsulate algorithms in disciplines such as bioinformatics (Köster's Rust-Bio), geosciences (the Geo-Rust project) and mathematics (nalgebra). Still, says Nichols, "that could definitely tip the balance away from Rust, if the libraries you need are just not in Rust". Programmers can sometimes bridge that gap using Rust's 'foreign function interface', however.

RUST RISING

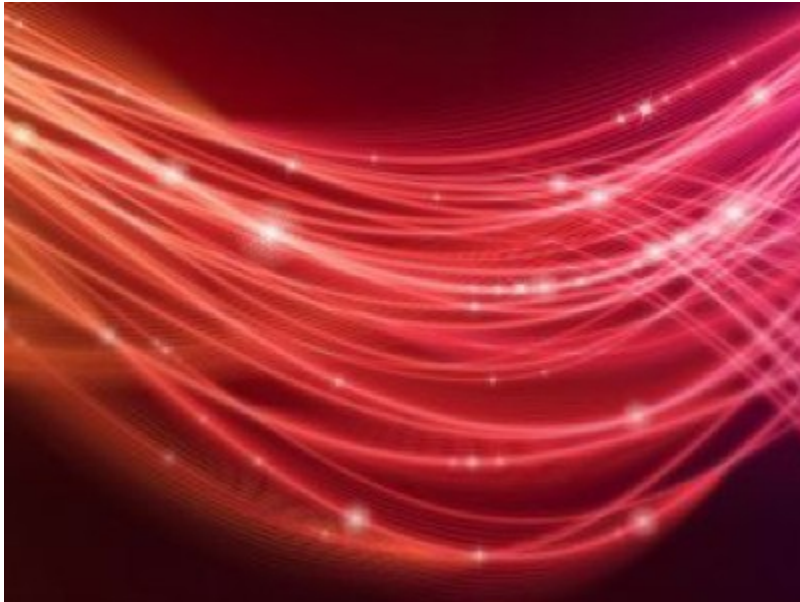
The Rust packages repository crates.io has grown sharply since 2016, mirroring the rapid uptake of the language.



Source: <http://www.modulecounts.com>

Oxidized code

Coding logistics aside, what's undeniable is that Rust is fast. In May, bioinformatician Heng Li at the Dana-Farber Cancer Institute in Boston, Massachusetts, tested multiple languages on a computational-biology task that involved parsing 5.7 million sequence records. Rust edged out C to take the top spot. "When we want to write a high-performance program using multiple threads, and also if you need it to be very fast and also compact in memory, then Rust is the ideal choice," Li says.



NatureTech hub

Luiz Irber, a bioinformatician at the University of California, Davis, used Rust to recode (or ‘oxidize’, in Rust parlance) a tool called Sourmash — which performs genomic searches and taxonomic profiling — to ease software maintenance, gain access to modern language features and make the code work in a web browser, he says.

Led by graduate student Hirak Sarkar, Patro’s team used Rust to build a gene-expression analysis tool called Terminus after team member Avi Srivastava returned from an internship at 10x Genomics, a biotechnology company in Pleasanton, California, that uses Rust to develop open-source tools. “The beauty of Rust is, it makes the task of debugging very easy, because memory management is much, much better,” explains Srivastava, who is now at the New York Genome Center.

But for many Rustaceans, the human element is equally compelling. Hauck, a member of the LGBT+ community, says that Rust users have gone out of their way to make her feel welcome. The community, she says, has “always made an effort to be extremely inclusive — like, very much aware of how diversity impacts things; very aware of how to write a code of conduct and enforce that code of conduct”.

“That’s probably a majority of the reason I’m still writing Rust,” Hauck says. “It’s because the community is so fantastic.”

Nature **588**, 185-186 (2020)

doi: <https://doi.org/10.1038/d41586-020-03382-2>

Updates & Corrections

- **Correction 02 December 2020:** An earlier version of this story gave the wrong source for the graphic.

Jobs from Nature Careers

- - **All jobs**
 -
- **Gene Therapy Lab & Research Manager**

University of Hawai'i at Manoa (UH Mānoa)
Honolulu, United States
JOB POST
- **RN Case Manager**

Oklahoma Medical Research Foundation (OMRF)
Oklahoma City, United States
JOB POST
- **Research Associate**

The University of British Columbia (UBC)

Vancouver, Canada

JOB POST

▪ **Postdoctoral Fellows in Quantum Mathematics**

University of Southern Denmark (SDU)

Odense M, Denmark

JOB POST

This article was downloaded by **calibre** from <https://www.nature.com/articles/d41586-020-03382-2>

| [Section menu](#) | [Main menu](#) |

WHERE I WORK
30 November 2020

Watching the sentinels

Immunologist Federica Benvenuti investigates the guard dogs of the immune system while training young scientists from developing nations.

Amber Dance

Amber Dance is a freelance writer in Los Angeles, California.

Search for this author in:

- [Pub Med](#)
- [Nature.com](#)
- [Google Scholar](#)



Federica Benvenuti working in her laboratory in Trieste, Italy.

Federica Benvenuti is a group leader in cellular immunology at the International Centre for Genetic Engineering and Biotechnology, Trieste, Italy. Credit: Rocco Ceselin for *Nature*

I've been working for 16 years to understand a particular type of immune cell, often called the sentinel of the immune system, that is found in humans and other mammals. Named dendritic cells, they detect dangers, such as pathogenic microorganisms, by collecting molecules from their environment. They show these molecules to other immune-system cells, instructing them to fight the enemy.

In my laboratory at the International Centre for Genetic Engineering and Biotechnology (ICGEB) we study dendritic cells' functioning — how they detect a pathogen, for example — and we also study immunodeficiencies in

which the dendritic cells stop working. We're trying to understand why they don't work properly, and how we might eventually correct them.

A few years ago, I decided also to investigate how dendritic cells interact with cancer. I've worked on immunity and cancer before, so it's been exciting to return to it. We're investigating how dendritic cells recognize tumours, and then tell the immune-system's 'soldiers' to start destroying the cancer cells.

For example, we compare dendritic cells that have been in contact with tumour cells with those that have not, looking for different molecules they might display. We use a micropipette, as I'm holding here, to precisely transfer tiny amounts of the antibodies we use to detect those molecules.

The ICGEB is special because it combines top-level research with a strong commitment to training students, postdocs and visitors from developing countries. I currently have six people, including graduate students and a postdoc, in my lab.

I love to see how members of my team, who might come from a background such as genomics or pharmacology, fall in love with immunology. Although the immune system is complex, it's clever and well organized. People get passionate about that, as I am.

Nature 588, 188 (2020)

doi: <https://doi.org/10.1038/d41586-020-03383-1>

Jobs from Nature Careers

- - - [All jobs](#)
 - - [Gene Therapy Lab & Research Manager](#)

[University of Hawai'i at Manoa \(UH Mānoa\)](#)

[Honolulu, United States](#)

[JOB POST](#)

▪ [**RN Case Manager**](#)

[Oklahoma Medical Research Foundation \(OMRF\)](#)

[Oklahoma City, United States](#)

[JOB POST](#)

▪ [**Research Associate**](#)

[The University of British Columbia \(UBC\)](#)

[Vancouver, Canada](#)

[JOB POST](#)

▪ [**Postdoctoral Fellows in Quantum Mathematics**](#)

[University of Southern Denmark \(SDU\)](#)

[Odense M, Denmark](#)

[JOB POST](#)

This article was downloaded by **calibre** from <https://www.nature.com/articles/d41586-020-03383-1>

Research

- **[Autonomous balloons take flight with artificial intelligence](#)**

[02 December 2020]

News & Views • An artificially intelligent controller can station a stratospheric balloon for weeks at a time without full knowledge of surrounding winds, opening up the prospect of unsupervised environmental monitoring.

- **[Sight restored by turning back the epigenetic clock](#)**

[02 December 2020]

News & Views • Neurons progressively deteriorate with age and lose resilience to injury. It emerges that treatment with three transcription factors can re-endow neurons in the mature eye with youthful characteristics and the capacity to regenerate.

- **[Building a chemical blueprint for human blood](#)**

[11 November 2020]

News & Views • What determines the chemical make-up of human blood? Measurement of the contributions of factors ranging from genetics to lifestyle has now identified diet and gut microbes as key predictors of blood's molecular composition.

- **[Standard model of particle physics tested by the fine-structure constant](#)**

[02 December 2020]

News & Views • A highly precise measurement of a physical constant known as the fine-structure constant provides a stringent test of the standard model of particle physics, and sets strong limits on the existence of speculative particles.

- **[Inference in artificial intelligence with deep optics and photonics](#)**

[02 December 2020]

Perspective • Recent work on optical computing for artificial intelligence applications is reviewed and the potential and challenges of all-optical and hybrid optical networks are discussed.

- **[Organized crime in the fisheries sector threatens a sustainable ocean economy](#)**

[11 November 2020]

Perspective • The authors review how the presence of organized crime in the fisheries sector hinders progress towards the development of a sustainable ocean economy and highlight practical opportunities to address this problem at both the local and the global level.

- **[Enhanced triple- \$\alpha\$ reaction reduces proton-rich](#)**

[nucleosynthesis in supernovae](#)

[02 December 2020]

Article • The triple- α reaction rate in proton-rich core-collapse supernovae is found to be enhanced at high nucleon densities, suppressing the formation of proton-rich nuclei from gallium to cadmium.

- **Determination of the fine-structure constant with an accuracy of 81 parts per trillion** [02 December 2020]
Article • The fine-structure constant is determined with an accuracy of 81 parts per trillion using matter-wave interferometry to measure the rubidium atom recoil velocity.
- **Electrical switching of magnetic order in an orbital Chern insulator** [23 November 2020]
Article • Non-volatile electrical switching of magnetic order in an orbital Chern insulator is experimentally demonstrated using a moiré heterostructure and analysis shows that the effect is driven by topological edge states.
- **Unconventional ferroelectricity in moiré heterostructures** [23 November 2020]
Article • Electronic ferroelectricity is observed in a graphene-based moiré heterostructure, which is explained using a spontaneous interlayer charge-transfer model driven by layer-specific on-site Coulomb repulsion.
- **Autonomous navigation of stratospheric balloons using reinforcement learning** [02 December 2020]
Article • Data augmentation and a self-correcting design are used to develop a reinforcement-learning algorithm for the autonomous navigation of Loon superpressure balloons in challenging stratospheric weather conditions.
- **Computational planning of the synthesis of complex natural products** [13 October 2020]
Article • A synthetic route-planning algorithm, augmented with causal relationships that allow it to strategize over multiple steps, can design complex natural-product syntheses that are indistinguishable from those designed by human experts.
- **Thermochemical lithosphere differentiation and the origin of cratonic mantle** [02 December 2020]
Article • A model is proposed for the origin of cratonic lithospheric mantle in which rifting and melting in the hot, early Earth mantle leave behind large volumes of stiffer, depleted mantle.
- **The future of food from the sea** [19 August 2020]
Article • Modelled supply curves show that, with policy reform and technological innovation, the production of food from the sea may increase sustainably, perhaps supplying 25% of the increase in demand for meat products by 2050.

- [An early Cambrian euarthropod with radiodont-like raptorial appendages](#) [04 November 2020]
Article • Kylinxia zhangi is a transitional fossil that is an evolutionary ‘missing link’ between radiodonts (also known as anomalocaridids) and true arthropods, providing insights into the origin and early evolution of Arthropoda.
- [Contrasting signatures of genomic divergence during sympatric speciation](#) [28 October 2020]
Article • Population genomic analyses of Midas cichlid fishes in young Nicaraguan crater lakes suggest that sympatric speciation is promoted by polygenic architectures.
- [The cellular basis of distinct thirst modalities](#) [14 October 2020]
Article • The authors uncover the diverse transcriptomic cell types of thirst-driving neurons in the lamina terminalis and show that unique combinations of neuron types respond to and mediate distinct thirst states.
- [A measure of smell enables the creation of olfactory metamers](#) [11 November 2020]
Article • By collecting nearly 50,000 perceptual estimates of smell, a reliable physicochemical measure that links odorant structure to odorant perception at a resolution that enables the creation of olfactory metamers was derived.
- [Reprogramming to recover youthful epigenetic information and restore vision](#) [02 December 2020]
Article • Expression of three Yamanaka transcription factors in mouse retinal ganglion cells restores youthful DNA methylation patterns, promotes axon regeneration after injury, and reverses vision loss in a mouse model of glaucoma and in aged mice, suggesting that mammalian tissues retain a record of youthful epigenetic information that can be accessed to improve tissue function.
- [Tension heterogeneity directs form and fate to pattern the myocardial wall](#) [18 November 2020]
Article • Differences in the mechanical properties of individual cardiomyocytes drive their segregation into compact versus trabecular layer, thereby transforming the myocardium in a developing heart from a simple epithelium into an intricately patterned tissue with distinct cell fates.
- [A reference map of potential determinants for the human serum metabolome](#) [11 November 2020]
Article • The levels of 1,251 metabolites are measured in 475 phenotyped individuals, and machine-learning algorithms reveal that diet and the microbiome are the determinants with the strongest predictive power for the levels of these metabolites.

- **Widespread endogenization of giant viruses shapes genomes of green algae** [18 November 2020]
Article • The authors show that large endogenous viral elements derived from giant viruses are prominent components of green algal genomes.
- **Association of COVID-19 inflammation with activation of the C5a–C5aR1 axis** [29 July 2020]
Article • Blockade of the C5a–C5aR1 axis using anti-C5aR1 monoclonal antibodies prevented inflammation associated with COVID-19.
- **Inhibition of LT β R signalling activates WNT-induced regeneration in lung** [04 November 2020]
Article • Blockade of lymphotoxin β -receptor (LT β R) signalling restores WNT signalling and epithelial repair in a model of chronic obstructive pulmonary disease.
- **Splicing factor YBX1 mediates persistence of JAK2-mutated neoplasms** [25 November 2020]
Article • Inhibition of YBX1, a downstream target of the Janus kinase JAK2, sensitizes myeloproliferative neoplasm cells to JAK and could provide a means to eradicate such cells in human haematopoietic cancers.
- **Small-molecule-induced polymerization triggers degradation of BCL6** [18 November 2020]
Article • Binding of the small molecule BI-3802 to the oncogenic transcription factor B cell lymphoma 6 (BCL6) induces polymerization of BCL6, leading to its ubiquitination by SIAH1 and proteasomal degradation.
- **SLC25A51 is a mammalian mitochondrial NAD $^{+}$ transporter** [09 September 2020]
Article • SLC25A51 is identified as a transporter of intact NAD $^{+}$ into mammalian mitochondria and is required to maintain the mitochondrial NAD $^{+}$ pool and respiratory function.

NEWS AND VIEWS

02 December 2020

Autonomous balloons take flight with artificial intelligence

An artificially intelligent controller can station a stratospheric balloon for weeks at a time without full knowledge of surrounding winds, opening up the prospect of unsupervised environmental monitoring.

Scott M. Osprey

Scott M. Osprey is at the National Centre for Atmospheric Science, UK, and is based in the Department of Atmospheric, Oceanic and Planetary Physics, University of Oxford, Oxford OX1 3PU, UK.

[Contact](#)

Search for this author in:

- [Pub Med](#)
- [Nature.com](#)
- [Google Scholar](#)



Figure 1 | An unmanned balloon in the stratosphere. Project Loon is using balloons such as this to set up an aerial wireless network for telecommunications. Credit: Loon

The goal of an autonomous machine is to achieve an objective by making decisions while negotiating a dynamic environment. Given complete knowledge of a system's current state, artificial intelligence and machine learning can excel at this, and even outperform humans at certain tasks — for example, when playing arcade and turn-based board games¹. But beyond the idealized world of games, real-world deployment of automated machines is hampered by environments that can be noisy and chaotic, and which are not adequately observed. The difficulty of devising long-term strategies from incomplete data can also hinder the operation of independent AI agents in real-world challenges. [Writing in Nature](#), Bellemare *et al.*² describe a way forward by demonstrating that stratospheric balloons, guided by AI, can

pursue a long-term strategy for positioning themselves about a location on the Equator, even when precise knowledge of buffeting winds is not known.

Fixed-volume balloons, known as super-pressure balloons, are often used to carry out unmanned experiments in the upper atmosphere (Fig. 1). Station-keeping is the act of maintaining the position of such a balloon within a certain horizontal distance of a ground location (the station). This involves changing the balloon's height to move it between regions in which winds blow in different directions — when the balloon is driven away from its station by winds at one height, it moves to a different height where the winds can blow it back again (Fig. 2).

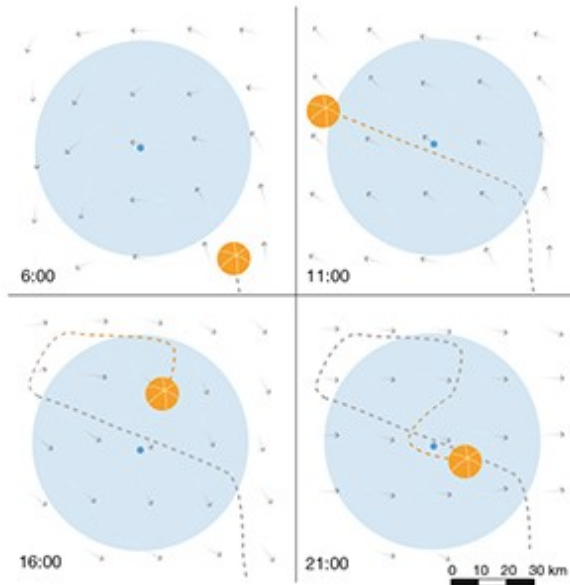
Figure 2

Figure 2 | Station-keeping for stratospheric balloons. Unmanned balloons, known as super-pressure balloons, are used to carry out experiments in the upper atmosphere. Station-keeping is the act of maintaining the position of a balloon within a certain range of a specific position on the ground. The balloon's height is altered during the day to move it between altitudes at which winds blow in different directions — when the balloon is driven away from its station by winds at one height, it moves to a different height at which the winds can blow it back again.

Bellemare *et al.*² report that a type of machine learning, known as reinforcement learning, can be used to train an autonomous control system for station-keeping that outperforms previously used control systems.

Self-navigating balloons do one of two things to stay within range of their stations. When a balloon is outside its range, the onboard controller seeks winds pointing to within a small angle of the station. However, the balloon preferentially seeks out lighter winds when inside the target range and close to the station. Balloons that are more active in exploring winds above and below them are more likely to find suitable winds to help achieve station-keeping, but this comes at the expense of using battery power that might be needed for other tasks, such as relaying telecommunications or environmental monitoring. These competing factors need to be weighed up carefully.

A type of machine learning known as reinforcement learning can be used to train an artificial agent to make an optimal sequence of decisions. In the case of a super-pressure balloon, the decisions are whether to rise, fall or do nothing, and are based on a historical record of global winds³, local observed and forecast winds, and projected future flight paths. Crucially, the available wind data are sparse and do not fully constrain the flight controller's decision-making.



[Read the paper: Autonomous navigation of stratospheric balloons using reinforcement learnings](#)

In their system, Bellemare *et al.* filled in the gaps by adding randomly generated 'noise' to the wind data, to better map out the range of winds that could plausibly occur, and to improve assessments of the variety of paths the balloon might take in the future. The resulting wind information and its statistical uncertainty, together with a small number of balloon-relevant parameters, were used to train a machine-learning system known as an artificial neural network, and ultimately improved decision-making time

during flights compared with previously used control systems, using similar battery power.

Earlier applications of reinforcement learning, which included playing classic board and arcade games, were trained using complete information sets¹ — the same information that is available to human controllers⁴. These allowed like-for-like performance comparisons between humans and AI players. However, the challenge confronting Bellemare and colleagues was that incomplete knowledge of environmental winds not only makes it difficult to judge the optimal actions to take, but also makes forecasts of future states following these actions uncertain. These problems are further compounded by other practical uncertainties that don't affect game controllers, such as those associated with internal balloon motions, power management and battery health. Bellemare and co-workers' success therefore represents a big advance in the use of reinforcement learning for real-world applications.

Station-keeping performance is ultimately limited by the range of wind speeds and directions in the region surrounding the balloons (at heights of 15–20 kilometres, for the current study). The winds must also switch direction so that balloons can adjust their trajectory to stay within range of the station. These special conditions only persist for months at a time within the Equatorial stratosphere, where Bellemare and colleagues' study was carried out — and where a slow procession of opposing winds peak in strength near 30 km, before descending and dissipating near 15 km, switching direction every 14 months or so⁵.



Learning to play Go from scratch

Such wind diversity also occurs elsewhere, but is less reliable and generally occurs beyond the range of heights at which a single super-pressure balloon can operate. During the flight campaign described in the current study, larger wind disturbances originating from high latitudes occurred in the tropical stratosphere, and probably assisted station-keeping. Bellemare and colleagues' system might therefore struggle to achieve the same success at other locations. However, smaller, more rapid wind variations can also occur, including atmospheric waves of various types⁶, which a skilful controller could navigate to its advantage.

The advent of effective autonomous super-pressure balloons would open up a range of commercial and scientific applications for probing Earth's atmosphere and that of other planets. Such balloons are already used to study small and large-scale waves in the tropical stratosphere⁷, and to detect low-frequency sounds produced by the ocean⁸, lightning⁹ and earthquakes¹⁰. They have also been proposed for use in future explorations of Venus's atmosphere¹¹, to search for signs of active volcanism and chemical signatures of life¹². Moreover, the ability to fix a balloon's geographical position is crucial if balloons are to be used to build an aerial wireless

network for telecommunications — an early objective of Project Loon, the owners of the balloons used in Bellemare and colleagues' study.

Station-keeping a balloon for months at a time would allow long-term environmental monitoring, for example, of air quality over cities, of carbon fluxes from heat-stressed forests and of regions of thawing permafrost. Other applications include monitoring animal- migration routes and illicit trafficking of goods and people across borders. These applications will become increasingly relevant as the effects of climate change become more pronounced, as restrictions on movement are imposed by global events such as COVID-19, and as long-term climate-change mitigation involving aviation prompts the search for alternative platforms for making aerial observations.

Nature **588**, 33-34 (2020)

doi: <https://doi.org/10.1038/d41586-020-03313-1>

References

1. 1.
Silver, D. *et al.* Nature **550**, 354–359 (2017).
2. 2.
Bellemare, M. G. *et al.* Nature **588**, 77–82 (2020).
3. 3.
Hersbach, H. *et al.* Q. J. R. Meteorol. Soc. **146**, 1999–2049 (2020).
4. 4.
Mnih, V. *et al.* Nature **518**, 529–533 (2015).
5. 5.
Baldwin, M. P. *et al.* Rev. Geophys. **39**, 179–229 (2001).

6. 6.

Schoeberl, M. R. *et al.* *J. Geophys. Res. Atmos.* **122**, 8517–8524 (2017).

7. 7.

Haase, J. *et al.* *Eos* <https://doi.org/10.1029/2018EO091907> (2018).

8. 8.

Bowman, D. C. & Albert, S. A. *Geophys. J. Int.* **213**, 1524–1535 (2018).

9. 9.

Lamb, O. D., Lees, J. M. & Bowman, D. C. *Geophys. Res. Lett.* **45**, 7176–7183 (2018).

10. 10.

Krishnamoorthy, S. *et al.* *Geophys. Res. Lett.* **45**, 3393–3403 (2018).

11. 11.

Hall, J. L. in *AIAA Aviation 2019 Forum* (American Institute of Aeronautics and Astronautics, 2019), Available at <https://doi.org/10.2514/6.2019-3194>.

12. 12.

Greaves, J. S. *et al.* *Nature Astron.* <https://doi.org/10.1038/s41550-020-1174-4> (2020).

Jobs from Nature Careers

- - - [All jobs](#)
 -

- **Gene Therapy Lab & Research Manager**

University of Hawai'i at Manoa (UH Mānoa)

Honolulu, United States

JOB POST

- **RN Case Manager**

Oklahoma Medical Research Foundation (OMRF)

Oklahoma City, United States

JOB POST

- **Research Associate**

The University of British Columbia (UBC)

Vancouver, Canada

JOB POST

- **Postdoctoral Fellows in Quantum Mathematics**

University of Southern Denmark (SDU)

Odense M, Denmark

JOB POST

NEWS AND VIEWS

02 December 2020

Sight restored by turning back the epigenetic clock

Neurons progressively deteriorate with age and lose resilience to injury. It emerges that treatment with three transcription factors can re-endow neurons in the mature eye with youthful characteristics and the capacity to regenerate.

Andrew D. Huberman

Andrew D. Huberman is in the Department of Neurobiology and the Department of Ophthalmology, Stanford University School of Medicine, Stanford, California 94305, USA.

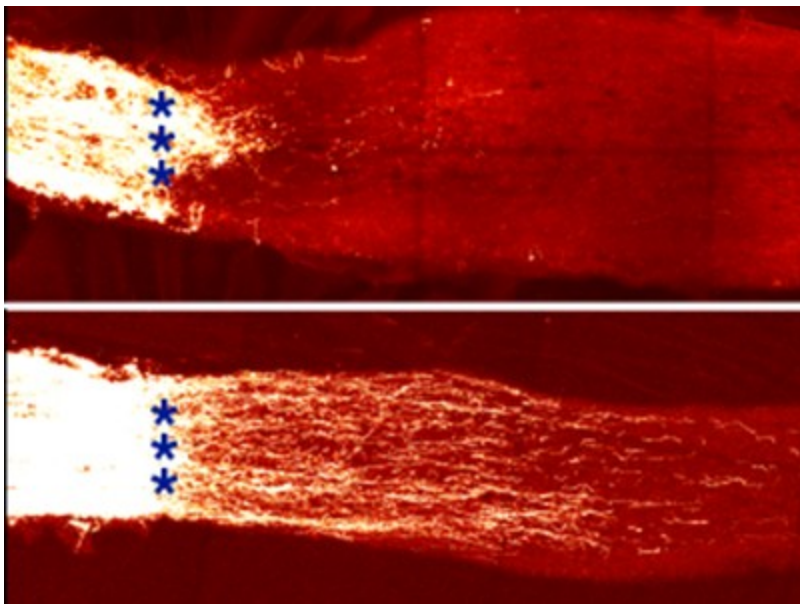
[Contact](#)

Search for this author in:

- [Pub Med](#)
- [Nature.com](#)
- [Google Scholar](#)

Ageing has negative consequences for all the cells and organs in our bodies. Our brains are no exception. Neurons in the developing brain form circuits that can adapt to change and regenerate in response to injury. These capacities have long been known¹ to diminish over time, but the molecular shifts that underlie this deterioration have remained mysterious. Lu *et al.*² show in [a paper in Nature](#) that neurons of the eye can be programmed to revert to a youthful state in which they reacquire their ability to resist injury and to regenerate. The authors' findings shed light on mechanisms of

ageing and point to a potent therapeutic target for age-related neuronal diseases.



[Read the paper: Reprogramming to recover youthful epigenetic information and restore vision](#)

Retinal ganglion cells (RGCs) reside in the eyes and thus outside the skull, but they are bona fide brain neurons. They initially develop as part of the forebrain. Subsequently, RGCs extend projections called axons out of the eye to make connections with neurons in the brain itself. These axons — which join together to form the optic nerve — survive and regenerate if they are damaged early in development, but not after they reach maturity^{3,4}. Evidence indicates^{3,5} that this shift is intrinsic to RGCs, rather than reflecting changes in the surrounding cells.

Myriad studies have searched for factors that can prevent or promote RGC survival and regeneration. A handful of such factors have been identified that can endow mature RGCs with some degree of survival and regenerative

capacity — but not enough to fully maintain or restore vision after damage to the optic nerve⁴.

Lu *et al.* asked whether it is possible to revert RGCs to a younger ‘age’, and whether doing so would allow the cells to regenerate. They infected RGCs in mice with adeno-associated viruses. These harmless viruses had been genetically engineered to induce expression of three of the ‘Yamanaka factors’ — a group of four transcription factors (Oct4, Sox2, Klf4 and c-Myc) that can trigger mature cell types to adopt an immature state⁶. Such an approach normally comes with hazards *in vivo*: Yamanaka factors can cause cells to adopt unwanted new identities and characteristics, leading to tumours or death⁷. Fortunately, Lu and co-workers found that they could circumvent these hazards by expressing just Oct4, Sox2 and Klf4 (together called OSK).

The authors tested the infected RGCs’ ability to regenerate if the cells’ axons were crushed. They found that the OSK-expressing viruses triggered RGC regeneration and long-distance axon extension following damage to the optic nerve (Fig. 1), with no apparent alterations to RGC identity, formation of retinal tumours or any other ill effects.

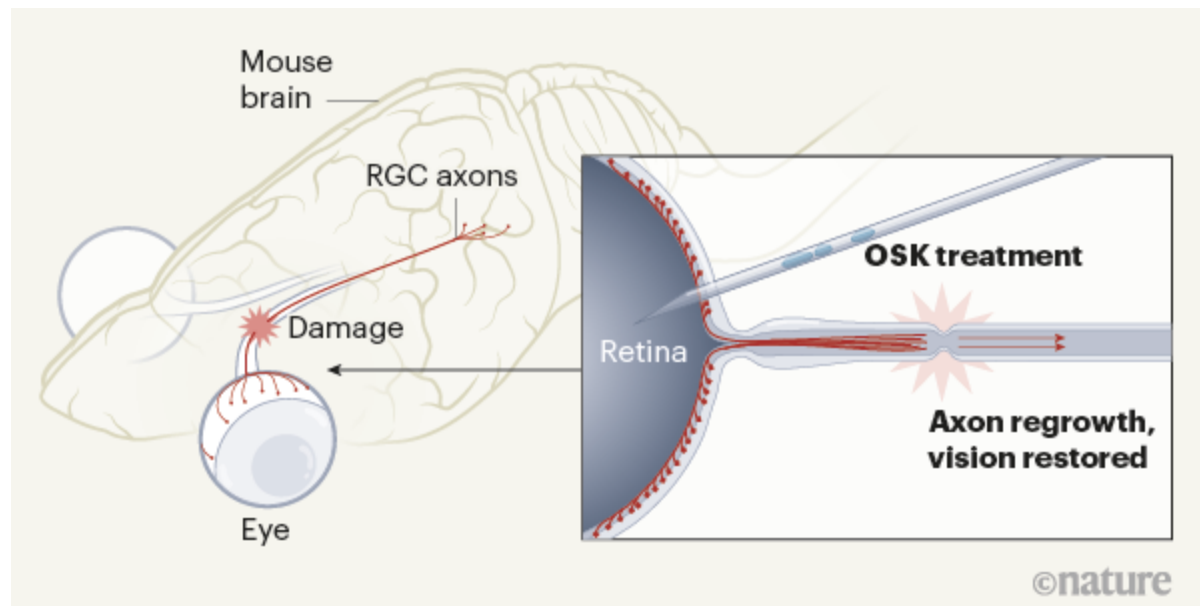
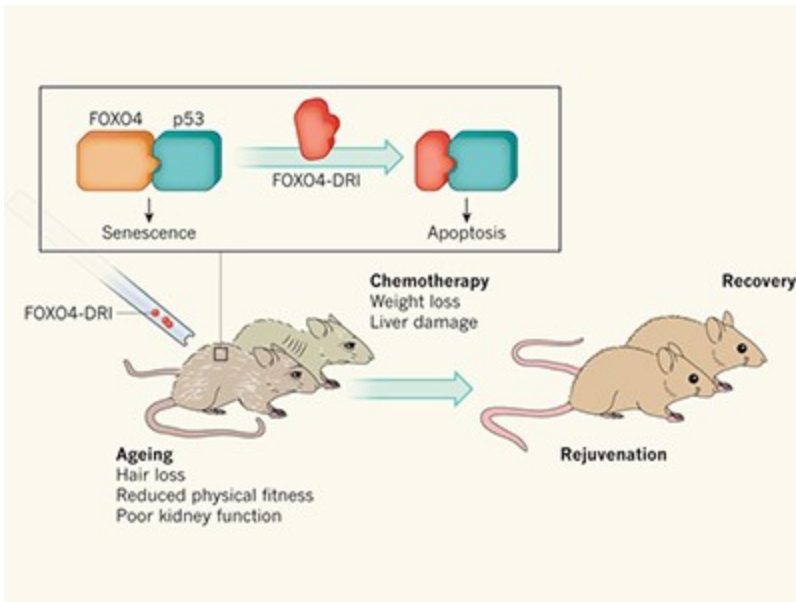


Figure 1 | Restoring vision in mice. Retinal ganglion cells (RGCs) transmit visual information from the eye to the brain along projections

called axons. Damage to the RGC axons prevents transmission of this information, leading to sight loss. Lu *et al.*² report that treatment of damaged RGCs with a transcription-factor cocktail called OSK restores the cells to a youthful state, leading to axon regeneration and restoration of sight in mice.

OSK expression had beneficial effects on RGC axon regeneration in both young and aged mice. In some cases, the regenerated axons extended all the way from the eye to the optic chiasm (the location at the base of the brain at which the optic nerves from each eye cross to the opposite brain hemisphere). It is notable that the effects of OSK are seen in older animals, because studies of RGC regeneration are often conducted in relatively young animals, which have a residual natural regenerative ability. Thus, the evidence suggests that Lu and colleagues' approach can fully restore long-distance regenerative capacity in mature RGCs — a milestone for the field.

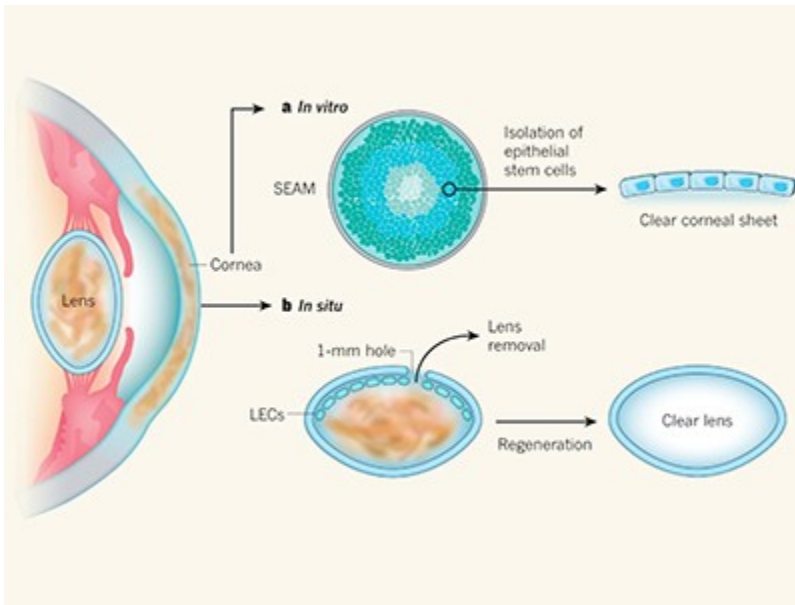
Almost all techniques previously used to enhance RGC survival and axon regrowth had to be performed before optic-nerve damage⁴ — a restriction incompatible with using a technique therapeutically. Excitingly, Lu and colleagues showed that they could induce OSK expression at different time points — even after axon injury — and still improve RGC survival and regeneration. These effects were not limited to optic-nerve injury; OSK expression also effectively reversed RGC and vision loss in a mouse model of glaucoma (the most common cause of human blindness). Expression of OSK in RGCs after axon and vision loss (but before the RGCs died) fully restored vision in these animals. The same was true for wild-type old mice: OSK allowed old mice to regain youthful eyesight.



Tools to eliminate senescent cells

Why might reprogramming old RGCs to a younger state promote regeneration and restore vision? An emerging model in the field of ageing is that, over time, cells accumulate epigenetic noise — molecular changes that alter patterns of gene expression⁸, including transcriptional changes and shifts in the patterns of methyl groups on DNA. Collectively, these changes cause cells to lose their identity and so to lose the DNA-, RNA- and protein-expression patterns that once promoted their youthful resilience^{9,10}. Given the growing excitement about DNA methylation as a marker of cell age, the authors asked whether OSK expression somehow counteracts the negative effects of ageing or axon injury on DNA methylation.

The RNA components of a cell's protein-synthesizing machine, called the ribosome, are encoded by ribosomal DNA genes that steadily accrue methyl marks with age. The ribosomal 'DNA methylation clock' is therefore considered to be a reliable estimate of cell age¹¹. Lu *et al.* found that damaging the axons of RGCs accelerated ribosomal DNA methylation in a way that mimicked accelerated cellular ageing, whereas OSK expression counteracted that acceleration, indicating that tissue injury in general might be a form of accelerated ageing.



Visionary stem-cell therapies

The group also tested whether the removal of DNA methylation is required for OSK to regenerate axons or restore vision in old mice. The TET enzymes (TET1, TET2 and TET3) catalyse the removal of DNA methylation¹². The authors showed that OSK induced expression of *TET1* and *TET2* genes, and that reducing TET1 and TET2 production blocked the effects of OSK on RGC regeneration and vision restoration in old mice. Thus, changes in DNA methylation seem essential for the effects of OSK. Indeed, Lu *et al.* found that OSK restored youthful DNA-methylation patterns across a broad set of genes involved in neuron survival, outgrowth and connectivity. These patterns occur at chromosomal regions that have high levels of PRC2 — a protein complex that alters methylation during development and ageing¹³. Going forward, it will be important to determine the exact extent to which the positive effects of OSK are mediated by resetting DNA-methylation patterns, and the downstream mechanisms that guide the cellular reset.

Are Lu and colleagues' findings likely to be relevant to humans? The authors found that OSK expression enhanced axon regrowth and cell survival in human neurons *in vitro*. The effects of OSK in people remain to

be tested, but the existing results suggest that OSK is likely to reprogram brain neurons across species.

Future research should also address whether OSK expression can have the same remarkable effects on neurons elsewhere in the brain and spinal cord. Given that RGCs are bona fide brain neurons, there is good reason to think they will. As such, the current findings are bound to ignite great excitement, not only in the field of vision restoration but also in those looking to understand epigenetic reprogramming of neurons and other cell types generally. For decades, it was argued that understanding normal neural developmental processes would one day lead to the tools to repair the aged or damaged brain. Lu and colleagues' work makes it clear: that era has now arrived.

Nature **588**, 34–36 (2020)

doi: <https://doi.org/10.1038/d41586-020-03119-1>

References

1. 1.
D.-B., D. *Nature* **125**, 230–231 (1930).
2. 2.
Lu, Y. *et al.* *Nature* **588**, 124–129 (2020).
3. 3.
Goldberg, J. L., Klassen, M. P., Hua, Y. & Barres, B. A. *Science* **296**, 1860–1864 (2002).
4. 4.
Laha, B., Stafford, B. K. & Huberman, A. D. *Science* **356**, 1031–1034 (2017).

5. 5.
Horsburgh, G. M., Lund, R. D. & Hankin, M. H. *J. Comp. Neurol.* **327**, 323–340 (1993).
6. 6.
Takahashi, K. & Yamanaka, S. *Cell* **126**, 663–676 (2006).
7. 7.
Abad, M. *et al.* *Nature* **502**, 340–345 (2013).
8. 8.
Oberdoerffer, P. *et al.* *Cell* **135**, 907–918 (2008)
9. 9.
López-Otín, C., Blasco, M. A., Partridge, L., Serrano, M. & Kroemer, G. *Cell* **153**, 1194–1217 (2013).
10. 10.
Horvath, S. *Genome Biol.* **14**, 3156 (2013).
11. 11.
Wang, M. & Lemos, B. *Genome Res.* **29**, 325–333 (2019).
12. 12.
Rasmussen, K. D. & Helin, K. *Genes Dev.* **30**, 733–750 (2016).
13. 13.
Laugesen, A., Højfeld, J. W. & Helin, K. *Mol. Cell* **74**, 8–18 (2019).

[**Jobs from Nature Careers**](#)

- - - [All jobs](#)
 - - [**Gene Therapy Lab & Research Manager**](#)
[University of Hawai'i at Manoa \(UH Mānoa\)](#)
[Honolulu, United States](#)
[JOB POST](#)
 - [**RN Case Manager**](#)
[Oklahoma Medical Research Foundation \(OMRF\)](#)
[Oklahoma City, United States](#)
[JOB POST](#)
 - [**Research Associate**](#)
[The University of British Columbia \(UBC\)](#)
[Vancouver, Canada](#)
[JOB POST](#)
 - [**Postdoctoral Fellows in Quantum Mathematics**](#)
[University of Southern Denmark \(SDU\)](#)
[Odense M, Denmark](#)
[JOB POST](#)

This article was downloaded by **calibre** from <https://www.nature.com/articles/d41586-020-03119-1>

| [Section menu](#) | [Main menu](#) |

NEWS AND VIEWS

11 November 2020

Building a chemical blueprint for human blood

What determines the chemical make-up of human blood? Measurement of the contributions of factors ranging from genetics to lifestyle has now identified diet and gut microbes as key predictors of blood's molecular composition.

Patrick H. Bradley &

Patrick H. Bradley is in the Department of Microbiology and the Infectious Diseases Institute, Ohio State University, Ohio 43210, USA.

[Contact](#)

Search for this author in:

- [Pub Med](#)
- [Nature.com](#)
- [Google Scholar](#)

Katherine S. Pollard

Katherine S. Pollard is at the Gladstone Institute of Data Science and Biotechnology, University of California, San Francisco, San Francisco, and the Chan Zuckerberg Biohub, San Francisco, California 94158, USA.

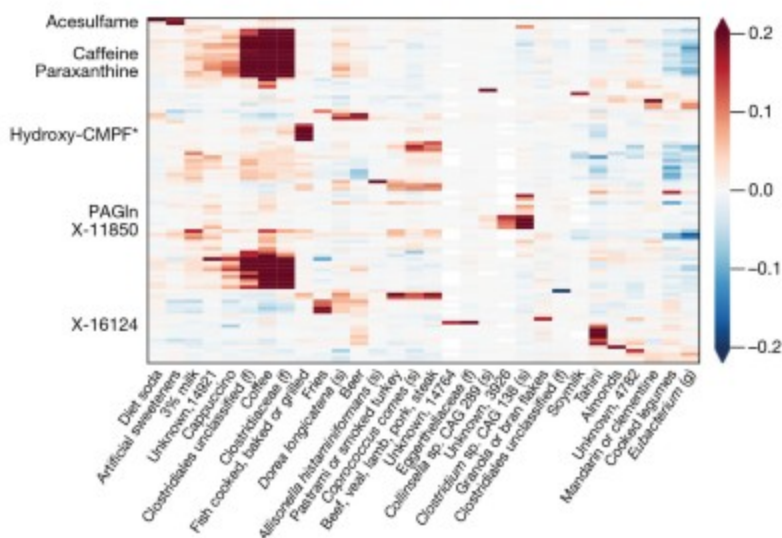
[Contact](#)

Search for this author in:

- [Pub Med](#)
- [Nature.com](#)
- [Google Scholar](#)

Our blood transports many chemicals besides oxygen and carbon dioxide. Some of these molecules provide useful indicators of the state of our health. Indeed, measuring such biomarkers is a common feature of clinical blood tests. Other molecules present, such as hormones and drugs, directly affect health by modulating processes such as metabolism and immune responses. [Writing in Nature](#), Bar *et al.*¹ shed light on the factors that affect the recipe for human blood's chemical brew.

The origin of most blood-borne molecules, and why they vary in concentration between individuals, is unknown. The list of possible regulators is long: for any given molecule, diet, drugs, medical conditions and history, genetic variants and gut microorganisms might all have a role. Furthermore, these factors can interact, as is the case for trimethylamine oxide. This molecule, which promotes the artery-narrowing disease atherosclerosis, is generated as a result of the metabolism, by both microbes and their host, of certain dietary compounds that are abundant in red meat². For molecules such as this, which directly affect health, understanding their metabolic regulation might help to yield new clinical treatments.



Read the paper: A reference map of potential determinants for the human serum metabolome

Bar *et al.* describe their efforts to tackle the question of what factors govern the molecules present in blood. This work requires not only measurement of the many variables potentially involved, but also the use of analytical methods that can capture complexity — such as the interactions between variables — while still ensuring that valid predictions can be made for individuals outside the study population.

The authors began by characterizing blood samples from a group of 491 healthy individuals in great detail. They quantified the molecules in serum — the liquid component of blood that remains after the proteins needed for clotting have been removed. The study participants provided detailed health information, and answered questionnaires about diet and lifestyle. They also gave stool samples, which were used for DNA sequencing, to determine the genetic signatures of the gut microbes present (also known as the microbiome).

As the authors acknowledge, this is a small study group by the standards of genome-wide association studies, which seek to find connections between genes and disease. Bar *et al.* are also not the first to link serum molecules to genetic variation or the microbiome^{3,4}. However, the authors' analysis of this group of individuals is unique in the number of data types that were systematically collected to investigate serum composition.

Next, Bar *et al.* used a machine-learning approach to link factors such as human genetics and microbiome information to the molecules in the blood. By carrying out many analyses omitting different data subsets, the authors found that diet, the microbiome and clinical variables such as prescription-drug use and blood pressure had the most associations with serum molecules. Although the authors found some genetic associations, confirming 46 previously reported gene–metabolite links, they concluded

that the association effects for genetic factors were smaller than were those for diet, clinical variables and the microbiome. These various data types are not exactly comparable, but the authors' estimates of the genetic effects are in line with results from previous work, providing support for their conclusion that diet and the microbiome have larger and more pervasive influences on serum composition than do genetic factors.

Diet and the microbiome could predict the data for some molecules with similar levels of accuracy, as would be expected, given that diet can affect microbiome composition. But Bar and colleagues showed that these data types provide non-overlapping information, too. For example, dietary information uniquely predicted particular metabolites associated with the consumption of citrus fruit, whereas the presence of a type of microbe belonging to the Lachnospiraceae family strongly predicted the presence of indoxyl sulfate — a bacterial breakdown product of the amino acid tryptophan, previously linked to diseases of the kidney and vasculature⁵.

To make predictions about the concentrations of molecules present in blood samples, Bar *et al.* used a machine-learning method called gradient-boosted decision trees, which can capture complex interactions. Decision trees learn simple 'if–then' rules to make predictions (Fig. 1). This method layers individual decision trees, successively improving them by training new models that focus specifically on reducing the prediction errors of the older ones.

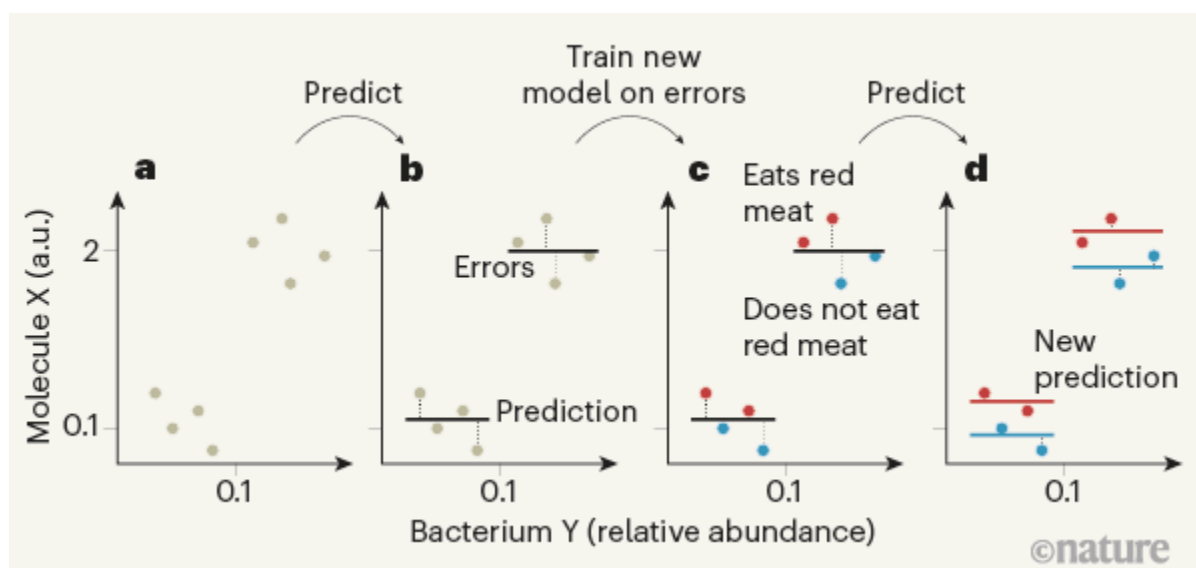


Figure 1 | A way to predict blood's molecular composition. Bar *et al.*¹ obtained human blood samples and identified many of the molecules present. The authors also gathered information about a range of factors, such as diet and gut microbes, that might have affected the molecules found. Using a computational method called gradient-boosted decision trees, Bar and colleagues predicted the molecular composition of an individual's blood. **a**, In this hypothetical example, data points show an individual's concentration of molecule X in arbitrary units (a.u.) and the relative abundance of a type of gut bacterium Y. **b**, The model uses an 'if–then' classification to predict (black horizontal lines) the relationship between bacterial abundance and the concentration of X. The prediction in this case is that if the bacterial abundance is more than 0.1, the concentration of X is 2, and if this abundance is less than 0.1, the concentration of X is 0.1. Dotted lines show the prediction errors. **c**, The model is then refined by taking into account another factor, such as whether the person eats red meat (red) or not (blue). **d**, After another 'if–then' classification that includes this dietary factor, the model generates refined predictions (red and blue horizontal lines) with lower errors that link the predicted concentration of X to dietary and bacterial factors.

Bar and colleagues interpreted these models using an approach called feature-attribution analysis. This yields specific hypotheses about how individual factors, such as microbes, foods and genetic variants, influence a particular prediction, here, the molecular composition of blood. More-complex models can be prone to 'overfitting' — making erroneous predictions that are based on noise or irrelevant details. The authors therefore fitted and evaluated their models conservatively, but, even more importantly, they confirmed many of their predicted microbe-to-metabolite links in two large, independent study groups. Finally, Bar *et al.* tested one set of their predictions in a smaller study, identifying molecules (cytosine and betaine) associated with the consumption of wholewheat bread, and then showing that individuals randomly assigned to eat the bread had the expected changes in these metabolites.

This study is comprehensive, but plenty of room remains for future exploration. The authors used the well-validated and standardized Metabolon platform to measure serum metabolites, but no such

metabolomic analysis method can cover the full range of blood-borne compounds. Certain types of molecule, such as blood lipids, might therefore be under-sampled compared with others. This might explain why the authors mostly detected metabolite associations with only one of the two most abundant lineages of gut bacteria^{6,7}. Metabolomics can detect molecules whose identity is unknown beyond their molecular weight, and, indeed, the authors report several associations with such unknown metabolites. Although these might point to previously unknown aspects of biology (interestingly, for example, one such association was linked to the age of the participant), without metabolite identification, only limited conclusions can be drawn.

The authors' microbiome data provide DNA information for all the genomes present in stool extracts. However, Bar *et al.* distil these data down to the level of abundances of bacterial species, excluding non-bacteria such as yeasts or protozoan organisms. Limiting analyses to the species level also obscures the fact that strains of the same bacterial species can differ in gene content. For example, the metabolism of the drug digoxin *in vivo* by the bacterium *Eggerthella lenta* requires a gene that is present in only certain strains of *E. lenta*⁸. Finally, the authors were unable to link serum metabolites to specific bacterial enzymes responsible for their generation, which would have helped to connect the associated links to the underlying molecular mechanisms.

These limitations should not detract from the most useful aspect of this paper. By making the full data set available to the research community, Bar and colleagues could help enable the development of future computational methods, potentially resolving some of these limitations, or even providing ways to answer new questions. Their data are likely to be a rich and valuable resource for scientists interested in the mechanisms by which diet, the microbiome and genetics affect our biochemistry and physiology.

Nature 588, 36-37 (2020)

doi: <https://doi.org/10.1038/d41586-020-03122-6>

References

1. 1.

Bar, N. *et al.* *Nature* **588**, 135–140 (2020).

2. 2.

Koeth, R. A. *et al.* *Nature Med.* **19**, 576–585 (2013).

3. 3.

Visconti, A. *et al.* *Nature Commun.* **10**, 4505 (2019).

4. 4.

Shin, S.-Y. *et al.* *Nature Genet.* **46**, 543–550 (2014).

5. 5.

Hung, S.-C., Kuo, K.-L., Wu, C.-C. & Tarng, D.-C. *J. Am. Heart Assoc.* **6**, e005022 (2017).

6. 6.

Nemati, R. *et al.* *J. Lipid Res.* **58**, 1999–2007 (2017).

7. 7.

Farrokhi, V. *et al.* *Clin. Transl. Immunol.* **2**, e8 (2013).

8. 8.

Koppel, N., Bisanz, J. E., Pandelia, M.-E., Turnbaugh, P. J. & Balskus, E. P. *eLife* **7**, e33953 (2018).

Jobs from Nature Careers



- [All jobs](#)

o

- **Gene Therapy Lab & Research Manager**

University of Hawai'i at Manoa (UH Mānoa)

Honolulu, United States

JOB POST

- **RN Case Manager**

Oklahoma Medical Research Foundation (OMRF)

Oklahoma City, United States

JOB POST

- **Research Associate**

The University of British Columbia (UBC)

Vancouver, Canada

JOB POST

- **Postdoctoral Fellows in Quantum Mathematics**

University of Southern Denmark (SDU)

Odense M, Denmark

JOB POST

| [Section menu](#) | [Main menu](#) |

NEWS AND VIEWS

02 December 2020

Standard model of particle physics tested by the fine-structure constant

A highly precise measurement of a physical constant known as the fine-structure constant provides a stringent test of the standard model of particle physics, and sets strong limits on the existence of speculative particles.

Holger Müller

Holger Müller is in the Department of Physics, University of California, Berkeley, Berkeley, California 94720, USA.

[Contact](#)

Search for this author in:

- [Pub Med](#)
- [Nature.com](#)
- [Google Scholar](#)

Every physicist knows the approximate value (1/137) of a fundamental constant called the fine-structure constant, α . This constant describes the strength of the electromagnetic force between elementary particles in the standard model of particle physics and is therefore central to the foundations of physics. For example, the binding energy of a hydrogen atom — the energy required to break apart the atom's electron and proton — is about $\alpha^2/2$ times the energy associated with an electron's mass. Moreover, the magnetic moment of an electron is subtly larger than that expected for a charged, point-like particle by a factor of roughly $1 + \alpha/(2\pi)$.

This ‘anomaly’ of the magnetic moment has been verified to ever-increasing accuracy, becoming “the standard model’s greatest triumph”¹. [Writing in Nature](#), Morel *et al.*² report a measurement of α with an accuracy of 81 parts per trillion (p.p.t.), a 2.5-fold improvement over the previous best determination³.

The measurement of α involves three steps. First, a laser beam makes an atom absorb and emit multiple photons and, in doing so, recoil (Fig. 1a). The mass of the atom is deduced by measuring the kinetic energy of this recoil. Second, the electron’s mass is calculated using the precisely known ratio of the atom’s mass to the mass of an electron^{4,5} (Fig. 1b). Third, α is determined from the electron’s mass and the binding energy of a hydrogen atom, which is known from spectroscopy⁶ (Fig. 1c).

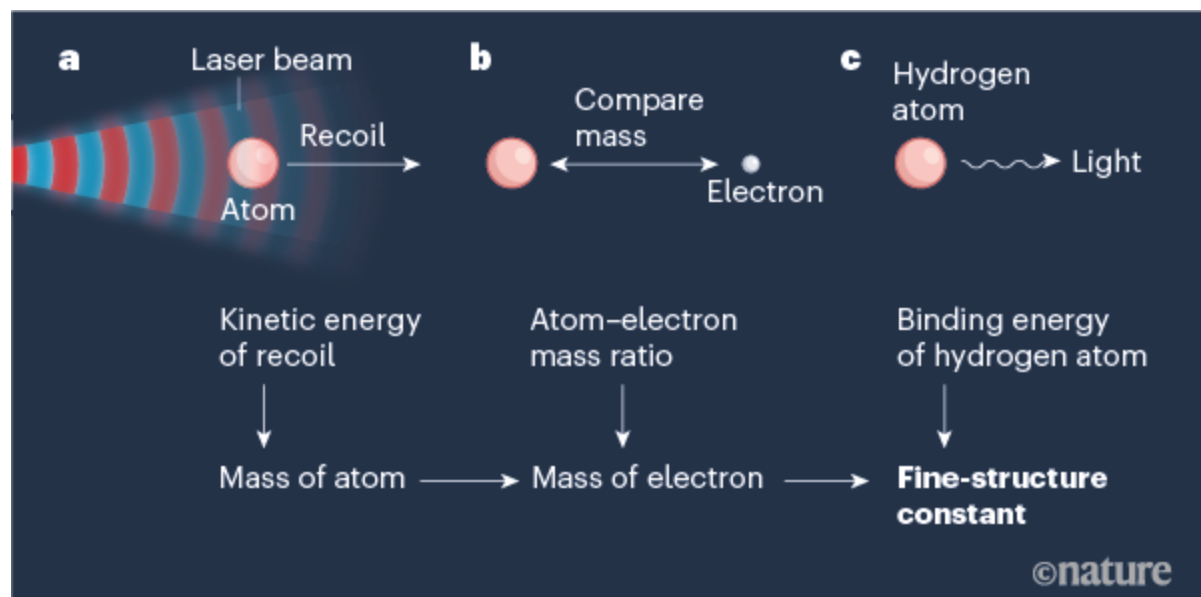


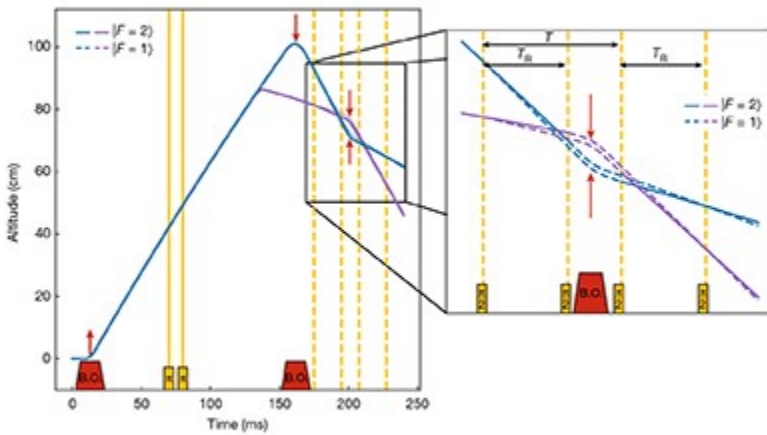
Figure 1 | Process for measuring the fine-structure constant. Morel *et al.*² report a highly precise determination of the fine-structure constant — the physical constant that defines the strength of the electromagnetic force between elementary particles. **a**, In the measurement of this constant, a beam of light from a laser causes an atom to recoil. The red and blue colours correspond to the light wave’s peaks and troughs, respectively. The kinetic energy of the recoil is used to deduce the atom’s mass. **b**, The value of the atom’s mass is then combined with the precisely known ratio of the atom’s mass to the electron’s mass^{4,5} to infer the mass of an electron. **c**,

Finally, the electron's mass and the binding energy of a hydrogen atom are used to determine the fine-structure constant. The binding energy is known from spectroscopy⁶, whereby light emitted from a hydrogen atom is analysed.

However, the recoil energy is tiny and therefore hard to measure. Laser-based cooling of atoms has enabled physicists to carry out atom interferometry — a measurement technique that uses the interference of matter waves associated with the atoms. In an atom interferometer, atoms have a 50% probability of interacting with photons from laser pulses. Consequently, such atoms exist in two quantum states simultaneously: one in which they are at rest and the other in which they move, having absorbed the momentum of the photons.

This situation is equivalent to the production of two partial matter waves that move away from each other. These matter waves are recombined by firing more laser pulses, generating constructive or destructive interference (whereby the waves reinforce or cancel each other) and therefore a high or low probability of observing the atoms. The phase shift between the interfering waves — the displacement of one wave with respect to the other — is proportional to their travel time and the recoil energy.

Subsequent improvements to this approach have realized long travel times and interactions with many photons. In 2011, the research group behind the current breakthrough, at the Kastler–Brossel Laboratory in Paris, used the technique to determine α with an accuracy⁷ of 660 p.p.t. In the following year, scientists carried out a measurement of the electron's anomalous magnetic moment to derive a standard-model prediction for α with an accuracy⁸ of 250 p.p.t. And in 2018, my team at the University of California, Berkeley, published an atom-interferometry determination of α that agreed with the previous one but pushed the accuracy³ to 200 p.p.t.



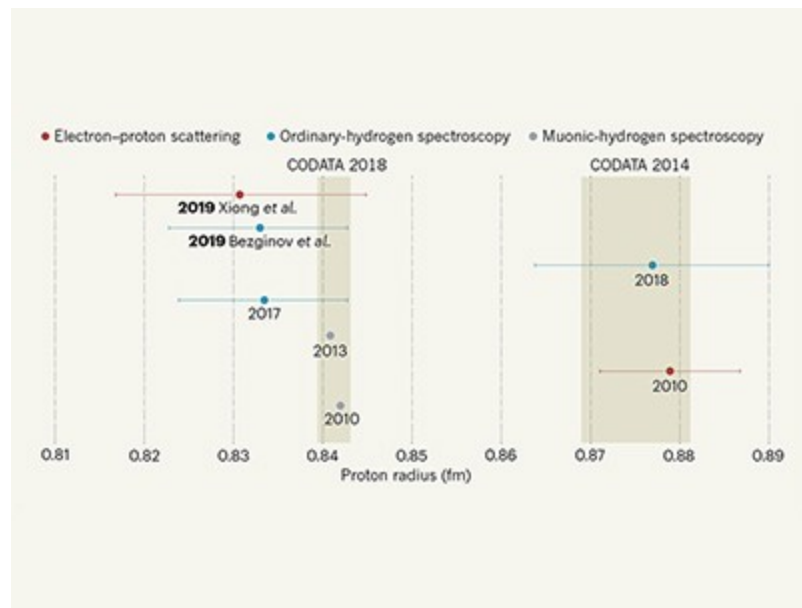
Read the paper: Determination of the fine-structure constant with an accuracy of 81 parts per trillion

Now, Morel *et al.* have improved the accuracy to 81 p.p.t. In another triumph for the standard model, the measured value of α agrees with the standard-model prediction from the anomalous magnetic moment, even at such precision. This result confirms, for example, that the electron has no substructure and is truly an elementary particle. If it were made of smaller constituents, it would have a different magnetic moment, contrary to observation.

The measurement also places strong bounds on the existence of certain dark-sector particles, a speculative family of particles, some of which might constitute dark matter — the unseen matter component of the Universe. In quantum field theory, empty space is a sea of ‘virtual’ particles that spring into a brief existence. Virtual dark-sector particles would shift the electron’s magnetic moment in subtle, yet measurable ways.

However, there is a remaining puzzle. Although there is only a slight tension between each of the determinations of α and the standard-model prediction from the anomalous magnetic moment, there is a strong tension between Morel and colleagues' latest measurement and its two predecessors. As shown in Figure 1 of their paper², this situation is possible because the latest measurement and its predecessors deviate from the standard-model prediction in opposite directions.

The authors suggest that the difference between their research group's own measurements could be caused by speckle — small-scale spatial variations of the laser intensity — or by a phase shift arising in electronic-signal processing. However, it is no longer possible to evaluate such a shift in the group's earlier experiment, and speckle should produce a variation between the measurements in the opposite direction to that needed to explain the discrepancy.



Progress on the proton-radius puzzle

Morel and colleagues also leave open the reason for the disparity with the 2018 measurement. The two experiments differ in the use of rubidium

versus caesium atoms, in the types of atom–light interaction used and in how the laser beams are prepared and aligned. These choices imply different influences of the environment on the atoms.

For example, the largest corrections applied to data taken in both experiments arise from the laser beams. Both the speckle mentioned earlier and the overall beam profiles affect the magnitude and direction of the atom recoil. The discrepancy between the results could be explained if my team had over-corrected for these effects or Morel *et al.* had under-corrected. Most probably, it will take further experimental work to tell.

Experimenters are therefore gearing up to clarify the origin of this discrepancy and to challenge the standard model yet again. For example, my team is aiming to further improve the precision in the measured value of α by building an atom interferometer that enables unprecedented control over the laser-beam shape. Moreover, necessary improved measurements of atomic masses are already under way⁵. And finally, a refined determination of the electron’s anomalous magnetic moment is being prepared at Northwestern University in Illinois⁹. Together, these improvements will allow physicists to approach an accuracy of 10 p.p.t. At that point, the effects of the tau lepton — a heavier cousin of the electron — will be observed in the experiments and many hypothesized dark-sector theories could be probed.

Nature **588**, 37–38 (2020)

doi: <https://doi.org/10.1038/d41586-020-03314-0>

References

1. 1.

Gabrielse, G. *Phys. Today* **66**, 64–65 (2013).

2. 2.

Morel, L., Yao, Z., Cladé, P. & Guellati-Khélifa, S. *Nature* **588**, 61–65 (2020).

3. 3.

Parker, R. H., Yu, C., Zhong, W., Estey, B. & Müller, H. *Science* **360**, 191–195 (2018).

4. 4.

Sturm, S. *et al.* *Nature* **506**, 467–470 (2014).

5. 5.

Myers, E. G. *Atoms* **7**, 37 (2019).

6. 6.

Udem, T. *Nature Phys.* **14**, 632 (2018).

7. 7.

Bouchendira, R., Cladé, P., Guellati-Khélifa, S., Nez, F. & Biraben, F. *Phys. Rev. Lett.* **106**, 080801 (2011).

8. 8.

Aoyama, T., Hayakawa, M., Kinoshita, T. & Nio, M. *Phys. Rev. Lett.* **109**, 111807 (2012).

9. 9.

Gabrielse, G., Fayer, S. E., Myers, T. G. & Fan, X. *Atoms* **7**, 45 (2019).

Jobs from Nature Careers



- [All jobs](#)

o

- **Gene Therapy Lab & Research Manager**

University of Hawai'i at Manoa (UH Mānoa)

Honolulu, United States

JOB POST

- **RN Case Manager**

Oklahoma Medical Research Foundation (OMRF)

Oklahoma City, United States

JOB POST

- **Research Associate**

The University of British Columbia (UBC)

Vancouver, Canada

JOB POST

- **Postdoctoral Fellows in Quantum Mathematics**

University of Southern Denmark (SDU)

Odense M, Denmark

JOB POST

| [Section menu](#) | [Main menu](#) |

- Perspective
- [Published: 02 December 2020](#)

Inference in artificial intelligence with deep optics and photonics

- [Gordon Wetzstein](#) [ORCID: orcid.org/0000-0002-9243-6885¹](#),
- [Aydogan Ozcan](#) [ORCID: orcid.org/0000-0002-0717-683X²](#),
- [Sylvain Gigan](#) [ORCID: orcid.org/0000-0002-9914-6231³](#),
- [Shanhui Fan¹](#),
- [Dirk Englund](#) [ORCID: orcid.org/0000-0002-1043-3489⁴](#),
- [Marin Soljačić](#) [ORCID: orcid.org/0000-0002-7184-5831⁴](#),
- [Cornelia Denz⁵](#),
- [David A. B. Miller](#) [ORCID: orcid.org/0000-0002-3633-7479¹](#) &
- [Demetri Psaltis⁶](#)

[Nature](#) volume 588, pages39–47(2020) [Cite this article](#)

- 505 Accesses
- 52 Altmetric
- [Metrics details](#)

Abstract

Artificial intelligence tasks across numerous applications require accelerators for fast and low-power execution. Optical computing systems may be able to meet these domain-specific needs but, despite half a century of research, general-purpose optical computing systems have yet to mature into a practical technology. Artificial intelligence inference, however, especially for visual computing applications, may offer opportunities for

inference based on optical and photonic systems. In this Perspective, we review recent work on optical computing for artificial intelligence applications and discuss its promise and challenges.

[Access through your institution](#)

[Change institution](#)

[Buy or subscribe](#)

Access options

Subscribe to Journal

Get full journal access for 1 year

185,98 €

only 3,58 € per issue

[Subscribe](#)

All prices are NET prices.

VAT will be added later in the checkout.

Rent or Buy article

Get time limited or full article access on ReadCube.

from \$8.99

[Rent or Buy](#)

All prices are NET prices.

Additional access options:

- [Log in](#)
- [Access through your institution](#)
- [Learn about institutional subscriptions](#)

Fig. 1: Timeline of artificial intelligence and related optical and photonic implementations.

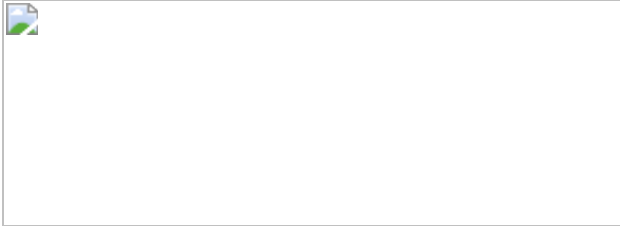


Fig. 2: Overview of optical wave propagation.



Fig. 3: Illustration of an optical encoder–electronic decoder system.

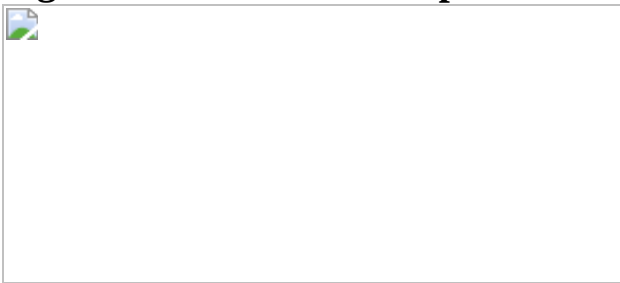


Fig. 4: Overview of deep optics and photonics applications I.





Fig. 5: Overview of deep optics and photonics applications II.



References

1. 1.

LeCun, Y. et al. Handwritten digit recognition with a back-propagation network. In *Advances in Neural Information Processing Systems 2 (NIPS 1989)* (ed. Touretzky, D. S.) 396–404 (1990).

2. 2.

Krizhevsky, A., Sutskever, I. & Hinton, G. E. ImageNet classification with deep convolutional neural networks. In *Advances in Neural Information Processing Systems 25 (NIPS 2012)* (eds Pereira, F. et al.) 1097–1105 (2012).

3. 3.

LeCun, Y., Bengio, Y. & Hinton, G. Deep learning. *Nature* **521**, 436–444 (2015).

[ADS](#) [CAS](#) [PubMed](#) [Google Scholar](#)

4. 4.

Miller, D. A. B. Waves, modes, communications, and optics: a tutorial. *Adv. Opt. Photonics* **11**, 679–825 (2019).

[ADS](#) [Google Scholar](#)

5. 5.

Brunner, D., Soriano, M. C., Mirasso, C. R. & Fischer, I. Parallel photonic information processing at gigabyte per second data rates using transient states. *Nat. Commun.* **4**, 1364 (2013).

[ADS](#) [PubMed](#) [PubMed Central](#) [Google Scholar](#)

6. 6.

Goodman, J. W., Leonberger, F. J., Kung, S.-Y. & Athale, R. A. Optical interconnections for VLSI systems. *Proc. IEEE* **72**, 850–866 (1984). **The first paper to provide a substantial analysis and reasons for the use of optics in interconnection (rather than for logic) in digital systems.**

[ADS](#) [Google Scholar](#)

7. 7.

Miller, D. A. B. Rationale and challenges for optical interconnects to electronic chips. *Proc. IEEE* **88**, 728–749 (2000).

[Google Scholar](#)

8. 8.

Miller, D. A. B. Attojoule optoelectronics for low-energy information processing and communications. *J. Lightwave Technol.* **35**, 346–396 (2017).

[ADS](#) [CAS](#) [Google Scholar](#)

9. 9.

Miller, D. A. B. Are optical transistors the logical next step? *Nat. Photon.* **4**, 3–5 (2010).

[ADS](#) [CAS](#) [Google Scholar](#)

10. 10.

Athale, R. & Psaltis, D. Optical computing: past and future. *Opt. Photon. News* **27**, 32–39 (2016).

[Google Scholar](#)

11. 11.

Goodman, J. W. *Introduction to Fourier Optics* (Roberts and Co, 2005).

12. 12.

Liutkus, A. et al. Imaging with nature: compressive imaging using a multiply scattering medium. *Sci. Rep.* **4**, 5552 (2014).

[CAS](#) [PubMed](#) [PubMed Central](#) [Google Scholar](#)

13. 13.

Saade, A. et al. Random projections through multiple optical scattering: approximating kernels at the speed of light. In *2016 IEEE Intl Conf. Acoustics, Speech and Signal Processing (ICASSP)* 6215–6219 (IEEE, 2016).

14. 14.

Lin, X. et al. All-optical machine learning using diffractive deep neural networks. *Science* **361**, 1004–1008 (2018). **An optical implementation using multiple optimized layers for all-optical image classification.**

[ADS](#) [MathSciNet](#) [CAS](#) [MATH](#) [PubMed](#) [Google Scholar](#)

15. 15.

Chang, J., Sitzmann, V., Dun, X., Heidrich, W. & Wetzstein, G. Hybrid optical–electronic convolutional neural networks with optimized diffractive optics for image classification. *Sci. Rep.* **8**, 12324 (2018). **An optical implementation of a single CNN layer demonstrated for hybrid optical–electronic image classification.**

[ADS](#) [PubMed](#) [PubMed Central](#) [Google Scholar](#)

16. 16.

Rosenblatt, F. *The Perceptron, A Perceiving and Recognizing Automaton* Report no. 85-460-1 (Project Para, Cornell Aeronautical Laboratory, 1957).

17. 17.

Hebb, D. O. *The Organization of Behavior* (Wiley, 1949).

18. 18.

Widrow, B. & Hoff, M. E. Adaptive switching circuits. In *1960 IRE WESCON Convention Record* 96–104 (Institute of Radio Engineers, 1960).

19. 19.

Hopfield, J. J. Neural networks and physical systems with emergent collective computational abilities. *Proc. Natl Acad. Sci. USA* **79**, 2554–2558 (1982).

[ADS](#) [MathSciNet](#) [CAS](#) [MATH](#) [PubMed](#) [Google Scholar](#)

20. 20.

Carpenter, G. A. & Grossberg, S. A massively parallel architecture for a self-organizing neural pattern recognition machine. *Comput. Vis. Graph. Image Process.* **37**, 54–115 (1987).

[MATH](#) [Google Scholar](#)

21. 21.

Kohonen, T. Self-organized formation of topologically correct feature maps. *Biol. Cybern.* **43**, 59–69 (1982).

[MathSciNet](#) [MATH](#) [Google Scholar](#)

22. 22.

Rumelhart, D. E., Hinton, G. E. & Williams, R. J. Learning representations by back-propagating errors. *Nature* **323**, 533–536 (1986).

[ADS](#) [MATH](#) [Google Scholar](#)

23. 23.

Mead, C. Neuromorphic electronic systems. *Proc. IEEE* **78**, 1629–1636 (1990).

[Google Scholar](#)

24. 24.

Farhat, N. H., Psaltis, D., Prata, A. & Paek, E. Optical implementation of the Hopfield model. *Appl. Opt.* **24**, 1469–1475 (1985). **Optical implementation of content-addressable associative memory based on the Hopfield model for neural networks and on the addition of nonlinear iterative feedback to a vector–matrix multiplier.**

[ADS](#) [CAS](#) [PubMed](#) [Google Scholar](#)

25. 25.

Denz, C. *Optical Neural Networks* (Springer Science & Business Media, 2013).

26. 26.

Psaltis, D., Brady, D., Gu, X.-G. & Lin, S. Holography in artificial neural networks. *Nature* **343**, 325–330 (1990). **Introduction of nonlinear photorefractive crystals for optical computing.**

[ADS](#) [CAS](#) [PubMed](#) [Google Scholar](#)

27. 27.

Li, H.-Y. S., Qiao, Y. & Psaltis, D. Optical network for real-time face recognition. *Appl. Opt.* **32**, 5026–5035 (1993).

[ADS](#) [CAS](#) [PubMed](#) [Google Scholar](#)

28. 28.

Miller, D. A. B. Self-configuring universal linear optical component. *Photon. Res.* **1**, 1–15 (2013). **Proof that arbitrary linear operations such as singular value decompositions can be performed in optics—not just Fourier transforms and convolutions as in early optical computing.**

[ADS](#) [Google Scholar](#)

29. 29.

Shen, Y. et al. Deep learning with coherent nanophotonic circuits. *Nat. Photon.* **11**, 441 (2017). **A silicon photonic neural network using meshes of MZIs for vowel recognition.**

[ADS](#) [CAS](#) [Google Scholar](#)

30. 30.

Fang, M. Y.-S., Manipatruni, S., Wierzynski, C., Khosrowshahi, A. & DeWeese, M. R. Design of optical neural networks with component imprecisions. *Opt. Express* **27**, 14009–14029 (2019).

[ADS](#) [CAS](#) [PubMed](#) [Google Scholar](#)

31. 31.

Wilkes, C. M. et al. 60 dB high-extinction auto-configured Mach–Zehnder interferometer. *Opt. Lett.* **41**, 5318–5321 (2016).

[ADS](#) [CAS](#) [PubMed](#) [Google Scholar](#)

32. 32.

Hughes, T. W., Minkov, M., Shi, Y. & Fan, S. Training of photonic neural networks through in situ backpropagation and gradient measurement. *Optica* **5**, 864–871 (2018).

[ADS](#) [Google Scholar](#)

33. 33.

Feldmann, J., Youngblood, N., Wright, C. D., Bhaskaran, H. & Pernice, W. H. P. All-optical spiking neurosynaptic networks with self-learning capabilities. *Nature* **569**, 208–214 (2019). **A photonic circuit**

that exploits wavelength division multiplexing techniques for pattern recognition directly in the optical domain.

[ADS](#) [CAS](#) [PubMed](#) [PubMed Central](#) [Google Scholar](#)

34. 34.

Tait, A. N. et al. Neuromorphic photonic networks using silicon photonic weight banks. *Sci. Rep.* **7**, 7430 (2017).

[ADS](#) [PubMed](#) [PubMed Central](#) [Google Scholar](#)

35. 35.

Huang, C. et al. Giant enhancement in signal contrast using integrated all-optical nonlinear thresholding. In *2019 Optical Fiber Communications Conference and Exhibition (OFC)* 415–417 (IEEE, 2019).

36. 36.

Nahmias, M. A., Shastri, B. J., Tait, A. N. & Prucnal, P. R. A leaky integrate-and-fire laser neuron for ultrafast cognitive computing. *IEEE J. Sel. Top. Quantum Electron.* **19**, 1800212 (2013).

[Google Scholar](#)

37. 37.

Amin, R. et al. ITO-based electro-absorption modulator for photonic neural activation function. *APL Mater.* **7**, 081112 (2019).

[ADS](#) [Google Scholar](#)

38. 38.

Williamson, I. A. D. et al. Reprogrammable electro-optic nonlinear activation functions for optical neural networks. *IEEE J. Sel. Top. Quantum Electron.* **26**, 7700412 (2020).

[CAS](#) [Google Scholar](#)

39. 39.

Miller, D. A. B. Novel analog self-electrooptic-effect devices. *IEEE J. Quantum Electron.* **29**, 678–698 (1993).

[ADS](#) [Google Scholar](#)

40. 40.

Srinivasan, S. A. et al. High absorption contrast quantum confined stark effect in ultra-thin Ge/SiGe quantum well stacks grown on Si. *IEEE J. Quantum Electron.* **56**, 5200207 (2020).

[Google Scholar](#)

41. 41.

Ferreira de Lima, T., Shastri, B. J., Tait, A. N., Nahmias, M. A. & Prucnal, P. R. Progress in neuromorphic photonics. *Nanophotonics* **6**, 577–599 (2017).

[Google Scholar](#)

42. 42.

Nahmias, M. A. et al. Photonic multiply–accumulate operations for neural networks. *IEEE J. Sel. Top. Quantum Electron.* **26**, 7701518 (2020). **A review article on the state-of-the-art of photonic MACs along with detailed characterizations and comparisons of the performance of photonic and comparable electronic hardware.**

[CAS](#) [Google Scholar](#)

43. 43.

Gupta, S., Agrawal, A., Gopalakrishnan, K. & Narayanan, P. Deep learning with limited numerical precision. In *Proc. 32nd Intl Conf.*

Machine Learning (eds Bach, F. & Blei, D.) 1737–1746 (PMLR, 2015).

44. 44.

Hamerly, R., Bernstein, L., Sludds, A., Soljačić, M. & Englund, D. Large-scale optical neural networks based on photoelectric multiplication. *Phys. Rev. X* **9**, 021032 (2019).

[CAS](#) [Google Scholar](#)

45. 45.

Lugt, A. V. Signal detection by complex spatial filtering. *IEEE Trans. Inf. Theory* **10**, 139–145 (1964). **The introduction of optical correlators.**

[MATH](#) [Google Scholar](#)

46. 46.

Gregory, D. A. Real-time pattern recognition using a modified liquid crystal television in a coherent optical correlator. *Appl. Opt.* **25**, 467–469 (1986).

[ADS](#) [CAS](#) [PubMed](#) [Google Scholar](#)

47. 47.

Manzur, T., Zeller, J. & Serati, S. Optical-correlator-based target detection, recognition, classification, and tracking. *Appl. Opt.* **51**, 4976–4983 (2012).

[ADS](#) [PubMed](#) [Google Scholar](#)

48. 48.

Javidi, B., Li, J. & Tang, Q. Optical implementation of neural networks for face recognition by the use of nonlinear joint transform correlators.

Appl. Opt. **34**, 3950–3962 (1995).

[ADS](#) [CAS](#) [PubMed](#) [Google Scholar](#)

49. 49.

Koppal, S. J., Gkioulekas, I., Zickler, T. & Barrows, G. L. Wide-angle micro sensors for vision on a tight budget. In *2011 IEEE Conf. Computer Vision and Pattern Recognition (CVPR 2011)* 361–368 (IEEE, 2011).

50. 50.

Hughes, T. W., Williamson, I. A. D., Minkov, M. & Fan, S. Wave physics as an analog recurrent neural network. *Sci. Adv.* **5**, eaay6946 (2019).

[ADS](#) [PubMed](#) [PubMed Central](#) [Google Scholar](#)

51. 51.

Duarte, M. F. et al. Single-pixel imaging via compressive sampling. *IEEE Signal Process. Mag.* **25**, 83–91 (2008).

[ADS](#) [Google Scholar](#)

52. 52.

Moretti, C. & Gigan, S. Readout of fluorescence functional signals through highly scattering tissue. *Nat. Photonics* **14**, 361–364 (2020).

[ADS](#) [CAS](#) [Google Scholar](#)

53. 53.

Rahmani, B., Loterie, D., Konstantinou, G., Psaltis, D. & Moser, C. Multimode optical fiber transmission with a deep learning network. *Light Sci. Appl.* **7**, 69 (2018).

[ADS](#) [PubMed](#) [PubMed Central](#) [Google Scholar](#)

54. 54.

Caramazza, P., Moran, O., Murray-Smith, R. & Faccio, D. Transmission of natural scene images through a multimode fibre. *Nat. Commun.* **10**, 2029 (2019).

[ADS](#) [PubMed](#) [PubMed Central](#) [Google Scholar](#)

55. 55.

Li, Y., Xue, Y. & Tian, L. Deep speckle correlation: a deep learning approach toward scalable imaging through scattering media. *Optica* **5**, 1181–1190 (2018).

[ADS](#) [Google Scholar](#)

56. 56.

Horisaki, R., Takagi, R. & Tanida, J. Learning-based imaging through scattering media. *Opt. Express* **24**, 13738–13743 (2016).

[ADS](#) [PubMed](#) [Google Scholar](#)

57. 57.

Ando, T., Horisaki, R. & Tanida, J. Speckle-learning-based object recognition through scattering media. *Opt. Express* **23**, 33902–33910 (2015).

[ADS](#) [CAS](#) [PubMed](#) [Google Scholar](#)

58. 58.

Mahoney, M. W. *Randomized Algorithms for Matrices and Data* (Now Publishers, 2011).

59. 59.

Dong, J., Rafayelyan, M., Krzakala, F. & Gigan, S. Optical reservoir computing using multiple light scattering for chaotic systems prediction. *IEEE J. Sel. Top. Quantum Electron.* **26**, 7701012 (2019).

[Google Scholar](#)

60. 60.

Gupta, S., Gribonval, R., Daudet, L. & Dokmanić, I. Don't take it lightly: phasing optical random projections with unknown operators. In *Advances in Neural Information Processing Systems 32 (NeurIPS 2019)* (eds Wallach, H. et al.) 14855–14865 (2019).

61. 61.

Marshall, J. & Oberwinkler, J. The colourful world of the mantis shrimp. *Nature* **401**, 873–874 (1999).

[ADS](#) [CAS](#) [PubMed](#) [Google Scholar](#)

62. 62.

Thoen, H. T., How, M. J., Chiou, T.-H. & Marshall, J. A different form of color vision in mantis shrimp. *Science* **343**, 411–413 (2014).

[ADS](#) [CAS](#) [PubMed](#) [Google Scholar](#)

63. 63.

Wetzstein, G., Ihrke, I., Lanman, D. & Heidrich, W. Computational plenoptic imaging. *Comput. Graph. Forum* **30**, 2397–2426 (2011).

[Google Scholar](#)

64. 64.

Hinton, G. E. & Salakhutdinov, R. R. Reducing the dimensionality of data with neural networks. *Science* **313**, 504–507 (2006).

[ADS](#) [MathSciNet](#) [CAS](#) [MATH](#) [PubMed](#) [PubMed Central](#) [Google Scholar](#)

65. 65.

Sitzmann, V. et al. End-to-end optimization of optics and image processing for achromatic extended depth of field and super-resolution imaging. *ACM Trans. Graph.* **37**, 114 (2018). **The first demonstration of end-to-end optimization of optics and image processing for a computational camera design with computer vision applications.**

[Google Scholar](#)

66. 66.

Chakrabarti, A. Learning sensor multiplexing design through back-propagation. In *Advances in Neural Information Processing Systems 29 (NIPS 2016)* (eds Lee, D. D. et al.) 3081–3089 (2016).

67. 67.

Martel, J. N. P., Muller, L. K., Carey, S., Dudek, P. & Wetzstein, G. Neural sensors: learning pixel exposures for HDR imaging and video compressive sensing with programmable sensors. *IEEE Trans. Pattern Anal. Mach. Intell.* **42**, 1642–1653 (2020).

[PubMed](#) [Google Scholar](#)

68. 68.

Horstmeier, R., Chen, R. Y., Kappes, B. & Judkewitz, B. Convolutional neural networks that teach microscopes how to image. Preprint at <https://arxiv.org/abs/1709.07223> (2017).

69. 69.

Marco, J. et al. DeepToF: off-the-shelf real-time correction of multipath interference in time-of-flight imaging. *ACM Trans. Graph.*

36, 219 (2017).

[Google Scholar](#)

70. 70.

Su, S., Heide, F., Wetzstein, G. & Heidrich, W. Deep end-to-end time-of-flight imaging. In *2018 IEEE Conf. Computer Vision and Pattern Recognition (CVPR)* 6383–6392 (IEEE, 2018).

71. 71.

Kellman, M., Bostan, E., Repina, N. & Waller, L. Physics-based learned design: optimized coded-illumination for quantitative phase imaging. *IEEE Trans. Comput. Imaging* **5**, 344–353 (2019).

[Google Scholar](#)

72. 72.

Sinha, A., Lee, J., Li, S. & Barbastathis, G. Lensless computational imaging through deep learning. *Optica* **4**, 1117–1125 (2017).

[ADS](#) [Google Scholar](#)

73. 73.

Metzler, C. A., Ikoma, H., Peng, Y. & Wetzstein, G. Deep optics for single-shot high-dynamic-range imaging. In *2020 IEEE/CVF Conf. Computer Vision and Pattern Recognition (CVPR)* 1372–1382 (IEEE, 2020).

74. 74.

Luo, Y. et al. Design of task-specific optical systems using broadband diffractive neural networks. *Light Sci. Appl.* **8**, 112 (2019).

[ADS](#) [PubMed](#) [PubMed Central](#) [Google Scholar](#)

75. 75.

Haim, H., Elmalem, S., Giryes, R., Bronstein, A. M. & Marom, E. Depth estimation from a single image using deep learned phase coded mask. *IEEE Trans. Comput. Imaging* **4**, 298–310 (2018).

[Google Scholar](#)

76. 76.

Chang, J. & Wetzstein, G. Deep optics for monocular depth estimation and 3D object detection. In *2019 IEEE/CVF Intl Conf. Computer Vision (ICCV)* 10192–10211 (IEEE, 2019).

77. 77.

Wu, Y., Boominathan, V., Chen, H., Sankaranarayanan, A. & Veeraraghavan, A. Phasecam3D—learning phase masks for passive single view depth estimation. In *2019 IEEE Intl Conf. Computational Photography (ICCP)* 19–30 (IEEE, 2019).

78. 78.

Bertero, M. & Boccacci, P. *Introduction to Inverse Problems in Imaging* (CRC Press, 1998).

79. 79.

Barbastathis, G., Ozcan, A. & Situ, G. On the use of deep learning for computational imaging. *Optica* **6**, 921–943 (2019).

[ADS](#) [Google Scholar](#)

80. 80.

Rivenson, Y. et al. Deep learning microscopy. *Optica* **4**, 1437–1443 (2017).

[ADS](#) [Google Scholar](#)

81. 81.

Wu, Y. et al. Extended depth-of-field in holographic imaging using deep-learning-based autofocusing and phase recovery. *Optica* **5**, 704–710 (2018).

[ADS](#) [Google Scholar](#)

82. 82.

Nehme, E. & Weiss, L. E., Michaeli, T. & Shechtman, Y. Deep-storm: super-resolution single-molecule microscopy by deep learning. *Optica* **5**, 458–464 (2018).

[ADS](#) [CAS](#) [Google Scholar](#)

83. 83.

Ouyang, W., Aristov, A., Lelek, M., Hao, X. & Zimmer, C. Deep learning massively accelerates super-resolution localization microscopy. *Nat. Biotechnol.* **36**, 460–468 (2018).

[CAS](#) [PubMed](#) [Google Scholar](#)

84. 84.

Christiansen, E. M. et al. In silico labeling: predicting fluorescent labels in unlabeled images. *Cell* **173**, 792–803 (2018).

[CAS](#) [PubMed](#) [PubMed Central](#) [Google Scholar](#)

85. 85.

Wu, Y. et al. Three-dimensional virtual refocusing of fluorescence microscopy images using deep learning. *Nat. Methods* **16**, 1323–1331 (2019).

[CAS](#) [PubMed](#) [Google Scholar](#)

86. 86.

Wang, H. et al. Deep learning enables cross-modality super-resolution in fluorescence microscopy. *Nat. Methods* **16**, 103–110 (2019).

[CAS](#) [PubMed](#) [Google Scholar](#)

87. 87.

Rivenson, Y., Zhang, Y., Günaydin, H., Teng, D. & Ozcan, A. Phase recovery and holographic image reconstruction using deep learning in neural networks. *Light Sci. Appl.* **7**, 17141 (2018).

[CAS](#) [PubMed](#) [PubMed Central](#) [Google Scholar](#)

88. 88.

Boyd, N., Jonas, E., Babcock, H. & Recht, B. DeepLoco: Fast 3D localization microscopy using neural networks. Preprint at <https://doi.org/10.1101/267096> (2018).

89. 89.

Weigert, M. et al. Content-aware image restoration: pushing the limits of fluorescence microscopy. *Nat. Methods* **15**, 1090 (2018).

[CAS](#) [PubMed](#) [Google Scholar](#)

90. 90.

Nehme, E. et al. DeepSTORM3D: dense 3D localization microscopy and PSF design by deep learning. *Nat. Methods* **17**, 734–740 (2020).
An end-to-end optimization approach for point spread function engineering and neural-network-based locations for 3D fluorescence superresolution microscopy.

[CAS](#) [PubMed](#) [Google Scholar](#)

91. 91.

Liu, T. et al. Deep learning-based super-resolution in coherent imaging systems. *Sci. Rep.* **9**, 3926 (2019).

[ADS](#) [PubMed](#) [PubMed Central](#) [Google Scholar](#)

92. 92.

Zhang, H. et al. High-throughput, high-resolution deep learning microscopy based on registration-free generative adversarial network. *Biomed. Opt. Express* **10**, 1044–1063 (2019).

[PubMed](#) [PubMed Central](#) [Google Scholar](#)

93. 93.

Escudero, M. C. et al. Digitally stained confocal microscopy through deep learning. In *Proc. 2nd Intl Conf. Medical Imaging with Deep Learning* (eds Cardoso, M. J. et al.) 121–129 (PMLR, 2019).

94. 94.

Rivenson, Y. et al. Deep learning enhanced mobile-phone microscopy. *ACS Photonics* **5**, 2354–2364 (2018).

[CAS](#) [Google Scholar](#)

95. 95.

Goy, A., Arthur, K., Li, S. & Barbastathis, G. Low photon count phase retrieval using deep learning. *Phys. Rev. Lett.* **121**, 243902 (2018).

[ADS](#) [CAS](#) [PubMed](#) [Google Scholar](#)

96. 96.

Rivenson, Y. et al. Virtual histological staining of unlabelled tissue-autofluorescence images via deep learning. *Nat. Biomed. Eng.* **3**, 466–477 (2019).

[CAS](#) [PubMed](#) [Google Scholar](#)

97. 97.

Wu, Y. et al. Bright-field holography: cross-modality deep learning enables snapshot 3D imaging with bright-field contrast using a single hologram. *Light Sci. Appl.* **8**, 25 (2019).

[ADS](#) [PubMed](#) [PubMed Central](#) [Google Scholar](#)

98. 98.

Rivenson, Y. et al. PhaseStain: the digital staining of label-free quantitative phase microscopy images using deep learning. *Light Sci. Appl.* **8**, 23 (2019).

[ADS](#) [PubMed](#) [PubMed Central](#) [Google Scholar](#)

99. 99.

Mengu, D., Luo, Y., Rivenson, Y. & Ozcan, A. Analysis of diffractive optical neural networks and their integration with electronic neural networks. *IEEE J. Sel. Top. Quantum Electron.* **26**, 3700114 (2019).

[PubMed](#) [Google Scholar](#)

100. 100.

Dagenais, M., Sharfin, W. F. & Seymour, R. J. Optical digital matrix multiplication apparatus. EU patent EP0330710A1 (1988).

[Download references](#)

Acknowledgements

We thank E. Otte for help designing figures. G.W. was supported by an NSF CAREER Award (IIS 1553333), a Sloan Fellowship, by the KAUST Office of Sponsored Research through the Visual Computing Center CCF grant,

and a PECASE by the US Army Research Office. A.O. was supported by an NSF ERC (PATHS-UP) grant. S.G. acknowledges funding from the European Research Council (ERC; H2020, SMARTIES-724473) and support from the Institut Universitaire de France. S.F. was supported by the US Air Force Office of Scientific Research (AFOSR) through the MURI project (grant no. FA9550-17-1-0002). D.E. and M.S. were in part supported by the US Army Research Office through the Institute for Soldier Nanotechnologies (grant no. W911NF-18-2-0048). D.E. also acknowledges support from an NSF EAGER programme. D.A.B.M. was supported by the Air Force Office of Scientific Research (award no. FA9550-17-1-0002). P.D. acknowledges discussions and a long-term collaboration with N. Farhat.

Author information

Affiliations

1. Stanford University, Stanford, CA, USA

Gordon Wetzstein, Shanhui Fan & David A. B. Miller

2. University of California, Los Angeles, Los Angeles, CA, USA

Aydogan Ozcan

3. Laboratoire Kastler Brossel, Sorbonne Université, École Normale Supérieure, Collège de France, CNRS UMR 8552, Paris, France

Sylvain Gigan

4. Massachusetts Institute of Technology, Cambridge, MA, USA

Dirk Englund & Marin Soljačić

5. University of Münster, Münster, Germany

Cornelia Denz

6. École Polytechnique Fédérale de Lausanne, Lausanne, Switzerland

Demetri Psaltis

Authors

1. Gordon Wetzstein

[View author publications](#)

You can also search for this author in [PubMed](#) [Google Scholar](#)

2. Aydogan Ozcan

[View author publications](#)

You can also search for this author in [PubMed](#) [Google Scholar](#)

3. Sylvain Gigan

[View author publications](#)

You can also search for this author in [PubMed](#) [Google Scholar](#)

4. Shanhui Fan

[View author publications](#)

You can also search for this author in [PubMed](#) [Google Scholar](#)

5. Dirk Englund

[View author publications](#)

You can also search for this author in [PubMed](#) [Google Scholar](#)

6. Marin Soljačić

[View author publications](#)

You can also search for this author in [PubMed](#) [Google Scholar](#)

7. Cornelia Denz

[View author publications](#)

You can also search for this author in [PubMed](#) [Google Scholar](#)

8. David A. B. Miller

[View author publications](#)

You can also search for this author in [PubMed](#) [Google Scholar](#)

9. Demetri Psaltis

[View author publications](#)

You can also search for this author in [PubMed](#) [Google Scholar](#)

Contributions

G.W. conceived the idea, coordinated the writing process, wrote parts of the paper, and edited all sections. A.O., S.G., S.F., D.E., M.S., C.D., D.A.B.M. and D.P. wrote parts of the paper and provided feedback on all other parts.

Corresponding author

Correspondence to [Gordon Wetzstein](#).

Ethics declarations

Competing interests

M.S. owns stocks of Lightelligence, Inc. S.G. owns stocks of LightOn. D.E. and D.A.B.M. own stocks in Lightmatter Inc. The other authors declare no competing financial interests.

Additional information

Peer review information *Nature* thanks Geoffrey W. Burr and Nathan Youngblood for their contribution to the peer review of this work.

Publisher's note Springer Nature remains neutral with regard to jurisdictional claims in published maps and institutional affiliations.

Rights and permissions

[Reprints and Permissions](#)

About this article



Check for
updates

Cite this article

Wetzstein, G., Ozcan, A., Gigan, S. *et al.* Inference in artificial intelligence with deep optics and photonics. *Nature* **588**, 39–47 (2020).
<https://doi.org/10.1038/s41586-020-2973-6>

[Download citation](#)

- Received: 28 November 2019
- Accepted: 20 August 2020
- Published: 02 December 2020
- Issue Date: 03 December 2020
- DOI: <https://doi.org/10.1038/s41586-020-2973-6>

Comments

By submitting a comment you agree to abide by our [Terms](#) and [Community Guidelines](#). If you find something abusive or that does not comply with our terms or guidelines please flag it as inappropriate.

[Access through your institution](#)

[Change institution](#)

[Buy or subscribe](#)

This article was downloaded by **calibre** from <https://www.nature.com/articles/s41586-020-2973-6>

| [Section menu](#) | [Main menu](#) |

- Perspective
- [Published: 11 November 2020](#)

Organized crime in the fisheries sector threatens a sustainable ocean economy

- [Emma Witbooi](#)^{1,2},
- [Kamal-Deen Ali](#)³,
- [Mas Achmad Santosa](#)⁴,
- [Gail Hurley](#)⁵,
- [Yunus Husein](#)⁴,
- [Sarika Maharaj](#)⁶,
- [Ifesinachi Okafor-Yarwood](#) ORCID: orcid.org/0000-0003-4952-9979⁷,
- [Inés Arroyo Quiroz](#)⁸ &
- [Omar Salas](#)⁹

[Nature](#) volume 588, pages48–56(2020) [Cite this article](#)

- 8809 Accesses
- 1 Citations
- 129 Altmetric
- [Metrics details](#)

Subjects

- [Law](#)

- [Sustainability](#)

Abstract

The threat of criminal activity in the fisheries sector has concerned the international community for a number of years. In more recent times, the presence of organized crime in fisheries has come to the fore. In 2008, the United Nations General Assembly asked all states to contribute to increasing our understanding the connection between illegal fishing and transnational organized crime at sea. Policy-makers, researchers and members of civil society are increasing their knowledge of the dynamics and destructiveness of the blue shadow economy and the role of organized crime within this economy. Anecdotal, scientific and example-based evidence of the various manifestations of organized crime in fisheries, its widespread adverse impacts on economies, societies and the environment globally and its potential security consequences is now publicly available. Here we present the current state of knowledge on organized crime in the fisheries sector. We show how the many facets of organized crime in this sector, including fraud, drug trafficking and forced labour, hinder progress towards the development of a sustainable ocean economy. With reference to worldwide promising practices, we highlight practical opportunities for action to address the problem. We emphasize the need for a shared understanding of the challenge and for the implementation of intelligence-led, skills-based cooperative law enforcement action at a global level and a community-based approach for targeting organized crime in the supply chain of organized criminal networks at a local level, facilitated by legislative frameworks and increased transparency.

[Download PDF](#)

Main

The global community has for a number of years raised concern about the threat of criminality in the fisheries sector. In 2008, the United Nations (UN) General Assembly sounded an alarm about the “possible connection[s] between international organized crime and illegal fishing in

certain regions of the world”¹. It urged states to research the links between these two phenomena and the evidence thereof, “bearing in mind the distinct legal regimes and remedies under international law applicable to illegal fishing and international organized crime”, respectively¹. In 2019, the UN Security Council further considered transnational organized crime at sea, including crime in fisheries, a threat to international peace and security². In 2011, a comprehensive report that highlights the vulnerability of the global fishing industry to multiple crime types, many of which were organized crimes, and global evidence thereof, was produced. The report recommended a cooperative criminal law enforcement response to the problem, subsequently echoed by the UN Commission for Crime Prevention and Criminal Justice, to prevent transnational organized crime at sea³. INTERPOL established a Fisheries Crime Working Group in 2013 as a conduit for joint law enforcement operations that target transnational organized fisheries crime networks. Lessons learned were shared with the global community, including high-level politicians, at annual international symposia, which led to the adoption of a Ministerial Declaration on Transnational Organized Crime in the Global Fishing Industry (Copenhagen Declaration) in 2018. The Declaration, which is currently supported by 28 states, maps a course of global commitment to combat transnational organized fisheries crime to help to foster a sustainable blue economy.

This Perspective is a distillation of the 16th Blue Paper commissioned by the High Level Panel for a Sustainable Ocean Economy, which presents the current state of knowledge on the question of how organized crime in the fisheries sector impedes the realization of a sustainable ocean economy, including an examination of the various crime types that fall under the term ‘fisheries crime’, and what practical measures can be taken to counter this⁴.

Defining organized crime in the fisheries sector

The modern fisheries sector is, as with many other economic sectors, globalized, industrialized and integrated into the worldwide financial market; it is therefore similarly exposed to organized crime. Organized crime in the fisheries sector is not a new problem; the infamous gangster and businessman Al Capone, for instance, exploited the fishing industry for

rum running in the 1920s^{5,6}. More probably, it is a recent labelling of this phenomenon borne from the current focus on sustainable fisheries management in the context of a sustainable ocean economy that has focused attention on the role of organized crime in the emerging parallel shadow blue economy.

Numerous definitions of organized crime exist⁷. Organized crime is often associated with hierarchical, exclusive and monopolistic groups—with a strong ethnic or societal commonality—that lean towards violence, a criminal subculture or otherwise deviant behaviour⁸. A broader understanding of organized crime, which is used here, is that it consists of networks of individuals that converge and collaborate over time to commit crime, with the profile of those networks varying from loosely knit flat structures to hierarchical chains of command, with correspondingly diverse crime scripts (modus operandi)⁹. Organized criminal groups may share characteristics with ‘conventional’ businesses, such as their structure and capability¹⁰, and frequently operate in the ‘white-collar’ realm¹¹. The ability of the network to protect its operations (the ‘protection economy’)—through violence, bribery or extortion—is a common, but not necessarily defining, feature of organized crime¹².

From a legal perspective, organized crime is defined in the UN Convention on Transnational Organized Crime (the Palermo Convention)¹³ as a ‘serious crime’ (an offence “punishable by a minimum deprivation of liberty of at least four years or a more serious penalty”) committed by a structured group of three or more people with the aim of obtaining financial or other material benefits.

Although international instruments provide a clear legal benchmark of what constitutes organized crime, outside the letter of the law, both conceptually and in practice, there is often ambiguity around what is regarded as criminal behaviour and, in particular, the extent to which criminal economies associated with organized crime are normalized in any given community¹⁴.

Crime in the fisheries sector is often referred to as fisheries crime or fisheries-related crime^{15,16}. It includes a range of criminal offences throughout the value chain from the preparatory stage to at-sea activities to

landing, processing, transportation, trade and sale¹⁷. Criminal offences may thus be committed at sea, on land, at the coastal interface or in cyberspace, including through the use of the darknet¹⁸. A commonality is that the offences are profit-driven—that is, they are an economic crime¹⁵. Many offences are conducted or continued extraterritorially, on the high seas and in other areas beyond national jurisdiction, such as regional seas, making most fisheries crime cases a transnational crime with the added complication of jurisdictional obscurity¹⁹. Organized crime may take place within the fishing industry or from outside, using the sector as a cover for other criminal activities²⁰. In practice many of the same issues pertaining to law enforcement will arise regardless of whether the organized crime is embedded in the industry or not²¹.

Two recent illustrative examples show how organized crime in the fisheries sector may unfold.

The *Viking* case

In February 2016, the Indonesian Navy intercepted and detained the fishing vessel *Viking* in Indonesian waters. The vessel was the subject of an INTERPOL Purple Notice, informing law enforcement agencies globally of the network's use of numerous vessel identities and nationalities (flag states) and the unclear ownership structures of the vessel, making it difficult to identify which country had jurisdiction over the vessel and was responsible for its activities. The owners and operators of the *Viking* landed and marketed illegally caught Patagonian toothfish from the Southern Ocean for more than a decade in contravention of the multilateral fisheries management regime in the area.

The documents presented on behalf of the vessel were forgeries and the vessel thus sailed under a false identity and flag. As the authorities were unable to trace the vessel's stated owner (suggesting it was a fictional company), the vessel was determined to be stateless and subject to the Indonesian jurisdiction. In Indonesia, document forgery is punishable with imprisonment of up to six years; gillnets were also found in the hold that exceeded 2.5 km in length, which is a further infringement of the

Indonesian law and subject to imprisonment for five years and a criminal penalty of up to US\$150,000. Investigations revealed three alleged core members of the network's organization: the vessel's master, an Australian national based in Singapore (who acted as the operator of the vessel) and a Spanish national who was domiciled in South Africa (the likely beneficial owner of the vessel). The vessel operated out of ports across Southeast Asia and Africa using forged documents, landing, shipping and trading Patagonian toothfish; they sourced crew, supplies and fuel across the world.

The rock lobster case

In May 2001, after a tip-off, South African officials seized and opened a container destined for the USA that belonged to the South African company Hout Bay Fishing Industries (Pty) Ltd. The container's contents included unlawfully harvested lobster tails and Patagonian toothfish. The US authorities were alerted and subsequently intercepted the next container exported by the company to the USA. A protracted cooperative investigation followed involving South African and US authorities, culminating in the arrest of the company's main director and two others in 2003 and criminal proceedings in both South Africa and the USA.

Investigations revealed that from 1987 to 2001 the network illegally harvested large quantities of west and south coast rock lobster in South African waters for export to the USA, systematically exceeding their authorized quota. The network bribed a large number of government fisheries officers and laundered their profits in a complex web of properties and offshore banks and trusts.

In South Africa, the main director of Hout Bay Fishing Industries was charged with fraud, corruption, bribery, racketeering, violations of the fisheries law and customs offences. In the USA, the directors were found guilty of violating the Lacey Act (which renders it illegal to introduce into the USA any fish or wildlife taken in contravention of the laws of another country) as well as smuggling and conspiracy and were sentenced to imprisonment and forfeiture. A US court initially awarded the South African government around US\$22.5 million in restitution for damages²² (although investigators struggled to locate and freeze the main director's

assets to secure the restitution amount) and in September 2018, around 15 years later, a final settlement agreement of US\$7.5 million was ordered.

The above examples shed light on how the various elements of organized crime may aggregate in a sophisticated criminal operation in a commercial fisheries context and the associated law enforcement challenges. It should be noted that the examples are merely illustrative and are not intended to be representative of how organized crime in fisheries necessarily unfolds, including in the context of vulnerable coastal communities; examples of the latter are discussed below (see ‘Drug trafficking’).

Organized crime impedes a sustainable ocean economy

To reach a sustainable ocean economy requires balancing the use of the ocean space and its resources with the long-term carrying capacity of the ocean’s ecosystems²³. In line with the three-pillared concept of sustainable development under the Rio process, a sustainable ocean economy should be based on the sustainable use of the ocean from an economic, social and environmental perspective²⁴. Agenda 2030 (adopted at the UN Sustainable Development Summit on 25 September 2015) extends the three dimensions of sustainability to five areas of critical importance (namely, people, prosperity, peace, partnership and planet), which should inform synergized interagency policy interventions that will enable the achievement of the Sustainable Development Goals (SDGs).

Organized crime in the fisheries sector has the potential to severely undermine the efforts of the member states to achieve a range of SDGs, including ‘zero hunger’ (SDG2), ‘decent work and economic growth’ (SDG8), ‘responsible consumption and production’ (SDG12) and ‘life below water’ (SDG14). SDG16 (peace, justice and strong institutions) is a core enabler of the other SDGs²⁵, and the targets of SDG16 have particular resonance in the context of addressing manifestations of organized crime in fisheries²⁵. This is especially important for vulnerable coastal communities with few alternative livelihood options, which renders them susceptible to recruitment by organized criminal networks.

In the sections below, we introduce the most common serious offences that may comprise manifestations of organized crime in the fisheries sector. Illustrative examples are included to highlight how the effects of these crimes may impede the pursuit of a sustainable ocean economy. The cited examples underscore how the various types of crimes interact and how these crimes, when they converge in the real world—particularly in vulnerable communities—may give rise to a range of complex adverse impacts.

Fraud

A large amount of documentation is produced along the fisheries value chain, which generates considerable potential for fraud (that is, the deliberate misrepresentation or concealing of facts for undue benefit)^{[17](#)}. For example, in the *Viking* case, false vessel registration documents were submitted at port, comprising text that had clearly been cut and pasted from Google translate and using ordinary word-processing software^{[19](#)}. Fishing vessel identity fraud occurs when a vessel's identity is changed by, for example, not flying the correct flag at port or by physically hiding a vessel's name to render it anonymous^{[19](#)}. This is associated with 'flag hopping', a pattern of re-registering a vessel with new flag states to confound investigations into its illegal operations, as occurred with the *Viking*^{[19](#)}.

Fraudulent practices harm the reputation of both the legitimate fishing industry and the flag state in question. Furthermore, fraudulent fishing licences deprive coastal states of revenue from the legitimate allocation of fishing rights.

On the basis of fraudulent landing certificates, Trinidad and Tobago is cited as the world's sixth largest shark fin exporter to Hong Kong^{[26](#)}; the fins, in fact, are landed by foreign fishing vessels and merely transit Trinidad and Tobago ports (Republic of Trinidad and Tobago Fisheries Division, personal communication), contributing to the global international illegal trade of shark fins^{[27](#)}. In 2014, Trinidad and Tobago was also cited by the Convention for the Conservation of Antarctic Marine Living Resources (CCAMLR) as trading in Patagonian toothfish, which is in conflict with the region's fisheries management agreement; however, it was discovered that

the trade documents attached to the toothfish exports to Canada that cited Trinidad and Tobago as the port of origin were fraudulent. Fraudulent practices can also give rise to food hygiene risks. At landing, for example, false customs and health documentation can disguise the origin of the catch or the flag of the vessel to avoid paying import tariffs or complying with food hygiene regulations^{[17](#)}.

In some instances, fish and fish products are fraudulently labelled to avoid paying higher customs duty on high-value species, enabling tax crime^{[28,29](#)} and thereby depriving coastal states of a further stream of economic revenue.

Tax crime and money laundering

The fisheries sector lends itself to tax crime given the ease with which criminals can change a vessel's country of origin and identity and use fictitious companies as registered vessel owners; this facilitates channelling profits to shell companies in tax havens to avoid paying tax where the profit was generated^{[19](#)}. Tax havens (secrecy jurisdictions) are jurisdictions that lack transparency around the beneficial ownership of bank accounts and companies, making it particularly difficult to identify and prove tax crimes.

Tax crime covers a range of violations of tax and revenue rules that are criminalized in law. The loss of tax revenue through tax crimes in fisheries is estimated to be considerable, which severely undermines the development benefits of the sector and particularly adversely affects states in the Global South^{[28](#)}. In Indonesia, an audit of 187 fishing companies by the Tax Directorate General in 2016 identified potential unpaid tax revenues of around IDR235 billion (more than US\$16 million). The introduction of law enforcement and policy reform in Indonesia against fisheries crime has contributed to a marked increase in tax revenue from the fisheries sector (US\$113 million in 2018)^{[30](#)} (along with an increase in fish stocks^{[31,32](#)}).

Money laundering—the intentional concealing or disguising of the illicit origins of the proceeds of crime^{[13](#)}—is a type of tax crime and may also be an indication of corruption. Organized criminal networks engage in money laundering in the fisheries sector to integrate the proceeds of crimes

committed along the fisheries value chain, or the proceeds from illicit activities outside the sector³³, into the legitimate economy²⁸. Money laundering hampers investigations into organized crime in the fisheries sector and hinders prosecution, including asset recovery, forfeiture of the proceeds of the crime and restitution of illicit gains. In Russia, for instance, the ‘crab mafia’³⁴ has been linked to money laundering (as well as illegal fishing and even assassinations of high-ranking public officials and competitors)³⁵. Many offences committed by organized crime groups in fisheries are ‘predicate offences’ (that is, offences that are a component of a ‘primary’ crime) to money laundering. In Indonesia, fisheries crime is cited as a predicate offence under the Prevention and Eradication of Money Laundering (Anti Money Laundering) Law³⁶.

Corruption

Although there is substantial anecdotal evidence of corruption in the fishing industry, and it is suspected to be an enabling factor of many other crimes in the sector, there is limited formal literature, and few decided cases, on the subject¹⁵. Corruption is the giving, soliciting or receiving of any undue advantage that is aimed at causing an official to act or refrain from acting³⁷. This can include, for example, political figures or senior government officials using their positions to influence the allocation of fishing licences to companies in which they have a personal business interest (that is, the abuse of function)^{17,38,39}. An illustrative case that is currently under investigation involves an Icelandic fishing company that allegedly used a bank of a neighbouring country and shell companies in the Pacific to channel bribes to obtain fishing licences in Namibia⁴⁰.

Corruption may take the form of bribes paid to reduce penalties⁴¹, to ignore illegal harvesting of fish^{15,17} or to endorse landing data that are clearly false, as occurred in the rock lobster case. Bribery may extend throughout the criminal supply chain, as in a San Diego case in which it was alleged that a US company brought approximately US\$17 million worth of sea cucumber from Mexico into the USA by illegally bribing officials along the entire supply chain^{17,42,43}.

Corruption in the fisheries sector diverts the revenue that is due to states to the shadow economy and severely undermines advancement towards achieving SDG16, in particular the goal to substantially reduce corruption and bribery.

Drug trafficking

Fishing vessels are ideal modes of transport for the movement of drugs given their legitimate presence at sea, the lack of transparency around their movement, identity and ownership, and their ability to tranship and access small harbours. The use of fishing vessels to facilitate drug trafficking (the illicit trade of substances that are subject to drug prohibition laws⁴⁴) is well documented, as fishing vessels can be used as mother ships from which smaller vessels traffic drugs, as support vessels for go-fast boats transiting trafficking routes (for example, in the Caribbean) or as smaller vessels that can traffic drugs directly to and from coastal landing sites and tranship the drugs to mother ships beyond coastal jurisdiction²⁰, for example in the Gulf of Guinea⁴¹.

Fishing vessels may traffic drugs in conjunction with transporting other illicit goods as well as with the smuggling of migrants. In Trinidad and Tobago, for example, artisanal fishing vessels transport drugs and guns from Venezuela to Trinidad and Tobago as well as illegal migrants and, in Jamaica, fishing canoes transport marijuana to Haiti where it is traded for illegal weapons (the ‘drugs-for-guns’ trade) or cocaine^{45,46,47}. In the Gulf of Guinea, in 2006, a fishing vessel—the MV *Benjamin* flying a Ghanaian flag—trafficked about 78 parcels (2,340 kg) of cocaine into Ghana labelled as shrimps⁴⁸.

There is evidence of a close connection between poaching of some high-value species and drug trafficking networks in some parts of the world. In South Africa, for example, poached abalone is bartered with local gangs for the ingredients to manufacture the synthetic drug Mandrax as part of organized criminal networks that illegally export abalone to the East^{49,50}. In Mexico, an intricate transnational poaching, drug trafficking and human trafficking network controls the supply chain of illegally harvested Totoaba bladders, which are exported to China^{51,52,53}. In Colombia, organized drug

trafficking in the fisheries sector interfaces with a range of inter-related offences including the trafficking of illegal arms, human trafficking, smuggling of fuel and other contraband, large-scale illegal fishing and wildlife trafficking, the response to which requires coordinated operations between the national police, navy and air forces⁵⁴.

The influx of drugs through sea routes, often in conjunction with illicit arms, appears to have a range of negative effects on the coastal communities through which they transit, including a rise in the levels of local violence and associated increased security costs for local businesses (for example, in Trinidad and Tobago⁵⁵), weakened social cohesion and sense of security (for example, in the Yucatán Peninsula (Mexico), associated with the illegal sea cucumber fishery)⁴² and increased gang-related activity, for example, in Jamaica^{47,56,57,58}. In South Africa, research indicates that remote coastal communities, such as Buffeljagsbaai, are under siege by organized criminal gangs that illegally harvest abalone on their doorsteps^{50,59}, with women in the woman-lead households becoming accomplices to organized poaching operations with the result that they are subject to criminal prosecution⁵⁹. Given the central role of communities in the supply chain of organized criminal networks, a community-based approach to complement a law enforcement response is arguably valuable and the community, similarly, has a potential preventative role^{59,60,61,62}.

Crime in the labour market

Forced labour—that is, work or services exacted from a person under the threat of a penalty and for which the person did not offer himself or herself voluntarily⁶³—is increasingly highlighted as pervasive in the fisheries sector globally. It is often a consequence of human trafficking⁶⁴ or ‘trafficking in persons’ (that is, the procuring of and trading in human beings for the purposes of exploitation)¹³. The problem is documented in a growing body of literature^{65,66} and is increasingly exposed in the media. For example, in 2017, employees of a Scottish family-owned company operating a fleet of scallop dredgers were arrested in southern England after nine individuals who had been trafficked were found on one of their vessels⁶⁷. In the port of Puntarenas, Costa Rica, police rescued 36 Asian

individuals who had been subjected to labour exploitation on two fishing boats in 2014, arresting four individuals who were charged with human trafficking offences⁶⁸. In the fishing industry, indicators of forced labour include deception, physical and sexual violence, intimidation, retention of identity documents, withholding of wages, debt bondage and abusive working conditions⁶⁴. Recruitment agencies play a central part in facilitating human trafficking for forced labour⁶⁶. In 2016, a foreign network operating out of north Norway in the Barents Sea crab fisheries was identified as making use of forced labour^{69,70}; allegedly a Seychelles recruitment agency, together with Norwegian port agents, facilitated the smuggling of migrant fishers from Indonesia to Norway.

Criminal networks in fisheries use forced labour to cut costs and boost profits⁷¹. In addition to the implications for human rights, this results in unfair competition with legal operators, which, in turn, can influence legitimate fishing companies to breach domestic crewing regulations in an attempt to remain competitive, such as in the Norwegian snow-crab sector^{69,70,72} and in Russia⁷³.

Fisheries offences

Illegal fishing—fishing in violation of fisheries laws and measures—may also be a criminal offence if it is criminalized under the law of the relevant jurisdiction. Some jurisdictions have severe criminal penalties for fisheries offences, such as Norway, in which grave offences attract a prison sentence of up to six years plus asset forfeiture. Illegal fishing is criminalized in many jurisdictions around the world, including Ghana, Indonesia and South Africa^{74,75}. In practice, regardless of whether or not illegal fishing has been criminalized in a jurisdiction, illegal, unreported and unregulated (IUU) fishing is a strong risk indicator of fisheries crime^{76,77}.

The adverse effects of large-scale overfishing are well documented⁷⁸. This includes the severe negative impacts on the state of commercially exploitable fish stocks: 2009 data estimated that 18% of the global catch, valued at US\$10–23.5 billion, between 2000 and 2003 was lost to illegal or unreported fishing⁷⁹. The latest figures of the UN Food and Agriculture

Organization (2015 data) estimate that 59.9% of the world's commercial fish stocks are now fully fished and a third of the global fish stocks are overexploited⁸⁰. As fish stocks decline, the resource becomes more valuable, attracting increasing involvement of transnational organized crime syndicates²⁰. Successful prosecution of organized networks can have positive effects on the targeted stocks, as illustrated by the rock lobster case, which resulted in the marked recovery of the targeted species (south coast rock lobster)⁸¹.

Large-scale illegal fishing can cause severe economic loss to coastal states: the combined annual economic losses due to illegal fishing to Mauritania, Senegal, The Gambia, Guinea Bissau, Guinea and Sierra Leone, for example, are estimated at US\$2.3 billion^{48,82}. A recent global study⁸³ estimates that between 7.7 and 14.0 million metric tons of unreported fish catches are potentially traded illicitly each year, suggesting that gross revenues of between US\$8.9 and US\$17.2 billion are annually redirected out of the legitimate market through illicit trade. Asia, Africa and South America account for approximately 85% of total catch losses to likely illicit trade globally. Africa is estimated to experience between US\$7.6 and US\$13.9 billion and US\$1.8 and US\$3.3 billion in losses annually in economic and income impacts, respectively, owing to the redirection of catches from legitimate to illicit seafood trade⁸³.

In fishing communities with few alternative livelihood options, low-level poaching may change into, or co-exist alongside, organized criminal activity. In South Africa, this is evident in the context of abalone and west coast rock lobster fishing, where the boundaries between 'protest poaching', opportunistic poaching and facilitation of, or involvement in, organized criminal activity are porous and often overlap⁵⁹. The overexploitation of west coast rock lobster⁸⁴, for example, has led to thousands of subsistence fishers being unable to secure sufficient quotas with the result that some have turned to illegal alternative-income-generating activities⁸⁵.

The UN Special Rapporteur on the Right to Food⁸⁶ has underscored the importance of curtailing illegal fishing to prevent further adverse effects on food security. Fisheries provide an estimated 17% of animal protein consumed worldwide, with the highest per capita consumption in

developing small-island states⁸⁰. In the West African region of the Gulf of Guinea, where around 40% of the population resides in coastal areas, fish is the predominant (and sometimes, only) source of animal protein consumed in coastal communities⁸⁷. In Jamaica, where large-scale overfishing has left most reef fish stocks overexploited⁸⁸, the country is almost entirely dependent on imported fish for domestic consumption.

The marine environment and associated ecosystems may also be negatively affected by organized crime in fisheries: piracy and armed robbery at sea in the Gulf of Guinea pose threats to the marine environment because of the risk of oil or chemical spills caused by the use of destructive weapons to attack vessels and the transfer of the targeted vessel's cargo⁸⁹. In Nigeria, some local fishers struggling to sustain their livelihoods engage in illegal fishing in the vicinity of oil pipeline installations, which risks causing oil leaks and marine pollution⁹⁰. In Mexico, fishers adversely affected by the poorly regulated governmental conservation measures in the Gulf of California have turned to totoaba poaching because of the lack of legitimate alternative livelihoods⁵². The use of gill nets in this illegal activity has brought the vaquita porpoise (caught as bycatch) to the brink of extinction and resulted in severe damage to the large marine ecosystem of the Upper Gulf of California^{51,91}. Illegal dynamite ('blast') fishing, associated with explosives trafficking, off the Tanzanian coast is highly destructive to the affected marine habitat, including coral reefs, and fish stocks, and has broad food security ramifications^{92,93}.

Smuggling

The fishing industry provides ideal cover for smuggling of otherwise legal goods from one jurisdiction to another in violation of the law (often to avoid customs duties). In Ecuador, for example, artisanal fishers smuggle subsidized Ecuadorian fuel to the neighbouring coast of Colombia, where it is sold at considerable profit⁹⁴ and Trinidad and Tobago fishing vessels have been implicated in the illegal trade of fuel. Ghana is reportedly at risk of losing about GHS1.5 billion (US\$300 million) to the smuggling of fuel, which is trafficked by fishing vessels and canoes⁹⁵. Fuel is often smuggled

alongside illicit goods, such as drugs, illegal weapons and illegally harvested fish, as well as people⁹⁴.

The use of fishing vessels to smuggle migrants (that is, to facilitate or assist migrants to enter a country illegally for financial or material benefit¹³) is alleged to be prevalent, but is less well documented formally. The public media reports that artisanal fishing vessels are the mode of transport to traffic migrant women from South America to Trinidad and Tobago, where some are forced into prostitution and others are transported to the USA⁹⁶. There are also indications that fishing vessels are linked to migrant smuggling in the Mediterranean Sea^{20,97,98,99}, Australia¹⁰⁰ and Thailand¹⁰¹.

Security threats at sea

Various offences that occur at sea present a threat to peace and security; this can include offences falling within the ambit of organized crime in fisheries. ‘Fisheries conflicts’—which may arise from a combination of factors, including illegal fishing (along with climate change and food security concerns)—are recognized as a potential threat to maritime security and livelihoods and there is a growing body of literature on the topic^{90,102,103,104}. In the Gulf of Guinea, numerous organized criminal activities at sea threaten peace and security, including piracy and armed robbery, kidnapping for ransom, fuel and gas robbery and smuggling, drugs and arms trafficking and illegal fishing². This adversely affects the economic bases of the region’s states through, for example, increased insurance premiums for cargo vessels, which hinders the movement of goods and services and results in lost income for businesses and governments and an increase in the price of goods and services^{105,106}. In Nigeria, for example, piracy and armed robbery at sea is associated with a diminished contribution from the domestic fishing sector to the gross domestic product (GDP) as fewer licensed fee-paying vessels are willing to go to sea^{90,107}. Furthermore, coastal fishers who fear putting out to sea in Nigeria due to violent attacks from illegal fishing vessels have been recruited by organized criminal networks engaging in armed robbery at sea and oil smuggling, and fishmongers—who are predominantly women—have in some instances turned to prostitution to make ends meet^{90,108}.

A recent Security Council Resolution expressed concern over the links between international terrorism and organized crime, including transnational organized crime at sea^{[109](#)}. The Security Council has further highlighted the complex relationship between large-scale illegal fishing and the international crime of piracy (as defined in the UN International Law of the Sea)^{[110](#)}, in Somali waters in the Indian Ocean^{[111,112,113](#)}; a similar link has been argued in the case of Southeast Asia^{[114](#)}.

Challenges and positive practices

In this section, we highlight particular challenges associated with tackling organized crime in the fisheries sector and, with reference to worldwide promising practices, we present practical opportunities for action to address these challenges.

Challenges

There are a number of globally identifiable law enforcement challenges concerning the identification, investigation and successful prosecution of organized crime in the fisheries sector. The following challenges are often highlighted in reports and outcome documents from expert group meetings and relevant international gatherings, which draw on operational experience. (1) Low national prioritization of organized crime in fisheries at political and operational levels. “In many countries, crime linked to the fisheries value chain will not be investigated because it is not seen as a major priority and it is difficult to investigate”^{[17](#)}. (2) The lack of coordination between government departments and agencies nationally and across borders^{[17,19](#)}. (3) Inadequate criminal and criminal procedural legislative frameworks^{[17,19](#)}. (4) The lack of clarity of jurisdiction at sea and extraterritorial jurisdiction: as a result, fisheries crime at sea (beyond national waters) is often not investigated or prosecuted^{[19](#)}. (5) The lack in capacity and skills of law enforcement agencies and the criminal justice system, particularly around associated financial investigations^{[15,20,115](#)}. (6) The lack of transparency in the fisheries sector and financial sector^{[19,20,115](#)}.

Positive practices

The complexity of organized crime in fisheries, the potential harm it may cause and the resources needed to combat it all suggest that any strategy should place great emphasis on crime prevention. In this regard, identifying socio-economic drivers of criminal activities is key, including increasing knowledge of demand-driven markets, along with crime-disruption strategies and robust legislative frameworks that criminalize serious offences and attach sufficiently deterrent penalties. As evidence suggests that many criminal networks have already manifested themselves in the fisheries sector, the section that follows thus focuses on enforcement responses, rather than preventative measures. That said, it is worth underscoring that in vulnerable coastal communities, in particular, strengthening the inhabitants' capacity to withstand the intrusion of organized criminal activities is a valuable complement to any law enforcement response^{[59](#)}. As administrative measures alone are inadequate to deter the illicit operations of criminal networks—the networks absorb such penalties as part of their business models^{[76](#)}—it is important to identify effective means to address their activities, underpinned by robust cooperative criminal law enforcement and criminal procedural efforts. In the following sections, we describe some of the promising practices globally in this regard that, subject to critical analyses, could potentially offer ideas for practical ways forward.

Interagency cooperation at national level

Countries use different cooperative interagency enforcement models to address organized crime in fisheries. Indonesia, for example, uses a ‘single-roof’ enforcement agency that brings together five enforcement agencies (the Ministry of Marine Affairs and Fisheries, the navy, the marine police, the coast guard and the Attorney-General’s Office) under the Minister of Marine Affairs and Fisheries; Norway’s National Advisory Group on Fisheries Crime and IUU Fishing (Fiskeriforvaltningens Analysenettverk) brings together representatives from the coast guard, the police, fisheries, maritime, tax, customs and labour authorities regularly to discuss fisheries cases; and Tanzania’s multi-agency task team on environmental and wildlife crime Multi Agency Task Team, led by the Ministry of Home Affairs along with the Ministries of Livestock and Fisheries Development, the Ministry of Energy and Minerals, the Ministry of Natural Resources and the Tanzanian

police force, coordinates efforts to target fisheries crime in the region⁹². The Copenhagen Declaration underscores the necessity of effective interagency cooperation; critical research on suitable governance models is therefore important.

Regional and global cooperation

Given the transnational nature of organized crime in the fisheries sector, cross-border cooperation is imperative in investigations, including through the use of mutual legal assistance, INTERPOL tools and judicial requests to cooperate with other countries. The value of such collaboration was highlighted in the *Viking* case, in which Indonesia invited a multilateral team of experts and INTERPOL to help to facilitate information sharing and analysis. Successful cross-border investigative cooperation also facilitated prosecution in the rock lobster case.

Law reviews and reforms

Many jurisdictions criminalize fisheries offences and have harsh deterrent penalties. For example, the Ghanaian courts may impose a maximum penalty of two years' imprisonment for the illegal exportation of fish under the terms of the 2002 Fisheries Act and in South Africa violations of most provisions of the 1998 Marine Living Resources Act are a criminal offence, attracting a fine of up to ZAR5 million (US\$338,000). Legislation criminalizing other offences that fall under the fisheries crime umbrella is also valuable, such as Indonesian Law 25/2003 on the Crime of Money Laundering, as is organized crime legislation such as South Africa's 1998 Prevention of Organized Crime Act, which criminalizes racketeering and triggers asset forfeiture. The introduction of legislation against human rights abuse on fishing vessels is gaining traction: for example, in February 2019, Thailand ratified the International Labour Organization (ILO) Work in Fishing Convention No. 188 with a view to amend the existing laws in lights of its provisions¹¹⁶.

Capacity building and skills training in the criminal justice system

Capacity building can hone enforcement efforts against organized crime in fisheries. Indonesia and Norway, for instance, offer professional accredited training through the International FishFORCE Academy of Indonesia (established in December 2016) and the Norwegian Police University College (since 2010), respectively. The enhancement of skills is particularly valuable to conduct financial investigations that pertain to organized criminal activities in the fisheries sector^{[15](#)}.

Information exchange and awareness raising

International networks that facilitate information exchange (mindful of data-protection laws and principles)^{[117](#)} and intelligence-led law enforcement efforts enhance law enforcement skills to address organized crime in fisheries. International government organizations and international knowledge-sharing symposiums can facilitate this. Legitimate businesses in the fishing industry should also be made aware of organized crime in the sector to encourage corporate social responsibility^{[118](#)} practices that improve transparency in the supply chain. Illustrative examples exposed in the media —such as the 2014 revelation in *The Guardian* that the world's largest Thailand-based prawn farmer was purchasing fishmeal for its prawns from suppliers that were linked to fishing vessels that used individuals who were subjected to human trafficking for forced labour and selling the prawns to the public through top retailers^{[119](#)}—have heightened public demand for improved transparency of seafood production practices. Civil society can play a part in influencing the substantial content of corporate social responsibility practices and holding companies accountable for their implementation^{[120](#)}.

Opportunities for action

With notable exceptions, the world community remains ill-informed that transnational organized crime in fisheries is a distinct problem alongside unsustainable harvesting practices in global fisheries. States are thus largely

unaware of the most suitable legal tools to address organized crime in fisheries and, furthermore, that these measures differ from (yet compliment) instruments aimed at improved fisheries management. We suggest that states should first develop a common understanding of organized crime in the global fishing industry at a political level. Thereafter, at an operational level, they should identify and implement suitable technical and practical measures to address the challenges. Mindful of the fact that, globally, states are at various levels of understanding the problem, this should not be interpreted to mean that states should wait for official international consensus of the problem before seeking to address the matter internally. Rather, states with a sufficient grasp of the issue—such as those supporting the Copenhagen Declaration—should be encouraged to proceed to cooperatively implement suitable measures. The suggestions below are formulated as contributions towards the ‘solutions-oriented report’ of the High Level Panel for a Sustainable Ocean Economy, the content of which is guided by pragmatism, cost effectiveness and political feasibility¹²¹. To this end, they do not purport to suggest actions aimed at addressing the drivers of organized crime in fisheries; however, effectively addressing organized crime in fisheries will facilitate the achievement of a number of UN SDGs, which, in turn, may contribute to reducing the prevalence of involvement in organized crime in fisheries, particularly among vulnerable coastal communities.

In summary, to address organized crime in the fisheries sector, action in two stages is required. First, a common understanding of transnational organized crime in the fisheries sector at a global level is needed, coupled with the political will to cooperatively address the challenge. Second, political will must be translated into action by states harnessing practical tools to strengthen their law enforcement capacity to effectively tackle organized crime in the fisheries sector.

In more detail, we suggest the following actions should be taken. First, states should be encouraged initially to: (1) report to the UN General Assembly in response to the call made by UN GA Resolution 63/112 to examine connections between illegal fishing and organized crime in fisheries; (2) raise the security implications of transnational organized crime in fisheries at the UN Security Council; (3) formally support the 2018

International Declaration against Transnational Organized Crime (the Copenhagen Declaration); (4) report annually on transnational organized crime in fisheries to the UN Commission for Crime Prevention and Criminal Justice (CCPCJ) and (5) participate in regular international knowledge-sharing forums on organized crime in fisheries.

Second, at a practical level, drawing on the positive practices identified above, armed with a common understanding of the problem, and making use of best-available knowledge, states should be encouraged to strengthen national interagency cooperation, enhance cross-border cooperation and provide for enabling legal frameworks; improve the capacity and skills of criminal law enforcement; strengthen community-based crime prevention, with a focus on gendered implications, which will in turn strengthen the resilience of vulnerable coastal communities and their ability to respond to organized fisheries crime; facilitate civil society engagement with the fishing industry on corporate social responsibility; and support increased publishable research on organized crime in the fisheries sector.

Outlook

There is ample anecdotal, scientific and case-based evidence of the many manifestations of organized crime in the fisheries sector and its widespread adverse effects on economies, societies and the environment, including its broader security implications. We show that organized crime in the fisheries sector is widespread in the sense that it is not restricted to specific geographical locations but, rather, that examples are found globally. That said, criminals will tend to seek out the most vulnerable regions of the world in which to conduct their activities, and fisheries crime thus appears to affect most adversely the coastal populations of states with limited resources to prevent and combat it.

There is a noticeable knowledge deficit with regards to the scale of organized crime in the fisheries sector. To date, there is no publicly available statistical data that estimate the extent of organized fisheries crime or that map the incidents and their location at a global level. Existing scientific output and data on criminality in the fisheries sector almost exclusively describe illegal or unreported fishing, which does not take into

account the range of criminal offences that occur throughout the fisheries value chain. There is a need to gain further scientific and criminological knowledge of the dynamics and scale of organized fisheries crime and the criminal networks involved therein, including data on the offences in which the criminal networks engage, to identify, evaluate and implement the best measures to address the drivers thereof.

Organized crime in the fisheries sector has the potential to severely undermine the premises for a sustainable ocean economy with notable adverse social, economic and environmental implications. The problem is recognized as sufficiently severe to warrant states' mobilization to take political action. The rate at which support of the Copenhagen Declaration is gaining momentum—particularly among states from the Global South—attests to the fact that states are increasingly acknowledging the existence, extent and adverse impacts of organized fisheries crime. Furthermore, states acknowledge that a failure to effectively address organized fisheries crime will result in a widespread inability to fulfil, among others, the SDG16 goal of 'peace, justice and strong institutions' and, ultimately, will hinder the realization of a sustainable ocean economy. A next important step will be for states that support the Declaration to identify practical measures to operationalize their political commitments on the ground.

References

1. 1.

UN General Assembly. *Sustainable fisheries, including through the 1995 Agreement for the Implementation of the Provisions of the United Nations Convention on the Law of the Sea of 10 December 1982 relating to the Conservation and Management of Straddling Fish Stocks and Highly Migratory Fish Stocks, and related instruments*. UN Resolution A/RES/63/112 <https://undocs.org/en/A/RES/63/112> (2008).

2. 2.

UN Security Council. *Maintenance of International Peace and Security. Transnational Organized Crime at Sea as a Threat to*

International Peace and Security. 8457th Meeting of the United Nations Security Council Report No. S/PV.8457 (UNSC, 2019).

3. 3.

Commission on Crime Prevention and Criminal Justice. *Statements of Financial Implications presented to the Commission on Crime Prevention and Criminal Justice before its Consideration of Draft Resolutions at its Twentieth Session*. Report No. E/CN.15/2011/21 (UN ODC, 2019).

4. 4.

Witbooi, E. et al. *Organised Crime in the Fisheries Sector*.
<https://oceanpanel.org/blue-papers/organised-crime-associated-fisheries> (World Resources Institute, 2020).

5. 5.

Ensign, E. S. *Intelligence in the Rum War at Sea, 1920–1933* (Joint Military Intelligence College, 2001).

6. 6.

Demont, J. *Maritime Drug Smuggling and Rum-Running*.
<https://www.thecanadianencyclopedia.ca/en/article/maritime-drug-smuggling-and-rum-running> (The Canadian Encyclopedia, 17 March 2003).

7. 7.

Varese, F. in *Redefining Organized Crime: A Challenge for the European Union?* (eds Carnevale, S. et al.) 27–56 (Hart Publishing, 2017).

8. 8.

Abadinski, H. *Organized Crime* 8th edn (Thomson Wadsworth, 2007).

9. 9.

Madsen, F. *Transnational Organized Crime* (Routledge, 2009).

10. 10.

Australian Crime Commission. *Organized Crime in Australia: 2009* (Australian Government, 2009).

11. 11.

Gottschalk, P. *White-collar Criminals: Cases and Theories of Financial Crime* (Unipub, 2012).

12. 12.

Shaw, M. & Kemp, W. *Spotting the Spoilers: A Guide to Analyzing Organized Crime in Fragile States* (International Peace Institute, 2012).

13. 13.

UNODC. *United Nations Convention Against Transnational Organized Crime and the Protocols Thereto.*

<https://www.unodc.org/documents/middleeastandnorthafrica/organised>

=

[crime/UNITED NATIONS CONVENTION AGAINST TRANSNATIONAL ORGANIZED CRIME AND THE PROTOCOLS THERETO.pdf](#) (UN, 2004). This United Nations Convention—which contains the most widely accepted legal definition internationally (through state ratifications) of organized crime and includes a dedicated protocol to combat human trafficking—promotes the use of law enforcement tools, such as mutual legal assistance, to cooperatively combat transnational organized crime globally.

14. 14.

Shaw, M. *Africa's Changing Place in the Global Criminal Economy.*

<https://globalinitiative.net/wp-content/uploads/2017/09/2017-09-26->

[enact-continental-report1.pdf](#) (ENACT, 2017).

15. 15.

UNODC. *Rotten Fish: A Guide on Addressing Corruption in the Fisheries Sector.* https://www.unodc.org/documents/Rotten_Fish.pdf (UN, 2019). This guide provides an overview of the potential for corruption along the fisheries value chain and provides guidance to authorities in identifying the specific areas in their legal and regulatory frameworks that are susceptible to corruption, and how to address those weaknesses to reduce its impact and develop safeguards to prevent its return.

16. 16.

FAO. *Draft: Guidance on Social Responsibility in Fisheries and Aquaculture Value Chains* (FAO, 2019).

17. 17.

UNODC. *Stretching the Fishnet: Identifying Opportunities to Address Fisheries Crime.* <https://bluejustice.org/publication/stretching-the-fishnet-addressing-crimes-in-the-fisheries-value-chain/> (UN, 2017).

18. 18.

Wright, J. Darknet usage in the illegal wildlife trade. Preprint at <https://doi.org/10.31235/osf.io/fgr9d> (2019). There is a growing body of literature on the role of the darknet in the illicit trade of wildlife such as this recent article; there is a paucity of literature that specifically pertains to illicit flows from organized crime in the fisheries sector.

19. 19.

North Atlantic Fisheries Intelligence Group. *Chasing Red Herring: Flags of Convenience, Secrecy and the Impact on Fisheries Crime Law Enforcement* (NA-FIG, 2017). This report draws on case examples

to highlight how the lack of transparency around beneficial ownership of fishing vessels and associated corporate financial bodies hinders investigations into organized fisheries crime.

20. 20.

UNODC. *Transnational Organized Crime in the Fishing Industry: Focus on: Trafficking in Persons Smuggling of Migrants Illicit Drugs Trafficking*. https://www.unodc.org/documents/human-trafficking/Issue_Paper_-_TOC_in_the_Fishing_Industry.pdf (UN, 2011). This comprehensive study highlights the vulnerability of the fishing industry to transnational organized fisheries crime, chronicles examples thereof globally and recommends addressing the problem using a criminal law enforcement approach.

21. 21.

Telesetsky, A. Laundering fish in the global undercurrents: illegal, unreported, and unregulated fishing and transnational organized crime. *Ecol. Law Q.* **41**, 939–996 (2015).

[Google Scholar](#)

22. 22.

United States v. Bengis et al. US District Court Southern District of New York S 1 03 Crim. 0308 (LAK) (2013).

23. 23.

Kraemer, R. A. *A Sustainable Ocean Economy, Innovation and Growth: A G20 Initiative*. CIGI Policy Brief No. 113 <https://www.cigionline.org/publications/sustainable-ocean-economy-innovation-and-growth-g20-initiative> (Centre for International Governance Innovation, 2017).

24. 24.

UN. *The Future We Want: Outcome Document of the United Nations Conference on Sustainable Development.*
<https://sustainabledevelopment.un.org/content/documents/733FutureWeWant.pdf> (UN, 2012).

25. 25.

Kercher, J. Fisheries crime and the SDGs: the call and the tools for interagency cooperation. *FishCRIME 2018* (UN, 2018). **This presentation outlines the value of locating and addressing organized crime in the fisheries sector in the context of government efforts to achieve the UN SDGs, with particular emphasis on institutional cooperation.**

26. 26.

The Pew Charitable Trusts Environmental Group. *Navigating Global Shark Conservation: Current Measures and Gaps.* (Pew, 2012).

27. 27.

Clancy, N. *Peru Wildlife Agency Eases Export of Illegal Shark Fins.* <https://www.insightcrime.org/news/brief/peru-wildlife-agency-eases-export-of-illegal-shark-fins/> (InSight Crime, 2019). **This report describes the links between illegal shark fin trade and organized crime.**

28. 28.

Organization for Economic Cooperation and Development. *Evading the Net: Tax Crime in the Fisheries Sector.*
<http://www.oecd.org/ctp/crime/evading-the-net-tax-crime-fisheries-sector.pdf> (OECD, 2013). **The extent, nature and implications of tax crime that takes place in the global fishing industry are documented.**

29. 29.

EUROPOL. *Fraud on a Plate: Over 3 600 Tonnes of Dangerous Food Removed from Consumer Market.*

<https://www.europol.europa.eu/newsroom/news/fraud-plate-over-3-600-tonnes-of-dangerous-food-removed-consumer-market>

(EUROPOL, 2018).

30. 30.

Indonesian Ministry of Finance. *Government Revenue Model* (Indonesian Ministry of Finance, 2019).

31. 31.

Ministry of Maritime and Fisheries Affairs Indonesia. *Sea for the Future of the Nation* (Ministry of Maritime and Fisheries Affairs Indonesia, 2018).

32. 32.

Cabral, R. B. et al. Rapid and lasting gains from solving illegal fishing. *Nat. Ecol. Evol.* **2**, 650–658 (2018).

[Article](#) [PubMed](#) [Google Scholar](#)

33. 33.

Parks, I. in *Following the Proceeds of Environmental Crime: Forests, Fish and Filthy Lucre* (ed. Rose, G.) 116–139 (Routledge, 2014).

34. 34.

Akhmirova, R. Глава Росрыболовства Андрей Крайний: мы побеждаем мафию! (Head of the Federal Agency for Fishery Andrei Kainy: we are defeating the mafia!) *Sobesednik Ru*
<https://sobesednik.ru/politika/20120709-glava-rosrybolovstva-andrei-krainii-my-pobezhdaem-mafiyu> (2012).

35. 35.

Otto, R. S. in *King Crabs of the World: Biology and Fisheries Management* (ed. Stevens, B. G.) (CRC, 2014).

36. 36.

Husein, Y. in *Following the Proceeds of Environmental Crime: Forests, Fish and Filthy Lucre* (ed. Rose, G.) 71–80 (Routledge, 2014).

37. 37.

UN. *United Nations Convention Against Corruption*.
https://www.unodc.org/documents/brussels/UN_Convention_Against_Corruption.pdf (UN, 2004).

38. 38.

Standing, A. *Corruption and Commercial Fisheries in Africa*. CMI Institute U4 Brief 23 <https://www.cmi.no/publications/3189-corruption-and-commercial-fisheries-in-africa> (CMI Institute, 2008).

39. 39.

Standing, A. *Corruption and State-Corporate Crime in Fisheries*. CMI Institute U4 Brief 15 <https://www.cmi.no/publications/5589-corruption-and-state-corporate-crime-in-fisheries> (CMI Institute, 2015).

40. 40.

Wilhjálmsson, I. F. An Icelandic fishing company bribed officials in Namibia and used Norway's largest bank to transfer 70 million dollars to a tax haven. *Stundin* <https://stundin.is/grein/9920/> (12 November 2019).

41. 41.

INTERPOL. *Study on Fisheries Crime in the West African Coastal Region* (INTERPOL, 2014).

42. 42.

Kaplan-Hallam, M., Bennett, N. J. & Satterfield, T. Catching sea cucumber fever in coastal communities: conceptualizing the impacts of shocks versus trends on social-ecological systems. *Glob. Environ. Change* **45**, 89–98 (2017).

[Article](#) [Google Scholar](#)

43. 43.

US Attorney's Office. Three charged with illegal trafficking of \$17 million worth of sea cucumbers. <https://www.justice.gov/usao-sdca/pr/three-charged-illegal-trafficking-17-million-worth-sea-cucumbers> (US Department of Justice, 2017).

44. 44.

UNODC. *Drug Trafficking*. <https://www.unodc.org/unodc/en/drug-trafficking/index.html> (UN, 2019).

45. 45.

Bureau for International Narcotics and Law Enforcement Affairs. *2018 International Narcotics Control Strategy Report* Vol. I <https://www.state.gov/2018-international-narcotics-control-strategy-report/> (US Department of State, 2018).

46. 46.

Neil, J. A. *IUU Fishing: A Gateway to Transnational Crimes in Jamaica*. MSc thesis, World Maritime Univ. (2018).

47. 47.

Witbooi, E. *Criminality and Resilience: Rocky Point, Jamaica*. Research Report <https://globalinitiative.net/wp-content/uploads/2020/02/Jamaica-report.26.02.v1.pdf> (Global Initiative Against Transnational Organized Crime, 2020).

48. 48.

Ali, K.-D. *Maritime Security Cooperation in the Gulf of Guinea: Prospects and Challenges* (Brill/Nijhoff, 2015). **This book provides a comprehensive, in-depth analysis of maritime security prospects and challenges in the Gulf of Guinea.**

49. 49.

Steinberg, J. *The Illicit Abalone Trade in South Africa*. ISS Paper No. 105 (Institute for Security Studies, 2005).

50. 50.

de Greef, K. & Raemaekers, S. *South Africa's Illicit Abalone Trade: An Updated Overview and Knowledge Gap Analysis*.
<https://www.traffic.org/site/assets/files/8469/south-africas-illicit-abalone.pdf> (Traffic International, 2014). **This report provides a synthesis of knowledge about South Africa's illegal abalone fishery, drawing on both available literature and unpublished research spotlighting the history, drivers, impacts and modus operandi of this country's illicit abalone trade.**

51. 51.

Alvarado Martínez, I. & Martínez, E. R. in *Green Crime in Mexico: A Collection of Case Studies* (eds Arroyo Quiroz, I. & Wyatt, T) 149–170 (Palgrave Macmillan, 2018).

52. 52.

Crosta, A., Sutherland, K., Talerico, C., Layolle, I. & Fantacci, B. *Operation Fake Gold. The Totoaba Supply Chain – From Mexico's Totoaba Cartels to China's Totoaba Maw Wholesalers – An Illegal Trade Killing the Vaquita*. <http://earthleagueinternational.org/wp-content/uploads/2018/07/EAL-Operation-Fake-Gold-Final.pdf> (Elephant Action League, 2018).

53. 53.

Miranda, F. Ligan al crimen organizado con extinción de vaquita marina. (Extinction of vaquita marina linked to organized crime.) *Milenio* <https://www.milenio.com/cultura/ligan-crimen-organizado-extincion-vaquita-marina> (1 January 2018).

54. 54.

Armada de Colombia. Activación de la Fuerza de Tarea contra el Narcotráfico en el Caribe. (Activation of the Task Force against Drug Trafficking in the Caribbean.) <https://www.armada.mil.co/es/content/activacion-de-la-fuerza-de-tarea-contra-el-narcotrafico-en-el-caribe> (2015).

55. 55.

Sutton, H. in *The Cost of Crime and Violence: New Evidence and Insights in Latin America and the Caribbean* (ed. Jaitman, L.) Ch. 7 (Inter-American Development Bank, 2017).

56. 56.

Fisher, H. Rocky Point residents beg for peace. *The Jamaica Star* (13 April 2016).

57. 57.

Robinson, C. It's a 'rocky road': gangsters make life miserable for residents of once-peaceful fishing village. *The Jamaica Gleaner* (15 January 2017).

58. 58.

Leslie, G. *Confronting the Don: The Political Economy of Gang Violence in Jamaica* (Small Arms Survey, 2010).

59. 59.

Isaacs, M. & Witbooi, E. Fisheries crime, human rights and small-scale fisheries in South Africa: a case of bigger fish to fry. *Mar. Policy* **105**, 158–168 (2019). **Using empirical research in South Africa, this paper highlights the adverse impacts of organized crime in fisheries on vulnerable coastal communities, with a particular focus on gendered implications, and discusses potentially suitable law enforcement approaches to address the problem.**

[Article](#) [Google Scholar](#)

60. 60.

Hübschle, A. & Shearing, C. *Ending Wildlife Trafficking: Local Communities as Change Agents*. <http://globalinitiative.net/wp-content/uploads/2018/08/TGIATOC-Wildlife-Trafficking-Report-WEB-4.pdf> (Global Initiative Against Transnational Organized Crime, 2018).

61. 61.

Cooney, R., Roe, D. Dublin, H. & Booker, F. *Wild Life, Wild Livelihoods: Involving Communities in Sustainable Wildlife Management and Combating Illegal Wildlife Trade* (UN Environment Programme, 2018).

62. 62.

Hauck, M. & Sweijd, N. A. A case study of abalone poaching in South Africa and its impact on fisheries management. *ICES J. Mar. Sci.* **56**, 1024–1032 (1999).

[Article](#) [Google Scholar](#)

63. 63.

International Labour Organization. *Co29 - Forced Labour Convention, 1930* (No. 29). Article 2 <https://www.ilo.org/dyn/normlex/en/f?>

[p=NORMLEXPUB:12100:0::NO::P12100_ILO_CODE:C029](#) (ILO, 1930).

64. 64.

International Labour Organization. *Fishers First: Good Practices to End Labour Exploitation at Sea.*

[\[https://www.ilo.org/wcmsp5/groups/public/---ed_norm/---declaration/documents/publication/wcms_515365.pdf\]\(https://www.ilo.org/wcmsp5/groups/public/---ed_norm/---declaration/documents/publication/wcms_515365.pdf\)](#) (ILO, 2016).

This report by the ILO presents analyses of labour exploitation and includes good practices and interventions to help to eradicating forced labour and other forms of labour exploitation in the global fishing industry.

65. 65.

Stringer, C. & Harre, T. Human trafficking as fisheries crime? An application of the concept to the New Zealand context. *Mar. Policy* **105**, 169–176 (2019).

[Article](#) [Google Scholar](#)

66. 66.

Surtees, R. Trapped at sea. Using the legal and regulatory framework to prevent and combat the trafficking of seafarers and fishers. *Groningen J. Int. Law* **1**, 91–151 (2013). **This article provides a comprehensive overview of the chain of illegalities associated with human trafficking for forced labour in the fisheries sector with use of global illustrative examples.**

[Article](#) [Google Scholar](#)

67. 67.

Lawrence, F. & McSweeney, E. UK police rescue nine suspected victims of slavery from British trawlers. *The Guardian* (December 12 2017).

68. 68.

Zueras, D. Costa Rica: (in)human trafficking. *IPS News* <http://www.ipsnews.net/2010/04/costa-rica-inhuman-trafficking/> (15 April 2010).

69. 69.

Thorenfeldt, G. et al. The deadliest catch. *Dagbladet* <https://www.dagbladet.no/arkivert/magasinet/the-deadliest-catch/70534450> (11 December 2018).

70. 70.

Gedde-Dahl, S., Thorenfeldt, G., Stang, L. & Strømman, O. De skjulte slavekontraktene. (The Hidden Slave Contracts.) *Dagbladet* <https://www.dagbladet.no/nyheter/de-skjulte-slavekontraktene/70460627> (17 November 2018).

71. 71.

Tickler, D. et al. Modern slavery and the race to fish. *Nat. Commun.* **9**, 4643 (2018).

[ADS](#) [Article](#) [PubMed](#) [PubMed Central](#) [Google Scholar](#)

72. 72.

Fenstadt A. & Kvile, K. «Polaris»-reder lover å rydde opp i mannskapsrot («Polaris»-owner promises to clean up mess with crew.) *Fiskeribladet* <https://www.fiskeribladet.no/nyheter/-polaris-reder-lover-a-rydde-opp-i-mannskapsrot/8-1-46419> (14 April 2016.).

73. 73.

Krivoshapko, J. Рыба! Антимонопольная служба раскрыла схемы, с помощью которых иностранцы незаконно ловят нашу рыбу (A fish! The antimonopoly service has uncovered schemes by which foreigners illegally catch our fish.) *Rossiyskaya Gazeta*

<https://rg.ru/2017/06/20/fas-raskryla-shemy-po-nezakonomu-lovu-rossijskoj-ryby-inostrancami.html> (20 June 2017).

74. 74.

SHERLOC. *Database of Legislation*.

<https://sherloc.unodc.org/cld/v3/sherloc/legdb/> (UN ODC, accessed 12 October 2019).

75. 75.

FAO Legal Office. Survey of practice on fisheries law enforcement process: administrative v criminal v both. Presentation at Our Ocean 2019 (FAO, 2019).

76. 76.

de Coning, E. in *Handbook of Transnational Environmental Crime* (ed. Elliot, L. & Schaedla, W. H.) 146–167 (Edward Elgar Publishing, 2016). **This book chapter explores the concept of fisheries crime from a compliance strategy, legal–procedural and socio-legal perspective, drawing out and expanding on the law enforcement implications of fisheries crime.**

77. 77.

INTERPOL. *International Law Enforcement Cooperation in the Fisheries Sector: A Guide for Law Enforcement Practitioners* (INTERPOL, 2018).

78. 78.

Widjaja, S. et al. *Illegal, Unreported and Unregulated Fishing and Associated Drivers*. Blue Paper 15
<https://oceanpanel.org/sites/default/files/2020-02/HLP%20Blue%20Paper%20on%20IUU%20Fishing%20and%20Associated%20Drivers.pdf> (World Resources Institute, 2020).

79. 79.

Agnew, D. J. et al. Estimating the worldwide extent of illegal fishing. *PLoS ONE* **4**, e4570 (2009). **This paper was one of the first to publicly estimate the extent and economic impact of illegal and unreported fishing globally and, in so doing, drew attention to the urgent need to address the problem and the associated enforcement challenges.**

[ADS](#) [Article](#) [PubMed](#) [PubMed Central](#) [Google Scholar](#)

80. 80.

FAO. *The State of World Fisheries and Aquaculture: Meeting the Sustainable Development Goals 2018.*

<http://www.fao.org/3/i9540en/i9540en.pdf> (FAO, 2018).

81. 81.

Johnston, S. J. & Butterworth, D. S. Summary of south coast rock lobster (*Palinurus gilchristi*) fishery. *International Fisheries Stock Assessment Review Workshop* (Department of Mathematics and Applied Mathematics, Univ. Cape Town, 2017).

82. 82.

Doumbouya, A. et al. Assessing the effectiveness of monitoring control and surveillance of illegal fishing: the case of West Africa. *Front. Mar. Sci.* **7**, 50 (2017).

[Google Scholar](#)

83. 83.

Sumaila, U. R. et al. Illicit trade in marine fish catch and its effects on ecosystems and people worldwide. *Sci. Adv.* **6**, eaaz3801 (2020).

[ADS](#) [CAS](#) [Article](#) [PubMed](#) [PubMed Central](#) [Google Scholar](#)

84. 84.

WWF South Africa v Minister of Agriculture, Forestry and Fisheries and Others (11478/18) [2018] ZAWCHC 127.

85. 85.

Cochrane, K. Department will be judged harshly if it fails to protect rock lobster. *Cape Times* (26 September 2017).

86. 86.

UN General Assembly. *Fisheries: Interim Report of the Special Rapporteur on the Right to Food*. A/67/268 (UN, 2012).

87. 87.

Okafor-Yarwood, I. Illegal, unreported and unregulated fishing, and the complexities of the sustainable development goals (SDGs) for countries in the Gulf of Guinea. *Mar. Policy* **99**, 414–422 (2019).

[Article](#) [Google Scholar](#)

88. 88.

The World Bank. *Promoting Community-based Climate Resilience in the Fisheries Sector* (World Bank, 2017).

89. 89.

International Maritime Bureau. *Piracy and Armed Robbery against Ships: Report of the Period 1 Jan.–31 Dec. 2012* (International Maritime Bureau, 2013).

90. 90.

Okafor-Yarwood, I. The cyclical nature of maritime security threats: illegal, unreported and unregulated fishing as a threat to human and national security in the Gulf of Guinea. *Afr. Secur.* **31**, 116–146 (2020).

[Article](#) [Google Scholar](#)

91. 91.

Santos-Fita, D. Subsistence hunting in rural communities: incompatibilities and opportunities within Mexican environmental legislation. *J. Ethnobiol.* **38**, 356–371 (2018).

[Article](#) [Google Scholar](#)

92. 92.

Talma, J., Kotze, J. D., Markovina, M. & Snijman, P. *A Multi-Agency Task Team Working Together to End Destructive Blast Fishing.* http://www.fao.org/fi/oldsite/eims_search/1_dett.asp?calling=simple_s_result&lang=zh&pub_id=317379 (FAO & IOC, 2015).

93. 93.

Galbraith, K. The horrors of fishing with dynamite. *The New York Times* (4 February 2015).

94. 94.

Ralby, I. & Soud, D. *Oil on the Water: Illicit Hydrocarbons Activity in the Maritime Domain* (The Atlantic Council, 2018).

95. 95.

Banaseh, M. Ghana risks losing GH¢ 1.5bn to fuel smuggling. *Graphic Online* (23 August 2017).

96. 96.

Surtees, J. Venezuelan refugees feared drowned on route to Trinidad. *The Guardian* (25 April 2019).

97. 97.

Dambach, K. Human traffickers arrested in Italy. *InfoMigrants* (6 June 2019).

98. 98.

Frontex detects mother boat smuggling people. *Frontex* <https://frontex.europa.eu/media-centre/news-release/frontex-detects-mother-boat-smuggling-people-dIBt9Q> (24 June 2019).

99. 99.

UNODC. *Report of the meeting of the Working Group on the Smuggling of Migrants held in Vienna from 11 to 13 September 2019*. CTOC/COP/WG.7/2019/6 (UN, 2019). **This reports describes the use of fishing vessels to smuggle migrants by sea in the Mediterranean before 2016.**

100. 100.

Lindley, J., Percy, S. & Techera, E. *Illegal Fishing and Australian Security*. <http://www.internationalaffairs.org.au/australianoutlook/illegal-fishing-australia/> (Australian Institute of International Affairs, 2018).

101. 101.

Lefevre, A. S. Thai fishermen convert boats to cash in on human-smuggling. *Reuters* <https://www.reuters.com/article/us-thailand-rohingya/thai-fishermen-convert-boats-to-cash-in-on-human-smuggling-idUSKCN0J40P120141120> (20 November 2015).

102. 102.

Spijkers, J. et al. Global patterns of fisheries conflict: forty years of data. *Glob. Environ. Change* 57, 101921 (2019).

[Article](#) [Google Scholar](#)

103. 103.

Pomeroy, R. et al. Fish wars: conflict and collaboration in fisheries management in Southeast Asia. *Mar. Policy* **31** 645–656 (2019).

[Article](#) [Google Scholar](#)

104. 104.

Sumaila, U. R. & Bawumia, M. Fisheries, ecosystem justice and piracy: a case study of Somalia. *Fish. Res.* **157**, 154–163 (2019).

[Article](#) [Google Scholar](#)

105. 105.

Chatham House. *Maritime Security in the Gulf of Guinea* (The Royal Institute of International Affairs, 2013).

106. 106.

Gilpin, R. *Enhancing Maritime Security in the Gulf of Guinea*. Strategic Studies Vol. VI (Center for Contemporary Conflict, 2007).

107. 107.

Onuoha, F. *Piracy and Maritime Security in the Gulf of Guinea: Nigeria as a Microcosm* (Al Jazeera Centre for Studies, 2012).

108. 108.

Okafor-Yarwood, I. The effects of oil pollution on the marine environment in the Gulf of Guinea—the Bonga Oil Field example. *Transnatl Legal Theory* **9**, 254–271 (2018).

[Article](#) [Google Scholar](#)

109. 109.

UN Security Council. *Threats to International Peace and Security*. Security Council Resolution 2842/2019. 8582nd Meeting of the United

Nations Security Council Report No. S/RES/2842 (UNSC, 2019).

110. 110.

UN. *International Law of the Sea*. Article 101 (UN, 1982).

111. 111.

UN Security Council. 7805th Meeting of the United Nations Security Council Report No. S/RES/2316 (UNSC, 2016).

112. 112.

Samatar, A. I., Lindberg, M. & Mahayni, B. The dialectics of piracy in Somalia: the rich versus the poor. *Third World Q.* **31**, 1377–1394 (2010).

[Article](#) [Google Scholar](#)

113. 113.

Devlin, C., Glaser, S. M., Villegas, C. & Poinsatte, N. *Rough Seas: The Causes and Consequences of Fisheries Conflict in Somali Waters*. <https://securefisheries.org/rough-seas-fisheries-conflict-somali-waters> (One Earth Future, 2020).

114. 114.

Liss, C. The roots of piracy in Southeast Asia. *APSNet Policy Forum* (22 October 2007).

115. 115.

CCPCJ. *Outcome of the 2nd International Symposium on Fisheries Crime, 10–11 October 2016, Yogyakarta, Indonesia*. E/CN.15/2017/CRP.3 (UN ODC, 2017).

116. 116.

Tavornmas, A. From EU IUU yellow to green card: Thailand's sustainable fisheries, 2019. *ASEAN Regional Forum* (2019).

117. 117.

European Commission. *EU Data Protection Rules*.

https://ec.europa.eu/commission/priorities/justice-and-fundamental-rights/data-protection/2018-reform-eu-data-protection-rules/eu-data-protection-rules_en (2019).

118. 118.

Blowfield, M. & Flynas, J. G. Setting new agendas: critical perspectives on corporate social responsibility in the developing world. *Int. Aff.* **81**, 499–513 (2005).

[Article](#) [Google Scholar](#)

119. 119.

Hodal, K., Kelly, C. & Lawrence, F. Revealed: Asian slave labour producing prawns in supermarkets in US, UK. *The Guardian* (10 June 2014).

120. 120.

Packer, H., Swarz, W., Ota, Y. & Baily, M. Corporate social responsibility (CSR) practices of the largest seafood suppliers in the wild capture fisheries sector: from vision to action. *Sustainability* **11**, 2254 (2019).

[Article](#) [Google Scholar](#)

121. 121.

High Level Panel on a Sustainable Ocean Economy. *Towards a Sustainable Ocean Economy Report*. <https://www.oceanpanel.org/the-report> (2020).

[Download references](#)

Acknowledgements

This manuscript is adapted from a Blue Paper commissioned by the High Level Panel for a Sustainable Ocean Economy entitled ‘Organized Crime in the Fisheries Sector’. We thank T. Edmunds and D. G. Webster for their insightful input.

Author information

Affiliations

1. Nelson Mandela University, Port Elizabeth, South Africa
Emma Witbooi
2. PescaDOLUS International Fisheries Crime Research Network, Cape Town, South Africa
Emma Witbooi
3. Centre for Maritime Law and Security Africa, Accra, Ghana
Kamal-Deen Ali
4. Indonesia Presidential Task Force to Combat Illegal Fishing, Jakarta, Indonesia
Mas Achmad Santosa & Yunus Husein
5. Development Finance, United Nations Development Programme (UNDP) Bureau for Policy and Programme Support, Copenhagen, Denmark
Gail Hurley

6. Fisheries Inspectorate Fisheries Division, Ministry of Agriculture, Land and Fisheries, Government of the Republic of Trinidad and Tobago, Port of Spain, Trinidad and Tobago

Sarika Maharaj

7. The Centre for Strategic Research and Studies, National Defence College, Abuja, Nigeria

Ifesinachi Okafor-Yarwood

8. Programa de Estudios Socioambientales, Centro Regional de Investigaciones Multidisciplinarias, Universidad Nacional Autónoma de México, Cuernavaca, Mexico

Inés Arroyo Quiroz

9. Security and Government National Planning Department, Agency for Reincorporation and Normalization (ARN) Presidency of Colombia, Bogotá, Colombia

Omar Salas

Authors

1. Emma Witbooi

[View author publications](#)

You can also search for this author in [PubMed](#) [Google Scholar](#)

2. Kamal-Deen Ali

[View author publications](#)

You can also search for this author in [PubMed](#) [Google Scholar](#)

3. Mas Achmad Santosa

[View author publications](#)

You can also search for this author in [PubMed](#) [Google Scholar](#)

4. Gail Hurley

[View author publications](#)

You can also search for this author in [PubMed](#) [Google Scholar](#)

5. Yunus Husein

[View author publications](#)

You can also search for this author in [PubMed](#) [Google Scholar](#)

6. Sarika Maharaj

[View author publications](#)

You can also search for this author in [PubMed](#) [Google Scholar](#)

7. Ifesinachi Okafor-Yarwood

[View author publications](#)

You can also search for this author in [PubMed](#) [Google Scholar](#)

8. Inés Arroyo Quiroz

[View author publications](#)

You can also search for this author in [PubMed](#) [Google Scholar](#)

9. Omar Salas

[View author publications](#)

You can also search for this author in [PubMed](#) [Google Scholar](#)

Contributions

E.W. is the first co-lead author; she was originally approached by the High Level Panel for a Sustainable Ocean Economy to lead the commissioned Blue Paper 16 on Organized Crime in the fisheries sector; she was tasked with the responsibility of appointing co-lead authors and contributing authors and the delivery of the final product. She wrote a substantial part of the text of the original draft framework paper, assigned writing roles and

thereafter coordinated all input and led the reformulation of the paper. She further provided input on organized crime in fisheries in the South African context. E.W. drafted this Perspective with input from the co-lead authors. M.A.S. is a co-lead author. He provided substantial input for the draft framework paper, with specific reference to Indonesian examples, assisted in shaping the content of the paper, provided support throughout the writing process and contributed to the reformulation of the Blue paper and the Perspective. K.D.-A. is the third co-lead author. He provided substantial input for the draft framework paper, with specific reference to Gulf of Guinea examples and with particular input on maritime security concerns in the context of organized crime in the fisheries sector, assisted in shaping the content of the paper, provided support throughout the writing process and contributed to the reformulation of the Blue Paper and the Perspective. G.H. is a contributing author. She provided substantial input on sections concerning financial crime in the fisheries sector. Y.H. is a contributing author. He provided substantial input on sections concerning money laundering in the fisheries sector, specifically in the Indonesian context. S.M. is a contributing author. She provided substantial input on sections concerning organized crime in the fisheries sector in the Caribbean context. I.O.-Y. is a contributing author. She provided substantial input on sections concerning the impact of organized crime in the fisheries sector on coastal communities, particularly in the Nigerian context as well as in the broader Gulf of Guinea context. I.A.Q. is a contributing author. She provided substantial input on sections concerning the interface between environmental crime and organized crime in the fisheries sector in the Mexican context. O.S. is a contributing author. He provided substantial input on sections concerning organized crime in fisheries in the context of Colombia.

Corresponding author

Correspondence to [Emma Witbooi](#).

Ethics declarations

Competing interests

The authors declare no competing interests.

Additional information

Peer review information *Nature* thanks Timothy Edmunds and D. G. Webster for their contribution to the peer review of this work.

Publisher's note Springer Nature remains neutral with regard to jurisdictional claims in published maps and institutional affiliations.

Supplementary information

Supplementary Information

This file contains appendix A, the Copenhagen Declaration 2018.

Rights and permissions

Reprints and Permissions

About this article



Check for
updates

Cite this article

Witbooi, E., Ali, KD., Santosa, M.A. *et al.* Organized crime in the fisheries sector threatens a sustainable ocean economy. *Nature* **588**, 48–56 (2020). <https://doi.org/10.1038/s41586-020-2913-5>

Download citation

- Received: 09 December 2019

- Accepted: 20 August 2020
- Published: 11 November 2020
- Issue Date: 03 December 2020
- DOI: <https://doi.org/10.1038/s41586-020-2913-5>

Further reading

- **Five priorities for a sustainable ocean economy**
 - Jane Lubchenco
 - , Peter M. Haugan
 - & Mari Elka Pangestu

Nature (2020)

Comments

By submitting a comment you agree to abide by our [Terms](#) and [Community Guidelines](#). If you find something abusive or that does not comply with our terms or guidelines please flag it as inappropriate.

[Download PDF](#)

Associated Content

Special

[**The ocean in humanity's future**](#)

| [Section menu](#) | [Main menu](#) |

- Article
- [Published: 02 December 2020](#)

Enhanced triple- α reaction reduces proton-rich nucleosynthesis in supernovae

- [Shilun Jin](#) ORCID: orcid.org/0000-0002-2868-8658^{1,2,3},
- [Luke F. Roberts](#) ORCID: orcid.org/0000-0001-7364-7946^{1,2},
- [Sam M. Austin](#)^{1,2} &
- [Hendrik Schatz](#)^{1,2}

Nature volume **588**, pages 57–60(2020) [Cite this article](#)

- 76 Altmetric
- [Metrics details](#)

Subjects

- [Nuclear astrophysics](#)
- [Stars](#)

Abstract

The rate of the triple- α reaction that forms ^{12}C affects^{1,2} the synthesis of heavy elements in the Ga–Cd range in proton-rich neutrino-driven outflows of core-collapse supernovae^{3,4,5}. Initially, these outflows contain only protons and neutrons; these later combine to form α particles, then ^{12}C nuclei via the triple- α reaction, and eventually heavier nuclei as the material expands and cools. Previous experimental work^{6,7} demonstrated that despite

the high temperatures encountered in these environments, the reaction is dominated by the well characterized Hoyle state resonance in ^{12}C nuclei. At sufficiently high nucleon densities, however, proton- and neutron-scattering processes may alter the effective width of the Hoyle state^{8,9}. This raises the questions of what the reaction rate in supernova outflows is, and how changes affect nucleosynthesis predictions. Here we report that in proton-rich core-collapse supernova outflows, these hitherto neglected processes enhance the triple- α reaction rate by up to an order of magnitude. The larger reaction rate suppresses the production of heavy proton-rich isotopes that are formed by the νp process^{3,4,5} (where ν is the neutrino and p is the proton) in the innermost ejected material of supernovae^{10,11,12,13}. Previous work on the rate enhancement mechanism⁹ did not anticipate the importance of this enhancement for proton-rich nucleosynthesis. Because the in-medium contribution to the triple- α reaction rate must be present at high densities, this effect needs to be included in supernova nucleosynthesis models. This enhancement also differs from earlier sensitivity studies that explored variations of the unenhanced rate by a constant factor^{1,2}, because the enhancement depends on the evolving thermodynamic conditions. The resulting suppression of heavy-element nucleosynthesis for realistic conditions casts doubt on the νp process being the explanation for the anomalously high abundances of $^{92,94}\text{Mo}$ and $^{96,98}\text{Ru}$ isotopes in the Solar System^{1,3,14} and for the signatures of early Universe element synthesis in the Ga–Cd range found in the spectra of ancient metal-poor stars^{15,16,17,18,19,20}.

[Access through your institution](#)

[Change institution](#)

[Buy or subscribe](#)

Access options

Subscribe to Journal

Get full journal access for 1 year

185,98 €

only 3,58 € per issue

[Subscribe](#)

All prices are NET prices.
VAT will be added later in the checkout.

Rent or Buy article

Get time limited or full article access on ReadCube.
from \$8.99

[Rent or Buy](#)

All prices are NET prices.

Additional access options:

- [Log in](#)
- [Access through your institution](#)
- [Learn about institutional subscriptions](#)

Fig. 1: Enhancement of seed nuclei production.

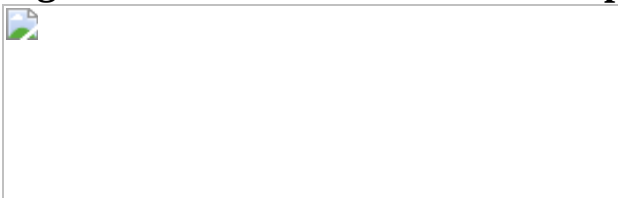


Fig. 2: The total in-medium enhanced triple- α reaction rate.



Fig. 3: Nucleosynthesis results.



Fig. 4: Nucleosynthesis results with the rate enhancement at the upper end of the estimated nuclear uncertainty.



Fig. 5: Effect of the enhancement on p-nuclide production.



Data availability

The simulation data that support these findings is available from the corresponding author upon reasonable request.

Code availability

The reaction network library SkyNet used for this work is publicly available at <https://bitbucket.org/jlippuner/skynet>. The code used to run and analyse the simulations described here (which relies on the SkyNet library) is publicly available at <https://bitbucket.org/lroberts/triplealphainmediumenhancement>.

References

1. 1.

Wanajo, S., Janka, H.-T. & Kubono, S. Uncertainties in the νp -process: supernova dynamics versus nuclear physics. *Astrophys. J.* **729**, 46 (2011).

[ADS](#) [Article](#) [Google Scholar](#)

2. 2.

Nishimura, N. et al. Uncertainties in νp -process nucleosynthesis from Monte Carlo variation of reaction rates. *Mon. Not. R. Astron. Soc.* **489**, 1379–1396 (2019).

[ADS](#) [CAS](#) [Article](#) [Google Scholar](#)

3. 3.

Fröhlich, C. et al. Neutrino-induced nucleosynthesis of $A > 64$ nuclei: the νp process. *Phys. Rev. Lett.* **96**, 142502 (2006).

[ADS](#) [Article](#) [PubMed](#) [Google Scholar](#)

4. 4.

Pruet, J., Hoffman, R. D., Woosley, S. E., Janka, H. T. & Buras, R. Nucleosynthesis in early supernova winds. II. The role of neutrinos. *Astrophys. J.* **644**, 1028–1039 (2006).

[ADS](#) [CAS](#) [Article](#) [Google Scholar](#)

5. 5.

Wanajo, S. The rp-process in neutrino-driven winds. *Astrophys. J.* **647**, 1323–1340 (2006).

[ADS](#) [CAS](#) [Article](#) [Google Scholar](#)

6. 6.

Fynbo, H. O. U. et al. Revised rates for the stellar triple- α process from measurement of ^{12}C nuclear resonances. *Nature* **433**, 136–139 (2005).

[ADS](#) [CAS](#) [Article](#) [PubMed](#) [Google Scholar](#)

7. 7.

Freer, M. & Fynbo, H. O. U. The Hoyle state in ^{12}C . *Prog. Part. Nucl. Phys.* **78**, 1–23 (2014).

[ADS](#) [CAS](#) [Article](#) [Google Scholar](#)

8. 8.

Truran, J. W. & Kozlovsky, B. Z. The enhancement of the ${}^3\text{He} \rightarrow {}^{12}\text{C}$ reaction rate in dense matter by inelastic-scattering processes. *Astrophys. J.* **158**, 1021–1032 (1969).

[ADS](#) [CAS](#) [Article](#) [Google Scholar](#)

9. 9.

Beard, M., Austin, S. M. & Cyburt, R. Enhancement of the triple alpha rate in a hot dense medium. *Phys. Rev. Lett.* **119**, 112701 (2017).

[ADS](#) [Article](#) [PubMed](#) [Google Scholar](#)

10. 10.

Meyer, B. S., Mathews, G. J., Howard, W. M., Woosley, S. E. & Hoffman, R. D. r -process nucleosynthesis in the high-entropy supernova bubble. *Astrophys. J.* **399**, 656–664 (1992).

[ADS](#) [CAS](#) [Article](#) [Google Scholar](#)

11. 11.

Woosley, S. E. & Hoffman, R. D. The α -process and the r-process. *Astrophys. J.* **395**, 202–239 (1992).

[ADS](#) [CAS](#) [Article](#) [Google Scholar](#)

12. 12.

Hüdepohl, L., Müller, B., Janka, H. T., Marek, A. & Raffelt, G. G. Neutrino signal of electron-capture supernovae from core collapse to cooling. *Phys. Rev. Lett.* **104**, 251101 (2010).

[ADS](#) [Article](#) [PubMed](#) [Google Scholar](#)

13. 13.

Fischer, T., Whitehouse, S. C., Mezzacappa, A., Thielemann, F. K. & Liebendörfer, M. Protoneutron star evolution and the neutrino-driven wind in general relativistic neutrino radiation hydrodynamics simulations. *Astron. Astrophys.* **517**, A80 (2010).

[Article](#) [Google Scholar](#)

14. 14.

Rayet, M., Arnould, M. & Prantzos, N. The p-process revisited. *Astron. Astrophys.* **227**, 271–281 (1990).

[ADS](#) [CAS](#) [Article](#) [Google Scholar](#)

15. 15.

Travaglio, C. et al. Galactic evolution of Sr, Y, and Zr: a multiplicity of nucleosynthetic processes. *Astrophys. J.* **601**, 864–884 (2004).

[ADS](#) [CAS](#) [Article](#) [Google Scholar](#)

16. 16.

Montes, F. et al. Nucleosynthesis in the early Galaxy. *Astrophys. J.* **671**, 1685–1695 (2007).

[ADS](#) [CAS](#) [Article](#) [Google Scholar](#)

17. 17.

Qian, Y. Z. & Wasserburg, G. J. Abundances of Sr, Y, and Zr in metal-poor stars and implications for chemical evolution in the early Galaxy. *Astrophys. J.* **687**, 272–286 (2008).

[ADS](#) [CAS](#) [Article](#) [Google Scholar](#)

18. 18.

Hansen, C. J., Montes, F. & Arcones, A. How many nucleosynthesis processes exist at low metallicity? *Astrophys. J.* **797**, 123 (2014).

[ADS](#) [Article](#) [Google Scholar](#)

19. 19.

Eichler, M. et al. Nucleosynthesis in 2D core-collapse supernovae of 11.2 and 17.0 M_{\odot} progenitors: implications for Mo and Ru production. *J. Phys. G* **45**, 014001 (2018).

[ADS](#) [Article](#) [Google Scholar](#)

20. 20.

Bliss, J., Arcones, A. & Qian, Y. Z. Production of Mo and Ru isotopes in neutrino-driven winds: implications for solar abundances and presolar grains. *Astrophys. J.* **866**, 105 (2018).

[ADS](#) [Article](#) [Google Scholar](#)

21. 21.

Angulo, C. et al. A compilation of charged-particle induced thermonuclear reaction rates. *Nucl. Phys. A* **656**, 3–183 (1999).

[ADS](#) [Article](#) [Google Scholar](#)

22. 22.

Arcones, A. & Thielemann, F.-K. Neutrino-driven wind simulations and nucleosynthesis of heavy elements. *J. Phys. G* **40**, 013201 (2013).

[ADS](#) [Article](#) [Google Scholar](#)

23. 23.

Hoffman, R. D., Woosley, S. E. & Qian, Y. Z. Nucleosynthesis in neutrino-driven winds. II. Implications for heavy element synthesis.

Astrophys. J. **482**, 951–962 (1997).

[ADS](#) [CAS](#) [Article](#) [Google Scholar](#)

24. 24.

Wanajo, S., Müller, B., Janka, H.-T. & Heger, A. Nucleosynthesis in the innermost ejecta of neutrino-driven supernova explosions in two dimensions. *Astrophys. J.* **852**, 40 (2018).

[ADS](#) [Article](#) [Google Scholar](#)

25. 25.

Davids, C. N. & Bonner, T. Enhancement of the ${}^3\text{He} \rightarrow {}^{12}\text{C}$ reaction rate by inelastic proton scattering. *Astrophys. J.* **166**, 405–410 (1971).

[ADS](#) [CAS](#) [Article](#) [Google Scholar](#)

26. 26.

Freer, M., Horiuchi, H., Kanada-En'yo, Y., Lee, D. & Meißner, U.-G. Microscopic clustering in light nuclei. *Rev. Mod. Phys.* **90**, 035004 (2018).

[ADS](#) [MathSciNet](#) [CAS](#) [Article](#) [Google Scholar](#)

27. 27.

Zimmerman, W. R. et al. Unambiguous identification of the second 2^+ state in ${}^{12}\text{C}$ and the structure of the Hoyle state. *Phys. Rev. Lett.* **110**, 152502 (2013).

[ADS](#) [CAS](#) [Article](#) [PubMed](#) [Google Scholar](#)

28. 28.

Zimmerman, W. R. *Direct Observation of the Second 2^+ State in ${}^{12}\text{C}$.* PhD thesis, Univ. of Connecticut (2013).

29. 29.

Lippuner, J. & Roberts, L. SkyNet: a modular nuclear reaction network library. *Astrophys. J. Suppl. Ser.* **233**, 18 (2017).

[ADS](#) [Article](#) [Google Scholar](#)

30. 30.

Timmes, F. X. & Swesty, F. D. The accuracy, consistency, and speed of an electron–positron equation of state based on table interpolation of the Helmholtz free energy. *Astrophys. J. Suppl. Ser.* **126**, 501–516 (2000).

[ADS](#) [Article](#) [Google Scholar](#)

31. 31.

Cyburt, R. H. et al. The JINA REACLIB database: its recent updates and impact on type-I X-ray bursts. *Astrophys. J.* **189**, 240–252 (2010).

[CAS](#) [Article](#) [Google Scholar](#)

32. 32.

Caughlan, G. R. & Fowler, W. A. Thermonuclear reaction rates V. *At. Data Nucl. Data Tables* **40**, 283–334 (1988).

[ADS](#) [CAS](#) [Article](#) [Google Scholar](#)

33. 33.

Arnold, C. W. et al. Cross-section measurement of ${}^9\text{Be}(\gamma, n){}^8\text{Be}$ and implications for $\alpha + \alpha + n \rightarrow {}^9\text{Be}$ in the r process. *Phys. Rev. C* **85**, 044605 (2012).

[ADS](#) [Article](#) [Google Scholar](#)

34. 34.

Radice, D. et al. Binary neutron star mergers: mass ejection, electromagnetic counterparts, and nucleosynthesis. *Astrophys. J.* **869**, 130 (2018).

[ADS](#) [CAS](#) [Article](#) [Google Scholar](#)

35. 35.

Roberts, L. et al. The influence of neutrinos on r-process nucleosynthesis in the ejecta of black hole-neutron star mergers. *Mon. Not. R. Astron. Soc.* **464**, 3907 (2017).

[ADS](#) [CAS](#) [Article](#) [Google Scholar](#)

[Download references](#)

Acknowledgements

We thank A. Arcones, J. Bliss, H. O. U. Fynbo, G. M. Hale, D. Lee and H. Weller for discussions. We acknowledge support from NSF awards PHY-1430152 (JINA Center for the Evolution of the Elements), PHY-1913554 and PHY-1102511. S.J. is supported by CSC-FRIB Postdoctoral Fellowship grant 201600090331. L.F.R. was partially supported by the US Department of Energy through the Advanced Computing (SciDAC) programme under award number DE-SC0017955.

Author information

Affiliations

1. National Superconducting Cyclotron Laboratory, East Lansing, MI, USA

Shilun Jin, Luke F. Roberts, Sam M. Austin & Hendrik Schatz

2. Joint Institute for Nuclear Astrophysics – Center for the Evolution of the Elements, Michigan State University, East Lansing, MI, USA

Shilun Jin, Luke F. Roberts, Sam M. Austin & Hendrik Schatz

3. Institute of Modern Physics, Chinese Academy of Sciences, Lanzhou, China

Shilun Jin

Authors

1. Shilun Jin

[View author publications](#)

You can also search for this author in [PubMed](#) [Google Scholar](#)

2. Luke F. Roberts

[View author publications](#)

You can also search for this author in [PubMed](#) [Google Scholar](#)

3. Sam M. Austin

[View author publications](#)

You can also search for this author in [PubMed](#) [Google Scholar](#)

4. Hendrik Schatz

[View author publications](#)

You can also search for this author in [PubMed](#) [Google Scholar](#)

Contributions

S.J. and L.F.R. carried out the calculations and analysis. S.M.A. carried out enhancement factor calculations. All authors contributed to the motivation, analysis and interpretation as well as the writing of the manuscript.

Corresponding author

Correspondence to [Luke F. Roberts](#).

Ethics declarations

Competing interests

The authors declare no competing interests.

Additional information

Peer review information *Nature* thanks the anonymous reviewer(s) for their contribution to the peer review of this work. Peer reviewer reports are available.

Publisher's note Springer Nature remains neutral with regard to jurisdictional claims in published maps and institutional affiliations.

Supplementary information

[Peer Review File](#)

Rights and permissions

[Reprints and Permissions](#)

About this article



Check for
updates

Cite this article

Jin, S., Roberts, L.F., Austin, S.M. *et al.* Enhanced triple- α reaction reduces

proton-rich nucleosynthesis in supernovae. *Nature* **588**, 57–60 (2020).

<https://doi.org/10.1038/s41586-020-2948-7>

Download citation

- Received: 09 March 2020
- Accepted: 25 September 2020
- Published: 02 December 2020
- Issue Date: 03 December 2020
- DOI: <https://doi.org/10.1038/s41586-020-2948-7>

Comments

By submitting a comment you agree to abide by our [Terms](#) and [Community Guidelines](#). If you find something abusive or that does not comply with our terms or guidelines please flag it as inappropriate.

[Access through your institution](#)

[Change institution](#)

[Buy or subscribe](#)

This article was downloaded by **calibre** from <https://www.nature.com/articles/s41586-020-2948-7>

- Article
- [Published: 02 December 2020](#)

Determination of the fine-structure constant with an accuracy of 81 parts per trillion

- [Léo Morel](#) [ORCID: orcid.org/0000-0002-1122-008X¹](#),
- [Zhibin Yao¹](#),
- [Pierre Cladé¹](#) &
- [Saïda Guellati-Khélifa](#) [ORCID: orcid.org/0000-0002-8412-411X^{1,2}](#)

[Nature](#) volume **588**, pages 61–65(2020) [Cite this article](#)

- 521 Accesses
- 148 Altmetric
- [Metrics details](#)

Subjects

- [Matter waves and particle beams](#)
- [Quantum metrology](#)

Abstract

The standard model of particle physics is remarkably successful because it is consistent with (almost) all experimental results. However, it fails to explain dark matter, dark energy and the imbalance between matter and antimatter in the Universe. Because discrepancies between standard-model

predictions and experimental observations may provide evidence of new physics, an accurate evaluation of these predictions requires highly precise values of the fundamental physical constants. Among them, the fine-structure constant α is of particular importance because it sets the strength of the electromagnetic interaction between light and charged elementary particles, such as the electron and the muon. Here we use matter-wave interferometry to measure the recoil velocity of a rubidium atom that absorbs a photon, and determine the fine-structure constant $\alpha^{-1} = 137.035999206(11)$ with a relative accuracy of 81 parts per trillion. The accuracy of eleven digits in α leads to an electron g factor^{1,2}—the most precise prediction of the standard model—that has a greatly reduced uncertainty. Our value of the fine-structure constant differs by more than 5 standard deviations from the best available result from caesium recoil measurements³. Our result modifies the constraints on possible candidate dark-matter particles proposed to explain the anomalous decays of excited states of ⁸Be nuclei⁴ and paves the way for testing the discrepancy observed in the magnetic moment anomaly of the muon⁵ in the electron sector⁶.

[Access through your institution](#)

[Change institution](#)

[Buy or subscribe](#)

Access options

Subscribe to Journal

Get full journal access for 1 year

185,98 €

only 3,58 € per issue

[Subscribe](#)

All prices are NET prices.

VAT will be added later in the checkout.

Rent or Buy article

Get time limited or full article access on ReadCube.

from \$8.99

[Rent or Buy](#)

All prices are NET prices.

Additional access options:

- [Log in](#)
- [Access through your institution](#)
- [Learn about institutional subscriptions](#)

Fig. 1: Precision measurements of the fine-structure constant.

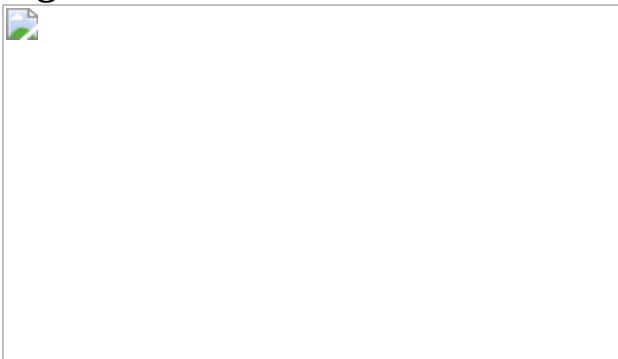


Fig. 2: Experimental setup.

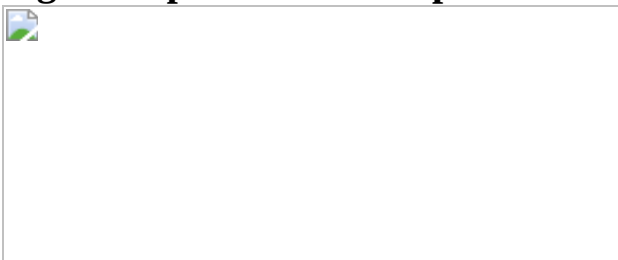


Fig. 3: Data analysis.



Fig. 4: Impact on the test of the standard-model prediction of a_e and limits on hypothetical X boson.



Data availability

The datasets generated and/or analysed during the current study are available from the corresponding author on reasonable request.

Code availability

The experimental data were analysed using a self-written analysis script, which is available from the corresponding author on reasonable request.

References

1. 1.

- Aoyama, T., Hayakawa, M., Kinoshita, T. & Nio, M. Tenth-order QED contribution to the electron $g - 2$ and an improved value of the fine structure constant. *Phys. Rev. Lett.* **109**, 111807 (2012).

[ADS](#) [Google Scholar](#)

2. 2.

Aoyama, T., Kinoshita, T. & Nio, M. Theory of the anomalous magnetic moment of the electron. *Atoms* **7**, 28 (2019).

[ADS](#) [CAS](#) [Google Scholar](#)

3. 3.

Parker, R. H., Yu, C., Zhong, W., Estey, B. & Müller, H. Measurement of the fine-structure constant as a test of the Standard Model. *Science* **360**, 191–195 (2018).

[ADS](#) [MathSciNet](#) [CAS](#) [MATH](#) [Google Scholar](#)

4. 4.

Krasznahorkay, A. J. et al. Observation of anomalous internal pair creation in ${}^8\text{Be}$: a possible indication of a light, neutral boson. *Phys. Rev. Lett.* **116**, 042501 (2016).

[ADS](#) [CAS](#) [Google Scholar](#)

5. 5.

Bennett, G. W. et al. Final report of the E821 muon anomalous magnetic moment measurement at BNL. *Phys. Rev. D* **73**, 072003 (2006).

[ADS](#) [Google Scholar](#)

6. 6.

Terranova, F. & Tino, G. M. Testing the a_μ anomaly in the electron sector through a precise measurement of h/M . *Phys. Rev. A* **89**, 052118 (2014).

[ADS](#) [Google Scholar](#)

7. 7.

Mohr, P. J., Newell, D. B. & Taylor, B. N. CODATA recommended values of the fundamental physical constants: 2014. *Rev. Mod. Phys.* **88**, 035009 (2016).

[ADS](#) [Google Scholar](#)

8. 8.

Laporta, S. High-precision calculation of the 4-loop contribution to the electron $g - 2$ in QED. *Phys. Lett. B* **772**, 232–238 (2017).

[ADS](#) [CAS](#) [Google Scholar](#)

9. 9.

Hanneke, D., Fogwell, S. & Gabrielse, G. New measurement of the electron magnetic moment and the fine structure constant. *Phys. Rev. Lett.* **100**, 120801 (2008).

[ADS](#) [CAS](#) [Google Scholar](#)

10. 10.

Wicht, A., Hensley, J. M., Sarajlic, E. & Chu, S. A preliminary measurement of the fine structure constant based on atom interferometry. *Phys. Scr.* **T102**, 82 (2002).

[ADS](#) [CAS](#) [Google Scholar](#)

11. 11.

Battesti, R. et al. Bloch oscillations of ultracold atoms: a tool for a metrological determination of h/m_{Rb} . *Phys. Rev. Lett.* **92**, 253001 (2004).

[ADS](#) [Google Scholar](#)

12. 12.

Mount, B. J., Redshaw, M. & Myers, E. G. Atomic masses of ${}^6\text{Li}$, ${}^{23}\text{Na}$, ${}^{39,41}\text{K}$, ${}^{85,87}\text{Rb}$, and ${}^{133}\text{Cs}$. *Phys. Rev. A* **82**, 042513 (2010).

[ADS](#) [Google Scholar](#)

13. 13.

Huang, W. et al. The AME2016 atomic mass evaluation (I). Evaluation of input data; and adjustment procedures. *Chin. Phys. C* **41**, 030002 (2017).

[ADS](#) [Google Scholar](#)

14. 14.

Sturm, S. et al. High-precision measurement of the atomic mass of the electron. *Nature* **506**, 467–470 (2014).

[ADS](#) [CAS](#) [Google Scholar](#)

15. 15.

Cladé, P., Guellati-Khélifa, S., Nez, F. & Biraben, F. Large momentum beam splitter using Bloch oscillations. *Phys. Rev. Lett.* **102**, 240402 (2009).

[ADS](#) [Google Scholar](#)

16. 16.

Müller, H., Chiow, S.-w., Long, Q., Herrmann, S. & Chu, S. Atom interferometry with up to 24-photon-momentum-transfer beam splitters. *Phys. Rev. Lett.* **100**, 180405 (2008).

[ADS](#) [Google Scholar](#)

17. 17.

Cadoret, M. et al. Combination of Bloch oscillations with a Ramsey–Bordé interferometer: new determination of the fine structure constant. *Phys. Rev. Lett.* **101**, 230801 (2008).

[ADS](#) [Google Scholar](#)

18. 18.

Bouchendira, R., Cladé, P., Guellati-Khélifa, S., Nez, F. & Biraben, F. New determination of the fine structure constant and test of the quantum electrodynamics. *Phys. Rev. Lett.* **106**, 080801 (2011).

[ADS](#) [Google Scholar](#)

19. 19.

Lan, S.-Y., Kuan, P.-C., Estey, B., Haslinger, P. & Müller, H. Influence of the Coriolis force in atom interferometry. *Phys. Rev. Lett.* **108**, 090402 (2012).

[ADS](#) [Google Scholar](#)

20. 20.

Jannin, R., Cladé, P. & Guellati-Khélifa, S. Phase shift due to atom–atom interactions in a light-pulse atom interferometer. *Phys. Rev. A* **92**, 013616 (2015).

[ADS](#) [Google Scholar](#)

21. 21.

Bade, S., Djadaojee, L., Andia, M., Cladé, P. & Guellati-Khelifa, S. Observation of extra photon recoil in a distorted optical field. *Phys. Rev. Lett.* **121**, 073603 (2018).

[ADS](#) [CAS](#) [Google Scholar](#)

22. 22.

Gillot, P., Cheng, B., Merlet, S. & Pereira Dos Santos, F. Limits to the symmetry of a Mach-Zehnder-type atom interferometer. *Phys. Rev. A* **93**, 013609 (2016).

[ADS](#) [Google Scholar](#)

23. 23.

Morel, L., Yao, Z., Cladé, P. & Guellati-Khélifa, S. Velocity-dependent phase shift in a light-pulse atom interferometer. Preprint at <https://arxiv.org/abs/2006.14354> (2020).

24. 24.

Yu, C. et al. Atom-interferometry measurement of the fine structure constant. *Ann. Phys.* **531**, 1800346 (2019).

[Google Scholar](#)

25. 25.

Brodsky, S. J. & Drell, S. D. Anomalous magnetic moment and limits on fermion substructure. *Phys. Rev. D* **22**, 2236–2243 (1980).

[ADS](#) [CAS](#) [Google Scholar](#)

26. 26.

Bourilkov, D. Hint for axial-vector contact interactions in the data on $e^+e^- \rightarrow e^+e^-(\gamma)$ at center-of-mass energies 192–208 GeV. *Phys. Rev. D* **64**, 071701 (2001).

[ADS](#) [Google Scholar](#)

27. 27.

Aoyama, T., Kinoshita, T. & Nio, M. Revised and improved value of the QED tenth-order electron anomalous magnetic moment. *Phys. Rev. D* **97**, 036001 (2018).

[ADS](#) [CAS](#) [Google Scholar](#)

28. 28.

Davoudiasl, H., Lee, H.-S. & Marciano, W. J. Muon $g-2$, rare kaon decays, and parity violation from dark bosons. *Phys. Rev. D* **89**, 095006 (2014).

[ADS](#) [Google Scholar](#)

29. 29.

Gabrielse, G., Fayer, S. E., Myers, T. G. & Fan, X. Towards an improved test of the standard model's most precise prediction. *Atoms* **7**, 45 (2019).

[ADS](#) [CAS](#) [Google Scholar](#)

30. 30.

Feng, J. L. et al. Protophobic fifth-force interpretation of the observed anomaly in ${}^8\text{Be}$ nuclear transitions. *Phys. Rev. Lett.* **117**, 071803 (2016).

[ADS](#) [Google Scholar](#)

31. 31.

Riordan E. M. et al. Search for short-lived axions in an electron-beam-dump experiment. *Phys. Rev. Lett.* **59**, 755–758 (1987).

[ADS](#) [CAS](#) [Google Scholar](#)

32. 32.

NA64 Collaboration. Search for a hypothetical 16.7 MeV gauge boson and dark photons in the NA64 experiment at CERN. *Phys. Rev. Lett.* **120**, 231802 (2018).

[ADS](#) [Google Scholar](#)

33. 33.

Banerjee, D. et al. Improved limits on a hypothetical $X(16.7)$ boson and a dark photon decaying into e^+e^- pairs. *Phys. Rev. D* **101**, 071101 (2020).

[ADS](#) [CAS](#) [Google Scholar](#)

34. 34.

Van Dyck, R. S., Schwinberg, P. & Dehmelt, H. New high-precision comparison of electron and positron g factors. *Phys. Rev. Lett.* **59**, 26–29 (1987).

[ADS](#) [Google Scholar](#)

35. 35.

BABAR Collaboration. Search for a dark photon in e^+e^- collisions at BaBar. *Phys. Rev. Lett.* **113**, 201801 (2014).

[ADS](#) [Google Scholar](#)

36. 36.

Andia, M., Wodey, É., Biraben, F., Cladé, P. & Guellati-Khélifa, S. Bloch oscillations in an optical lattice generated by a laser source based on a fiber amplifier: decoherence effects due to amplified spontaneous emission. *J. Opt. Soc. Am. B* **32**, 1038–1042 (2015).

[ADS](#) [CAS](#) [Google Scholar](#)

37. 37.

Wolf, P. & Tourrenc, P. Gravimetry using atom interferometers: some systematic effects. *Phys. Lett. A* **251**, 241–246 (1999).

[ADS](#) [CAS](#) [Google Scholar](#)

38. 38.

Storey, P. & Cohen-Tannoudji, C. The Feynman path integral approach to atomic interferometry. A tutorial. *J. Phys. II France* **4**, 1999–2027 (1994).

[CAS](#) [Google Scholar](#)

39. 39.

Weiss, D. S., Young, B. C. & Chu, S. Precision measurement of \hbar/m_{Cs} based on photon recoil using laser-cooled atoms and atomic interferometry. *Appl. Phys. B* **59**, 217–256 (1994).

[ADS](#) [Google Scholar](#)

40. 40.

Glück, M., Kolovsky, A. R. & Korsch, H. J. Wannier–Stark resonances in optical and semiconductor superlattices. *Phys. Rep.* **366**, 103–182 (2002).

[ADS](#) [MathSciNet](#) [MATH](#) [Google Scholar](#)

41. 41.

Cladé, P., Andia, M. & Guellati-Khélifa, S. Improving efficiency of Bloch oscillations in the tight-binding limit. *Phys. Rev. A* **95**, 063604 (2017).

[ADS](#) [Google Scholar](#)

42. 42.

Touahri, D. et al. Frequency measurement of the two-photon transition in rubidium. *Opt. Commun.* **133**, 471–478 (1997).

[ADS](#) [CAS](#) [Google Scholar](#)

43. 43.

Louchet-Chauvet, A. et al. The influence of transverse motion within an atomic gravimeter. *New J. Phys.* **13**, 065025 (2011).

[ADS](#) [Google Scholar](#)

44. 44.

Hogan, J. M., Johnson, D. M. S. & Kasevich, M. A. Light-pulse atom interferometry. In *Proc. of the International School of Physics Enrico Fermi Course CLXVIII on Atom Optics and Space Physics* (eds. Arimondo, E. et al.) 411 (IOS Press, 2008).

[Download references](#)

Acknowledgements

This work was supported by the US National Institute of Standards and Technology (NIST) Precision Measurement Grant Program under award number 60NANB16D271 and by the LABEX Cluster of Excellence FIRST-TF (ANR-10-LABX-48-01), within the *Programme investissements d'avenir* operated by the French National Research Agency (ANR). We are particularly grateful to R. Jannin and C. Courvoisier, who participated actively to the construction of the experimental setup, which was initially funded by the ANR, INAQED Project number ANR-12-JS04-0009.

Author information

Affiliations

1. Laboratoire Kastler Brossel (LKB), Sorbonne University, CNRS, ENS-PSL University, Collège de France, Paris, France

Léo Morel, Zhibin Yao, Pierre Cladé & Saïda Guellati-Khélifa

2. Conservatoire National des Arts et Métiers, Paris, France

Saïda Guellati-Khélifa

Authors

1. Léo Morel

[View author publications](#)

You can also search for this author in [PubMed](#) [Google Scholar](#)

2. Zhibin Yao

[View author publications](#)

You can also search for this author in [PubMed](#) [Google Scholar](#)

3. Pierre Cladé

[View author publications](#)

You can also search for this author in [PubMed](#) [Google Scholar](#)

4. Saïda Guellati-Khélifa

[View author publications](#)

You can also search for this author in [PubMed](#) [Google Scholar](#)

Contributions

The experiment was performed by L.M., Y.Z., P.C. and S.G.-K. The data were analysed by L.M., P.C. and S.G.-K. The main text was written by S.G.-K. and the Methods section by L.M. and P.C. All authors discussed and approved the data as well as the manuscript.

Corresponding author

Correspondence to [Saïda Guellati-Khélifa](#).

Ethics declarations

Competing interests

The authors declare no competing interests.

Additional information

Peer review information *Nature* thanks Gerald Gabrielse and the other, anonymous, reviewer(s) for their contribution to the peer review of this work. Peer reviewer reports are available.

Publisher's note Springer Nature remains neutral with regard to jurisdictional claims in published maps and institutional affiliations.

Extended data figures and tables

Extended Data Fig. 1 Laser beam setup and detection.

a, Vacuum cell and laser beams used for the Raman transition and Bloch oscillations. **b**, Detection setup consisting of three horizontal retro-reflected light sheets, through which the atoms fall successively. The thick red line represents the probe beams of circular polarization, which are resonant with the atoms in the state $|F = 2\rangle$. The black line represents the beam that repumps atoms from $|F = 1\rangle$ to $|F = 2\rangle$. **c**, Light pulse sequence implemented for the measurement protocol. Shown are the temporal variables used in Methods.

Extended Data Fig. 2 Control of the laser beam alignment and the magnetic field.

a, Distributions of the shot-to-shot variations of the auto-alignment procedure for mirrors M1 and M2 (see Extended Data Fig. 1a). **b**, Scatter plot of the contrast with respect to the sweep rate of the piezoelectric transducer of the mirror mounts (M2) for a 700-ms-long interferometer. **c**, Raw determinations of integrated h/m with and without Earth rotation compensation. Each point correspond to 400 sets of four spectra. The total interrogation time is 60 h. **d**, Blue: measured magnetic field, obtained by

measuring the resonance of the magnetically sensitive $|F = 1, m_F = 1\rangle \rightarrow |F = 2, m_F = -1\rangle$ transition. Orange: interpolation used for the modelling of the systematic effect. **e**, Allan deviation of the frequency measurement.

Extended Data Fig. 3 Frequency control of Raman lasers.

a, Raman phase-lock system. Top left: laser arrangement used to extract a beat note between the two lasers. Bottom left: radio-frequency chain for the phase lock. Right: setup used for the measurement of the phase between the two lasers. NKT, fibre laser from NKT photonics; RIO, diode laser from RIO lasers; EDFA, erbium-doped fiber amplifier; SHG-PPLN, second-harmonic generation using a periodic crystal; AOM, acousto-optic modulator; PID, proportional-integral-derivative controller. **b**, Frequency of the radio-frequency generator of the PLL for each Raman direction (red and blue lines). ω_C is changed with the Raman direction (right) to obtain symmetrized ramps. **c**, Average interferometric phase with respect to the average correction deduced from the phase of the beat note.

Extended Data Fig. 4 Analysis of the effect of local fluctuations on laser intensity.

a, Typical intensity profile of the laser beam. **b**, Characterization of the short-scale noise on the beam intensity. The intensity of the laser used for Bloch oscillations is reduced, leading to losses of atoms in the experiment (bottom). This induces a systematic effect on the recoil measurement (upper). To match the experimental data with the Monte Carlo simulation results, we added a small noise (2% at a scale of 50 μm) to the pictures recorded with a camera. **c**, Correction from the intensity profile calculated for each configuration. Only independent uncertainties are displayed, obtained from the Monte Carlo simulation. **d**, Results of the Monte Carlo simulation for the estimation of the effect of the one-photon light shift for different initial velocity and Raman inversion compensation (orange points: perfect compensation; blue and green points: one-photon light shift is 20% greater for one or the other Raman direction). The simulation was performed for all interferometer configurations (top: Raman high power;

bottom: Raman low power) and different (T_R , N_B , τ_B) values (from left to right).

Extended Data Table 1 Time sequence data

[Full size table](#)

Extended Data Table 2 Light shifts

[Full size table](#)

Supplementary information

[Peer Review File](#)

Rights and permissions

[Reprints and Permissions](#)

About this article



Check for
updates

Cite this article

Morel, L., Yao, Z., Cladé, P. *et al.* Determination of the fine-structure constant with an accuracy of 81 parts per trillion. *Nature* **588**, 61–65 (2020). <https://doi.org/10.1038/s41586-020-2964-7>

[Download citation](#)

- Received: 07 May 2020
- Accepted: 16 October 2020
- Published: 02 December 2020

- Issue Date: 03 December 2020
- DOI: <https://doi.org/10.1038/s41586-020-2964-7>

Comments

By submitting a comment you agree to abide by our [Terms](#) and [Community Guidelines](#). If you find something abusive or that does not comply with our terms or guidelines please flag it as inappropriate.

[Access through your institution](#)

[Change institution](#)

[Buy or subscribe](#)

Associated Content

Nature | News & Views

[Standard model of particle physics tested by the fine-structure constant](#)

- Holger Müller

This article was downloaded by **calibre** from <https://www.nature.com/articles/s41586-020-2964-7>

- Article
- [Published: 23 November 2020](#)

Electrical switching of magnetic order in an orbital Chern insulator

- [H. Polshyn](#) ORCID: orcid.org/0000-0001-8223-8896¹,
- [J. Zhu](#)²,
- [M. A. Kumar](#)¹,
- [Y. Zhang](#) ORCID: orcid.org/0000-0003-0369-0230¹,
- [F. Yang](#) ORCID: orcid.org/0000-0001-8418-7383¹,
- [C. L. Tschirhart](#)¹,
- [M. Serlin](#)¹,
- [K. Watanabe](#) ORCID: orcid.org/0000-0003-3701-8119³,
- [T. Taniguchi](#) ORCID: orcid.org/0000-0002-1467-3105⁴,
- [A. H. MacDonald](#)² &
- [A. F. Young](#) ORCID: orcid.org/0000-0001-5954-8028¹

[Nature](#) volume 588, pages66–70(2020) [Cite this article](#)

- 3572 Accesses
- 25 Altmetric
- [Metrics details](#)

Subjects

- [Electronic properties and devices](#)
- [Magnetic properties and materials](#)
- [Quantum Hall](#)
- [Surfaces, interfaces and thin films](#)

- [Topological insulators](#)

Abstract

Magnetism typically arises from the joint effect of Fermi statistics and repulsive Coulomb interactions, which favours ground states with non-zero electron spin. As a result, controlling spin magnetism with electric fields—a longstanding technological goal in spintronics and multiferroics^{1,2}—can be achieved only indirectly. Here we experimentally demonstrate direct electric-field control of magnetic states in an orbital Chern insulator^{3,4,5,6}, a magnetic system in which non-trivial band topology favours long-range order of orbital angular momentum but the spins are thought to remain disordered^{7,8,9,10,11,12,13,14}. We use van der Waals heterostructures consisting of a graphene monolayer rotationally faulted with respect to a Bernal-stacked bilayer to realize narrow and topologically non-trivial valley-projected moiré minibands^{15,16,17}. At fillings of one and three electrons per moiré unit cell within these bands, we observe quantized anomalous Hall effects¹⁸ with transverse resistance approximately equal to $h/2e^2$ (where h is Planck’s constant and e is the charge on the electron), which is indicative of spontaneous polarization of the system into a single-valley-projected band with a Chern number equal to two. At a filling of three electrons per moiré unit cell, we find that the sign of the quantum anomalous Hall effect can be reversed via field-effect control of the chemical potential; moreover, this transition is hysteretic, which we use to demonstrate non-volatile electric-field-induced reversal of the magnetic state. A theoretical analysis¹⁹ indicates that the effect arises from the topological edge states, which drive a change in sign of the magnetization and thus a reversal in the favoured magnetic state. Voltage control of magnetic states can be used to electrically pattern non-volatile magnetic-domain structures hosting chiral edge states, with applications ranging from reconfigurable microwave circuit elements to ultralow-power magnetic memories.

[Access through your institution](#)

[Change institution](#)

[Buy or subscribe](#)

Access options

Subscribe to Journal

Get full journal access for 1 year

185,98 €

only 3,58 € per issue

[Subscribe](#)

All prices are NET prices.

VAT will be added later in the checkout.

Rent or Buy article

Get time limited or full article access on ReadCube.

from \$8.99

[Rent or Buy](#)

All prices are NET prices.

Additional access options:

- [Log in](#)
- [Access through your institution](#)
- [Learn about institutional subscriptions](#)

Fig. 1: Twisted monolayer–bilayer graphene.



Fig. 2: Orbital Chern insulators with $C = 2$.



Fig. 3: Doping induced magnetization reversal.



Fig. 4: Non-volatile electrical control of a magnetic state at $T = 6.4$ K.



Data availability

Source data are available for this paper. All other data that support the plots within this paper and other findings of this study are available from the corresponding author upon reasonable request. [Source data](#) are provided with this paper.

References

1. 1.

Matsukura, F., Tokura, Y. & Ohno, H. Control of magnetism by electric fields. *Nat. Nanotechnol.* **10**, 209–220 (2015).

[ADS](#) [CAS](#) [Article](#) [PubMed](#) [Google Scholar](#)

2. 2.

Jiang, S., Shan, J. & Mak, K. F. Electric-field switching of two-dimensional van der Waals magnets. *Nat. Mater.* **17**, 406–410 (2018).

[ADS](#) [CAS](#) [Article](#) [PubMed](#) [Google Scholar](#)

3. 3.

Sharpe, A. L. et al. Emergent ferromagnetism near three-quarters filling in twisted bilayer graphene. *Science* **365**, 605–608 (2019).

[ADS](#) [CAS](#) [Article](#) [PubMed](#) [Google Scholar](#)

4. 4.

Serlin, M. et al. Intrinsic quantized anomalous Hall effect in a moiré heterostructure. *Science* **367**, 900–903 (2020).

[ADS](#) [CAS](#) [Article](#) [PubMed](#) [Google Scholar](#)

5. 5.

Chen, G. et al. Tunable correlated Chern insulator and ferromagnetism in a moiré superlattice. *Nature* **579**, 56–61 (2020); correction **581**, E3 (2020).

[ADS](#) [CAS](#) [Article](#) [PubMed](#) [Google Scholar](#)

6. 6.

Lu, X. et al. Superconductors, orbital magnets and correlated states in magic-angle bilayer graphene. *Nature* **574**, 653–657 (2019).

[ADS](#) [CAS](#) [Article](#) [PubMed](#) [Google Scholar](#)

7. 7.

Xie, M. & MacDonald, A. Nature of the correlated insulator states in twisted bilayer graphene. *Phys. Rev. Lett.* **124**, 097601 (2020).

[ADS](#) [CAS](#) [Article](#) [PubMed](#) [Google Scholar](#)

8. 8.

Bultinck, N., Chatterjee, S. & Zaletel, M. P. Mechanism for anomalous Hall ferromagnetism in twisted bilayer graphene. *Phys. Rev. Lett.* **124**, 166601 (2020).

[ADS](#) [MathSciNet](#) [CAS](#) [Article](#) [PubMed](#) [Google Scholar](#)

9. 9.

Zhang, Y.-H., Mao, D. & Senthil, T. Twisted bilayer graphene aligned with hexagonal boron nitride: anomalous Hall effect and a lattice model. *Phys. Rev. Res.* **1**, 033126 (2019).

[CAS](#) [Article](#) [Google Scholar](#)

10. 10.

Liu, J. & Dai, X. Theories for the correlated insulating states and quantum anomalous Hall phenomena in twisted bilayer graphene. Preprint at <https://arxiv.org/abs/1911.03760> (2020).

11. 11.

Wu, F. & Das Sarma, S. Collective excitations of quantum anomalous Hall ferromagnets in twisted bilayer graphene. *Phys. Rev. Lett.* **124**, 046403 (2020).

[ADS](#) [CAS](#) [Article](#) [PubMed](#) [Google Scholar](#)

12. 12.

Chatterjee, S., Bultinck, N. & Zaletel, M. P. Symmetry breaking and skyrmionic transport in twisted bilayer graphene. *Phys. Rev. B* **101**, 165141 (2020).

[ADS](#) [CAS](#) [Article](#) [Google Scholar](#)

13. 13.

Repellin, C., Dong, Z., Zhang, Y.-H. & Senthil, T. Ferromagnetism in narrow bands of moiré superlattices. *Phys. Rev. Lett.* **124**, 187601 (2020).

[ADS](#) [CAS](#) [Article](#) [PubMed](#) [Google Scholar](#)

14. 14.

Alavirad, Y. & Sau, J. D. Ferromagnetism and its stability from the one-magnon spectrum in twisted bilayer graphene. Preprint at <https://arxiv.org/abs/1907.13633> (2019).

15. 15.

Ma, Z. et al. Topological flat bands in twisted trilayer graphene. Preprint at <https://arxiv.org/abs/1905.00622> (2019).

16. 16.

Park, Y., Chittari, B. L. & Jung, J. Gate-tunable topological flat bands in twisted monolayer-bilayer graphene. *Phys. Rev. B* **102**, 035411 (2020).

[ADS](#) [CAS](#) [Article](#) [Google Scholar](#)

17. 17.

Rademaker, L., Protopopov, I. V. & Abanin, D. A. Topological flat bands and correlated states in twisted monolayer-bilayer graphene. *Phys. Rev. Res.* **2**, 033150 (2020).

[CAS](#) [Article](#) [Google Scholar](#)

18. 18.

Chang, C.-Z. et al. Experimental observation of the quantum anomalous Hall effect in a magnetic topological insulator. *Science* **340**, 167–170 (2013).

[ADS](#) [CAS](#) [Article](#) [PubMed](#) [Google Scholar](#)

19. 19.

Zhu, J., Su, J.-J. & MacDonald, A. H. The curious magnetic properties of orbital Chern insulators. Preprint at <https://arxiv.org/abs/2001.05084> (2020).

20. 20.

Haldane, F. D. M. Model for a quantum Hall effect without Landau levels: condensed-matter realization of the “parity anomaly”. *Phys. Rev. Lett.* **61**, 2015–2018 (1988).

[ADS](#) [CAS](#) [Article](#) [PubMed](#) [Google Scholar](#)

21. 21.

Song, J. C. W., Samutpraphoot, P. & Levitov, L. S. Topological Bloch bands in graphene superlattices. *Proc. Natl Acad. Sci. USA* **112**, 10879–10883 (2015).

[ADS](#) [MathSciNet](#) [CAS](#) [Article](#) [PubMed](#) [Google Scholar](#)

22. 22.

Zhang, Y.-H., Mao, D., Cao, Y., Jarillo-Herrero, P. & Senthil, T. Nearly flat Chern bands in moiré superlattices. *Phys. Rev. B* **99**, 075127 (2019).

[ADS](#) [CAS](#) [Article](#) [Google Scholar](#)

23. 23.

Liu, J., Ma, Z., Gao, J. & Dai, X. Quantum valley Hall effect, orbital magnetism, and anomalous Hall effect in twisted multilayer graphene systems. *Phys. Rev. X* **9**, 031021 (2019).

[CAS](#) [Google Scholar](#)

24. 24.

Bistritzer, R. & MacDonald, A. H. Moiré bands in twisted double-layer graphene. *Proc. Natl Acad. Sci. USA* **108**, 12233–12237 (2011).

[ADS](#) [CAS](#) [Article](#) [PubMed](#) [Google Scholar](#)

25. 25.

Cao, Y. et al. Correlated insulator behaviour at half-filling in magic-angle graphene superlattices. *Nature* **556**, 80–84 (2018).

[ADS](#) [CAS](#) [Article](#) [PubMed](#) [Google Scholar](#)

26. 26.

Chen, G. et al. Evidence of a gate-tunable Mott insulator in a trilayer graphene moiré superlattice. *Nat. Phys.* **15**, 237–241 (2019).

[CAS](#) [Article](#) [Google Scholar](#)

27. 27.

Shen, C. et al. Correlated states in twisted double bilayer graphene. *Nat. Phys.* **16**, 520–525 (2020).

[CAS](#) [Article](#) [Google Scholar](#)

28. 28.

Liu, X. et al. Tunable spin-polarized correlated states in twisted double bilayer graphene. *Nature* **583**, 221–225 (2020).

[ADS](#) [CAS](#) [Article](#) [PubMed](#) [Google Scholar](#)

29. 29.

Cao, Y. et al. Tunable correlated states and spin-polarized phases in twisted bilayer–bilayer graphene. *Nature* **583**, 215–220 (2020); correction **583**, E27 (2020).

[ADS](#) [CAS](#) [Article](#) [PubMed](#) [Google Scholar](#)

30. 30.

Burg, G. W. et al. Correlated insulating states in twisted double bilayer graphene. *Phys. Rev. Lett.* **123**, 197702 (2019).

[ADS](#) [CAS](#) [Article](#) [PubMed](#) [Google Scholar](#)

31. 31.

He, M. et al. Symmetry breaking in twisted double bilayer graphene. *Nat. Phys.* <https://doi.org/10.1038/s41567-020-1030-6> (2020).

32. 32.

Streda, P. Quantised Hall effect in a two-dimensional periodic potential. *J. Phys. C* **15**, L1299 (1982).

[ADS](#) [CAS](#) [Article](#) [Google Scholar](#)

33. 33.

Tschirhart, C. L. et al. Imaging orbital ferromagnetism in a moiré Chern insulator. Preprint at <https://arxiv.org/abs/2006.08053> (2020).

34. 34.

Chiba, D. et al. Anomalous Hall effect in field-effect structures of (Ga,Mn)As. *Phys. Rev. Lett.* **104**, 106601 (2010).

[ADS](#) [CAS](#) [Article](#) [PubMed](#) [Google Scholar](#)

35. 35.

Zhang, S. et al. Experimental observation of the gate-controlled reversal of the anomalous Hall effect in the intrinsic magnetic topological insulator MnBi₂Te₄ device. *Nano Lett.* **20**, 709–714 (2020).

[ADS](#) [Article](#) [PubMed](#) [Google Scholar](#)

36. 36.

Beekman, M., Heideman, C. L. & Johnson, D. C. Ferecrystals: non-epitaxial layered intergrowths. *Semicond. Sci. Technol.* **29**, 064012 (2014).

[ADS](#) [Article](#) [Google Scholar](#)

37. 37.

Viola, G. & DiVincenzo, D. P. Hall effect gyrators and circulators. *Phys. Rev. X* **4**, 021019 (2014).

[Google Scholar](#)

38. 38.

Lian, B., Sun, X.-Q., Vaezi, A., Qi, X.-L. & Zhang, S.-C. Topological quantum computation based on chiral Majorana fermions. *Proc. Natl Acad. Sci. USA* **115**, 10938–10942 (2018).

[ADS](#) [MathSciNet](#) [CAS](#) [Article](#) [PubMed](#) [Google Scholar](#)

[Download references](#)

Acknowledgements

We acknowledge discussions with J. Checkelsky, S. Chen, C. Dean, M. Yankowitz, D. Reilly, I. Sodemann and M. Zaletel. Work at UCSB was primarily supported by the ARO under MURI W911NF-16-1-0361. Measurements of twisted bilayer graphene (Extended Data Fig. [8](#)) and measurements at elevated temperatures (Extended Data Fig. [3](#)) were supported by a SEED grant and made use of shared facilities of the UCSB MRSEC (NSF DMR 1720256), a member of the Materials Research Facilities Network (www.mrfn.org). A.F.Y. acknowledges the support of the David and Lucille Packard Foundation under award 2016-65145. A.H.M. and J.Z. were supported by the National Science Foundation through the Center for Dynamics and Control of Materials, an NSF MRSEC under Cooperative Agreement number DMR-1720595, and by the Welch Foundation under grant TBF1473. C.L.T. acknowledges support from the Hertz Foundation and from the National Science Foundation Graduate Research Fellowship Program under grant 1650114. K.W. and T.T. acknowledge support from the Elemental Strategy Initiative conducted by the MEXT, Japan, Grant Number JPMXP0112101001, JSPS KAKENHI grant numbers JP20H00354 and the CREST(JPMJCR15F3), JST.

Author information

Affiliations

1. Department of Physics, University of California, Santa Barbara, Santa Barbara, CA, USA

H. Polshyn, M. A. Kumar, Y. Zhang, F. Yang, C. L. Tschirhart, M. Serlin & A. F. Young

2. Department of Physics, University of Texas, Austin, TX, USA

J. Zhu & A. H. MacDonald

3. Research Center for Functional Materials, National Institute for Materials Science, Tsukuba, Japan

K. Watanabe

4. International Center for Materials Nanoarchitectonics, National Institute for Materials Science, Tsukuba, Japan

T. Taniguchi

Authors

1. H. Polshyn

[View author publications](#)

You can also search for this author in [PubMed](#) [Google Scholar](#)

2. J. Zhu

[View author publications](#)

You can also search for this author in [PubMed](#) [Google Scholar](#)

3. M. A. Kumar

[View author publications](#)

You can also search for this author in [PubMed](#) [Google Scholar](#)

4. Y. Zhang

[View author publications](#)

You can also search for this author in [PubMed](#) [Google Scholar](#)

5. F. Yang

[View author publications](#)

You can also search for this author in [PubMed](#) [Google Scholar](#)

6. C. L. Tschirhart

[View author publications](#)

You can also search for this author in [PubMed](#) [Google Scholar](#)

7. M. Serlin

[View author publications](#)

You can also search for this author in [PubMed](#) [Google Scholar](#)

8. K. Watanabe

[View author publications](#)

You can also search for this author in [PubMed](#) [Google Scholar](#)

9. T. Taniguchi

[View author publications](#)

You can also search for this author in [PubMed](#) [Google Scholar](#)

10. A. H. MacDonald

[View author publications](#)

You can also search for this author in [PubMed](#) [Google Scholar](#)

11. A. F. Young

[View author publications](#)

You can also search for this author in [PubMed](#) [Google Scholar](#)

Contributions

H.P., M.A.K. and Y.Z. fabricated the devices. H.P., F.Y., C.L.T. and M.S. performed the measurements, advised by A.F.Y. J.Z. and A.H.M. performed the band structure calculations. K.W. and T.T. grew the hexagonal boron nitride crystals. H.P., A.H.M. and A.F.Y. wrote the manuscript with input from all other authors.

Corresponding author

Correspondence to [A. F. Young](#).

Ethics declarations

Competing interests

The authors declare no competing interests.

Additional information

Peer review information *Nature* thanks the anonymous reviewers for their contribution to the peer review of this work. Peer reviewer reports are available.

Publisher's note Springer Nature remains neutral with regard to jurisdictional claims in published maps and institutional affiliations.

Extended data figures and tables

[Extended Data Fig. 1 tMBG devices.](#)

a, Optical image of a typical graphene flake containing both MLG and BLG domains. **b**, The same image as in **a** but in greyscale and with enhanced contrast to clearly show the graphene flake. Dashed lines show the lines along which the flake was cut using atomic force microscopy. **c–f**, Optical images of completed tMBG devices D1 (**c**), D2 (**d**), D3 (**e**) and D4 (**f**). All scale bars, 10 μm .

[Extended Data Fig. 2 Longitudinal resistance of tMBG devices with different twist angles.](#)

a–d, Longitudinal resistance R_{xx} of devices D1 with $\theta \approx 1.25(1)^\circ$ (**a**), D2 with $\theta \approx 1.25(1)^\circ$ (**b**), D3 with $\theta = 1.385(5)^\circ$ (**c**) and D4 with $\theta \approx 0.90(1)^\circ$

(d). The numbers in parentheses indicate the uncertainty in the final digit. All measurements are performed at zero magnetic field and $T \approx 20$ mK.

Extended Data Fig. 3 Temperature dependence of the correlated states in device D1.

a, Temperature-dependent resistance measured at $D = 0.43$ V nm $^{-1}$ in device D1. **b, c**, Temperature-dependent resistance at selected carrier densities, marked by the arrows in **a**, for $n < 0$ (**b**) and $n > 0$ (**c**).

Extended Data Fig. 4 Development of Hall resistance at different n and D in device D1.

a, Longitudinal resistance R_{xx} of the correlated region at $B = 0$ T. **b–e**, Hall resistance R_{yx} measured at n and D marked by the dots in **a**. The colour of the dots in **a** corresponds to the colour of curves in **b–e**. Panels **b** and **c** show curves taken at small negative and positive dopings of $v = 1$. Panels **d** and **e** show curves taken at small negative and positive dopings of $v = 2$. **f**, Zoom-in of R_{xx} around $v = 1$. **g–i**, R_{yx} measured along the line cuts I (**g**), II (**h**) and III (**i**). R_{yx} in the plots are shifted by an offset.

Extended Data Fig. 5 Development of Hall resistance in device D3.

a, Longitudinal resistance R_{xx} of the correlated region at $B = 0$ T. **b**, Hall resistance R_{yx} of the same region as in **a**. **c**, Temperature dependence of R_{yx} at $v = 1$. The anomalous Hall effect disappears at 4.2 K. **d**, R_{xx} of the correlated region measured at $B = 2$ T. **e–i**, R_{yx} along the line cuts I (**e**), II (**f**), III (**g**), IV (**h**) and V (**i**).

Extended Data Fig. 6 Temperature dependence of the hysteresis at $v = 1$ and $v = 3$ in device D1.

a, b, Temperature dependence of the Hall resistance R_{yx} measured at $v = 1$ (**a**) and $v = 3$ (**b**). Insets show the temperature dependence of the height of the hysteresis loop height, as defined in Fig. 3a.

Extended Data Fig. 7 n and B dependence of the measured anomalous Hall effect, plotted at selected temperatures for $D = 0.4 \text{ V nm}^{-1}$ in device D1.

Temperatures are labelled on the individual panels.

Extended Data Fig. 8 Magnetization reversal in tBLG.

a, Anomalous Hall resistance ΔR_{yx} associated with tBLG ferromagnetism, extracted by subtracting $R_{yx}(B)$ as B is increased from $R_{yx}(B)$ as B is decreased. The tBLG device is the same as in ref. 4. The colour scale is fixed to the von Klitzing constant in the top of the plot to show the range of filling factors for which a robust quantum anomalous Hall effect is observed. The colour scale axis is dramatically reduced in the bottom plot to illustrate weak features in $\Delta R_{yx}(v)$. For $v < 3$, the coercive field of the ferromagnetic order increases dramatically, peaking at $v = 2.82$ electrons per moiré unit cell. For $v < 2.82$, ΔR_{yx} switches sign, indicating that the valley polarization of the ground state of the system at finite magnetic field has switched. **b**, A robust $C = 1$ quantum anomalous Hall effect at $v = 3.1$. **c**, Ferromagnetic hysteresis plots on opposite sides of the divergence of the coercive field close to $v = 2.82$ (with offset). Note the change in the relative sign of ΔR_{yx} .

Extended Data Fig. 9 Repeatability of magnetization switching with B and n measured in device D1.

a, Repeated magnetic-field hysteresis loops. **b**, Repeated doping hysteresis loops. Both panels taken under conditions analogous to those in Fig. 4b, described in the main text.

Supplementary information

Supplementary Information

This file contains Supplementary Text and Data Sections 1–3, including Supplementary Figures 1–4 and Supplementary References.

Peer Review File

Source data

Source Data Fig. 1

Source Data Fig. 2

Source Data Fig. 3

Source Data Fig. 4

Rights and permissions

Reprints and Permissions

About this article



Check for
updates

Cite this article

Polshyn, H., Zhu, J., Kumar, M.A. *et al.* Electrical switching of magnetic order in an orbital Chern insulator. *Nature* **588**, 66–70 (2020).
<https://doi.org/10.1038/s41586-020-2963-8>

Download citation

- Received: 16 April 2020
- Accepted: 01 September 2020
- Published: 23 November 2020
- Issue Date: 03 December 2020
- DOI: <https://doi.org/10.1038/s41586-020-2963-8>

Comments

By submitting a comment you agree to abide by our [Terms](#) and [Community Guidelines](#). If you find something abusive or that does not comply with our terms or guidelines please flag it as inappropriate.

[Access through your institution](#)

[Change institution](#)

[Buy or subscribe](#)

This article was downloaded by **calibre** from <https://www.nature.com/articles/s41586-020-2963-8>

- Article
- [Published: 23 November 2020](#)

Unconventional ferroelectricity in moiré heterostructures

- [Zhiren Zheng^{1 na1}](#),
- [Qiong Ma](#) [ORCID: orcid.org/0000-0002-5103-6973^{1,2 na1}](#),
- [Zhen Bi](#) [ORCID: orcid.org/0000-0003-0351-3963¹](#),
- [Sergio de la Barrera](#) [ORCID: orcid.org/0000-0002-5974-9476¹](#),
- [Ming-Hao Liu³](#),
- [Nannan Mao^{4,5}](#),
- [Yang Zhang¹](#),
- [Natasha Kiper¹](#),
- [Kenji Watanabe](#) [ORCID: orcid.org/0000-0003-3701-8119⁶](#),
- [Takashi Taniguchi](#) [ORCID: orcid.org/0000-0002-1467-3105⁷](#),
- [Jing Kong⁴](#),
- [William A. Tisdale](#) [ORCID: orcid.org/0000-0002-6615-5342⁵](#),
- [Ray Ashoori](#) [ORCID: orcid.org/0000-0001-5031-1673¹](#),
- [Nuh Gedik](#) [ORCID: orcid.org/0000-0002-6394-4987¹](#),
- [Liang Fu¹](#),
- [Su-Yang Xu^{1,8}](#) &
- [Pablo Jarillo-Herrero](#) [ORCID: orcid.org/0000-0001-8217-8213¹](#)

[Nature](#) volume 588, pages 71–76(2020) [Cite this article](#)

- 6002 Accesses
- 17 Altmetric
- [Metrics details](#)

Subjects

- [Electronic properties and materials](#)
- [Two-dimensional materials](#)

Abstract

The constituent particles of matter can arrange themselves in various ways, giving rise to emergent phenomena that can be surprisingly rich and often cannot be understood by studying only the individual constituents.

Discovering and understanding the emergence of such phenomena in quantum materials—especially those in which multiple degrees of freedom or energy scales are delicately balanced—is of fundamental interest to condensed-matter research^{1,2}. Here we report on the surprising observation of emergent ferroelectricity in graphene-based moiré heterostructures. Ferroelectric materials show electrically switchable electric dipoles, which are usually formed by spatial separation between the average centres of positive and negative charge within the unit cell. On this basis, it is difficult to imagine graphene—a material composed of only carbon atoms—exhibiting ferroelectricity³. However, in this work we realize switchable ferroelectricity in Bernal-stacked bilayer graphene sandwiched between two hexagonal boron nitride layers. By introducing a moiré superlattice potential (via aligning bilayer graphene with the top and/or bottom boron nitride crystals), we observe prominent and robust hysteretic behaviour of the graphene resistance with an externally applied out-of-plane displacement field. Our systematic transport measurements reveal a rich and striking response as a function of displacement field and electron filling, and beyond the framework of conventional ferroelectrics. We further directly probe the ferroelectric polarization through a non-local monolayer graphene sensor. Our results suggest an unconventional, odd-parity electronic ordering in the bilayer graphene/boron nitride moiré system. This emergent moiré ferroelectricity may enable ultrafast, programmable and atomically thin carbon-based memory devices.

[Access through your institution](#)

[Change institution](#)

[Buy or subscribe](#)

Access options

Subscribe to Journal

Get full journal access for 1 year

185,98 €

only 3,58 € per issue

[Subscribe](#)

All prices are NET prices.

VAT will be added later in the checkout.

Rent or Buy article

Get time limited or full article access on ReadCube.

from \$8.99

[Rent or Buy](#)

All prices are NET prices.

Additional access options:

- [Log in](#)
- [Access through your institution](#)
- [Learn about institutional subscriptions](#)

Fig. 1: Quadratic, chiral fermions on a moiré potential in a BLG/BN moiré superlattice.

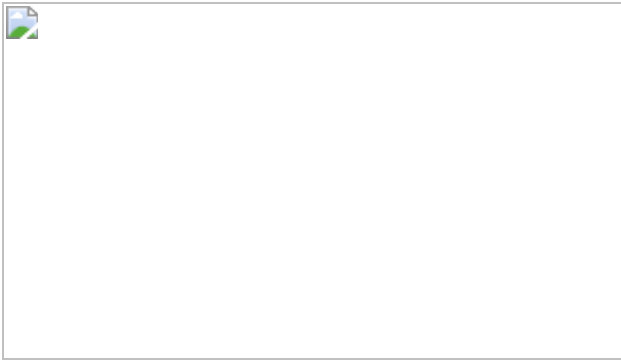


Fig. 2: Hysteretic transport behaviour for device H4.

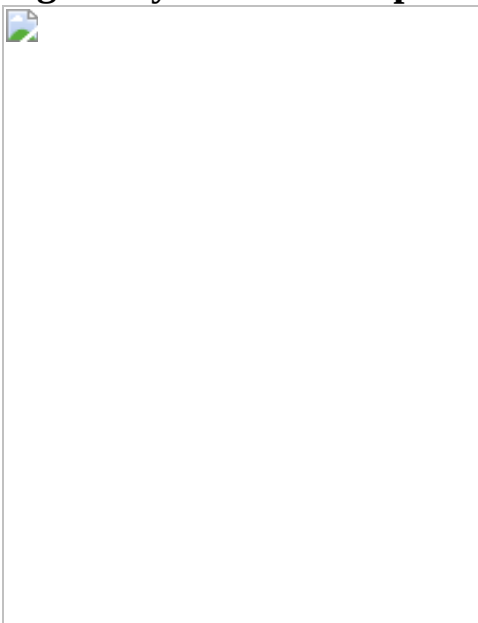


Fig. 3: Measuring the out-of-plane electric polarization and a possible microscopic picture based on interlayer charge transfer.



Fig. 4: Robustness of the ferroelectric switching in the graphene/BN moiré system.



Data availability

The data that support the plots within this paper and other findings of this study are available from the corresponding authors upon reasonable request.

References

1. 1.

Keimer, B. & Moore, J. E. The physics of quantum materials. *Nat. Phys.* **13**, 1045–1055 (2017).

[CAS](#) [Google Scholar](#)

2. 2.

Tokura, Y., Kawasaki, M. & Nagaosa, N. Emergent functions of quantum materials. *Nat. Phys.* **13**, 1056–1068 (2017).

[CAS](#) [Google Scholar](#)

3. 3.

Castro Neto, A. H., Guinea, F., Peres, N. M. R., Novoselov, K. S. & Geim, A. K. The electronic properties of graphene. *Rev. Mod. Phys.* **81**, 109–162 (2009).

[ADS](#) [CAS](#) [Google Scholar](#)

4. 4.

Armitage, N. P., Mele, E. J. & Vishwanath, A. Weyl and Dirac semimetals in three-dimensional solids. *Rev. Mod. Phys.* **90**, 015001 (2018).

[ADS](#) [MathSciNet](#) [CAS](#) [Google Scholar](#)

5. 5.

Suárez Morell, E., Correa, J., Vargas, P., Pacheco, M. & Barticevic, Z. Flat bands in slightly twisted bilayer graphene: tight-binding calculations. *Phys. Rev. B* **82**, 121407 (2010).

[ADS](#) [Google Scholar](#)

6. 6.

Li, G. et al. Observation of van Hove singularities in twisted graphene layers. *Nat. Phys.* **6**, 109–113 (2010).

[Google Scholar](#)

7. 7.

Bistritzer, R. & MacDonald, A. H. Moiré bands in twisted double-layer graphene. *Proc. Natl Acad. Sci. USA* **108**, 12233–12237 (2011).

[ADS](#) [CAS](#) [PubMed](#) [Google Scholar](#)

8. 8.

Cao, Y. et al. Unconventional superconductivity in magic-angle graphene superlattices. *Nature* **556**, 43–50 (2018).

[ADS](#) [CAS](#) [PubMed](#) [Google Scholar](#)

9. 9.

Cao, Y. et al. Correlated insulator behaviour at half-filling in magic-angle graphene superlattices. *Nature* **556**, 80–84 (2018).

[ADS](#) [CAS](#) [PubMed](#) [Google Scholar](#)

10. 10.

Yankowitz, M. et al. Tuning superconductivity in twisted bilayer graphene. *Science* **363**, 1059–1064 (2019).

[ADS](#) [CAS](#) [PubMed](#) [Google Scholar](#)

11. 11.

Sharpe, A. L. et al. Emergent ferromagnetism near three-quarters filling in twisted bilayer graphene. *Science* **365**, 605–608 (2019).

[ADS](#) [CAS](#) [PubMed](#) [Google Scholar](#)

12. 12.

Serlin, M. et al. Intrinsic quantized anomalous Hall effect in a moiré heterostructure. *Science* **367**, 900–903 (2020).

[ADS](#) [CAS](#) [PubMed](#) [Google Scholar](#)

13. 13.

Chen, G. et al. Evidence of a gate-tunable Mott insulator in a trilayer graphene moiré superlattice. *Nat. Phys.* **15**, 237–241 (2019).

[CAS](#) [Google Scholar](#)

14. 14.

Chen, G. et al. Tunable correlated Chern insulator and ferromagnetism in a moiré superlattice. *Nature* **579**, 56–61 (2020); correction **581**, E3 (2020).

[ADS](#) [CAS](#) [PubMed](#) [Google Scholar](#)

15. 15.

Burg, G. W. et al. Correlated insulating states in twisted double bilayer graphene. *Phys. Rev. Lett.* **123**, 197702 (2019).

[ADS](#) [CAS](#) [PubMed](#) [Google Scholar](#)

16. 16.

Liu, X. et al. Spin-polarized correlated insulator and superconductor in twisted double bilayer graphene. *Nature* **583**, 221–225 (2020).

[ADS](#) [CAS](#) [PubMed](#) [Google Scholar](#)

17. 17.

Cao, Y. et al. Tunable correlated states and spin-polarized phases in twisted bilayer–bilayer graphene. *Nature* **583**, 215–220 (2020); correction **583**, 215–220 (2020).

[ADS](#) [CAS](#) [PubMed](#) [Google Scholar](#)

18. 18.

Shen, C. et al. Correlated states in twisted double bilayer graphene. *Nat. Phys.* **16**, 520–525 (2020).

[CAS](#) [Google Scholar](#)

19. 19.

Wang, L. et al. Correlated electronic phases in twisted bilayer transition metal dichalcogenides. *Nat. Mater.* **19**, 861–866 (2020).

[CAS](#) [PubMed](#) [Google Scholar](#)

20. 20.

Regan, E. C. et al. Mott and generalized Wigner crystal states in WSe₂/WS₂ moiré superlattices. *Nature* **579**, 359–363 (2020).

[ADS](#) [CAS](#) [PubMed](#) [Google Scholar](#)

21. 21.

Tang, Y. et al. Simulation of Hubbard model physics in WSe₂/WS₂ moiré superlattices. *Nature* **579**, 353–358 (2020).

[ADS](#) [CAS](#) [PubMed](#) [Google Scholar](#)

22. 22.

Nandkishore, R. & Levitov, L. Dynamical screening and excitonic instability in bilayer graphene. *Phys. Rev. Lett.* **104**, 156803 (2010).

[ADS](#) [PubMed](#) [Google Scholar](#)

23. 23.

Fradkin, E., Kivelson, S. A., Lawler, M. J., Eisenstein, J. P. & Mackenzie, A. P. Nematic Fermi fluids in condensed matter physics. *Annu. Rev. Condens. Matter Phys.* **1**, 153–178 (2010).

[ADS](#) [CAS](#) [Google Scholar](#)

24. 24.

Fu, L. Parity-breaking phases of spin-orbit-coupled metals with gyrotropic, ferroelectric, and multipolar orders. *Phys. Rev. Lett.* **115**, 026401 (2015).

[ADS](#) [PubMed](#) [Google Scholar](#)

25. 25.

Fernandes, R. M. & Venderbos, J. W. Nematicity with a twist: rotational symmetry breaking in a moiré superlattice. *Sci. Adv.* **6**, eaba8834 (2020).

[ADS](#) [CAS](#) [PubMed](#) [PubMed Central](#) [Google Scholar](#)

26. 26.

Kozii, V. & Fu, L. Odd-parity superconductivity in the vicinity of inversion symmetry breaking in spin–orbit-coupled systems. *Phys. Rev. Lett.* **115**, 207002 (2015).

[ADS](#) [PubMed](#) [Google Scholar](#)

27. 27.

Mishra, A. & Lee, S. Topological multiferroic phases in the extended Kane–Mele–Hubbard model in the Hofstadter regime. *Phys. Rev. B* **98**, 235124 (2018).

[ADS](#) [CAS](#) [Google Scholar](#)

28. 28.

Cao, Y. et al. Nematicity and competing orders in superconducting magic-angle graphene. Preprint at <https://arxiv.org/abs/2004.04148> (2020).

29. 29.

Jiang, Y. et al. Charge order and broken rotational symmetry in magic-angle twisted bilayer graphene. *Nature* **573**, 91–95 (2019).

[ADS](#) [CAS](#) [PubMed](#) [Google Scholar](#)

30. 30.

Choi, Y. et al. Imaging electronic correlations in twisted bilayer graphene near the magic angle. *Nat. Phys.* **15**, 1174–1180 (2019); correction **15**, 1205 (2019).

[CAS](#) [Google Scholar](#)

31. 31.

Zhang, Y.-H., Mao, D., Cao, Y., Jarillo-Herrero, P. & Senthil, T. Nearly flat Chern bands in moiré superlattices. *Phys. Rev. B* **99**, 075127 (2019).

[ADS](#) [CAS](#) [Google Scholar](#)

32. 32.

McCann, E. & Koshino, M. The electronic properties of bilayer graphene. *Rep. Prog. Phys.* **76**, 056503 (2013).

[ADS](#) [PubMed](#) [Google Scholar](#)

33. 33.

Li, J., Martin, I., Büttiker, M. & Morpurgo, A. F. Topological origin of subgap conductance in insulating bilayer graphene. *Nat. Phys.* **7**, 38–42 (2011).

[CAS](#) [Google Scholar](#)

34. 34.

Ju, L. et al. Topological valley transport at bilayer graphene domain walls. *Nature* **520**, 650–655 (2015).

[ADS](#) [CAS](#) [PubMed](#) [Google Scholar](#)

35. 35.

Sui, M. et al. Gate-tunable topological valley transport in bilayer graphene. *Nat. Phys.* **11**, 1027–1031 (2015).

[CAS](#) [Google Scholar](#)

36. 36.

Shimazaki, Y. et al. Generation and detection of pure valley current by electrically induced Berry curvature in bilayer graphene. *Nat. Phys.* **11**,

1032–1036 (2015).

[CAS](#) [Google Scholar](#)

37. 37.

Ju, L. et al. Tunable excitons in bilayer graphene. *Science* **358**, 907–910 (2017).

[ADS](#) [CAS](#) [PubMed](#) [Google Scholar](#)

38. 38.

Maher, P. et al. Evidence for a spin phase transition at charge neutrality in bilayer graphene. *Nat. Phys.* **9**, 154–158 (2013).

[CAS](#) [Google Scholar](#)

39. 39.

Hunt, B. et al. Direct measurement of discrete valley and orbital quantum numbers in bilayer graphene. *Nat. Commun.* **8**, 948 (2017).

[ADS](#) [CAS](#) [PubMed](#) [PubMed Central](#) [Google Scholar](#)

40. 40.

Weitz, R. T., Allen, M., Feldman, B., Martin, J. & Yacoby, A. Broken-symmetry states in doubly gated suspended bilayer graphene. *Science* **330**, 812–816 (2010).

[ADS](#) [CAS](#) [PubMed](#) [Google Scholar](#)

41. 41.

Bao, W. et al. Evidence for a spontaneous gapped state in ultraclean bilayer graphene. *Proc. Natl Acad. Sci. USA* **109**, 10802–10805 (2012).

[ADS](#) [CAS](#) [PubMed](#) [Google Scholar](#)

42. 42.

Freitag, F., Trbovic, J., Weiss, M. & Schönenberger, C. Spontaneously gapped ground state in suspended bilayer graphene. *Phys. Rev. Lett.* **108**, 076602 (2012).

[ADS](#) [CAS](#) [PubMed](#) [Google Scholar](#)

43. 43.

Nam, Y., Ki, D.-K., Soler-Delgado, D. & Morpurgo, A. F. A family of finite-temperature electronic phase transitions in graphene multilayers. *Science* **362**, 324–328 (2018).

[ADS](#) [CAS](#) [PubMed](#) [Google Scholar](#)

44. 44.

Fei, Z. et al. Ferroelectric switching of a two-dimensional metal. *Nature* **560**, 336–339 (2018).

[ADS](#) [CAS](#) [PubMed](#) [Google Scholar](#)

45. 45.

Zhang, Y., Yuan, N. F. & Fu, L. Moiré quantum chemistry: charge transfer in transition metal dichalcogenide superlattices. Preprint at <https://arxiv.org/abs/1910.14061> (2019).

46. 46.

Katayama, Y., Tsui, D., Manoharan, H., Parihar, S. & Shayegan, M. Charge transfer at double-layer to single-layer transition in double-quantum-well systems. *Phys. Rev. B* **52**, 14817–14824 (1995).

[ADS](#) [CAS](#) [Google Scholar](#)

47. 47.

Zhang, Y. et al. Direct observation of a widely tunable bandgap in bilayer graphene. *Nature* **459**, 820–823 (2009).

[ADS](#) [CAS](#) [PubMed](#) [Google Scholar](#)

48. 48.

Young, A. F. & Levitov, L. S. Capacitance of graphene bilayer as a probe of layer-specific properties. *Phys. Rev. B* **84**, 085441 (2011).

[ADS](#) [Google Scholar](#)

49. 49.

Li, Y. et al. Probing symmetry properties of few-layer MoS₂ and h-BN by optical second-harmonic generation. *Nano Lett.* **13**, 3329–3333 (2013).

[ADS](#) [CAS](#) [PubMed](#) [Google Scholar](#)

50. 50.

Yankowitz, M. et al. Emergence of superlattice Dirac points in graphene on hexagonal boron nitride. *Nat. Phys.* **8**, 382–386 (2012).

[CAS](#) [Google Scholar](#)

51. 51.

Dean, C. R. et al. Hofstadter’s butterfly and the fractal quantum Hall effect in moiré superlattices. *Nature* **497**, 598–602 (2013).

[ADS](#) [CAS](#) [PubMed](#) [Google Scholar](#)

52. 52.

Ponomarenko, L. et al. Cloning of Dirac fermions in graphene superlattices. *Nature* **497**, 594–597 (2013).

[ADS](#) [CAS](#) [PubMed](#) [Google Scholar](#)

53. 53.

Hunt, B. et al. Massive Dirac fermions and Hofstadter butterfly in a van der Waals heterostructure. *Science* **340**, 1427–1430 (2013).

[ADS](#) [CAS](#) [PubMed](#) [Google Scholar](#)

54. 54.

Finney, N. R. et al. Tunable crystal symmetry in graphene–boron nitride heterostructures with coexisting moiré superlattices. *Nat. Nanotechnol.* **14**, 1029–1034 (2019).

[ADS](#) [CAS](#) [PubMed](#) [Google Scholar](#)

55. 55.

Novoselov, K. S. et al. Unconventional quantum Hall effect and Berry’s phase of 2π in bilayer graphene. *Nat. Phys.* **2**, 177–180 (2006).

[Google Scholar](#)

56. 56.

Craciun, M. et al. Trilayer graphene is a semimetal with a gate-tunable band overlap. *Nat. Nanotechnol.* **4**, 383–388 (2009).

[ADS](#) [CAS](#) [PubMed](#) [Google Scholar](#)

57. 57.

Jhang, S. H. et al. Stacking-order dependent transport properties of trilayer graphene. *Phys. Rev. B* **84**, 161408 (2011).

[ADS](#) [Google Scholar](#)

58. 58.

Wang, H., Wu, Y., Cong, C., Shang, J. & Yu, T. Hysteresis of electronic transport in graphene transistors. *ACS Nano* **4**, 7221–7228 (2010).

[CAS](#) [PubMed](#) [Google Scholar](#)

59. 59.

McGilly, L. et al. Visualization of moiré superlattices. *Nat. Nanotechnol.* **15**, 580–584 (2020).

[ADS](#) [CAS](#) [PubMed](#) [Google Scholar](#)

[Download references](#)

Acknowledgements

We thank D. Bandurin, V. Fatemi, L. Levitov, Y. Lin, J. Mundy, R. Ramesh, J. Sanchez-Yamagishi, H. Shen, J. Song, S. Todadri, A. Vishwanath and N. Yuan for discussions; and T. Dinh for initial efforts on this project. Work in the P.J.-H. group was supported by the US DOE, BES Office, Division of Materials Sciences and Engineering under award DE-SC0001819 (device fabrication and transport measurements), the Center for the Advancement of Topological Semimetals, an Energy Frontier Research Center funded by the US Department of Energy Office of Science, through the Ames Laboratory under contract DE-AC02-07CH11358 (data analysis), and the Gordon and Betty Moore Foundation’s EPiQS Initiative through grant GBMF9643 to P.J.-H. The development of new nanofabrication and characterization techniques enabling this work has been supported by the US DOE Office of Science, BES, under award DE-SC0019300. Partial support for measurement and characterization training was through AFOSR grant FA9550-16-1-0382. This work made use of the Materials Research Science and Engineering Center Shared Experimental Facilities supported

by the National Science Foundation (NSF) (grant number DMR-0819762). N.G. and S.-Y.X. acknowledge support from DOE, BES DMSE (data taking and analysis), and National Science Foundation under grant number DMR-1809815 (manuscript writing). K.W. and T.T. acknowledge support from the Elemental Strategy Initiative conducted by the MEXT, Japan, grant number JPMXP0112101001, JSPS KAKENHI grant numbers JP20H00354 and the CREST(JPMJCR15F3), JST. R.A. (capacitance measurements), Z.B., Y.Z. and L.F. (theory) acknowledge support from NSF Science and Technology Center for Integrated Quantum Materials grant DMR-1231319. M.-H.L. was supported by Taiwan Ministry of Science and Technology (MOST) under grant numbers 109-2112-M-006-020-MY3 and 108-2638-M-006-002-MY2. N.M. and J.K. acknowledge the support by the US Department of Energy (DOE), Office of Science, Basic Energy Sciences (BES) under award DE-SC0020042.

Author information

Author notes

1. These authors contributed equally: Zhiren Zheng, Qiong Ma

Affiliations

1. Department of Physics, Massachusetts Institute of Technology, Cambridge, MA, USA

Zhiren Zheng, Qiong Ma, Zhen Bi, Sergio de la Barrera, Yang Zhang, Natasha Kiper, Ray Ashoori, Nuh Gedik, Liang Fu, Su-Yang Xu & Pablo Jarillo-Herrero

2. Department of Physics, Boston College, Chestnut Hill, MA, USA

Qiong Ma

3. Department of Physics, National Cheng Kung University, Tainan, Taiwan

Ming-Hao Liu

4. Department of Electrical Engineering and Computer Science,
Massachusetts Institute of Technology, Cambridge, MA, USA

Nannan Mao & Jing Kong

5. Department of Chemical Engineering, Massachusetts Institute of
Technology, Cambridge, MA, USA

Nannan Mao & William A. Tisdale

6. Research Center for Functional Materials, National Institute for
Materials Science, Tsukuba, Japan

Kenji Watanabe

7. International Center for Material Nanoarchitectonics, National Institute
for Materials Science, Tsukuba, Japan

Takashi Taniguchi

8. Department of Chemistry and Chemical Biology, Harvard University,
Cambridge, MA, USA

Su-Yang Xu

Authors

1. Zhiren Zheng

[View author publications](#)

You can also search for this author in [PubMed](#) [Google Scholar](#)

2. Qiong Ma

[View author publications](#)

You can also search for this author in [PubMed](#) [Google Scholar](#)

3. Zhen Bi

[View author publications](#)

You can also search for this author in [PubMed](#) [Google Scholar](#)

4. Sergio de la Barrera

[View author publications](#)

You can also search for this author in [PubMed](#) [Google Scholar](#)

5. Ming-Hao Liu

[View author publications](#)

You can also search for this author in [PubMed](#) [Google Scholar](#)

6. Nannan Mao

[View author publications](#)

You can also search for this author in [PubMed](#) [Google Scholar](#)

7. Yang Zhang

[View author publications](#)

You can also search for this author in [PubMed](#) [Google Scholar](#)

8. Natasha Kiper

[View author publications](#)

You can also search for this author in [PubMed](#) [Google Scholar](#)

9. Kenji Watanabe

[View author publications](#)

You can also search for this author in [PubMed](#) [Google Scholar](#)

10. Takashi Taniguchi

[View author publications](#)

You can also search for this author in [PubMed](#) [Google Scholar](#)

11. Jing Kong

[View author publications](#)

You can also search for this author in [PubMed](#) [Google Scholar](#)

12. William A. Tisdale

[View author publications](#)

You can also search for this author in [PubMed](#) [Google Scholar](#)

13. Ray Ashoori

[View author publications](#)

You can also search for this author in [PubMed](#) [Google Scholar](#)

14. Nuh Gedik

[View author publications](#)

You can also search for this author in [PubMed](#) [Google Scholar](#)

15. Liang Fu

[View author publications](#)

You can also search for this author in [PubMed](#) [Google Scholar](#)

16. Su-Yang Xu

[View author publications](#)

You can also search for this author in [PubMed](#) [Google Scholar](#)

17. Pablo Jarillo-Herrero

[View author publications](#)

You can also search for this author in [PubMed](#) [Google Scholar](#)

Contributions

Q.M. and S.-Y.X. conceived the idea and experiment. Z.Z. fabricated devices, performed transport measurements and analysed data under the

supervision of Q.M. and P.J.-H. S.d.l.B. performed capacitance measurements with the help of Z.Z. under the supervision of R.A. Z.B., Y.Z. and N.K. performed theoretical modelling and bandstructure calculations under the supervision of S.-Y.X., Q.M., N.G. and L.F. M.-H.L. performed the simulation of the transport behaviours for the hysteretic devices. N.M. performed second-harmonic generation measurements of BN flakes under the supervision of J.K. and W.A.T. K.W. and T.T. grew the bulk BN single crystals. All authors discussed the results and wrote the manuscript.

Corresponding authors

Correspondence to [Qiong Ma](#) or [Pablo Jarillo-Herrero](#).

Ethics declarations

Competing interests

The authors declare no competing interests.

Additional information

Peer review information *Nature* thanks Kayoung Lee and the other, anonymous, reviewer(s) for their contribution to the peer review of this work.

Publisher's note Springer Nature remains neutral with regard to jurisdictional claims in published maps and institutional affiliations.

Extended data figures and tables

[Extended Data Fig. 1 Resistance data summary for devices M1, N0, T1, H1 and H4.](#)

Device schematic (**a**, **d**, **g**, **j**, **n**), dual-gate resistance map (**b**, **e**, **h**, **k**, **o**), n - D map (forward and backward) (**l**, **p**), and resistance as a function of externally applied displacement field at zero doping (**c**, **f**, **i**, **m**, **q**) for representative devices M1 (**a**–**c**), N0 (**d**–**f**), T1 (**g**–**i**), H1 (**j**–**m**) and H4 (**n**–**q**). The line traces along the electric-field direction are marked by black dashed lines. The superlattice resistance peaks are marked by cyan dashed lines. Note that the horizontal resistance line in **h** stems from a region of the sample that is only controlled by the top gate. Note that line traces in **q** are taken at $n_{\text{ext}} = 0$ from the n - D map (**p**), whereas line traces in Fig. 1f in the main text are taken at $V_{\text{TG}} = 0$ from the dual-gate map (Supplementary Fig. 25e, f), hence the difference in resistance magnitude.

Extended Data Fig. 2 Shifting of the hysteretic behaviour in device H4.

a–**c**, Forward (**a**) and backward (**b**) scans of the four-probe longitudinal resistance as a function of V_{TG} and V_{BG} and their difference (**c**). **d**–**f**, **g**–**i**, Same measurements as in **a**–**c**, except that V_{BG} is swept between 0 V and 50 V (**d**–**f**) and between –40 V and 0 V (**g**–**i**). We present a phenomenological model to simulate the resistance maps in [Supplementary Section V.3.2](#).

Extended Data Fig. 3 Hysteretic transport behaviour for device H2.

a–**d**, The four-probe resistance as a function of V_{BG} (range, –10 V to 10 V) and V_{TG} with ranges from 0 V to 5 V (**a**), from 5 V to –5 V (**b**), from –5 V to 10 V (**c**), and from 10 V to –5 V (**d**). The scan sequences are specified in the insets.

Extended Data Fig. 4 Shifting of the hysteretic behaviour in device H2.

a–**c**, Four-probe longitudinal resistance as a function of V_{TG} and V_{BG} for the forward (**a**) and backward (**b**) scans and their difference (**c**). **d**–**i**, Same

measurements as in **a–c**, except that V_{TG} is measured within 0 V to 5 V (**d–f**) and within −5 V to 0 V (**g–i**).

Extended Data Fig. 5 Hysteretic signature in Hall measurements for device H2.

a, b, The resistance measured while sweeping the externally applied displacement field D_{ext} in the forward (**a**) and backward (**b**) direction at each fixed carrier density n_{ext} . The carrier density scan direction is from the negative to positive values. **c–e**, Carrier density extracted from Hall measurements along the lines L1 (**c**), L2 (**d**) and L3 (**e**) denoted in **a**. Red and blue curves were taken during the forward and backward scan of D_{ext} , respectively.

Extended Data Fig. 6 Probing the out-of-plane electrical polarization using the top MLG sensor in device H4.

a, Experimental configuration for measurements of the conductance of the BLG. **b**, Measured conductance of the BLG as a function of V_{BG} (top gate is grounded). The red and blue curves correspond to the forward and backward V_{BG} scans, respectively. The vertical dashed lines denote the V_{BG} values that correspond to the charge-neutrality point of the BLG for forward and backward scans. **c**, Experimental configuration for the measurements of the conductance of the tp-MLG with gate voltage V_{BG} applied to bottom metal gate and the BLG grounded. **d**, Measured conductance of the tp-MLG as a function of V_{BG} with the experimental configuration in **c**. The gate voltages are the same as in **b** (Methods). The red and blue dots denote the conductance of the tp-MLG when the BLG is charge neutral. **e**, Experimental configuration for the measurements of the conductance of the tp-MLG with gate voltage V_{BL} applied to the BLG. **f**, Measurements of the conductance of the tp-MLG as a function of V_{BL} with the experimental configuration in **e**. The conductance of the monolayer at the red and blue dots in **d** can be inversely mapped to two different V_{BL} values, which corresponds to the difference of electrostatic potentials on the top surface of

BLG induced by ferroelectric switching (Methods). The in-plane bias voltage V_{SD} was kept below 1 mV for all the measurements.

Extended Data Fig. 7 Hysteresis signature in the bulk electronic compressibility of device H2.

a, b, Bottom capacitance C_b between the bottom gate and BLG as a function of the externally applied field, D_{ext} as the fast-scan axis, and gate-defined carrier density, n_{ext} as the slow-scan axis. The white arrows indicate the sweep direction of D_{ext} in each panel. Deviations of the capacitance from the geometric value reflect modulations in the electronic compressibility, $\partial n / \partial \mu$, from the total area of BLG overlapping the bottom gate. Data were collected by sweeping the displacement field at each fixed carrier density, as in Fig. 2*h, i*. Dark features indicate regions of incompressibility resulting from the opening of a gap in the BLG. The gapless point, a compressible state with high C_b , is achieved at a finite D_{ext} that depends on the sweep direction. **c**, Forward and backward traces from **a** and **b** at a fixed n_{ext} . **d**, Resistance traces at the same density showing resistance peaks corresponding to the incompressible features in **c**. **e**, Circuit schematic of the bottom gate capacitance measurement, including a two-stage cryogenic amplifier (enclosed in dashed box). Capacitance is measured by applying a small a.c. excitation voltage to the bottom gate, δV_{BG} , while also applying a nearly 180° out-of-phase signal, δV_{ref} , to a reference capacitor, C_{ref} to null the voltage at the bridge balance point, (B). Deviations in the balanced signal caused by variations in compressibility are amplified by two high electron-mobility transistors and measured at the drain of the second stage, δV_{out} . Carrier density n_{ext} and external field D_{ext} are controlled by top- and bottom-gate d.c. voltages V_{TG} and V_{BG} , in the same way as in the transport measurements.

Extended Data Fig. 8 Independence of the hysteretic behaviour on the sweep rate.

a–c, Forward (red) and backward (blue) sweeps of the bottom-gate capacitance, C_b , from device H2 at fixed carrier density n_{ext} with sweep rates of $2.2 \text{ mV nm}^{-1} \text{ s}^{-1}$ (**a**), $4.5 \text{ mV nm}^{-1} \text{ s}^{-1}$ (**b**), and $9.8 \text{ mV nm}^{-1} \text{ s}^{-1}$ (**c**). Sweep rates shown in each panel denote the rate at which the externally applied displacement field $D_{\text{ext}}/\epsilon_0$ was ramped in the BN dielectric layers. No noticeable variation was observed in the capacitance features for the large range of sweep rates.

Extended Data Table 1 Device parameters and characteristics for devices M1, N0, T1 and H1–H4

[Full size table](#)

Supplementary information

[Supplementary Information](#)

This file contains Supplementary Notes and Discussions and includes Supplementary Figures 1–33.

Rights and permissions

[Reprints and Permissions](#)

About this article



Check for
updates

Cite this article

Zheng, Z., Ma, Q., Bi, Z. *et al.* Unconventional ferroelectricity in moiré heterostructures. *Nature* **588**, 71–76 (2020). <https://doi.org/10.1038/s41586-020-2970-9>

Download citation

- Received: 06 May 2020
- Accepted: 07 October 2020
- Published: 23 November 2020
- Issue Date: 03 December 2020
- DOI: <https://doi.org/10.1038/s41586-020-2970-9>

Comments

By submitting a comment you agree to abide by our [Terms](#) and [Community Guidelines](#). If you find something abusive or that does not comply with our terms or guidelines please flag it as inappropriate.

[Access through your institution](#)

[Change institution](#)

[Buy or subscribe](#)

This article was downloaded by **calibre** from <https://www.nature.com/articles/s41586-020-2970-9>

- Article
- [Published: 02 December 2020](#)

Autonomous navigation of stratospheric balloons using reinforcement learning

- [Marc G. Bellemare](#) ORCID: orcid.org/0000-0002-6096-0105¹,
- [Salvatore Candido](#) ORCID: orcid.org/0000-0002-5847-0617³,
- [Pablo Samuel Castro](#)¹,
- [Jun Gong](#)³,
- [Marlos C. Machado](#)¹,
- [Subhodeep Moitra](#)¹,
- [Sameera S. Ponda](#)³ &
- [Ziyu Wang](#)²

[Nature](#) volume 588, pages 77–82(2020) [Cite this article](#)

- 265 Altmetric
- [Metrics details](#)

Subjects

- [Aerospace engineering](#)
- [Computer science](#)

Abstract

Efficiently navigating a superpressure balloon in the stratosphere¹ requires the integration of a multitude of cues, such as wind speed and solar

elevation, and the process is complicated by forecast errors and sparse wind measurements. Coupled with the need to make decisions in real time, these factors rule out the use of conventional control techniques^{2,3}. Here we describe the use of reinforcement learning^{4,5} to create a high-performing flight controller. Our algorithm uses data augmentation^{6,7} and a self-correcting design to overcome the key technical challenge of reinforcement learning from imperfect data, which has proved to be a major obstacle to its application to physical systems⁸. We deployed our controller to station Loon superpressure balloons at multiple locations across the globe, including a 39-day controlled experiment over the Pacific Ocean. Analyses show that the controller outperforms Loon's previous algorithm and is robust to the natural diversity in stratospheric winds. These results demonstrate that reinforcement learning is an effective solution to real-world autonomous control problems in which neither conventional methods nor human intervention suffice, offering clues about what may be needed to create artificially intelligent agents that continuously interact with real, dynamic environments.

[Access through your institution](#)

[Change institution](#)

[Buy or subscribe](#)

Access options

Subscribe to Journal

Get full journal access for 1 year

185,98 €

only 3,58 € per issue

[Subscribe](#)

All prices are NET prices.

VAT will be added later in the checkout.

Rent or Buy article

Get time limited or full article access on ReadCube.

from \$8.99

[Rent or Buy](#)

All prices are NET prices.

Additional access options:

- [Log in](#)
- [Access through your institution](#)
- [Learn about institutional subscriptions](#)

Fig. 1: Station-keeping with a superpressure balloon.



Fig. 2: Effect of parameters on controller performance.



Fig. 3: Performance profile of the reinforcement-learning controller in simulation.

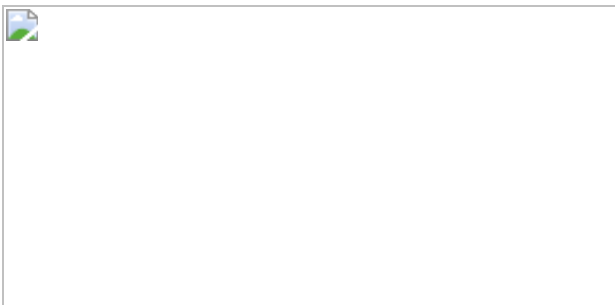


Fig. 4: Flight characteristics of controllers tested in the Pacific Ocean experiment.



Data availability

The data analysed in this paper are available from the corresponding authors on reasonable request.

Code availability

The code used to train the flight controllers is proprietary. The code used to analyse the generated data is available from the corresponding authors on reasonable request.

References

1. 1.

Lally, V. E. *Superpressure Balloons for Horizontal Soundings of the Atmosphere* Technical report (National Center for Atmospheric Research, 1967).

2. 2.

Anderson, B. & Moore, B. J. *Optimal Control: Linear Quadratic Methods* (Prentice-Hall, 1989).

3. 3.

Camacho, E. F. & Bordons, C. *Model Predictive Control* (Springer, 2007).

4. 4.

Bellman, R. E. *Dynamic Programming* (Princeton Univ. Press, 1957).

5. 5.

Sutton, R. S. & Barto, A. G. *Reinforcement Learning: An Introduction* 2nd edn (MIT Press, 2018).

6. 6.

Jakobi, N., Husbands, P. & Harvey, I. Noise and the reality gap: the use of simulation in evolutionary robotics. In *Proc. European Conf. Artificial Life* (eds Moran, F. et al.) 704–720 (Springer, 1995).

7. 7.

Tobin, J. et al. Domain randomization and generative models for robotic grasping. In *Proc. Intl Conf. Intelligent Robots and Systems* 3482–3489 (IEEE, 2018).

8. 8.

Levine, S., Kumar, A., Tucker, G. & Fu, J. Offline reinforcement learning: tutorial, review, and perspectives on open problems. Preprint at <https://arxiv.org/abs/2005.01643> (2020).

9. 9.

Kaelbling, L. P., Littman, M. L. & Cassandra, A. R. Planning and acting in partially observable stochastic domains. *Artif. Intell.* **101**, 99–134 (1998).

[MathSciNet](#) [Article](#) [Google Scholar](#)

10. 10.

Tesauro, G. Temporal difference learning and TD-Gammon. *Commun. ACM* **38**, 58–68 (1995).

[Article](#) [Google Scholar](#)

11. 11.

Mnih, V. et al. Human-level control through deep reinforcement learning. *Nature* **518**, 529–533 (2015).

[ADS](#) [CAS](#) [Article](#) [PubMed](#) [Google Scholar](#)

12. 12.

Silver, D. et al. Mastering the game of Go with deep neural networks and tree search. *Nature* **529**, 484–489 (2016).

[ADS](#) [CAS](#) [Article](#) [PubMed](#) [Google Scholar](#)

13. 13.

Lauer, C. J., Montgomery, C. A. & Dietterich, T. G. Managing fragmented fire-threatened landscapes with spatial externalities. *For. Sci.* **66**, 443–456 (2020).

[Article](#) [Google Scholar](#)

14. 14.

Simão, H. P. et al. An approximate dynamic programming algorithm for large-scale fleet management: a case application. *Transport. Sci.* **43**, 178–197 (2009).

[Article](#) [Google Scholar](#)

15. 15.

Mannion, P., Duggan, J. & Howley, E. An experimental review of reinforcement learning algorithms for adaptive traffic signal control. In

Autonomic Road Transport Support Systems (eds McCluskey, T. L. et al.) 47–66 (Springer, 2016).

16. 16.

Mirhoseini, A. et al. Chip placement with deep reinforcement learning. Preprint at <https://arxiv.org/abs/2004.10746> (2020).

17. 17.

Nevmyvaka, Y., Feng, Y. & Kearns, M. Reinforcement learning for optimized trade execution. In *Proc. Intl Conf. Machine Learning* (eds Cohen, W. W. & Moore, A.) 673–680 (ACM, 2006).

18. 18.

Pineau, J., Bellemare, M. G., Rush, A. J., Ghizaru, A. & Murphy, S. A. Constructing evidence-based treatment strategies using methods from computer science. *Drug Alcohol Depend.* **88**, S52–S60 (2007).

[Article](#) [PubMed](#) [PubMed Central](#) [Google Scholar](#)

19. 19.

Anderson, R. N., Boulanger, A., Powell, W. B. & Scott, W. Adaptive stochastic control for the smart grid. *Proc. IEEE* **99**, 1098–1115 (2011).

[Article](#) [Google Scholar](#)

20. 20.

Glavic, M., Fonteneau, R. & Ernst, D. Reinforcement learning for electric power system decision and control: past considerations and perspectives. *IFAC PapersOnLine* **50**, 6918–6927 (2017).

[Article](#) [Google Scholar](#)

21. 21.

Theocharous, G., Thomas, P. S. & Ghavazamdeh, M. Personalized ad recommendation systems for life-time value optimization with guarantees. In *Proc. Intl Joint Conf. Artificial Intelligence* (eds Yang, Q. & Wooldridge, M.) 1806–1812 (AAAI Press, IJCAI, 2015).

22. 22.

Ie, E. et al. SlateQ: a tractable decomposition for reinforcement learning with recommendation sets. In *Proc. Intl Joint Conf. Artificial Intelligence* (ed. Kraus, S.) 2592–2599 (IJCAI, 2019).

23. 23.

Ross, S., Gordon, G. & Bagnell, D. A reduction of imitation learning and structured prediction to no-regret online learning. In *Proc. 14th Intl Conf. Artificial Intelligence and Statistics*, (eds Gordon, G. et al.) 627–635 (PMLR, 2011).

24. 24.

Tan, J. et al. Sim-to-real: learning agile locomotion for quadruped robots. In *Proc. Robotics: Science and Systems XIV* (eds Kress-Gazir, H. et al.) 10 (2018).

25. 25.

Ng, A. Y., Kim, H. J., Jordan, M. I. & Sastry, S. Autonomous helicopter flight via reinforcement learning. In *Advances in Neural Information Processing Systems 16 (NIPS 2003)* (eds Saul, L. K. et al.) 799–806 (2004).

26. 26.

Abbeel, P., Coates, A., Quigley, M. & Ng, A. Y. An application of reinforcement learning to aerobatic helicopter flight. In *Advances in Neural Information Processing Systems 19 (NIPS 2006)* (eds Schölkopf, B. et al.) 1–8 (MIT Press, 2007).

27. 27.

Reddy, G., Wong-Ng, J., Celani, A., Sejnowski, T. J. & Vergassola, M. Glider soaring via reinforcement learning in the field. *Nature* **562**, 236–239 (2018).

[ADS](#) [CAS](#) [Article](#) [PubMed](#) [Google Scholar](#)

28. 28.

Lange, S., Riedmiller, M. & Voigtländer, A. Autonomous reinforcement learning on raw visual input data in a real world application. In *Proc. Intl Joint Conf. Neural Networks* <https://doi.org/10.1109/IJCNN.2012.6252823> (IEEE, 2012).

29. 29.

Levine, S., Pastor, P., Krizhevsky, A., Ibarz, J. & Quillen, D. Learning hand-eye coordination for robotic grasping with deep learning and large-scale data collection. *Int. J. Robot. Res.* **37**, 421–436 (2018).

[Article](#) [Google Scholar](#)

30. 30.

Kalashnikov, D. et al. Scalable deep reinforcement learning for vision-based robotic manipulation. In *Proc. Conf. Robot Learning* Vol. 87 (eds Billard, A. et al.) 651–673 (PMLR, 2018).

31. 31.

Andrychowicz, O. M. et al. Learning dexterous in-hand manipulation. *Int. J. Robot. Res.* **39**, 3–20 (2020).

[Article](#) [Google Scholar](#)

32. 32.

Zhang, C. Madden–Julian Oscillation. *Rev. Geophys.* **43**, RG2003 (2005).

[ADS](#) [Google Scholar](#)

33. 33.

Domeisen, D. I., Garfinkel, C. I. & Butler, A. H. The teleconnection of El Niño Southern Oscillation to the stratosphere. *Rev. Geophys.* **57**, 5–47 (2018).

[ADS](#) [Article](#) [Google Scholar](#)

34. 34.

Baldwin, M. et al. The quasi-biennial oscillation. *Rev. Geophys.* **39**, 179–229 (2001).

[ADS](#) [Article](#) [Google Scholar](#)

35. 35.

Friedrich, L. S. et al. A comparison of Loon balloon observations and stratospheric reanalysis products. *Atmos. Chem. Phys.* **17**, 855–866 (2017).

[ADS](#) [CAS](#) [Article](#) [Google Scholar](#)

36. 36.

Coy, L., Schoeberl, M. R., Pawson, S., Candido, S. & Carver, R. W. Global assimilation of Loon stratospheric balloon observations. *J. Geophys. Res. D* **124**, 3005–3019 (2019).

[ADS](#) [Article](#) [Google Scholar](#)

37. 37.

Rasmussen, C. E. & Williams, C. K. I. *Gaussian Processes for Machine Learning* (MIT Press, 2006).

38. 38.

Sondik, E. *The Optimal Control of Partially Observable Markov Processes*. PhD thesis, Stanford Univ. (1971).

39. 39.

Hersbach, H. et al. The ERA5 global reanalysis. *Q. J. R. Meteorol. Soc.* **146**, 1999–2049 (2020).

[ADS](#) [Article](#) [Google Scholar](#)

40. 40.

Perlin, K. An image synthesizer. *Comput. Graph.* **19**, 287–296 (1985).

[Article](#) [Google Scholar](#)

41. 41.

Bellemare, M. G., Naddaf, Y., Veness, J. & Bowling, M. The Arcade Learning Environment: an evaluation platform for general agents. *J. Artif. Intell. Res.* **47**, 253–279 (2013).

[Article](#) [Google Scholar](#)

42. 42.

Kolter, Z. J. & Ng, A. Y. Policy search via the signed derivative. In *Proc. Robotics: Science and Systems V* (eds Trinkle, J. et al.) 27 (MIT Press, 2009).

43. 43.

Levine, S. & Koltun, V. Guided policy search. In *Proc. Intl Conf. Machine Learning* Vol. 28-3 (eds Dasgupta, S. & McAllester, D.) 1–9 (ICML, 2013).

44. 44.

Lin, L. Self-improving reactive agents based on reinforcement learning, planning and teaching. *Mach. Learn.* **8**, 293–321 (1992).

[Google Scholar](#)

45. 45.

Nair, V. & Hinton, G. E. Rectified linear units improve restricted Boltzmann machines. In *Proc. 27th Intl Conf. Machine Learning* (ed. Fürnkranz, J.) 807–814 (ICML, 2010).

46. 46.

Dabney, W., Rowland, M., Bellemare, M. G. & Munos, R. Distributional reinforcement learning with quantile regression. In *Proc. AAAI Conf. Artificial Intelligence* 2892–2901 (AAAI Press, 2018).

47. 47.

Mnih, V. et al. Asynchronous methods for deep reinforcement learning. In *Proc. Intl Conf. Machine Learning* Vol. 48 (eds Balcan, M.-F. & Weinberger, K. Q.) 1928–1937 (ICML, 2016).

48. 48.

Munos, R. From bandits to Monte-Carlo tree search: the optimistic principle applied to optimization and planning. *Found. Trends Mach. Learn.* **7**, 1–129 (2014).

[ADS Article](#) [Google Scholar](#)

49. 49.

Gibson, J. J. *The Ecological Approach to Visual Perception* (Taylor & Francis, 1979).

50. 50.

Brooks, R. Elephants don't play chess. *Robot. Auton. Syst.* **6**, 3–15 (1990).

[Article](#) [Google Scholar](#)

51. 51.

Alexander, M., Grimsdell, A., Stephan, C. & Hoffmann, L. MJO-related intraseasonal variation in the stratosphere: gravity waves and zonal winds. *J. Geophys. Res. D Atmospheres* **123**, 775–788 (2018).

[ADS](#) [Article](#) [Google Scholar](#)

52. 52.

Watkins, C. J. C. H. *Learning from Delayed Rewards*. PhD thesis, Cambridge Univ. (1989).

53. 53.

Castro, P. S., Moitra, S., Gelada, C., Kumar, S. & Bellemare, M. G. Dopamine: a research framework for deep reinforcement learning. Preprint at <https://arxiv.org/abs/1812.06110> (2018).

54. 54.

Bellemare, M. G., Dabney, W. & Munos, R. A distributional perspective on reinforcement learning. In *Proc. Intl Conf. Machine Learning* Vol. 70 (eds Precup, D. & Teh, Y. W.) 449–458 (PMLR, 2017).

55. 55.

Kingma, D. & Ba, J. Adam: A method for stochastic optimization. In *Proc. Intl Conf. Learning Representations* (eds Benigo, Y. & LeCun, Y.) (2015).

56. 56.

Golovin, D. et al. Google Vizier: a service for black-box optimization. In *Proc. ACM SIGKDD Intl Conf. Knowledge Discovery and Data Mining* (eds Matwin, S. et al.) 1487–1496 (ACM, 2017).

[Download references](#)

Acknowledgements

We are grateful to J. Davidson for early ideation and prototyping. We thank V. Vanhoucke, K. Choromanski, V. Sindhwani, C. Boutilier, D. Precup, S. Mourad, S. Levine, K. Murphy, A. Faust, H. Larochelle and J. Platt for discussions; M. Bowling, A. Guez, D. Tarlow, J. Drouin, and M. Brenner for feedback on earlier versions of the manuscript; W. Dabney for feedback and help with design; T. Larivee for help with visuals; N. Mainville for project management support; R. Carver for information on weather phenomena; and the Loon operations team.

Author information

Affiliations

1. Brain Team, Google Research, Montreal, Quebec, Canada

Marc G. Bellemare, Pablo Samuel Castro, Marlos C. Machado & Subhodeep Moitra

2. Brain Team, Google Research, Toronto, Ontario, Canada

Ziyu Wang

3. Loon, Mountain View, CA, USA

Salvatore Candido, Jun Gong & Sameera S. Ponda

Authors

1. Marc G. Bellemare

[View author publications](#)

You can also search for this author in [PubMed](#) [Google Scholar](#)

2. Salvatore Candido

[View author publications](#)

You can also search for this author in [PubMed](#) [Google Scholar](#)

3. Pablo Samuel Castro

[View author publications](#)

You can also search for this author in [PubMed](#) [Google Scholar](#)

4. Jun Gong

[View author publications](#)

You can also search for this author in [PubMed](#) [Google Scholar](#)

5. Marlos C. Machado

[View author publications](#)

You can also search for this author in [PubMed](#) [Google Scholar](#)

6. Subhodeep Moitra

[View author publications](#)

You can also search for this author in [PubMed](#) [Google Scholar](#)

7. Sameera S. Ponda

[View author publications](#)

You can also search for this author in [PubMed](#) [Google Scholar](#)

8. Ziyu Wang

[View author publications](#)

You can also search for this author in [PubMed](#) [Google Scholar](#)

Contributions

S.C. conceptualized the problem. J.G., S.C., S.S.P., P.S.C. and S.M. built the technical infrastructure. S.C., M.G.B., J.G., M.C.M. and P.S.C. developed and tested the algorithm. M.C.M., M.G.B., P.S.C., S.C., S.S.P., J.G. and Z.W. performed experimentation and data analysis. M.G.B. and S.C. managed the project. M.G.B., S.C., M.C.M., P.S.C. and S.S.P. wrote the paper. Authors are listed alphabetically by surname.

Corresponding authors

Correspondence to [Marc G. Bellemare](#) or [Salvatore Candido](#).

Ethics declarations

Competing interests

M.G.B., S.C., J.G. and M.C.M. have filed patent applications relating to navigating aerial vehicles using deep reinforcement learning. The remaining authors declare no competing financial interests.

Additional information

Peer review information *Nature* thanks Scott Osprey and the other, anonymous, reviewer(s) for their contribution to the peer review of this work. Peer reviewer reports are available.

Publisher's note Springer Nature remains neutral with regard to jurisdictional claims in published maps and institutional affiliations.

Extended data figures and tables

[Extended Data Fig. 1 Flight paths of the reinforcement-learning controller during the Pacific Ocean experiment.](#)

The x and y axes represent longitude and latitude.

Extended Data Fig. 2 Flight paths of StationSeeker during the Pacific Ocean experiment, 1 of 2.

The x and y axes represent longitude and latitude, respectively.

Extended Data Fig. 3 Flight paths of StationSeeker during the Pacific Ocean experiment, 2 of 2.

The x and y axes represent longitude and latitude, respectively.

Extended Data Fig. 4 TWR50 and power consumption for different parametrizations of StationSeeker's score function.

Grey points indicate settings chosen uniformly at random from the following ranges: $w_A \in [0.4, 0.8]$ (at close range), $k_1 \in [0.01, 0.15]$, $g_{\text{unknown}} \in [0.4, 0.6]$ and $k_2 \in [0, 0.2]$. Each parameter was also varied in isolation (coloured points). Semantically interesting parameter choices are highlighted.

Extended Data Fig. 5 Distribution of returns predicted by the neural network.

Each panel indicates the predicted distributions for a particular state and action. The 51 quantiles output by the network are smoothed using kernel density estimation (σ determined from Scott's rule with interquartile range scaling). The dashed lines indicate the average of these locations. The states with depicted distributions are from different times (0, 3, 6 and 9 h) into the July 2002 simulation. We use the largest quantile to estimate the return that could be realized in the absence of partial observability.

Extended Data Fig. 6 Average distances and pairwise distances for perturbations of 12 initial conditions.

a, Distance to station, averaged over 125 perturbations. These numbers highlight how the 1 January to 1 June 2002 simulations (May excluded) were challenging station-keeping conditions. The 1 January configuration, in particular, lacked wind diversity. **b**, Average distance between pairs of balloons (7,750 pairs). Our controller exhibits greater robustness to challenging conditions.

[Extended Data Fig. 7 Scaled response of controllers to wind bearing and magnitude as a function of distance.](#)

We use the derivative of the network's action-value estimates, or response, as a proxy for the relative weight of an input. The two inputs tested here are the wind bearing and magnitude at the balloon's altitude; the curves report the derivative for the 'stay' action.

Extended Data Table 1 Inputs to the flight controller

[Full size table](#)

Extended Data Table 2 Hyperparameters defining the deep reinforcement-learning algorithm

[Full size table](#)

Supplementary information

[Video 1](#)

: Simulation of 125 balloons station keeping in challenging conditions. Simulation of 125 balloons starting from perturbations of a single initial position, either using the learned controller or StationSeeker. The station is denoted by an 'X', and the 50 km range by a dashed line. Unlike StationSeeker, the learned controller is able to remain near the station irrespective of initial conditions, despite a highly challenging wind field. It achieves this by navigating away from the station to avoid strong winds and remain in a relatively calm area, visible from 0:06 into the video.

[Video 2](#)

: Simulation of 125 balloons station keeping in easy conditions. Simulation of 125 balloons starting from perturbations of a single initial position, either using the learned controller or StationSeeker. In this relatively easy scenario, the learned controller arrives at the station faster than StationSeeker and regroups more quickly after the second night. Its performance is generally less dependent on the initial condition.

[Video 3](#)

: Flight #16 from the Pacific Ocean experiment. This video depicts flight #16 (learned controller) over the Pacific Ocean. The right panel depicts the controller's observed wind column, with colour representing uncertainty. StationSeeker's proposed choices are highlighted in that panel. When possible, the learned controller remains stationary by remaining at the interface between opposing wind sheets. Its station keeping patterns make use of the full 50 km range, providing it with additional energy late into the night.

[Peer Review File](#)

Rights and permissions

[Reprints and Permissions](#)

About this article



Check for
updates

Cite this article

Bellemare, M.G., Candido, S., Castro, P.S. *et al.* Autonomous navigation of stratospheric balloons using reinforcement learning. *Nature* **588**, 77–82 (2020). <https://doi.org/10.1038/s41586-020-2939-8>

Download citation

- Received: 01 April 2020
- Accepted: 29 September 2020
- Published: 02 December 2020
- Issue Date: 03 December 2020
- DOI: <https://doi.org/10.1038/s41586-020-2939-8>

Comments

By submitting a comment you agree to abide by our [Terms](#) and [Community Guidelines](#). If you find something abusive or that does not comply with our terms or guidelines please flag it as inappropriate.

[Access through your institution](#)

[Change institution](#)

[Buy or subscribe](#)

This article was downloaded by **calibre** from <https://www.nature.com/articles/s41586-020-2939-8>

- Article
- [Published: 13 October 2020](#)

Computational planning of the synthesis of complex natural products

- [Barbara Mikulak-Klucznik](#) ORCID: orcid.org/0000-0001-5263-0731¹,
- [Patrycja Gołębiowska](#)¹,
- [Alison A. Bayly](#)²,
- [Oskar Popik](#) ORCID: orcid.org/0000-0003-4224-5850¹,
- [Tomasz Klucznik](#) ORCID: orcid.org/0000-0001-9375-9945¹,
- [Sara Szymkuć](#)¹,
- [Ewa P. Gajewska](#)¹,
- [Piotr Dittwald](#)¹,
- [Olga Staszewska-Krajewska](#)¹,
- [Wiktor Beker](#)¹,
- [Tomasz Badowski](#)¹,
- [Karl A. Scheidt](#) ORCID: orcid.org/0000-0003-4856-3569²,
- [Karol Molga](#) ORCID: orcid.org/0000-0003-4808-7910¹,
- [Jacek Mlynarski](#) ORCID: orcid.org/0000-0002-1794-306X¹,
- [Milan Mrksich](#) ORCID: orcid.org/0000-0002-4964-796X² &
- [Bartosz A. Grzybowski](#) ORCID: orcid.org/0000-0001-6613-4261^{1,3,4}

[Nature](#) volume 588, pages83–88(2020) [Cite this article](#)

- 10k Accesses
- 196 Altmetric

- [Metrics details](#)

Subjects

- [Automation](#)
- [Cheminformatics](#)
- [Natural product synthesis](#)
- [Chemical synthesis](#)

Abstract

Training algorithms to computationally plan multistep organic syntheses has been a challenge for more than 50 years^{1,2,3,4,5,6,7}. However, the field has progressed greatly since the development of early programs such as LHASA^{1,7}, for which reaction choices at each step were made by human operators. Multiple software platforms^{6,8,9,10,11,12,13,14} are now capable of completely autonomous planning. But these programs ‘think’ only one step at a time and have so far been limited to relatively simple targets, the syntheses of which could arguably be designed by human chemists within minutes, without the help of a computer. Furthermore, no algorithm has yet been able to design plausible routes to complex natural products, for which much more far-sighted, multistep planning is necessary^{15,16} and closely related literature precedents cannot be relied on. Here we demonstrate that such computational synthesis planning is possible, provided that the program’s knowledge of organic chemistry and data-based artificial intelligence routines are augmented with causal relationships^{17,18}, allowing it to ‘strategize’ over multiple synthetic steps. Using a Turing-like test administered to synthesis experts, we show that the routes designed by such a program are largely indistinguishable from those designed by humans. We also successfully validated three computer-designed syntheses of natural products in the laboratory. Taken together, these results indicate that expert-level automated synthetic planning is feasible, pending continued improvements to the reaction knowledge base and further code optimization.

[Access through your institution](#)

[Change institution](#)

[Buy or subscribe](#)

Access options

Subscribe to Journal

Get full journal access for 1 year

185,98 €

only 3,58 € per issue

[Subscribe](#)

All prices are NET prices.

VAT will be added later in the checkout.

Rent or Buy article

Get time limited or full article access on ReadCube.

from \$8.99

[Rent or Buy](#)

All prices are NET prices.

Additional access options:

- [Log in](#)
- [Access through your institution](#)
- [Learn about institutional subscriptions](#)

Fig. 1: Automatic synthesis planning over large networks of possible reactions.



Fig. 2: Synthesis Turing test.



Fig. 3: Synthesis of dauricine.



Fig. 4: Total enantioselective synthesis of (*R,R,S*)-tacamonidine.

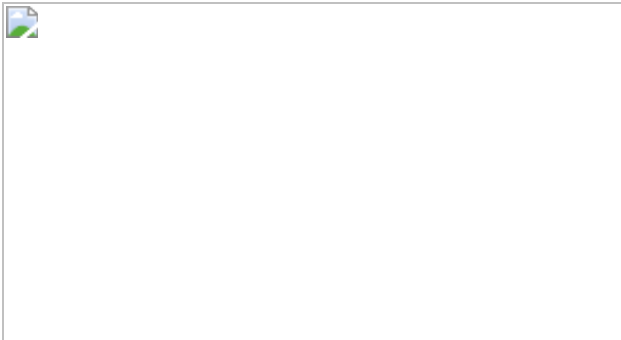
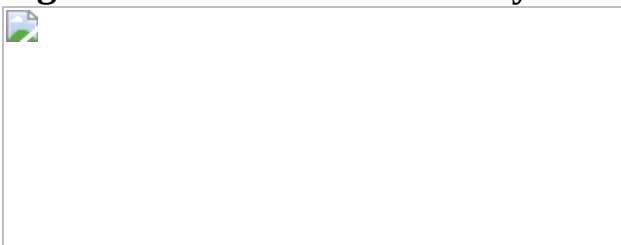


Fig. 5: Total enantioselective synthesis of lamellodysidine A.



Data availability

All data that support the findings of this study are available within the paper and its Supplementary Information, or from the corresponding authors on reasonable request.

Code availability

In Supplementary Data, we provide the pseudocode for the multistep retrosynthetic design, pathway generation and retrieval (PSEUDOCODE_Aug2.pdf), an example of one of the reaction rules as coded in Chematica (RULE.pdf), and additional details of the availability and execution of the software (README_Aug2.pdf).

References

1. 1.

Corey, E. J. & Wipke, W. T. Computer-assisted design of complex organic syntheses. *Science* **166**, 178–192 (1969).

[CAS](#) [ADS](#) [Google Scholar](#)

2. 2.

Gelernter, H. L. et al. Empirical explorations of SYNCHEM. *Science* **197**, 1041–1049 (1977).

[CAS](#) [ADS](#) [Google Scholar](#)

3. 3.

Hanessian, S., Franco, J. & Larouche, B. The psychobiological basis of heuristic synthesis planning - man, machine and the Chiron approach. *Pure Appl. Chem.* **62**, 1887–1910 (1990).

[CAS](#) [Google Scholar](#)

4. 4.

Hendrickson, J. B. Systematic synthesis design. 6. Yield analysis and convergency. *J. Am. Chem. Soc.* **99**, 5439–5450 (1977).

[CAS](#) [Google Scholar](#)

5. 5.

Ugi, I. et al. Computer-assisted solution of chemical problems - the historical development and the present state of the art of a new discipline of chemistry. *Angew. Chem. Int. Edn Engl.* **32**, 201–227 (1993).

[Google Scholar](#)

6. 6.

Todd, M. H. Computer-aided organic synthesis. *Chem. Soc. Rev.* **34**, 247–266 (2005).

[CAS](#) [Google Scholar](#)

7. 7.

Ravitz, O. Data-driven computer aided synthesis design. *Drug Discov. Today. Technol.* **10**, e443–e449 (2013).

[Google Scholar](#)

8. 8.

Szymkuć, S. et al. Computer-assisted synthetic planning: the end of the beginning. *Angew. Chem. Int. Ed.* **55**, 5904–5937 (2016).

[Google Scholar](#)

9. 9.

Klucznik, T. et al. Efficient syntheses of diverse, medicinally relevant targets planned by computer and executed in the laboratory. *Chem* **4**, 522–532 (2018).

[CAS](#) [Google Scholar](#)

10. 10.

Segler, M. H. S., Preuss, M. & Waller, M. P. Planning chemical syntheses with deep neural networks and symbolic AI. *Nature* **555**, 604–610 (2018).

[CAS](#) [ADS](#) [Google Scholar](#)

11. 11.

Coley, C. W. et al. A robotic platform for flow synthesis of organic compounds informed by AI planning. *Science* **365**, eaax1566 (2019).

[CAS](#) [Google Scholar](#)

12. 12.

SciFinderⁿ, <https://scifinder-n.cas.org> (accessed 20 July 2020).

13. 13.

Lee, A. A. et al. Molecular transformer unifies reaction prediction and retrosynthesis across pharma chemical space. *Chem. Commun.* **55**, 12152–12155 (2019).

[CAS](#) [Google Scholar](#)

14. 14.

Schwaller, P. et al. Predicting retrosynthetic pathways using transformer-based models and a hyper-graph exploration strategy. *Chem. Sci.* **11**, 3316–3325 (2020).

[CAS](#) [Google Scholar](#)

15. 15.

Nicolaou, K. C. *Classics in Total Synthesis II: More Targets, Strategies, Methods* (Wiley-VCH, 2003).

16. 16.

Huang, P. *Efficiency in Natural Product Total Synthesis* (Wiley, 2018).

17. 17.

Yi, K. et al. CLEVERER: collision events for video representation and reasoning. Preprint at <https://arxiv.org/abs/1910.01442> (2020).

18. 18.

Bergstein, B. *What AI still can't do*. MIT Technical Review
<https://www.technologyreview.com/s/615189/what-ai-still-cant-do/> (2020).

19. 19.

Kowalik, M. et al. Parallel optimization of synthetic pathways within the network of organic chemistry. *Angew. Chem. Int. Ed.* **51**, 7928–7932 (2012).

[CAS](#) [Google Scholar](#)

20. 20.

Lin, Y. et al. Reinforcing the supply chain of COVID-19 therapeutics with expert-coded retrosynthetic software. Preprint at <https://doi.org/10.26434/chemrxiv.12765410.v1> (2020).

21. 21.

Beker, W., Gajewska, E. P., Badowski, T. & Grzybowski, B. A. Prediction of major regio-, site-, and diastereoisomers in Diels-Alder reactions by using machine-learning: the importance of physically meaningful descriptors. *Angew. Chem. Int. Ed.* **58**, 4515–4519 (2019).

[CAS](#) [Google Scholar](#)

22. 22.

Badowski, T., Gajewska, E. P., Molga, K. & Grzybowski, B. A. Synergy between expert and machine-learning approaches allows for improved retrosynthetic planning. *Angew. Chem. Int. Ed.* **59**, 725–730 (2020).

[CAS](#) [Google Scholar](#)

23. 23.

Badowski, T., Molga, K. & Grzybowski, B. A. Selection of cost-effective yet chemically diverse pathways from the networks of computer-generated retrosynthetic plans. *Chem. Sci.* **10**, 4640–4651 (2019).

[CAS](#) [PubMed](#) [PubMed Central](#) [Google Scholar](#)

24. 24.

Molga, K., Dittwald, P. & Grzybowski, B. A. Computational design of syntheses leading to compound libraries or isotopically labelled targets. *Chem. Sci.* **10**, 9219–9232 (2019).

[CAS](#) [PubMed](#) [PubMed Central](#) [Google Scholar](#)

25. 25.

Molga, K., Dittwald, P. & Grzybowski, B. A. Navigating around patented routes by preserving specific motifs along computer-planned retrosynthetic pathways. *Chem* **5**, 460–473 (2019).

[CAS](#) [Google Scholar](#)

26. 26.

Gajewska, E. P. et al. Algorithmic discovery of tactical combinations for advanced organic syntheses. *Chem* **6**, 280–293 (2020).

[Google Scholar](#)

27. 27.

Molga, K., Gajewska, E. P., Szymkuć, S. & Grzybowski, B. A. The logic of translating chemical knowledge into machine-processable forms: a modern playground for physical-organic chemistry. *React. Chem. Eng.* **4**, 1506–1521 (2019).

[CAS](#) [Google Scholar](#)

28. 28.

Emami, F. E. et al. A priori estimation of organic reaction yields. *Angew. Chem. Int. Ed.* **54**, 10797–10801 (2015).

[CAS](#) [Google Scholar](#)

29. 29.

Skoraczyński, G. et al. Predicting the outcomes of organic reactions via machine learning: are current descriptors sufficient? *Sci. Rep.* **7**, 3582 (2017).

[ADS](#) [PubMed](#) [PubMed Central](#) [Google Scholar](#)

30. 30.

Corey, E. J. & Cheng, X.-M. *The Logic of Chemical Synthesis* (Wiley, 1995).

31. 31.

Serratosa, F. *Organic Chemistry in Action: The Design of Organic Synthesis* (Elsevier, 1996).

32. 32.

Copeland, B. J. (ed.) *The Essential Turing: The Ideas That Gave Birth to the Computer Age* (Oxford Univ. Press, 2004).

33. 33.

Shah, H., Warwick, K., Vallverdú, J. & Wu, D. Can machines talk? Comparison of Eliza with modern dialogue systems. *Comput. Human Behav.* **58**, 278–295 (2016).

[Google Scholar](#)

34. 34.

Yang, Z. et al. Dauricine induces apoptosis, inhibits proliferation and invasion through inhibiting NF-κB signaling pathway in colon cancer cells. *J. Cell. Physiol.* **225**, 266–275 (2010).

[CAS](#) [Google Scholar](#)

35. 35.

Kametani, T. & Fukumoto, K. Total synthesis of (\pm)-dauricine. *Tetrahedr. Lett.* **5**, 2771–2775 (1964).

[Google Scholar](#)

36. 36.

Lim, K.-H. et al. Ibogan, tacaman, and cytotoxic bisindole alkaloids from *Tabernaemontana*. Cononusine, an iboga alkaloid with unusual incorporation of a pyrrolidone moiety. *J. Nat. Prod.* **78**, 1129–1138 (2015).

[CAS](#) [Google Scholar](#)

37. 37.

Torii, M. et al. Lamellodysidines A and B, sesquiterpenes isolated from the marine sponge *Lamellodysidea herbacea*. *J. Nat. Prod.* **80**, 2536–2541 (2017).

[CAS](#) [Google Scholar](#)

38. 38.

Fialkowski, M., Bishop, K. J. M., Chubukov, V. A., Campbell, C. J. & Grzybowski, B. A. Architecture and evolution of organic chemistry. *Angew. Chem. Int. Ed.* **44**, 7263–7269 (2005).

[CAS](#) [Google Scholar](#)

39. 39.

Grzybowski, B. A., Bishop, K. J. M., Kowalczyk, B. & Wilmer, C. E. The ‘wired’ universe of organic chemistry. *Nat. Chem.* **1**, 31–36 (2009).

[CAS](#) [PubMed](#) [PubMed Central](#) [Google Scholar](#)

40. 40.

Sammut, C. in *Encyclopedia of Machine Learning and Data Mining* (eds Sammut, C. & Webb, G. I.) 120 (Springer, 2017).

41. 41.

Gremmen, C., Willemse, B., Wanner, M. J. & Koomen, G.-J. Enantiopure tetrahydro- β -carbolines via Pictet–Spengler reactions with N-sulfinyl tryptamines. *Org. Lett.* **2**, 1955–1958 (2000).

[CAS](#) [Google Scholar](#)

42. 42.

Gansäuer, A., Worgull, D., Knebel, K., Huth, I. & Schnakenburg, G. 4-exo cyclizations by template catalysis. *Angew. Chem. Int. Ed.* **48**, 8882–8885 (2009).

[Google Scholar](#)

43. 43.

Hadjaz, F., Yous, S., Lebegue, N., Berthelot, P. & Carato, P. A mild and efficient route to 2-benzyl tryptamine derivatives via ring-opening of β -carbolines. *Tetrahedron* **64**, 10004–10008 (2008).

[CAS](#) [Google Scholar](#)

44. 44.

Taylor, M. S. & Jacobsen, E. N. Highly enantioselective catalytic acyl-Pictet–Spengler reactions. *J. Am. Chem. Soc.* **126**, 10558–10559 (2004).

[CAS](#) [Google Scholar](#)

45. 45.

Goetz, A. E., Silberstein, A. L., Corsello, M. A. & Garg, N. K. Concise enantiospecific total synthesis of tubingensin A. *J. Am. Chem. Soc.* **136**, 3036–3039 (2014).

[CAS](#) [PubMed](#) [PubMed Central](#) [Google Scholar](#)

46. 46.

White, J. D., Grether, U. M. & Lee, Ch.-S. (R)-(+)-3,4-dimethylcyclohex-2-en-1-one. *Org. Synth.* **82**, 108 (2005).

[CAS](#) [Google Scholar](#)

47. 47.

Nicolaou, K. C., Zhong, Y.-L. & Baran, P. S. A new method for the one-step synthesis of α,β -unsaturated carbonyl systems from saturated alcohols and carbonyl compounds. *J. Am. Chem. Soc.* **122**, 7596–7597 (2000).

[CAS](#) [Google Scholar](#)

48. 48.

Xu, L., Wang, C., Gao, Z. & Zhao, Y.-M. Total synthesis of (\pm)-cephanolides B and C via a palladium-catalyzed cascade cyclization and late-stage sp^3 C–H bond oxidation. *J. Am. Chem. Soc.* **140**, 5653–5658 (2018).

[CAS](#) [Google Scholar](#)

49. 49.

Xu, B., Xun, W., Su, S. & Zhai, H. Total syntheses of (–)-conidiogenone B, (–)-conidiogenone, and (–)-conidiogenol. *Angew. Chem. Int. Ed.* **59**, 16475 (2020).

[CAS](#) [Google Scholar](#)

50. 50.

Hafeman, N. J. et al. The total synthesis of (−)-scabrolide A. *J. Am. Chem. Soc.* **142**, 8585–8590 (2020).

[CAS](#) [Google Scholar](#)

51. 51.

Wilde, N. C., Isomura, M., Mendoza, A. & Baran, P. S. Two-phase synthesis of (−)-taxuyunnanine D. *J. Am. Chem. Soc.* **136**, 4909–4912 (2014).

[CAS](#) [PubMed](#) [PubMed Central](#) [Google Scholar](#)

52. 52.

Zhang, Y. & Danishefsky, S. J. Total synthesis of (\pm)-aplykurodinone-1: traceless stereochemical guidance. *J. Am. Chem. Soc.* **132**, 9567–9569 (2010).

[CAS](#) [PubMed](#) [PubMed Central](#) [Google Scholar](#)

53. 53.

Guo, L., Frey, W. & Plietker, B. Catalytic enantioselective total synthesis of the picrotoxane alkaloids (−)-dendrobine, (−)-mubironine B, and (−)-dendroxine. *Org. Lett.* **20**, 4328–4331 (2018).

[CAS](#) [Google Scholar](#)

54. 54.

Nicolaou, K. C. et al. Total synthesis and structural revision of antibiotic CJ-16,264. *Angew. Chem. Int. Ed.* **54**, 9203–9208 (2015).

[CAS](#) [Google Scholar](#)

55. 55.

Chuang, K. V., Xu, C. & Reisman, S. E. A 15-step synthesis of (+)-ryanodol. *Science* **353**, 912–915 (2016).

[CAS](#) [ADS](#) [PubMed](#) [PubMed Central](#) [Google Scholar](#)

56. 56.

Kanda, Y. et al. Two-phase synthesis of taxol. *J. Am. Chem. Soc.* **142**, 10526–10533 (2020).

[CAS](#) [Google Scholar](#)

57. 57.

Lambert, T. H. & Danishefsky, S. J. Total synthesis of UCS1025A. *J. Am. Chem. Soc.* **128**, 426–427 (2006).

[CAS](#) [Google Scholar](#)

58. 58.

Roszak, R., Beker, W., Molga, K. & Grzybowski, B. A. Rapid and accurate prediction of pKa values of C–H acids using graph convolutional neural networks. *J. Am. Chem. Soc.* **141**, 17142–17149 (2019).

[CAS](#) [Google Scholar](#)

59. 59.

Crosby, S. R., Harding, J. R., King, C. D., Parker, G. D. & Willis, C. L. Oxonia-Cope rearrangement and side-chain exchange in the Prins cyclization. *Org. Lett.* **4**, 577–580 (2002).

[CAS](#) [Google Scholar](#)

60. 60.

Kormann, C., Heinemann, F. W. & Gmeiner, P. A consecutive Diels–Alder approach toward a Tet repressor directed combinatorial library. *Tetrahedron* **62**, 6899–6908 (2006).

[CAS](#) [Google Scholar](#)

61. 61.

Owens, K. R. et al. Total synthesis of the diterpenoid alkaloid Arcutinidine using a strategy inspired by chemical network analysis. *J. Am. Chem. Soc.* **141**, 13713–13717 (2019).

[CAS](#) [Google Scholar](#)

62. 62.

Jung, M. E. & Davidov, P. Efficient synthesis of a tricyclic BCD analogue of ouabain: Lewis acid catalyzed Diels–Alder reactions of sterically hindered systems. *Angew. Chem. Int. Ed.* **41**, 4125–4128 (2002).

[CAS](#) [Google Scholar](#)

63. 63.

Sheu, J.-H., Ahmed, A. F., Shiue, R.-T., Dai, C.-F. & Kuo, Y.-H. Scabrolides A–D, four new norditerpenoids isolated from the soft coral *Sinularia scabra*. *J. Nat. Prod.* **65**, 1904–1908 (2002).

[CAS](#) [Google Scholar](#)

64. 64.

Cui, W.-X. et al. Polycyclic furanobutenolide-derived norditerpenoids from the South China Sea soft corals *Sinularia scabra* and *Sinularia polydactyla* with immunosuppressive activity. *Bioorg. Chem.* **94**, 103350 (2020)

[CAS](#) [Google Scholar](#)

65. 65.

Mendoza, A., Ishihara, Y. & Baran, P. S. Scalable enantioselective total synthesis of taxanes. *Nat. Chem.* **4**, 21–25 (2012).

[CAS](#) [Google Scholar](#)

66. 66.

Liao, W. & Yu, Z.-X. DFT study of the mechanism and stereochemistry of the Rh(I)-catalyzed Diels–Alder reactions between electronically neutral dienes and dienophiles. *J. Org. Chem.* **79**, 11949–11960 (2014).

[CAS](#) [Google Scholar](#)

67. 67.

Xu, B., Xun, W., Wang, T. & Qiu, F. G. Total synthesis of (+)-aplykurodinone-1. *Org. Lett.* **19**, 4861–4863 (2017).

[CAS](#) [Google Scholar](#)

68. 68.

Wang, Y.-M., Bruno, N. C., Placeres, Á. L., Zhu, S. & Buchwald, S. L. Enantioselective synthesis of carbo- and heterocycles through a CuH-catalyzed hydroalkylation approach. *J. Am. Chem. Soc.* **137**, 10524–10527 (2015).

[CAS](#) [PubMed](#) [PubMed Central](#) [Google Scholar](#)

[Download references](#)

Acknowledgements

Development of Chematica was partly supported by US DARPA under the Make-It Award, 69461-CH-DRP #W911NF1610384 (K.M., S.S., E.P.G.,

P.D., T.B., B.A.G.); the same award also supported the synthesis of dauricine (A.A.B., M.M.). Synthesis of tacamonidine was supported in part (B.M.-K., T.K., B.A.G.) by the National Science Center, NCN, Poland under the Symfonia Award (#2014/12/W/ST5/00592). Synthesis of lamellobodysidine A was supported in part (P.G., B.A.G.) by the National Science Center, NCN, Poland under the Maestro Award (#2018/30/A/ST5/00529). J.M. and O.P. thank the Foundation for Polish Science for financial support under award TEAM/2017-4/38. B.A.G. acknowledges support from the Institute for Basic Science Korea, project code IBS-R020-D1. We thank B. Sieredzińska for help in the synthesis of tacamonidine and S. Trice (Merck, KGaA) for help in organizing the Turing test. We thank the following experts for their participation in the Turing test (in alphabetical order): P. Baran (Scripps), J. Bode (ETH Zurich), M. Burke (University of Illinois), M. Christmann (Freie Universität Berlin), H. Davies (Emory University), M. Giedyk (ICHO PAN), D. Huryn (University of Pittsburgh), M. Krische (University of Texas), S. Matsubara (Kyoto University), N. Maulide (Universität Wien), G. Molander (University of Pennsylvania), R. Sarpong (Berkeley), P. Schreiner (Justus Liebig University Giessen) and J. Siitonen (Rice University), as well as four others, who prefer to remain anonymous.

Author information

Affiliations

1. Institute of Organic Chemistry, Polish Academy of Sciences, Warsaw, Poland

Barbara Mikulak-Klucznik, Patrycja Gołębiowska, Oskar Popik, Tomasz Klucznik, Sara Szymkuć, Ewa P. Gajewska, Piotr Dittwald, Olga Staszewska-Krajewska, Wiktor Beker, Tomasz Badowski, Karol Molga, Jacek Mlynarski & Bartosz A. Grzybowski

2. Department of Chemistry, Northwestern University, Evanston, IL, USA

Alison A. Bayly, Karl A. Scheidt & Milan Mrksich

3. IBS Center for Soft and Living Matter, Ulsan, South Korea

Bartosz A. Grzybowski

4. Department of Chemistry, UNIST, Ulsan, South Korea

Bartosz A. Grzybowski

Authors

1. Barbara Mikulak-Klucznik

[View author publications](#)

You can also search for this author in [PubMed](#) [Google Scholar](#)

2. Patrycja Gołębiowska

[View author publications](#)

You can also search for this author in [PubMed](#) [Google Scholar](#)

3. Alison A. Bayly

[View author publications](#)

You can also search for this author in [PubMed](#) [Google Scholar](#)

4. Oskar Popik

[View author publications](#)

You can also search for this author in [PubMed](#) [Google Scholar](#)

5. Tomasz Klucznik

[View author publications](#)

You can also search for this author in [PubMed](#) [Google Scholar](#)

6. Sara Szymkuć

[View author publications](#)

You can also search for this author in [PubMed](#) [Google Scholar](#)

7. Ewa P. Gajewska

[View author publications](#)

You can also search for this author in [PubMed](#) [Google Scholar](#)

8. Piotr Dittwald

[View author publications](#)

You can also search for this author in [PubMed](#) [Google Scholar](#)

9. Olga Staszewska-Krajewska

[View author publications](#)

You can also search for this author in [PubMed](#) [Google Scholar](#)

10. Wiktor Beker

[View author publications](#)

You can also search for this author in [PubMed](#) [Google Scholar](#)

11. Tomasz Badowski

[View author publications](#)

You can also search for this author in [PubMed](#) [Google Scholar](#)

12. Karl A. Scheidt

[View author publications](#)

You can also search for this author in [PubMed](#) [Google Scholar](#)

13. Karol Molga

[View author publications](#)

You can also search for this author in [PubMed](#) [Google Scholar](#)

14. Jacek Mlynarski

[View author publications](#)

You can also search for this author in [PubMed](#) [Google Scholar](#)

15. Milan Mrksich

[View author publications](#)

You can also search for this author in [PubMed](#) [Google Scholar](#)

16. Bartosz A. Grzybowski

[View author publications](#)

You can also search for this author in [PubMed](#) [Google Scholar](#)

Contributions

B.M.-K. and T.K. synthesized tacamonidine. P.G. and O.P. synthesized lamellodysidine A. A.A.B. synthesized dauricine. K.M., S.S., E.P.G., P.D. and T.B. were key developers of Chematica; K.M., S.S., E.P.G. and P.D. implemented the Turing test. O.S.-K. determined the structures and relative configuration of compounds **(R,R)-21**, **(R,S)-21** and final **(R,R,S)-tacamonidine**. K.M. and W.B. performed analyses of the Turing-test results. K.A.S. and M.M. supervised synthesis of dauricine. J.M. supervised synthesis of lamellodysidine A. B.A.G. supervised the synthesis of tacamonidine, designed the Turing test and supervised, along with K.M., its administration, and conceived and directed the development of Chematica from its inception 20 years ago. K.M. and B.A.G. wrote the paper, with contributions from other authors.

Corresponding authors

Correspondence to [Karol Molga](#) or [Jacek Mlynarski](#) or [Milan Mrksich](#) or [Bartosz A. Grzybowski](#).

Ethics declarations

Competing interests

Although Chematica was originally developed and owned by B.A.G.'s Grzybowski Scientific Inventions, LLC, neither he nor the co-authors currently hold any stock in this company, which is now property of Merck

KGaA, Darmstadt, Germany. S.S., E.P.G. P.D., T.B., K.M. and B.A.G. continue to collaborate with Merck KGaA, Darmstadt. The algorithms described in this paper are currently being transitioned into Chematica's commercial version, called SynthiaTM. All queries about access options to Chematica/SynthiaTM, including academic collaborations, should be directed to S. Trice (sarah.trice@sial.com).

Additional information

Peer review information *Nature* thanks the anonymous reviewer(s) for their contribution to the peer review of this work.

Publisher's note Springer Nature remains neutral with regard to jurisdictional claims in published maps and institutional affiliations.

Extended data figures and tables

[Extended Data Fig. 1 New components of Chematica essential to its ability to plan the syntheses of complex, natural-product targets.](#)

Only key algorithmic improvements (since the publication of ref. ⁹) are highlighted. **a**, Increase in the knowledge base of reactions rules to more than 100,000, including a large fraction of advanced stereoselective transforms. **b**, Implementation of various machine-learning molecular mechanics and quantum-mechanics routines to further evaluate the correctness of the reaction prediction. Illustrated here is the machine-learning method (random forest classifier) that evaluates the applicability of Diels–Alder cyclizations²¹. **c**, Information about specific motifs in the synthons that are not only too strained (top)⁸ but also prone to side reactions. An electron-rich allylic alcohol substrate in the Prins cyclization may undergo a competitive oxonia-Cope rearrangement⁵⁹ (bottom). **d**, Scoring functions, either improved heuristics-based or best-in-class neural networks²². **e**, Search algorithms that combine two strategies: searching broadly to explore wide spectrum of options and deeply to reach stop-point

substrates as soon as possible. Each search strategy maintains its own priority queue (PQ), with different queues sharing results. **f**, Large numbers of previously unrecognized two-step reaction sequences that allow the program to overcome local maxima of structural complexity. Image reproduced with permission from ref. [26](#) (<https://doi.org/10.1016/j.chempr.2019.11.016>; Elsevier), which is published under a Creative Commons license (CC BY-NC-ND 4.0; <http://creativecommons.org/licenses/by-nc-nd/4.0/>). **g**, Hard-coded sequences of some 100 FGIs to rapidly reach less reactive synthons. **h**, Bypasses—that is, routines that navigate around intermittent reactivity conflicts (red reaction arrow), by first converting the conflicting group into a non-conflicting one (here, a primary alcohol into an alkene or a silyl ether) and only then performing a high-gain, structure-simplifying step (here, stereoselective alkylation of cyclohexenone). Without the bypass algorithm, the search would explore other, less-structure-simplifying options such as the allylic oxidation indicated by blue arrow. **i**, The ability to perform two different reactions on the retron simultaneously, if multiple reaction loci are reactive under the reaction conditions. Here, treatment with hydrogen and Pd catalyst should remove both phosphonate esters and benzyl ethers (left). Under these conditions, only esters or only ethers cannot be selectively removed. Attempting such selective removal, Chematica would see the unremoved groups (marked in red) as incompatible; in effect, it would not be able to perform the desired global deprotection. Similarly, global debenzylation of an aminoalcohol should be performed in a single step (right).

[Extended Data Fig. 2 Enantioselective synthesis of a pentacyclic diterpenoid, cephanolide B, designed by Chematica.](#)

This target was recently prepared in racemic form in 12 steps⁴⁸, with Pd-catalysed carbonylative cyclization as the key step. In its design, Chematica used 13 steps to reach commercially available crotonyl chloride and a known iodoalkyne **2** (available in two steps from the commercially available oxirane and TMS-acetylene). The synthesis commences with the formation of enantioenriched diene **5** via stereoselective alkylation of the enolate (with stereochemistry controlled by a chiral auxiliary) and subsequent metathesis of the enyne **4**. Subsequently, addition of a Grignard

reagent derived from bromide **6**, cyanation, reduction of ketone, lactonization, methylenation and oxidation of the less hindered allylic position derives triene **12**. This is then used in an elegant, intramolecular Diels–Alder cycloaddition (the feasibility of which was confirmed separately by molecular-mechanics calculations) to form the tetracyclic skeleton of cephalolide B. The synthesis of the target is then accomplished via the (non-intuitive) construction of the aromatic part via Robinson annulation of **13** with butanone **14** and oxidation of the thus-obtained enone.

Extended Data Fig. 3 Enantioselective synthesis of a cyclopane diterpene, conidiogenone B, and its derivative designed by Chematica.

Synthesis of conidiogenone B, which includes a challenging 6–5–5–5 ring system and six contiguous stereocentres (of which three are quaternary), was recently accomplished in 14 steps⁴⁹ (starting from trimethylcyclopentenone, itself one step from a buyable substrate) and relied on a substrate-controlled Nicholas/Pauson–Khand reaction and Danheiser annulation. Chematica’s plan (top panel) also uses 14 steps and relies on intramolecular alkylations to construct five-membered rings and Diels–Alder cycloaddition to build the six-membered ring of conidiogenone B. The synthesis commences with the chiral-auxiliary-controlled alkylation of cyclopentenone **4** with protected bromoethanol **5** to install the first stereocentre. Subsequent Stork–Danheiser transposition is followed by a substrate-controlled addition of a tertiary organocuprate and intramolecular alkylation to yield the bicyclic ketone **10**, which is further methylenated to enone **11**. Formation of the six-membered ring of conidiogenone B is accomplished via the Diels–Alder reaction of **11** with diene **12** to give the tricyclic ketone **13**, which is further elaborated into iodoketone **17**. Formation of the last ring of conidiogenone B is accomplished via the intramolecular alkylation of the ketone. In the bottom panel, Chematica was asked to design a plan for a more complex derivative of conidiogenone B, which differs by an extra methyl group (at a new quaternary stereocentre). Within 18 steps from the target, Chematica reached a known enantioenriched ketoester **4** (marked with a yellow asterisk) which was then sourced, in a few minutes of additional searching, to the commercially

available and inexpensive **1**. The synthesis commences with the reduction of the ketone (with stereochemistry controlled by Noyori's catalyst). Subsequent substrate-controlled alkylation and oxidation are followed by elaboration of ester **4** into iodoenone **10**. Stereoselective alkylation with protected bromoethanol **11** and subsequent cyclization yields the bicyclic ketone **13**, which is further elaborated to tricyclic enone **17**. We make two notes here. First, owing to the presence of a matched stereocentre, conversion of **10** to **12** could probably be performed as one step, without Enders' auxiliary to control the stereochemical outcome. Chematica did not recognize this possibility, probably because it has not yet been taught detailed rules that govern substrate-directed alkylations controlled by quaternary stereocentres. Second, desmethyl analogue of enone **17** was also used in the published synthesis of conidiogenone B, but, to form the six-membered ring, it was subjected to Danheiser annulation followed by ozonolysis-aldol condensation rather than to Diels–Alder cyclization. The formation of the last ring of conidiogenone B is accomplished via intermolecular Diels–Alder reaction with electron-rich diene **18** (available in a single step from pent-3-enal) approaching from the less hindered face of the enone (see refs. [60,61,62](#) for similar Diels–Alder cyclizations promoted by Lewis-acid catalysts). From this point, the target molecule is obtained in three straightforward steps.

[Extended Data Fig. 4 Chematica's synthetic plan for scabrolide A.](#)

Scabrolide A is a polycyclic furanobutenolide-derived norcembranoid diterpenoid that belongs to a family of marine natural products isolated from *Sinularia* soft corals^{[63,64](#)}. The molecule poses a synthetic challenge owing to its compact, densely functionalized core: a fused 5–6–7 carbocyclic scaffold decorated with five adjacent stereocentres and one additional remote stereocentre on the seven-membered ring. A recent literature pathway^{[50](#)} (to the enantiomer from ref. [64](#)) comprises 21 synthetic steps and relies on the intramolecular Diels–Alder cycloaddition and late-stage [2+2] photocycloaddition/fragmentation sequence. During computer planning of the enantiomer from ref. [63](#), several constraints were imposed; for example, Chematica was asked to design an enantioselective strategy

(using the REMOVE_DIAST variable to exclude reactions that lead to a single racemic diastereoisomer), and was not allowed to use SAMP or RAMP hydrazones (to minimize the use of chiral auxiliaries), or highly strained bridgehead intermediates. The route proposed by the software is longer (about 30 steps) and more conservative in the sense that it relies on only broadly applicable chemistries. When planning its route, Chematica did not know the highly scaffold-specific (though elegant) fragmentation–recombination–elimination sequence of steps used towards the end of the literature pathway. The synthesis proposed by the machine relies on an intramolecular aldol addition of **17** followed by FGI, which sets the scene for the closure of a six-membered ring via alkylation reaction to yield intermediate **20**. Subsequent substrate-controlled, stereoselective addition installs the tertiary alcohol. Reduction (with double-bond migration) of intermediate **21** followed by reductive ozonolysis sets the scene for the construction of the second five-membered ring of scabrolide’s scaffold. The fourth and final, seven-membered ring is closed via Pd-mediated coupling. The starting material initially identified by the software (aldehyde **11**) is not commercially available, but can be sourced in four steps from (\pm)-*cis*-bicyclo[3.2.0]hept-2-en-6-one. Looking for alternative endings of the pathways, that terminate in commercially available, achiral and inexpensive starting materials, we restarted the search from a node marked in the graph view (top) by a yellow asterisk (bicyclic intermediate **18**). The alternative ending (blue reaction arrows in the bottom scheme) was found within about half an hour and commenced from readily available, protected hydroxyaldehyde and cyclopentanone. The initial ending, starting from the aldehyde **11**, is marked by green arrows.

Extended Data Fig. 5 Chematica-designed, enantioselective synthesis of taxuyunnanine D, a less oxidized taxane.

The previous synthesis^{51,65} of this target was accomplished in 12 steps via a two-phase cyclase-oxidase strategy, and required extensive exploration of conditions to achieve satisfactory selectivity during C–H oxidations. Here, within 14 steps from the target molecule, Chematica reached simple and known starting materials: iodocyclohexenone **6** and protected iodoethanol **7**. The synthesis commences with the Pd-mediated coupling of **6** and **7**. Subsequent catalyst-controlled methylation and oxidation introduce the all-

carbon quaternary and C5 hydroxylated stereocentres of taxuyunnanine D. Subsequently, protection of alcohol, stereoselective alkylation of cyclohexanone (with proposed Enders' auxiliary controlling the stereochemical outcome, but probably also feasible when performed directly; see notes in the caption of Extended Data Fig. 3), Hofmann elimination, removal of protecting groups and Appel reaction yield iodide 15, which is coupled with iododiene 5 (available in four steps from enone 1) to give triene 16, setting the scene for the key formation of the taxane skeleton via electron-neutral intramolecular Diels–Alder cycloaddition (such an electronically neutral system that lacks electron-withdrawing groups may require activation with high temperature or a transition-metal catalyst⁶⁶). Formation of taxuyunnanine D from the [4+2] cycloadduct 18 is then accomplished in two steps and requires olefination of ketone and allylic oxidation. The latter step appears less risky compared to the known solution⁵¹, because 19 lacks any competitive allylic CH₂ groups, which are prone to oxidation and could cause selectivity problems.

Extended Data Fig. 6 Chematica-designed, enantioselective synthesis of a marine steroid, aplykurodinone-1.

Prior syntheses⁶⁷ of this target, featuring six contiguous stereocentres, either relied on the late-stage introduction of the side chain via Michael addition to cyclopentenone (which suffers from low selectivity), or started⁶⁷ from chiral building blocks (in the latter case, in 11 steps but from much more advanced, chiral substrates). Chematica used 17 steps to reach achiral and commercially available substrates: crotonyl chloride, allyl bromide and bromochloropropane 2. This synthesis commences with the installation of two contiguous stereocentres via stereoselective *vic*-difunctionalization of unsaturated amide and subsequent hydroboration and bisoxidation, followed by McMurry coupling to give cyclopentene 7. From there on, oxidation of the less hindered allylic position, methylation of cyclopentenone, reoxidation and formation of imine (elegantly ensuring that a single regioisomer would form in the Diels–Alder reaction) with aminodiene 10 (available in four steps from ethyl sorbate) derives triene 11, which is then used in an intramolecular Diels–Alder cycloaddition that forms the desired 6–5 ring system of aplykurodinone-1. Hydrolysis of the

imine linker and conversion of the primary amine to the carboxylic acid via oxidation and hydrolysis yields **15**, which is then subjected to iodolactonization followed by dehalogenation to form the entire 5–6–5 ring system. The synthesis is completed by elaborating the remaining alkyl chloride to the desired alkene.

[Extended Data Fig. 7 Chematica-designed enantioselective synthesis of a tetracyclic alkaloid, dendrobine.](#)

Synthesis of this target, which features a challenging 5–6–5–5 ring system and seven contiguous stereocentres, was performed recently⁵³ in 11 steps, taking advantage of enantioselective Diels–Alder reaction, substrate-controlled hydroboration and reduction of imine as the key steps. In Chematica’s synthetic plan, within 14 steps from the target, the software reached the commercially available crotonyl chloride and known 3-iodopropanol (that is, simpler starting materials than the Danishefsky’s diene and unsaturated imide used in the literature synthesis). The synthesis commences with the chiral-auxiliary-controlled alkylation of the amide enolate. Ensuing steps allow for the preparation of enoate **10**. Further homologation with allylic phosphonate **11** (available in two steps from an appropriate alcohol) and hydrolysis yield the triene **13**, setting the scene for an intramolecular Diels–Alder reaction that forms the desired 6–5 ring system. Subsequent hydroxylactonization gives tricyclic alcohol **15**, which is then efficiently transformed into the target molecule via stereoretentive chlorination of the alcohol, Cbz removal and substitution of chloride.

[Extended Data Fig. 8 Enantioselective synthesis of mevastatin designed by Chematica with all its reaction knowledge and on exclusion of user-specified reaction types.](#)

Top, synthetic plan obtained when the program was allowed to use all of its reaction knowledge base. Under these circumstances, the planned route relies on an intramolecular Diels–Alder reaction to construct mevastatin’s 6–6 ring system. The synthesis commences with stereoselective reduction of a ketone to give iodoalcohol **2**, which is transformed in five steps into triene **8**. Subsequent cycloaddition (note that such an electronically neutral

system that lacks electron-withdrawing groups may require activation with high temperature or a transition-metal catalyst⁶⁶) and elaboration of the side chain give the target molecule in the total of 14 steps. Bottom, synthetic plan designed by Chematica when it was forbidden from using the key Diels–Alder reaction and was thus forced to come up with a completely different approach; the synthesis is now much longer. The formation of each ring is accomplished via ring-closing metathesis.

Extended Data Fig. 9 Pathways leading to rameleton designed by the software with and without multistep strategizing routines.

The top synthetic pathway was designed without the new, multistep heuristics. The scaffold of the target was constructed via Cu-catalysed hydroalkylation of alkenes⁶⁸. Although the pathway does not contain chemically erroneous steps, it is long, relies heavily on reductions and oxidations, and involves many FGIs. The bottom route, designed with the new strategizing routines, is more concise and elegant. The key element in this path is a strategy that relies on Robinson annulation followed by dehydrogenation of enones (in the retrosynthetic direction, when planning the route, the program strategizes and first performs a seemingly unproductive dearomatization of a phenol, which then enables Robinson annulation).

Extended Data Fig. 10 Pathways leading to tybost designed by the software with and without multistep strategizing routines.

The top synthetic pathway was designed without the new multistep algorithms. This route is longer and requires additional protection and deprotection operations on intermediate **11** (node in blue halo). The program was not able to find better routes even after hours of searching. In the bottom route, when the program was allowed to strategize, it found a more elegant route that relies on two bypasses (two sets of red reaction arrows) and one FGI (pair of violet reaction arrows). The software navigated the pathways to starting materials that already had relevant

groups protected (such that no protections were required mid-way into the pathway) and were easily available from appropriate amino acids.

Supplementary information

Supplementary Information

This file contains additional synthetic, spectroscopic, chromatographic, and statistical details and includes Supplementary Figures 1-89.

Supplementary Data

This zipped folder contains 3 files. The pseudocode for the multistep retrosynthetic design, pathway generation and retrieval can be found in the PSEUDOCODE_Aug2.pdf file. An example of one of the reaction rules as coded in Chematica is provided in the RULE.pdf file. Additional details of the software's availability and execution are given in the README_Aug2.pdf file.

Rights and permissions

Reprints and Permissions

About this article



Check for
updates

Cite this article

Mikulak-Klucznik, B., Gołębiowska, P., Bayly, A.A. *et al.* Computational planning of the synthesis of complex natural products. *Nature* **588**, 83–88 (2020). <https://doi.org/10.1038/s41586-020-2855-y>

Download citation

- Received: 25 July 2020
- Accepted: 06 October 2020
- Published: 13 October 2020
- Issue Date: 03 December 2020
- DOI: <https://doi.org/10.1038/s41586-020-2855-y>

Comments

By submitting a comment you agree to abide by our [Terms](#) and [Community Guidelines](#). If you find something abusive or that does not comply with our terms or guidelines please flag it as inappropriate.

[Access through your institution](#)

[Change institution](#)

[Buy or subscribe](#)

This article was downloaded by **calibre** from <https://www.nature.com/articles/s41586-020-2855-y>

- Article
- [Published: 02 December 2020](#)

Thermochemical lithosphere differentiation and the origin of cratonic mantle

- [Fabio A. Capitanio](#) ORCID: orcid.org/0000-0003-2131-8723¹,
- [Oliver Nebel](#)¹ &
- [Peter A. Cawood](#)¹

[Nature](#) volume 588, pages89–94(2020)[Cite this article](#)

- 170 Accesses
- 77 Altmetric
- [Metrics details](#)

Subjects

- [Geodynamics](#)
- [Petrology](#)
- [Tectonics](#)

Abstract

Cratons record the early history of continental lithosphere formation, yet how they became the most enduring part of the lithosphere on Earth remains unknown¹. Here we propose a mechanism for the formation of large volumes of melt-depleted cratonic lithospheric mantle (CLM) and its

evolution to stable cratons. Numerical models show large decompression melting of a hot, early Earth mantle beneath a stretching lithosphere, where melt extraction leaves large volumes of depleted mantle at depth. The dehydrated, stiffer mantle resists further deformation, forcing strain migration and cooling, thereby assimilating depleted mantle into the lithosphere. The negative feedback between strain localization and stiffening sustains long-term diffused extension and emplacement of large amounts of depleted CLM. The formation of CLM at low pressure and its deeper re-equilibration reproduces the evolution of Archaean lithosphere constrained by depth–temperature conditions^{1,2}, whereas large degrees of depletion^{3,4} and melt volumes⁵ in Archaean cratons are best matched by models with lower lithospheric strength. Under these conditions, which are otherwise viable for plate tectonics^{6,7}, thermochemical differentiation effectively prevents yielding and formation of margins: rifting and lithosphere subduction are short lived and embedded in the cooling CLM as relict structures, reproducing the recycling and reworking environments that are found in Archaean cratons^{8,9}. Although they undergo major melting and extensive recycling during an early stage lasting approximately 500 million years, the modelled lithospheres progressively differentiate and stabilize, and then recycling and reworking become episodic. Early major melting and recycling events explain the production and loss of primordial Hadean lithosphere and crust¹⁰, whereas later stabilization and episodic reworking provides a context for the creation of continental cratons in the Archaean era^{4,8}.

[Access through your institution](#)

[Change institution](#)

[Buy or subscribe](#)

Access options

Subscribe to Journal

Get full journal access for 1 year

185,98 €

only 3,58 € per issue

[Subscribe](#)

All prices are NET prices.
VAT will be added later in the checkout.

Rent or Buy article

Get time limited or full article access on ReadCube.
from \$8.99

[Rent or Buy](#)

All prices are NET prices.

Additional access options:

- [Log in](#)
- [Access through your institution](#)
- [Learn about institutional subscriptions](#)

Fig. 1: Viscosity distribution, velocity field, surface strain rate and surface heat flow during lithosphere stretching and rifting and formation of depleted, stiffer continental lithospheric mantle.



Fig. 2: Viscosity distribution, surface strain rate and surface heat flow after about 1 Gyr of model time and comparisons with P - T conditions in Archaean and Proterozoic cratons.



Fig. 3: Surface velocity and distribution of depletion degree, crust and recycled lithosphere in models developing plate tectonics-like features.



Fig. 4: Melt, melt rates and growth of the crust for different strengths tested versus model time.

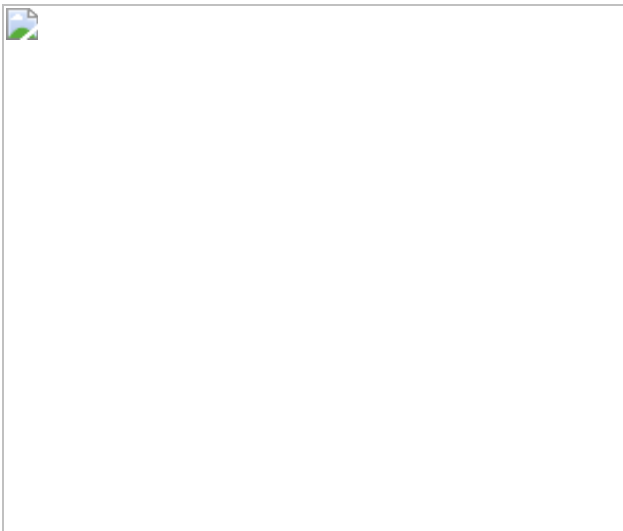
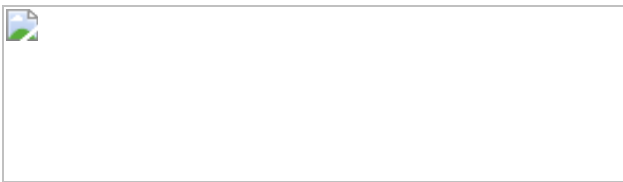


Fig. 5: Sketch of the thermochemical differentiation of the lithosphere and the stabilization to form a craton.



Data availability

All data are generated using Underworld2 version 2.8.1b, available at <https://doi.org/10.5281/zenodo.3384283>. Data generated are included at <https://doi.org/10.26180/5e40f7dcfbe58>, licensed under a CC BY 4.0 license. Data in Fig. 2 are from refs. [1](#),[2](#).

References

1. 1.

Lee, C.-T. A., Luffi, P. & Chin, E. J. Building and destroying continental mantle. *Annu. Rev. Earth Planet. Sci.* **39**, 59–90 (2011).

[CAS](#) [ADS](#) [Google Scholar](#)

2. 2.

Artemieva, I. M. The continental lithosphere: reconciling thermal, seismic, and petrologic data. *Lithos* **109**, 23–46 (2009).

[CAS](#) [ADS](#) [Google Scholar](#)

3. 3.

Herzberg, C., Condie, K. & Korenaga, J. Thermal history of the Earth and its petrological expression. *Earth Planet. Sci. Lett.* **292**, 79–88 (2010).

[CAS](#) [ADS](#) [Google Scholar](#)

4. 4.

Pearson, D. G. & Wittig, N. The formation and evolution of cratonic mantle lithosphere – evidence from mantle xenoliths. In *Treatise on Geochemistry* Vol. 3 (eds Turekian, K. K. & Holland, H. D.) 255–292 (Elsevier, 2014).

5. 5.

Griffin, W. L. et al. The origin and evolution of Archean lithospheric mantle. *Precambr. Res.* **127**, 19–41 (2003).

[CAS](#) [ADS](#) [Google Scholar](#)

6. 6.

Korenaga, J. Initiation and evolution of plate tectonics on Earth: theories and observations. *Annu. Rev. Earth Planet. Sci.* **41**, 117–151 (2013).

[CAS](#) [ADS](#) [Google Scholar](#)

7. 7.

O'Neill, C., Lenardic, A., Moresi, L. N., Torsvik, T. H. & Lee, C.-T. A. Episodic Precambrian subduction. *Earth Planet. Sci. Lett.* **262**, 552–562 (2007).

[ADS](#) [Google Scholar](#)

8. 8.

Van Kranendonk, M. J., Smithies, R. H., Hickman, A. H. & Champion, D. C. Secular tectonic evolution of Archean continental crust: interplay between horizontal and vertical processes in the formation of the Pilbara Craton, Australia. *Terra Nova* **19**, 1–38 (2007).

[ADS](#) [Google Scholar](#)

9. 9.

van Hunen, J. & Moyen, J. F. Archean subduction: fact or fiction? *Annu. Rev. Earth Planet. Sci.* **40**, 195–219 (2012).

[ADS](#) [Google Scholar](#)

10. 10.

O'Neil, J. & Carlson, R. W. Building Archean cratons from Hadean mafic crust. *Science* **355**, 1199–1202 (2017).

[ADS](#) [PubMed](#) [Google Scholar](#)

11. 11.

Jordan, T. H. Structure and formation of the continental tectosphere. *J. Petrol.* **1**, 11–37 (1988).

[Google Scholar](#)

12. 12.

Kemp, A. I. S. et al. Hadean crustal evolution revisited: new constraints from Pb–Hf isotope systematics of the Jack Hills zircons. *Earth Planet. Sci. Lett.* **296**, 45–56 (2010).

[CAS](#) [ADS](#) [Google Scholar](#)

13. 13.

Dhuime, B., Hawkesworth, C. J., Cawood, P. A. & Storey, C. D. A change in the geodynamics of continental growth 3 billion years ago. *Science* **335**, 1334–1336 (2012).

[CAS](#) [ADS](#) [PubMed](#) [Google Scholar](#)

14. 14.

Wang, H., van Hunen, J., Pearson, D. G. & Allen, M. B. Craton stability and longevity: the roles of composition-dependent rheology and buoyancy. *Earth Planet. Sci. Lett.* **391**, 224–233 (2014).

[CAS](#) [ADS](#) [Google Scholar](#)

15. 15.

Simon, N. S. C., Carlson, R. W., Pearson, D. G. & Davis, G. R. The origin and evolution of the Kaapvaal cratonic lithospheric mantle. *J. Petrol.* **48**, 589–625 (2007).

[CAS](#) [ADS](#) [Google Scholar](#)

16. 16.

Fischer, R. & Gerya, T. V. Early Earth plume-lid tectonics: a high-resolution 3D numerical modelling approach. *J. Geodyn.* **100**, 198–214 (2016).

[Google Scholar](#)

17. 17.

van Thienen, P., Van den Berg, A. P. & Vlaar, N. J. Production and recycling of oceanic crust in the early Earth. *Tectonophysics* **386**, 41–65 (2004).

[ADS](#) [Google Scholar](#)

18. 18.

Korenaga, J. Archean geodynamics and the thermal evolution of Earth. In *Archean Geodynamics and Environments* (eds Benn, K. et al.) 7–32 (American Geophysical Union, 2006).

19. 19.

Johnson, T. E., Brown, M., Kaus, B. J. P. & VanTongeren, J. A. Delamination and recycling of Archaean crust caused by gravitational instabilities. *Nat. Geosci.* **7**, 47–52 (2014).

[CAS](#) [ADS](#) [Google Scholar](#)

20. 20.

Lenardic, A. & Moresi, L. N. Some thoughts on the stability of cratonic lithosphere: effects of buoyancy and viscosity. *J. Geophys. Res.* **104**, 12747–12758 (1999).

[ADS](#) [Google Scholar](#)

21. 21.

Cooper, C. M. & Miller, M. S. Craton formation: internal structure inherited from closing of the early oceans. *Lithosphere* **6**, 35–42 (2014).

[ADS](#) [Google Scholar](#)

22. 22.

Wang, H., van Hunen, J. & Pearson, D. G. Making Archean cratonic roots by lateral compression: a two-stage thickening and stabilization model. *Tectonophysics* **746**, 562–571 (2018).

[ADS](#) [Google Scholar](#)

23. 23.

Moore, W. B. & Webb, A. G. Heat-pipe Earth. *Nature* **501**, 501–505 (2013).

[CAS](#) [ADS](#) [PubMed](#) [Google Scholar](#)

24. 24.

Rozel, A. B., Golabek, G. J., Jain, C., Tackley, P. J. & Gerya, T. V. Continental crust formation on early Earth controlled by intrusive magmatism. *Nature* **545**, 332–335 (2017).

[CAS](#) [ADS](#) [PubMed](#) [Google Scholar](#)

25. 25.

Sizova, E., Gerya, T. V., Stüwe, K. & Brown, M. Generation of felsic crust in the Archean: a geodynamic modeling perspective. *Precambr. Res.* **271**, 198–224 (2015).

[CAS](#) [ADS](#) [Google Scholar](#)

26. 26.

England, P. Constraints on the extension of continental lithosphere. *J. Geophys. Res.* **88**, 1145–1152 (1983).

[ADS](#) [Google Scholar](#)

27. 27.

van Wijk, J. W. & Cloetingh, S. Basin migration caused by slow lithospheric extension. *Earth Planet. Sci. Lett.* **198**, 275–288 (2002).

[ADS](#) [Google Scholar](#)

28. 28.

Arndt, N. T., Lewin, E. & Albarède, F. Strange partners: formation and survival of continental crust and lithospheric mantle. In *The Early Earth: Physical, Chemical and Biological Development* (eds Fowler, C. M. R. et al.) 91–103 (The Geological Society of London, 2002).

29. 29.

Lee, C.-T. A. & Chin, E. J. Calculating melting temperatures and pressures of peridotite protoliths: implications for the origin of cratonic mantle. *Earth Planet. Sci. Lett.* **403**, 273–286 (2014).

[CAS](#) [ADS](#) [Google Scholar](#)

30. 30.

Kopylova, M. G. & Russell, J. K. Chemical stratification of cratonic lithosphere: constraints from the northern Slave Craton, Canada. *Earth Planet. Sci. Lett.* **181**, 71–87 (2000).

[CAS](#) [ADS](#) [Google Scholar](#)

31. 31.

Moresi, L. et al. Computational approaches to studying non-linear dynamics of the crust and mantle. *Phys. Earth Planet. Inter.* **163**, 69–82 (2007).

[ADS](#) [Google Scholar](#)

32. 32.

Turcotte, D. L. & Schubert, G. *Geodynamics, Application of Continuum Mechanics to Geological Problems* (John Wiley & Sons, 1982).

33. 33.

Schutt, D. L. & Lesher, C. E. Effects of melt depletion on the density and seismic velocity of garnet and spinel lherzolite. *J. Geophys. Res. Solid Earth* **111**, B05401 (2006).

[ADS](#) [Google Scholar](#)

34. 34.

Ballmer, M. D., van Hunen, J., Ito, G., Tackley, P. J. & Bianco, T. Non-hotspot volcano chains originating from small-scale sublithospheric convection. *Geophys. Res. Lett.* **34**, (2007).

35. 35.

Ballmer, M. D., Ito, G., van Hunen, J. & Tackley, P. J. Spatial and temporal variability in Hawaiian hotspot volcanism induced by small-scale convection. *Nat. Geosci.* **4**, 457–460 (2011).

[CAS](#) [ADS](#) [Google Scholar](#)

36. 36.

Mei, S. & Kohlstedt, D. L. Influence of water on plastic deformation of olivine aggregates. *J. Geophys. Res.* **105**, 21457–21469 (2000).

[CAS](#) [ADS](#) [Google Scholar](#)

37. 37.

Hirth, G. & Kohlstedt, D. L. Water in the oceanic upper mantle: implications for rheology, melt extraction and the evolution of the lithosphere. *Earth Planet. Sci. Lett.* **144**, 93–108 (1996).

[CAS](#) [ADS](#) [Google Scholar](#)

38. 38.

McKenzie, D. & Bickle, M. J. The volume and composition of melt generated by extension of the lithosphere. *J. Petrol.* **29**, 625–679 (1988).

[CAS](#) [ADS](#) [Google Scholar](#)

39. 39.

Crameri, F. & Tackley, P. J. Parameters controlling dynamically self-consistent plate tectonics and single-sided subduction in global models of mantle convection. *J. Geophys. Res. Solid Earth* **120**, 3680–3706 (2015).

[ADS](#) [Google Scholar](#)

40. 40.

Rozel, A., Golabek, G. J., Näf, R. & Tackley, P. J. Formation of ridges in a stable lithosphere in mantle convection models with a viscoplastic rheology. *Geophys. Res. Lett.* **42**, 4770–4777 (2015).

[CAS](#) [ADS](#) [PubMed](#) [PubMed Central](#) [Google Scholar](#)

41. 41.

Rolf, T., Capitanio, F. A. & Tackley, P. J. Constraints on mantle viscosity structure from continental drift histories in spherical mantle convection models. *Tectonophysics* **746**, 339–351 (2018).

[ADS](#) [Google Scholar](#)

42. 42.

Karato, S. I. & Wu, P. Rheology of the upper mantle – a synthesis. *Science* **260**, 771–778 (1993).

[CAS](#) [ADS](#) [PubMed](#) [Google Scholar](#)

43. 43.

Keller, T., May, D. A. & Kaus, B. J. P. Numerical modelling of magma dynamics coupled to tectonic deformation of lithosphere and crust. *Geophys. J. Int.* **195**, 1406–1442 (2013).

[ADS](#) [Google Scholar](#)

44. 44.

Dannberg, J. & Heister, T. Compressible magma/mantle dynamics: 3-D, adaptive simulations in ASPECT. *Geophys. J. Int.* **207**, 1343–1366 (2016).

[ADS](#) [Google Scholar](#)

45. 45.

Kohlstedt, D. L. & Hansen, L. N. Constitutive equations, rheological behavior, and viscosity of rocks. In *Treatise on Geophysics* Vol. 2 (ed. Schubert, G.) 441–472 (2015).

46. 46.

Pinkerton, H. & Stevenson, R. J. Methods of determining the rheological properties of magmas at subliquidus temperatures. *J. Volcanol. Geotherm. Res.* **53**, 47–66 (1992).

[ADS](#) [Google Scholar](#)

47. 47.

Karato, S. I. *Deformation of Earth Materials: An Introduction to the Rheology of Solid Earth* (Cambridge Univ. Press, 2008).

48. 48.

Phipps Morgan, J. The generation of a compositional lithosphere by mid-ocean ridge melting and its effect on subsequent off-axis hotspot upwelling and melting. *Earth Planet. Sci. Lett.* **146**, 213–232 (1997).

[CAS](#) [ADS](#) [Google Scholar](#)

49. 49.

Ito, G., Shen, Y., Hirth, G. & Wolfe, C. J. Mantle flow, melting, and dehydration of the Iceland mantle plume. *Earth Planet. Sci. Lett.* **165**, 81–96 (1999).

[CAS](#) [ADS](#) [Google Scholar](#)

50. 50.

Gerya, T. V. *Introduction to Numerical Geodynamical Modelling* (Cambridge Univ. Press, 2009).

51. 51.

Moresi, L. & Solomatov, V. S. Mantle convection with a brittle lithosphere: thoughts on the global tectonic styles of the Earth and Venus. *Geophys. J. Int.* **133**, 669–682 (1998).

[ADS](#) [Google Scholar](#)

52. 52.

Rey, P. F., Coltice, N. & Flament, N. Spreading continents kick-started plate tectonics. *Nature* **513**, 405–408 (2014).

[CAS](#) [ADS](#) [PubMed](#) [Google Scholar](#)

53. 53.

Capitanio, F. A., Nebel, O., Cawood, P. A., Weinberg, R. F. & Chowdhury, P. Reconciling thermal regimes and tectonics of the early Earth. *Geology* **47**, 923–927 (2019).

[CAS](#) [ADS](#) [Google Scholar](#)

54. 54.

Capitanio, F. A., Nebel, O., Cawood, P. A., Weinberg, R. F. & Clos, F. Lithosphere differentiation in the early Earth controls Archean tectonics. *Earth Planet. Sci. Lett.* **525**, 115755 (2019).

[CAS](#) [Google Scholar](#)

55. 55.

Davies, G. F. Effect of plate bending on the Urey ratio and the thermal evolution of the mantle. *Earth Planet. Sci. Lett.* **287**, 513–518 (2009).

[CAS](#) [ADS](#) [Google Scholar](#)

56. 56.

Jain, C., Rozel, A. B., Tackley, P. J., Sanan, P. & Gerya, T. V. Growing primordial continental crust self-consistently in global mantle convection models. *Gondwana Res.* **73**, 96–122 (2019).

[CAS](#) [ADS](#) [Google Scholar](#)

57. 57.

van Thienen, P., Vlaar, N. J. & van den Berg, A. P. Plate tectonics on the terrestrial planets. *Phys. Earth Planet. Inter.* **142**, 61–74 (2004).

[ADS](#) [Google Scholar](#)

58. 58.

Parsons, B. E. & McKenzie, D. Mantle convection and thermal structure of plates. *J. Geophys. Res.* **83**, 4485–4496 (1978).

[ADS](#) [Google Scholar](#)

59. 59.

O'Farrell, K. A. & Lowman, J. P. Emulating the thermal structure of spherical shell convection in plane-layer geometry mantle convection models. *Phys. Earth Planet. Inter.* **182**, 73–84 (2010).

[ADS](#) [Google Scholar](#)

60. 60.

Katz, R. F., Spiegelman, M. & Langmuir, C. H. A new parameterization of hydrous mantle melting. *Geochem. Geophys. Geosyst.* **4**, 1073 (2003).

[ADS](#) [Google Scholar](#)

[Download references](#)

Acknowledgements

We thank T. Gerya, C. Herzberg and G. Pearson for comments on the manuscript. We acknowledge support from Australian Research Council grants FT170100254 (to F.A.C.) and FL160100168 (to P.A.C.). We acknowledge the provision of resources and services from the National Computational Infrastructure (NCI), which is supported by the Australian Government.

Author information

Affiliations

1. School of Earth Atmosphere and Environment, Monash University, Clayton, Victoria, Australia

Fabio A. Capitanio, Oliver Nebel & Peter A. Cawood

Authors

1. Fabio A. Capitanio

[View author publications](#)

You can also search for this author in [PubMed](#) [Google Scholar](#)

2. Oliver Nebel

[View author publications](#)

You can also search for this author in [PubMed](#) [Google Scholar](#)

3. Peter A. Cawood

[View author publications](#)

You can also search for this author in [PubMed](#) [Google Scholar](#)

Contributions

F.A.C. and O.N. designed the models. F.A.C. implemented and ran the numerical simulations. All authors contributed to the manuscript.

Corresponding author

Correspondence to [Fabio A. Capitanio](#).

Ethics declarations

Competing interests

The authors declare no competing interests.

Additional information

Peer review information *Nature* thanks Taras Gerya, Claude Herzberg and D. Graham Pearson for their contribution to the peer review of this work.

Publisher's note Springer Nature remains neutral with regard to jurisdictional claims in published maps and institutional affiliations.

Extended data figures and tables

Extended Data Fig. 1 Mantle adiabats for different potential temperatures, depletion degrees and density difference, for different water-content values versus depth.

Left, potential temperatures for the early Earth are estimated between 1,430 °C and 1,560 °C (blue and green) with respect to the present day (magenta). Right, depletion fraction and potential-density change $\Delta\rho_p$, that is, the differential density due to the difference with potential temperature, for dry solidus (T_{sol} , solid lines), wet solidus with minimum (dashed lines) and average (dotted lines) estimates of water content³⁷ \(\langle X \rangle_{\langle \langle \langle \rm H \rangle \rangle \rangle_2 \langle \rm O \rangle \rangle}\), and water-saturated solidus T_{sat} . The yellow area brackets the depletion values inferred for the Archaean³.

Extended Data Fig. 2 Mantle adiabats for present-day mantle potential temperatures at a mid-oceanic ridge and viscosity for different water contents, versus depth.

Left, potential temperatures for the present day and solidi for dry, wet, with different water-content values, and water-saturated mantle, from ref. ³⁷. Right, viscosities of wet (dashed lines), dry (solid thick line) and wet-to-dry transition (thin black line). In grey, the effective viscosity used in this study. Viscosities are calculated using a background strain rate $\dot{\varepsilon} = 10^{-15} \text{ s}^{-1}$.

Extended Data Fig. 3 Mantle adiabats for mantle potential temperatures ranging from that of the present-day to that inferred for early Earth at a mid-oceanic ridge, depletion degrees and potential-density difference, for dry and wet mantle, and viscosities, versus depth.

Left, potential temperatures for the early Earth are estimated between 1,430 °C and 1,560 °C (magenta and green) with respect to present day (cyan). Solids for dry and wet, with average water content from ref. [37](#). Center, depletion fraction and potential density contrast for dry (solid lines) and wet (dashed lines) adiabats. The shaded area brackets the depletion values inferred for the Archaean³. Right panel, corresponding effective viscosities used in this study, calculated using a background strain rate $\dot{\varepsilon} = 10^{-15} \text{ s}^{-1}$.

Extended Data Fig. 4 Lithospheric geotherms for different thicknesses, depletion fraction, density contrast, and rheology, for an early-Earth-like mantle potential temperature.

Left, the geotherms (half-space cooling) reproduce the effect of thinning of a thick (magenta) lithosphere into a thinner one (blue and indigo). Thin lines for the dry and water-saturated solids. Centre, the depletion degree and volumes increase with thinning during rifting, and become increasingly shallow. Right, the viscosity of the lithosphere during rifting increases with thinning, as larger melting is produced and embedded in the mechanical boundary layer. Thin lines are viscosities for η_0 , $10\eta_0$, $10^2\eta_0$ and $10^3\eta_0$ for the temperature-dependent viscosity $\eta(T)$ and temperature- and depletion-dependent viscosity $\eta(T, F)$. Plastic viscosities are η_Y for the lithospheric yielding and η_C for the crust. The viscosity is calculated using $\sigma_0 = 50 \text{ MPa}$ for the lithosphere and background strain rate $\dot{\varepsilon} = 10^{-15} \text{ s}^{-1}$.

Extended Data Fig. 5 The strength ratio of the thermochemical boundary layer, with depletion-dependent rheology and the thermal boundary layer versus the thickness of the lithosphere.

Potential temperatures tested are present-day, $T_P = 1,300 \text{ }^\circ\text{C}$, and early-Earth-like, $T_P = 1,560 \text{ }^\circ\text{C}$.

Extended Data Fig. 6 Initial adiabatic temperature distribution.

a, Model configuration after 500 Myr of convection with $\text{Ra} = 10^7$. The crust is shown in magenta. **b**, Horizontally averaged temperature. The crust (magenta) is defined by the isotherm $T = 330 \text{ }^\circ\text{C}$ (vertical line; see [Methods](#) section ‘Initial conditions’) chosen to yield a mean crust thickness of 20 km. The dashed line represents the lower boundary of the magnification given in **c**. **c**, All model geotherms in grey and the mean geotherm in black; magnification of region in **b** bounded by the horizontal dashed line and the solid vertical line. The crustal thickness in the initial condition varies between approximately 14 and 35 km.

Extended Data Fig. 7 Melt production and melt rate versus time.

The solid lines are the models presented herein and the dashed lines indicate the models with higher (short-dashed line) and lower (long-dashed line) viscosity cut-offs for three models with low, intermediate and high cohesion (grey, magenta and blue, respectively).

Extended Data Table 1 Symbols, definitions and values of the dimensional reference parameters used in this study

[Full size table](#)

Extended Data Table 2 List of the model runs and their modelling parameters

[Full size table](#)

Rights and permissions

[Reprints and Permissions](#)

About this article



Check for
updates

Cite this article

Capitanio, F.A., Nebel, O. & Cawood, P.A. Thermochemical lithosphere differentiation and the origin of cratonic mantle. *Nature* **588**, 89–94 (2020). <https://doi.org/10.1038/s41586-020-2976-3>

[Download citation](#)

- Received: 25 January 2020
- Accepted: 17 September 2020
- Published: 02 December 2020
- Issue Date: 03 December 2020
- DOI: <https://doi.org/10.1038/s41586-020-2976-3>

Comments

By submitting a comment you agree to abide by our [Terms](#) and [Community Guidelines](#). If you find something abusive or that does not comply with our terms or guidelines please flag it as inappropriate.

[Access through your institution](#)

[Change institution](#)

[Buy or subscribe](#)

This article was downloaded by **calibre** from <https://www.nature.com/articles/s41586-020-2976-3>

The future of food from the sea

[Download PDF](#)

- Article
- [Published: 19 August 2020](#)

The future of food from the sea

- [Christopher Costello](#) ORCID: [orcid.org/0000-0002-9646-7806^{1,2 na1}](https://orcid.org/0000-0002-9646-7806),
- [Ling Cao](#) ^{3 na1},
- [Stefan Gelcich](#) ORCID: [orcid.org/0000-0002-5976-9311^{4,5 na1}](https://orcid.org/0000-0002-5976-9311),
- [Miguel Á. Cisneros-Mata](#) ORCID: [orcid.org/0000-0001-5525-5498⁶](https://orcid.org/0000-0001-5525-5498),
- [Christopher M. Free](#)^{1,2},
- [Halley E. Froehlich](#)^{7,8},
- [Christopher D. Golden](#) ORCID: [orcid.org/0000-0002-0358-4625^{9,10}](https://orcid.org/0000-0002-0358-4625),
- [Gakushi Ishimura](#)^{11,12},
- [Jason Maier](#)¹,
- [Ilan Macadam-Somer](#)^{1,2},
- [Tracey Mangin](#) ORCID: [orcid.org/0000-0001-6111-0914^{1,2}](https://orcid.org/0000-0001-6111-0914),
- [Michael C. Melnychuk](#)¹³,
- [Masanori Miyahara](#)¹⁴,
- [Carryn L. de Moor](#)¹⁵,
- [Rosamond Naylor](#)^{16,17},
- [Linda Nøstbakken](#)¹⁸,
- [Elena Ojea](#)¹⁹,
- [Erin O'Reilly](#)^{1,2},
- [Ana M. Parma](#)²⁰,
- [Andrew J. Plantinga](#)^{1,2},
- [Shakuntala H. Thilsted](#)²¹ &
- [Jane Lubchenco](#) ORCID: [orcid.org/0000-0003-3540-5879²²](https://orcid.org/0000-0003-3540-5879)

[Nature](#) volume 588, pages95–100(2020)Cite this article

- 26k Accesses
- 5 Citations

- 503 Altmetric
- [Metrics details](#)

Subjects

- [Ecosystem services](#)
- [Environmental sciences](#)

Abstract

Global food demand is rising, and serious questions remain about whether supply can increase sustainably¹. Land-based expansion is possible but may exacerbate climate change and biodiversity loss, and compromise the delivery of other ecosystem services^{2,3,4,5,6}. As food from the sea represents only 17% of the current production of edible meat, we ask how much food we can expect the ocean to sustainably produce by 2050. Here we examine the main food-producing sectors in the ocean—wild fisheries, finfish mariculture and bivalve mariculture—to estimate ‘sustainable supply curves’ that account for ecological, economic, regulatory and technological constraints. We overlay these supply curves with demand scenarios to estimate future seafood production. We find that under our estimated demand shifts and supply scenarios (which account for policy reform and technology improvements), edible food from the sea could increase by 21–44 million tonnes by 2050, a 36–74% increase compared to current yields. This represents 12–25% of the estimated increase in all meat needed to feed 9.8 billion people by 2050. Increases in all three sectors are likely, but are most pronounced for mariculture. Whether these production potentials are realized sustainably will depend on factors such as policy reforms, technological innovation and the extent of future shifts in demand.

[Download PDF](#)

Main

Human population growth, rising incomes and preference shifts will considerably increase global demand for nutritious food in the coming decades. Malnutrition and hunger still plague many countries^{1,7}, and projections of population and income by 2050 suggest a future need for more than 500 megatonnes (Mt) of meat per year for human consumption (Supplementary Information section [1.1.6](#)). Scaling up the production of land-derived food crops is challenging, because of declining yield rates and competition for scarce land and water resources². Land-derived seafood

(freshwater aquaculture and inland capture fisheries; we use seafood to denote any aquatic food resource, and food from the sea for marine resources specifically) has an important role in food security and global supply, but its expansion is also constrained. Similar to other land-based production, the expansion of land-based aquaculture has resulted in substantial environmental externalities that affect water, soil, biodiversity and climate, and which compromise the ability of the environment to produce food^{3,4,5,6}. Despite the importance of terrestrial aquaculture in seafood production (Supplementary Fig. 3), many countries—notably China, the largest inland-aquaculture producer—have restricted the use of land and public waters for this purpose, which constrains expansion⁸. Although inland capture fisheries are important for food security, their contribution to total global seafood production is limited (Supplementary Table 1) and expansion is hampered by ecosystem constraints. Thus, to meet future needs (and recognizing that land-based sources of fish and other foods are also part of the solution), we ask whether the sustainable production of food from the sea has an important role in future supply.

Food from the sea is produced from wild fisheries and species farmed in the ocean (mariculture), and currently accounts for 17% of the global production of edible meat^{9,10,11,12} (Supplementary Information section 1.1, Supplementary Tables 1–3). In addition to protein, food from the sea contains bioavailable micronutrients and essential fatty acids that are not easily found in land-based foods, and is thus uniquely poised to contribute to global food and nutrition security^{13,14,15,16}.

Widely publicized reports about climate change, overfishing, pollution and unsustainable mariculture give the impression that sustainably increasing the supply of food from the sea is impossible. On the other hand, unsustainable practices, regulatory barriers, perverse incentives and other constraints may be limiting seafood production, and shifts in policies and practices could support both food provisioning and conservation goals^{17,18}. In this study, we investigate the potential of expanding the economically and environmentally sustainable production of food from the sea for meeting global food demand in 2050. We do so by estimating the extent to which food from the sea could plausibly increase under a range of scenarios, including demand scenarios under which land-based fish act as market substitutes.

The future contribution of food from the sea to global food supply will depend on a range of ecological, economic, policy and technological factors. Estimates based solely on ecological capacity are useful, but do not capture the responses of producers to incentives and do not account for changes in demand, input costs or technology^{19,20}. To account for these realities, we construct global supply curves of food from the sea that explicitly account for economic feasibility and feed

constraints. We first derive the conceptual pathways through which food could be increased in wild fisheries and in mariculture sectors. We then empirically derive the magnitudes of these pathways to estimate the sustainable supply of food from each seafood sector at any given price²¹. Finally, we match these supply curves with future demand scenarios to estimate the likely future production of sustainable seafood at the global level.

Sustainably increasing food from the sea

We describe four main pathways by which food supply from the ocean could increase: (1) improving the management of wild fisheries; (2) implementing policy reforms of mariculture; (3) advancing feed technologies for fed mariculture; and (4) shifting demand, which affects the quantity supplied from all three production sectors.

Although mariculture production has grown steadily over the past 60 years (Fig. 1) and provides an important contribution to food security²², the vast majority (over 80%) of edible meat from the sea comes from wild fisheries⁹ (Fig. 1b). Over the past 30 years, supply from this wild food source has stabilized globally despite growing demand worldwide, which has raised concerns about our ability to sustainably increase production. Of nearly 400 fish stocks around the world that have been monitored since the 1970s by the UN Food and Agriculture Organization (FAO), approximately one third are currently not fished within sustainable limits¹. Indeed, overfishing occurs often in poorly managed ('open access') fisheries. This is disproportionately true in regions with food and nutrition security concerns¹. In open-access fisheries, fishing pressure increases as the price rises: this can result in a 'backward-bending' supply curve^{23,24} (the OA curve in Fig. 2a), in which higher prices result in the depletion of fish stocks and reduced productivity—and thus reduced equilibrium food provision.

Fig. 1: Marine harvest and food from the sea over time (excluding aquatic plants).



Data are from ref. ⁹. **a, b**, Harvests (live-weight production) (**a**) are converted to food equivalents (edible production)¹⁰ (**b**). In **b**, there is also an assumption that 18% of the annual landings of marine wild fisheries are directed towards non-food purposes⁴⁷.

[Full size image](#)

Fig. 2: Hypothetical supply curves for wild fisheries and mariculture, showing the influence of price on production quantity.



a, Wild fisheries. Curves represent poorly managed (open access) fisheries (OA); management reform for all fisheries (MSY); and economically rational management reform (R). **b**, Mariculture. Curves represent weak regulations that allow for

ecologically unsustainable production (M1); overly restrictive policies (M2); policies that allow for sustainable expansion (M3); and a reduced dependence on limited feed ingredients for fed-mariculture production (M4).

[Full size image](#)

Fishery management allows overexploited stocks to rebuild, which can increase long-term food production from wild fisheries^{25,26}. We present two hypothetical pathways by which wild fisheries could adopt improved management (Fig. 2a). First, independent of economic conditions, governments can impose reforms in fishery management. The resulting production in 2050 from this pathway—assuming that fisheries are managed for maximum sustainable yield (MSY)—is represented by the MSY curve in Fig. 2a, and is independent of price. The second pathway explicitly recognizes that wild fisheries are expensive to monitor (for example, via stock assessments) and manage (for example, via quotas)—management reforms are adopted only by fisheries for which future profits outweigh the associated costs of improved management. When management entities respond to economic incentives, the number of fisheries for which the benefits of improved management outweigh the costs increases as demand (and thus price) increases. This economically rational management endogenously determines which fisheries are well-managed, and thus how much food production they deliver, resulting in supply curve designated R in Fig. 2a.

Although the production of wild fisheries is approaching its ecological limits, current mariculture production is far below its ecological limits and could be increased through policy reforms, technological advancements and increased demand^{19,27}. We present explanations for why food production from mariculture is currently limited, and describe how the relaxation of these constraints gives rise to distinct pathways for expansion (Fig. 2b). The first pathway recognizes that ineffective policies have limited the supply^{28,29}. Lax regulations in some regions have resulted in poor environmental stewardship, disease and even collapse, which have compromised the viability of food production in the long run (curve M1 in Fig. 2b). In other regions, regulations are overly restrictive, convoluted and poorly defined^{30,31}, and thus limit production (curve M2 in Fig. 2b). In both cases, improved policies and implementation can increase food production by preventing and ending environmentally damaging mariculture practices (the shift from M1 to M3 in Fig. 2b) and allowing for environmentally sustainable expansion (the shift from M2 to M3 in Fig. 2b).

The second pathway to sustainably increase mariculture production is through further technological advances in finfish feeds. Currently, most mariculture

production (75%) requires some feed input (such as fishmeal and fish oil) that is largely derived from wild forage fisheries¹. If fed mariculture continues using fishmeal and fish oil at the current rate, its growth will be constrained by the ecological limits of these wild fisheries³². Alternative feed ingredients—including terrestrial plant- or animal-based proteins, seafood processing waste, microbial ingredients, insects, algae and genetically modified plants—are rapidly being developed and are increasingly used in mariculture feeds^{33,34,35,36}. These innovations could decouple fed mariculture from wild fisheries (but may refocus pressure on terrestrial ecosystems) and could catalyse considerable expansion in some regions^{37,38}. This has already begun for many fed species, such as Atlantic salmon—for which fish-based ingredient use has been reduced from 90% in the 1990s to just 25% at present³⁹. A reduced reliance on fishmeal and fish oil is expected to shift the supply curve of fed mariculture to the right (curve M4 in Fig. 2b).

The final pathway is a shift in demand (aggregated across all global fish consumers), which affects all three production sectors. When the sustainable supply curve is upward-sloping, an increase in demand (rightward shift; for example, from rising population, income or preferences) increases food production.

Estimated sustainable supply curves

We estimate supply curves of food from the sea in 2050 for the three largest food sectors in the ocean: wild fisheries, finfish mariculture and bivalve mariculture. We construct global supply curves for marine wild fisheries using projected future production for 4,702 fisheries under alternative management scenarios (Fig. 3a). We model future production with a bioeconomic model based on ref. ¹⁷, which tracks annual biomass, harvest and profit, and accounts for costs associated with extraction and management (see Methods and Supplementary Information for details).

Managing all fisheries to maximize food production (MSY) would result in 57.4 Mt of food in 2050 (derived from 89.3 Mt of total harvest, hereafter noted as live-weight equivalent), representing a 16% increase compared to the current food production (Fig. 3a). Under a scenario of economically rational reform (in which the management approach and exploitation rate of fisheries depend on profitability), the price influences production (Fig. 3a). At current mean global prices, this scenario would result in 51.3 Mt of food (77.4 Mt live-weight equivalent)—a 4% increase compared to current food production. These management-induced shifts in supply are ultimately limited by the carrying capacity of the ecosystem. If current fishing pressure is maintained for each fish stock when profitable (F current, referring to the current fishing mortality rate), food production from wild fisheries is lower for most

prices than under the two reform scenarios (owing to fishing too intensively on some stocks, and too conservatively on others)²⁵. this supply curve is not backward-bending, as it reflects constant fishing pressures.

Fig. 3: Estimated sustainable supply curves for wild fisheries, finfish mariculture and bivalve mariculture.

 [figure3](#)

a–c, Points represent current production and average price in each sector: marine wild fisheries (**a**), finfish mariculture (**b**) and bivalve mariculture (**c**). In **a**, supply curves for annual steady-state edible production from wild fisheries are shown under three different management scenarios: production in 2050 under current fishing effort assuming that fishing only occurs in fisheries that are profitable (*F* current); the economically rational supply curve aimed at maximizing profitability (rational reform); and a reform policy aimed at maximizing food production, regardless of the economic considerations (MSY). In **b**, supply curves for finfish (fed) mariculture show: future steady-state production under current feed assumptions and policy reform (policy reform); sustainable production assuming policy reform and a 50% reduction in fishmeal and fish oil feed requirements (technological innovation); and sustainable production assuming policy reform and a 95% reduction in fishmeal and fish oil feed requirements (technological innovation (ambitious)). In all cases, feed ingredients are from the economically rational reform of wild fisheries.

[Full size image](#)

We estimate the production potential of mariculture at a resolution of 0.217° around the world for finfish and bivalves. Ecological conditions—sea surface temperature, dissolved oxygen and primary productivity—determine the suitability of each pixel for mariculture production. We build on previous models¹⁹ by including economic considerations (including the capital costs of vessels and equipment, and the operating costs of wages, fuel, feed, insurance and maintenance; Supplementary Tables 5–7) to determine whether farming an ecologically suitable area is economically profitable at any given price. Summing economically viable production for each sector at the global level for different prices produces two mariculture supply curves. This approach assumes that the most profitable sites will be developed first, but does not explicitly include challenges such as the cost of public regulation and the delineation of property rights. Farm design is based on best practice for sustainable production, and we therefore interpret the results as an environmentally sustainable supply. We examine a range of assumptions regarding production costs, and explore different technological assumptions with respect to the species type farmed for finfish mariculture (Methods, Supplementary Information section 1.3, Supplementary Table 9). The supply curve for finfish mariculture differs substantially among future feed-technology scenarios, although all of these scenarios foretell a substantial increase in annual food supply in the future compared to the current production of the sector (6.8 Mt of food) (Fig. 3b). However, the policy reform scenario—which assumes mariculture policies are neither too restrictive nor lax (curve M3 in Fig. 2b), but that fishmeal and fish oil requirements match present-day conditions—produces a modest additional 1.4 Mt of food at current prices. In this scenario, marine-based feed inputs limit mariculture expansion even as the price increases considerably.

Two feed-innovation scenarios—representing policy reform plus a 50% or 95% reduction in fishmeal and fish oil requirements, which we refer to as ‘technological innovation’ and ‘technological innovation (ambitious)’, respectively—can substantially shift the supply curve.

At current prices, future supply under these scenarios is predicted to increase substantially to 17.2 Mt and 174.5 Mt of food for technological innovation and technological innovation (ambitious) scenarios, respectively (Fig. 3b). Bivalve mariculture is constrained by current policy but not by feed limitations, and is poised to expand substantially under policy reform scenarios. At current prices, economically rational production could lead to an increase from 2.9 Mt to 80.5 Mt of food (Fig. 3c). Even if our model underestimates costs by 50%, policy reforms would increase the production potential of both fed and unfed mariculture at current prices. For fed mariculture, this remains true even when evaluating mariculture species with different feed demands (Atlantic salmon, milkfish and barramundi).

Estimates of future food from the sea

Our supply curves suggest that all three sectors of ocean food production are capable of sustainably producing much more food than they do at present. The quantity of seafood demanded will also respond to price. We present three demand-curve estimates, shown in Fig. 4 (Methods, Supplementary Information). The intersections of future demand and sustainable supply curves provide an estimate of future food production from the sea. Because it is a substantial contributor to fish supply and—in some instances—acts as a market substitute for seafood, we also account for land-based aquatic food production (from freshwater aquaculture and inland capture fisheries; Supplementary Information section 1.4, Supplementary Tables 10–12). Estimates of future production from this fourth sector ('inland fisheries') are shown side-by-side in Supplementary Fig. 3 and Supplementary Tables 13, 14 (for quantities of food) and in Supplementary Tables 15, 16 (for live-weight equivalents), and are discussed with the results on food from the sea.

Fig. 4: Supply and demand curves of food from the sea for the three sectors.



a–c, Supply and demand curves for marine wild fisheries (**a**), finfish mariculture (**b**) and bivalve mariculture (**c**). In each panel, the solid black line is the supply curve from Fig. 3: for wild fisheries, the rational reform scenario is shown, and for finfish mariculture the technological innovation (ambitious) scenario is shown. Future demand refers to estimated demand in 2050; extreme demand represents a doubling of the estimated demand in 2050. The intersections of demand and sustainable supply curve (indicated with crosses) provide an estimate of the future food from the sea. Points represent current production and average price in each sector.

[Full size image](#)

Even under current demand curves (green curves in Fig. 4), the economically rational reform of marine wild fisheries and sustainable mariculture policies (stocking densities consistent with European organic standards⁴⁰) under the technological innovation (ambitious) scenario could result in a combined total of 62 Mt of food from the sea per year, 5% more than the current levels (59 Mt). But we know that demand will increase as incomes rise and populations expand. Under the ‘future demand’ scenario (purple curves in Fig. 4), total food from the sea is projected to increase to 80 Mt. If demand shifts even more (as represented by our ‘extreme demand’ scenario; red curves in Fig. 4), the intersection of supply and demand is expected to increase to 103 Mt of food. Using the approach used by the FAO to estimate future needs, the world will require an additional 177 Mt of meat by 2050 (Supplementary Information section 1.1.6)—our results suggest that additional food from the sea alone could plausibly contribute 12–25% of this need. Another possibility we consider is that future consumers will not distinguish between fish-producing sectors, such that all sources of fish (including land-based) would be substitutes for each other. Adopting that assumption alters the supply-and-demand equilibrium, and implies that the increase among all sources of fish (sea and land) relative to the present could be between 90–212 Mt of food; under this scenario, expansion of aquatic foods alone could possibly exceed the 177-Mt benchmark.

Our results also suggest that the future composition of food from the sea will differ substantially from the present (Fig. 5). Although wild fisheries dominate edible marine production at present, we project that by 2050 up to 44% of edible marine production could come from mariculture (rising to 76% when all fish are substitutes and land-based fish are included under extreme demand scenarios (Supplementary Fig. 3, Supplementary Table 14)), although all sectors could increase production. Although even more substantial increases are technically possible (for example, fed mariculture alone is capable of generating at least the benchmark 177 Mt of additional meat), actually realizing these gains would require enormous shifts in demand.

Fig. 5: Composition of current and future food from the sea under three alternative demand scenarios.



a, Composition of current (initial production) food from the sea. **b–d**, Composition of future (2050) food from the sea under scenarios of current (**b**), future (**c**) and extreme (**d**) demand. The sustainable supply curves assumed for these predictions are: rational reform for wild fisheries; technological innovation (ambitious) for finfish mariculture; and policy reform for bivalve mariculture, as shown in Fig. 3. The total production of food from the sea per year is shown in the centre in each panel.

[Full size image](#)

Our models rely on a number of assumptions and parameters that are uncertain, and which may interact in nonlinear ways. To test the robustness of our main conclusions, we examine a range of scenarios and run an extensive sensitivity analysis (Supplementary Information). Across a wide range of cost, technology and demand scenarios, we find that sustainably harvested food from the sea: (1) has the potential to increase considerably in the coming decades; (2) will change in composition, with a greater future share coming from mariculture; and (3), in

aggregate, could have an outsized role in meeting future meat demands around the world (Supplementary Figs. [1–4](#), Supplementary Tables [13–17](#)).

Conclusions

Global food demand is rising, and expanding land-based production is fraught with environmental and health concerns. Because seafood is nutritionally diverse and avoids or lessens many of the environmental burdens of terrestrial food production, it is uniquely positioned to contribute to both food provision and future global food and nutrition security. Our estimated sustainable supply curves of food from the sea suggest substantial possibilities for future expansion in both wild fisheries and mariculture. The potential for increased global production from wild fisheries hinges on maintaining fish populations near their most-productive levels. For underutilized stocks, this will require expanding existing markets. For overfished stocks, this will require adopting or improving management practices that prevent overfishing and allow depleted stocks to rebuild. Effective management practices commonly involve setting and enforcing science-based limits on catch or fishing effort, but appropriate interventions will depend on the biological, socioeconomic, cultural and governance contexts of individual fisheries. Effective management will be further challenged by climate change, species composition changes in marine ecosystems and illegal fishing. Directing resources away from subsidies that enhance fishing capacity towards building institutional and technical capacity for fisheries research, management and enforcement will help to meet these challenges. Increased mariculture production will require management practices and policies that allow for environmentally sustainable expansion, while balancing the associated trade-offs to the greatest extent possible; this principle underpins the entire analysis. We find that substantial expansion is realistic, given the costs of production and the likely future increase in demand.

We have identified a variety of ways that sustainable supply curves can shift outward. These shifts interact with future demand to determine the plausible future equilibrium quantity of food produced from the sea. We find that although supply could increase to more than six times the current level (primarily via expanded mariculture), the demand shift required to engage this level of supply is unlikely. Under more realistic demand scenarios and appropriate reforms of the supply, we find that food from the sea could increase in all three sectors (wild fisheries, finfish mariculture and bivalve mariculture) to a total of 80–103 Mt of food in 2050 versus 59 Mt at present (in live-weight equivalents, 159–227 Mt compared to 102 Mt at present). When combined with projected inland production, this represents an 18–44% per decade increase in live-weight production, which is somewhat higher than the 14% increase that the Organisation for Economic Co-operation and

Development (OECD) and the FAO project for total fish production during the next decade⁴¹. Under some scenarios, future production could represent a disproportionate fraction of the estimated total increase in global food production that will be required to feed 9.8 billion people by 2050. Substantial growth in mariculture will rely partly on public perceptions. Although there is some evidence of a negative public perception of aquaculture, it is highly variable by region and by context^{42,43}, and certifications and the provision of other information can help to alleviate concerns and expand demand⁴⁴.

These global projections will not have uniform implications around the world. For example, improved policies that shift the supply curve outward will decrease prices, but income-induced demand shifts will increase prices. Both effects increase production, but have vastly different consequences for low-income consumers. Bivalves may contribute substantially to food security by providing relatively low-cost and thus accessible food, because they have a high production potential at low costs compared to finfish production (Fig. 3). If all seafood is perfectly substitutable, bivalves could contribute 43% and 34% of future aquatic food under future and extreme demand scenarios, respectively (Supplementary Fig. 3)—which suggests potential large increases in production, provided demand is high enough. Trade also has an important role in distributing seafood from high-production to low-production regions, and in overcoming regional mismatches in price. The rate of international trade of seafood products has increased over past decades, and 27% of seafood products were traded in 2016¹, although major economic disruptions—such as the COVID-19 pandemic—can jointly reduce both supply and demand of traded seafood. On the other hand, trade may become increasingly relied upon as climate change alters regional productivity.

Substantially expanding the production of food from the sea will bring co-benefits and trade-offs, and will require national and interregional governance, as well as local capacity to ensure equity and sustainability. The improved management of wild fisheries can not only increase fish biomass, but also brings the co-benefit of improved livelihoods of fishers. However, there will be some short-term costs as overfished stocks rebuild to levels that support greater food provision. As mariculture expands, interactions with wild fisheries and other ecosystem services (via spatial overlaps, pollution and so on) must be constantly addressed. Ambitious technical innovation (that is, the substitution of marine ingredients with terrestrial-sourced proteins) can help to decouple fed mariculture from wild fisheries, but will probably refocus some pressure on terrestrial ecosystems. Climate change will further challenge food security. Estimates suggest that active adaptation to climate-induced changes will be crucial in both wild fisheries⁴⁵ and mariculture⁴⁶. Climate-adaptive management of wild fisheries and decisions regarding mariculture

production (for example, the type of feed used, species produced and farm siting) could improve food provision from the sea under conditions of climate change.

We have shown that the sea can be a much larger contributor to sustainable food production than is currently the case, and that this comes about by implementing a range of plausible and actionable mechanisms. The price mechanism—when it motivates improved fishery management and the sustainable expansion of mariculture into new areas—arises from change in demand, and acts on its own without any explicit intervention. The feed technology mechanism is driven by incentives to innovate, and thus acquire intellectual property rights to new technologies. When intellectual property is not ensured, or to achieve other social goals, there may be a role for public subsidies or other investments in these technologies. The policy mechanism pervades all three production sectors, and could make—or break—the ability of food from the sea to sustainably, equitably and efficiently expand in the future.

Methods

Sample size was a census of all available fisheries data. No experiments were conducted.

Here we describe our methods in brief: detailed methods, sensitivity analyses and robustness checks are provided in the Supplementary Information.

Sustainable supply curves

The supply of food from marine wild fisheries is jointly determined by ecosystem constraints, fishery policy and prevailing economic conditions. Estimated supply curves show the projected 2050 production quantity at a given price, incorporating harvesting costs, management costs and fishery-specific engagement decisions for individual fisheries. Current management of the 4,702 marine fisheries included in our study range from open access to strong target-based management¹⁷. Using data from the RAM Legacy Stock Assessment Database⁴⁸, the FAO⁹ and refs. ^{17,49,50}, we calculate three supply curves that represent summed global production from established wild fisheries for a range of prices (Fig. 3). The first (F current) assumes that all fisheries in the world maintain their current fishing mortality rate if profitable (that is, fisheries for which current fishing pressure would result in steady-state profit < 0 are not fished). The second (rational reform) assumes that fisheries are reformed to maximize long-term food production (that is, adopt F_{MSY} , the fishing mortality rate that results in maximum sustainable yield (MSY)), but

only at prices for which reform results in greater future profit than that of current management. Importantly, adopting reform is associated with greater management costs for fisheries that are currently weakly managed. If a fishery is managed, its production changes, which alters the supply curve. Production occurs in a given fishery only if future profit > 0 . The third supply curve (MSY) assumes that all fisheries are managed to maximize sustainable yield, regardless of the cost or benefit of doing so (Fig. 3). Supply curves under alternative cost assumptions yield results similar to those presented in Fig. 3 (Supplementary Fig. 1).

To construct supply curves for finfish and bivalve mariculture (which account for 83% of current production of edible animal products from mariculture¹¹), we use a previously published¹⁹ global suitability dataset at a resolution of 0.217° . Ecological conditions (that is, surface temperature, dissolved oxygen and primary productivity (bivalves only)) determine the suitability of different areas for production. We build on ref. ¹⁹ by including economic considerations (for example, the capital costs of vessels and equipment and operating costs of wages, fuel, feed, insurance and maintenance; see Supplementary Information section 1.3, Supplementary Tables 5–7 for more details) to determine whether an ecologically suitable area is also economically profitable to farm at a given price. For any given price, we estimate the potential production and profitability of each pixel, and determine the global set of economically viable pixels for mariculture production of finfish and bivalves; we allow for production of both kinds of mariculture in the same pixel, provided the pixel is economically suitable for both. Summing production in this manner at the global level provides a point on the supply curve, at which farm design (Supplementary Table 4) is based on best practices for sustainable production (that is, stocking densities consistent with European organic standards⁴⁰). We then derive supply curves under different assumptions regarding mariculture policy and technological innovation, which affect the parameters of the supply model.

We estimate supply curves for finfish mariculture under three scenarios, all of which assume that wild fisheries are rationally managed; this pins down the potential supply of wild fish that can be used as feed in mariculture (Supplementary Table 8). We display three supply curves for fed mariculture (Fig. 3). The policy reforms scenario represents a future in which regulatory barriers are removed, unsustainable production is prevented and mariculture continues to use feed ingredients from wild fisheries at the current rate (that is, feed conversion ratios remain static, fishmeal and fish oil inclusion rates in feed remain the same, and feed availability depends on production from wild fisheries). This scenario represents the economically rational sustainable production given the current feed context. Two technological innovation scenarios represent policy reform plus a 50% and (a more ambitious) 95% reduction in fishmeal and fish oil requirements for fed mariculture production. The supply

curve for bivalve (unfed) mariculture (Fig. 3) reflects production in the set of pixels for which unfed mariculture can be profitably produced at any given price.

Supply meets demand

To estimate how food from the sea might help to meet future increases in demand at the global level, we require estimates of the current and future demand curves of food from the sea. The intersection of future demand curves and our estimated sustainable supply curves provides an estimate of food from the sea in 2050. As a benchmark, we assume that the three sectors are independent, but that increases in demand are parametric, so each of the three sectors experiences a proportional increase in future demand—for example, as global population and per capita incomes rise (see Supplementary Information for detailed results, assuming all aquatic foods are perfect substitutes). We assume a straightforward structure in which each sector faces an isoelastic demand (for example, see ref. 51, with own price elasticity = -0.382 ; ref. 52; and sector-specific income elasticities estimated from ref. 51). Using these elasticities, the coefficient on current-demand curve in each sector (current, in Fig. 4) is tuned so the demand curve passes through the current price of seafood in that sector (averaged across fish from that sector) given the current global gross domestic product and population. Effectively, this approach assumes that all fish within a sector are substitutes. We do not explicitly estimate a current supply curve because it is not required to perform our calculations and—for reasons stated in the Article—we do not necessarily regard the current supply as sustainable.

To project future demand at the global level, we develop two scenarios that we term future and extreme (Fig. 4). The future demand represents the demand curve for food from the sea in each sector given exogenous estimates of future population size and global income in 2050^{53,54}, which are entered as parameters in the demand curve (Supplementary Information). The extreme scenario doubles the quantity demanded at any given price in 2050, relative to the future scenario; we regard demand shifts larger than this amount as unlikely.

The Supplementary Information contains an extensive set of robustness checks and sensitivity analyses. One important alternative to the model in the Article is to allow all fish to be perfect substitutes in the future. Under that model, land-based fish production (aquaculture and capture) must be accounted for because those fish act as substitutes for food from the sea. Although this tends to increase the final estimates of food production from the sea, our qualitative findings are robust to this assumption and the Supplementary Information reports how this changes the model results described in the Article.

Reporting summary

Further information on research design is available in the [Nature Research Reporting Summary](#) linked to this paper.

Data availability

All datasets analysed during the current study are available in a Dryad repository at <https://datadryad.org/stash/dataset/doi:10.25349/D96G6H>.

Code availability

All code used to conduct the study are available in a GitHub repository: https://github.com/emlab-ucsb/future_food_from_sea.

References

1. 1.

FAO. *The State of World Fisheries and Aquaculture* (FAO, 2018).

2. 2.

Olsen, Y. Resources for fish feed in future mariculture. *Aquacult. Environ. Interact.* **1**, 187–200 (2011).

[Google Scholar](#)

3. 3.

Foley, J. A. et al. Solutions for a cultivated planet. *Nature* **478**, 337–342 (2011).

[CAS Article](#) [ADS](#) [PubMed](#) [Google Scholar](#)

4. 4.

Foley, J. A. et al. Global consequences of land use. *Science* **309**, 570–574 (2005).

[CAS Article](#) [ADS](#) [PubMed](#) [PubMed Central](#) [Google Scholar](#)

5. 5.

Mbow, C. et al. in *Climate Change and Land (IPCC Special Report)* (eds Shukla, P. R. et al.) Ch. 5 (IPCC, 2019).

6. 6.

Amundson, R. et al. Soil and human security in the 21st century. *Science* **348**, 1261071 (2015).

[Article](#) [PubMed](#) [Google Scholar](#)

7. 7.

UNDP. Sustainable Development Goal 2, *Sustainable Development Goals*. <https://sustainabledevelopment.un.org/sdg2> (accessed 27 July 2020).

8. 8.

De Silva, S. & Davy, F. *Success Stories in Asian Aquaculture* (Springer 2010).

9. 9.

FAO Fisheries and Aquaculture Department. *FishStatJ – Software for Fishery and Aquaculture Statistical Time Series*. <http://www.fao.org/fishery/statistics/software/fishstatj/en> (2019).

10. 10.

Edwards, P., Zhang, W., Belton, B. & Little, D. C. Misunderstandings, myths and mantras in aquaculture: its contribution to world food supplies has been systematically over reported. *Mar. Policy* **106**, 103547 (2019).

[Article](#) [Google Scholar](#)

11. 11.

FAO. FAOSTAT. <http://www.fao.org/faostat/en/#home> (2020).

12. 12.

Nijdam, D., Rood, T. & Westhoek, H. The price of protein: review of land use and carbon footprints from life cycle assessments of animal food products and

their substitutes. *Food Policy* **37**, 760–770 (2012).

[Article](#) [Google Scholar](#)

13. 13.

Kawarazuka, N. & Béné, C. Linking small-scale fisheries and aquaculture to household nutritional security: an overview. *Food Secur.* **2**, 343–357 (2010).

[Article](#) [Google Scholar](#)

14. 14.

Allison, E. H. *Aquaculture, Fisheries, Poverty and Food Security (Working Paper 2011–65)* (WorldFish Center, 2011).

15. 15.

Golden, C. D. et al. Fall in fish catch threatens human health. *Nature* **534**, 317–320 (2016).

[Article](#) [ADS](#) [PubMed](#) [Google Scholar](#)

16. 16.

Hicks, C. C. et al. Harnessing global fisheries to tackle micronutrient deficiencies. *Nature* **574**, 95–98 (2019).

[CAS](#) [Article](#) [ADS](#) [PubMed](#) [Google Scholar](#)

17. 17.

Costello, C. et al. Global fishery prospects under contrasting management regimes. *Proc. Natl Acad. Sci. USA* **113**, 5125–5129 (2016).

[CAS](#) [Article](#) [ADS](#) [PubMed](#) [Google Scholar](#)

18. 18.

Ye, Y. & Gutierrez, N. L. Ending fishery overexploitation by expanding from local successes to globalized solutions. *Nat. Ecol. Evol.* **1**, 0179 (2017).

[Article](#) [Google Scholar](#)

19. 19.

Gentry, R. R. et al. Mapping the global potential for marine aquaculture. *Nat. Ecol. Evol.* **1**, 1317–1324 (2017).

[Article](#) [PubMed](#) [Google Scholar](#)

20. 20.

Troell, M., Jonell, M. & Henriksson, P. J. G. Ocean space for seafood. *Nat. Ecol. Evol.* **1**, 1224–1225 (2017).

[Article](#) [PubMed](#) [Google Scholar](#)

21. 21.

Costello, C. et al. *The Future of Food from the Sea*
<http://oceanpanel.org/future-food-sea> (World Resources Institute, 2019).

22. 22.

Belton, B., Bush, S. R. & Little, D. C. Not just for the wealthy: rethinking farmed fish consumption in the Global South. *Glob. Food Secur.* **16**, 85–92 (2018).

[Article](#) [Google Scholar](#)

23. 23.

Copes, P. The backward-bending supply curve of the fishing industry. *Scott. J. Polit. Econ.* **17**, 69–77 (1970).

[Article](#) [Google Scholar](#)

24. 24.

Nielsen, M. Trade liberalisation, resource sustainability and welfare: the case of East Baltic cod. *Ecol. Econ.* **58**, 650–664 (2006).

[Article](#) [Google Scholar](#)

25. 25.

Hilborn, R. & Costello, C. The potential for blue growth in marine fish yield, profit and abundance of fish in the ocean. *Mar. Policy* **87**, 350–355 (2018).

[Article](#) [Google Scholar](#)

26. 26.

Hilborn, R. et al. Effective fisheries management instrumental in improving fish stock status. *Proc. Natl Acad. Sci. USA* **117**, 2218–2224 (2020).

[CAS](#) [Article](#) [PubMed](#) [Google Scholar](#)

27. 27.

Joffre, O. M., Klerkx, L., Dickson, M. & Verdegem, M. How is innovation in aquaculture conceptualized and managed? A systematic literature review and reflection framework to inform analysis and action. *Aquaculture* **470**, 129–148 (2017).

[Article](#) [Google Scholar](#)

28. 28.

Abate, T. G., Nielsen, R. & Tveterås, R. Stringency of environmental regulation and aquaculture growth: a cross-country analysis. *Aquac. Econ. Manag.* **20**, 201–221 (2016).

[Article](#) [Google Scholar](#)

29. 29.

Gentry, R. R., Ruff, E. O. & Lester, S. E. Temporal patterns of adoption of mariculture innovation globally. *Nat. Sustain.* **2**, 949–956 (2019).

[Article](#) [Google Scholar](#)

30. 30.

The Sea Grant Law Center. *Overcoming Impediments to Shellfish Aquaculture Through Legal Research and Outreach: Case Studies* (NOAA, 2019).

31. 31.

Davies, I. P. et al. Governance of marine aquaculture: pitfalls, potential, and pathways forward. *Mar. Policy* **104**, 29–36 (2019).

[Article](#) [Google Scholar](#)

32. 32.

Froehlich, H. E., Jacobsen, N. S., Essington, T. E., Clavelle, T. & Halpern, B. S. Avoiding the ecological limits of forage fish for fed aquaculture. *Nat. Sustain.* **1**, 298–303 (2018).

[Article](#) [Google Scholar](#)

33. 33.

Klinger, D. & Naylor, R. Searching for solutions in aquaculture: charting a sustainable course. *Annu. Rev. Environ. Resour.* **37**, 247–276 (2012).

[Article](#) [Google Scholar](#)

34. 34.

Cao, L. et al. China’s aquaculture and the world’s wild fisheries. *Science* **347**, 133–135 (2015).

[CAS](#) [Article](#) [ADS](#) [PubMed](#) [Google Scholar](#)

35. 35.

Little, D. C., Newton, R. W. & Beveridge, M. C. M. Aquaculture: a rapidly growing and significant source of sustainable food? Status, transitions and potential. *Proc. Nutr. Soc.* **75**, 274–286 (2016).

[CAS](#) [Article](#) [PubMed](#) [Google Scholar](#)

36. 36.

Shah, M. R. et al. Microalgae in aquafeeds for a sustainable aquaculture industry. *J. Appl. Phycol.* **30**, 197–213 (2018).

[Article](#) [Google Scholar](#)

37. 37.

Troell, M. et al. Does aquaculture add resilience to the global food system? *Proc. Natl Acad. Sci. USA* **111**, 13257–13263 (2014).

[CAS](#) [Article](#) [ADS](#) [PubMed](#) [Google Scholar](#)

38. 38.

Froehlich, H. E., Runge, C. A., Gentry, R. R., Gaines, S. D. & Halpern, B. S. Comparative terrestrial feed and land use of an aquaculture-dominant world. *Proc. Natl Acad. Sci. USA* **115**, 5295–5300 (2018).

[CAS](#) [Article](#) [PubMed](#) [Google Scholar](#)

39. 39.

Aas, T. S., Ytrestøyl, T. & Åsgård, T. Utilization of feed resources in the production of Atlantic salmon (*Salmo salar*) in Norway: An update for 2016. *Aquacult. Rep.* **15**, 100216 (2019).

[Article](#) [Google Scholar](#)

40. 40.

European Union. Commission Regulation (EC) No 889/2008 of 5 September 2008 laying down detailed rules for the implementation of Council Regulation (EC) No 834/2007 on organic production and labelling of organic products with regard to organic production, labelling and control. *Offic. J. EU L* **250**, 1–84 (2008).

[Google Scholar](#)

41. 41.

OECD & Food and Agriculture Organization of the United Nations. *OECD-FAO Agricultural Outlook 2019–2028* (OECD, 2019).

42. 42.

Froehlich, H. E., Gentry, R. R., Rust, M. B., Grimm, D. & Halpern, B. S. Public perceptions of aquaculture: evaluating spatiotemporal patterns of sentiment around the world. *PLoS ONE* **12**, e0169281 (2017).

[Article](#) [PubMed](#) [PubMed Central](#) [Google Scholar](#)

43. 43.

Bacher, K. *Perceptions and Misconceptions of Aquaculture: A Global Overview* (GLOBEFISH, 2015).

44. 44.

Bronnmann, J. & Asche, F. Sustainable seafood from aquaculture and wild fisheries: insights from a discrete choice experiment in Germany. *Ecol. Econ.* **142**, 113–119 (2017).

[Article](#) [Google Scholar](#)

45. 45.

Gaines, S. D. et al. Improved fisheries management could offset many negative effects of climate change. *Sci. Adv.* **4**, eaao1378 (2018).

[Article](#) [ADS](#) [PubMed](#) [PubMed Central](#) [Google Scholar](#)

46. 46.

Froehlich, H. E., Gentry, R. R. & Halpern, B. S. Global change in marine aquaculture production potential under climate change. *Nat. Ecol. Evol.* **2**, 1745–1750 (2018).

[Article](#) [PubMed](#) [Google Scholar](#)

47. 47.

Cashion, T., Tyedmers, P. & Parker, R. W. R. Global reduction fisheries and their products in the context of sustainable limits. *Fish Fish.* **18**, 1026–1037 (2017).

[Article](#) [Google Scholar](#)

48. 48.

Ricard, D., Minto, C., Jensen, O. P. & Baum, J. K. Examining the knowledge base and status of commercially exploited marine species with the RAM Legacy Stock Assessment Database. *Fish Fish.* **13**, 380–398 (2012).

[Article](#) [Google Scholar](#)

49. 49.

Melnichuk, M. C., Clavelle, T., Owashi, B. & Strauss, K. Reconstruction of global ex-vessel prices of fished species. *ICES J. Mar. Sci.* **74**, 121–133 (2017).

[Article](#) [Google Scholar](#)

50. 50.

Mangin, T. et al. Are fishery management upgrades worth the cost? *PLoS ONE* **13**, e0204258 (2018).

[Article](#) [PubMed](#) [PubMed Central](#) [Google Scholar](#)

51. 51.

Cai, J. & Leung, P. *Short-term Projection of Global Fish Demand and Supply Gaps* (FAO, 2017).

52. 52.

Muhammad, A., Seale, J. L. Jr, Meade, B. & Regmi, A. *International Evidence on Food Consumption Patterns: An Update Using 2005 International Comparison Program Data*. Technical Bulletin No. TB-1929 (United States Department of Agriculture, 2011).

53. 53.

PwC. *The Long View: How will the global economic order change by 2050?* <https://www.pwc.com/gx/en/world-2050/assets/pwc-the-world-in-2050-full-report-feb-2017.pdf> (2017).

54. 54.

United Nations. World population projected to reach 9.8 billion in 2050, and 11.2 billion in 2100. *World population projected to reach 9.8 billion in 2050, and 11.2 billion in 2100*

<https://www.un.org/development/desa/en/news/population/world-population-prospects-2017.html> (2017).

[Download references](#)

Acknowledgements

This research is adapted from a Blue Paper commissioned by the High Level Panel for a Sustainable Ocean Economy entitled ‘The Future of Food from the Sea’. We thank the high-level panel for a sustainable ocean economy, N. Frost, K. Teleki, T. Clavelle and A. Merkl for inspiration and comments. We thank SYSTEMIQ (C.C., C.M.F., T.M., E.O’R. and A.J.P.), World Resources Institute (C.C., C.M.F., T.M., E.O’R. and A.J.P.), the David and Lucile Packard Foundation (L.C. and S.G.), the European Research Council (679812) (E.O.), ANID PIA/BASAL 0002 (S.G.) and GAIN-Xunta de Galicia (E.O.) for financial support.

Author information

Author notes

1. These authors jointly supervised this work: Christopher Costello, Ling Cao, Stefan Gelcich

Affiliations

1. Bren School of Environmental Science and Management, University of California, Santa Barbara, Santa Barbara, CA, USA
Christopher Costello, Christopher M. Free, Jason Maier, Ilan Macadam-Somer, Tracey Mangin, Erin O'Reilly & Andrew J. Plantinga
2. Environmental Market Solutions Lab, University of California, Santa Barbara, Santa Barbara, CA, USA
Christopher Costello, Christopher M. Free, Ilan Macadam-Somer, Tracey Mangin, Erin O'Reilly & Andrew J. Plantinga
3. School of Oceanography, Shanghai Jiao Tong University, Shanghai, China
Ling Cao
4. Center of Applied Ecology and Sustainability, Pontificia Universidad Católica de Chile, Santiago, Chile
Stefan Gelcich
5. Center for the Study of Multiple-Drivers on Marine Socio-Ecological Systems, Pontificia Universidad Católica de Chile, Santiago, Chile

Stefan Gelcich

6. Instituto Nacional de Pesca y Acuacultura, Guaymas, Mexico

Miguel Á. Cisneros-Mata

7. Ecology, Evolution and Marine Biology, University of California, Santa Barbara, Santa Barbara, CA, USA

Halley E. Froehlich

8. Environmental Studies, University of California, Santa Barbara, Santa Barbara, CA, USA

Halley E. Froehlich

9. Department of Nutrition, Harvard T. H. Chan School of Public Health, Boston, MA, USA

Christopher D. Golden

10. Department of Environmental Health, Harvard T. H. Chan School of Public Health, Boston, MA, USA

Christopher D. Golden

11. Faculty of Agriculture, Iwate University, Morioka, Japan

Gakushi Ishimura

12. National Research Institute for Environmental Studies, Tsukuba, Japan

Gakushi Ishimura

13. School of Aquatic and Fishery Sciences, University of Washington, Seattle, WA, USA

Michael C. Melnychuk

14. Fisheries Research and Education Agency of Japan, Yokohama, Japan

Masanori Miyahara

15. Marine Resource Assessment and Management (MARAM) Group, Department of Mathematics and Applied Mathematics, University of Cape Town, Rondebosch, South Africa

Carryn L. de Moor

16. Department of Earth System Science, Stanford University, Stanford, CA, USA

Rosamond Naylor

17. Center on Food Security and the Environment, Stanford University, Stanford, CA, USA

Rosamond Naylor

18. Department of Economics, Norwegian School of Economics, Bergen, Norway

Linda Nøstbakken

19. Future Oceans Lab, CIM-University of Vigo, Vigo, Spain

Elena Ojea

20. Center for the Study of Marine Systems, National Scientific and Technical Research Council of Argentina, Buenos Aires, Argentina

Ana M. Parma

21. WorldFish, Bayan Lepas, Malaysia

Shakuntala H. Thilsted

22. Department of Integrative Biology, Oregon State University, Corvallis, OR, USA

Jane Lubchenco

Authors

1. Christopher Costello

[View author publications](#)

You can also search for this author in [PubMed](#) [Google Scholar](#)

2. Ling Cao

[View author publications](#)

You can also search for this author in [PubMed](#) [Google Scholar](#)

3. Stefan Gelcich

[View author publications](#)

You can also search for this author in [PubMed](#) [Google Scholar](#)

4. Miguel Á. Cisneros-Mata

[View author publications](#)

You can also search for this author in [PubMed](#) [Google Scholar](#)

5. Christopher M. Free

[View author publications](#)

You can also search for this author in [PubMed](#) [Google Scholar](#)

6. Halley E. Froehlich

[View author publications](#)

You can also search for this author in [PubMed](#) [Google Scholar](#)

7. Christopher D. Golden

[View author publications](#)

You can also search for this author in [PubMed](#) [Google Scholar](#)

8. Gakushi Ishimura

[View author publications](#)

You can also search for this author in [PubMed](#) [Google Scholar](#)

9. Jason Maier

[View author publications](#)

You can also search for this author in [PubMed](#) [Google Scholar](#)

10. Ilan Macadam-Somer

[View author publications](#)

You can also search for this author in [PubMed](#) [Google Scholar](#)

11. Tracey Mangin

[View author publications](#)

You can also search for this author in [PubMed](#) [Google Scholar](#)

12. Michael C. Melnychuk

[View author publications](#)

You can also search for this author in [PubMed](#) [Google Scholar](#)

13. Masanori Miyahara

[View author publications](#)

You can also search for this author in [PubMed](#) [Google Scholar](#)

14. Carryn L. de Moor

[View author publications](#)

You can also search for this author in [PubMed](#) [Google Scholar](#)

15. Rosamond Naylor

[View author publications](#)

You can also search for this author in [PubMed](#) [Google Scholar](#)

16. Linda Nøstbakken

[View author publications](#)

You can also search for this author in [PubMed](#) [Google Scholar](#)

17. Elena Ojea

[View author publications](#)

You can also search for this author in [PubMed](#) [Google Scholar](#)

18. Erin O'Reilly

[View author publications](#)

You can also search for this author in [PubMed](#) [Google Scholar](#)

19. Ana M. Parma

[View author publications](#)

You can also search for this author in [PubMed](#) [Google Scholar](#)

20. Andrew J. Plantinga

[View author publications](#)

You can also search for this author in [PubMed](#) [Google Scholar](#)

21. Shakuntala H. Thilsted

[View author publications](#)

You can also search for this author in [PubMed](#) [Google Scholar](#)

22. Jane Lubchenco

[View author publications](#)

You can also search for this author in [PubMed](#) [Google Scholar](#)

Contributions

C.C., L.C., S.G. and A.J.P. conceived the study. C.C., L.C., C.M.F., H.E.F., S.G., T.M. and A.J.P. contributed to the study design. C.C., L.C., C.M.F., J.M., T.M., R.N. and A.J.P. contributed to the acquisition and analysis of data. C.C., L.C., M.Á.C.-M., C.M.F., H.E.F., S.G., T.M., R.N., A.J.P. and S.H.T. contributed to the interpretation of results. C.C., L.C., M.A.C., H.E.F., S.G., C.D.G., G.I., I.M.-S., J.M., T.M., M.C.M., M.M., C.L.d.M., R.N., L.N., E.O., E.O'R., A.M.P, A.J.P., J.L. and S.H.T. wrote and edited the manuscript.

Corresponding authors

Correspondence to [Christopher Costello](#) or [Ling Cao](#) or [Stefan Gelcich](#).

Ethics declarations

Competing interests

C.C. serves as trustee for Environmental Defense Fund and Global Fishing Watch. H.E.F. serves as a scientific advisor on the Technical Advisory Group for the Aquaculture Stewardship Council. R.N. serves on the scientific advisory board for Oceana and *Nature Food*. C.L.d.M. has undertaken work funded by government agencies, fishery industry organizations and regional fisheries management organizations. C.D.G. serves on the scientific advisory board for Oceana.

Additional information

Peer review information *Nature* thanks Dale Squires and the other, anonymous, reviewer(s) for their contribution to the peer review of this work.

Publisher's note Springer Nature remains neutral with regard to jurisdictional claims in published maps and institutional affiliations.

Supplementary information

[Supplementary Information](#)

This file contains Supplementary Methods, Supplementary Tables 1-17, Supplementary Figs 1-4 and Supplementary References.

[Reporting Summary](#)

Rights and permissions

[Reprints and Permissions](#)

About this article



Check for
updates

Cite this article

Costello, C., Cao, L., Gelcich, S. *et al.* The future of food from the sea. *Nature* **588**, 95–100 (2020). <https://doi.org/10.1038/s41586-020-2616-y>

[Download citation](#)

- Received: 19 December 2019
- Accepted: 29 June 2020
- Published: 19 August 2020
- Issue Date: 03 December 2020
- DOI: <https://doi.org/10.1038/s41586-020-2616-y>

Further reading

- [**Harnessing Kenya's Blue Economy: prospects and challenges**](#)
 - Joseph O. Rasowo
 - , Paul Orina
 - , Betty Nyonje

- , Salome Awuor
- & Robert Olendi

Journal of the Indian Ocean Region (2020)

- **Reconciling sustainability, economic efficiency and equity in marine fisheries: Has there been progress in the last 20 years?**

- Kevern L. Cochrane

Fish and Fisheries (2020)

- **Five priorities for a sustainable ocean economy**

- Jane Lubchenco
- , Peter M. Haugan
- & Mari Elka Pangestu

Nature (2020)

- **A transition to sustainable ocean governance**

- Tanya Brodie Rudolph
- , Mary Ruckelshaus
- , Mark Swilling
- , Edward H. Allison
- , Henrik Österblom
- , Stefan Gelcich
- & Philile Mbatha

Nature Communications (2020)

- **Transdisciplinary Research Priorities for Human and Planetary Health in the Context of the 2030 Agenda for Sustainable Development**

- Kristie L. Ebi
- , Frances Harris
- , Giles B. Sioen
- , Chadia Wannous
- , Assaf Anyamba
- , Peng Bi
- , Melanie Boeckmann
- , Kathryn Bowen
- , Guéladio Cissé
- , Purnamita Dasgupta
- , Gabriel O. Dida
- , Alexandros Gasparatos
- , Franz Gatzweiler
- , Firouzeh Javadi
- , Sakiko Kanbara
- , Brama Kone
- , Bruce Maycock
- , Andy Morse
- , Takahiro Murakami
- , Adetoun Mustapha
- , Montira Pongsiri
- , Gerardo Suzán
- , Chiho Watanabe
- & Anthony Capon

International Journal of Environmental Research and Public Health
(2020)

Comments

By submitting a comment you agree to abide by our [Terms](#) and [Community Guidelines](#). If you find something abusive or that does not comply with our terms or guidelines please flag it as inappropriate.

[Download PDF](#)

Associated Content

Special

The ocean in humanity's future

This article was downloaded by **calibre** from <https://www.nature.com/articles/s41586-020-2616-y>.

| [Section menu](#) | [Main menu](#) |

- Article
- [Published: 04 November 2020](#)

An early Cambrian euarthropod with radiodont-like raptorial appendages

- [Han Zeng](#) ORCID: orcid.org/0000-0002-5728-7896^{1,2,3},
- [Fangchen Zhao](#) ORCID: orcid.org/0000-0001-8473-4439^{1,2,4},
- [Kecheng Niu](#)⁵,
- [Maoyan Zhu](#) ORCID: orcid.org/0000-0001-7327-9856^{1,2,4} &
- [Diying Huang](#) ORCID: orcid.org/0000-0002-5637-4867^{1,2}

Nature volume 588, pages101–105(2020)[Cite this article](#)

- 4331 Accesses
- 694 Altmetric
- [Metrics details](#)

Subjects

- [Palaeontology](#)
- [Phylogenetics](#)

Abstract

Resolving the early evolution of euarthropods is one of the most challenging problems in metazoan evolution^{1,2}. Exceptionally preserved fossils from the Cambrian period have contributed important

palaeontological data to deciphering this evolutionary process^{3,4}. Phylogenetic studies have resolved Radiodonta (also known as anomalocaridids) as the closest group to all euarthropods that have frontalmost appendages on the second head segment (Deuteropoda)^{5,6,7,8,9}. However, the interrelationships among major Cambrian euarthropod groups remain disputed^{1,2,4,7}, which impedes our understanding of the evolutionary gap between Radiodonta and Deuteropoda. Here we describe *Kylinxia zhangi* gen. et. sp. nov., a euarthropod from the early Cambrian Chengjiang biota of China. *Kylinxia* possesses not only deuteropod characteristics such as a fused head shield, a fully arthrodized trunk and jointed endopodites, but also five eyes (as in *Opabinia*) as well as radiodont-like raptorial frontalmost appendages. Our phylogenetic reconstruction recovers *Kylinxia* as a transitional taxon that bridges Radiodonta and Deuteropoda. The most basal deuteropods are retrieved as a paraphyletic lineage that features plesiomorphic raptorial frontalmost appendages and includes *Kylinxia*, megacheirans, panchelicerates, ‘great-appendage’ bivalved euarthropods and isoxyids. This phylogenetic topology supports the idea that the radiodont and megacheiran frontalmost appendages are homologous, that the chelicerae of Chelicerata originated from megacheiran great appendages and that the sensorial antennae in Mandibulata derived from ancestral raptorial forms. *Kylinxia* thus provides important insights into the phylogenetic relationships among early euarthropods, the evolutionary transformations and disparity of frontalmost appendages, and the origin of crucial evolutionary innovations in this clade.

[Access through your institution](#)

[Change institution](#)

[Buy or subscribe](#)

Access options

Subscribe to Journal

Get full journal access for 1 year

185,98 €

only 3,58 € per issue

[Subscribe](#)

All prices are NET prices.
VAT will be added later in the checkout.

Rent or Buy article

Get time limited or full article access on ReadCube.
from \$8.99

[Rent or Buy](#)

All prices are NET prices.

Additional access options:

- [Log in](#)
- [Access through your institution](#)
- [Learn about institutional subscriptions](#)

Fig. 1: Anatomy of *Kylinxia zhangi* from the early Cambrian Chengjiang biota.

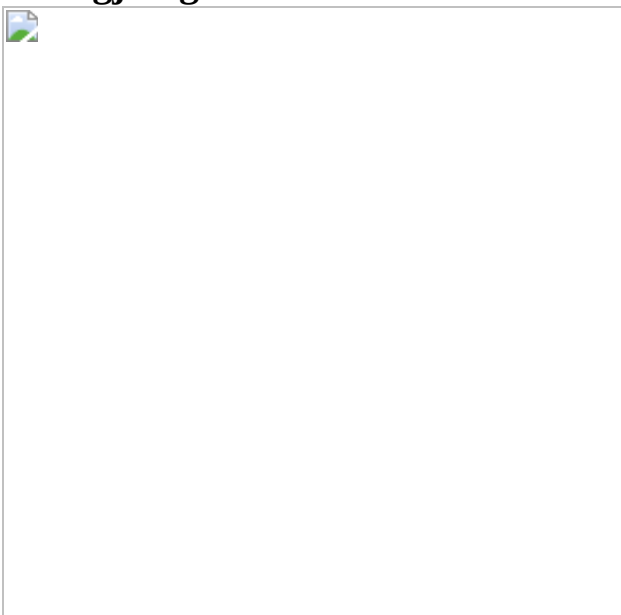


Fig. 2: Comparative anatomy of head structures in *Kylinxia zhangi*, *Opabinia regalis*, radiodonts and megacheirans.

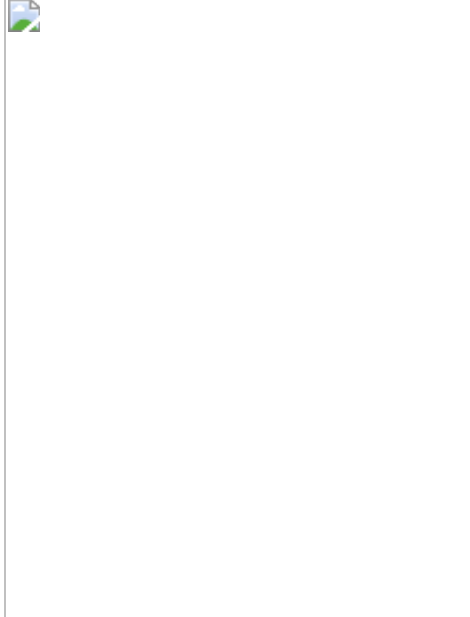
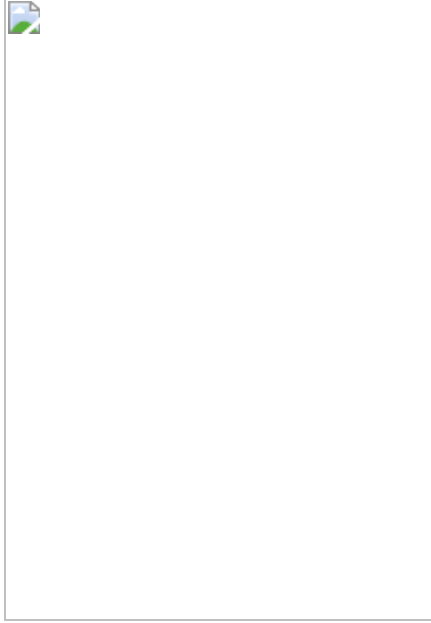


Fig. 3: Reconstruction of *Kylinxia* and evolution of the frontalmost appendages in early euarthropods.



Data availability

All data analysed in this paper, including the phylogenetic datasets, are available as part of the Article, Extended Data Figs. [1–10](#) or [Supplementary](#).

[Information](#). The nomenclatural acts in this publication have been registered at ZooBank (LSID: urn:lsid:zoobank.org:pub:3B79BB94-239D-4C0A-93E5-62E90DAE6469).

Code availability

The phylogenetic datasets and the commands necessary to run the MrBayes analyses, are included as NEXUS formatted files (Supplementary Data [1](#), [2](#)).

References

1. 1.

Giribet, G. & Edgecombe, G. D. The phylogeny and evolutionary history of arthropods. *Curr. Biol.* **29**, R592–R602 (2019).

[CAS](#) [Article](#) [PubMed](#) [Google Scholar](#)

2. 2.

Budd, G. E. & Telford, M. J. The origin and evolution of arthropods. *Nature* **457**, 812–817 (2009).

[ADS](#) [CAS](#) [Article](#) [PubMed](#) [Google Scholar](#)

3. 3.

Edgecombe, G. D. & Legg, D. A. Origins and early evolution of arthropods. *Palaeontology* **57**, 457–468 (2014).

[Article](#) [Google Scholar](#)

4. 4.

Daley, A. C., Antcliffe, J. B., Drage, H. B. & Pates, S. Early fossil record of Euarthropoda and the Cambrian Explosion. *Proc. Natl Acad.*

Sci. USA **115**, 5323–5331 (2018).

[ADS](#) [CAS](#) [Article](#) [PubMed](#) [Google Scholar](#)

5. 5.

Daley, A. C., Budd, G. E., Caron, J.-B., Edgecombe, G. D. & Collins, D. The Burgess Shale anomalocaridid *Hurdia* and its significance for early euarthropod evolution. *Science* **323**, 1597–1600 (2009).

[ADS](#) [CAS](#) [Article](#) [PubMed](#) [Google Scholar](#)

6. 6.

Legg, D. A., Sutton, M. D. & Edgecombe, G. D. Arthropod fossil data increase congruence of morphological and molecular phylogenies. *Nat. Commun.* **4**, 2485 (2013).

[ADS](#) [Article](#) [PubMed](#) [Google Scholar](#)

7. 7.

Ortega-Hernández, J. Making sense of ‘lower’ and ‘upper’ stem-group Euarthropoda, with comments on the strict use of the name Arthropoda von Siebold, 1848. *Biol. Rev.* **91**, 255–273 (2016).

[Article](#) [PubMed](#) [Google Scholar](#)

8. 8.

Aria, C. & Caron, J.-B. Burgess Shale fossils illustrate the origin of the mandibulate body plan. *Nature* **545**, 89–92 (2017).

[ADS](#) [CAS](#) [Article](#) [PubMed](#) [Google Scholar](#)

9. 9.

Aria, C. & Caron, J.-B. A middle Cambrian arthropod with chelicerae and proto-book gills. *Nature* **573**, 586–589 (2019).

[ADS](#) [CAS](#) [Article](#) [PubMed](#) [Google Scholar](#)

10. 10.

Whittington, H. B. The enigmatic animal *Opabinia regalis*, Middle Cambrian, Burgess Shale, British Columbia. *Phil. Trans. R. Soc. Lond. B* **271**, 1–43 (1975).

[ADS](#) [Article](#) [Google Scholar](#)

11. 11.

Ortega-Hernández, J. Homology of head sclerites in Burgess Shale euarthropods. *Curr. Biol.* **25**, 1625–1631 (2015).

[Article](#) [PubMed](#) [Google Scholar](#)

12. 12.

Daley, A. C. & Edgecombe, G. D. Morphology of *Anomalocaris canadensis* from the Burgess Shale. *J. Paleontol.* **88**, 68–91 (2014).

[Article](#) [Google Scholar](#)

13. 13.

Cong, P. et al. New radiodonts with gnathobase-like structures from the Cambrian Chengjiang biota and implications for the systematics of Radiodonta. *Pap. Palaeontol.* **4**, 605–621 (2018).

[Article](#) [Google Scholar](#)

14. 14.

Chen, J., Waloszek, D. & Maas, A. A new ‘great-appendage’ arthropod from the Lower Cambrian of China and homology of chelicerate chelicerae and raptorial antero-ventral appendages. *Lethaia* **37**, 3–20 (2004).

[Article](#) [Google Scholar](#)

15. 15.

Hou, X. New rare bivalved arthropods from the Lower Cambrian Chengjiang Fauna, Yunnan, China. *J. Paleontol.* **73**, 102–116 (1999).

[Article](#) [Google Scholar](#)

16. 16.

Fu, D., Zhang, X. & Shu, D. Soft anatomy of the early Cambrian arthropod *Isoxys curvirostratus* from the Chengjiang biota of south China with a discussion on the origination of great appendages. *Acta Palaeontol. Pol.* **56**, 843–852 (2011).

[Article](#) [Google Scholar](#)

17. 17.

Legg, D. A. & Vannier, J. The affinities of the cosmopolitan arthropod *Isoxys* and its implications for the origin of arthropods. *Lethaia* **46**, 540–550 (2013).

[Article](#) [Google Scholar](#)

18. 18.

Hou, X. et al. *The Cambrian Fossils of Chengjiang, China: The Flowering of Early Animal Life* 2nd edn (John Wiley & Sons, 2017).

19. 19.

Aria, C., Zhao, F., Zeng, H., Guo, J. & Zhu, M. Fossils from South China redefine the ancestral euarthropod body plan. *BMC Evol. Biol.* **20**, 4 (2020).

[Article](#) [PubMed](#) [PubMed Central](#) [Google Scholar](#)

20. 20.

Ortega-Hernández, J., Lerosey-Aubril, R. & Pates, S. Proclivity of nervous system preservation in Cambrian Burgess Shale-type deposits. *Proc. R. Soc. Lond. B* **286**, 20192370 (2019).

[Google Scholar](#)

21. 21.

Yang, J., Ortega-Hernández, J., Butterfield, N. J. & Zhang, X. Specialized appendages in fuxianhuiids and the head organization of early euarthropods. *Nature* **494**, 468–471 (2013).

[ADS](#) [CAS](#) [Article](#) [PubMed](#) [Google Scholar](#)

22. 22.

Tanaka, G., Hou, X., Ma, X., Edgecombe, G. D. & Strausfeld, N. J. Chelicerate neural ground pattern in a Cambrian great appendage arthropod. *Nature* **502**, 364–367 (2013).

[ADS](#) [CAS](#) [Article](#) [PubMed](#) [Google Scholar](#)

23. 23.

Haug, J. T., Waloszek, D., Maas, A., Liu, Y. & Haug, C. Functional morphology, ontogeny and evolution of mantis shrimp-like predators in the Cambrian. *Palaeontology* **55**, 369–399 (2012).

[Article](#) [Google Scholar](#)

24. 24.

Ortega-Hernández, J., Janssen, R. & Budd, G. E. Origin and evolution of the panarthropod head — a palaeobiological and developmental perspective. *Arthropod Struct. Dev.* **46**, 354–379 (2017).

[Article](#) [PubMed](#) [Google Scholar](#)

25. 25.

Scholtz, G. & Edgecombe, G. D. The evolution of arthropod heads: reconciling morphological, developmental and palaeontological evidence. *Dev. Genes Evol.* **216**, 395–415 (2006).

[Article](#) [PubMed](#) [Google Scholar](#)

26. 26.

Cong, P., Ma, X., Hou, X., Edgecombe, G. D. & Strausfeld, N. J. Brain structure resolves the segmental affinity of anomalocaridid appendages. *Nature* **513**, 538–542 (2014).

[ADS](#) [CAS](#) [Article](#) [PubMed](#) [Google Scholar](#)

27. 27.

Stein, M. A new arthropod from the Early Cambrian of North Greenland, with a ‘great appendage’-like antennula. *Zool. J. Linn. Soc.* **158**, 477–500 (2010).

[Article](#) [Google Scholar](#)

28. 28.

Yang, J., Ortega-Hernández, J., Lan, T., Hou, J. & Zhang, X. A predatory bivalved euarthropod from the Cambrian (Stage 3) Xiaoshiba Lagerstätte, South China. *Sci. Rep.* **6**, 27709 (2016).

[ADS](#) [CAS](#) [Article](#) [PubMed](#) [PubMed Central](#) [Google Scholar](#)

29. 29.

Fu, D., Zhang, X., Budd, G. E., Liu, W. & Pan, X. Ontogeny and dimorphism of *Isoxys auritus* (Arthropoda) from the Early Cambrian Chengjiang biota, South China. *Gondwana Res.* **25**, 975–982 (2014).

[ADS](#) [Article](#) [Google Scholar](#)

30. 30.

Aria, C. & Caron, J.-B. Cephalic and limb anatomy of a new isoxyid from the Burgess Shale and the role of “stem bivalved arthropods” in the disparity of the frontalmost appendage. *PLoS ONE* **10**, e0124979 (2015).

[Article](#) [PubMed](#) [PubMed Central](#) [Google Scholar](#)

31. 31.

Zhao, F., Caron, J.-B., Hu, S. & Zhu, M. Quantitative analysis of taphofacies and paleocommunities in the Early Cambrian Chengjiang Lagerstätte. *Palaeos* **24**, 826–839 (2009).

[ADS](#) [CAS](#) [Article](#) [Google Scholar](#)

32. 32.

Ronquist, F. et al. MrBayes 3.2: efficient Bayesian phylogenetic inference and model choice across a large model space. *Syst. Biol.* **61**, 539–542 (2012).

[Article](#) [PubMed](#) [PubMed Central](#) [Google Scholar](#)

33. 33.

Lewis, P. O. A likelihood approach to estimating phylogeny from discrete morphological character data. *Syst. Biol.* **50**, 913–925 (2001).

[CAS](#) [Article](#) [PubMed](#) [Google Scholar](#)

34. 34.

Rambaut, A., Drummond, A. J., Xie, D., Baele, G. & Suchard, M. A. Posterior summarization in Bayesian phylogenetics using Tracer 1.7. *Syst. Biol.* **67**, 901–904 (2018).

[CAS](#) [Article](#) [PubMed](#) [PubMed Central](#) [Google Scholar](#)

35. 35.

Goloboff, P. A. Estimating character weights during tree search. *Cladistics* **9**, 83–91 (1993).

[Article](#) [Google Scholar](#)

36. 36.

Goloboff, P. A. & Catalano, S. A. TNT, version 1.5, with a full implementation of phylogenetic morphometrics. *Cladistics* **32**, 221–238 (2016).

[Article](#) [Google Scholar](#)

[Download references](#)

Acknowledgements

This study was supported by the Strategic Priority Research Program (B) of the Chinese Academy of Sciences (XDB26000000 and XDB18000000), the National Natural Science Foundation of China (41921002, 41902014 and 41925008), Jiangsu Basic Research Project (BK20191102), State Key Laboratory of Paleobiology and Stratigraphy, Nanjing Institute of Geology and Palaeontology, CAS (20192111 and 20181105) and IGCP Project 668. H.Z. was supported by a Smithsonian post-doctoral fellowship. We thank J. Chen and S. Hu for access to their collections of Chengjiang fossils, J. Li and T. Alima (Electron Microscopy Laboratory, IGGCAS) for efforts to maintain operation during scanning electron microscopy and energy-dispersive X-ray spectroscopy experiments, H. Xu and Y. Chen (Geobiodiversity Database, NIGPAS) for maintaining the computers used in the phylogenetic analysis, J. Sun for artistic reconstructions, D. Briggs for discussion, J.-B. Caron for access to the radiodont specimens at the Royal Ontario Museum, and D. Erwin for comments on the manuscript and access to the Burgess Shale collection at the Smithsonian Institution.

Author information

Affiliations

1. State Key Laboratory of Palaeobiology and Stratigraphy, Nanjing Institute of Geology and Palaeontology, Chinese Academy of Sciences, Nanjing, China

Han Zeng, Fangchen Zhao, Maoyan Zhu & Diying Huang

2. Center for Excellence in Life and Palaeoenvironment, Chinese Academy of Sciences, Nanjing, China

Han Zeng, Fangchen Zhao, Maoyan Zhu & Diying Huang

3. Department of Paleobiology, National Museum of Natural History, Smithsonian Institution, Washington, DC, USA

Han Zeng

4. College of Earth and Planetary Sciences, University of Chinese Academy of Sciences, Beijing, China

Fangchen Zhao & Maoyan Zhu

5. Yingliang Stone Natural History Museum, Nan'an, China

Kecheng Niu

Authors

1. Han Zeng

[View author publications](#)

You can also search for this author in [PubMed](#) [Google Scholar](#)

2. Fangchen Zhao

[View author publications](#)

You can also search for this author in [PubMed](#) [Google Scholar](#)

3. Kecheng Niu

[View author publications](#)

You can also search for this author in [PubMed](#) [Google Scholar](#)

4. Maoyan Zhu

[View author publications](#)

You can also search for this author in [PubMed](#) [Google Scholar](#)

5. Diying Huang

[View author publications](#)

You can also search for this author in [PubMed](#) [Google Scholar](#)

Contributions

D.H. designed the research. M.Z. secured the funding and prompted completion of the project. F.Z. collected all of the material of *Kylinxia zhangi* except for the paratype, which was collected by K.N. H.Z. conducted the geochemical and phylogenetic analyses. H.Z. wrote the paper with input from all other authors. All authors participated in the interpretation of the material and the discussions.

Corresponding authors

Correspondence to [Fangchen Zhao](#) or [Diying Huang](#).

Ethics declarations

Competing interests

The authors declare no competing interests.

Additional information

Peer review information *Nature* thanks Jean Vannier and the other, anonymous, reviewer(s) for their contribution to the peer review of this work.

Publisher's note Springer Nature remains neutral with regard to jurisdictional claims in published maps and institutional affiliations.

Extended data figures and tables

[Extended Data Fig. 1 Additional photographs and camera lucida drawings of type specimens of *Kylinxia zhangi*.](#)

a–c, Photographs taken under low-angle illumination. **a, b**, Holotype, NIGP 171304. **a**, Part, NIGP 171304a. **b**, Counterpart, NIGP 171304b. **c**, Paratype, YLSNHM 01124. **d, e**, Camera lucida drawings of **a, c**, respectively. Abbreviations as in Figs. [1](#), [2](#).

[Extended Data Fig. 2 Additional specimens of *Kylinxia zhangi* in different post-embryonic developmental stages.](#)

a, b, Nearly complete specimen, NIGP 171305a, part. **c, d**, Incomplete specimen showing anterior body part, NIGP 171306. **e–g**, Complete larger juvenile specimen, NIGP 171307a, part. **h, i**, Complete smaller juvenile specimen, NIGP 171308. **a, c, e, g**, Whole specimens. **b, d, f, i**, Head regions in **a, c, e, h**, respectively. **g**, Magnification of the alimentary canal shown in **e**, showing paired digestive glands. **ts**, spine on head shield. Other abbreviations as in Figs. [1](#), [2](#).

[Extended Data Fig. 3 Head and eyes of Cambrian euarthropods discussed in this study.](#)

a–d, g, h, *Opabinia regalis*. **a**, USNM 155600b. **b**, USNM 205259. **c**, USNM 205258. **d**, USNM 131217. **e**, *Anomalocaris* sp., ELRC 20001. **f**, *Haikoucaris ercaiensis*, ELRC EC11051a. **g–i**, Ocular regions in **c–e**, respectively. **j, l**, *Odaraia alata*, USNM 189232. **k, m**, *Helmetia expansa*, USNM 83952. **l, m**, Ocular regions in **j, k**, respectively. **n, o**, Head regions

of *Kylinxia zhangi* in Extended Data Fig. 1a, b, respectively, NIGP 171304. n, Part, NIGP 171304a. o, Counterpart, NIGP 171304b. as, anterior sclerite; me, median eye. Other abbreviations as in Figs. 1, 2.

Extended Data Fig. 4 Drawings of the head region in *Kylinxia* and comparison of frontalmost appendages in *Kylinxia* and *Anomalocaris*.

a–g, *K. zhangi*. a–e, Camera lucida drawings of head regions, see colours of different anatomical structures at the bottom. a, YLSNHM 01124, as in Fig. 2g. b, NIGP 171304a, as in Extended Data Fig. 2d. c, NIGP 171307a, as in Extended Data Fig. 2f. d, NIGP 171305a, as in Extended Data Fig. 2b. e, NIGP 171308, as in Extended Data Fig. 2i. f, g, Frontalmost appendages of *Kylinxia*. f, YLSNHM 01124. g, NIGP 171304a. h–k, Frontal appendages of *Anomalocaris canadensis*. h, i, Full appendages. h, GSC 75535. i, ROMIP 51212. j, k, Shaft region. j, ROMIP 51215. k, ROMIP 59947. Abbreviations as in Figs. 1, 2 and Extended Data Fig. 2.

Extended Data Fig. 5 Anatomy and geochemical analysis of cephalic soft tissues in *Kylinxia zhangi*, holotype NIGP 171304a.

a, Magnification of the head and anteriormost trunk under visible light. b, Interpretive drawing of a by integrating observations under visible light and from geochemical analysis, see Extended Data Fig. 4 for a colour key. c, Backscatter scanning electron image of a under a scanning electronic microscope. d–h, Elemental maps of a from energy-dispersive X-ray spectroscopy. d, C map, showing alimentary canal with positive signal. e, Fe map, showing nervous tissue with positive signal. f, Overlay image of C and Fe maps with the blending mode of filtering colour in Adobe Photoshop CS6, showing the compositional differences between alimentary canal and nervous tissues. g, P map, showing putative digestive glands with positive signal. h, Si map, showing soft tissues in negative relief. pr, protocerebral tissue. Other abbreviations as in Figs. 1, 2.

Extended Data Fig. 6 Morphological details of trunk in *Kylinxia zhangi*.

a–d, Soft tissue in trunk. Arrowheads indicate putative bifurcating nerves into paired trunk appendages. **a**, YLSNHM 01124. **b**, NIGP 171304a. **c**, NIGP 171305a. **d**, NIGP 171306. **e–h**, Tail region. **e**, NIGP 171307a. **f**, NIGP 171308. **g**, NIGP 171304a. **h**, YLSNHM 01124. **i**, Magnification of the tail flaps in **g**, showing setae. **a**, trunk appendage; **st**, setae. Other abbreviations as in Figs. [1](#), [2](#).

Extended Data Fig. 7 Frontalmost appendages of Cambrian megacheirans, isoxyids and artiopodans.

a–i, Great appendages of megacheirans. **a**, **d**, *Haikoucaris ercaiensis*, NIGP 171309. **a**, Whole specimen. **d**, Great appendage in **a**. **b**, **e**, *Fortiforceps foliosa*, NIGP 169954. **b**, Whole specimen. **e**, Great appendage in **b**. **c**, **f**, **g**, *Yohoia tenuis*, USNM 179053. **c**, Whole specimen. **f**, Great appendage in **c**. **g**, Endites in **f**, arrowheads indicate auxiliary spines. **h**, **i**, *Parapeytoia yunnanensis*, NIGP 171310. **h**, Great appendage. **i**, Endite showing auxiliary spines in **h**. **j–q**, Frontalmost appendages showing raptorial features in isoxyids and artiopodans. **j**, **k**, *Isoxys curvirostratus*, NIGP 171311. **j**, Whole specimen. **k**, Frontalmost appendage in **j**, note the frontalmost appendages are disarticulated and oriented downward. **l–o**, *I. auritus*. **l**, **m**, YDKS 43. **n**, **o**, NIGP 171312. **l**, **n**, Whole specimen. **m**, **o**, Frontalmost appendage in **l**, **n**, respectively. **p**, **q**, *Kuamaia lata*, NIGP 172294. **p**, Head region. **q**, Antenna in **p**. Yellow arrowheads indicate endites. **l**, **m**, Specimen courtesy of S. Hu. **ba**, basis of great appendage; **pd**, peduncle podomere. Other abbreviations as in Figs. [1](#), [2](#).

Extended Data Fig. 8 Ecological reconstruction of *Kylinxia zhangi* in the early Cambrian Chengjiang biota.

Artistic reconstruction by J. Sun.

Extended Data Fig. 9 Consensus trees from Bayesian and parsimony analyses of panarthropod relationships based on a matrix of 81 taxa and 283 characters.

a, The 50% majority-rule consensus tree from a Bayesian analysis. Nodal supports are posterior probabilities. Major taxonomic groups are indicated by bars on the right of tips. **b**, Strict consensus of a single most parsimonious tree of 51.91166 steps (consistency index = 0.507; retention index = 0.871) from a parsimony analysis using implied character weighting (concavity constant $k = 3$). Nodal supports are group present and contradicted frequency differences. In **a**, **b**, nodal supports of 100% are not shown, and the ordering of tips is the same. The consensus results from Bayesian analysis and parsimony analyses with equal and various implied character weighting settings (concavity constant $k = 2, 3, 5, 10$) are consistent on the position of *Kylinxia zhangi* (in red) and the main topologies between major taxonomic groups (indicated by bars in **a**), except for the alternatively monophyletic or paraphyletic grouping of great-appendage bivalved forms and Isoxyida and the questionable relationships of mandibulate-related groups including Hymenocarina (indicated by asterisks in **a**, **b**).

Extended Data Fig. 10 Consensus trees from Bayesian and parsimony analyses of panarthropod relationships with *Kylinxia zhangi* omitted.

a, The 50% majority-rule consensus tree from a Bayesian analysis. Nodal supports are posterior probabilities. Major taxonomic groups are indicated by bars on the right of tips. **b**, Strict consensus of a single most parsimonious tree of 49.60546 steps (consistency index = 0.518, retention index = 0.874) from a parsimony analysis using implied character weighting (concavity constant $k = 3$). Nodal supports are group present and contradicted frequency differences. In **a**, **b**, nodal supports of 100% are not shown. Note that Isoxyida and great-appendage bivalved forms (both in red) are placed at a more basal position than Megacheira and Panchelicerata when *K. zhangi* is omitted, which is a major difference from the results with *K. zhangi* included (Extended Data Fig. 9).

Supplementary information

Supplementary Discussion

This file contains detailed morphological description, additional remarks and the character list used for phylogenetic analyses.

Reporting Summary

Supplementary Data 1

Morphological matrix, MrBayes code and consensus trees found in the phylogenetic analyses with *Kylinxia zhangi* included.

Supplementary Data 2

Morphological matrix, MrBayes code and consensus trees found in the phylogenetic analyses with *Kylinxia zhangi* omitted.

Rights and permissions

Reprints and Permissions

About this article



Check for
updates

Cite this article

Zeng, H., Zhao, F., Niu, K. *et al.* An early Cambrian euarthropod with radiodont-like raptorial appendages. *Nature* **588**, 101–105 (2020).
<https://doi.org/10.1038/s41586-020-2883-7>

Download citation

- Received: 07 October 2019

- Accepted: 14 August 2020
- Published: 04 November 2020
- Issue Date: 03 December 2020
- DOI: <https://doi.org/10.1038/s41586-020-2883-7>

Comments

By submitting a comment you agree to abide by our [Terms](#) and [Community Guidelines](#). If you find something abusive or that does not comply with our terms or guidelines please flag it as inappropriate.

[Access through your institution](#)

[Change institution](#)

[Buy or subscribe](#)

This article was downloaded by **calibre** from <https://www.nature.com/articles/s41586-020-2883-7>

| [Section menu](#) | [Main menu](#) |

- Article
- [Published: 28 October 2020](#)

Contrasting signatures of genomic divergence during sympatric speciation

- [Andreas F. Kautt](#) [ORCID: orcid.org/0000-0001-7792-0735](#)^{1 na1 nAff4},
- [Claudius F. Kratochwil](#) [ORCID: orcid.org/0000-0002-5646-3114](#)^{1 na1},
- [Alexander Nater](#) [ORCID: orcid.org/0000-0002-4805-5575](#)^{1 na1},
- [Gonzalo Machado-Schiaffino](#)^{1 nAff5},
- [Melisa Olave](#)^{1 nAff6},
- [Frederico Henning](#)^{1 nAff7},
- [Julían Torres-Dowdall](#) [ORCID: orcid.org/0000-0003-2729-6246](#)¹,
- [Andreas Härer](#) [ORCID: orcid.org/0000-0003-2894-5041](#)^{1 nAff8},
- [C. Darrin Hulsey](#)¹,
- [Paolo Franchini](#) [ORCID: orcid.org/0000-0002-8184-1463](#)¹,
- [Martin Pippel](#) [ORCID: orcid.org/0000-0002-8134-5929](#)^{2,3},
- [Eugene W. Myers](#) [ORCID: orcid.org/0000-0002-6580-7839](#)^{2,3} &
- [Axel Meyer](#) [ORCID: orcid.org/0000-0002-0888-8193](#)¹

[Nature](#) volume 588, pages106–111(2020) [Cite this article](#)

- 7234 Accesses
- 158 Altmetric
- [Metrics details](#)

Subjects

- [Adaptive radiation](#)
- [Evolutionary genetics](#)
- [Genomics](#)
- [Molecular evolution](#)
- [Population genetics](#)

Abstract

The transition from ‘well-marked varieties’ of a single species into ‘well-defined species’—especially in the absence of geographic barriers to gene flow (sympatric speciation)—has puzzled evolutionary biologists ever since Darwin^{1,2}. Gene flow counteracts the buildup of genome-wide differentiation, which is a hallmark of speciation and increases the likelihood of the evolution of irreversible reproductive barriers (incompatibilities) that complete the speciation process³. Theory predicts that the genetic architecture of divergently selected traits can influence whether sympatric speciation occurs⁴, but empirical tests of this theory are scant because comprehensive data are difficult to collect and synthesize across species, owing to their unique biologies and evolutionary histories⁵. Here, within a young species complex of neotropical cichlid fishes (*Amphilophus* spp.), we analysed genomic divergence among populations and species. By generating a new genome assembly and re-sequencing 453 genomes, we uncovered the genetic architecture of traits that have been suggested to be important for divergence. Species that differ in monogenic or oligogenic traits that affect ecological performance and/or mate choice show remarkably localized genomic differentiation. By contrast, differentiation among species that have diverged in polygenic traits is genomically widespread and much higher overall, consistent with the evolution of effective and stable genome-wide barriers to gene flow. Thus, we conclude that simple trait architectures are not always as conducive to speciation with gene flow as previously suggested, whereas polygenic architectures can promote rapid and stable speciation in sympatry.

[Access through your institution](#)

[Change institution](#)

[Buy or subscribe](#)

Access options

Subscribe to Journal

Get full journal access for 1 year

185,98 €

only 3,58 € per issue

[Subscribe](#)

All prices are NET prices.

VAT will be added later in the checkout.

Rent or Buy article

Get time limited or full article access on ReadCube.

from \$8.99

[Rent or Buy](#)

All prices are NET prices.

Additional access options:

- [Log in](#)
- [Access through your institution](#)
- [Learn about institutional subscriptions](#)

Fig. 1: Evolutionary relationships among all members of the Midas cichlid species complex.



Fig. 2: Genotype–phenotype association mapping.



Fig. 3: Genomic differentiation across the species complex.



Data availability

The genome assembly has been deposited at DDBJ/ENA/GenBank under accession [JACBYM000000000](#). The version described in this paper is version [JACBYM010000000](#). Whole-genome resequencing data for all 453 samples in the form of unmapped BAM files ([PRJEB38173](#)) and unpublished transcriptomic data ([PRJNA635556](#)) have been uploaded to ENA and NCBI/SRA, respectively. Geometric morphometric data, information on samples, and downstream data to reproduce our results can be downloaded from Dryad (<https://doi.org/10.5061/dryad.bcc2fqz91>)⁵¹. [Source data](#) are provided with this paper.

Code availability

Custom code used for the genome assembly (<https://github.com/MartinPippel/DAmar>) and custom code for genomic and morphometric analyses (<https://github.com/alexnater/midas-genomics>) can be accessed on GitHub.

References

1. 1.

Richards, E. J., Servedio, M. R. & Martin, C. H. Searching for sympatric speciation in the genomic era. *BioEssays* **41**, e1900047 (2019).

[PubMed](#) [Google Scholar](#)

2. 2.

Westram, A. M. et al. Clines on the seashore: the genomic architecture underlying rapid divergence in the face of gene flow. *Evol. Lett.* **2**, 297–309 (2018).

[PubMed](#) [PubMed Central](#) [Google Scholar](#)

3. 3.

Coyne, J. A. & Orr, H. A. *Speciation* (Sinauer, 2004).

4. 4.

Gavrilets, S. *Fitness Landscapes and the Origin of Species* (Princeton Univ. Press, 2004).

5. 5.

Nosil, P., Feder, J. L., Flaxman, S. M. & Gompert, Z. Tipping points in the dynamics of speciation. *Nat. Ecol. Evol.* **1**, 0001 (2017).

[Google Scholar](#)

6. 6.

Maynard Smith, J. Sympatric speciation. *Am. Nat.* **100**, 637–650 (1966).

[Google Scholar](#)

7. 7.

Servedio, M. R., Van Doorn, G. S., Kopp, M., Frame, A. M. & Nosil, P. Magic traits in speciation: ‘magic’ but not rare? *Trends Ecol. Evol.* **26**, 389–397 (2011).

[PubMed](#) [Google Scholar](#)

8. 8.

Smadja, C. M. & Butlin, R. K. A framework for comparing processes of speciation in the presence of gene flow. *Mol. Ecol.* **20**, 5123–5140 (2011).

[PubMed](#) [Google Scholar](#)

9. 9.

Gavrilets, S. & Vose, A. Dynamic patterns of adaptive radiation. *Proc. Natl Acad. Sci. USA* **102**, 18040–18045 (2005).

[ADS](#) [CAS](#) [PubMed](#) [Google Scholar](#)

10. 10.

Seehausen, O. et al. Genomics and the origin of species. *Nat. Rev. Genet.* **15**, 176–192 (2014).

[CAS](#) [PubMed](#) [Google Scholar](#)

11. 11.

Poelstra, J. W. et al. The genomic landscape underlying phenotypic integrity in the face of gene flow in crows. *Science* **344**, 1410–1414

(2014).

[ADS](#) [CAS](#) [PubMed](#) [Google Scholar](#)

12. 12.

Malinsky, M. et al. Genomic islands of speciation separate cichlid ecomorphs in an East African crater lake. *Science* **350**, 1493–1498 (2015).

[ADS](#) [CAS](#) [PubMed](#) [PubMed Central](#) [Google Scholar](#)

13. 13.

Riesch, R. et al. Transitions between phases of genomic differentiation during stick-insect speciation. *Nat. Ecol. Evol.* **1**, 82 (2017).

[PubMed](#) [Google Scholar](#)

14. 14.

Marques, D. A. et al. Genomics of rapid incipient speciation in sympatric threespine stickleback. *PLoS Genet.* **12**, e1005887 (2016).

[PubMed](#) [PubMed Central](#) [Google Scholar](#)

15. 15.

Barton, N. & Bengtsson, B. O. The barrier to genetic exchange between hybridising populations. *Heredity* **57**, 357–376 (1986).

[PubMed](#) [Google Scholar](#)

16. 16.

Barton, N. H. Multilocus clines. *Evolution* **37**, 454–471 (1983).

[CAS](#) [PubMed](#) [Google Scholar](#)

17. 17.

Feder, J. L. et al. Genome-wide congealing and rapid transitions across the speciation continuum during speciation with gene flow. *J. Hered.* **105** (Suppl. 1), 810–820 (2014).

[PubMed](#) [Google Scholar](#)

18. 18.

Flaxman, S. M., Wacholder, A. C., Feder, J. L. & Nosil, P. Theoretical models of the influence of genomic architecture on the dynamics of speciation. *Mol. Ecol.* **23**, 4074–4088 (2014).

[PubMed](#) [Google Scholar](#)

19. 19.

Elmer, K. R. et al. Parallel evolution of Nicaraguan crater lake cichlid fishes via non-parallel routes. *Nat. Commun.* **5**, 5168 (2014).

[ADS](#) [CAS](#) [PubMed](#) [Google Scholar](#)

20. 20.

Barluenga, M., Stölting, K. N., Salzburger, W., Muschick, M. & Meyer, A. Sympatric speciation in Nicaraguan crater lake cichlid fish. *Nature* **439**, 719–723 (2006).

[ADS](#) [CAS](#) [PubMed](#) [Google Scholar](#)

21. 21.

Kautt, A. F., Machado-Schiaffino, G. & Meyer, A. Multispecies outcomes of sympatric speciation after admixture with the source population in two radiations of Nicaraguan crater lake cichlids. *PLoS Genet.* **12**, e1006157 (2016).

[PubMed](#) [PubMed Central](#) [Google Scholar](#)

22. 22.

Elmer, K. R., Kusche, H., Lehtonen, T. K. & Meyer, A. Local variation and parallel evolution: morphological and genetic diversity across a species complex of neotropical crater lake cichlid fishes. *Philos. Trans. R. Soc. Lond. B Biol. Sci.* **365**, 1763–1782 (2010).

[PubMed](#) [PubMed Central](#) [Google Scholar](#)

23. 23.

Machado-Schiaffino, G. et al. Incipient speciation driven by hypertrophied lips in Midas cichlid fishes? *Mol. Ecol.* **26**, 2348–2362 (2017).

[CAS](#) [PubMed](#) [Google Scholar](#)

24. 24.

Kusche, H., Elmer, K. R. & Meyer, A. Sympatric ecological divergence associated with a color polymorphism. *BMC Biol.* **13**, 82 (2015).

[PubMed](#) [PubMed Central](#) [Google Scholar](#)

25. 25.

Barlow, G. W. in *Investigations of the Ichthyology of Nicaraguan Lakes* (ed. Thorson, T. B.) 333–358 (Univ. Nebraska Press, 1976).

26. 26.

Elmer, K. R., Lehtonen, T. K. & Meyer, A. Color assortative mating contributes to sympatric divergence of neotropical cichlid fish. *Evolution* **63**, 2750–2757 (2009).

[PubMed](#) [Google Scholar](#)

27. 27.

Fruciano, C. et al. Genetic linkage of distinct adaptive traits in sympatrically speciating crater lake cichlid fish. *Nat. Commun.* **7**, 12736 (2016).

[ADS](#) [CAS](#) [PubMed](#) [PubMed Central](#) [Google Scholar](#)

28. 28.

Henning, F., Jones, J. C., Franchini, P. & Meyer, A. Transcriptomics of morphological color change in polychromatic Midas cichlids. *BMC Genomics* **14**, 171 (2013).

[CAS](#) [PubMed](#) [PubMed Central](#) [Google Scholar](#)

29. 29.

Kautt, A. F., Machado-Schiaffino, G. & Meyer, A. Lessons from a natural experiment: allopatric morphological divergence and sympatric diversification in the Midas cichlid species complex are largely influenced by ecology in a deterministic way. *Evol. Lett.* **2**, 323–340 (2018).

[PubMed](#) [PubMed Central](#) [Google Scholar](#)

30. 30.

Freundt, A., Kutterolf, S., Wehrmann, H., Schmincke, H. U. & Strauch, W. Eruption of the dacite to andesite zoned Mateare Tephra, and associated tsunamis in Lake Managua, Nicaragua. *J. Volcanol. Geotherm. Res.* **149**, 103–123 (2006).

[ADS](#) [CAS](#) [Google Scholar](#)

31. 31.

Rundle, H. D., Nagel, L., Wenrick Boughman, J. & Schlüter, D. Natural selection and parallel speciation in sympatric sticklebacks. *Science* **287**, 306–308 (2000).

[ADS](#) [CAS](#) [PubMed](#) [Google Scholar](#)

32. 32.

Cruickshank, T. E. & Hahn, M. W. Reanalysis suggests that genomic islands of speciation are due to reduced diversity, not reduced gene flow. *Mol. Ecol.* **23**, 3133–3157 (2014).

[PubMed](#) [Google Scholar](#)

33. 33.

Martin, S. H., Davey, J. W., Salazar, C. & Jiggins, C. D. Recombination rate variation shapes barriers to introgression across butterfly genomes. *PLoS Biol.* **17**, e2006288 (2019).

[CAS](#) [PubMed](#) [PubMed Central](#) [Google Scholar](#)

34. 34.

Feder, J. L. & Nosil, P. The efficacy of divergence hitchhiking in generating genomic islands during ecological speciation. *Evolution* **64**, 1729–1747 (2010).

[PubMed](#) [Google Scholar](#)

35. 35.

Grohme, M. A. et al. The genome of *Schmidtea mediterranea* and the evolution of core cellular mechanisms. *Nature* **554**, 56–61 (2018).

[ADS](#) [CAS](#) [PubMed](#) [PubMed Central](#) [Google Scholar](#)

36. 36.

Nowoshilow, S. et al. The axolotl genome and the evolution of key tissue formation regulators. *Nature* **554**, 50–55 (2018).

[ADS](#) [CAS](#) [PubMed](#) [Google Scholar](#)

37. 37.

Dudchenko, O. et al. De novo assembly of the *Aedes aegypti* genome using Hi-C yields chromosome-length scaffolds. *Science* **356**, 92–95 (2017).

[ADS](#) [CAS](#) [PubMed](#) [PubMed Central](#) [Google Scholar](#)

38. 38.

Durand, N. C. et al. Juicer provides a one-click system for analyzing loop-resolution hi-C experiments. *Cell Syst.* **3**, 95–98 (2016).

[CAS](#) [PubMed](#) [PubMed Central](#) [Google Scholar](#)

39. 39.

Thompson, K. W. Cytotaxonomy of 41 species of neotropical cichlidae. *Copeia* 679–691 (1979).

40. 40.

Garrison, E. & Marth, G. Haplotype-based variant detection from short-read sequencing. Preprint at <https://arxiv.org/abs/1207.3907> (2012).

41. 41.

Li, H. et al. The Sequence Alignment/Map format and SAMtools. *Bioinformatics* **25**, 2078–2079 (2009).

[PubMed](#) [PubMed Central](#) [Google Scholar](#)

42. 42.

Conte, M. A., Gammerdinger, W. J., Bartie, K. L., Penman, D. J. & Kocher, T. D. A high quality assembly of the Nile Tilapia (*Oreochromis niloticus*) genome reveals the structure of two sex determination regions. *BMC Genomics* **18**, 341 (2017).

[PubMed](#) [PubMed Central](#) [Google Scholar](#)

43. 43.

Harris, R. S. *Improved Pairwise Alignment of Genomic DNA* (Pennsylvania State Univ., 2007).

44. 44.

Xu, B. et al. The complete mitochondrial genome of the Midas cichlid (*Amphilophus citrinellus*). *Mitochondrial DNA A. DNA Mapp. Seq. Anal.* **27**, 3895–3896 (2016).

[CAS](#) [PubMed](#) [Google Scholar](#)

45. 45.

Haas, B. J. et al. Automated eukaryotic gene structure annotation using EVidenceModeler and the Program to Assemble Spliced Alignments. *Genome Biol.* **9**, R7 (2008).

[PubMed](#) [PubMed Central](#) [Google Scholar](#)

46. 46.

Hoff, K. J., Lange, S., Lomsadze, A., Borodovsky, M. & Stanke, M. BRAKER1: unsupervised RNA-seq-based genome annotation with GeneMark-ET and AUGUSTUS. *Bioinformatics* **32**, 767–769 (2016).

[CAS](#) [PubMed](#) [Google Scholar](#)

47. 47.

Franchini, P., Xiong, P., Fruciano, C. & Meyer, A. The role of microRNAs in the repeated parallel diversification of lineages of Midas cichlid fish from Nicaragua. *Genome Biol. Evol.* **8**, 1543–1555 (2016).

[CAS](#) [PubMed](#) [PubMed Central](#) [Google Scholar](#)

48. 48.

Manousaki, T. et al. Parsing parallel evolution: ecological divergence and differential gene expression in the adaptive radiations of thick-lipped Midas cichlid fishes from Nicaragua. *Mol. Ecol.* **22**, 650–669 (2013).

[CAS](#) [PubMed](#) [Google Scholar](#)

49. 49.

Fruciano, C., Meyer, A. & Franchini, P. Divergent allometric trajectories in gene expression and coexpression produce species differences in sympatrically speciating Midas cichlid fish. *Genome Biol. Evol.* **11**, 1644–1657 (2019).

[CAS](#) [PubMed](#) [PubMed Central](#) [Google Scholar](#)

50. 50.

Härer, A., Meyer, A. & Torres-Dowdall, J. Convergent phenotypic evolution of the visual system via different molecular routes: how neotropical cichlid fishes adapt to novel light environments. *Evol. Lett.* **2**, 341–354 (2018).

[PubMed](#) [PubMed Central](#) [Google Scholar](#)

51. 51.

Kautt, A. F. et al. Data from: Contrasting signatures of genomic divergence during sympatric speciation. *Dryad* <https://doi.org/10.5061/dryad.bcc2fqz91> (2020).

52. 52.

Kim, D., Langmead, B. & Salzberg, S. L. HISAT: a fast spliced aligner with low memory requirements. *Nat. Methods* **12**, 357–360 (2015).

[CAS](#) [PubMed](#) [PubMed Central](#) [Google Scholar](#)

53. 53.

Pertea, M. et al. StringTie enables improved reconstruction of a transcriptome from RNA-seq reads. *Nat. Biotechnol.* **33**, 290–295 (2015).

[CAS](#) [PubMed](#) [PubMed Central](#) [Google Scholar](#)

54. 54.

Slater, G. S. & Birney, E. Automated generation of heuristics for biological sequence comparison. *BMC Bioinformatics* **6**, 31 (2005).

[PubMed](#) [PubMed Central](#) [Google Scholar](#)

55. 55.

Haas, B. J. et al. Improving the *Arabidopsis* genome annotation using maximal transcript alignment assemblies. *Nucleic Acids Res.* **31**, 5654–5666 (2003).

[CAS](#) [PubMed](#) [PubMed Central](#) [Google Scholar](#)

56. 56.

Grabherr, M. G. et al. Full-length transcriptome assembly from RNA-seq data without a reference genome. *Nat. Biotechnol.* **29**, 644–652 (2011).

[CAS](#) [PubMed](#) [PubMed Central](#) [Google Scholar](#)

57. 57.

Trapnell, C. et al. Transcript assembly and quantification by RNA-seq reveals unannotated transcripts and isoform switching during cell differentiation. *Nat. Biotechnol.* **28**, 511–515 (2010).

[CAS](#) [PubMed](#) [PubMed Central](#) [Google Scholar](#)

58. 58.

Nishimura, O., Hara, Y. & Kuraku, S. gVolante for standardizing completeness assessment of genome and transcriptome assemblies. *Bioinformatics* **33**, 3635–3637 (2017).

[CAS](#) [PubMed](#) [PubMed Central](#) [Google Scholar](#)

59. 59.

Simão, F. A., Waterhouse, R. M., Ioannidis, P., Kriventseva, E. V. & Zdobnov, E. M. BUSCO: assessing genome assembly and annotation completeness with single-copy orthologs. *Bioinformatics* **31**, 3210–3212 (2015).

[PubMed](#) [Google Scholar](#)

60. 60.

Hara, Y. et al. Optimizing and benchmarking de novo transcriptome sequencing: from library preparation to assembly evaluation. *BMC Genomics* **16**, 977 (2015).

[PubMed](#) [PubMed Central](#) [Google Scholar](#)

61. 61.

Pertea, G. & Pertea, M. GFF Utilities: GffRead and GffCompare. *F1000 Res.* **9**, 304 (2020).

[Google Scholar](#)

62. 62.

Li, H. & Durbin, R. Fast and accurate short read alignment with Burrows-Wheeler transform. *Bioinformatics* **25**, 1754–1760 (2009).

[CAS](#) [PubMed](#) [PubMed Central](#) [Google Scholar](#)

63. 63.

Tan, A., Abecasis, G. R. & Kang, H. M. Unified representation of genetic variants. *Bioinformatics* **31**, 2202–2204 (2015).

[CAS](#) [PubMed](#) [PubMed Central](#) [Google Scholar](#)

64. 64.

Danecek, P. et al. The variant call format and VCFtools. *Bioinformatics* **27**, 2156–2158 (2011).

[CAS](#) [PubMed](#) [PubMed Central](#) [Google Scholar](#)

65. 65.

Purcell, S. et al. PLINK: a tool set for whole-genome association and population-based linkage analyses. *Am. J. Hum. Genet.* **81**, 559–575 (2007).

[CAS](#) [PubMed](#) [PubMed Central](#) [Google Scholar](#)

66. 66.

Derrien, T. et al. Fast computation and applications of genome mappability. *PLoS One* **7**, e30377 (2012).

[ADS](#) [CAS](#) [PubMed](#) [PubMed Central](#) [Google Scholar](#)

67. 67.

Delaneau, O., Marchini, J. & Zagury, J. F. A linear complexity phasing method for thousands of genomes. *Nat. Methods* **9**, 179–181 (2011).

[PubMed](#) [Google Scholar](#)

68. 68.

Delaneau, O., Howie, B., Cox, A. J., Zagury, J. F. & Marchini, J. Haplotype estimation using sequencing reads. *Am. J. Hum. Genet.* **93**, 687–696 (2013).

[CAS](#) [PubMed](#) [PubMed Central](#) [Google Scholar](#)

69. 69.

Gao, F., Ming, C., Hu, W. & Li, H. New software for the fast estimation of population recombination rates (FastEPRR) in the genomic era. *G3* **6**, 1563–1571 (2016).

[CAS](#) [PubMed](#) [Google Scholar](#)

70. 70.

Stamatakis, A. RAxML version 8: a tool for phylogenetic analysis and post-analysis of large phylogenies. *Bioinformatics* **30**, 1312–1313 (2014).

[CAS](#) [PubMed](#) [PubMed Central](#) [Google Scholar](#)

71. 71.

Zhang, C., Rabiee, M., Sayyari, E. & Mirarab, S. ASTRAL-III: polynomial time species tree reconstruction from partially resolved gene trees. *BMC Bioinformatics* **19** (Suppl. 6), 153 (2018).

[PubMed](#) [PubMed Central](#) [Google Scholar](#)

72. 72.

Bouckaert, R. et al. BEAST 2: a software platform for Bayesian evolutionary analysis. *PLOS Comput. Biol.* **10**, e1003537 (2014).

[PubMed](#) [PubMed Central](#) [Google Scholar](#)

73. 73.

Smith, S. A., Moore, M. J., Brown, J. W. & Yang, Y. Analysis of phylogenomic datasets reveals conflict, concordance, and gene duplications with examples from animals and plants. *BMC Evol. Biol.* **15**, 150 (2015).

[PubMed](#) [PubMed Central](#) [Google Scholar](#)

74. 74.

Robinson, D. F. & Foulds, L. R. Comparison of phylogenetic trees. *Math. Biosci.* **53**, 131–147 (1981).

[MathSciNet](#) [MATH](#) [Google Scholar](#)

75. 75.

Kuhner, M. K. & Felsenstein, J. A simulation comparison of phylogeny algorithms under equal and unequal evolutionary rates. *Mol. Biol. Evol.* **11**, 459–468 (1994).

[CAS](#) [PubMed](#) [Google Scholar](#)

76. 76.

Salichos, L., Stamatakis, A. & Rokas, A. Novel information theory-based measures for quantifying incongruence among phylogenetic trees. *Mol. Biol. Evol.* **31**, 1261–1271 (2014).

[CAS](#) [PubMed](#) [Google Scholar](#)

77. 77.

Lawson, D. J., Hellenthal, G., Myers, S. & Falush, D. Inference of population structure using dense haplotype data. *PLoS Genet.* **8**, e1002453 (2012).

[CAS](#) [PubMed](#) [PubMed Central](#) [Google Scholar](#)

78. 78.

Hellenthal, G. et al. A genetic atlas of human admixture history. *Science* **343**, 747–751 (2014).

[ADS](#) [CAS](#) [PubMed](#) [PubMed Central](#) [Google Scholar](#)

79. 79.

Malaspinas, A. S. et al. A genomic history of Aboriginal Australia. *Nature* **538**, 207–214 (2016).

[ADS](#) [CAS](#) [PubMed](#) [Google Scholar](#)

80. 80.

Malinsky, M. et al. Whole-genome sequences of Malawi cichlids reveal multiple radiations interconnected by gene flow. *Nat. Ecol. Evol.* **2**, 1940–1955 (2018).

[PubMed](#) [PubMed Central](#) [Google Scholar](#)

81. 81.

Excoffier, L., Dupanloup, I., Huerta-Sánchez, E., Sousa, V. C. & Foll, M. Robust demographic inference from genomic and SNP data. *PLoS Genet.* **9**, e1003905 (2013).

[PubMed](#) [PubMed Central](#) [Google Scholar](#)

82. 82.

Korneliussen, T. S., Albrechtsen, A. & Nielsen, R. ANGSD: analysis of next generation sequencing data. *BMC Bioinformatics* **15**, 356 (2014).

[PubMed](#) [PubMed Central](#) [Google Scholar](#)

83. 83.

McKenna, A. et al. The Genome Analysis Toolkit: a MapReduce framework for analyzing next-generation DNA sequencing data. *Genome Res.* **20**, 1297–1303 (2010).

[CAS](#) [PubMed](#) [PubMed Central](#) [Google Scholar](#)

84. 84.

van der Maaten, L. & Hinton, G. Visualizing data using t-SNE. *J. Mach. Learn. Res.* **9**, 2579–2605 (2008).

[MATH](#) [Google Scholar](#)

85. 85.

Diaz-Papkovich, A., Anderson-Trocmé, L., Ben-Eghan, C. & Gravel, S. UMAP reveals cryptic population structure and phenotype heterogeneity in large genomic cohorts. *PLoS Genet.* **15**, e1008432 (2019).

[PubMed](#) [PubMed Central](#) [Google Scholar](#)

86. 86.

Patterson, N., Price, A. L. & Reich, D. Population structure and eigenanalysis. *PLoS Genet.* **2**, e190 (2006).

[PubMed](#) [PubMed Central](#) [Google Scholar](#)

87. 87.

Alexander, D. H., Novembre, J. & Lange, K. Fast model-based estimation of ancestry in unrelated individuals. *Genome Res.* **19**, 1655–1664 (2009).

[CAS](#) [PubMed](#) [PubMed Central](#) [Google Scholar](#)

88. 88.

Bhatia, G., Patterson, N., Sankararaman, S. & Price, A. L. Estimating and interpreting FST: the impact of rare variants. *Genome Res.* **23**, 1514–1521 (2013).

[CAS](#) [PubMed](#) [PubMed Central](#) [Google Scholar](#)

89. 89.

Kang, H. M. et al. Variance component model to account for sample structure in genome-wide association studies. *Nat. Genet.* **42**, 348–354 (2010).

[CAS](#) [PubMed](#) [PubMed Central](#) [Google Scholar](#)

90. 90.

Hudson, R. R., Slatkin, M. & Maddison, W. P. Estimation of levels of gene flow from DNA sequence data. *Genetics* **132**, 583–589 (1992).

[CAS](#) [PubMed](#) [PubMed Central](#) [Google Scholar](#)

91. 91.

Zamani, N. et al. Unsupervised genome-wide recognition of local relationship patterns. *BMC Genomics* **14**, 347 (2013).

[CAS](#) [PubMed](#) [PubMed Central](#) [Google Scholar](#)

92. 92.

Paradis, E. pegas: an R package for population genetics with an integrated-modular approach. *Bioinformatics* **26**, 419–420 (2010).

[CAS](#) [PubMed](#) [Google Scholar](#)

93. 93.

Speidel, L., Forest, M., Shi, S. & Myers, S. R. A method for genome-wide genealogy estimation for thousands of samples. *Nat. Genet.* **51**,

1321–1329 (2019).

[CAS](#) [PubMed](#) [Google Scholar](#)

94. 94.

Kern, A. D. & Schrider, D. R. diploS/HIC: an updated approach to classifying selective sweeps. *G3* **8**, 1959–1970 (2018).

[PubMed](#) [Google Scholar](#)

95. 95.

Ewing, G. & Hermisson, J. MSMS: a coalescent simulation program including recombination, demographic structure and selection at a single locus. *Bioinformatics* **26**, 2064–2065 (2010).

[CAS](#) [PubMed](#) [PubMed Central](#) [Google Scholar](#)

96. 96.

Thornton, K. Libsequence: a C++ class library for evolutionary genetic analysis. *Bioinformatics* **19**, 2325–2327 (2003).

[CAS](#) [PubMed](#) [Google Scholar](#)

97. 97.

Garud, N. R., Messer, P. W., Buzbas, E. O. & Petrov, D. A. Recent selective sweeps in North American *Drosophila melanogaster* show signatures of soft sweeps. *PLoS Genet.* **11**, e1005004 (2015).

[PubMed](#) [PubMed Central](#) [Google Scholar](#)

98. 98.

Ronen, R. et al. Predicting carriers of ongoing selective sweeps without knowledge of the favored allele. *PLoS Genet.* **11**, e1005527 (2015).

[PubMed](#) [PubMed Central](#) [Google Scholar](#)

99. 99.

Geneva, A. J., Muirhead, C. A., Kingan, S. B. & Garrigan, D. A new method to scan genomes for introgression in a secondary contact model. *PLoS One* **10**, e0118621 (2015).

[PubMed](#) [PubMed Central](#) [Google Scholar](#)

100. 100.

Harris, A. M. & DeGiorgio, M. Identifying and classifying shared selective sweeps from multilocus data. *Genetics* **215**, 143–171 (2020).

[CAS](#) [PubMed](#) [Google Scholar](#)

101. 101.

Chen, H. VennDiagram: generate high-resolution Venn and Euler plots. R package version 1.6.20 <https://CRAN.R-project.org/package=VennDiagram> (2018).

102. 102.

Quinlan, A. R. BEDTools: the Swiss-army tool for genome feature analysis. *Curr. Protoc. Bioinformatics* **47**, 11.12.11–11.12.34 (2014).

[Google Scholar](#)

103. 103.

Ge, S. X., Jung, D. & Yao, R. ShinyGO: a graphical gene-set enrichment tool for animals and plants. *Bioinformatics* **36**, 2628–2629 (2020).

[CAS](#) [PubMed](#) [Google Scholar](#)

104. 104.

Gautier, M., Klassmann, A. & Vitalis, R. rehh 2.0: a reimplementation of the R package rehh to detect positive selection from haplotype structure. *Mol. Ecol. Resour.* **17**, 78–90 (2017).

[CAS](#) [PubMed](#) [Google Scholar](#)

105. 105.

Gutenkunst, R. N., Hernandez, R. D., Williamson, S. H. & Bustamante, C. D. Inferring the joint demographic history of multiple populations from multidimensional SNP frequency data. *PLoS Genet.* **5**, e1000695 (2009).

[PubMed](#) [PubMed Central](#) [Google Scholar](#)

106. 106.

Machado-Schiaffino, G., Henning, F. & Meyer, A. Species-specific differences in adaptive phenotypic plasticity in an ecologically relevant trophic trait: hypertrophic lips in Midas cichlid fishes. *Evolution* **68**, 2086–2091 (2014).

[PubMed](#) [Google Scholar](#)

107. 107.

Rohlf, F. J. TPSDIG2. A program for landmark development and analysis. (Department of Ecology and Evolution, State University of New York at Stony Brook, 2001).

108. 108.

Adams, D. C. & Otarola-Castillo, E. geomorph: an R package for the collection and analysis of geometric morphometric shape data. *Methods Ecol. Evol.* **4**, 393–399 (2013).

[Google Scholar](#)

109. 109.

Ripley, B. et al. MASS: support functions and datasets for venables and Ripley's MASS. R package version 7.3-51.3 <https://CRAN.R-project.org/package=MASS> (2019).

110. 110.

Sanchez, G. plsdepot: partial least squares (PLS) data analysis methods. R package version 0.1.17 <https://CRAN.R-project.org/package=plsdepot> (2012).

111. 111.

Mehmood, T., Martens, H., Sæbø, S., Warringer, J. & Snipen, L. A partial least squares based algorithm for parsimonious variable selection. *Algorithms Mol. Biol.* **6**, 27 (2011).

[PubMed](#) [PubMed Central](#) [Google Scholar](#)

112. 112.

Franchini, P. et al. Genomic architecture of ecologically divergent body shape in a pair of sympatric crater lake cichlid fishes. *Mol. Ecol.* **23**, 1828–1845 (2014).

[PubMed](#) [Google Scholar](#)

113. 113.

Bolger, A. M., Lohse, M. & Usadel, B. Trimmomatic: a flexible trimmer for Illumina sequence data. *Bioinformatics* **30**, 2114–2120 (2014).

[CAS](#) [PubMed](#) [PubMed Central](#) [Google Scholar](#)

114. 114.

Van Ooijen, J. JoinMap 4. <https://www.kyazma.nl/index.php/JoinMap/> (2006).

115. 115.

Arends, D., Prins, P., Jansen, R. C. & Broman, K. W. R/qtl: high-throughput multiple QTL mapping. *Bioinformatics* **26**, 2990–2992 (2010).

[CAS](#) [PubMed](#) [PubMed Central](#) [Google Scholar](#)

116. 116.

Haley, C. S. & Knott, S. A. A simple regression method for mapping quantitative trait loci in line crosses using flanking markers. *Heredity* **69**, 315–324 (1992).

[CAS](#) [PubMed](#) [PubMed Central](#) [Google Scholar](#)

117. 117.

RStudio Team. *RStudio: Integrated Development for R* (RStudio, 2019).

118. 118.

R Development Core Team. *R: A Language and Environment for Statistical Computing* (R Foundation for Statistical Computing, 2019).

119. 119.

Wei, T. et al. corrplot: visualization of a correlation matrix. R package version 0.84 <https://CRAN.R-project.org/package=corrplot> (2017).

120. 120.

Wilke, C. O. cowplot: streamlined plot theme and plot annotations for ‘ggplot2’. R package version 0.9.4 <https://CRAN.R-project.org/package=cowplot> (2019).

121. 121.

Signorell, A. DescTools: tools for descriptive statistics. R package version 99.28 <https://CRAN.R-project.org/package=DescTools> (2019).

122. 122.

Wickham, H., François, R., Henry, L. & Müller, K. dplyr: a grammar of data manipulation. R package version 0.8.0.1 <https://CRAN.R-project.org/package=dplyr> (2019).

123. 123.

Ren, K. formattable: create ‘formattable’ data structures. R package version 0.2.0.1 <https://CRAN.R-project.org/package=formattable> (2016).

124. 124.

Wickham, H. et al. ggplot2: create elegant data visualisations using the grammar of graphics. R package version 3.1.1 <https://CRAN.R-project.org/package=ggplot2> (2019).

125. 125.

Kassambara, A. ggpubr: ‘ggplot2’ based publication ready plots. R package version 0.2 <https://CRAN.R-project.org/package=ggpubr> (2018).

126. 126.

Wilke, C. O. ggridges: ridgeline plots in ‘ggplot2’. R package version 0.5.1 <https://CRAN.R-project.org/package=ggridges> (2018).

127. 127.

Harrell, F. E. Hmisc: Harrell miscellaneous. R package version 4.2-0 <https://cran.r-project.org/web/packages/Hmisc/index.html> (2019).

128. 128.

Sarkar, D. lattice: Trellis graphics for R. R package version 0.20-38 <https://CRAN.R-project.org/package=lattice> (2018).

129. 129.

Kolde, R. pheatmap: pretty heatmaps. R package version 1.0.12 <https://CRAN.R-project.org/package=pheatmap> (2019).

130. 130.

Neuwirth, E. RColorBrewer: ColorBrewer palettes. R package version 1.1-2 <https://CRAN.R-project.org/package=RColorBrewer> (2014).

131. 131.

Ligges, U., Maechler, M. & Schnackenberg, S. scatterplot3d: 3D scatter plot. R package version 0.3-41 <https://CRAN.R-project.org/package=scatterplot3d> (2018).

132. 132.

Wickham, H. stringr: simple, consistent wrappers for common string operations. R package version 1.4.0 <https://CRAN.R-project.org/package=stringr> (2019).

133. 133.

Wickham, H. & Henry, L. tidyverse: tidy messy data. R package version 0.8.3 <https://CRAN.R-project.org/package=tidyverse> (2019).

134. 134.

Meek, S. E. *Synopsis of the Fishes of the Great Lakes of Nicaragua* 97–132 (Field Columbian Museum, 1907).

135. 135.

Torres-Dowdall, J., Machado-Schiaffino, G., Kautt, A. F., Kusche, H. & Meyer, A. Differential predation on the two colour morphs of Nicaraguan Crater lake Midas cichlid fish: implications for the maintenance of its gold-dark polymorphism. *Biol. J. Linn. Soc.* **112**, 123–131 (2014).

[Google Scholar](#)

136. 136.

McKaye, K. R. & Barlow, G. W. in *Investigations of the Ichthyofauna of Nicaraguan Lakes* (ed. Thorson, T. B.) 465–475 (Univ. Nebraska Press, 1976).

137. 137.

Cross, T. G. et al. Serine/threonine protein kinases and apoptosis. *Exp. Cell Res.* **256**, 34–41 (2000).

[CAS](#) [PubMed](#) [Google Scholar](#)

138. 138.

Adams, D. S. et al. Bioelectric signalling via potassium channels: a mechanism for craniofacial dysmorphogenesis in KCNJ2-associated Andersen-Tawil syndrome. *J. Physiol. (Lond.)* **594**, 3245–3270 (2016).

[CAS](#) [Google Scholar](#)

139. 139.

Liu, Y. et al. The human inward rectifier K⁺ channel subunit kir5.1 (KCNJ16) maps to chromosome 17q25 and is expressed in kidney and pancreas. *Cytogenet. Cell Genet.* **90**, 60–63 (2000).

[CAS](#) [PubMed](#) [Google Scholar](#)

140. 140.

Kabashima, K. et al. Prostaglandin E₂–EP4 signaling initiates skin immune responses by promoting migration and maturation of Langerhans cells. *Nat. Med.* **9**, 744–749 (2003).

[CAS](#) [PubMed](#) [Google Scholar](#)

141. 141.

Baylis, J. R. Quantitative study of long-term courtship: 1. ethological isolation between sympatric populations of the Midas cichlid, *Cichlasoma citrinellum*, and the arrow cichlid, *C. zeliosum*. *Behaviour* **59**, 59–69 (1976).

[Google Scholar](#)

142. 142.

Stauffer, J. R., McCrary, J. K. & Black, K. E. Three new species of cichlid fishes (Teleostei: Cichlidae) from Lake Apoyo, Nicaragua. *Proc. Biol. Soc. Wash.* **121**, 117–129 (2008).

[Google Scholar](#)

[Download references](#)

Acknowledgements

We thank the scientific computing cluster (SCC) and the animal research facility (TFA) of the University of Konstanz; the Long Read Project Team of the DRESDEN-concept Genome Center for their support; the Zoologische Staatssammlung München (Germany) for tissue samples and photographs of holotypes and paratypes of *A. globosus* ($n = 11$) and *A. supercilius* ($n = 10$); the Nicaraguan Ministerio del Ambiente y los Recursos Naturales (MARENA); the Empresa Nicaragüense de Acueductos y Alcantarillados Sanitarios (ENACAL); current and previous members of the Meyer laboratory for their help; and J. Feder, S. Flaxman, S. Gavrilets, Z. Gompert, and J. Wolf for comments and discussions. This work was principally supported by an European Research Council Advanced Grant (ERC “GenAdap” 293700) to A.M., the Zukunftskolleg of the University of Konstanz to A.F.K. and M.O., a European Molecular Biology Organization fellowship to A.F.K., a Swiss National Science Foundation fellowship to A.N. (P300PA_177852), Alexander von Humboldt fellowships to G.M.-S. and M.O., the Deutsche Forschungsgemeinschaft (DFG) to C.F.K., G.M.-S., P.F., C.D.H., and A.M. (5363031, 219669982, 243870899, 253390846, 290977748, 366312182, 423396155), and a grant of the Federal Ministry of Education and Research (01IS18026C) to M.P.

Author information

Author notes

1. Andreas F. Kautt

Present address: Department of Organismic and Evolutionary Biology, Harvard University, Cambridge, MA, USA

2. Gonzalo Machado-Schiaffino

Present address: Department of Functional Biology, Area of Genetics, University of Oviedo, Oviedo, Spain

3. Melisa Olave

Present address: Argentine Dryland Research Institute of the National Council for Scientific Research (IADIZA-CONICET), Mendoza, Argentina

4. Frederico Henning

Present address: Department of Genetics, Institute of Biology, Federal University of Rio de Janeiro (UFRJ), Rio de Janeiro, Brazil

5. Andreas Härer

Present address: Division of Biological Sciences, Section of Ecology, Behavior & Evolution, University of California San Diego, La Jolla, CA, USA

6. These authors contributed equally: Andreas F. Kautt, Claudius F. Kratochwil, Alexander Nater

Affiliations

1. Department of Biology, University of Konstanz, Konstanz, Germany

Andreas F. Kautt, Claudius F. Kratochwil, Alexander Nater, Gonzalo Machado-Schiaffino, Melisa Olave, Frederico Henning, Julián Torres-Dowdall, Andreas Härer, C. Darrin Hulsey, Paolo Franchini & Axel Meyer

2. Max Planck Institute of Molecular Cell Biology and Genetics, Dresden, Germany

Martin Pippel & Eugene W. Myers

3. Center for Systems Biology Dresden, Dresden, Germany

Martin Pippel & Eugene W. Myers

Authors

1. Andreas F. Kautt

[View author publications](#)

You can also search for this author in [PubMed](#) [Google Scholar](#)

2. Claudio F. Kratochwil

[View author publications](#)

You can also search for this author in [PubMed](#) [Google Scholar](#)

3. Alexander Nater

[View author publications](#)

You can also search for this author in [PubMed](#) [Google Scholar](#)

4. Gonzalo Machado-Schiaffino

[View author publications](#)

You can also search for this author in [PubMed](#) [Google Scholar](#)

5. Melisa Olave

[View author publications](#)

You can also search for this author in [PubMed](#) [Google Scholar](#)

6. Frederico Henning

[View author publications](#)

You can also search for this author in [PubMed](#) [Google Scholar](#)

7. Julián Torres-Dowdall

[View author publications](#)

You can also search for this author in [PubMed](#) [Google Scholar](#)

8. Andreas Härer

[View author publications](#)

You can also search for this author in [PubMed](#) [Google Scholar](#)

9. C. Darrin Hulsey

[View author publications](#)

You can also search for this author in [PubMed](#) [Google Scholar](#)

10. Paolo Franchini

[View author publications](#)

You can also search for this author in [PubMed](#) [Google Scholar](#)

11. Martin Pippel

[View author publications](#)

You can also search for this author in [PubMed](#) [Google Scholar](#)

12. Eugene W. Myers

[View author publications](#)

You can also search for this author in [PubMed](#) [Google Scholar](#)

13. Axel Meyer

[View author publications](#)

You can also search for this author in [PubMed](#) [Google Scholar](#)

Contributions

Sample collection: A.F.K., G.M.-S., J.T.-D., A.H., M.O., A.M.; sample selection, extraction and library preparation: A.F.K., G.M.-S.; sequencing coordination: A.F.K.; genome assembly: M.P., A.F.K., E.W.M., genome annotation: A.F.K., P.F.; mapping, variant and genotype calling, phasing: A.F.K., A.N.; phenotyping and analyses: C.F.K., M.O., C.D.H., A.F.K.; population structure, phylogenetic and demographic analyses, selection tests: A.N., A.F.K., M.O.; gold mapping panel: C.F.K., F.H.; QTL mapping: P.F., F.H., C.F.K.; mate choice experiments: A.F.K., G.M.-S., J.T.-D.; funding acquisition: A.M., E.W.M., G.M.-S., A.F.K.; conceptualization: A.F.K., C.F.K., A.N., G.M.-S., A.M.; manuscript draft and figures: A.F.K., C.F.K., A.N., A.M. All authors contributed to, improved and approved the final manuscript.

Corresponding author

Correspondence to [Axel Meyer](#).

Ethics declarations

Competing interests

The authors declare no competing interests.

Additional information

Peer review information *Nature* thanks Fritz Sedlazeck and the other, anonymous, reviewer(s) for their contribution to the peer review of this work. Peer reviewer reports are available.

Publisher's note Springer Nature remains neutral with regard to jurisdictional claims in published maps and institutional affiliations.

Extended data figures and tables

Extended Data Fig. 1 Ancestry relationships in the Midas cichlid species complex.

a, Inferred ASTRAL species tree, together with node support, DensiTree visualization of bootstrapped species trees, and detected levels of gene tree – species tree discordance. Numbers after species names denote genome-wide π estimates, symbols before species names indicate colour code used in the rest of the figure (left half colour for lakes, right half colour for species). **b–d**, Clustering based on the first three dimensions of principal component analyses (PCAs) across all lakes (**b**), only CL Apoyo (**c**) and only CL Xiloá (**d**). Empty symbols indicate hybrids (that is, individuals with >25% admixed ancestry). **e–k**, Clustering based on the first two dimensions of principal component analyses of genomic variation in GLs Managua (**e**) and Nicaragua (**f**), CLs Apoyeque (**g**), As. León (**h**), As. Managua (**i**), Masaya (**j**), and Tiscapa (**k**). Please note the proportion of variation explained depends on the number of samples in an analysis and is influenced by the overall variation (which is small in single species lakes). **l–z**, Proportions of ancestry derived (using ChromoPainter) from the two great lake species, *A. citrinellus* (lighter green/violet) and *A. labiatus* (darker green/violet) inhabiting the two great lakes Nicaragua (violet) and Managua (green) for each crater lake population/species and chromosome. CL Apoyo (**l–q**) fish derive their ancestry from GL Nicaragua. CLs As. León (**r**), As. Managua (**s**), Apoyeque (**t**), Tiscapa (**v**), and Xiloá (**w–z**) fish derive their ancestry from GL Managua. CL Masaya (**u**) has mixed contributions from both GL Managua and GL Nicaragua. [Source data](#)

Extended Data Fig. 2 Multiple sequentially Markovian coalescent (MSMC) inferences.

a–d, Inferred effective population sizes through time in GL Nicaragua (**a**), GL Managua (**b**), CLs Apoyo, Masaya and Xiloá (**c**) and CLs Apoyeque, As. León, As. Managua, and Tiscapa (**d**). **e–l**, Inferred relative cross-coalescence rates for CL populations/species and GL source populations (**e** and **f**) and between sympatric species in GLs Managua and Nicaragua (**g**),

CLs Apoyo (**h** and **i**), thin- and thick-lipped ecotypes in CLs Masaya and Apoyeque (**j**), Xiloá (**k** and **l**). g = generation time in years, mu = mutation rate per site per generation. Comparisons not highlighted in the respective plots are indicated as thin grey lines. [Source data](#)

Extended Data Fig. 3 Schematic illustrations of all tested main demographic models.

a–f, Models of great lake species divergence, including colonization of GL Managua from GL Nicaragua after species divergence within GL Nicaragua (**a**; most supported model), colonization of GL Managua from GL Nicaragua before species divergence within GL Nicaragua (**b**), colonization of GL Nicaragua from GL Managua before species divergence within GL Managua (**c**), colonization of GL Managua from GL Nicaragua, but species divergence within both GLs (**d**), colonization of GL Nicaragua from GL Managua after species divergence within GL Managua (**e**), and colonization of GL Nicaragua from GL Managua from GL Managua, but species divergence within both GLs (**f**). **g–i**, Models of colonization and sympatric speciation in CL Apoyo, with colonization and subsequent intralacustrine divergence from GL Nicaragua after GL species divergence with (**g**; most supported model) and without (**h**) admixture, and with colonization of CL Apoyo and subsequent intralacustrine divergence from GL Nicaragua before GL species divergence (**i**). **j–l**, Models of colonization and sympatric speciation in CL Xiloá, with colonization and subsequent intralacustrine divergence from GL Managua after GL species divergence with (**j**; most supported model) and without (**l**) admixture, and with colonization of CL Xiloá and subsequent intralacustrine divergence from GL Managua before GL species divergence (**k**). **m, n**, Models for colonization of CL Masaya, which has support for both GLs acting as source populations, with (**m**; most supported model) and without (**n**) admixture from the source populations. **o, p**, Models for all other CLs with one species (Apoyeque, As. Managua, As. León, Masaya, and Tiscapa), with (**o**; most supported model) and without (**p**) admixture from the source populations of GL Managua. Parameters for time (T), population size (N), migration rate (M), admixture (A) and population growth (R) are indicated in the most supported models. Maximum-likelihood point estimates and confidence intervals for these parameters are provided in Extended Data Table 1. Abbreviations: A, admixture

(proportion of gene pool that was replaced); adm, admixture event; ama, *A. amarillo*; anc, ancestral population; asl, CL As León; ast, *A. astorquii*; aye, CL Apoyeque; bot, bottleneck; cit, *A. citrinellus*; cl, crater lake; col/col1: (first) colonization event; col2, second colonization event; div/div1, (first) divergence event (speciation in GLs); div2, second divergence event; lab, *A. labiatus*; M, symmetric migration rate (probability of lineages to move between populations per generation); man, GL Managua; mas, CL Masaya; N, population size (in individuals); nic, GL Nicaragua; R, population growth; sag, *A. sagittae*; T, time (in generations); tsc, CL Tiscapa; zal, *A. zaliosus*.

Extended Data Fig. 4 Focal phenotypic traits and their relationship to population divergence.

a–i, Variable Importance in Projection (VIP) scores (black point; based on complete data) together with 95% confidence intervals (error bars) and distributions of $n = 1,000$ non-parametric bootstrap replicates (coloured points; based on re-sampling with replacement) of partial least squares (PLS) regressions of focal traits with the primary axes of genomic divergence within GLs Nicaragua (**a**) and Managua (**b**) and CLs Masaya (**c**), Apoyo (**d**), Xiloá (**e**), Apoyeque (**f**), As. Managua (**g**), As. León (**h**) and Tiscapa (**i**). Trait VIP scores for which the lower CI bounds exceed 1, and which are thus deemed important for genomic divergence, are highlighted with an arrowhead. Note that coloration was excluded in **d**, **h** and **i**, because golden fish are virtually absent in these lakes (**o**). Pharyngeal jaw data was only available for lakes with evident population structure (**a–e**) and CL Apoyeque (**f**). **j–n**, Phenotypic distributions for lip size (**j**) (normalized by body area and \log_{10} -transformed), the first three axes of a principal component analysis on geometric morphometric data (**k–m**), and maximum pharyngeal tooth area (**n**) (normalized). Box plots are shown as median (solid line), interquartile range (IQR, that is, 25th–75th percentiles, box), and $\pm 1.5 \times \text{IQR}$ (whiskers) of the trait values. **o**, Number of golden specimens in our data set and estimated frequencies in the wild^{25,26,134,135,136}. **p, q**, t-SNE based on linear discriminant scores of geometric morphometric landmark data shows that all six and four described, endemic, sympatric species in CL Apoyo (**p**) and CL Xiloá (**q**), differ in body shapes, respectively. Admixed individuals were excluded

from these analyses. **r**, Landmark positions used for geometric morphometric analyses. [Source data](#)

Extended Data Fig. 5 Analyses of candidate regions underlying focal traits.

a–d, Genotype-phenotype association in an F_2 mapping panel of a cross of a homozygote golden (GG) and dark (DD) individual. Genotypes are based on microsatellite data at chr. 11 position 7,085,452 confirming that the dark/gold phenotype constitutes a dominant Mendelian trait with high penetrance (>99%) (**a**). Three recombinants localize the causal region to a 230-kb interval (11:6,890,589–7,119,761), which overlaps with the peak of high genotype-phenotype association in natural populations (Fig. 2a) (**b**). A haplotype network of the locus containing the top-associated SNP reveals that a single haplotype is associated with the dark/gold polymorphism (**c**; phenotype colour-coded) and is shared across all lakes with golden morphs (**d**; lake colour-coded with golden individuals in brighter colours). **e–p**, Genome-wide association mapping in the four lakes that harbour thick-lipped fish identifies two regions of high association, one on chr. 8 and another slightly weaker one on chr. 24. The locus on chr. 8 is also the most highly associated one in each of the four lakes separately, whereas association on chr. 24 is strong in GL Nicaragua (**e**), much weaker in GL Managua (**f**) and CL Masaya (**g**), and essentially absent in CL Apoyeque (**h**). Cross-population extended haplotype homozygosity (XP-EHH) analyses show that haplotypes within the most highly associated region on chr. 8 (see **e–h**) are on average much shorter in thin- than thick-lipped fish for GLs Nicaragua (**i**), Managua (**j**) and CLs Masaya (**k**) and Apoyeque (**l**), providing evidence for a strong selective sweep in thick-lipped fish. Independent of their lake of origin, most haplotypes cluster by lip phenotype, suggesting that a shared genetic basis underlies lip size in all populations (**n** and **o**). Estimation of the age of the lip haplotype suggests that it is much older (30–260,000 years) than the divergence time of thin- and thick-lipped species in the great lakes (~16,730 years) (**m**). Lip size is bimodally distributed in all four lakes that harbour thick-lipped fish (**p**).

[Source data](#)

Extended Data Fig. 6 The genomic bases of adaptive divergence in Midas cichlids.

a–c, Gene annotation of the gold locus on chr. 11, with a serine-threonine kinase (*stk*) as a candidate gene (**a**). Serine/threonine-protein kinases regulate cell division and apoptosis and could therefore explain the progressive pigment cell loss¹³⁷. The lip loci located on chr. 8 (**b**) and 24 (**c**) include two inward rectifier potassium channels (*kcnj2* and *kcnj16*) and a g-protein coupled receptor (*ptger4*) as top candidate genes, respectively. *Kcnj2* has been associated with Andersen–Tawil Syndrome, which involves craniofacial dysmorphogenesis¹³⁸. *Kcnj16* has been linked to fluid balance¹³⁹ and could therefore trigger tissue swelling in thick-lipped individuals. *Ptger4* influences tissue swelling as part of immune responses in mice¹⁴⁰. **d, e**, Genome-wide association (GWA) mapping of pharyngeal jaw (maximum tooth size) (**d**) and body morphology (geometric morphometrics PC1 scores) (**e**). The lack of high association signals ($-\log_{10}(P) > 10$) is consistent with a polygenic bases for these traits. **f, g**, Sharing of genomic windows under divergent selection among comparisons of thin- and thick-lipped ecotypes and species (**f**) and among sympatric species of CLs Apoyo and Xiloá. The three windows shared in **f** are three consecutive windows centred around the lip locus (see **b**). No windows are shared among all CL Apoyo and Xiloá species, suggesting that different loci are associated with divergence of the species. **h, i**, Gene ontology (GO) term enrichment analysis of genomic windows classified to be under divergent selection between CL Apoyo and CL Xiloá species (see **g** and Fig. 3v–y) reveals an overrepresentation of several biological processes linked to morphological variation (for example, animal organ development, anatomical structure development, cellular component organization).

[Source data](#)

Extended Data Fig. 7 Pairwise *FST* comparisons.

Genomic landscapes of differentiation among sympatric species in CLs Apoyo and Xiloá (**a–u**), between thin- versus thick-lipped fish (**v, x, y** and **ad**), and between dark versus golden-coloured fish within

populations/species (**w**, **z–ac** and **ae–ag**). Panels are sorted by decreasing levels of overall genetic differentiation (Hudson's F_{ST}). Manhattan plots show F_{ST} values in 10-kb non-overlapping windows and red lines indicate loess-smoothed values. [Source data](#)

Extended Data Fig. 8 Effective gene flow and the role of genetic drift in genomic differentiation among Crater Lake Apoyo and Xiloá species.

a, b, Estimates of effective gene flow (migration rate per generation) between CL Apoyo (**a**) and CL Xiloá (**b**) species pairs as well as between the species *A. citrinellus* and *A. labiatus* in GL Nicaragua (**a**) and GL Managua (**b**). Shown are maximum likelihood point estimates together with error bars denoting 95% confidence intervals obtained from $n = 100$ parametric bootstrap replicates. **c–j**, Distributions of F_{ST} values in 10-kb windows of the empirical data (**c, g**) and genome-scale simulations (**d, h**—based on the inferred maximum-likelihood parameter estimates of our most supported demographic models). Genome-scale simulations with matched past and present population sizes from crater lake (**e, i**) and great lake species (**f, j**) demonstrate that crater lake species pair comparisons retain a consistently higher mean F_{ST} compared to the great lake comparisons, even though divergence times are more recent in the crater lakes (Extended Data Table 1). Violin plots in **d–f** and **h–j** show 100 replicates plotted on top of each other, horizontal bars are box plots of the mean values of the 100 replicates demonstrating little variance across simulation runs. Transparent parts of violin plots in **e, f, i, j** correspond to the respective estimates from **d, h** for ease of comparisons. Box plots are shown as median (solid line), interquartile (that is, 25th–75th percentiles, box), and $\pm 1.5 \times \text{IQR}$ (whiskers) of the mean values (not visible due to low variance). [Source data](#)

Extended Data Table 1 Parameter estimates of demographic models

[Full size table](#)

Extended Data Table 2 Mate choice experiments

[Full size table](#)

Supplementary information

Supplementary Notes

This file contains Supplementary Notes on the inferred demographic history of the Midas cichlid species complex, the pedigree-based association and fine-mapping of the gold locus, sampling, frequencies, and population structure of gold morphs as well as mate choice experiments.

Reporting Summary

Peer Review File

Source data

Source Data Fig. 1

Source Data Fig. 2

Source Data Fig. 3

Source Data Extended Data Fig. 1

Source Data Extended Data Fig. 2

Source Data Extended Data Fig. 4

Source Data Extended Data Fig. 5

Source Data Extended Data Fig. 6

Source Data Extended Data Fig. 7

Source Data Extended Data Fig. 8

Rights and permissions

[Reprints and Permissions](#)

About this article



Check for
updates

Cite this article

Kautt, A.F., Kratochwil, C.F., Nater, A. *et al.* Contrasting signatures of genomic divergence during sympatric speciation. *Nature* **588**, 106–111 (2020). <https://doi.org/10.1038/s41586-020-2845-0>

[Download citation](#)

- Received: 30 March 2020
- Accepted: 23 July 2020
- Published: 28 October 2020
- Issue Date: 03 December 2020
- DOI: <https://doi.org/10.1038/s41586-020-2845-0>

Comments

By submitting a comment you agree to abide by our [Terms](#) and [Community Guidelines](#). If you find something abusive or that does not comply with our terms or guidelines please flag it as inappropriate.

[Access through your institution](#)

[Change institution](#)

[Buy or subscribe](#)

This article was downloaded by **calibre** from <https://www.nature.com/articles/s41586-020-2845-0>

| [Section menu](#) | [Main menu](#) |

- Article
- [Published: 14 October 2020](#)

The cellular basis of distinct thirst modalities

- [Allan-Hermann Pool¹,](#)
- [Tongtong Wang ORCID: orcid.org/0000-0002-0408-2571^{1,2},](#)
- [David A. Stafford³,](#)
- [Rebecca K. Chance ORCID: orcid.org/0000-0001-7059-6119³,](#)
- [Sangjun Lee¹,](#)
- [John Ngai³ nAff4](#) &
- [Yuki Oka ORCID: orcid.org/0000-0003-2686-0677¹](#)

[Nature](#) volume 588, pages112–117(2020)[Cite this article](#)

- 5973 Accesses
- 521 Altmetric
- [Metrics details](#)

Subjects

- [Feeding behaviour](#)
- [Molecular neuroscience](#)
- [Neural circuits](#)

Abstract

Fluid intake is an essential innate behaviour that is mainly caused by two distinct types of thirst^{1,2,3}. Increased blood osmolality induces osmotic

thirst that drives animals to consume pure water. Conversely, the loss of body fluid induces hypovolaemic thirst, in which animals seek both water and minerals (salts) to recover blood volume. Circumventricular organs in the lamina terminalis are critical sites for sensing both types of thirst-inducing stimulus^{4,5,6}. However, how different thirst modalities are encoded in the brain remains unknown. Here we employed stimulus-to-cell-type mapping using single-cell RNA sequencing to identify the cellular substrates that underlie distinct types of thirst. These studies revealed diverse types of excitatory and inhibitory neuron in each circumventricular organ structure. We show that unique combinations of these neuron types are activated under osmotic and hypovolaemic stresses. These results elucidate the cellular logic that underlies distinct thirst modalities. Furthermore, optogenetic gain of function in thirst-modality-specific cell types recapitulated water-specific and non-specific fluid appetite caused by the two distinct dipsogenic stimuli. Together, these results show that thirst is a multimodal physiological state, and that different thirst states are mediated by specific neuron types in the mammalian brain.

[Access through your institution](#)

[Change institution](#)

[Buy or subscribe](#)

Access options

Subscribe to Journal

Get full journal access for 1 year

185,98 €

only 3,58 € per issue

[Subscribe](#)

All prices are NET prices.

VAT will be added later in the checkout.

Rent or Buy article

Get time limited or full article access on ReadCube.

from \$8.99

[Rent or Buy](#)

All prices are NET prices.

Additional access options:

- [Log in](#)
- [Access through your institution](#)
- [Learn about institutional subscriptions](#)

Fig. 1: Fluid consumption, physiological changes and neural activation pattern under distinct thirst states.



Fig. 2: Major cell classes and neuron types in the SFO and the OVLT.



Fig. 3: Stimulus-to-cell-type mapping reveals neuron types tuned to distinct thirst states.



Fig. 4: Activation of thirst-state-specific cell populations in the SFO and the OVLT recapitulates thirst modality-specific drinking patterns.



Data availability

The behavioural and histological data that support the findings are available from the corresponding author on reasonable request. Raw and fully processed scRNA-seq data are available at the NCBI Gene Expression Omnibus (GEO accession no. GSE154048).

Code availability

The R code used to perform the scRNA-seq analysis is available from the corresponding author on reasonable request.

References

1. 1.

Fitzsimons, J. T. The physiology of thirst and sodium appetite. *Monogr. Physiol. Soc.* **35**, 1–572 (1979).

[Google Scholar](#)

2. 2.

Leib, D. E., Zimmerman, C. A. & Knight, Z. A. Thirst. *Curr. Biol.* **26**, R1260–R1265 (2016).

[CAS](#) [PubMed](#) [PubMed Central](#) [Google Scholar](#)

3. 3.

McKinley, M. J. & Johnson, A. K. The physiological regulation of thirst and fluid intake. *News Physiol. Sci.* **19**, 1–6 (2004).

[PubMed](#) [Google Scholar](#)

4. 4.

Augustine, V., Lee, S. & Oka, Y. Neural control and modulation of thirst, sodium appetite, and hunger. *Cell* **180**, 25–32 (2020).

[CAS](#) [PubMed](#) [PubMed Central](#) [Google Scholar](#)

5. 5.

Bourque, C. W. Central mechanisms of osmosensation and systemic osmoregulation. *Nat. Rev. Neurosci.* **9**, 519–531 (2008).

[CAS](#) [PubMed](#) [Google Scholar](#)

6. 6.

Zimmerman, C. A., Leib, D. E. & Knight, Z. A. Neural circuits underlying thirst and fluid homeostasis. *Nat. Rev. Neurosci.* **18**, 459–469 (2017).

[CAS](#) [PubMed](#) [PubMed Central](#) [Google Scholar](#)

7. 7.

McKinley, M. J. et al. The sensory circumventricular organs of the mammalian brain. *Adv. Anat. Embryol. Cell Biol.* **172**, III–XII, 1–122, back cover (2003).

[CAS](#) [PubMed](#) [Google Scholar](#)

8. 8.

Augustine, V. et al. Hierarchical neural architecture underlying thirst regulation. *Nature* **555**, 204–209 (2018).

[ADS](#) [CAS](#) [PubMed](#) [PubMed Central](#) [Google Scholar](#)

9. 9.

Leib, D. E. et al. The forebrain thirst circuit drives drinking through negative reinforcement. *Neuron* **96**, 1272–1281.e4 (2017).

[CAS](#) [PubMed](#) [PubMed Central](#) [Google Scholar](#)

10. 10.

Oka, Y., Ye, M. & Zuker, C. S. Thirst driving and suppressing signals encoded by distinct neural populations in the brain. *Nature* **520**, 349–352 (2015).

[ADS](#) [CAS](#) [PubMed](#) [PubMed Central](#) [Google Scholar](#)

11. 11.

Stricker, E. M. Osmoregulation and volume regulation in rats: inhibition of hypovolemic thirst by water. *Am. J. Physiol.* **217**, 98–105 (1969).

[CAS](#) [PubMed](#) [Google Scholar](#)

12. 12.

Jalowiec, J. E., Crapanzano, J. E. & Stricker, E. M. Specificity of salt appetite elicited by hypovolemia. *Psychon. Sci.* **6**, 331–332 (1966).

[Google Scholar](#)

13. 13.

Allen, W. E. et al. Thirst-associated preoptic neurons encode an aversive motivational drive. *Science* **357**, 1149–1155 (2017).

[ADS](#) [CAS](#) [PubMed](#) [PubMed Central](#) [Google Scholar](#)

14. 14.

Johnson, A. K. & Gross, P. M. Sensory circumventricular organs and brain homeostatic pathways. *FASEB J.* **7**, 678–686 (1993).

[CAS](#) [PubMed](#) [Google Scholar](#)

15. 15.

Johnson, A. K., Zardetto-Smith, A. M. & Edwards, G. L. Integrative mechanisms and the maintenance of cardiovascular and body fluid homeostasis: the central processing of sensory input derived from the circumventricular organs of the lamina terminalis. *Prog. Brain Res.* **91**, 381–393 (1992).

[CAS](#) [PubMed](#) [Google Scholar](#)

16. 16.

Butler, A., Hoffman, P., Smibert, P., Papalex, E. & Satija, R. Integrating single-cell transcriptomic data across different conditions, technologies, and species. *Nat. Biotechnol.* **36**, 411–420 (2018).

[CAS](#) [PubMed](#) [PubMed Central](#) [Google Scholar](#)

17. 17.

Stuart, T. et al. Comprehensive integration of single-cell data. *Cell* **177**, 1888–1902.e21 (2019).

[CAS](#) [PubMed](#) [PubMed Central](#) [Google Scholar](#)

18. 18.

Benz, F. et al. Low WNT/β-catenin signaling determines leaky vessels in the subfornical organ and affects water homeostasis in mice. *eLife* **8**, e43818 (2019).

[PubMed](#) [PubMed Central](#) [Google Scholar](#)

19. 19.

Bourque, C. W., Oliet, S. H. & Richard, D. Osmoreceptors, osmoreception, and osmoregulation. *Front. Neuroendocrinol.* **15**, 231–274 (1994).

[CAS](#) [PubMed](#) [Google Scholar](#)

20. 20.

Sharif-Naeini, R., Ciura, S., Zhang, Z. & Bourque, C. W. Contribution of TRPV channels to osmosensory transduction, thirst, and vasopressin release. *Kidney Int.* **73**, 811–815 (2008).

[CAS](#) [PubMed](#) [Google Scholar](#)

21. 21.

Hrvatin, S. et al. Single-cell analysis of experience-dependent transcriptomic states in the mouse visual cortex. *Nat. Neurosci.* **21**, 120–129 (2018).

[CAS](#) [PubMed](#) [Google Scholar](#)

22. 22.

Wu, Y. E., Pan, L., Zuo, Y. N., Li, X. M. & Hong, W. Z. Detecting activated cell populations using single-cell RNA-seq. *Neuron* **96**, 313–329.e6 (2017).

[CAS](#) [PubMed](#) [Google Scholar](#)

23. 23.

Betley, J. N. et al. Neurons for hunger and thirst transmit a negative-valence teaching signal. *Nature* **521**, 180–185 (2015).

[ADS](#) [CAS](#) [PubMed](#) [PubMed Central](#) [Google Scholar](#)

24. 24.

Campbell, J. N. et al. A molecular census of arcuate hypothalamus and median eminence cell types. *Nat. Neurosci.* **20**, 484–496 (2017).

[CAS](#) [PubMed](#) [PubMed Central](#) [Google Scholar](#)

25. 25.

Moffitt, J. R. et al. Molecular, spatial, and functional single-cell profiling of the hypothalamic preoptic region. *Science* **362**, eaau5324 (2018).

[ADS](#) [PubMed](#) [PubMed Central](#) [Google Scholar](#)

26. 26.

Geerling, J. C. & Loewy, A. D. Central regulation of sodium appetite. *Exp. Physiol.* **93**, 177–209 (2008).

[CAS](#) [PubMed](#) [Google Scholar](#)

27. 27.

Lee, S. et al. Chemosensory modulation of neural circuits for sodium appetite. *Nature* **568**, 93–97 (2019).

[ADS](#) [CAS](#) [PubMed](#) [PubMed Central](#) [Google Scholar](#)

28. 28.

Fitzsimons, J. T. Angiotensin, thirst, and sodium appetite. *Physiol. Rev.* **78**, 583–686 (1998).

[CAS](#) [PubMed](#) [Google Scholar](#)

29. 29.

Gizowski, C. & Bourque, C. W. The neural basis of homeostatic and anticipatory thirst. *Nat. Rev. Nephrol.* **14**, 11–25 (2018).

[CAS](#) [PubMed](#) [Google Scholar](#)

30. 30.

Hiyama, T. Y., Watanabe, E., Okado, H. & Noda, M. The subfornical organ is the primary locus of sodium-level sensing by Na_x sodium channels for the control of salt-intake behavior. *J. Neurosci.* **24**, 9276–9281 (2004).

[CAS](#) [PubMed](#) [PubMed Central](#) [Google Scholar](#)

31. 31.

Guenthner, C. J., Miyamichi, K., Yang, H. H., Heller, H. C. & Luo, L. Permanent genetic access to transiently active neurons via TRAP: targeted recombination in active populations. *Neuron* **78**, 773–784 (2013).

[CAS](#) [PubMed](#) [PubMed Central](#) [Google Scholar](#)

32. 32.

Lein, E. S. et al. Genome-wide atlas of gene expression in the adult mouse brain. *Nature* **445**, 168–176 (2007).

[ADS](#) [CAS](#) [PubMed](#) [Google Scholar](#)

33. 33.

Antunes-Rodrigues, J., McCann, S. M., Rogers, L. C. & Samson, W. K. Atrial natriuretic factor inhibits dehydration- and angiotensin II-induced water intake in the conscious, unrestrained rat. *Proc. Natl Acad. Sci. USA* **82**, 8720–8723 (1985).

[ADS](#) [CAS](#) [PubMed](#) [Google Scholar](#)

34. 34.

Ciura, S. & Bourque, C. W. Transient receptor potential vanilloid 1 is required for intrinsic osmoreception in organum vasculosum lamina terminalis neurons and for normal thirst responses to systemic hyperosmolality. *J. Neurosci.* **26**, 9069–9075 (2006).

[CAS](#) [PubMed](#) [PubMed Central](#) [Google Scholar](#)

35. 35.

Gizowski, C., Zaelzer, C. & Bourque, C. W. Clock-driven vasopressin neurotransmission mediates anticipatory thirst prior to sleep. *Nature* **537**, 685–688 (2016).

[ADS](#) [CAS](#) [PubMed](#) [Google Scholar](#)

36. 36.

Kinsman, B. et al. Osmoregulatory thirst in mice lacking the transient receptor potential vanilloid type 1 (TRPV1) and/or type 4 (TRPV4) receptor. *Am. J. Physiol. Regul. Integr. Comp. Physiol.* **307**, R1092–R1100 (2014).

[CAS](#) [PubMed](#) [PubMed Central](#) [Google Scholar](#)

37. 37.

Liedtke, W. & Friedman, J. M. Abnormal osmotic regulation in *Trpv4*^{-/-} mice. *Proc. Natl Acad. Sci. USA* **100**, 13698–13703 (2003).

[ADS](#) [CAS](#) [PubMed](#) [Google Scholar](#)

38. 38.

Miller, R. L. & Loewy, A. D. ENaC γ-expressing astrocytes in the circumventricular organs, white matter, and ventral medullary surface: sites for Na⁺ regulation by glial cells. *J. Chem. Neuroanat.* **53**, 72–80 (2013).

[CAS](#) [PubMed](#) [PubMed Central](#) [Google Scholar](#)

39. 39.

Miller, R. L., Wang, M. H., Gray, P. A., Salkoff, L. B. & Loewy, A. D. ENaC-expressing neurons in the sensory circumventricular organs become c-Fos activated following systemic sodium changes. *Am. J. Physiol. Regul. Integr. Comp. Physiol.* **305**, R1141–R1152 (2013).

[CAS](#) [PubMed](#) [PubMed Central](#) [Google Scholar](#)

40. 40.

Nomura, K. et al. [Na⁺] increases in body fluids sensed by central Nax induce sympathetically mediated blood pressure elevations via H⁺-dependent activation of ASIC1a. *Neuron* **101**, 60–75.e6 (2019).

[CAS](#) [PubMed](#) [Google Scholar](#)

41. 41.

Samson, W. K. et al. Central nervous system action of endothelin-3 to inhibit water drinking in the rat. *Brain Res.* **539**, 347–351 (1991).

[CAS](#) [PubMed](#) [Google Scholar](#)

42. 42.

Sunn, N. et al. Circulating relaxin acts on subfornical organ neurons to stimulate water drinking in the rat. *Proc. Natl Acad. Sci. USA* **99**, 1701–1706 (2002).

[ADS](#) [CAS](#) [PubMed](#) [Google Scholar](#)

43. 43.

Tang-Christensen, M. et al. Central administration of GLP-1-(7-36) amide inhibits food and water intake in rats. *Am. J. Physiol.* **271**, R848–R856 (1996).

[CAS](#) [PubMed](#) [Google Scholar](#)

44. 44.

Watanabe, E. et al. Nav2/NaG channel is involved in control of salt-intake behavior in the CNS. *J. Neurosci.* **20**, 7743–7751 (2000).

[CAS](#) [PubMed](#) [PubMed Central](#) [Google Scholar](#)

[Download references](#)

Acknowledgements

We thank the members of the Oka laboratory, D. J. Anderson, M. Thomson and S. Chen for helpful discussion and comments; B. Ho and A. Koranne for maintaining and genotyping animal lines; J. Park and the Single-Cell Profiling Center (SPEC) in the Beckman Institute at Caltech for technical assistance with scRNA-seq; B. Lowell and M. Krashes for generously sharing *Pdyn-Cre* mice; and L. Luo for a generous gift of TRAP2 mice. This work was supported by Startup funds from the President and Provost of the California Institute of Technology and the Biology and Biological Engineering Division of California Institute of Technology. Y.O. is also supported by the Searle Scholars Program, the Mallinckrodt Foundation, the McKnight Foundation, the Klingenstein-Simons Foundation, the New York Stem Cell Foundation and the NIH (R56MH113030 and R01NS109997). J.N. is supported by the NIH (U19MH114830).

Author information

Author notes

1. John Ngai

Present address: National Institute of Neurological Disorders and Stroke, National Institutes of Health, Bethesda, MD, USA

Affiliations

1. Division of Biology and Biological Engineering, California Institute of Technology, Pasadena, CA, USA

Allan-Hermann Pool, Tongtong Wang, Sangjun Lee & Yuki Oka

2. College of Life Sciences, Nankai University, Tianjin, China

Tongtong Wang

3. Department of Molecular & Cell Biology, University of California, Berkeley, Berkeley, CA, USA

David A. Stafford, Rebecca K. Chance & John Ngai

Authors

1. Allan-Hermann Pool

[View author publications](#)

You can also search for this author in [PubMed](#) [Google Scholar](#)

2. Tongtong Wang

[View author publications](#)

You can also search for this author in [PubMed](#) [Google Scholar](#)

3. David A. Stafford

[View author publications](#)

You can also search for this author in [PubMed](#) [Google Scholar](#)

4. Rebecca K. Chance

[View author publications](#)

You can also search for this author in [PubMed](#) [Google Scholar](#)

5. Sangjun Lee

[View author publications](#)

You can also search for this author in [PubMed](#) [Google Scholar](#)

6. John Ngai

[View author publications](#)

You can also search for this author in [PubMed](#) [Google Scholar](#)

7. Yuki Oka

[View author publications](#)

You can also search for this author in [PubMed](#) [Google Scholar](#)

Contributions

A.-H.P. and Y.O. conceived the research programme and designed experiments. A.-H.P. and T.W. carried out the experiments and analysed the data. J.N., R.K.C. and D.A.S. generated and characterized *Rxfp1-2A-Cre* mice. S.L. maintained and characterized *Pdyn-Cre* mice. A.-H.P. and Y.O. wrote the paper. Y.O. supervised the entire work.

Corresponding author

Correspondence to [Yuki Oka](#).

Ethics declarations

Competing interests

The authors declare no competing interests.

Additional information

Peer review information *Nature* thanks Benjamin R. Arenkiel, Charles W. Bourque and the other, anonymous, reviewer(s) for their contribution to the peer review of this work.

Publisher's note Springer Nature remains neutral with regard to jurisdictional claims in published maps and institutional affiliations.

Extended data figures and tables

[Extended Data Fig. 1 Thirst-state-dependent drinking behaviour and genetic labelling of active neurons.](#)

a, FOS expression in the SFO (left) and the OVLT (right) under the four thirst states (SFO: $n = 6$ sections from 4 mice for control, $n = 6$ sections from 6 mice for osmotic thirst, $n = 5$ sections from 4 mice for hypovolaemic thirst, and $n = 6$ sections from 6 mice for water deprivation; OVLT: $n = 3$ sections from 3 mice for control, $n = 8$ sections from 7 mice for osmotic thirst, $n = 5$ sections from 4 mice for hypovolaemic thirst, $n = 7$ sections from 7 mice for water deprivation). **b**, Water and 0.3M NaCl consumption in sated control animals. The number of total licks for water (grey) and 0.3M saline (red) were quantified during a one-hour session ($n = 9$ mice for each group). **c**, Water (grey) and 0.3M KCl intake (orange) under osmotic and hypovolaemic thirst states. The number of total licks was quantified during a one-hour session ($n = 6$ mice). **d**, Experimental diagram for TRAP2 activity-dependent genetic labelling. TRAP2/Ai14 double transgenic animals were challenged with osmotic stress by i.p. injection of NaCl solution in the presence of 4-OHT. Osmolality sensitive cells (upper) express Cre-ER under the promoter of *Fos* gene, which turns on *tdTomato* expression (red). In osmolality insensitive cells, the same stimulus does not induce *tdTomato* expression (bottom). **e**, Genetic labelling of thirst-sensitive

neurons in the OVLT of TRAP2/Ai14 mice. Experimental design to label activated neurons under osmotic thirst and hypovolaemic thirst (top). Osmolality sensitive neurons (Osm-TRAP, red) in the OVLT (bottom) overlapped with NaCl-induced acute FOS expression (green). Individual labelling and merged images are shown. By contrast, a significantly smaller fraction of Osm-TRAP neurons was co-labelled with hypovolaemia-induced FOS. Scale bars, 50 µm. **f**, Quantification of OVLT TRAP2 experiments ($n = 6$ sections from 4 mice for Osm-Osm, $n = 5$ sections from 5 mice for Osm-Hvol). **g**, TRAP labelling in the SFO and the OVLT of sated control animals ($n = 6$ sections from 3 mice for SFO, $n = 3$ sections from 2 mice for OVLT). * $P < 0.05$, ** $P < 0.01$, *** $P < 0.001$ by two-tailed Wilcoxon matched-pairs signed rank test or Mann–Whitney test. Data are shown as mean ± s.e.m.

[Extended Data Fig. 2 Profiling of cell and neuron types in the SFO and the OVLT.](#)

a, b, Violin plots of log-normalized expression of cell-type-defining genes for SFO (**a**) and OVLT (**b**) major cell classes with maximum counts per million (max CPM). Bar graph shows profiling resolution per cell type in median genes/cell. **c, d**, Heat maps of cell-type-specific gene expression in the major cell classes of SFO (**c**) and OVLT (**d**). Gene expression data are z-scored with warmer colours indicating higher gene expression. **e**, Transcriptomic neuron types in the OVLT region ($n = 4109$ cells) shown in a UMAP embedding (left). Based on in situ hybridization data from Allen Brain Atlas, cell types were annotated into three anatomic classes: OVLT internal (green), external(red), and regional (both inside and outside of the OVLT) (yellow). We excluded non-OVLT cell types (red) for further analyses (Fig. 2, Extended Data Fig. 2h). **f**, Violin plot of log-normalized gene expression for all neuron types in the OVLT area. Neuron types outside the OVLT are shown in grey. **g, h**, Heat map of neuron-type-specific gene expression in the SFO (**g**) and the OVLT (**h**).

[Extended Data Fig. 3 Expression of putative osmoregulatory channels or hormone receptors and cellular comparison between the SFO and the OVLT.](#)

a, Dotplot of cell-type-specific expression for putative osmosensory ion channels and receptor genes for osmoregulatory hormone systems in major cell classes in the SFO and the OVLT (dot size is proportional to % of cells with transcript count >0 expression, colour scale represents z-scored average gene expression, $n = 7,950$ and $6,161$ cells for SFO and OVLT respectively). **b**, Dotplot of neuron-type-specific expression for putative osmosensory ion channels and receptor genes for osmoregulatory hormone systems in neuron types in the SFO and OVLT^{30,33,34,35,36,37,38,39,40,41,42,43,44}. Although some of the putative genes are not enriched in the SFO or OVLT, they may function outside the LT to regulate thirst ($n = 2,642$ and $1,511$ neurons for SFO and OVLT respectively). **c**, Evaluation of transcriptional homology between SFO and OVLT cell classes based on Spearman correlation between average expression of top 850 most variable genes from the SFO and OVLT, respectively ($n = 1,224$ genes total). Euclidean distance matrix between cell types was calculated based on the Spearman correlation coefficients between cell types, which were then hierarchically clustered using Ward agglomeration. **d**, Same analysis on transcriptional homology between SFO and OVLT neuron types based on top 200 most variable genes from the SFO and OVLT ($n = 315$ genes total).

[Extended Data Fig. 4 Stimulus-to-cell-type mapping in the SFO and the OVLT.](#)

a, A diagram of scRNA-seq-based stimulus-to-cell-type mapping protocol. As previously reported, regular scRNA-seq results in artificial induction of IEGs in all neuron types stemming from tissue dissociation^{21,22}. Performing scRNA-seq with a transcriptional blocker during tissue dissociation suppresses artificial induction of IEGs revealing the stimulus or behaviour induced IEG expression pattern. **b**, Regular scRNA-seq induces high levels of *Fos* expression in all SFO and OVLT neuron types. Data are shown as a violin plot of log-normalized *Fos* transcript count data. **c**, In the presence of actinomycin D, artificial induction of IEGs in non-stimulated SFO and OVLT neurons is abolished. 10x Chromium Controller image was provided by 10x Genomics. **d**, Expression of *Fos* in SFO and OVLT major cell classes under distinct thirst states (SFO excitatory neurons $n = 931, 689, 775, 706$; SFO inhibitory neurons $n = 935, 714, 997, 793$; SFO LT

astrocytes $n = 2,085, 1,907, 2,544, 3,177$; SFO astrocytes $n = 110, 138, 97, 265$; OVLT area excitatory neurons $n = 2,623, 3,027, 2,115, 2,489$; OVLT area inhibitory neurons $n = 853, 831, 661, 773$; OVLT LT astrocytes $n = 1,229, 1,087, 1,133, 1,238$; OVLT astrocytes $n = 1,736, 1,225, 1,384, 1,353$). Data are shown as mean \pm s.e.m. **e**, Expression of other IEGs (*Nr4a1* and *Fosl2*) in SFO and OVLT neuron types under distinct thirst states. All data were analysed with two-tailed Kruskal–Wallis test with Dunn’s post-test. P -values are shown on a $\log_{10}(p)$ scale.

Extended Data Fig. 5 Canonical correlation analysis based alignment of transcriptomic neuron types under different physiological conditions.

a, A diagram illustrating the misalignment of cell types under distinct physiological states with regular graph-based clustering analysis. **b**, The canonical correlation analysis (CCA) workflow for realigning cell types for joint analysis of transcriptomic data sets. **c**, UMAP embedded scRNA-seq data from SFO and OVLT neurons under distinct thirst states without alignment (left panel), with CCA alignment (middle panel) and cell-type identification on CCA aligned data (right panel). **d, e**, Violin plots of cell-type defining marker genes in CCA aligned stimulus-to-cell-type mapping data sets for SFO (**e**) and OVLT (**d**) respectively.

Extended Data Fig. 6 Multi-colour *in situ* hybridization for anatomical validation of transcriptomic cell types.

a, Quantification of SFO *Htr7*- and *Rxfp1*-positive cells and their overlap in the SFO ($n = 17$ sections from 6 animals). Scale bar, 20 μm . Nuclei are visualized by DAPI staining (white). **b**, Quantification of *Bmp3*- and *Rxfp1*-positive cells and their overlap in the OVLT ($n = 15$ sections from 8 animals). Scale bar, 20 μm . **c**, *Rxfp1*-and *Pdyn*-positive cells co-express *Fos* under water deprived conditions. Representative images from 8, 3, 8 and 3 sections from 2 independent experiments for SFO RXFP1/FOS, OVLT RXFP1/FOS, SFO PDYN/FOS and OVLT PDYN/FOS stains respectively. Scale bar, 10 μm . **d**, Cell types labelled by *Rxfp3* (SFO) and *Cpne4* (OVLT) express *Fos* under osmotic thirst conditions (left). Cell types labelled by

Htr7 (SFO) and *Bmp3* (OVLT) express *Fos* under hypovolaemic thirst (right). Representative images from 2, 2, 3 and 2 sections from 2 independent experiments for SFO RXFP3/FOS, OVLT CPNE4/FOS, SFO HTR7/FOS and OVLT BMP3/FOS stains respectively. Scale bar, 10 µm.

Extended Data Fig. 7 Genetic targeting of osmotic and hypovolaemic thirst-activated cell populations in the SFO and the OVLT.

a, Spearman correlation between *Fos* expression under distinct thirst states and cell-type-specific and thirst-state-specific marker genes. Thirst-state-specific marker genes (*Rxfp1* and *Pdyn*) show higher correlation with *Fos* expression compared to cell-type-specific genes. **b**, Two-colour *in situ* hybridization of *Pdyn* and *Rxfp1*. These gene expression patterns are mostly distinct with minor overlap (arrowhead). Representative images from 8 and 2 slices from 2 independent experiments for SFO (left) and OVLT (right) respectively. Scale bar, 10 µm. **c**, Validation of Cre expression in *Pdyn-Cre* and *Rxfp1-Cre* lines. 95.5% of *Pdyn-Cre* and 100% of *Rxfp1-Cre* expression matched endogenous gene expression. Representative images from 4 and 2 slices from 2 independent experiments for PDYN/CRE and RXFP1/CRE labelling, respectively. Scale bar, 10 µm. **d**, Immunostaining of the SFO (top) and OVLT (bottom). Shown are PDYN-positive neurons in *Pdyn-Cre/Ai3* animals (representative images out of 8 slices from 4 mice for SFO and out of 2 slices from 2 mice for OVLT, left) and RXFP1-positive neurons in *Rxfp1-Cre/Ai14* animals (representative images out of 6 slices from 3 mice for both SFO and OVLT, right). PDYN- and RXFP1-positive neurons (red) are a partial population of ETV1-positive excitatory neurons (green). Almost all (>90%) PDYN- and RXFP1-positive neurons expressed *Etv1*. RXFP1 and PDYN data are from Fig. 4d. Scale bar, 10 µm.

Extended Data Fig. 8 Characterization of *Rxfp1-Cre* and *Pdyn-Cre* activation-derived consumption phenotypes.

a, Photostimulation of RXFP1 neurons in the SFO triggered robust drinking preference to pure water ($n = 9$ mice), while photostimulation of SFO^{Pdyn} neurons induced indiscriminate intake of both water and 0.5 M KCl ($n = 6$

mice). We observed similar preference in OVLT neurons ($n = 6$ mice for *Rxfp1-Cre*, and $n = 4$ mice for *Pdyn-Cre*). **b**, Drinking patterns of *Rxfp1-Cre* and *Pdyn-Cre* animals to different concentrations and various salts.

Photoactivation of SFO^{Rxfp1} induced robust pure water drinking, while the same animal avoided NaCl (0.3 M, $n = 4$ mice), KCl (0.3 M, $n = 5$ mice), MgCl₂ (0.05 M, $n = 5$) and CaCl₂ (0.05M, $n = 5$). Animals that receive stimulation in SFO^{Pdyn} neurons accepted all of the above solutions ($n = 7$ mice for NaCl and KCl, 5 mice for MgCl₂ and CaCl₂). **c**, Photostimulation of SFO^{Pdyn} and SFO^{Rxfp1} neurons triggered comparable total fluid intake ($n = 7$ mice for SFO^{Pdyn}, $n = 5$ mice for SFO^{Rxfp1}). The total lick number over 20 trials was quantified. **d**, Photostimulation of SFO^{Pdyn} neurons did not drive sodium-licking behaviour ($n = 6$ animals). Schematic of rock salt behaviour test (left). Representative salt licking raster plots under sodium deprivation (-Sodium), sated (- Light) and photostimulation (+ Light) are presented (middle). Triangle marks the start time of recording. The total bout duration is quantified (right). **e**, Hypovolaemic stress failed to activate sodium appetite neurons in Pre-LC. Representative images of FOS (red) and FOXP2 expression (a genetic marker for sodium appetite neurons, green) under sated (Control), hypovolaemic thirst (Furosemide) and sodium deprived conditions (Sodium deprivation). Quantification shows percentage of activated sodium appetite neurons (double positive / FOXP2 positive neurons, right, $n = 4$ mice per group). Scale bar, 50 μm. * $P < 0.05$, ** $P < 0.01$, by two-tailed Wilcoxon matched-pairs signed-rank test, Mann–Whitney test, Friedman test or Kruskal–Wallis test followed by a Dunn’s post-test. Data are shown as mean ± s.e.m.

Supplementary information

Supplementary Table 1

| Statistical summary table.

Reporting Summary

Video 1

Optogenetic stimulation of SFO^{Rxfp1} neurons. Optogenetic activation of Rxfp1 neurons in SFO induced robust pure water consumption (left) but the same animals avoided hyperosmotic saline (0.5M NaCl, right). Light was delivered for 10 sec.

[Video 2](#)

Optogenetic stimulation of SFO^{Pdyn} neurons. Optogenetic stimulation of Pdyn neurons in SFO triggered consumption of both water (left) and hyperosmotic salt solution (0.5M NaCl, right). Light was delivered for 10 sec.

Rights and permissions

[Reprints and Permissions](#)

About this article



Check for
updates

Cite this article

Pool, AH., Wang, T., Stafford, D. *et al.* The cellular basis of distinct thirst modalities. *Nature* **588**, 112–117 (2020). <https://doi.org/10.1038/s41586-020-2821-8>

[Download citation](#)

- Received: 29 January 2020
- Accepted: 16 July 2020
- Published: 14 October 2020

- Issue Date: 03 December 2020
- DOI: <https://doi.org/10.1038/s41586-020-2821-8>

Comments

By submitting a comment you agree to abide by our [Terms](#) and [Community Guidelines](#). If you find something abusive or that does not comply with our terms or guidelines please flag it as inappropriate.

[Access through your institution](#)

[Change institution](#)

[Buy or subscribe](#)

This article was downloaded by **calibre** from <https://www.nature.com/articles/s41586-020-2821-8>

| [Section menu](#) | [Main menu](#) |

- Article
- [Published: 11 November 2020](#)

A measure of smell enables the creation of olfactory metamers

- [Aharon Ravia](#) [ORCID: orcid.org/0000-0003-2183-9254](#)¹,
- [Kobi Snitz](#)¹,
- [Danielle Honigstein](#)¹,
- [Maya Finkel](#)¹,
- [Rotem Zirler](#)¹,
- [Ofer Perl](#)¹,
- [Lavi Secundo](#)¹,
- [Christophe Laudamiel](#)²,
- [David Harel](#)³ &
- [Noam Sobel](#) [ORCID: orcid.org/0000-0002-3232-9391](#)¹

[Nature](#) volume 588, pages118–123(2020)[Cite this article](#)

- 2919 Accesses
- 124 Altmetric
- [Metrics details](#)

Subjects

- [Computational neuroscience](#)
- [Intellectual-property rights](#)
- [Olfactory system](#)

Abstract

Wavelength is a physical measure of light, and the intricate understanding of its link to perceived colour enables the creation of perceptual entities such as metamers—non-overlapping spectral compositions that generate identical colour percepts¹. By contrast, scientists have been unable to develop a physical measure linked to perceived smell, even one that merely reflects the extent of perceptual similarity between odorants². Here, to generate such a measure, we collected perceptual similarity estimates of 49,788 pairwise odorants from 199 participants who smelled 242 different multicomponent odorants and used these data to refine a predictive model that links odorant structure to odorant perception³. The resulting measure combines 21 physicochemical features of the odorants into a single number—expressed in radians—that accurately predicts the extent of perceptual similarity between multicomponent odorant pairs. To assess the usefulness of this measure, we investigated whether we could use it to create olfactory metamers. To this end, we first identified a cut-off in the measure: pairs of multicomponent odorants that were within 0.05 radians of each other or less were very difficult to discriminate. Using this cut-off, we were able to design olfactory metamers—pairs of non-overlapping molecular compositions that generated identical odour percepts. The accurate predictions of perceptual similarity, and the ensuing creation of olfactory metamers, suggest that we have obtained a valid olfactory measure, one that may enable the digitization of smell.

[Access through your institution](#)

[Change institution](#)

[Buy or subscribe](#)

Access options

Subscribe to Journal

Get full journal access for 1 year

185,98 €

only 3,58 € per issue

Subscribe

All prices are NET prices.
VAT will be added later in the checkout.

Rent or Buy article

Get time limited or full article access on ReadCube.

from \$8.99

Rent or Buy

All prices are NET prices.

Additional access options:

- [Log in](#)
- [Access through your institution](#)
- [Learn about institutional subscriptions](#)

Fig. 1: The measure of smell predicts perceived similarity of real-world multicomponent odorants.

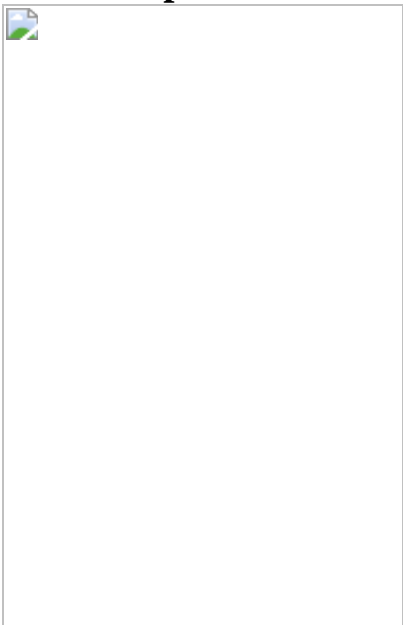


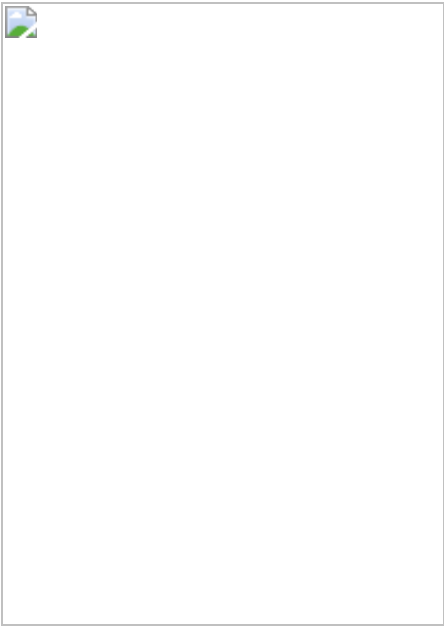
Fig. 2: The measure of smell predicts the perceived similarity of rose, violet and asafoetida.



Fig. 3: The measure of smell predicts performance in olfactory discrimination tasks.



Fig. 4: The measure of smell enables the creation of an olfactory metamer.



Data availability

All data generated during this study are included in the Article and its [Supplementary Information](#). All the odorants used are included in Supplementary Table [1](#), all behavioural similarity results are included in Supplementary Table [2](#) and all behavioural discrimination results are included in Supplementary Table [3](#). An additional external dataset used can be found in the supplementary material of a previously published study^{[15](#)}.

Code availability

The custom code used to process the data collected in this study is available at <https://gitlab.com/AharonR/olfaction>.

References

1. 1. Wandell, B. A. *Foundations of Vision* (Sinauer Associates, 1995).
2. 2.

Bell, A. G. Discovery and invention. *Natl Geogr. Mag.* **25**, 649–655 (1914).

[Google Scholar](#)

3. 3.

Snitz, K. et al. Predicting odor perceptual similarity from odor structure. *PLOS Comput. Biol.* **9**, e1003184 (2013).

[CAS](#) [Article](#) [PubMed](#) [PubMed Central](#) [Google Scholar](#)

4. 4.

Khan, R. M. et al. Predicting odor pleasantness from odorant structure: pleasantness as a reflection of the physical world. *J. Neurosci.* **27**, 10015–10023 (2007).

[CAS](#) [Article](#) [PubMed](#) [PubMed Central](#) [Google Scholar](#)

5. 5.

Zarzo, M. & Stanton, D. T. Understanding the underlying dimensions in perfumers' odor perception space as a basis for developing meaningful odor maps. *Atten. Percept. Psychophys.* **71**, 225–247 (2009).

[Article](#) [PubMed](#) [Google Scholar](#)

6. 6.

Koulakov, A. A., Kolterman, B. E., Enikolopov, A. G. & Rinberg, D. In search of the structure of human olfactory space. *Front. Syst. Neurosci.* **5**, 65 (2011).

[Article](#) [PubMed](#) [PubMed Central](#) [Google Scholar](#)

7. 7.

Keller, A. et al. Predicting human olfactory perception from chemical features of odor molecules. *Science* **355**, 820–826 (2017).

[ADS](#) [CAS](#) [Article](#) [PubMed](#) [PubMed Central](#) [Google Scholar](#)

8. 8.

Weiss, T. et al. Perceptual convergence of multi-component mixtures in olfaction implies an olfactory white. *Proc. Natl Acad. Sci. USA* **109**, 19959–19964 (2012).

[ADS](#) [CAS](#) [Article](#) [PubMed](#) [Google Scholar](#)

9. 9.

Zhou, Y., Smith, B. H. & Sharpee, T. O. Hyperbolic geometry of the olfactory space. *Sci. Adv.* **4**, eaaq1458 (2018).

[ADS](#) [Article](#) [PubMed](#) [PubMed Central](#) [Google Scholar](#)

10. 10.

Cain, W. S. Odor intensity: differences in the exponent of the psychophysical function. *Percept. Psychophys.* **6**, 349–354 (1969).

[Article](#) [Google Scholar](#)

11. 11.

Olsson, M. J. An integrated model of intensity and quality of odor mixtures. *Ann. NY Acad. Sci.* **855**, 837–840 (1998).

[ADS](#) [CAS](#) [Article](#) [PubMed](#) [Google Scholar](#)

12. 12.

Halpern, S. D., Andrews, T. J. & Purves, D. Interindividual variation in human visual performance. *J. Cogn. Neurosci.* **11**, 521–534 (1999).

[CAS](#) [Article](#) [PubMed](#) [Google Scholar](#)

13. 13.

Thiede, T. et al. PEAQ—the ITU standard for objective measurement of perceived audio quality. *J. Audio Eng. Soc.* **48**, 3–29 (2000).

[Google Scholar](#)

14. 14.

Yuhong, Y. et al. Auditory attention based mobile audio quality assessment. In *IEEE International Conference on Acoustics, Speech and Signal Processing (ICASSP)* 1389–1393 (IEEE, 2014).

15. 15.

Bushdid, C., Magnasco, M. O., Vosshall, L. B. & Keller, A. Humans can discriminate more than 1 trillion olfactory stimuli. *Science* **343**, 1370–1372 (2014).

[ADS](#) [CAS](#) [Article](#) [PubMed](#) [PubMed Central](#) [Google Scholar](#)

16. 16.

Cain, W. S. Differential sensitivity for smell: “noise” at the nose. *Science* **195**, 796–798 (1977).

[ADS](#) [CAS](#) [Article](#) [PubMed](#) [Google Scholar](#)

17. 17.

Booth, D. A. & Freeman, R. P. Discriminative feature integration by individuals. *Acta Psychol. (Amst.)* **84**, 1–16 (1993).

[CAS](#) [Article](#) [Google Scholar](#)

18. 18.

Prins, N. *Psychophysics: A Practical Introduction* (Academic, 2016).

19. 19.

Ennis, J. M., Ennis, D. M., Yip, D. & O'Mahony, M. Thurstonian models for variants of the method of tetrads. *Br. J. Math. Stat. Psychol.* **51**, 205–215 (1998).

[Article](#) [Google Scholar](#)

20. 20.

Ennis, D. M. The power of sensory discrimination methods. *J. Sens. Stud.* **8**, 353–370 (1993).

[Article](#) [Google Scholar](#)

21. 21.

Hamwi, V. & Landis, C. Memory for color. *J. Psychol.* **39**, 183–194 (1955).

[Article](#) [Google Scholar](#)

22. 22.

Rousseau, B. Meyer, A. & O'Mahony, M. Power and sensitivity of the same-different test: comparison with triangle and duo-trio methods. *J. Sens. Stud.* **13**, 149–173 (1998).

[Article](#) [Google Scholar](#)

23. 23.

Stillman, J. A. & Irwin, R. J. Advantages of the same-different method over the triangular method for the measurement of taste discrimination. *J. Sens. Stud.* **10**, 261–272 (1995).

[Article](#) [Google Scholar](#)

24. 24.

Laska, M. & Teubner, P. Olfactory discrimination ability of human subjects for ten pairs of enantiomers. *Chem. Senses* **24**, 161–170 (1999).

[CAS](#) [Article](#) [PubMed](#) [Google Scholar](#)

25. 25.

Sela, L. & Sobel, N. Human olfaction: a constant state of change-blindness. *Exp. Brain Res.* **205**, 13–29 (2010).

[Article](#) [PubMed](#) [PubMed Central](#) [Google Scholar](#)

26. 26.

Mainland, J. D. et al. The missense of smell: functional variability in the human odorant receptor repertoire. *Nat. Neurosci.* **17**, 114–120 (2014).

[CAS](#) [Article](#) [PubMed](#) [Google Scholar](#)

27. 27.

Brainard, D. H. & Hurlbert, A. C. Colour vision: understanding #TheDress. *Curr. Biol.* **25**, R551–R554 (2015).

[CAS](#) [Article](#) [PubMed](#) [Google Scholar](#)

28. 28.

Jameson, D. & Hurvich, L. M. Theoretical analysis of anomalous trichromatic color vision. *J. Opt. Soc. Am.* **46**, 1075–1089 (1956).

[ADS](#) [Article](#) [PubMed](#) [Google Scholar](#)

29. 29.

Rüfer, F. et al. Age-corrected reference values for the Heidelberg multi-color anomaloscope. *Graefes Arch. Clin. Exp. Ophthalmol.* **250**, 1267–1273 (2012).

[Article](#) [PubMed](#) [Google Scholar](#)

30. 30.

Meister, M. On the dimensionality of odor space. *eLife* **4**, e07865 (2015).

[Article](#) [PubMed](#) [PubMed Central](#) [Google Scholar](#)

31. 31.

Gerkin, R. C. & Castro, J. B. The number of olfactory stimuli that humans can discriminate is still unknown. *eLife* **4**, e08127 (2015).

[Article](#) [PubMed](#) [PubMed Central](#) [Google Scholar](#)

32. 32.

Mamlouk, A. M., Chee-Ruiter, C., Hofmann, U. G. & Bower, J. M. Quantifying olfactory perception: mapping olfactory perception space by using multidimensional scaling and self-organizing maps. *Neurocomputing* **52–54**, 591–597 (2003).

[Article](#) [Google Scholar](#)

33. 33.

Fan, M., Qiao, H. & Zhang, B. Intrinsic dimension estimation of manifolds by incising balls. *Pattern Recognit.* **42**, 780–787 (2009).

[Article](#) [Google Scholar](#)

34. 34.

Camastra, F. Data dimensionality estimation methods: a survey. *Pattern Recognit.* **36**, 2945–2954 (2003).

[Article](#) [Google Scholar](#)

35. 35.

Haddad, R. et al. Global features of neural activity in the olfactory system form a parallel code that predicts olfactory behavior and perception. *J. Neurosci.* **30**, 9017–9026 (2010).

[CAS](#) [Article](#) [PubMed](#) [PubMed Central](#) [Google Scholar](#)

36. 36.

Kleiner, M. et al. What's new in psychtoolbox-3. *Perception* **36**, 1–16 (2007).

37. 37.

Pelli, D. G. The VideoToolbox software for visual psychophysics: transforming numbers into movies. *Spat. Vis.* **10**, 437–442 (1997).

[CAS](#) [Article](#) [PubMed](#) [Google Scholar](#)

38. 38.

Brainard, D. H. The psychophysics toolbox. *Spat. Vis.* **10**, 433–436 (1997).

[CAS](#) [Article](#) [PubMed](#) [PubMed Central](#) [Google Scholar](#)

39. 39.

Dragon: software for the calculation of molecular descriptors v.6.0 (Talete srl, 2011).

40. 40.

Macmillan, N. A. & Creelman, C. D. *Detection Theory: A User's Guide* (Psychology Press, 2004).

41. 41.

Rousseau, B. & Ennis, D. M. A Thurstonian model for the dual pair (4IAX) discrimination method. *Percept. Psychophys.* **63**, 1083–1090 (2001).

[CAS](#) [Article](#) [PubMed](#) [Google Scholar](#)

42. 42.

Kaplan, H. L., Macmillan, N. A. & Creelman, C. D. Tables of d' for variable-standard discrimination paradigms. *Behav. Res. Meth. Instrum.* **10**, 796–813 (1978).

[Article](#) [Google Scholar](#)

[Download references](#)

Acknowledgements

This work was primarily supported by the Horizon 2020 FET Open project NanoSmell (662629). Additional support from grant 1599/14 from the Israel Science Foundation, by a grant from Unilever, and by the Rob and Cheryl McEwen Fund for Brain Research.

Author information

Affiliations

1. Department of Neurobiology, Weizmann Institute of Science, Rehovot, Israel

Aharon Ravia, Kobi Snitz, Danielle Honigstein, Maya Finkel, Rotem Zirler, Ofer Perl, Lavi Secundo & Noam Sobel

2. DreamAir LLC, New York, NY, USA

Christophe Laudamiel

3. Department of Computer Science and Applied Mathematics,
Weizmann Institute of Science, Rehovot, Israel

David Harel

Authors

1. Aharon Ravia

[View author publications](#)

You can also search for this author in [PubMed](#) [Google Scholar](#)

2. Kobi Snitz

[View author publications](#)

You can also search for this author in [PubMed](#) [Google Scholar](#)

3. Danielle Honigstein

[View author publications](#)

You can also search for this author in [PubMed](#) [Google Scholar](#)

4. Maya Finkel

[View author publications](#)

You can also search for this author in [PubMed](#) [Google Scholar](#)

5. Rotem Zirler

[View author publications](#)

You can also search for this author in [PubMed](#) [Google Scholar](#)

6. Ofer Perl

[View author publications](#)

You can also search for this author in [PubMed](#) [Google Scholar](#)

7. Lavi Secundo

[View author publications](#)

You can also search for this author in [PubMed](#) [Google Scholar](#)

8. Christophe Laudamiel

[View author publications](#)

You can also search for this author in [PubMed](#) [Google Scholar](#)

9. David Harel

[View author publications](#)

You can also search for this author in [PubMed](#) [Google Scholar](#)

10. Noam Sobel

[View author publications](#)

You can also search for this author in [PubMed](#) [Google Scholar](#)

Contributions

A.R., K.S., L.S., D. Harel and N.S. developed the concepts. A.R. and N.S. designed experiments. A.R., R.Z. and M.F. ran experiments. A.R., K.S., O.P. and N.S. analysed data. C.L. developed scent formulas. A.R., D. Honigstein, K.S., O.P. and N.S. constructed the web-tool. A.R., O.P., D. Harel and N.S. wrote the paper.

Corresponding authors

Correspondence to [Aharon Ravia](#) or [Noam Sobel](#).

Ethics declarations

Competing interests

The Office of Technology Licensing at the Weizmann Institute of Science is filing for patents on the algorithms developed in this study. A small portion of this work was supported by a research grant from Unilever, a company with interests in the fragrance industry. Unilever had no input or impact on the design of experiments, or on analysis and presentation of the results. C.L. is the owner of DreamAir LLC, a company with interests in the fragrance industry. DreamAir had no input or impact on the analysis and presentation of the results.

Additional information

Peer review information *Nature* thanks Tatyana Sharpee and the other, anonymous, reviewer(s) for their contribution to the peer review of this work.

Publisher's note Springer Nature remains neutral with regard to jurisdictional claims in published maps and institutional affiliations.

Extended data figures and tables

Extended Data Fig. 1 The odorants used projected into perceptual space.

a, As in the main text, the 148 molecules used across experiments overlaid on 4,046 molecules within the first and second principal components of the 21-descriptor physicochemical space. **b**, The same molecules within the first and second principal components of perceptual space. Perceptual space data for 470 molecules as background (data from previously published studies^{4,7}), containing 115 of the 148 molecules that we used. **c**, Histograms showing the experiment odorant distribution on each principal component (PC) in the range of PC1–PC6. The principal components were computed as in **a**, on the 21-descriptor physicochemical space. There is a large decline in the explained variance from the third principal component onward. **d**, Histograms showing the distances between all odorant pairs, per experiment. The distances are summed (black line) for the overall distribution. Although monomolecules were not used as a stimulus for

discrimination, this is to show that there was no bias in their selection, because for each experiment the distances of the pairs spanned a range of distances.

Extended Data Fig. 2 Experimental flowchart.

Ordered depiction of the tasks across the seven reported experiments.

Extended Data Fig. 3 Factoring and predicting odorant intensity.

a, b, Factoring odorant intensity. **a**, In experiment 1, the overall MC-odorant intensity could have been used to determine similarity, $n = 23$ participants for intensity ratings and 22 participants for similarity ratings. Correlation coefficient $r = -0.61$, $P < 6 \times 10^{-11}$, $n = 95$ ($r = -0.57$, $P < 6 \times 10^{-11}$, $n = 91$, for comparisons excluding identical pairs). To check whether intensity similarity and angle-distance similarity account for overlapping information, we built a linear model considering the two factors. We found that this two-factor model could account for larger variability than each of the models alone (adjusted $R^2 = 0.37$ versus adjusted $R^2 = 0.32$ for intensity difference and adjusted $R^2 = 0.16$ for angle distance). Both factors were significant in this model (both $P < 0.005$). In other words, although intensity differences could explain variance in the results, angle distance was a significant factor as well, and could explain independent variance. **b**, The same analysis for experiment 2. Here, MC-odorant intensity was weakly, albeit significantly correlated with MC-odorant similarity ($n = 30$ participants for intensity ratings and 29 participants for similarity ratings, correlation coefficient $r = -0.22$, $P = 0.03$, $n = 95$) and this correlation was entirely explained by comparing odorants to themselves, and once these comparisons were removed, the correlation was lost altogether ($r = 0.04$, $P = 0.68$, $n = 91$ for comparisons excluding identical pairs). Thus, experiment 2 largely negated this overall concern. **c–i**, Predicting odorant intensity. **c**, Estimated performance of predicted intensity model as correlation between actual and predicted intensity on k -fold test-set ([Supplementary Methods](#)). Expected variance estimated using cross-validation (k varied according to the number of

molecules (n) used in each concentration; $k = 8, 10, 10$ and 5 , and $n = 134, 422, 346$ and 58 for concentrations of $10^{-1}, 10^{-3}, 10^{-5}$ and 10^{-7} , respectively). In the violin plot large points are averages of k -folds, vertical lines are quartiles 2–3. All four models have correlations significantly larger than zero, with peak at the 10^{-3} concentration (average $r = 0.67$). **d–i**, We used the 10^{-3} concentration data ([Supplementary Methods](#)) to devise a predictive model for intensity ratings, this time excluding molecules used in experiments 1 and 2 to avoid overfitting. **d, g**, Intensity predictions generated by this model for monomolecule intensities in experiments 1 (**d**) and 2 (**g**). The x axis is actual intensity (averages of $n = 23$ participants, 2 repetitions each for experiment 1; and $n = 29$ participants, 3 repetitions each for experiment 2) and the y axis is predicted intensity. We show correlations in black and in red to be compatible with other panels, although no zero intensity odours were included. **d**, Correlation coefficient $r = 0.36$, $P < 0.02$, $n = 44$ monomolecules. **g**, Correlation coefficient $r = 0.68$, $P < 7 \times 10^{-7}$, $n = 43$ monomolecules. **e, h**, Angle distance estimation using the intensity factor. The intensity factor was calculated based on predicted intensity (**d, g**) as in Fig. [1e](#); these predicted factors were then used to model MC-odorants. Finally, angle distances between pairs of MC-odorants were calculated according to predicted intensity compared to those obtained by rated intensity (as used in the main text). **e**, Correlation coefficient $r = 0.53$, $P < 3 \times 10^{-8}$, $n = 95$ ($r = 0.29$, $P < 6 \times 10^{-3}$, $n = 91$ for comparisons excluding identical pairs). **h**, Correlation coefficient $r = 0.73$, $P < 2 \times 10^{-17}$, $n = 95$ ($r = 0.56$, $P < 7 \times 10^{-9}$, $n = 91$ for comparisons excluding identical pairs). **f, i**, Prediction of measured similarity from angle distances calculated using predicted intensity (similar to Figs. [1f, 2c](#)). In the scatter plot, each dot is a pairwise comparison of MC-odorants; the y axis shows their actual similarity as rated by participants (for experiment 1, $n = 22$, 2 repetitions; for experiment 2, $n = 29$, 2 repetitions) and the x axis shows their angle distance according to predicted intensity. Red regression lines include comparisons of identical MC-odorants (zero angle distance), black regression lines are with those comparisons removed. **f**, Correlation coefficient $r = -0.50$, $P < 3 \times 10^{-7}$, $n = 95$ ($r = -0.29$, $P < 6 \times 10^{-3}$, $n = 91$ for comparisons excluding identical pairs). **i**, Correlation coefficient $r = 0.74$, $P < 9 \times 10^{-19}$, $n = 95$ ($r = 0.54$, $P < 5 \times 10^{-8}$, $n = 91$ for comparisons excluding identical pairs). **f, i**, Correlations between previous

and current results were not significantly different. **f**, Experiment 1, difference between result using rated and predicted monomolecule intensities ($r = -0.41$ and $r = -0.29$, respectively) was not significantly different ($Z = 0.91$, $P = 0.36$, two-tailed, $n = 91$ comparisons). **i**, Experiment 2, same procedure, difference between $r = -0.69$ and $r = -0.54$ was not significantly different ($Z = -1.62$, $P = 0.011$, two-tailed, $n = 91$ comparisons). We summarize that this is a promising direction for the future, but beyond the scope of this manuscript.

Extended Data Fig. 4 Variability in predictions of perceptual similarity from structure in olfaction and audition.

a, Recreation of Fig. 2c, which shows our underlying results, with the point of maximal variance highlighted with a blue ellipse. **b**, Data extracted from figure 22 from a previously published study¹³, which shows the state-of-the-art predictions from around ad 2000 of sound similarity from sound structure (overlaying points may be missing, as these data were extracted from the graph). Correlation coefficient $r = -0.80$, $P < 2 \times 10^{-103}$, $n = 462$. **c**, Data extracted from figure 3 of a previously published study¹⁴, which shows the state-of-the-art predictions from around ad 2014 of sound similarity from sound structure. Note that we formatted the data to compare the datapoints to our data by putting the data into the same graph colour and structure and by reversing the axes. Correlation coefficient $r = -0.84$, $P < 3 \times 10^{-26}$, $n = 96$. **d**, Comparison of points of maximal variance across datasets (blue, olfaction; red and green, audition). In audition technology, the major standard is PEAQ—the ITU standard for objective measurement of perceived audio quality. PEAQ defines the subjective difference grade, which is the equivalent of our ‘perceived similarity’, and the objective difference grade (ODG), which is the equivalent of our ‘angle distance’. The field is tasked with developing different objective difference grades, which can be made of various combined measures such as frequency, timbre, power, and so on. We observe that the overall correlation in audition is not very different from olfaction, and that the variability at a given physical distance is perhaps even greater in audition compared with olfaction.

Extended Data Fig. 5 From angle distance to perceived similarity.

a, c, Scatter plots on which each dot is a pairwise comparison of two odorants; the *y* axis shows their actual similarity as rated by participants and the *x* axis shows their distance according to the model. **a**, Data from the experiment containing rose, violet, asafoetida and 11 additional MC-odorants. All comparisons containing rose are shown in red, all comparisons containing violet in violet and all comparisons containing asafoetida are shown in mustard ($n = 29$ participants, 2 repetitions each). Correlation coefficient $r = -0.55$, $P < 3 \times 10^{-5}$, $n = 52$ ($r = -0.31$, $P < 0.03$, $n = 48$ for comparisons excluding identical pairs). **b**, Rated similarity versus angle distance between rose, violet and asafoetida comparisons in this experiment. The rated similarity data (dark blue) are the average of $n = 29$ participants, mean of 2 repetitions. Data are mean \pm s.e.m. Blue circles are individual ratings of similarity. **c**, Data from experiments 1 and 2 used for model building, taken from Figs. 1f, 2c. Correlation coefficient $r = -0.66$, $P < 3 \times 10^{-25}$, $n = 190$ ($r = -0.55$, $P < 2 \times 10^{-15}$, $n = 182$ for comparisons excluding identical pairs). **d**, End result of predicted versus actual similarity of rose, violet and asafoetida, rated similarity (dark blue) is as in **b**. Data for predicted similarity (light blue) presented as mean prediction using the linear regression model described in **c** (red line); the error bars show the confidence intervals ($P = 0.05$) for this model prediction. See [Supplementary Methods](#) for transformation from angle distance to predicted similarity.

Extended Data Fig. 6 Variability in individual performance.

a, Performance displayed by individual participant rather than by odorant comparison, sorted by performance. The *z* axis and colour both code participant performance accuracy. White, 41.8% accuracy or $d' = 1$; red, $d' < 1$; blue, $d' > 1$. **b**, Performance displayed by individual participants rather than by odorant comparison, sorted by performance. Colour codes are shown for the participant d' as estimated in Fig. 3c. white, $d' = 1$; red, $d' < 1$; blue, $d' > 1$.

Extended Data Fig. 7 Testing of significance by shuffling.

We randomly shuffled performance outcome in the previously published dataset¹⁵, and in experiments 4–6. For each MC-odorant pair, we assigned performance (means of the participants) randomly 10,000 times, and then computed the correlation between angle distance and ‘shuffled’ performance. **a**, A copy of Fig. 3b. **b**, A set of 100 traces (randomly picked for visualization purposes) of a moving average of shuffled data, similar to the black line in **a**. Red dashed line in **a** and **b** is performance of $d' = 1$ (41.8% correct). **c–f**, Histogram of correlations between angle distance and shuffled performance. Red line is the correlation of the observed data. **c**, The previously published data¹⁵. The correlation of observed data ($r = 0.50$, $n = 310$ comparisons) outperforms the correlation of shuffled data ($P < 10^{-4}$, $n = 10,000$ repetitions). **d–f**, Angle distance is shown on a log scale. **d**, Experiment 4, the correlation of observed data ($r = 0.51$, $n = 50$ comparisons) outperforms the correlation of shuffled data ($P < 10^{-4}$, $n = 10,000$ repetitions). **e**, Experiment 5, the correlation of observed data ($r = 0.42$, $n = 50$ comparisons) is significantly stronger than the correlation of shuffled data ($P = 0.0009$, $n = 10,000$ repetitions). **f**, Experiment 6, the correlation of observed data ($r = 0.53$, $n = 40$ comparisons) is significantly stronger than the correlation of shuffled data ($P = 0.0013$, $n = 10,000$ repetitions). **g–i**, Same as **d–f**, only here angle distance was analysed using a linear rather than logarithmic scale. **g**, Experiment 4, the correlation of observed data ($r = 0.61$, $n = 50$ comparisons) outperforms the correlation of shuffled data ($P < 10^{-4}$, $n = 10,000$ repetitions). **h**, Experiment 5, the correlation of observed data ($r = 0.43$, $n = 50$ comparisons) is significantly stronger than the correlation of shuffled data ($P = 0.0015$, $n = 10,000$ repetitions). **i**, Experiment 6, the correlation of observed data ($r = 0.45$, $n = 40$ comparisons) outperforms the correlation of shuffled data ($P < 10^{-4}$, $n = 10,000$ repetitions). **j–l**, Here we verify the validity of the choice of performance threshold, namely $d' = 1$, in our data. For this verification, we calculate the null distribution for d' for the discrimination tasks in experiments 4–6. To generate a meaningful distribution, we carefully choose the shuffling in this analysis. For our data, we shuffled the correct responses for each participant in each session, and assigned the responses to different MC-odorant pairs. For each participant, we used a different label

assignment; this way we disentangle the difficulty of the task, and produce a statistic on the frequency at which one would expect each d' by chance. The histograms of performance in the different experiments are shown in the case in which the data of the participants have been shuffled participants. the red areas show the bottom and top 5%; the grey line is $d' = 1$. **j**, Experiment 4. **k**, Experiment 5. **l**, Experiment 6.

Extended Data Fig. 8 Perceptual independence of metamers.

We wondered whether metamers are simply instances of ‘olfactory white’. This would imply that the difference between (not within) the 3 metamer pairs would be under 0.05 radians. To address this question, we measured the distances between the 3 metamer pairs, which are as follows: pair 1 and pair 2, 0.11 radians; pair 1 and pair 3, 0.13 radians; pair 2 and pair 3, 0.07 radians. In other words, each metamer is a distinct odour. Moreover, we next compared the metamers to ‘olfactory white’. We selected the ‘best’ white from a previously published study⁸ and measured its distance from each of the metamers. The obtained minimal distances were 0.25, 0.24 and 0.24, all of which are much higher than 0.05 radians. One may note that the white in the previous study⁸ may not have been ‘true White’, as indeed that study did not have the underlying computational framework developed here. Moreover, that study was restricted to about 30 components. To address this, we generated 1,000 virtual versions of white odours, by combining different sets of 100 components. We observe that all mean distances between the metamers and these whites are above 0.1 radians, and that the minimal distance of any pair to any white is larger than 0.05 radians. **a–c**, Histograms show distances between current metamer pairs to the 1,000 different white odours that we generated. Distance between one odour (of the metamer pair) to the whites is shown in blue, and distance between the other odour (of the metamer pair) to the whites is shown in red. Circular points show distances of each odour in the pair to the three previously described white odours⁸. Each panel shows one of the three metamer pairs reported in this paper.

Extended Data Table 1 The 21 physicochemical descriptors used for the optimized angle model

[Full size table](#)

Extended Data Table 2 Formulas for rose, violet, asafoetida and for three olfactory metamers

[Full size table](#)

Supplementary information

Supplementary Information

Supplementary Information document containing Supplementary Discussion and Supplementary Methods.

Reporting Summary

Supplementary Table

Supplementary Table 1: containing all manuscript odorants and their intensities.

Supplementary Table

Supplementary Table 2: containing all manuscript similarity ratings.

Supplementary Table

Supplementary Table 3: containing all manuscript discrimination results.

Rights and permissions

Reprints and Permissions

About this article



Check for
updates

Cite this article

Ravia, A., Snitz, K., Honigstein, D. *et al.* A measure of smell enables the creation of olfactory metamers. *Nature* **588**, 118–123 (2020).
<https://doi.org/10.1038/s41586-020-2891-7>

[Download citation](#)

- Received: 20 December 2018
- Accepted: 19 August 2020
- Published: 11 November 2020
- Issue Date: 03 December 2020
- DOI: <https://doi.org/10.1038/s41586-020-2891-7>

Comments

By submitting a comment you agree to abide by our [Terms](#) and [Community Guidelines](#). If you find something abusive or that does not comply with our terms or guidelines please flag it as inappropriate.

[Access through your institution](#)

[Change institution](#)

[Buy or subscribe](#)

This article was downloaded by **calibre** from <https://www.nature.com/articles/s41586-020-2891-7>

- Article
- [Published: 02 December 2020](#)

Reprogramming to recover youthful epigenetic information and restore vision

- [Yuancheng Lu](#) ORCID: orcid.org/0000-0002-5982-3963¹,
- [Benedikt Brommer](#)^{2,3 na1},
- [Xiao Tian](#) ORCID: orcid.org/0000-0001-5300-3596^{1 na1},
- [Anitha Krishnan](#)^{3,4 na1},
- [Margarita Meer](#)^{5,6 na1},
- [Chen Wang](#)^{2,3},
- [Daniel L. Vera](#)¹,
- [Qiurui Zeng](#)¹,
- [Doudou Yu](#)¹,
- [Michael S. Bonkowski](#)¹,
- [Jae-Hyun Yang](#)¹,
- [Songlin Zhou](#)^{2,3},
- [Emma M. Hoffmann](#)^{3,4},
- [Margarete M. Karg](#)^{3,4},
- [Michael B. Schultz](#)¹,
- [Alice E. Kane](#)¹,
- [Noah Davidsohn](#) ORCID: orcid.org/0000-0002-4470-5665⁷,
- [Ekaterina Korobkina](#)^{3,4},
- [Karolina Chwalek](#)¹,
- [Luis A. Rajman](#)¹,
- [George M. Church](#) ORCID: orcid.org/0000-0003-3535-2076⁷,
- [Konrad Hochedlinger](#) ORCID: orcid.org/0000-0001-5811-5386⁸,
- [Vadim N. Gladyshev](#) ORCID: orcid.org/0000-0002-0372-7016⁵,

- [Steve Horvath ORCID: orcid.org/0000-0002-4110-3589⁹](#),
- [Morgan E. Levine⁶](#),
- [Meredith S. Gregory-Ksander^{3,4 na2}](#),
- [Bruce R. Ksander ORCID: orcid.org/0000-0001-5546-0360^{3,4 na2}](#),
- [Zhigang He ORCID: orcid.org/0000-0001-6080-6880^{2,3 na2}](#) &
- [David A. Sinclair ORCID: orcid.org/0000-0002-9936-436X^{1,10 na2}](#)

[Nature](#) volume 588, pages124–129(2020) [Cite this article](#)

- 2788 Accesses
- 743 Altmetric
- [Metrics details](#)

Subjects

- [Ageing](#)
- [DNA methylation](#)
- [Regeneration and repair in the nervous system](#)
- [Reprogramming](#)
- [Retina](#)

Abstract

Ageing is a degenerative process that leads to tissue dysfunction and death. A proposed cause of ageing is the accumulation of epigenetic noise that disrupts gene expression patterns, leading to decreases in tissue function and regenerative capacity^{1,2,3}. Changes to DNA methylation patterns over time form the basis of ageing clocks⁴, but whether older individuals retain the information needed to restore these patterns—and, if so, whether this could improve tissue function—is not known. Over time, the central nervous system (CNS) loses function and regenerative capacity^{5,6,7}. Using the eye as a model CNS tissue, here we show that ectopic expression of *Oct4* (also known as *Pou5f1*), *Sox2* and *Klf4* genes (OSK) in mouse retinal ganglion cells restores youthful DNA methylation patterns and

transcriptomes, promotes axon regeneration after injury, and reverses vision loss in a mouse model of glaucoma and in aged mice. The beneficial effects of OSK-induced reprogramming in axon regeneration and vision require the DNA demethylases TET1 and TET2. These data indicate that mammalian tissues retain a record of youthful epigenetic information—encoded in part by DNA methylation—that can be accessed to improve tissue function and promote regeneration *in vivo*.

[Access through your institution](#)

[Change institution](#)

[Buy or subscribe](#)

Access options

Subscribe to Journal

Get full journal access for 1 year

185,98 €

only 3,58 € per issue

[Subscribe](#)

All prices are NET prices.

VAT will be added later in the checkout.

Rent or Buy article

Get time limited or full article access on ReadCube.

from \$8.99

[Rent or Buy](#)

All prices are NET prices.

Additional access options:

- [Log in](#)
- [Access through your institution](#)
- [Learn about institutional subscriptions](#)

Fig. 1: AAV2-delivered polycistronic OSK promotes axon regeneration and RGC survival after optic nerve injury.

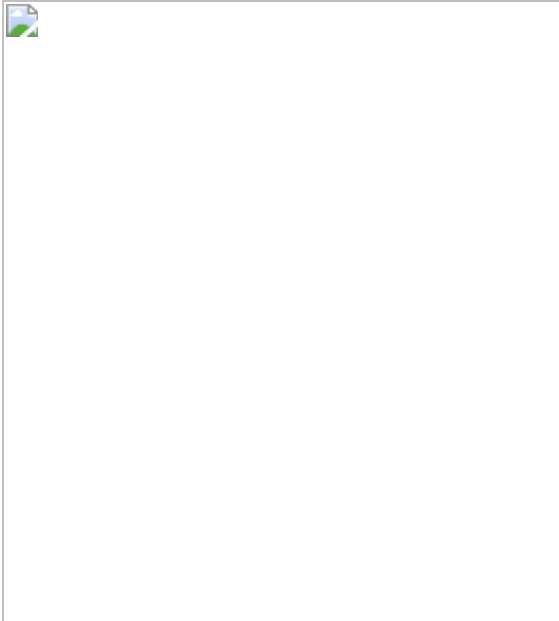


Fig. 2: DNA demethylation is required for OSK-induced axon regeneration after injury.



Fig. 3: Four weeks of OSK expression reverses vision loss after glaucomatous damage has already occurred.



Fig. 4: Restoration of youthful vision, transcriptome and DNA methylation ageing signature in old mice.



Data availability

RRBS data for DNA methylation analysis and RNA sequencing data are available in the BioSample database (NCBI) and under BioProject [PRJNA655981](#). Illumina Human Methylation EPIc array data are available in the Gene Expression Omnibus (GEO) database (NCBI) and under

[GSE147436](#). All other relevant data that support the findings of this study are available from the corresponding author upon reasonable request. [Source data](#) are provided with this paper.

Code availability

The code for determining methylation ageing signatures is provided in the Supplementary Information.

References

1. 1.

Sinclair, D. A., Mills, K. & Guarente, L. Accelerated aging and nucleolar fragmentation in yeast sgs1 mutants. *Science* **277**, 1313–1316 (1997).

[CAS](#) [Google Scholar](#)

2. 2.

Imai, S. & Kitano, H. Heterochromatin islands and their dynamic reorganization: a hypothesis for three distinctive features of cellular aging. *Exp. Gerontol.* **33**, 555–570 (1998).

[CAS](#) [Google Scholar](#)

3. 3.

Oberdoerffer, P. et al. SIRT1 redistribution on chromatin promotes genomic stability but alters gene expression during aging. *Cell* **135**, 907–918 (2008).

[CAS](#) [PubMed](#) [PubMed Central](#) [Google Scholar](#)

4. 4.

Horvath, S. DNA methylation age of human tissues and cell types. *Genome Biol.* **14**, 3156 (2013).

[Google Scholar](#)

5. 5.

Kennard, M. A. Relation of age to motor impairment in man and in subhuman primates. *Arch. Neurol. Psychiatry* **44**, 377–397 (1940).

[Google Scholar](#)

6. 6.

Goldberg, J. L., Klassen, M. P., Hua, Y. & Barres, B. A. Amacrine-signaled loss of intrinsic axon growth ability by retinal ganglion cells. *Science* **296**, 1860–1864 (2002).

[ADS](#) [CAS](#) [Google Scholar](#)

7. 7.

Yun, M. H. Changes in regenerative capacity through lifespan. *Int. J. Mol. Sci.* **16**, 25392–25432 (2015).

[CAS](#) [PubMed](#) [PubMed Central](#) [Google Scholar](#)

8. 8.

Waddington, C. H. & Kacser, H. *The Strategy of the Genes: a Discussion of Some Aspects of Theoretical Biology* (Allen & Unwin, 1957).

9. 9.

Sen, P., Shah, P. P., Nativio, R. & Berger, S. L. Epigenetic mechanisms of longevity and aging. *Cell* **166**, 822–839 (2016).

[CAS](#) [PubMed](#) [PubMed Central](#) [Google Scholar](#)

10. 10.

Sinclair, D. A. & LaPlante, M. D. *Lifespan: Why We Age—and Why We Don't Have To* 13–23, 158–175 (Simon & Schuster, 2019).

11. 11.

Shannon, C. E. A mathematical theory of communication. *Bell Syst. Tech. J.* **27**, 379–423 (1948).

[MathSciNet](#) [MATH](#) [Google Scholar](#)

12. 12.

López-Otín, C., Blasco, M. A., Partridge, L., Serrano, M. & Kroemer, G. The hallmarks of aging. *Cell* **153**, 1194–1217 (2013).

[PubMed](#) [PubMed Central](#) [Google Scholar](#)

13. 13.

Yang, J.-H. et al. Erosion of the epigenetic landscape and loss of cellular identity as a cause of aging in mammals. Preprint at <https://doi.org/10.1101/808642> (2019).

14. 14.

Takahashi, K. & Yamanaka, S. Induction of pluripotent stem cells from mouse embryonic and adult fibroblast cultures by defined factors. *Cell* **126**, 663–676 (2006).

[CAS](#) [PubMed](#) [PubMed Central](#) [Google Scholar](#)

15. 15.

Petkovich, D. A. et al. Using DNA methylation profiling to evaluate biological age and longevity interventions. *Cell Metab.* **25**, 954–960.e6 (2017).

[CAS](#) [PubMed](#) [PubMed Central](#) [Google Scholar](#)

16. 16.

Ocampo, A. et al. In vivo amelioration of age-associated hallmarks by partial reprogramming. *Cell* **167**, 1719–1733.e12 (2016).

[CAS](#) [PubMed](#) [PubMed Central](#) [Google Scholar](#)

17. 17.

Ohnishi, K. et al. Premature termination of reprogramming in vivo leads to cancer development through altered epigenetic regulation. *Cell* **156**, 663–677 (2014).

[CAS](#) [Google Scholar](#)

18. 18.

Abad, M. et al. Reprogramming in vivo produces teratomas and iPS cells with totipotency features. *Nature* **502**, 340–345 (2013).

[ADS](#) [CAS](#) [Google Scholar](#)

19. 19.

Senís, E. et al. AAV vector-mediated in vivo reprogramming into pluripotency. *Nat. Commun.* **9**, 2651 (2018).

[ADS](#) [PubMed](#) [PubMed Central](#) [Google Scholar](#)

20. 20.

Hofmann, J. W. et al. Reduced expression of MYC increases longevity and enhances healthspan. *Cell* **160**, 477–488 (2015).

[CAS](#) [PubMed](#) [PubMed Central](#) [Google Scholar](#)

21. 21.

Rand, T. A. et al. MYC releases early reprogrammed human cells from proliferation pause via retinoblastoma protein inhibition. *Cell Rep.* **23**, 361–375 (2018).

[CAS](#) [Google Scholar](#)

22. 22.

Laha, B., Stafford, B. K. & Huberman, A. D. Regenerating optic pathways from the eye to the brain. *Science* **356**, 1031–1034 (2017).

[ADS](#) [CAS](#) [PubMed](#) [PubMed Central](#) [Google Scholar](#)

23. 23.

Roska, B. & Sahel, J. A. Restoring vision. *Nature* **557**, 359–367 (2018).

[ADS](#) [CAS](#) [Google Scholar](#)

24. 24.

Moore, D. L. et al. KLF family members regulate intrinsic axon regeneration ability. *Science* **326**, 298–301 (2009).

[ADS](#) [CAS](#) [PubMed](#) [PubMed Central](#) [Google Scholar](#)

25. 25.

Geoffroy, C. G., Hilton, B. J., Tetzlaff, W. & Zheng, B. Evidence for an age-dependent decline in axon regeneration in the adult mammalian central nervous system. *Cell Rep.* **15**, 238–246 (2016).

[CAS](#) [PubMed](#) [PubMed Central](#) [Google Scholar](#)

26. 26.

Yao, K. et al. Restoration of vision after de novo genesis of rod photoreceptors in mammalian retinas. *Nature* **560**, 484–488 (2018).

[ADS](#) [CAS](#) [PubMed](#) [PubMed Central](#) [Google Scholar](#)

27. 27.

Zhang, Y. et al. Elevating growth factor responsiveness and axon regeneration by modulating presynaptic inputs. *Neuron* **103**, 39–51.e5 (2019).

[CAS](#) [PubMed](#) [PubMed Central](#) [Google Scholar](#)

28. 28.

Luo, X. et al. Enhanced transcriptional activity and mitochondrial localization of STAT3 co-induce axon regrowth in the adult central nervous system. *Cell Rep.* **15**, 398–410 (2016).

[CAS](#) [PubMed](#) [PubMed Central](#) [Google Scholar](#)

29. 29.

Park, K. K. et al. Promoting axon regeneration in the adult CNS by modulation of the PTEN/mTOR pathway. *Science* **322**, 963–966 (2008).

[ADS](#) [CAS](#) [PubMed](#) [PubMed Central](#) [Google Scholar](#)

30. 30.

Sun, F. et al. Sustained axon regeneration induced by co-deletion of PTEN and SOCS3. *Nature* **480**, 372–375 (2011).

[ADS](#) [CAS](#) [PubMed](#) [PubMed Central](#) [Google Scholar](#)

31. 31.

Olova, N., Simpson, D. J., Marioni, R. E. & Chandra, T. Partial reprogramming induces a steady decline in epigenetic age before loss of somatic identity. *Aging Cell* **18**, e12877 (2019).

[Google Scholar](#)

32. 32.

Sarkar, T. J. et al. Transient non-integrative expression of nuclear reprogramming factors promotes multifaceted amelioration of aging in human cells. *Nat. Commun.* **11**, 1545 (2020).

[ADS](#) [CAS](#) [PubMed](#) [PubMed Central](#) [Google Scholar](#)

33. 33.

Wang, M. & Lemos, B. Ribosomal DNA harbors an evolutionarily conserved clock of biological aging. *Genome Res.* **29**, 325–333 (2019).

[CAS](#) [PubMed](#) [PubMed Central](#) [Google Scholar](#)

34. 34.

Wu, X. & Zhang, Y. TET-mediated active DNA demethylation: mechanism, function and beyond. *Nat. Rev. Genet.* **18**, 517–534 (2017).

[CAS](#) [Google Scholar](#)

35. 35.

Koh, K. P. et al. Tet1 and Tet2 regulate 5-hydroxymethylcytosine production and cell lineage specification in mouse embryonic stem cells. *Cell Stem Cell* **8**, 200–213 (2011).

[CAS](#) [PubMed](#) [PubMed Central](#) [Google Scholar](#)

36. 36.

Gao, Y. et al. Replacement of Oct4 by Tet1 during iPSC induction reveals an important role of DNA methylation and hydroxymethylation in reprogramming. *Cell Stem Cell* **12**, 453–469 (2013).

[CAS](#) [Google Scholar](#)

37. 37.

Yu, H. et al. Tet3 regulates synaptic transmission and homeostatic plasticity via DNA oxidation and repair. *Nat. Neurosci.* **18**, 836–843 (2015).

[CAS](#) [PubMed](#) [PubMed Central](#) [Google Scholar](#)

38. 38.

Weng, Y.-L. et al. An intrinsic epigenetic barrier for functional axon regeneration. *Neuron* **94**, 337–346.e6 (2017).

[CAS](#) [PubMed](#) [PubMed Central](#) [Google Scholar](#)

39. 39.

Guo, J. U., Su, Y., Zhong, C., Ming, G. L. & Song, H. Hydroxylation of 5-methylcytosine by TET1 promotes active DNA demethylation in the adult brain. *Cell* **145**, 423–434 (2011).

[CAS](#) [PubMed](#) [PubMed Central](#) [Google Scholar](#)

40. 40.

Krishnan, A. et al. Overexpression of soluble Fas ligand following adeno-associated virus gene therapy prevents retinal ganglion cell death in chronic and acute murine models of glaucoma. *J. Immunol.* **197**, 4626–4638 (2016).

[CAS](#) [PubMed](#) [PubMed Central](#) [Google Scholar](#)

41. 41.

Almasieh, M. & Levin, L. A. Neuroprotection in glaucoma: animal models and clinical trials. *Ann. Rev. Vis. Sci.* **3**, 1–30 (2016).

[Google Scholar](#)

42. 42.

Levin, L. A. et al. Neuroprotection for glaucoma: requirements for clinical translation. *Exp. Eye Res.* **157**, 34–37 (2017).

[CAS](#) [Google Scholar](#)

43. 43.

McClellan, A. J. et al. Ocular surface disease and dacryoadenitis in aging C57BL/6 mice. *Am. J. Pathol.* **184**, 631–643 (2014).

[CAS](#) [PubMed](#) [PubMed Central](#) [Google Scholar](#)

44. 44.

Li, H. et al. Single-cell transcriptomes reveal diverse regulatory strategies for olfactory receptor expression and axon targeting. *Curr. Biol.* **30**, 1189–1198.e5 (2020).

[CAS](#) [Google Scholar](#)

45. 45.

Mackay, D. S., Bennett, T. M. & Shiels, A. Exome sequencing identifies a missense variant in EFEMP1 co-segregating in a family with autosomal dominant primary open-angle glaucoma. *PLoS ONE* **10**, e0132529 (2015).

[PubMed](#) [PubMed Central](#) [Google Scholar](#)

46. 46.

Marmorstein, L. Y. et al. Aberrant accumulation of EFEMP1 underlies drusen formation in Malattia Leventinese and age-related macular degeneration. *Proc. Natl Acad. Sci. USA* **99**, 13067–13072 (2002).

[ADS](#) [CAS](#) [PubMed](#) [Google Scholar](#)

47. 47.

Wu, X., Li, G. & Xie, R. Decoding the role of TET family dioxygenases in lineage specification. *Epigenetics Chromatin* **11**, 58 (2018).

[PubMed](#) [PubMed Central](#) [Google Scholar](#)

48. 48.

Neri, F. et al. Genome-wide analysis identifies a functional association of Tet1 and Polycomb repressive complex 2 in mouse embryonic stem cells. *Genome Biol.* **14**, R91 (2013).

[PubMed](#) [PubMed Central](#) [Google Scholar](#)

49. 49.

Margueron, R. & Reinberg, D. The Polycomb complex PRC2 and its mark in life. *Nature* **469**, 343–349 (2011).

[ADS](#) [CAS](#) [PubMed](#) [PubMed Central](#) [Google Scholar](#)

50. 50.

Mozhui, K. & Pandey, A. K. Conserved effect of aging on DNA methylation and association with EZH2 polycomb protein in mice and humans. *Mech. Ageing Dev.* **162**, 27–37 (2017).

[CAS](#) [PubMed](#) [PubMed Central](#) [Google Scholar](#)

51. 51.

Bar-Nur, O. et al. Small molecules facilitate rapid and synchronous iPSC generation. *Nat. Methods* **11**, 1170–1176 (2014).

[CAS](#) [PubMed](#) [PubMed Central](#) [Google Scholar](#)

52. 52.

Moran-Crusio, K. et al. Tet2 loss leads to increased hematopoietic stem cell self-renewal and myeloid transformation. *Cancer Cell* **20**, 11–24 (2011).

[CAS](#) [PubMed](#) [PubMed Central](#) [Google Scholar](#)

53. 53.

Mertens, J. et al. Directly reprogrammed human neurons retain aging-associated transcriptomic signatures and reveal age-related nucleocytoplasmic defects. *Cell Stem Cell* **17**, 705–718 (2015).

[CAS](#) [PubMed](#) [PubMed Central](#) [Google Scholar](#)

54. 54.

Shipley, M. M., Mangold, C. A. & Szpara, M. L. Differentiation of the SH-SY5Y human neuroblastoma cell line. *J. Vis. Exp.* **108**, e53193 (2016).

[Google Scholar](#)

55. 55.

Triche, T. J., Jr, Weisenberger, D. J., Van Den Berg, D., Laird, P. W. & Siegmund, K. D. Low-level processing of Illumina Infinium DNA Methylation BeadArrays. *Nucleic Acids Res.* **41**, e90 (2013).

[CAS](#) [PubMed](#) [PubMed Central](#) [Google Scholar](#)

56. 56.

Fortin, J. P., Triche, T. J., Jr & Hansen, K. D. Preprocessing, normalization and integration of the Illumina HumanMethylationEPIC array with minfi. *Bioinformatics* **33**, 558–560 (2017).

[CAS](#) [Google Scholar](#)

57. 57.

Horvath, S. et al. Epigenetic clock for skin and blood cells applied to Hutchinson Gilford Progeria Syndrome and *ex vivo* studies. *Aging (Albany NY)* **10**, 1758–1775 (2018).

[CAS](#) [Google Scholar](#)

58. 58.

Sun, D., Moore, S. & Jakobs, T. C. Optic nerve astrocyte reactivity protects function in experimental glaucoma and other nerve injuries. *J. Exp. Med.* **214**, 1411-1430 (2017).

[CAS](#) [PubMed](#) [PubMed Central](#) [Google Scholar](#)

59. 59.

Krishnan, A., Kocab, A. J., Zacks, D. N., Marshak-Rothstein, A. & Gregory-Ksander, M. A small peptide antagonist of the Fas receptor inhibits neuroinflammation and prevents axon degeneration and retinal ganglion cell death in an inducible mouse model of glaucoma. *J. Neuroinflammation* **16**, 184 (2019).

[PubMed](#) [PubMed Central](#) [Google Scholar](#)

60. 60.

Dordea, A. C. et al. An open-source computational tool to automatically quantify immunolabeled retinal ganglion cells. *Exp. Eye Res.* **147**, 1218–1235 (2013).

[Google Scholar](#)

61. 61.

Meer, M. V., Podolskiy, D. I., Tyshkovskiy, A. & Gladyshev, V. N. A whole lifespan mouse multi-tissue DNA methylation clock. *eLife* **7**, e40675 (2018).

[PubMed](#) [PubMed Central](#) [Google Scholar](#)

62. 62.

Thompson, M. J. et al. A multi-tissue full lifespan epigenetic clock for mice. *Aging (Albany NY)* **10**, 2832–2854 (2018).

[CAS](#) [Google Scholar](#)

63. 63.

Horvath, S. et al. The cerebellum ages slowly according to the epigenetic clock. *Aging (Albany NY)* **7**, 294–306 (2015).

[CAS](#) [Google Scholar](#)

64. 64.

Hoshino, A., Horvath, S., Sridhar, A., Chitsazan, A. & Reh, T. A. Synchrony and asynchrony between an epigenetic clock and developmental timing. *Sci. Rep.* **9**, 3770 (2019).

[ADS](#) [PubMed](#) [PubMed Central](#) [Google Scholar](#)

65. 65.

Levine, M. et al. A rat epigenetic clock recapitulates phenotypic aging and co-localizes with heterochromatin. *eLife* **9**, e59201 (2020).

66. 66.

Kim, D., Langmead, B. & Salzberg, S. L. HISAT: a fast spliced aligner with low memory requirements. *Nat. Methods* **12**, 357–360 (2015).

[CAS](#) [PubMed](#) [PubMed Central](#) [Google Scholar](#)

67. 67.

Liao, Y., Smyth, G. K. & Shi, W. featureCounts: an efficient general purpose program for assigning sequence reads to genomic features. *Bioinformatics* **30**, 923–930 (2014).

[CAS](#) [PubMed](#) [PubMed Central](#) [Google Scholar](#)

68. 68.

Robinson, M. D., McCarthy, D. J. & Smyth, G. K. edgeR: a Bioconductor package for differential expression analysis of digital gene expression data. *Bioinformatics* **26**, 139–140 (2010).

[CAS](#) [Google Scholar](#)

69. 69.

Carbon, S. et al. AmiGO: online access to ontology and annotation data. *Bioinformatics* **25**, 288–289 (2009).

[CAS](#) [Google Scholar](#)

70. 70.

Ashburner, M. et al. Gene Ontology: tool for the unification of biology. *Nat. Genet.* **25**, 25–29 (2000).

[CAS](#) [PubMed](#) [PubMed Central](#) [Google Scholar](#)

71. 71.

The Gene Ontology Consortium. The Gene Ontology Resource: 20 years and still GOing strong. *Nucleic Acids Res.* **47**, D330–D338 (2019).

[Google Scholar](#)

[Download references](#)

Acknowledgements

We thank A. Wagers, R. Mostoslavsky, Y. Shi, A. Das, A. Pogoutse, C. Petty, A. Coffey, B. Zhang, P. Dmitriev, K. Booher, E. Chen, J. Wang, D. Vogel, M. Thompson, A. Jacobi and S. Hou for advice and assistance; and Y. Weng, H. Song and F. Wang for reagents and mice. The work was supported by the Harvard Medical School Epigenetics Seed Grant and Development Grant; The Paul F. Glenn Foundation for Medical Research; a gift from E. Schulak; NIH awards R01AG019719 and R37AG028730 (to D.A.S.), R01EY026939 and R01EY021526 (to Z.H.), R01AG067782 and R01GM065204 (to V.N.G.) and R01AG065403 (to M.E.L. and V.N.G.). We thank Boston Children's Hospital Viral Core, which is supported by NIH5P30EY012196; and Schepens Eye Institute Core facilities, supported by NEI-P30EY003790. X.T. was supported by NIH award K99AG068303 and by NASA Postdoctoral Fellowship 80NSSC19K0439; D.L.V. was supported by NIH training grant T32AG023480; J.-H.Y. was partially supported by National Research Foundation of Korea (2012R1A6A3A03040476); B.R.K. was partially supported by the St Vincent de Paul Foundation and by NEI awards R24EY028767 and R01EY025794; and M.S.G.-K. by NEI award R21EY030276. We thank P. F. Glenn for his mentorship and support of ageing research.

Author information

Author notes

1. These authors contributed equally: Benedikt Brommer, Xiao Tian, Anitha Krishnan, Margarita Meer
2. These authors jointly supervised this work: Meredith S. Gregory-Ksander, Bruce R. Ksander, Zhigang He, David A. Sinclair

Affiliations

1. Department of Genetics, Blavatnik Institute, Paul F. Glenn Center for Biology of Aging Research, Harvard Medical School, Boston, MA,

USA

Yuancheng Lu, Xiao Tian, Daniel L. Vera, Qiurui Zeng, Doudou Yu, Michael S. Bonkowski, Jae-Hyun Yang, Michael B. Schultz, Alice E. Kane, Karolina Chwalek, Luis A. Rajman & David A. Sinclair

2. Department of Neurology, Boston Children's Hospital, Harvard Medical School, Boston, MA, USA

Benedikt Brommer, Chen Wang, Songlin Zhou & Zhigang He

3. Department of Ophthalmology, Harvard Medical School, Boston, MA, USA

Benedikt Brommer, Anitha Krishnan, Chen Wang, Songlin Zhou, Emma M. Hoffmann, Margarete M. Karg, Ekaterina Korobkina, Meredith S. Gregory-Ksander, Bruce R. Ksander & Zhigang He

4. Schepens Eye Research Institute of Mass Eye and Ear, Harvard Medical School, Boston, MA, USA

Anitha Krishnan, Emma M. Hoffmann, Margarete M. Karg, Ekaterina Korobkina, Meredith S. Gregory-Ksander & Bruce R. Ksander

5. Division of Genetics, Department of Medicine, Brigham and Women's Hospital, Harvard Medical School, Boston, MA, USA

Margarita Meer & Vadim N. Gladyshev

6. Department of Pathology, Yale School of Medicine, New Haven, CT, USA

Margarita Meer & Morgan E. Levine

7. Department of Genetics, Wyss Institute for Biologically Inspired Engineering, Harvard University, Boston, MA, USA

Noah Davidsohn & George M. Church

8. Department of Molecular Biology, Cancer Center and Center for Regenerative Medicine, Massachusetts General Hospital, Boston, MA, USA

Konrad Hochedlinger

9. Department of Human Genetics, David Geffen School of Medicine, University of California Los Angeles, Los Angeles, CA, USA

Steve Horvath

10. Laboratory for Ageing Research, Department of Pharmacology, School of Medical Sciences, The University of New South Wales, Sydney, New South Wales, Australia

David A. Sinclair

Authors

1. Yuancheng Lu

[View author publications](#)

You can also search for this author in [PubMed](#) [Google Scholar](#)

2. Benedikt Brommer

[View author publications](#)

You can also search for this author in [PubMed](#) [Google Scholar](#)

3. Xiao Tian

[View author publications](#)

You can also search for this author in [PubMed](#) [Google Scholar](#)

4. Anitha Krishnan

[View author publications](#)

You can also search for this author in [PubMed](#) [Google Scholar](#)

5. Margarita Meer

[View author publications](#)

You can also search for this author in [PubMed](#) [Google Scholar](#)

6. Chen Wang

[View author publications](#)

You can also search for this author in [PubMed](#) [Google Scholar](#)

7. Daniel L. Vera

[View author publications](#)

You can also search for this author in [PubMed](#) [Google Scholar](#)

8. Qiurui Zeng

[View author publications](#)

You can also search for this author in [PubMed](#) [Google Scholar](#)

9. Doudou Yu

[View author publications](#)

You can also search for this author in [PubMed](#) [Google Scholar](#)

10. Michael S. Bonkowski

[View author publications](#)

You can also search for this author in [PubMed](#) [Google Scholar](#)

11. Jae-Hyun Yang

[View author publications](#)

You can also search for this author in [PubMed](#) [Google Scholar](#)

12. Songlin Zhou

[View author publications](#)

You can also search for this author in [PubMed](#) [Google Scholar](#)

13. Emma M. Hoffmann

[View author publications](#)

You can also search for this author in [PubMed](#) [Google Scholar](#)

14. Margarete M. Karg

[View author publications](#)

You can also search for this author in [PubMed](#) [Google Scholar](#)

15. Michael B. Schultz

[View author publications](#)

You can also search for this author in [PubMed](#) [Google Scholar](#)

16. Alice E. Kane

[View author publications](#)

You can also search for this author in [PubMed](#) [Google Scholar](#)

17. Noah Davidsohn

[View author publications](#)

You can also search for this author in [PubMed](#) [Google Scholar](#)

18. Ekaterina Korobkina

[View author publications](#)

You can also search for this author in [PubMed](#) [Google Scholar](#)

19. Karolina Chwalek

[View author publications](#)

You can also search for this author in [PubMed](#) [Google Scholar](#)

20. Luis A. Rajman

[View author publications](#)

You can also search for this author in [PubMed](#) [Google Scholar](#)

21. George M. Church

[View author publications](#)

You can also search for this author in [PubMed](#) [Google Scholar](#)

22. Konrad Hochedlinger

[View author publications](#)

You can also search for this author in [PubMed](#) [Google Scholar](#)

23. Vadim N. Gladyshev

[View author publications](#)

You can also search for this author in [PubMed](#) [Google Scholar](#)

24. Steve Horvath

[View author publications](#)

You can also search for this author in [PubMed](#) [Google Scholar](#)

25. Morgan E. Levine

[View author publications](#)

You can also search for this author in [PubMed](#) [Google Scholar](#)

26. Meredith S. Gregory-Ksander

[View author publications](#)

You can also search for this author in [PubMed](#) [Google Scholar](#)

27. Bruce R. Ksander

[View author publications](#)

You can also search for this author in [PubMed](#) [Google Scholar](#)

28. Zhigang He

[View author publications](#)

You can also search for this author in [PubMed](#) [Google Scholar](#)

29. David A. Sinclair

[View author publications](#)

You can also search for this author in [PubMed](#) [Google Scholar](#)

Contributions

Y.L. and D.A.S. conceived the project. Y.L., X.T. and D.A.S. wrote the manuscript with input from all co-authors. Y.L. was involved in all experiments and analyses. M.S.B. and J.-H.Y. provided early training to Y.L. B.B., C.W., Q.Z., D.Y., S.Z. and Z.H. contributed to the optic nerve crush studies and imaging. A.K., D.Y., Q.Z., E.M.H., E.K., M.S.G.-K. and B.R.K. contributed to the glaucoma and ageing studies. M.M.K. and B.R.K. performed OCT imaging and analysis. M.M. and V.N.G. conducted ribosomal DNA methylation age analysis for mouse RGCs. M.E.L. developed the DNA methylation ageing signature. D.L.V. performed the RNA sequencing and gene association analysis. X.T. conducted human neuron experiments. S.H. conducted the human methylation clock analysis. X.T., J.-H.Y. and K.H. helped with the work on transgenic mouse fibroblasts. M.S.B., X.T., M.B.S., A.E.K. and L.A.R. helped with systemic AAV9 experiments. N.D. and G.M.C. helped with plasmid constructs and AAV9 production. K.C. helped with grant applications and project management.

Corresponding author

Correspondence to [David A. Sinclair](#).

Ethics declarations

Competing interests

D.A.S. is a consultant to, inventor of patents licensed to, board member of and equity owner of Iduna Therapeutics, a Life Biosciences company developing epigenetic reprogramming therapies. D.A.S. is an advisor to Zymo Research, an epigenetics tools company. Additional disclosures are at <https://genetics.med.harvard.edu/sinclair/people/sinclair-other.php>. Y.L., L.A.R. and S.H. are equity owners of Iduna Therapeutics, a Life Biosciences company. D.L.V. is an advisor to Liberty Biosecurity. M.S.B. is a shareholder in MetroBiotech. K.C. is an equity owner in Life Biosciences and affiliates. N.D. and G.M.C. are co-founders of Rejuvenate Bio. Disclosures for G.M.C. can be found at <http://arep.med.harvard.edu/gmc/tech.html>. M.E.L. is a bioinformatics advisor to Elysium Health. Y.L., N.D. and D.A.S. are inventors on patents arising from this work (WO/2020/069373 and WO/2020/069339), filed by the President and Fellows of Harvard College. The other authors declare no competing interests.

Additional information

Peer review information *Nature* thanks Andrew Huberman, Hongjun Song, Yasuhiro Yamada and the anonymous reviewer(s) for their contribution to the peer review of this work. Peer reviewer reports are available.

Publisher's note Springer Nature remains neutral with regard to jurisdictional claims in published maps and institutional affiliations.

Extended data figures and tables

[Extended Data Fig. 1 Effectiveness and safety of OSK reprogramming.](#)

a, Experimental outline for testing the effects of OSKM and OSK on gene expression in fibroblasts from young and old transgenic (TG) mice. **b, c**,

Expression of OSKM (**b**, R26^{rtTA}; Col1a1^{OSKM}, $n = 3$ biological replicates each condition) and OSK (**c**, R26^{rtTA}; Col1a1^{OKS-mCherry}, $n = 3$ and 8 biological replicates) rescue age-associated transcriptional changes without inducing *Nanog* mRNA. mo, month(s). qPCR primers are listed in Supplementary Table 2. **d**, AAV-ubiquitinC (UbC)-rtTA and AAV-TRE-Luc vectors for measuring tissue distribution. **e**, Luciferase imaging of WT mice 2 months after intravenous injection (retro-orbital) of AAV9-UbC-rtTA;TRE-Luc (1.0×10^{12} gene copies total). DOX was delivered in drinking water (1 mg ml^{-1}) for 7 days to +DOX mice. **f**, Luciferase imaging of the eye (Ey), brain (Br), pituitary gland (Pi), heart (He), thymus (Th), lung (Lu), liver (Li), kidney (Ki), spleen (Sp), pancreas (Pa), testis (Te), adipose (Ad), muscle (Mu), spinal cord (SC), stomach (St), small intestine (In) and caecum (Ce) 2 months after retro-orbital injection of AAV9-UbC-rtTA;TRE-Luc followed by treatment with DOX for 7 days. The luciferase signal was primarily in the liver. Imaging the same tissues with a longer exposure time (right) with the liver removed revealed a strong signal in the pancreas. **g**, Toxicity and safety studies in young and old mice after in vivo delivery of OSK-expressing AAVs. In **h**, **i**, at the age of 5 months, mice were intravenously injected with AAV9-rtTA;TRE-OSK (3 and 7×10^{11} gene copies of AAV per mouse). After 1 month, mice remained untreated (-DOX) or were treated with DOX (+DOX) for 18 months. WT mice were not injected with AAV. In **j–n**, at the age of 21 months, mice were injected intravenously with 5×10^{11} gene copies of AAV9-rtTA and 7×10^{11} of either AAV9-TRE-GFP (GFP) or TRE-OSK (OSK) per mouse. After 1 month, GFP, OSK, and non-injected WT mice were treated with DOX for 10 months. **h**, SOX2 expression in the liver of WT mice 2 months after intravenous delivery of OSK-expressing AAV9s with or without a month of DOX induction, and in the liver of OSK transgenic mice, 129S1/C57BL/6J mixed background. Uncropped scans are shown in Supplementary Fig. 1. **i**, Body weight of WT mice, OSK transgenic mice, and AAV-mediated OSK-expressing mice with or without DOX in the first 4 weeks (left; $n = 5$, 3, 6, 4, 4 and 3 mice) and after 17 months (right, $n = 5$, 3, 6 and 4 mice). **j**, Examples of liver sections from WT or GFP mice showing the infection of AAV9. Scale bar, $100 \mu\text{m}$. **k**, KLF4 and GFP protein levels in the livers of WT, GFP and OSK mice at 32 months of age. * indicates high OSK expression, + indicates induced protein expression levels in livers of OSK transgenic mice. Uncropped scans are shown in Supplementary Fig. 1. **l**,

Tumour incidence in WT, GFP, and OSK mice at age 32 months after 10 months of DOX induction. **m**, **n**, Liver tumour scores (**m**) and white blood cell counts (**n**) for WT, GFP and OSK groups at age 32 months after 10 months of DOX induction. OSK mice were defined as either high expression (indicated by * in **k**) or low expression (WT, $n = 11$ mice; GFP, $n = 10$ mice; OSK high, $n = 7$ mice; OSK low, $n = 8$ mice). For **m**, **n**, there was no difference between the groups using one-way ANOVA. All data are presented as mean \pm s.e.m. [Source data](#)

Extended Data Fig. 2 Normal architecture and absence of tumours in the retina after long-term OSK expression mediated by AAV2 delivery.

a, b, Representative wholemount retina display of RBPMS (a RGC marker) and *Klf4* immunofluorescence showing (**a**) expression from the AAV2 Tet-Off system can be turned off by DOX in drinking water (2 mg ml⁻¹, 3 days), and (**b**) expression from the AAV2 Tet-On system can be turned on by DOX (2 mg ml⁻¹, 2 days). Scale bars, 1 mm; $n = 4$ retinas for each condition. **c**, Corresponding retinal wholemount images stained for RBPMS and *Klf4* are shown for each group tested: top, no injection, $n = 6$; middle, -OSK (intravitreal injection of AAV2-rtTA;TRE-OSK without DOX induction), 10 months post-injection, $n = 3$; bottom, +OSK (intravitreal injection of AAV2-tTA;TRE-OSK with DOX induction), 15 months post-injection, $n = 6$. All retinas are from 16-month-old mice, showing similar expression within the group. Scale bars, 100 μ m. **d**, Volume intensity projection of en-face OCT (optical coherence tomography) retinal image with a white line indicating the location of **e**. **e**, Representative retinal cross-section B-scan images. White box indicates the location of the high magnification scans in **f** (retinal layers: GCL, ganglion cell layer; INL, inner nuclear layer; ONL, outer nuclear layer and choroid). Videos of complete retinal cross-section B-scan images of the entire globe are provided as Supplementary Videos 1–3. **g**, Low- and high-power representative images of haematoxylin and eosin (H&E)-stained cross-sections of corresponding eyes, verifying retinal layers. **h**, Quantitative measurements of retinal thickness, there was no difference between the groups at any location using two-way ANOVA with Bonferroni correction

($n = 6$, 3 and 6, respectively). **i**, Immunosuppressed NOD scid gamma mice received a subretinal injection of approximately 10,000 human retinoblastoma tumour cells. The OCT image shows a small retinal tumour and increased retinal thickness 14 days post-injection, demonstrating the ability of the OCT scan to detect tumours. *Rb indicates retinoblastoma.

[Source data](#)

Extended Data Fig. 3 Polycistronic OSK induces long-distance axon regeneration post-injury without RGC proliferation.

a, Proliferating cells in the optic nerve (for example, glial cells) in BrdU-injected mice as a positive control ($n = 2$ nerves). BrdU staining co-localized with Ki67, a proliferation marker. **b**, Representative retina wholemount staining shows OSK-expressing RGCs do not stain for BrdU in the first or second week after crush injury; $n = 4$ retinas. Scale bars, 100 μm . **c**, Imaging of optic nerves showing regenerating and sprouting axons with or without OSK AAV treatment, 12 weeks post-crush (wpc); $n = 2$ nerves. Scale bars, 200 μm . **d**, Whole-nerve imaging showing CTB-labelled regenerative axons at 16 wpc in WT mice with intravitreal injection of AAV2-tTA;TRE-OSK ($n = 2$ nerves). Scale bars, 200 μm . **e**, Survival of RBPMs-positive cells in the RGC layer transduced with different AAV2s, 16 dpc ($n = 6, 4, 4, 4, 4, 4, 8$ and 4 eyes). All data are mean \pm s.e.m. **f, g**, Representative immunofluorescence (**f**) and sub-population proportion (**g**) of wholemount retinas transduced with a polycistronic AAV vector expressing *Oct4*, *Sox2* and *Klf4* in the same cell. White arrows designate triple-positive cells. $n = 3$ retinas. Scale bars, 100 μm . **h, i**, Immunofluorescence (**h**) and sub-population proportion (**i**) of wholemount retinas transduced with AAVs separately encoding *Oct4*, *Sox2* and *Klf4*. Red, blue, and green arrows designate single-positive cells, with a white arrow marking a triple-positive cell, and other arrows marking double-positive cells. $n = 3$ retinas. Scale bar, 100 μm . One-way ANOVA with Bonferroni correction in **e**, with comparisons to d2EGFP shown. [Source data](#)

Extended Data Fig. 4 Regenerative and pro-survival effects of OSK are RGC-specific and cell-autonomous.

a, Effect of OSK expression on RGC survival in young (1-month-old, $n = 8$), adult (3-month-old, $n = 5$), and old (12-month-old, $n = 8$) mice after optic-nerve crush-injury compared to expression of d2EGFP as a negative control ($n = 6$, 5 and 6, respectively). **b**, Axon regeneration after OSK expression compared to d2EGFP controls in young (1-month-old, $n = 5, 6$), adult (3-month-old, $n = 6$), and old (12-month-old, $n = 4, 5$) mice, 2 wpc. **c**, Number of RGCs in the intact, 2 wpc or 5 wpc retinas of 12-month-old mice expressing GFP (AAV2-tTA;TRE-d2EGFP, $n = 7, 6$ and 6, respectively) or OSK (AAV2-tTA;TRE-OSK, $n = 5, 8$ and 6, respectively). **d**, Axon regeneration in 12-month-old mice with OSK AAV or control AAV (d2EGFP) treatment, 5 wpc ($n = 5$ nerves). **e**, Schematic of retinal structure showing Vglut2-Cre mice selectively expressing Cre in excitatory neurons such as RGCs, whereas Vgat-Cre mice selectively express Cre in inhibitory amacrine and horizontal cells. **f**, Schematic of the FLEX (flip-excision) Cre-switch system. AAV2-FLEX-tTA is inverted by Cre to express tTA and therefore induces OSK only in Cre-positive cells. **g**, Confocal image stack demonstrating delivery of AAV2-FLEX-tTA;TRE-OSK to intact Vglut2-Cre transgenic retinas, resulting in RGC-specific OSK expression (top) and robust axon regeneration in the optic nerve (bottom). White arrows indicate RBPMS+ (AP2-)-labelled RGCs that express *Klf4* (green). $n = 4$ independent replicates. **h**, Confocal image stack demonstrating delivery of AAV2-FLEX-tTA;TRE-OSK to intact Vgat-Cre transgenic retinas, resulting in amacrine-specific OSK expression (top) and poor axon regeneration in the optic nerve (bottom). White arrows indicate AP2+ (RBPMS-)labelled amacrine cells that express *Klf4* (green). $n = 4$ independent replicates. **i**, Representative image of AAV-expressing or non-expressing RGCs in intact and crushed retinas 2 wpc with AAVs expressing d2EGFP or OSK. d2EGFP: AAV2-tTA;TRE-d2EGFP, $n = 6$ retinas; OSK: AAV2-tTA;TRE-OSK, $n = 8$ retinas. **j**, RGC survival rate (crushed/intact) of d2EGFP- ($n = 6$ eyes) or *Klf4*-expressing cells ($n = 8$ eyes) and their surrounding non-expressing cells indicating a cell-autonomous pro-survival effect of OSK-expressing RGCs after crush, 2 wpc. **k**, Frequency of d2EGFP- or *Klf4*-positive RGCs pre- or 2 weeks post-injury ($n = 4, 6, 6$ and 8 eyes). Two-way ANOVA with Bonferroni correction in **a–d, j**; one-way ANOVA with Bonferroni correction in **k**. Scale bars (**g–i**), 100 μ m. All data are mean \pm s.e.m. [Source data](#)

Extended Data Fig. 5 OSK activates Stat3 in the absence of mTOR activation or global demethylation.

a, Representative images of retinal wholemounts transduced with AAV2-tTA (-OSK) or AAV2-tTA;TRE-OSK (+OSK) in the presence or absence of crush injury after 3 days. Retinal wholemounts immunostained for *pStat3*, *Klf4* and RBPMS. $n = 2$ retinas each condition. **b**, Representative images of retinal wholemounts transduced with d2EGFP- or OSK-encoding AAV2 in the presence or absence of a crush injury. Retinal wholemounts immunostained for RBPMS and mTOR activation marker phosphorylated S6 (pS6). $n = 4$ retinas for each condition. **c**, Percentage of pS6-positive RGCs in intact and crushed samples ($n = 4$ retinas for each condition). **d**, Representative images of d2EGFP in retina expressed from the Tet-On AAV system. No GFP expression was observed in the absence of DOX. GFP expression reached peak levels 2 days after DOX induction and remained at a similar level at day 5 after induction. $n = 2$ retinas each condition. **e**, Representative images of retinal d2EGFP expression using the Tet-Off AAV system with various durations of DOX treatments (2 mg ml^{-1}). Once pre-treated with DOX to suppress expression (on DOX), GFP was sparse even on day 8 after DOX withdrawal, lower than peak expression (Never DOX). $n = 2$ retinas each condition. **f**, Axon regeneration at 2 or 4 wpc in response to OSK induction either pre- or post-injury ($n = 4, 5, 5, 4$ and 4 eyes, respectively). **g**, Correlation between ribosomal DNA methylation (DNAm) age and chronological age of sorted mouse RGCs (1 month, $n = 6$; 12 months, $n = 2$; 30 months, $n = 5$), with the light blue region representing the confidence interval. P value of the linear regression is calculated by two-sided *F*-test of overall significance. In agreement with previous studies, DNA methylation age estimates of neurons tend to be lower than their chronological age but remain correlated (see [Methods](#)). **h**, Average DNA methylation levels across the mouse genome in RGCs from different ages and treatments, based on 703,583 shared CpG sites from RRBS of all samples (combined strands), $n = 6, 8, 2, 8, 6, 4, 8, 8, 6, 5, 6, 4$ and 5, respectively. **i**, Correlation of DNA methylation at each CpG site versus age (x-axis; 1 month, 12 months, 30 months) and versus injury (y-axis; intact, injured GFP). The heat map represents the number of sites located in each block of value coordinates. Pearson's correlation coefficient, $r = 0.34$, $P < 1e^{-200}$. **j**, Hierarchical clustered heat map of methylation

levels of 4,106 CpGs that significantly changed in RGCs after crush injury (intact vs injured GFP, $q < 0.05$) and the effect of OSK. **k**, Top biological processes associated with the 698 CpGs that were significantly altered by both injury and OSK. Two-way ANOVA with Bonferroni correction in **c, f**. Scale bars (**a, b, d, e**), 100 μ m. All data are mean \pm s.e.m. [Source data](#)

Extended Data Fig. 6 Protective and regenerative effect of OSK is dependent on TET1 and TET2.

a, Mouse *Tet1*, *Tet2* and *Tet3* mRNA levels with or without OSK expression in RGCs ($n = 6$ biological replicates each condition). The P value indicated with an asterisk was calculated using an unpaired one-tailed *t*-test. **b**, Representative images of retinal wholemounts transduced with AAV2-tTA;TRE-OSK in combination with a AAV2-shRNA-YFP (yellow fluorescent protein) having either a scrambled sequence (sh-Scr) or a hairpin sequence to knockdown *Tet1* (sh-Tet1) or *Tet2* (sh-Tet2) expression, at titre ratio 5:5:1. Retinal wholemounts immunostained for *Klf4*. $n = 3$ retinas for each condition. **c**, Quantification of shRNA-YFP AAV transduction in OSK-expressing RGCs ($n = 3$ retinas for each condition). **d**, Mouse *Tet1*, *Tet2* and *Tet3* mRNA levels with sh-Scr ($n = 5$), sh-Tet1 ($n = 4$) or sh-Tet2 ($n = 5$) YFP AAV2 in RGCs in the presence of OSK expression. **e, f**, Quantification of axon regeneration (**e**, $n = 4$ eyes each condition) and RGC survival (**f**, $n = 10$, 7 and 9 eyes) at 2 wpc in retinas co-transduced with AAV2-tTA;TRE-OSK;shRNA. **g**, Mouse *Stat3* mRNA levels after knockdown using sh-Scr ($n = 5$), sh-Tet1 ($n = 4$) or sh-Tet2 ($n = 5$) in RGCs in the presence of OSK expression. **h**, Cre-dependent Tomato expression in RGCs after intravitreal AAV2-Cre injection of Tomato reporter mice (Rosa-CAG-lox-STOP-lox-Tomato), and the co-expressed frequency of Cre and *Klf4* ($n = 3$ eyes). **i, j**, RGC survival (**i**) and representative longitudinal sections of regenerating axons in longitudinal sections (**j**) in response to OSK expression (AAV2-tTA;TRE-OSK, $n = 5$ for each condition) compared to no expression (saline, $n = 3$ and 4), 16 days after crush injury in *Tet2*^{fl/fl} mice injected with saline (Tet2 WT) or AAV2-Cre (Tet2 cKO). Scale bars (**b, h** and **j**), 100 μ m. Two-way ANOVA in **a, d, i**; unpaired two-tailed Student's *t*-test in **g**; one-way ANOVA in **e, f**. All data are mean \pm s.e.m. [Source data](#)

Extended Data Fig. 7 OSK-induced axon regeneration and survival require non-global active DNA demethylation through thymine DNA glycosylase.

a, Representative images of retinal wholemounts transduced with sh-Scr-H2B-GFP or sh-TDG-H2B-GFP AAV2 s for 4 weeks, demonstrating that knockdown of thymine DNA glycosylase (TDG) increased levels of 5-hydroxymethylcytosine (5-hmC). $n = 4$ retinas for each condition. **b**, Representative retinal wholemount images and images of longitudinal sections through the optic nerve showing CTB-labelled regenerative axons in WT mice, 16 dpc after an intravitreal injection of AAV2-tTA ;TRE-OSK in combination with AAV2-sh-Scr (sh-Scr) or AAV2-sh-TDG (sh-TDG) at titre ratio 5:5:1. $n = 4$ retinas for each condition. **c, d**, Quantification of regenerating axons (**c**) and RGC survival (**d**) in OSK-treated mice 16 dpc with AAVs carrying sh-Scr or sh-TDG ($n = 4$ nerves for each condition). **e**, Representative image of retinal wholemounts transduced with AAV2-tTA;TRE-OSK. Retinal wholemounts were immunostained for 5-methylcytosine (5-mC) and *Klf4*, showing a lack of global demethylation in OSK expressing RGCs. $n = 3$ retinas. **f**, Representative images of retinal wholemounts transduced with AAV2 vectors encoding the HA-TET1 catalytic domain (TET1-CD) or its catalytic mutant (TET1-mCD) for 4 weeks, demonstrating that overexpression of TET1-CD decreases global 5-mC levels. $n = 3$ retinas for each condition. **g, h**, Quantification of axon regeneration (**g**) and RGC survival (**h**) at 2 wpc in retinas transduced without or with AAV2 vectors encoding HA-TET1 CD mutant or HA-TET1 CD ($n = 3, 4$ and 3 eyes). **i**, A schematic diagram illustrating passive demethylation and TDG-dependent active DNA demethylation. Scale bars (**a, b, e, f**), 100 μ m. One-way ANOVA with Bonferroni's multiple comparison test in **c, g, h**; unpaired two-tailed Student's *t*-test in **d**. There was no difference between the groups in **g** and **h** using two-way ANOVA and one-way ANOVA, respectively. All data are mean \pm s.e.m. [Source data](#)

Extended Data Fig. 8 OSK induces axon regeneration and reversal of DNA methylation age in human neurons.

a, mRNA levels of mouse *Oct4*, *Sox2* and *Klf4* in human neurons transduced with vectors packaged by AAV-DJ, a recombinogenic hybrid capsid that is efficient for in vitro transduction. −OSK: AAV-DJ-tTA ($n = 3$); +OSK: AAV-DJ-tTA;TRE-OSK ($n = 3$). **b**, Percentage of cells in S phase, as measured by propidium iodide (PI)-staining ($n = 4$). **c**, FACS profiles of G1, S and G2 phases in undifferentiated SH-SY5Y cells and differentiated cells transduced with −OSK and +OSK vectors. **d**, Experimental outline for testing axon regeneration in human neurons after vincristine (VCS) damage. **e**, **f**, DNA methylation (DNAm) age of human neurons without damage (intact), and 1 or 9 days after VCS damage in the absence (**e**) or presence (**f**) of OSK expression, measured using the skin and blood clock suited to in vitro studies (see [Methods](#)). The linear regression P value in **e** ($P = 0.55$) indicates nonlinear DNA methylation age changes, and in **f** ($P = 0.008$) indicates a continuous decrease in DNA methylation age ($n = 3, 3$ and 6). **g**, Average DNA methylation levels among 850,000 probes from the EPIC array in human neurons without damage (intact), and 1 or 9 days after VCS damage in the absence or presence of OSK expression ($n = 3, 3$ and 6). **h**, **i**, Representative images (**h**, similar results were confirmed in two series of experiments) and quantification (**i**) of neurite area at different time points after VCS damage ($n = 6, 7, 5, 5, 7$ and 5 ; 2 independent experiments). Cells were not passaged after damage to avoid cell–cell contact for quantifying maximum axon regeneration. **j–l**, Human *TET1*, *TET2* and *TET3* mRNA level with scrambled shRNA (sh-Scr) or sh-Tet2 AAV in human neurons in the presence or absence of OSK expression ($n = 4$; 2 independent experiments). **m**, Representative images of human neurons in each AAV treated group, 9 days after VCS damage. Similar results were confirmed in three series of experiments. **n–p**, Neurite area (**n**), axon number (**o**) and axon length (**p**) in each AAV-treated group 9 days after VCS damage ($n = 20, 21, 24$ and 23 ; 3 independent experiments). **q**, Mouse *Oct4* mRNA levels (from OSK AAV) in human neurons with sh-Scr or sh-Tet2 AAV and in presence or absence of OSK AAV ($n = 4$). **r**, The effect of mTOR inhibition by rapamycin (Rap, 10 nM) on axon regeneration of differentiated neurons with or without OSK ($n = 18, 19, 13$ and 11 ; 2 independent experiments). **s**, S6 phosphorylation levels in human neurons 5 days after treatment with rapamycin (Rap, 10 nM). Similar results were seen in two independent experiments. Uncropped scans are shown in Supplementary Fig. [1](#). **t**, Neurite area of neurons expressing TET1

catalytic domain (TET1-CD) or its catalytic mutant (TET1-mCD) 9 days after VCS damage ($n = 24$, 28 and 21; 2 independent experiments). One-way ANOVA with Bonferroni's multiple comparison test in **b**, **e–g** and **t**; two-way ANOVA with Bonferroni's multiple comparison test in **a**, **i**, **j–l** and **n–r**. All bar graphs are mean \pm s.e.m. [Source data](#)

Extended Data Fig. 9 Vision restoration and regenerative effect of OSK rely on functional improvement of existing RGCs.

a, Axon density and representative photomicrographs of PPD-stained optic nerve cross-sections, 4 weeks after microbead or saline injection (baseline, $n = 5$ eyes each condition). Scale bars, 25 μm . **b**, Quantification of RGCs and representative confocal microscopic images from retinal flat-mounts stained with anti-Brn3a (red), an RGC-specific marker, and DAPI (4',6-diamidino-2-phenylindole, blue), a nuclear stain, 4 weeks after microbead or saline injection (baseline, $n = 5$ eyes each condition). Scale bar, 100 μm . **c**, Axon density and representative micrographs from PPD-stained optic nerve cross-sections, 4 weeks after AAV2 or PBS injection (treated, $n = 9$, 7, 6 and 8 eyes). Scale, 50 μm . **d**, Quantification of RGCs and representative confocal microscopic images 4 weeks after PBS or AAV injection (treated, $n = 7$, 5, 6 and 5 eyes). Scale bar, 100 μm . **e**, PERG measurement at different ages 4 weeks after –OSK ($n = 16$, 14 and 11 eyes) or +OSK treatment ($n = 20$, 12 and 14 eyes). Similar results from 2 independent experiments are combined. **f**, Visual acuity in 18-month-old mice treated with –OSK ($n = 11$ eyes) or +OSK ($n = 14$ eyes) AAV for 4 weeks. **g**, **h**, Axon (**g**; $n = 4$, 6, 10 and 9 nerves) and RGC (**h**; $n = 5$, 4, 10 and 8 retinas) density in 4- and 12-month-old-mice, 4 weeks after –OSK or +OSK AAV injection. **i**, Scatter plot of OSK-induced changes and age-associated changes in mRNA levels in RGCs, with differentially expressed genes labelled. Gene selection criteria are in Methods. **j**, Hierarchical clustered heat map showing relative mRNA levels of age-associated sensory perception genes in FACS-sorted RGCs from untreated young (5-month-old) or old (12-month-old) mice or old mice treated with either –OSK or +OSK AAV. Sensory genes were extracted from the mouse Sensory Perception (GO:0007600) category of the Gene Ontology database. Gene selection criteria are in Methods. –OSK: AAV2-rtTA;TRE-OSK for **c–h**, AAV2-TRE-OSK for **i**, **j**; +OSK: AAV2-tTA;TRE-OSK for **c–j**.

Unpaired two-tailed Student's *t*-test in **a, b, f**; one-way ANOVA with Bonferroni's multiple comparison test in **c, d**; two-way ANOVA with Bonferroni correction in **e, g, h**. All data are mean ± s.e.m. [Source data](#)

Extended Data Fig. 10 OSK expression in old RGCs restores youthful epigenetic signatures.

a, b, Top biological processes based on transcriptome data that were either lower expressed in old compared to young RGCs and reversed by OSK (**a**), or higher expressed in old RGCs compared to young and reversed by OSK (**b**). **c**, Heat map showing relative mRNA levels of genes involved in the negative regulation of neural projection development, among the 464 differentially expressed genes during ageing. The accumulation of the gene *Efemp1* during ageing is suspected to have a role in diseases of the retina. **d**, RGC *Efemp1* mRNA levels measured by qPCR (relative to GAPDH) compared between young mice, old mice, and old mice treated with -OSK or +OSK AAV. Old RGCs with sh-Scr, sh-Tet1 or sh-Tet2 knockdown combined with +OSK AAV are included for comparison ($n = 7, 6, 5, 4, 5, 5$ and 6 eyes). **e**, Principal component 1 value of 1 month, 12 month and 30 month RGC training samples in the PCA analysis. Values are standardized to have a mean = 0 and s.d. = 1 ($n = 6, 2$ and 6). **f**, DNA methylation ageing signatures of 6-week-old RGCs isolated from axon-intact retinas infected with GFP-expressing AAV, or from axon-injured retinas infected with GFP- or OSK- expressing AAV at 4 dpc ($n = 4, 4$ and 8 eyes). **g**, Top biological processes associated with the 1,226 signature CpG sites. **h, i**, Transcription factor (TF) binding (**h**) and histone modifications (**i**) specifically enriched at the 1,226 signature CpG sites, compared to five sets of randomly selected CpGs. **j**, Correlation of *Tet1* and *Tet2* knockdown-induced changes in methylation (5-mC and 5-hmC together) at the selected CpGs. $r = 0.4$, $P = 2.53e^{-45}$. **k**, Delta value of ribosomal DNA methylation age (months) of 12-month-old RGCs infected for 4 weeks with +OSK ($n = 5$ retinas). Values are relative to the average of RGCs infected with -OSK AAV. **l**, Ribosomal DNA methylation age (months) of 12-month-old OSK-treated RGCs infected for 4 weeks with sh-Tet1 or sh-Tet2 ($n = 4, 5$ retinas). Values are relative to the average of RGCs infected with sh-Scr. **m**, PERG amplitudes in old (12-month-old) mice treated with -OSK, +OSK or +OSK together with either sh-Scr or sh-Tet1/sh-Tet2-mediated knockdown for 4

weeks ($n = 8, 7, 5, 6$ and 6 eyes). **n**, Working model. The loss of youthful epigenetic information during ageing and injury (including genome-wide changes to DNA methylation, acceleration of the DNA methylation clock, and disruption of youthful gene expression patterns) causes a decline in tissue function and regenerative capacity. OSK-mediated reprogramming recovers youthful epigenetic information, reverses the DNA methylation clock, restores youthful gene expression patterns, and improves tissue function and regenerative capacity, a process that requires active DNA demethylation by TET1/TET2 and TDG. The PRC2 complex may serve to recruit TET1 and TET2 to specific sites in the genome, and DNA methylation by DNA methyltransferases (DNMTs) may be important as well. One-way ANOVA with Bonferroni's multiple comparison test in **d–f**, **m**. All data are mean \pm s.e.m. [Source data](#)

Supplementary information

Supplementary Information

This file contains Supplementary Figures 1-2, Supplementary Discussion, Supplementary Code and Supplementary Tables 1-7.

Reporting Summary

Peer Review File

Supplementary Data

DNAm.csv; DNAm values used for developing and analyzing the DNA methylation ageing signatures.

Video 1

Complete cross section B-scan images for an entire globe of a 16-month-old mouse retina, without intravitreal injection of AAV2.

Video 2

Complete cross section B-scan images for an entire globe of a 16-month-old mouse retina, 10 months post intravitreal injection of AAV2-rtTA;TRE-OSK (-OSK, no OSK expression).

Video 3

Complete cross section B-scan images for an entire globe of a 16-month-old mouse retina, 15 months post intravitreal injection of AAV2-tTA;TRE-OSK (+OSK, continuous OSK expression).

Source data

Source Data Fig. 1

[Source Data Fig. 2](#)

[Source Data Fig. 3](#)

[Source Data Fig. 4](#)

[Source Data Extended Data Fig. 1](#)

[Source Data Extended Data Fig. 2](#)

[Source Data Extended Data Fig. 3](#)

[Source Data Extended Data Fig. 4](#)

[Source Data Extended Data Fig. 5](#)

[Source Data Extended Data Fig. 6](#)

[Source Data Extended Data Fig. 7](#)

[Source Data Extended Data Fig. 8](#)

[Source Data Extended Data Fig. 9](#)

[Source Data Extended Data Fig. 10](#)

Rights and permissions

[Reprints and Permissions](#)

About this article



Check for
updates

Cite this article

Lu, Y., Brommer, B., Tian, X. *et al.* Reprogramming to recover youthful epigenetic information and restore vision. *Nature* **588**, 124–129 (2020). <https://doi.org/10.1038/s41586-020-2975-4>

[Download citation](#)

- Received: 31 July 2019
- Accepted: 22 October 2020
- Published: 02 December 2020
- Issue Date: 03 December 2020
- DOI: <https://doi.org/10.1038/s41586-020-2975-4>

Comments

By submitting a comment you agree to abide by our [Terms](#) and [Community Guidelines](#). If you find something abusive or that does not comply with our terms or guidelines please flag it as inappropriate.

[Access through your institution](#)

[Change institution](#)

[Buy or subscribe](#)

Associated Content

Nature | News & Views

Sight restored by turning back the epigenetic clock

- Andrew D. Huberman

This article was downloaded by **calibre** from <https://www.nature.com/articles/s41586-020-2975-4>

| [Section menu](#) | [Main menu](#) |

- Article
- [Published: 18 November 2020](#)

Tension heterogeneity directs form and fate to pattern the myocardial wall

- [Rashmi Priya](#) [ORCID: orcid.org/0000-0002-0510-7515^{1,2}](#),
- [Srinivas Allanki](#) [ORCID: orcid.org/0000-0002-5042-7550¹](#),
- [Alessandra Gentile](#) [ORCID: orcid.org/0000-0002-5423-7295^{1 na1}](#),
- [Shivani Mansingh](#) [ORCID: orcid.org/0000-0002-0144-1049^{1 na1}](#),
- [Veronica Uribe^{1 nAff3}](#),
- [Hans-Martin Maischein¹](#) &
- [Didier Y. R. Stainier](#) [ORCID: orcid.org/0000-0002-0382-0026^{1,2}](#)

[Nature](#) volume 588, pages130–134(2020)[Cite this article](#)

- 2673 Accesses
- 85 Altmetric
- [Metrics details](#)

Subjects

- [Cellular imaging](#)
- [Cytoskeleton](#)
- [Heart development](#)
- [Morphogenesis](#)
- [Zebrafish](#)

Abstract

How diverse cell fates and complex forms emerge and feed back to each other to sculpt functional organs remains unclear. In the developing heart, the myocardium transitions from a simple epithelium to an intricate tissue that consists of distinct layers: the outer compact and inner trabecular layers. Defects in this process, which is known as cardiac trabeculation, cause cardiomyopathies and embryonic lethality, yet how tissue symmetry is broken to specify trabecular cardiomyocytes is unknown. Here we show that local tension heterogeneity drives organ-scale patterning and cell-fate decisions during cardiac trabeculation in zebrafish. Proliferation-induced cellular crowding at the tissue scale triggers tension heterogeneity among cardiomyocytes of the compact layer and drives those with higher contractility to delaminate and seed the trabecular layer. Experimentally, increasing crowding within the compact layer cardiomyocytes augments delamination, whereas decreasing it abrogates delamination. Using genetic mosaics in trabeculation-deficient zebrafish models—that is, in the absence of critical upstream signals such as Nrg–Erbb2 or blood flow—we find that inducing actomyosin contractility rescues cardiomyocyte delamination and is sufficient to drive cardiomyocyte fate specification, as assessed by Notch reporter expression in compact layer cardiomyocytes. Furthermore, Notch signalling perturbs the actomyosin machinery in cardiomyocytes to restrict excessive delamination, thereby preserving the architecture of the myocardial wall. Thus, tissue-scale forces converge on local cellular mechanics to generate complex forms and modulate cell-fate choices, and these multiscale regulatory interactions ensure robust self-organized organ patterning.

[Access through your institution](#)

[Change institution](#)

[Buy or subscribe](#)

Access options

Subscribe to Journal

Get full journal access for 1 year

185,98 €

only 3,58 € per issue

[Subscribe](#)

All prices are NET prices.

VAT will be added later in the checkout.

Rent or Buy article

Get time limited or full article access on ReadCube.

from \$8.99

[Rent or Buy](#)

All prices are NET prices.

Additional access options:

- [Log in](#)
- [Access through your institution](#)
- [Learn about institutional subscriptions](#)

Fig. 1: Tension heterogeneity among cardiomyocytes at the onset of delamination.

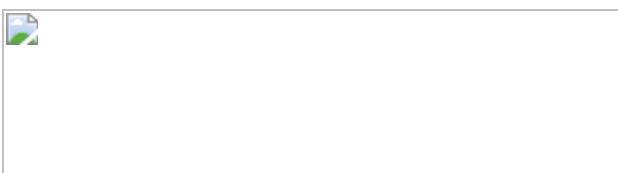


Fig. 2: Crowding-induced tension heterogeneity triggers cardiomyocyte delamination.



Fig. 3: Differential contractility is sufficient to induce cardiomyocyte delamination in the absence of Nrg–Erbb2 signalling.

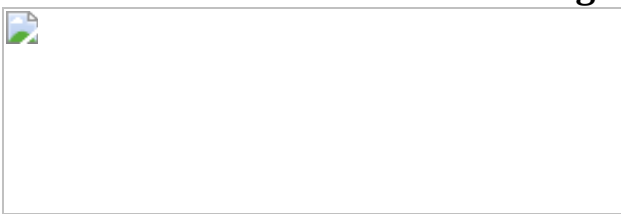


Fig. 4: Feedback interactions between mechanics and cell-fate cascades pattern the myocardial wall.



Data availability

All of the data supporting Figs. 1–4 and Extended Data Figs. 1–10 are available within the manuscript and its [Supplementary Information](#). [Source data](#) are provided with this paper.

Code availability

Custom script used for beating heart imaging is provided in the [Supplementary Methods](#).

References

1. 1.

Staudt, D. & Stainier, D. Uncovering the molecular and cellular mechanisms of heart development using the zebrafish. *Annu. Rev. Genet.* **46**, 397–418 (2012).

[CAS](#) [PubMed](#) [PubMed Central](#) [Google Scholar](#)

2. 2.

Liu, J. et al. A dual role for ErbB2 signaling in cardiac trabeculation. *Development* **137**, 3867–3875 (2010).

[CAS](#) [PubMed](#) [PubMed Central](#) [Google Scholar](#)

3. 3.

Staudt, D. W. et al. High-resolution imaging of cardiomyocyte behavior reveals two distinct steps in ventricular trabeculation. *Development* **141**, 585–593 (2014).

[CAS](#) [PubMed](#) [PubMed Central](#) [Google Scholar](#)

4. 4.

Maître, J. L. et al. Adhesion functions in cell sorting by mechanically coupling the cortices of adhering cells. *Science* **338**, 253–256 (2012).

[ADS](#) [PubMed](#) [Google Scholar](#)

5. 5.

Maître, J. L. et al. Asymmetric division of contractile domains couples cell positioning and fate specification. *Nature* **536**, 344–348 (2016).

[ADS](#) [PubMed](#) [PubMed Central](#) [Google Scholar](#)

6. 6.

Miroshnikova, Y. A. et al. Adhesion forces and cortical tension couple cell proliferation and differentiation to drive epidermal stratification. *Nat. Cell Biol.* **20**, 69–80 (2018).

[CAS](#) [PubMed](#) [Google Scholar](#)

7. 7.

Samarage, C. R. et al. Cortical tension allocates the first inner cells of the mammalian embryo. *Dev. Cell* **34**, 435–447 (2015).

[CAS](#) [PubMed](#) [Google Scholar](#)

8. 8.

Cherian, A. V., Fukuda, R., Augustine, S. M., Maischein, H. M. & Stainier, D. Y. N-cadherin relocalization during cardiac trabeculation. *Proc. Natl Acad. Sci. USA* **113**, 7569–7574 (2016).

[CAS](#) [PubMed](#) [Google Scholar](#)

9. 9.

Jiménez-Amilburu, V. & Stainier, D. Y. R. The transmembrane protein Crb2a regulates cardiomyocyte apicobasal polarity and adhesion in zebrafish. *Development* **146**, dev171207 (2019).

[PubMed](#) [Google Scholar](#)

10. 10.

Tinevez, J. Y. et al. Role of cortical tension in bleb growth. *Proc. Natl Acad. Sci. USA* **106**, 18581–18586 (2009).

[ADS](#) [CAS](#) [PubMed](#) [Google Scholar](#)

11. 11.

Yonemura, S., Wada, Y., Watanabe, T., Nagafuchi, A. & Shibata, M. α -Catenin as a tension transducer that induces adherens junction development. *Nat. Cell Biol.* **12**, 533–542 (2010).

[CAS](#) [PubMed](#) [Google Scholar](#)

12. 12.

Eisenhoffer, G. T. et al. Crowding induces live cell extrusion to maintain homeostatic cell numbers in epithelia. *Nature* **484**, 546–549 (2012).

[ADS](#) [CAS](#) [PubMed](#) [PubMed Central](#) [Google Scholar](#)

13. 13.

Eisenhoffer, G. T. & Rosenblatt, J. Bringing balance by force: live cell extrusion controls epithelial cell numbers. *Trends Cell Biol.* **23**, 185–192 (2013).

[CAS](#) [PubMed](#) [Google Scholar](#)

14. 14.

Saw, T. B. et al. Topological defects in epithelia govern cell death and extrusion. *Nature* **544**, 212–216 (2017).

[ADS](#) [CAS](#) [PubMed](#) [PubMed Central](#) [Google Scholar](#)

15. 15.

Marinari, E. et al. Live-cell delamination counterbalances epithelial growth to limit tissue overcrowding. *Nature* **484**, 542–545 (2012).

[ADS](#) [CAS](#) [PubMed](#) [Google Scholar](#)

16. 16.

Levayer, R., Dupont, C. & Moreno, E. Tissue crowding induces caspase-dependent competition for space. *Curr. Biol.* **26**, 670–677 (2016).

[CAS](#) [PubMed](#) [PubMed Central](#) [Google Scholar](#)

17. 17.

Han, Y. et al. Vitamin D stimulates cardiomyocyte proliferation and controls organ size and regeneration in zebrafish. *Dev. Cell* **48**, 853–863 (2019).

[CAS](#) [PubMed](#) [PubMed Central](#) [Google Scholar](#)

18. 18.

D’Uva, G. et al. ERBB2 triggers mammalian heart regeneration by promoting cardiomyocyte dedifferentiation and proliferation. *Nat. Cell Biol.* **17**, 627–638 (2015).

[PubMed](#) [Google Scholar](#)

19. 19.

Uribe, V. et al. In vivo analysis of cardiomyocyte proliferation during trabeculation. *Development* **145**, dev164194 (2018).

[PubMed](#) [Google Scholar](#)

20. 20.

Chugh, P. et al. Actin cortex architecture regulates cell surface tension. *Nat. Cell Biol.* **19**, 689–697 (2017).

[CAS](#) [PubMed](#) [PubMed Central](#) [Google Scholar](#)

21. 21.

Latorre, E. et al. Active superelasticity in three-dimensional epithelia of controlled shape. *Nature* **563**, 203–208 (2018).

[ADS](#) [CAS](#) [PubMed](#) [PubMed Central](#) [Google Scholar](#)

22. 22.

Sehnert, A. J. et al. Cardiac troponin T is essential in sarcomere assembly and cardiac contractility. *Nat. Genet.* **31**, 106–110 (2002).

[CAS](#) [PubMed](#) [Google Scholar](#)

23. 23.

Rasouli, S. J. & Stainier, D. Y. R. Regulation of cardiomyocyte behavior in zebrafish trabeculation by Neuregulin 2a signaling. *Nat. Commun.* **8**, 15281 (2017).

[ADS](#) [CAS](#) [PubMed](#) [PubMed Central](#) [Google Scholar](#)

24. 24.

Jiménez-Amilburu, V. et al. In vivo visualization of cardiomyocyte apicobasal polarity reveals epithelial to mesenchymal-like transition during cardiac trabeculation. *Cell Rep.* **17**, 2687–2699 (2016).

[PubMed](#) [Google Scholar](#)

25. 25.

Peshkovsky, C., Totong, R. & Yelon, D. Dependence of cardiac trabeculation on neuregulin signaling and blood flow in zebrafish. *Dev.*

Dyn. **240**, 446–456 (2011).

[PubMed](#) [Google Scholar](#)

26. 26.

Westcot, S. E. et al. Protein-trap insertional mutagenesis uncovers new genes involved in zebrafish skin development, including a *Neuregulin 2a*-based ErbB signaling pathway required during median fin fold morphogenesis. *PLoS One* **10**, e0130688 (2015).

[PubMed](#) [PubMed Central](#) [Google Scholar](#)

27. 27.

Auman, H. J. et al. Functional modulation of cardiac form through regionally confined cell shape changes. *PLoS Biol.* **5**, e53 (2007).

[PubMed](#) [PubMed Central](#) [Google Scholar](#)

28. 28.

Han, P. et al. Coordinating cardiomyocyte interactions to direct ventricular chamber morphogenesis. *Nature* **534**, 700–704 (2016).

[ADS](#) [CAS](#) [PubMed](#) [PubMed Central](#) [Google Scholar](#)

29. 29.

Ninov, N., Borius, M. & Stainier, D. Y. Different levels of Notch signaling regulate quiescence, renewal and differentiation in pancreatic endocrine progenitors. *Development* **139**, 1557–1567 (2012).

[CAS](#) [PubMed](#) [PubMed Central](#) [Google Scholar](#)

30. 30.

Shaya, O. et al. Cell–cell contact area affects Notch signaling and Notch-dependent patterning. *Dev. Cell* **40**, 505–511 (2017).

[CAS](#) [PubMed](#) [PubMed Central](#) [Google Scholar](#)

31. 31.

Bray, S. J. Notch signalling in context. *Nat. Rev. Mol. Cell Biol.* **17**, 722–735 (2016).

[CAS](#) [PubMed](#) [Google Scholar](#)

32. 32.

Shaya, O. & Sprinzak, D. From Notch signaling to fine-grained patterning: modeling meets experiments. *Curr. Opin. Genet. Dev.* **21**, 732–739 (2011).

[CAS](#) [PubMed](#) [Google Scholar](#)

33. 33.

del Monte-Nieto, G. et al. Control of cardiac jelly dynamics by NOTCH1 and NRG1 defines the building plan for trabeculation. *Nature* **557**, 439–445 (2018).

[ADS](#) [PubMed](#) [Google Scholar](#)

34. 34.

Beach, J. R., Licate, L. S., Crish, J. F. & Egelhoff, T. T. Analysis of the role of Ser1/Ser2/Thr9 phosphorylation on myosin II assembly and function in live cells. *BMC Cell Biol.* **12**, 52 (2011).

[CAS](#) [PubMed](#) [PubMed Central](#) [Google Scholar](#)

35. 35.

Bindels, D. S. et al. mScarlet: a bright monomeric red fluorescent protein for cellular imaging. *Nat. Methods* **14**, 53–56 (2017).

[CAS](#) [PubMed](#) [Google Scholar](#)

36. 36.

Subauste, M. C. et al. Rho family proteins modulate rapid apoptosis induced by cytotoxic T lymphocytes and Fas. *J. Biol. Chem.* **275**, 9725–9733 (2000).

[CAS](#) [PubMed](#) [Google Scholar](#)

37. 37.

Clark, B. S. et al. Loss of Llgl1 in retinal neuroepithelia reveals links between apical domain size, Notch activity and neurogenesis. *Development* **139**, 1599–1610 (2012).

[CAS](#) [PubMed](#) [PubMed Central](#) [Google Scholar](#)

38. 38.

Lin, Y. F., Swinburne, I. & Yelon, D. Multiple influences of blood flow on cardiomyocyte hypertrophy in the embryonic zebrafish heart. *Dev. Biol.* **362**, 242–253 (2012).

[CAS](#) [PubMed](#) [Google Scholar](#)

39. 39.

Mickoleit, M. et al. High-resolution reconstruction of the beating zebrafish heart. *Nat. Methods* **11**, 919–922 (2014).

[CAS](#) [PubMed](#) [PubMed Central](#) [Google Scholar](#)

40. 40.

D'Amico, L., Scott, I. C., Jungblut, B. & Stainier, D. Y. A mutation in zebrafish *hmgcr1b* reveals a role for isoprenoids in vertebrate heart-tube formation. *Curr. Biol.* **17**, 252–259 (2007).

[PubMed](#) [Google Scholar](#)

41. 41.

Reischauer, S., Arnaout, R., Ramadass, R. & Stainier, D. Y. R. Actin binding GFP allows 4D *in vivo* imaging of myofilament dynamics in the zebrafish heart and the identification of Erbb2 signaling as a remodeling factor of myofibril architecture. *Circ. Res.* **115**, 845–856 (2014).

[CAS](#) [PubMed](#) [PubMed Central](#) [Google Scholar](#)

42. 42.

Fukuda, R. et al. Proteolysis regulates cardiomyocyte maturation and tissue integration. *Nat. Commun.* **8**, 14495 (2017).

[ADS](#) [CAS](#) [PubMed](#) [PubMed Central](#) [Google Scholar](#)

43. 43.

Guerra, A. et al. Distinct myocardial lineages break atrial symmetry during cardiogenesis in zebrafish. *eLife* **7**, e32833 (2018).

[PubMed](#) [PubMed Central](#) [Google Scholar](#)

44. 44.

Revenu, C. et al. Quantitative cell polarity imaging defines leader-to-follower transitions during collective migration and the key role of microtubule-dependent adherens junction formation. *Development* **141**, 1282–1291 (2014).

[CAS](#) [PubMed](#) [Google Scholar](#)

45. 45.

Lyons, D. A. et al. *erbb3* and *erbb2* are essential for Schwann cell migration and myelination in zebrafish. *Curr. Biol.* **15**, 513–524 (2005).

[CAS](#) [PubMed](#) [Google Scholar](#)

46. 46.

Asakawa, K. & Kawakami, K. The *Tol2*-mediated Gal4-UAS method for gene and enhancer trapping in zebrafish. *Methods* **49**, 275–281 (2009).

[CAS](#) [PubMed](#) [PubMed Central](#) [Google Scholar](#)

47. 47.

Berdougo, E., Coleman, H., Lee, D. H., Stainier, D. Y. & Yelon, D. Mutation of weak atrium/atrial myosin heavy chain disrupts atrial function and influences ventricular morphogenesis in zebrafish. *Development* **130**, 6121–6129 (2003).

[CAS](#) [PubMed](#) [Google Scholar](#)

48. 48.

Schindelin, J. et al. Fiji: an open-source platform for biological-image analysis. *Nat. Methods* **9**, 676–682 (2012).

[CAS](#) [Google Scholar](#)

49. 49.

Bolte, S. & Cordelières, F. P. A guided tour into subcellular colocalization analysis in light microscopy. *J Microsc.* **224**, 213–232 (2006).

[MathSciNet](#) [CAS](#) [PubMed](#) [Google Scholar](#)

50. 50.

Bornhorst, D. et al. Biomechanical signaling within the developing zebrafish heart attunes endocardial growth to myocardial chamber dimensions. *Nat. Commun.* **10**, 4113 (2019).

[ADS](#) [PubMed](#) [PubMed Central](#) [Google Scholar](#)

51. 51.

Priya, R. & Gomez, G. A. Measurement of junctional protein dynamics using fluorescence recovery after photobleaching (FRAP). *Bio Protoc.* **3**, e937 (2013).

[Google Scholar](#)

52. 52.

Liang, X., Michael, M. & Gomez, G. A. Measurement of mechanical tension at cell–cell junctions using two-photon laser ablation. *Bio Protoc.* **6**, e2068 (2016).

[PubMed](#) [PubMed Central](#) [Google Scholar](#)

[Download references](#)

Acknowledgements

We are grateful to A. S. Yap, C. J. Chan, P. Panza, C. C. Wu, F. Gunawan, M. Collins, G. Boezio, A. Munjal, T. Tsai and E. H. Barriga for discussions and critical reading of the manuscript. We thank our laboratory colleagues for their support, S. Howard for technical assistance with injections, R. Ramadass for imaging support and our colleagues elsewhere for their gifts of reagents. R.P. acknowledges support by postdoctoral fellowships from EMBO (LTF 1569) and the Alexander von Humboldt Foundation, as well as a start-up grant from the Cardio-Pulmonary Institute (CPI) (EXC 2026, project ID 390649896). S.A. is supported by the DFG-CRC1213 project B01. Research in the Stainier laboratory is supported by the Max Planck Society, EU (ERC), DFG and Leducq Foundation.

Author information

Author notes

1. Veronica Uribe

Present address: Department of Physiology, The University of Melbourne, Melbourne, Victoria, Australia

2. These authors contributed equally: Alessandra Gentile, Shivani Mansingh

Affiliations

1. Department of Developmental Genetics, Max Planck Institute for Heart and Lung Research, Bad Nauheim, Germany

Rashmi Priya, Srinivas Allanki, Alessandra Gentile, Shivani Mansingh, Veronica Uribe, Hans-Martin Maischein & Didier Y. R. Stainier

2. German Centre for Cardiovascular Research (DZHK), Partner Site Rhine-Main, Bad Nauheim, Germany

Rashmi Priya & Didier Y. R. Stainier

Authors

1. Rashmi Priya

[View author publications](#)

You can also search for this author in [PubMed](#) [Google Scholar](#)

2. Srinivas Allanki

[View author publications](#)

You can also search for this author in [PubMed](#) [Google Scholar](#)

3. Alessandra Gentile

[View author publications](#)

You can also search for this author in [PubMed](#) [Google Scholar](#)

4. Shivani Mansingh

[View author publications](#)

You can also search for this author in [PubMed](#) [Google Scholar](#)

5. Veronica Uribe

[View author publications](#)

You can also search for this author in [PubMed](#) [Google Scholar](#)

6. Hans-Martin Maischein

[View author publications](#)

You can also search for this author in [PubMed](#) [Google Scholar](#)

7. Didier Y. R. Stainier

[View author publications](#)

You can also search for this author in [PubMed](#) [Google Scholar](#)

Contributions

R.P. conceived the project, designed and performed most of the experiments, analysed the data and wrote the manuscript with input from all authors. S.A. performed adult heart immunostaining and contributed to time-lapse imaging of beating hearts. A.G. performed some immunostaining and chemical treatment experiments. S.M. performed some immunostaining and chemical treatment experiments and contributed to data analysis. V.U. performed some mosaic experiments. H.-M.M. performed blastomere transplant experiments. D.Y.R.S. supervised the study and wrote the manuscript with input from all authors.

Corresponding authors

Correspondence to [Rashmi Priya](#) or [Didier Y. R. Stainier](#).

Ethics declarations

Competing interests

The authors declare no competing interests.

Additional information

Peer review information *Nature* thanks Jeroen Bakkers, Carl-Philipp Heisenberg and Sara Wickström for their contribution to the peer review of this work.

Publisher's note Springer Nature remains neutral with regard to jurisdictional claims in published maps and institutional affiliations.

Extended data figures and tables

[Extended Data Fig. 1 Cardiomyocytes delaminate in a stochastic fashion.](#)

a, Representative frames from time-lapse beating heart imaging to visualize cardiomyocyte (CM) delamination starting at 60 hpf ($n = 8/8$ hearts). **b–c'**, Representative mid-sagittal confocal images of 65 hpf (**b**), and 80 hpf (**c**) hearts, and distribution of delaminating (de) or TL cardiomyocytes along the compact layer at 65 hpf (**b'**, $n = 31$) and 80 hpf (**c'**, $n = 20$); red dashed line: position of first de or TL cardiomyocyte; blue dashed lines: relative distance between de or TL cardiomyocytes; white asterisks: TL cardiomyocytes; magenta asterisks: delaminating cardiomyocytes; arrowheads: CL cardiomyocytes. **d, d'**, 60 hpf heart immunostained for N-cadherin and GFP (membrane), and counterstained with DAPI; representative mid-sagittal confocal image (**d**), and fluorescence intensity (**d'**, $n = 49$). **e, e'**, Representative mid-sagittal confocal image of 67 hpf heart (**e**), and fluorescence intensity (**e'**, $n = 36$). **f, f'**, 60 hpf heart immunostained for ZO-1 and GFP (membrane), and counterstained with DAPI; representative mid-sagittal confocal image (**f**), and fluorescence intensity (**f'**, $n = 33$). **g, g'**, Representative mid-sagittal confocal image of 65 hpf heart (**g**), and fluorescence intensity (**g'**, $n = 27$). **h–h''**, 60 hpf heart immunostained for Crb2a and GFP (membrane), and counterstained with

DAPI; representative mid-sagittal confocal image (**h**), and fluorescence intensity (**h'**, $n = 31$), and number of delaminating cardiomyocytes with apical (yellow asterisk) or junctional (white asterisk) Crb2a localization (**h''**, $n = 49$). Data are mean \pm s.d. Two-tailed Wilcoxon test. n refers to the number of cardiomyocytes. Asterisks, delaminating cardiomyocytes; arrowheads, CL cardiomyocytes. Scale bars, 50 μm (**b**, **c**, **d**, **e**, **f**, **g**, **h**); 5 μm (**a**). For more details on statistics and reproducibility, see [Methods](#). [Source data](#)

[Extended Data Fig. 2 Proliferation-induced crowding triggers tension heterogeneity among cardiomyocytes.](#)

a, a', Representative mid-sagittal confocal image of 62 hpf heart (**a**), and fluorescence intensity (**a'**, $n = 53$). **b, b'**, Representative mid-sagittal confocal image of 65 hpf heart (**b**), and fluorescence intensity (**b'**, $n = 71$). **c, c'**, 62 hpf heart immunostained for GFP (membrane), and counterstained with phalloidin and DAPI; representative mid-sagittal confocal image (**c**), and fluorescence intensity (**c'**, $n = 60$). **d**, Representative mid-sagittal confocal image of 62 hpf heart immunostained for α -18 and GFP (membrane), and counterstained with DAPI, and fluorescence intensity profiles (**d'**, CL, $n = 76$; de, $n = 88$). **e, f**, Representative recovery profiles from FRAP of myosin (**e**, CL, $n = 18$; de, $n = 16$) and actin (**f**, CL, $n = 16$; de, $n = 12$) in CL and de cardiomyocytes. **g–g'**, Recoil velocity (**g**) and rate constant (k) (**g'**) of CL ($n = 44$) and de ($n = 47$) cardiomyocytes. **h**, Maximum intensity projection (MIP) of 48 and 62 hpf hearts corresponding to 3D object maps in Fig. [2a](#). **i**, Mid-sagittal confocal and corresponding binary images of 48- and 62 hpf hearts corresponding to NND calculations in Fig. [2a](#). **j–j''**, Representative MIP of 48- and 62 hpf hearts (**j**), apical cell surface area (**j'**, 48 hpf, $n = 175$; 62 hpf, $n = 200$) (**j'**), and aspect ratio (**j''**, 48 hpf, $n = 167$; 62 hpf, $n = 193$). **k, k'**, Representative maximum intensity projection (MIP) of 48 hpf heart (**k**), and number of mVenus-Gmnn⁺ (proliferating) cardiomyocytes (**k'**, $n = 37$). **l, l'**, 60 hpf hearts of DMSO-treated ($n = 28$), alfacalcidol-treated (Alfa, $n = 21$) or calcitriol-treated (Calci, $n = 20$) zebrafish embryos; representative MIP (**l**), and quantification (**l'**). **m, m'**, 60 hpf hearts of DMSO-treated ($n = 30$) or MEK inhibitor-treated ($n = 29$) zebrafish embryos; representative MIP (**m**), and quantification (**m'**). **n, n'**, 60 hpf hearts of DMSO-treated ($n = 25$) or Erbb2

inhibitor-treated ($n = 24$) zebrafish embryos; representative MIP (**n**), and quantification (**n'**). **o**, MIP of 60 hpf hearts of DMSO- or Alfa-treated zebrafish embryos corresponding to 3D object maps in Fig. 2b. **p**, MIP of 60 hpf hearts of DMSO-, MEK inhibitor- or Erbb2 inhibitor-treated zebrafish embryos corresponding to 3D object maps in Fig. 2d. **q, q'**, Representative mid-sagittal confocal images of 65 hpf hearts of DMSO-treated ($n = 22$) or MEK inhibitor-treated ($n = 23$) zebrafish embryos (**q**) and quantification (**q'**). Data are mean \pm s.d. except for **d', g, g'** (mean \pm s.e.m.). Two-tailed Wilcoxon test (**a', b', c'**); Kruskal–Wallis test (**l'**); two-tailed Student's *t*-test (**g', m', n', q'**). *n* refers to the number of hearts (**e, f, g, k', l', m', n', q'**) or number of cardiomyocytes (**a', b', c', d', j', j''**). All box-and-whisker plots show median, 25th and 75th percentiles, and all data points extending from minimum to maximum. Asterisks, delaminating or TL cardiomyocytes; arrowheads, CL cardiomyocytes. Scale bars, 50 μ m. For more details on statistics and reproducibility, see [Methods](#). [Source data](#)

[Extended Data Fig. 3 Inducing or abrogating the proliferation of CL cardiomyocytes increases or decreases cell morphology and tension heterogeneity.](#)

a, b, Representative mid-sagittal confocal images of 60 hpf hearts of zebrafish embryos treated with DMSO, alfacalcidol (Alfa), MEK inhibitor or Erbb2 inhibitor, immunostained for p-myo and GFP (membrane), and counterstained with DAPI, and quantification (**b**, DMSO, $n = 42$; Alfa, $n = 39$; MEK inhibitor, $n = 28$; Erbb2 inhibitor, $n = 33$). Boxed area indicates high-p-myo cardiomyocytes in DMSO- and Alfa-treated zebrafish embryos. **c–c''**, Representative MIP of 62 hpf hearts (**c**), apical cell surface area (**c'**, Erbb2 inhibitor, $n = 217$; Alfa, $n = 229$) and aspect ratio (**c''**, Erbb2 inhibitor, $n = 199$; Alfa, $n = 205$). **d, d'**, Representative MIP of 48- and 60 hpf hearts immunostained for p-myo and GFP (membrane), and counterstained with DAPI (**d**), and fluorescence intensity (**d'**, 48 hpf, $n = 91$; 60 hpf, $n = 89$). **e, e'**, Representative MIP of 60 hpf hearts of DMSO-, Alfa- and MEK inhibitor-treated zebrafish embryos immunostained for p-myo, GFP (membrane), and counterstained with DAPI (**e**), and fluorescence intensity (**e'**, DMSO, $n = 125$; Alfa, $n = 114$; MEK inhibitor, $n = 120$). Data are mean \pm s.d. One-way ANOVA (**b**), two-

tailed Mann–Whitney *U*-test (**d'**); Kruskal–Wallis test (**e'**). *n* refers to the number of hearts (**b**) or number of cardiomyocytes (**c'**, **c''**, **d'**, **e'**). All box-and-whisker plots show median, 25th and 75th percentiles, and all data points extending from minimum to maximum. Asterisks, delaminating cardiomyocytes; arrowheads, CL cardiomyocytes. Scale bars, 50 μm . For more details on statistics and reproducibility, see [Methods](#). [Source data](#)

Extended Data Fig. 4 Differential cellular contractility is necessary for cardiomyocyte delamination.

a–a'', Representative mid-sagittal confocal images of hearts of *WT-MYL9-GFP-* (*n* = 25), *DN-MYL9-GFP-* (*n* = 37) or *CA-MYL9-GFP-* (*n* = 34) injected 96 hpf zebrafish larvae. **b–c**, Hearts of *mScarlet-WT-RHOA-* (WT, *n* = 57), *mScarlet-DN-RHOA-* (DN, *n* = 37) or *mScarlet-CA-RHOA-* (CA, *n* = 31) injected 98 hpf zebrafish larvae; representative mid-sagittal confocal images (**b–b''**), and quantification (**c**). **d, d'**, Hearts of *mCherry-CAAX-* or *DN-shroom3-P2A-tdtomato*-injected 96 hpf zebrafish larvae; representative mid-sagittal confocal images (**d**), and quantification (**d'**, *n* = 27). **e**, Representative frames from time-lapse imaging of a beating heart (50 hpf) of a *CA-MYL9-mScarlet*-injected animal (*n* = 5/5 hearts). **f, f'**, Hearts of *mScarlet-DN-RHOA-* and *CA-MYL9-GFP*-injected 100 hpf zebrafish larvae; representative mid-sagittal confocal images (**f**), and quantification (**f'**, CA-MYL9, *n* = 32; DN-RHOA, *n* = 18; DN-RHOA + CA-MYL9, *n* = 36). **g–g''**, Heart of 98 hpf zebrafish larvae transplanted with control (ctrl) or *tnnt2a* morpholino (MO) -injected blastomeres; experimental plan (**g**), representative mid-sagittal confocal images (**g'**), and quantification (**g''**, *n* = 17). **h–h''**, Hearts of ctrl (*n* = 12) or *tnnt2a* (*n* = 27) MO-injected 75 hpf zebrafish larvae transplanted with *myl7: mKate-CAAX*blastomeres; experimental plan (**h**), representative mid-sagittal confocal images (**h'**), and quantification (**h''**). Data are mean \pm s.d. Kruskal–Wallis test (**c, f'**), two-tailed Student's *t*-test (**d', h''**). *n* refers to the number of hearts. Asterisks, delaminating or TL cardiomyocytes; arrowheads, CL cardiomyocytes. Scale bars, 50 μm (**a–a''**, **b–b''**, **d, f, g'**, **h'**); 5 μm (**e**). For more details on statistics and reproducibility, see [Methods](#). [Source data](#)

Extended Data Fig. 5 Differential cellular contractility augments cardiomyocyte delamination.

a, a', Heart of *CA-MYL9-GFP*-injected 58 hpf zebrafish embryos; representative mid-sagittal confocal images (**a**), and quantification of apical domain length (**a'**, $n = 12$). **b–c'**, Representative mid-sagittal confocal images of 61 hpf (**b**) and 70 hpf (**c**) hearts of control or *CA-MYL9-GFP*-injected zebrafish embryos, and quantification (**b'**, $n = 16$; **c'**, $n = 14$). **d, d'**, Representative mid-sagittal confocal images of 60 hpf (**d**, $n = 12/12$) and 70 hpf (**d'**, $n = 24/24$) hearts of *CA-MYL9-mScarlet*-injected zebrafish embryos; asterisks: depolarized TL cardiomyocytes. **e, e'**, Representative MIP of 60 hpf hearts of *H2B-BFP*- ($n = 19$) or *CA-MYL9-BFP*- ($n = 23$) injected zebrafish embryos (**e**), and quantification of the percentage of BFP and mVenus-Gmnn double-positive cardiomyocytes (**e'**); asterisks, BFP and mVenus-Gmnn double-positive cardiomyocytes. **f**, Representative confocal images of adult heart expressing *CA-MYL9-mScarlet*, and immunostained for MF-20 (myocardium) and counterstained with DAPI ($n = 5/5$). **g–h**, Representative MIP of 96 hpf hearts of control or *CA-MYL9-BFP*-injected zebrafish larvae treated with DMSO or Erbb2 inhibitor (**g**), and quantification (**h**; **g**, $n = 13$; **g'**, $n = 18$; **g''**, $n = 24$). Data are mean \pm s.d. Two-tailed Student's *t*-test (**a'**, **b'**, **c'**, **e'**); Kruskal–Wallis test (**h**). n refers to the number of hearts (**b'**, **c'**, **e'**, **h**); n = number of cardiomyocytes (**a'**). Asterisks: delaminating or TL cardiomyocytes; arrowheads: CL cardiomyocytes. Scale bars, 50 μm (**a, b, c, d, d', e, f, g–g''**), 200 μm (**f**). For more details on statistics and reproducibility, please see [Methods](#).

[Source data](#)

Extended Data Fig. 6 Differential cellular contractility is sufficient to drive cardiomyocyte delamination and apicobasal depolarization in the absence of Nrg–Erbb2 signalling.

a–b, Hearts of control or *CA-MYL9-mScarlet*-injected 96 hpf zebrafish larvae treated with DMSO or Erbb2 inhibitor; representative mid-sagittal confocal images (**a–a''**), and quantification (**b**; **a'**, $n = 30$; **a''**, $n = 27$). **c–c''**, Hearts of *nrg2a:mRFP;myl7:LIFEACT-GFP* 72 hpf zebrafish larvae injected with *CA-MYL9-BFP*; representative confocal images and 3D

surface-rendered images ($n = 17$). **d–e**, Hearts of *nrg2a:mRFP; myl7:eGFP-Podxl* 96 hpf zebrafish larvae injected with *CA-MYL9-BFP*; representative mid-sagittal confocal images (**e–e''**), and quantification (**d**; **e'**, $n = 12$; **e''**, $n = 15$). **f, f'**, Hearts of ctrl MO-, *amhc* MO- or *amhc* MO + *CA-MYL9-mScarlet*-injected 80 hpf zebrafish larvae; representative confocal images (**f**), and quantification (**f'**, $n = 18$). **g–g''** Hearts of ctrl- or *tnnt2a* MO- ($n = 26$) injected 70 hpf zebrafish embryos, transplanted with *myl7:MYL9-GFP* ($n = 22$) or *myl7:CA-MYL9-GFP* ($n = 32$) blastomeres; experimental plan (**g**), representative mid-sagittal confocal images (**g'**), and quantification (**g''**). Data are mean \pm s.d. Two-tailed Student's *t*-test (**f'**); Two-tailed Mann–Whitney *U*-test (**b, d**); Kruskal–Wallis test (**g''**). n refers to the number of hearts. Asterisks, delaminating or TL cardiomyocytes. Scale bars, 50 μm . For more details on statistics and reproducibility, see [Methods](#). [Source data](#)

[Extended Data Fig. 7 Contractility-induced spatial segregation of cardiomyocytes is necessary and sufficient to trigger Notch reporter expression in CL cardiomyocytes.](#)

a, Representative MIP of 48 hpf heart; Notch reporter expression is observed only in the endocardium ($n = 15/15$ hearts). **b, b'**, Hearts of DMSO- ($n = 20$) or alfacalcidol- (Alfa, $n = 27$) treated 60 hpf zebrafish embryos; representative mid-sagittal confocal images (**b**), and quantification (**b'**). **c, c'** Hearts of DMSO- ($n = 16$) or MEK inhibitor- ($n = 20$) treated 65 hpf zebrafish embryos; representative mid-sagittal confocal images (**c**), and quantification (**c'**). **d–d'**, Hearts of *nrg2a:mRFP;TP1:VenusPest* 100 hpf zebrafish larvae injected with *CA-MYL9-BFP* (**d**), and quantification (**d'**, *nrg2a*^{-/-}, $n = 40$; *nrg2a*^{-/-} + *CA-MYL9*, $n = 56$). **e, e'**, Hearts of *tnnt2a* MO-injected 72 hpf zebrafish larvae ($n = 22$) transplanted with *myl7:CA-MYL9-mScarlet* blastomeres ($n = 27$) (**e**), and quantification (**e'**). **f, f'**, Representative mid-sagittal confocal image of 62 hpf hearts (**f**), and quantification of apical domain length in Notch⁺ CL and Notch⁻ delaminating cardiomyocytes (**f'**, $n = 17$). Data are mean \pm s.d. Two-tailed Student's *t*-test (**b', c', d', f'**); two-tailed Mann–Whitney *U*-test (**e'**). n refers to the number of hearts (**b', c', d', e'**) or number of cardiomyocytes (**f'**). Red arrowheads, Notch⁺ cardiomyocytes;

yellow arrowheads, Notch⁺ endocardial cells; white arrowheads, CL cardiomyocytes; asterisks, delaminating or TL cardiomyocytes. Scale bars, 50 μ m. For more details on statistics and reproducibility, see [Methods](#).

[Source data](#)

[Extended Data Fig. 8 Notch signalling suppresses the actomyosin network in CL cardiomyocytes.](#)

a, a', Representative mid-sagittal confocal and skeletonized images of 70 hpf hearts of DMSO- or Notch-inhibitor-treated zebrafish embryos (**a**), and quantification (**a'**; DMSO, $n = 55$; LY411575, $n = 34$; RO4929097, $n = 35$). Asterisks, TL cardiomyocytes; arrowheads, Notch⁺ cardiomyocytes. **b, b'**, Representative mid-sagittal confocal images of 94 hpf hearts of zebrafish larvae injected with *NICD-P2A-tdTomato* and/or *CA-MYL9-GFP* (**b**), and quantification (**b'**; NICD, $n = 23$; CA-MYL9, $n = 41$; NICD + CA-MYL9, $n = 33$). **c, c'**, Actin localization in Notch⁻ and Notch⁺ (blue dashed line) CL cardiomyocytes of 62 hpf hearts; representative confocal images (en face view) (**c**), and quantification (**c'**, $n = 20$). **d–d''**, Phalloidin localization in Notch⁻ and Notch⁺ (blue dashed line) CL cardiomyocytes of 62 hpf hearts; representative confocal images (en face view) (**d**), and FI profiles (**d'**; Notch⁻, $n = 55$; Notch⁺, $n = 56$), and quantification (**d''**, $n = 21$). **e–e''**, p-myo localization in NICD⁻ and NICD⁺ cardiomyocytes; representative confocal images (en face view) (**e**), and FI profiles ($n = 42$) (**e'**), and quantification (**e''**; $n = 21$). **f–f''**, Representative frames from FRAP of myosin in Notch⁻ and Notch⁺ CL cardiomyocytes (**f**), and representative recovery profiles (**f'**, Notch⁻, $n = 11$; Notch⁺, $n = 12$), and mobile fraction values (**f''**, Notch⁻; $n = 43$; Notch⁺ $n = 47$). **g, g'**, Representative recovery profile (**g**, Notch⁻, $n = 12$; Notch⁺, $n = 9$) and mobile fraction values calculated from FRAP of actin in Notch⁻ ($n = 44$) and Notch⁺ ($n = 39$) CL cardiomyocytes (**g'**). Data are mean \pm s.d., except for **d'** and **e'** (mean \pm s.e.m.). Two-tailed Student's *t*-test (**d'', e'', f'', g'**); two-tailed Mann–Whitney *U*-test (**c'**); Kruskal–Wallis test (**a', b'**). n refers to the number of hearts (**a', b', c', d', e', f', g'**) or number of cardiomyocytes (**d', e'**). Asterisks, delaminating or TL cardiomyocytes; arrowheads, CL cardiomyocytes. Scale bars, 50 μ m (**a, b**); 20 μ m (**c, d, e**). For more details on statistics and reproducibility, see [Methods](#). [Source data](#)

Extended Data Fig. 9 Erbb2 signalling does not regulate actomyosin localization at the onset of trabeculation.

a–a”, Hearts of 65 hpf *erbb2^{+/−}* and *erbb2^{−/−}* zebrafish embryos, immunostained for Alcam, and counterstained with phalloidin and DAPI; representative MIP and en face view of boxed area (**a**), and FI profiles (**a'**, *erbb2^{+/−}*, *n* = 116; *erbb2^{−/−}*, *n* = 111), and quantification (**a”**, *n* = 17). **b, b’**, Hearts of 65 hpf *erbb2^{+/−}* and *erbb2^{−/−}* zebrafish embryos, immunostained for p-myo and counterstained with DAPI; representative MIP and en face view of boxed area (**b**), and quantification (**b’**, *erbb2^{+/−}*, *n* = 17; *erbb2^{−/−}*, *n* = 18). **c–c”**, Hearts of DMSO- or Erbb2 inhibitor-treated 60 hpf zebrafish embryos, immunostained for p-myo and Alcam, and counterstained with phalloidin and DAPI; representative MIP and en face view of boxed area (**c**), and FI profiles (**c’**, DMSO, *n* = 237; Erbb2 inhibitor, *n* = 166), and quantification (**c”**, DMSO, *n* = 26; Erbb2 inhibitor, *n* = 22; **c””**, DMSO, *n* = 19; Erbb2 inhibitor, *n* = 18). Data are mean ± s.d., except for **a’** and **c’** (mean ± s.e.m.). Two-tailed Student’s *t*-test. *n* refers to the number of hearts (**a”, b’, c”, c””**) or number of cardiomyocytes (**a’, c’**). Scale bars, 50 μm. For more details on statistics and reproducibility, see [Methods](#). [Source data](#)

Extended Data Fig. 10 Erbb2 signalling does not regulate actomyosin localization and stability at the onset of trabeculation.

a, a’, Representative MIP and en face view of boxed area of 62 hpf hearts of DMSO or Erbb2 inhibitor-treated zebrafish embryos (**a**), and quantification (**a’**, DMSO, *n* = 25; Erbb2 inhibitor, *n* = 27). **b–b”**, Representative MIP and en face view of boxed area of 62 hpf hearts of DMSO or Erbb2- inhibitor- treated zebrafish embryos (**b**), and FI profiles (**b’**, DMSO, *n* = 189; Erbb2 inhibitor, *n* = 183), and quantification (**b”**, DMSO, *n* = 22; Erbb2 inhibitor, *n* = 25). **c–c”**, FRAP of actin in CL cardiomyocytes of DMSO or Erbb2 inhibitor-treated zebrafish embryos; representative frames (**c**), and representative recovery profiles (**c’**, DMSO, *n* = 16; Erbb2 inhibitor, *n* = 17), and mobile fraction values (**c”**, DMSO, *n* = 39; Erbb2 inhibitor, *n* = 45). **d–d”**, FRAP of myosin in CL

cardiomyocytes of DMSO- or Erbb2 inhibitor-treated animals; representative frames (**d**), and recovery profiles (**d'**, $n = 43$), and mobile fraction values (**d''**, $n = 42$). Data are mean \pm s.d., except for **b'** (mean \pm s.e.m.). Two-tailed Mann–Whitney *U*-test (**a'**, **c''**, **d''**); two-tailed Student's *t*-test (**b''**). n refers to the number of hearts (**a'**, **b''**, **c'**, **c''**, **d'**, **d''**) or number of cardiomyocytes (**b'**). Scale bars, 50 μm . For more details on statistics and reproducibility, see [Methods](#). [Source data](#)

Supplementary information

[Supplementary Methods](#)

This file contains Supplementary Method 1: Macro for time-lapse live imaging of beating hearts on a Zeiss CSU-X1 Yokogawa spinning disk; and Supplementary Method 2: Laser nano-ablation data analysis.

[Reporting Summary](#)

[Supplementary Video 1](#)

Delaminating cardiomyocytes constrict their apical domain and exhibit enhanced myosin recruitment. Time-lapse imaging of a delaminating cardiomyocyte in a 60 hpf *myl7:HRAS-GFP* (green); *myl7:myl9-mScarlet* (magenta) heart. Scale bar, 10 μm .

[Supplementary Video 2](#)

Cardiomyocytes expressing CA-MYL9 delaminate to seed the trabecular layer. Time-lapse imaging of a 50 hpf *myl7:HRAS-GFP* (green) heart injected with *myl7:CA-MYL9-mScarlet* (magenta). Scale bar, 10 μm .

[Supplementary Video 3](#)

Cardiomyocytes expressing CA-MYL9 form trabecular ridges. Representative 3-D surface rendered animation of 15 dpf hearts of *myl7:GFP* or *myl7:CA-MYL9-GFP* injected animals. Scale bar, 30 μm .

Supplementary Video 4

Cardiomyocytes expressing CA-MYL9 form trabecular ridges in the absence of Erbb2 signalling. Representative 3-D surface rendered animation of 96 hpf hearts of control or *myl7:CA-MYL9-mScarlet* injected animals treated with DMSO or Erbb2 inhibitor. Scale bar, 20 μ m.

Supplementary Video 5

Cardiomyocytes expressing CA-MYL9 form trabecular ridges in the absence of Nrg2a signalling. Representative 3-D surface rendered animation of 72 hpf hearts of *nrg2a:mRFP; myl7:LIFEACT-GFP* animals injected with *myl7:CA-MYL9-BFP*. Scale Bar, 20 μ m.

Source data

[**Source Data Fig. 1**](#)

[**Source Data Fig. 2**](#)

[**Source Data Fig. 3**](#)

[**Source Data Fig. 4**](#)

[**Source Data Extended Data Fig. 1**](#)

[**Source Data Extended Data Fig. 2**](#)

[**Source Data Extended Data Fig. 3**](#)

[**Source Data Extended Data Fig. 4**](#)

[**Source Data Extended Data Fig. 5**](#)

[**Source Data Extended Data Fig. 6**](#)

[Source Data Extended Data Fig. 7](#)

[Source Data Extended Data Fig. 8](#)

[Source Data Extended Data Fig. 9](#)

[Source Data Extended Data Fig. 10](#)

Rights and permissions

[Reprints and Permissions](#)

About this article



Check for
updates

Cite this article

Priya, R., Allanki, S., Gentile, A. *et al.* Tension heterogeneity directs form and fate to pattern the myocardial wall. *Nature* **588**, 130–134 (2020).
<https://doi.org/10.1038/s41586-020-2946-9>

[Download citation](#)

- Received: 05 August 2019
- Accepted: 07 September 2020
- Published: 18 November 2020
- Issue Date: 03 December 2020
- DOI: <https://doi.org/10.1038/s41586-020-2946-9>

Comments

By submitting a comment you agree to abide by our [Terms](#) and [Community Guidelines](#). If you find something abusive or that does not comply with our terms or guidelines please flag it as inappropriate.

[Access through your institution](#)

[Change institution](#)

[Buy or subscribe](#)

This article was downloaded by **calibre** from <https://www.nature.com/articles/s41586-020-2946-9>

| [Section menu](#) | [Main menu](#) |

- Article
- [Published: 11 November 2020](#)

A reference map of potential determinants for the human serum metabolome

- [Noam Bar](#)^{1,2 na1},
- [Tal Korem](#) [ORCID: orcid.org/0000-0002-0609-0858](#)^{1,2,3,4,5 na1},
- [Omer Weissbrod](#)^{1,2,6},
- [David Zeevi](#) [ORCID: orcid.org/0000-0002-6492-6078](#)^{1,2,7},
- [Daphna Rothschild](#)^{1,2},
- [Sigal Leviatan](#)^{1,2},
- [Noa Kosower](#)^{1,2},
- [Maya Lotan-Pompan](#)^{1,2},
- [Adina Weinberger](#)^{1,2},
- [Caroline I. Le Roy](#) [ORCID: orcid.org/0000-0002-0341-751X](#)⁸,
- [Cristina Menni](#)⁸,
- [Alessia Visconti](#) [ORCID: orcid.org/0000-0003-4144-2019](#)⁸,
- [Mario Falchi](#)⁸,
- [Tim D. Spector](#) [ORCID: orcid.org/0000-0002-9795-0365](#)⁸,
- [The IMI DIRECT consortium](#),
- [Jerzy Adamski](#) [ORCID: orcid.org/0000-0001-9259-0199](#)^{9,10,11},
- [Paul W. Franks](#) [ORCID: orcid.org/0000-0002-0520-7604](#)^{12,13},
- [Oluf Pedersen](#) [ORCID: orcid.org/0000-0002-3321-3972](#)¹⁴ &
- [Eran Segal](#) [ORCID: orcid.org/0000-0002-6859-1164](#)^{1,2}

[Nature](#) volume 588, pages135–140(2020)[Cite this article](#)

- 12k Accesses

- 220 Altmetric
- [Metrics details](#)

Subjects

- [Databases](#)
- [Machine learning](#)
- [Metabolomics](#)
- [Microbiology](#)

Abstract

The serum metabolome contains a plethora of biomarkers and causative agents of various diseases, some of which are endogenously produced and some that have been taken up from the environment¹. The origins of specific compounds are known, including metabolites that are highly heritable^{2,3}, or those that are influenced by the gut microbiome⁴, by lifestyle choices such as smoking⁵, or by diet⁶. However, the key determinants of most metabolites are still poorly understood. Here we measured the levels of 1,251 metabolites in serum samples from a unique and deeply phenotyped healthy human cohort of 491 individuals. We applied machine-learning algorithms to predict metabolite levels in held-out individuals on the basis of host genetics, gut microbiome, clinical parameters, diet, lifestyle and anthropometric measurements, and obtained statistically significant predictions for more than 76% of the profiled metabolites. Diet and microbiome had the strongest predictive power, and each explained hundreds of metabolites—in some cases, explaining more than 50% of the observed variance. We further validated microbiome-related predictions by showing a high replication rate in two geographically independent cohorts^{7,8} that were not available to us when we trained the algorithms. We used feature attribution analysis⁹ to reveal specific dietary and bacterial interactions. We further demonstrate that some of these interactions might be causal, as some metabolites that we predicted to be positively associated with bread were found to increase after a randomized clinical trial of bread intervention. Overall, our results reveal potential determinants of more than

800 metabolites, paving the way towards a mechanistic understanding of alterations in metabolites under different conditions and to designing interventions for manipulating the levels of circulating metabolites.

[Access through your institution](#)

[Change institution](#)

[Buy or subscribe](#)

Access options

Subscribe to Journal

Get full journal access for 1 year

185,98 €

only 3,58 € per issue

[Subscribe](#)

All prices are NET prices.

VAT will be added later in the checkout.

Rent or Buy article

Get time limited or full article access on ReadCube.

from \$8.99

[Rent or Buy](#)

All prices are NET prices.

Additional access options:

- [Log in](#)
- [Access through your institution](#)
- [Learn about institutional subscriptions](#)

Fig. 1: Diet, gut microbiome, genetics and clinical data predict the levels of most serum metabolites.



Fig. 2: Validation of microbiome-based predictions of metabolites in two independent cohorts.



Fig. 3: Diet and gut microbiome data independently explain a wide range of biochemicals.



Fig. 4: Increases in levels of metabolites explained by bread after an intervention of increased bread consumption.



Data availability

The raw metagenomic sequencing data are available from the European Nucleotide Archive under accession numbers PRJEB11532, PRJEB17643, and for TwinsUK PRJEB32731. The raw metabolomics data and the phenotypic data are available from the European Genome–phenome Archive (EGA; <https://ega-archive.org/>) with accession number EGAS00001004512. Known links between genetic loci and serum metabolites were taken from the GWAS Catalog⁴⁶ (<https://www.ebi.ac.uk/gwas/>) and the GWAS server^{2,22} (<http://metabolomics.helmholtz-muenchen.de/gwas/>).

Code availability

Source code for analysis is available at
<https://github.com/noambar/SerumMetabolomePredictions>.

References

1. 1.

- Psychogios, N. et al. The human serum metabolome. *PLoS ONE* **6**, e16957 (2011).

[ADS](#) [CAS](#) [PubMed](#) [PubMed Central](#) [Google Scholar](#)

2. 2.

Shin, S.-Y. et al. An atlas of genetic influences on human blood metabolites. *Nat. Genet.* **46**, 543–550 (2014).

[CAS](#) [PubMed](#) [PubMed Central](#) [Google Scholar](#)

3. 3.

Long, T. et al. Whole-genome sequencing identifies common-to-rare variants associated with human blood metabolites. *Nat. Genet.* **49**, 568–578 (2017).

[CAS](#) [PubMed](#) [PubMed Central](#) [Google Scholar](#)

4. 4.

Wikoff, W. R. et al. Metabolomics analysis reveals large effects of gut microflora on mammalian blood metabolites. *Proc. Natl Acad. Sci. USA* **106**, 3698–3703 (2009).

[ADS](#) [CAS](#) [PubMed](#) [PubMed Central](#) [Google Scholar](#)

5. 5.

Xu, T. et al. Effects of smoking and smoking cessation on human serum metabolite profile: results from the KORA cohort study. *BMC Med.* **11**, 60 (2013).

[CAS](#) [PubMed](#) [PubMed Central](#) [Google Scholar](#)

6. 6.

Playdon, M. C. et al. Comparing metabolite profiles of habitual diet in serum and urine. *Am. J. Clin. Nutr.* **104**, 776–789 (2016).

[CAS](#) [PubMed](#) [PubMed Central](#) [Google Scholar](#)

7. 7.

Moayyeri, A., Hammond, C. J., Hart, D. J. & Spector, T. D. The UK Adult Twin Registry (TwinsUK Resource). *Twin Res. Hum. Genet.* **16**, 144–149 (2013).

[PubMed](#) [PubMed Central](#) [Google Scholar](#)

8. 8.

Koivula, R. W. et al. Discovery of biomarkers for glycaemic deterioration before and after the onset of type 2 diabetes: rationale and design of the epidemiological studies within the IMI DIRECT Consortium. *Diabetologia* **57**, 1132–1142 (2014).

[CAS](#) [PubMed](#) [PubMed Central](#) [Google Scholar](#)

9. 9.

Lundberg, S. M., Erion, G. G. & Lee, S.-I. Consistent individualized feature attribution for tree ensembles. Preprint at <https://arxiv.org/abs/1802.03888v3> (2018).

10. 10.

Zeevi, D. et al. Personalized nutrition by prediction of glycemic responses. *Cell* **163**, 1079–1094 (2015).

[CAS](#) [PubMed](#) [PubMed Central](#) [Google Scholar](#)

11. 11.

Yousri, N. A. et al. Long term conservation of human metabolic phenotypes and link to heritability. *Metabolomics* **10**, 1005–1017 (2014).

[CAS](#) [PubMed](#) [PubMed Central](#) [Google Scholar](#)

12. 12.

Ke, G. et al. LightGBM: a highly efficient gradient boosting decision tree. In *Advances in Neural Information Processing Systems 30* (eds Guyon, I. et al.) (Neural Information Processing Systems Foundation, 2017).

13. 13.

Cirulli, E. T. et al. Profound perturbation of the metabolome in obesity is associated with health risk. *Cell Metab.* **29**, 488–500.e2 (2019).

[CAS](#) [PubMed](#) [PubMed Central](#) [Google Scholar](#)

14. 14.

David, L. A. et al. Diet rapidly and reproducibly alters the human gut microbiome. *Nature* **505**, 559–563 (2014).

[ADS](#) [CAS](#) [Google Scholar](#)

15. 15.

Azam, S., Hadi, N., Khan, N. U. & Hadi, S. M. Antioxidant and prooxidant properties of caffeine, theobromine and xanthine. *Med. Sci. Monit.* **9**, BR325–BR330 (2003).

[CAS](#) [PubMed](#) [PubMed Central](#) [Google Scholar](#)

16. 16.

Tsutsumi, Y. et al. Renal disposition of a furan dicarboxylic acid and other uremic toxins in the rat. *J. Pharmacol. Exp. Ther.* **303**, 880–887 (2002).

[CAS](#) [PubMed](#) [PubMed Central](#) [Google Scholar](#)

17. 17.

Prentice, K. J. et al. CMPE, a metabolite formed upon prescription omega-3-acid ethyl ester supplementation, prevents and reverses

steatosis. *EBioMedicine* **27**, 200–213 (2018).

[PubMed](#) [PubMed Central](#) [Google Scholar](#)

18. 18.

Nemet, I. et al. A cardiovascular disease-linked gut microbial metabolite acts via adrenergic receptors. *Cell* **180**, 862–877.e22 (2020).

[CAS](#) [Google Scholar](#)

19. 19.

Hung, S.-C., Kuo, K.-L., Wu, C.-C. & Tarng, D.-C. Indoxyl sulfate: A novel cardiovascular risk factor in chronic kidney disease. *J. Am. Heart Assoc.* <https://doi.org/10.1161/JAHA.116.005022> (2017).

20. 20.

Evenepoel, P., Meijers, B. K. I., Bammens, B. R. M. & Verbeke, K. Uremic toxins originating from colonic microbial metabolism. *Kidney Int.* **76**, S12–S19 (2009).

[Google Scholar](#)

21. 21.

Youssi, N. A. et al. Whole-exome sequencing identifies common and rare variant metabolic QTLs in a Middle Eastern population. *Nat. Commun.* **9**, 333 (2018).

[ADS](#) [PubMed](#) [PubMed Central](#) [Google Scholar](#)

22. 22.

Suhre, K. et al. Human metabolic individuality in biomedical and pharmaceutical research. *Nature* **477**, 54–60 (2011).

[ADS](#) [CAS](#) [Google Scholar](#)

23. 23.

Gieger, C. et al. Genetics meets metabolomics: a genome-wide association study of metabolite profiles in human serum. *PLoS Genet.* **4**, e1000282 (2008).

[PubMed](#) [PubMed Central](#) [Google Scholar](#)

24. 24.

Kettunen, J. et al. Genome-wide association study identifies multiple loci influencing human serum metabolite levels. *Nat. Genet.* **44**, 269–276 (2012).

[CAS](#) [PubMed](#) [PubMed Central](#) [Google Scholar](#)

25. 25.

Capo-chichi, C. D. et al. Riboflavin and riboflavin-derived cofactors in adolescent girls with anorexia nervosa. *Am. J. Clin. Nutr.* **69**, 672–678 (1999).

[CAS](#) [PubMed](#) [PubMed Central](#) [Google Scholar](#)

26. 26.

Darst, B. F., Lu, Q., Johnson, S. C. & Engelman, C. D. Integrated analysis of genomics, longitudinal metabolomics, and Alzheimer's risk factors among 1,111 cohort participants. *Genet. Epidemiol.* **43**, 657–674 (2019).

[PubMed](#) [PubMed Central](#) [Google Scholar](#)

27. 27.

Sookoian, S., Castaño, G., Gianotti, T. F., Gemma, C. & Pirola, C. J. Polymorphisms of MRP2 (*ABCC2*) are associated with susceptibility

to nonalcoholic fatty liver disease. *J. Nutr. Biochem.* **20**, 765–770 (2009).

[CAS](#) [PubMed](#) [PubMed Central](#) [Google Scholar](#)

28. 28.

Hamaguchi, M. et al. Aging is a risk factor of nonalcoholic fatty liver disease in premenopausal women. *World J. Gastroenterol.* **18**, 237–243 (2012).

[PubMed](#) [PubMed Central](#) [Google Scholar](#)

29. 29.

Korem, T. et al. Bread affects clinical parameters and induces gut microbiome-associated personal glycemic responses. *Cell Metab.* **25**, 1243–1253.e5 (2017).

[CAS](#) [Google Scholar](#)

30. 30.

Olthof, M. R., van Vliet, T., Boelsma, E. & Verhoef, P. Low dose betaine supplementation leads to immediate and long term lowering of plasma homocysteine in healthy men and women. *J. Nutr.* **133**, 4135–4138 (2003).

[CAS](#) [PubMed](#) [PubMed Central](#) [Google Scholar](#)

31. 31.

Craig, S. A. S. Betaine in human nutrition. *Am. J. Clin. Nutr.* **80**, 539–549 (2004).

[CAS](#) [PubMed](#) [PubMed Central](#) [Google Scholar](#)

32. 32.

Liu, J. et al. Integration of epidemiologic, pharmacologic, genetic and gut microbiome data in a drug-metabolite atlas. *Nat. Med.* **26**, 110–117 (2020).

[CAS](#) [PubMed](#) [PubMed Central](#) [Google Scholar](#)

33. 33.

Rothschild, D. et al. Environment dominates over host genetics in shaping human gut microbiota. *Nature* **555**, 210–215 (2018).

[ADS](#) [CAS](#) [PubMed](#) [PubMed Central](#) [Google Scholar](#)

34. 34.

Segata, N. et al. Metagenomic microbial community profiling using unique clade-specific marker genes. *Nat. Methods* **9**, 811–814 (2012).

[CAS](#) [PubMed](#) [PubMed Central](#) [Google Scholar](#)

35. 35.

Li, J. et al. An integrated catalog of reference genes in the human gut microbiome. *Nat. Biotechnol.* **32**, 834–841 (2014).

[CAS](#) [PubMed](#) [PubMed Central](#) [Google Scholar](#)

36. 36.

Zeevi, D. et al. Structural variation in the gut microbiome associates with host health. *Nature* **568**, 43–48 (2019).

[ADS](#) [CAS](#) [PubMed](#) [PubMed Central](#) [Google Scholar](#)

37. 37.

Evans, A. M. et al. High resolution mass spectrometry improves data quantity and quality as compared to unit mass resolution mass

spectrometry in high-throughput profiling metabolomics.
Metabolomics **4**, 1000132 (2014).

[Google Scholar](#)

38. 38.

Zierer, J. et al. The fecal metabolome as a functional readout of the gut microbiome. *Nat. Genet.* **50**, 790–795 (2018).

[CAS](#) [PubMed](#) [PubMed Central](#) [Google Scholar](#)

39. 39.

Marco-Sola, S., Sammeth, M., Guigó, R. & Ribeca, P. The GEM mapper: fast, accurate and versatile alignment by filtration. *Nat. Methods* **9**, 1185–1188 (2012).

[CAS](#) [PubMed](#) [PubMed Central](#) [Google Scholar](#)

40. 40.

Pasolli, E. et al. Extensive unexplored human microbiome diversity revealed by over 150,000 genomes from metagenomes spanning age, geography, and lifestyle. *Cell* **176**, 649–662.e20 (2019).

[CAS](#) [PubMed](#) [PubMed Central](#) [Google Scholar](#)

41. 41.

Langmead, B. & Salzberg, S. L. Fast gapped-read alignment with Bowtie 2. *Nat. Methods* **9**, 357–359 (2012).

[CAS](#) [PubMed](#) [PubMed Central](#) [Google Scholar](#)

42. 42.

Korem, T. et al. Growth dynamics of gut microbiota in health and disease inferred from single metagenomic samples. *Science* **349**, 1101–

1106 (2015).

[ADS](#) [CAS](#) [PubMed](#) [PubMed Central](#) [Google Scholar](#)

43. 43.

Efron, B. & Tibshirani, R. J. *An Introduction to the Bootstrap* (Chapman and Hall, 1994).

44. 44.

Fisher, R. A. Frequency distribution of the values of the correlation coefficient in samples from an indefinitely large population. *Biometrika* **10**, 507 (1915).

[Google Scholar](#)

45. 45.

Wald, A. Sequential tests of statistical hypotheses. *Ann. Math. Stat.* **16**, 117–186 (1945).

[MathSciNet](#) [MATH](#) [Google Scholar](#)

46. 46.

Bunielo, A. et al. The NHGRI-EBI GWAS Catalog of published genome-wide association studies, targeted arrays and summary statistics 2019. *Nucleic Acids Res.* **47**, D1005–D1012 (2019).

[CAS](#) [PubMed](#) [PubMed Central](#) [Google Scholar](#)

47. 47.

Lundberg, S. & Lee, S.-I. A unified approach to interpreting model predictions. Preprint at <https://arxiv.org/abs/1705.07874v2> (2017).

48. 48.

Manor, O. & Borenstein, E. Systematic characterization and analysis of the taxonomic drivers of functional shifts in the human microbiome. *Cell Host Microbe* **21**, 254–267 (2017).

[PubMed](#) [PubMed Central](#) [Google Scholar](#)

49. 49.

SHAP <https://github.com/slundberg/shap>

50. 50.

Shannon, P. et al. Cytoscape: a software environment for integrated models of biomolecular interaction networks. *Genome Res.* **13**, 2498–2504 (2003).

[CAS](#) [PubMed](#) [PubMed Central](#) [Google Scholar](#)

51. 51.

Yang, J., Lee, S. H., Goddard, M. E. & Visscher, P. M. GCTA: a tool for genome-wide complex trait analysis. *Am. J. Hum. Genet.* **88**, 76–82 (2011).

[CAS](#) [PubMed](#) [PubMed Central](#) [Google Scholar](#)

52. 52.

Schweiger, R. et al. RL-SKAT: an exact and efficient score test for heritability and set tests. *Genetics* **207**, 1275–1283 (2017).

[PubMed](#) [PubMed Central](#) [Google Scholar](#)

[Download references](#)

Acknowledgements

We thank past and present members of the Segal group for discussions. N.B. received a PhD scholarship for Data Science by the Israeli Council for Higher Education (CHE) via the Weizmann Data Science Research Center and is supported by a research grant from Madame Olga Klein Astrachan. T.K. is a CIFAR Azrieli Global Scholar in the Humans & the Microbiome Program. E.S. is supported by the Crown Human Genome Center, by D. L. Schwarz, J. N. Halpern and L. Steinberg, and by grants funded by the European Research Council and the Israel Science Foundation. The work leading to this publication has received support from the Innovative Medicines Initiative Joint Undertaking under grant agreement no.115317 (DIRECT), resources of which are composed of financial contribution from the European Union's Seventh Framework Programme (FP7/2007-2013) and in-kind contribution from EFPIA companies. We thank A. Dutta for introducing us to the DIRECT consortium dataset.

Author information

Author notes

1. Ana Viñuela

Present address: Translational and Clinical Research Institute, Faculty of Medical Sciences, Newcastle University, Newcastle upon Tyne, UK

2. Mark McCarthy & Anubha Mahajan

Present address: Human Genetics, Genentech, South San Francisco, CA, USA

3. These authors contributed equally: Noam Bar, Tal Korem

Affiliations

1. Department of Computer Science and Applied Mathematics, Weizmann Institute of Science, Rehovot, Israel

Noam Bar, Tal Korem, Omer Weissbrod, David Zeevi, Daphna Rothschild, Sigal Leviatan, Noa Kosower, Maya Lotan-Pompan, Adina Weinberger & Eran Segal

2. Department of Molecular Cell Biology, Weizmann Institute of Science, Rehovot, Israel

Noam Bar, Tal Korem, Omer Weissbrod, David Zeevi, Daphna Rothschild, Sigal Leviatan, Noa Kosower, Maya Lotan-Pompan, Adina Weinberger & Eran Segal

3. Department of Systems Biology, Columbia University Irving Medical Center, New York, NY, USA

Tal Korem

4. Department of Obstetrics and Gynecology, Columbia University Irving Medical Center, New York, NY, USA

Tal Korem

5. CIFAR Azrieli Global Scholars Program, CIFAR, Toronto, Ontario, Canada

Tal Korem

6. Department of Epidemiology, Harvard T.H. Chan School of Public Health, Boston, MA, USA

Omer Weissbrod

7. Center for Studies in Physics and Biology, The Rockefeller University, New York, NY, USA

David Zeevi

8. Department for Twin Research & Genetic Epidemiology, King's College London, London, UK

Caroline I. Le Roy, Cristina Menni, Alessia Visconti, Mario Falchi & Tim D. Spector

9. Research Unit Molecular Endocrinology and Metabolism, Genome Analysis Center, Helmholtz Zentrum München, German Research Center for Environmental Health, Neuherberg, Germany

Jerzy Adamski

10. Lehrstuhl für Experimentelle Genetik, Technische Universität München, Freising-Weihenstephan, Germany

Jerzy Adamski

11. Department of Biochemistry, Yong Loo Lin School of Medicine, National University of Singapore, Singapore, Singapore

Jerzy Adamski

12. Lund University Diabetes Center, Department of Clinical Sciences, Lund University, Malmö, Sweden

Paul W. Franks

13. Harvard T.H. Chan School of Public Health, Boston, MA, USA

Paul W. Franks

14. The Novo Nordisk Foundation Center for Basic Metabolic Research, Faculty of Health and Medical Sciences, University of Copenhagen, Copenhagen, Denmark

Henrik Vestergaard, Manimozhiyan Arumugam, Torben Hansen, Kristine Allin, Tue Hansen & Oluf Pedersen

15. Bornholms Hospital, Rønne, Denmark

Henrik Vestergaard

16. Affinity Proteomics, Science for Life Laboratory, School of Engineering Sciences in Chemistry, Biotechnology and Health, KTH - Royal Institute of Technology, Solna, Sweden

Mun-Gwan Hong, Jochen Schwenk, Ragna Haussler & Matilda Dale

17. Biophysics Institute (IBF-CNR), National Research Council of Italy, Milan, Italy

Toni Giorgino

18. Department of Biosciences, University of Milan, Milan, Italy

Toni Giorgino

19. Biotech & Biomarkers Research Department, Institut de Recherches Internationales Servier, Croissy sur Seine, France

Marianne Rodriquez

20. Blood Sciences, Royal Devon and Exeter NHS Foundation Trust, Exeter, UK

Mandy Perry, Rachel Nice & Timothy McDonald

21. Institute of Clinical and Biological Sciences, University of Exeter Medical School, Exeter, UK

Timothy McDonald, Andrew Hattersley & Angus Jones

22. Therapeutic Area CNS, Retinopathies and Emerging Areas, Boehringer Ingelheim International GmbH, Ingelheim am Rhein, Germany

Ulrike Graefe-Mody

23. Translational Medicine & Clinical Pharmacology, Boehringer Ingelheim International GmbH, Biberach an der Riss, Germany

Patrick Baum & Rolf Grempler

24. Affinity Proteomics, Science for Life Laboratory, School of Biotechnology, KTH - Royal Institute of Technology, Solna, Sweden

Cecilia Engel Thomas

25. Disease Systems Biology Program, Novo Nordisk Foundation Center for Protein Research, Faculty of Health and Medical Sciences, University of Copenhagen, Copenhagen, Denmark

Cecilia Engel Thomas, Federico De Masi, Caroline Anna Brorsson, Gianluca Mazzoni, Rosa Allesøe, Simon Rasmussen, Valborg Gudmundsdóttir, Agnes Martine Nielsen, Karina Banasik, Konstantinos Tsirigos, Birgitte Nilsson, Helle Pedersen, Søren Brunak, Tugce Karaderi, Agnete Troen Lundgaard & Joachim Johansen

26. Section for Bioinformatics, Department of Health Technology, Technical University of Denmark, Kongens Lyngby, Denmark

Cecilia Engel Thomas, Federico De Masi, Caroline Anna Brorsson, Gianluca Mazzoni, Rosa Allesøe, Simon Rasmussen, Valborg Gudmundsdóttir, Agnes Martine Nielsen, Karina Banasik, Konstantinos Tsirigos, Birgitte Nilsson, Helle Pedersen, Søren Brunak, Tugce Karaderi, Agnete Troen Lundgaard, Joachim Johansen, Ramneek Gupta & Peter Wad Sackett

27. Clinical Operations, Sanofi-Aventis Deutschland GmbH, Frankfurt, Germany

Joachim Tillner

28. Clinical Pharmacy, Saarland University, Saarbrücken, Germany

Thorsten Lehr, Nina Scherer, Christiane Dings & Iryna Sihinevich

29. Clinical Research Centre, Ninewells Hospital and Medical School, University of Dundee, Dundee, UK

Heather Loftus & Louise Cabrelli

30. Clinical Research Facility, Royal Victoria Infirmary, Newcastle upon Tyne, UK

Donna McEvoy

31. CNR Institute of Neuroscience, Padova, Italy

Andrea Mari, Roberto Bizzotto & Andrea Tura

32. Department of Biomedical Data Sciences, Molecular Epidemiology Section, Leiden University Medical Center, Leiden, The Netherlands

Leen 't Hart

33. Department of Cell and Chemical Biology, Leiden University Medical Center, Leiden, The Netherlands

Leen 't Hart, Koen Dekkers, Nienke van Leeuwen & Roderick Slieker

34. Department of Epidemiology and Biostatistics, Amsterdam UMC- location VUmc, Amsterdam Public Health Research Institute, Amsterdam, The Netherlands

Leen 't Hart, Roderick Slieker, Femke Rutters, Joline Beulens, Giel Nijpels, Anita Koopman, Sabine van Oort & Lenka Groeneveld

35. Department of Clinical Sciences, Diabetes and Endocrinology Unit, Lund University, Skåne University Hospital Malmö, CRC, Malmö, Sweden

Leif Groop

36. Department of General Practice, Amsterdam UMC- location VUmc, Amsterdam Public Health Research Institute, Amsterdam, The Netherlands

Petra Elders

37. Department of Genetic Medicine and Development, University of Geneva Medical School, Geneva, Switzerland

Ana Viñuela, Anna Ramisch & Emmanouil Dermitzakis

38. Department of Mathematical Sciences, University of Bath, Bath, UK

Beate Ehrhardt & Christopher Jennison

39. Department of Metabolism, Digestion and Reproduction, Imperial College London, London, UK

Philippe Froguel

40. Université de Lille, INSERM UMR 1283, CNRS UMR 8199, Institut Pasteur de Lille, EGID, Lille, France

Philippe Froguel, Mickaël Canouil & Amélie Boneford

41. Diabetes Research Network, Royal Victoria Infirmary, Newcastle upon Tyne, UK

Ian McVittie & Dianne Wake

42. Digital and Data Sciences, Sanofi-Aventis Deutschland GmbH, Frankfurt, Germany

Francesca Frau

43. Center for Biological Sequence Analysis, Department of Systems Biology, Technical University of Denmark, Kongens Lyngby, Denmark

Hans-Henrik Staerfeldt

44. Eli Lilly and Company, Indianapolis, IN, USA

Kofi Adragni, Melissa Thomas & Han Wu

45. Eli Lilly Regional Operations GmbH, Vienna, Austria

Imre Pavo & Birgit Steckel-Hamann

46. Faculty of Medical and Health Sciences, University of Copenhagen,
Copenhagen, Denmark

Henrik Thomsen

47. Genetic and Molecular Epidemiology Unit, Lund University Diabetes
Centre, Department of Clinical Sciences, CRC, Lund University, SUS,
Malmö, Sweden

Giuseppe Nicola Giordano, Hugo Fitipaldi, Martin Ridderstråle, Azra
Kurbasic, Naeimeh Atabaki Pasdar, Hugo Pomares-Millan, Pascal
Mutie & Robert Koivula

48. Oxford Centre for Diabetes, Endocrinology and Metabolism, Radcliffe
Department of Medicine, University of Oxford, Oxford, UK

Robert Koivula, Nicky McRobert, Mark McCarthy & Agata
Wesolowska-Andersen

49. Oxford NIHR Biomedical Research Centre, Oxford University
Hospitals NHS Foundation Trust, John Radcliffe Hospital, Oxford, UK

Mark McCarthy

50. Wellcome Centre for Human Genetics, University of Oxford, Oxford,
UK

Mark McCarthy, Anubha Mahajan, Moustafa Abdalla & Juan
Fernandez

51. Institute for Epidemiology and Medical Biometry, ZIBMT, University
of Ulm, Ulm, Germany

Reinhard Holl

52. Institute of Cellular Medicine, Newcastle University, Newcastle upon Tyne, UK

Alison Heggie & Harshal Deshmukh

53. Therapeutic Area CardioMetabolism and Respiratory Medicine, Boehringer Ingelheim International GmbH, Ingelheim am Rhein, Germany

Anita Hennige, Susanna Bianzano & Hartmut Ruetten

54. Institute of Epidemiology II, Research Unit of Diabetes Epidemiology, Helmholtz Zentrum München, Neuherberg, Germany

Barbara Thorand

55. German Center for Diabetes Research (DZD), Neuherberg, Germany

Barbara Thorand, Sapna Sharma & Harald Grallert

56. Research Unit of Molecular Epidemiology, Institute of Epidemiology, Helmholtz Zentrum München, Neuherberg, Germany

Sapna Sharma, Harald Grallert, Jonathan Adam & Martina Troll

57. Medizinische Universitätsklinik Tübingen, Eberhard Karls Universität Tübingen, Tübingen, Germany

Andreas Fritzsche

58. NIHR Exeter Clinical Research Facility, University of Exeter Medical School, Exeter, UK

Anita Hill, Claire Thorne & Michelle Hudson

59. Internal Medicine, Institute of Clinical Medicine, University of Eastern Finland, Kuopio, Finland

Teemu Kuulasmaa, Jagadish Vangipurapu, Markku Laakso, Henna Cederberg & Tarja Kokkola

60. Oxford Centre for Diabetes, Endocrinology and Metabolism,
University of Oxford, Oxford, UK

Yunlong Jiao, Stephen Gough & Neil Robertson

61. Inserm, Université de Lille, CHU Lille, Lille Pasteur Institute, EGID,
Lille, France

Helene Verkindt, Violeta Raverdi, Robert Caiazzo & Francois Pattou

62. Population Health and Genomics, School of Medicine, University of
Dundee, Dundee, UK

Margaret White, Louise Donnelly, Andrew Brown, Colin
Palmer, David Davtian, Adem Dawed, Ian Forgie & Ewan Pearson

63. R&D Global Development, Translational Medicine & Clinical
Pharmacology (TMCP), Sanofi-Aventis Deutschland GmbH,
Frankfurt, Germany

Petra Musholt

64. Research Centre for Optimal Health, Department of Life Sciences,
University of Westminster, London, UK

Jimmy Bell, Elizabeth Louise Thomas & Brandon Whitcher

65. Research Unit of Molecular Endocrinology and Metabolism,
Helmholtz Zentrum München, Neuherberg, Germany

Mark Haid

66. Lilly Deutschland GmbH, Bad Homburg, Germany

Claudia Nicolay

67. Centre for Health, Law and Emerging Technologies (HeLEX), Faculty of Law, University of Oxford, Oxford, UK

Miranda Mourby, Jane Kaye, Nisha Shah & Harriet Teare

68. Technologies (HeLEX), Melbourne Law School, University of Melbourne, Carlton, Victoria, Australia

Jane Kaye

69. Section for Nutrition Research, Faculty of Medicine, Imperial College London, London, UK

Gary Frost

70. Strategy and Innovation, Sanofi-Aventis Deutschland GmbH, Frankfurt, Germany

Bernd Jablonka

71. Systems Biology, Science for Life Laboratory, School of Engineering Sciences in Chemistry, Biotechnology and Health, KTH - Royal Institute of Technology, Solna, Sweden

Mathias Uhlen

72. Section for Nutrition Research, Division of Digestive Diseases, Department of Metabolism, Digestion and Reproduction, Faculty of Medicine, Imperial College London, London, UK

Rebeca Eriksen

73. The Novo Nordisk Center for Basic Metabolic Research, Section of Metabolic Genetics, Faculty of Health and Medical Science, University of Copenhagen, Copenhagen, Denmark

Josef Vogt, Avirup Dutta, Anna Jonsson, Line Engelbrechtsen, Annemette Forman & Nadja Sondertoft

74. Translational and Clinical Research, Metabolism Innovation Pole,
Institut de Recherches Internationales Servier, Suresnes, France

Nathalie de Preville & Tania Baltauss

75. Translational and Clinical Research Institute, Faculty of Medical
Sciences, Newcastle University, Newcastle upon Tyne, UK

Mark Walker

76. Diabetes Division, Sanofi-Aventis Deutschland GmbH, Frankfurt,
Germany

Johann Gassenhuber

77. VO Endokrinologi, Enheten för Diabetesstudier, Skånes
Universitetssjukhus i Lund, Lund, Sweden

Maria Klintenberg & Margit Bergstrom

78. Institut d'Investigacions Biomediques August Pi i Sunye, Centre
Esther Koplowitz, Barcelona, Spain

Jorge Ferrer

Authors

1. Noam Bar

[View author publications](#)

You can also search for this author in [PubMed](#) [Google Scholar](#)

2. Tal Korem

[View author publications](#)

You can also search for this author in [PubMed](#) [Google Scholar](#)

3. Omer Weissbrod

[View author publications](#)

You can also search for this author in [PubMed](#) [Google Scholar](#)

4. David Zeevi

[View author publications](#)

You can also search for this author in [PubMed](#) [Google Scholar](#)

5. Daphna Rothschild

[View author publications](#)

You can also search for this author in [PubMed](#) [Google Scholar](#)

6. Sigal Leviatan

[View author publications](#)

You can also search for this author in [PubMed](#) [Google Scholar](#)

7. Noa Kosower

[View author publications](#)

You can also search for this author in [PubMed](#) [Google Scholar](#)

8. Maya Lotan-Pompan

[View author publications](#)

You can also search for this author in [PubMed](#) [Google Scholar](#)

9. Adina Weinberger

[View author publications](#)

You can also search for this author in [PubMed](#) [Google Scholar](#)

10. Caroline I. Le Roy

[View author publications](#)

You can also search for this author in [PubMed](#) [Google Scholar](#)

11. Cristina Menni

[View author publications](#)

You can also search for this author in [PubMed](#) [Google Scholar](#)

12. Alessia Visconti

[View author publications](#)

You can also search for this author in [PubMed](#) [Google Scholar](#)

13. Mario Falchi

[View author publications](#)

You can also search for this author in [PubMed](#) [Google Scholar](#)

14. Tim D. Spector

[View author publications](#)

You can also search for this author in [PubMed](#) [Google Scholar](#)

15. Jerzy Adamski

[View author publications](#)

You can also search for this author in [PubMed](#) [Google Scholar](#)

16. Paul W. Franks

[View author publications](#)

You can also search for this author in [PubMed](#) [Google Scholar](#)

17. Oluf Pedersen

[View author publications](#)

You can also search for this author in [PubMed](#) [Google Scholar](#)

18. Eran Segal

[View author publications](#)

You can also search for this author in [PubMed](#) [Google Scholar](#)

Consortia

The IMI DIRECT consortium

- , Henrik Vestergaard
- , Manimozhiyan Arumugam
- , Torben Hansen
- , Kristine Allin
- , Tue Hansen
- , Mun-Gwan Hong
- , Jochen Schwenk
- , Ragna Haussler
- , Matilda Dale
- , Toni Giorgino
- , Marianne Rodriguez
- , Mandy Perry
- , Rachel Nice
- , Timothy McDonald
- , Andrew Hattersley
- , Angus Jones
- , Ulrike Graefe-Mody
- , Patrick Baum
- , Rolf Grempler
- , Cecilia Engel Thomas
- , Federico De Masi
- , Caroline Anna Brorsson
- , Gianluca Mazzoni
- , Rosa Allesøe
- , Simon Rasmussen
- , Valborg Gudmundsdóttir
- , Agnes Martine Nielsen
- , Karina Banasik
- , Konstantinos Tsirigos
- , Birgitte Nilsson
- , Helle Pedersen
- , Søren Brunak
- , Tugce Karaderi
- , Agnete Troen Lundgaard
- , Joachim Johansen

- , Ramneek Gupta
- , Peter Wad Sackett
- , Joachim Tillner
- , Thorsten Lehr
- , Nina Scherer
- , Christiane Dings
- , Iryna Sihinevich
- , Heather Loftus
- , Louise Cabrelli
- , Donna McEvoy
- , Andrea Mari
- , Roberto Bizzotto
- , Andrea Tura
- , Leen 't Hart
- , Koen Dekkers
- , Nienke van Leeuwen
- , Roderick Slieker
- , Femke Rutters
- , Joline Beulens
- , Giel Nijpels
- , Anitra Koopman
- , Sabine van Oort
- , Lenka Groeneveld
- , Leif Groop
- , Petra Elders
- , Ana Viñuela
- , Anna Ramisch
- , Emmanouil Dermitzakis
- , Beate Ehrhardt
- , Christopher Jennison
- , Philippe Froguel
- , Mickaël Canouil
- , Amélie Boneford
- , Ian McVittie
- , Dianne Wake
- , Francesca Frau
- , Hans-Henrik Staerfeldt

- , Kofi Adragni
- , Melissa Thomas
- , Han Wu
- , Imre Pavo
- , Birgit Steckel-Hamann
- , Henrik Thomsen
- , Giuseppe Nicola Giordano
- , Hugo Fitipaldi
- , Martin Ridderstråle
- , Azra Kurbasic
- , Naeimeh Atabaki Pasdar
- , Hugo Pomares-Millan
- , Pascal Mutie
- , Robert Koivula
- , Nicky McRobert
- , Mark McCarthy
- , Agata Wesolowska-Andersen
- , Anubha Mahajan
- , Moustafa Abdalla
- , Juan Fernandez
- , Reinhard Holl
- , Alison Heggie
- , Harshal Deshmukh
- , Anita Hennige
- , Susanna Bianzano
- , Barbara Thorand
- , Sapna Sharma
- , Harald Grallert
- , Jonathan Adam
- , Martina Troll
- , Andreas Fritzsche
- , Anita Hill
- , Claire Thorne
- , Michelle Hudson
- , Teemu Kuulasmaa
- , Jagadish Vangipurapu
- , Markku Laakso

- , Henna Cederberg
- , Tarja Kokkola
- , Yunlong Jiao
- , Stephen Gough
- , Neil Robertson
- , Helene Verkindt
- , Violeta Raverdi
- , Robert Caiazzo
- , Francois Pattou
- , Margaret White
- , Louise Donnelly
- , Andrew Brown
- , Colin Palmer
- , David Davtian
- , Adem Dawed
- , Ian Forgie
- , Ewan Pearson
- , Hartmut Ruetten
- , Petra Musholt
- , Jimmy Bell
- , Elizabeth Louise Thomas
- , Brandon Whitcher
- , Mark Haid
- , Claudia Nicolay
- , Miranda Mourby
- , Jane Kaye
- , Nisha Shah
- , Harriet Teare
- , Gary Frost
- , Bernd Jablonka
- , Mathias Uhlen
- , Rebeca Eriksen
- , Josef Vogt
- , Avirup Dutta
- , Anna Jonsson
- , Line Engelbrechtsen
- , Annemette Forman

- , Nadja Sondertoft
- , Nathalie de Preville
- , Tania Baltauss
- , Mark Walker
- , Johann Gassenhuber
- , Maria Klintenberg
- , Margit Bergstrom
- & Jorge Ferrer

Contributions

N.B. and T.K. conceived the project, designed and conducted all analyses, interpreted the results and wrote the manuscript, and are listed in arbitrary order. O.W. and D.Z. designed statistical analyses. D.R. and S.L. conducted microbiome analysis. N.K. coordinated and designed data collection. M.L.-P. and A.W. developed protocols, performed microbiome sequencing and processed serum samples. A.W. designed the project and oversaw sample collection and processing. C.I.L.R., C.M., A.V., M.F. and T.D.S. performed the replication analysis on the TwinsUK cohort. J.A., P.W.F. and O.P. performed the replication analysis on the IMI DIRECT cohort. E.S. conceived and directed the project and analyses, designed the analyses, interpreted the results and wrote the manuscript.

Corresponding author

Correspondence to [Eran Segal](#).

Ethics declarations

Competing interests

The authors declare no competing interests.

Additional information

Peer review information *Nature* thanks Katherine Pollard, Eric Topol and the other, anonymous, reviewer(s) for their contribution to the peer review of this work.

Publisher's note Springer Nature remains neutral with regard to jurisdictional claims in published maps and institutional affiliations.

Extended data figures and tables

[Extended Data Fig. 1 Accurate and reproducible untargeted serum metabolomics.](#)

a, Breakdown of the 1,251 measured metabolites by type. **b**, Number of samples (*y* axis) in which each metabolite (*x* axis) was identified, sorted by prevalence. **c**, **d**, Mass-spectrometry measurements (*y* axis) versus standardized lab tests results (*x* axis; Methods) for creatinine (**c**; Pearson's $R = 0.87, P < 10^{-20}$) and cholesterol (**d**; $R = 0.79, P < 10^{-20}$). **e**, Spearman correlations (*y* axis: centre, median; box, IQR; whiskers, $1.5 \times$ IQR) between standardized metabolomic profiles (Methods) of different individuals ($n = 475$; median Spearman's $\rho 0.05$, s.d. 0.12) stratified by sex, and between standardized metabolomic profiles of the same participant ($n = 20$; median Spearman $\rho 0.68$, s.d. 0.06) taken one week apart. C&V, cofactors and vitamins; a.u., arbitrary units.

[Extended Data Fig. 2 Biological sub pathway prediction of unidentified molecules.](#)

Figure panels refer to the results of a leave-one-out cross validation prediction model of sub pathways of metabolites based on their normalized levels, raw mean, percentage of missing values, and SHAP values (Methods). Results shown are for a model trained using only sub pathways that include over 10 molecules in our data (28 sub pathways, 572 named metabolites). **a**, The overall accuracy of the sub pathway classifier (*y* axis) when a success is considered as having the true label in one of the top k predictions (*x* axis). **b**, The log loss of the classifier (*y* axis) computed over the resulting soft max (raw probabilities; blue) and a dichotomous matrix in

which for every metabolite we only keep the top predicted sub pathway as 1 and zero-out all other predictions (red). **c**, The overall accuracy of the model (left y axis; blue) and the corresponding fraction of metabolites (right y axis; red) when considering only metabolites for which the classifier predicted a maximal probability above some threshold (x axis). **d**, A confusion matrix showing the predicted sub pathways (x axis), determined as the label with the highest probability per metabolite, versus the true annotated sub pathways (y axis). Each cell in the matrix counts the number of metabolites of a certain true sub pathway (y axis) which were assigned with some predicted sub pathway (x axis) by our model. The rightmost column is the sum of every row and represents the number of metabolites annotated for every sub pathway. The matrix is ordered by the higher order biological pathway (super pathway). Cell colours are log scaled. **e**, Classification results summarizing the f1-score, precision and recall per sub pathway. Rows correspond to the sub pathway annotation in **d**. **f**, For every sub pathway (y axis) shown are the fraction of metabolites truly annotated as such (black), predicted as such by the classifier (blue; out of the named molecules in the support of the model), and the fraction of unidentified molecules predicted as such (out of all unidentified molecules). M., metabolism; Xeno., xenobiotics; Ptds, peptides; AAs, amino acids.

Extended Data Fig. 3 Comparative analysis of linear versus nonlinear models and in-sample versus out-of-sample predictions.

a, Metabolite prediction R^2 of GBDT versus Lasso regression models using diet data. Shown are only metabolites for which at least one model achieved significant predictions with R^2 greater than 0.05. **b**, Histogram of the differences between the R^2 of GBDT compared to Lasso regression using the diet data. **c**, The levels of the metabolite hydroxy-CMPF* (y axis: centre, median; box, IQR; whiskers, $1.5 \times$ IQR) versus the monthly consumption of cooked, baked or grilled fish as reported in a food frequency questionnaire. The comparison of Spearman's and Pearson's correlation coefficients suggests that the relationship between the metabolite and the numerical values of the question are monotonic yet nonlinear, which explains why GBDT performs better in predicting the

levels of hydroxy-CMPF* from diet data. The x axis is not to scale. **d, e**, Same as **a, b** for microbiome. **f**, Estimations of gut microbiome explainability (b^2) of metabolite levels obtained via applying a linear mixed model on the bacterial species composition as previously described (y axis) versus the explained variance (R^2) of metabolites from out-of-sample prediction models based on the same gut microbiome data. Shown are only metabolites with significant b^2 estimates (5% FDR). **g**, Histogram of the differences between the b^2 estimates and the R^2 of out-of-sample prediction using the gut microbiome data.

[Extended Data Fig. 4 Comparison of explained variance of metabolites for every pair of feature groups.](#)

Dot plots of the explained variance of the metabolite groups (y axis) from models based on every pair of feature groups (x axis). Panels on the diagonal show the marginal distribution of explained variance of metabolite groups for a certain feature group.

[Extended Data Fig. 5 Comparative analysis of different feature groups.](#)

a, Spearman correlations computed between the EV of metabolites for every pair of feature groups. **b**, The proportion of variance explained by each of the first 400 principal components (left y axis; black) and their cumulative EV (right y axis; blue). **c**, R^2 multiplied by the sign of the Pearson correlation coefficient (x axis) between metabolite levels and BMI in our study, versus the mean R^2 multiplied by the sign of the Pearson correlation coefficient (y axis) of BMI associated metabolites recently reported by a different group¹³. Shown are 36 (out of 49) BMI associated metabolites that were also measured in this cohort. P value for the Pearson correlation, $P = 7 \times 10^{-11}$. Line and shaded colouring represent the fitting of a linear model and the 95% confidence interval. **d**, The EV of every metabolite from prediction models based on the gut microbiome (x axis) versus diet (y axis). Dashed red line is $y = x$. **e**, Same for prediction models based on both gut microbiome and diet (x axis) compared to using only diet

(y axis). **f**, Same for prediction models based on diet and permuted gut microbiome (x axis) compared to using only diet (y axis). MB, microbiome.

Extended Data Fig. 6 Networks of interactions between phenotypes explain diverse metabolites.

Interactions between features from different feature groups predictive of similar metabolites are presented in a graphical layout, in which nodes are either metabolites or features, and edges are the directional mean absolute SHAP values (Methods) computed from models trained only on features from the respective feature group. Circular nodes, metabolites; predictive feature nodes, squares; both coloured by relevant categories. Shown are only edges with a mean absolute SHAP value greater than 0.12. **a**, Network of associations for the following feature groups: macronutrients, diet, microbiome, lifestyle, drugs and seasonal effects. **b**, A large group of metabolites for which predictions are mainly driven by the reported consumption of coffee and the relative abundance of a bacteria from the Clostridiales order. **c**, Metabolites explained by seasonal fruit consumption. **d**, Selected examples of interactions between metabolites and features in predictive models.

Extended Data Fig. 7 Specific dietary features and bacterial taxa underlie the accurate prediction of circulating metabolites.

a–f, Predicted (y axis) versus measured (x axis) levels (arbitrary units) of X-16124 (**a**; Pearson's $R = 0.77, P < 10^{-20}$), phenylacetylglutamine (**b**; $R = 0.63, P < 10^{-20}$), *p*-cresol-glucuronide (**c**; $R = 0.64, P < 10^{-20}$), caffeine (**d**; $R = 0.68, P < 10^{-20}$), hydroxy-CMPF (**e**; $R = 0.72, P < 10^{-20}$) and stachydrine (**f**; $R = 0.5, P < 10^{-20}$). Predictions of **a–c** are based only on microbiome data, and coloured by the relative abundance of the bacterial taxa having the highest mean absolute SHAP value for each metabolite. Predictions of **d–f** are based only on diet data, and coloured by the reported consumption of the dietary item having the highest mean absolute SHAP value for each metabolite. P values for prediction were estimated via bootstrapping. **g**, Heat map showing the directional mean absolute SHAP values (Methods) of various features (x axis) computed from fivefold cross

validation models that predict metabolite levels (*y* axis) using two separate models, one based on diet and another on gut microbiome data. Positive (negative) SHAP values indicate that higher (lower) feature values lead, on average, to higher predicted values. Shown are the top 150 predicted metabolites using diet and gut microbiome, and the top 40 features by maximum mean absolute SHAP value across all metabolites.

[Extended Data Fig. 8 Distribution of phyla and a taxa from the Eggerthellaceae family.](#)

a, Stacked bar plots per sample (*x* axis) showing the relative abundance of bacterial phyla (*y* axis). Samples are sorted by the relative abundance of the most abundant phylum, Firmicutes. Bacteroidetes is the second most abundant phylum in our cohort. Relative abundance of a phylum is computed as the sum over relative abundances of all bacterial features belonging to that phylum. **b**, The levels of the unidentified compound X-16124 in individuals for which the bacterial taxa from the Eggerthellaceae family was detectable in stool versus individuals for which it was not ($P < 10^{-20}$, two-sided Mann–Whitney *U*-test).

[Extended Data Fig. 9 The unidentified molecule X-21441 associates with rs8187710 independent of age.](#)

a, A table showing the coefficients, standard errors and *P* values resulted from a multiple linear regression model with levels of the unidentified molecule X-21441 as the dependent variable, the allele dosage of rs8187710 (0–2) and age (years) as the independent variables: $y_{X-21441} = \text{constant} + \beta_1 \times \text{rs8187710} + \beta_2 \times \text{Age}$. **b**, The levels of X-21441 (*y* axis; centre, median; box, IQR; whiskers, $1.5 \times \text{IQR}$) versus the genotype of the participants (*x* axis). The number of participants with each genotype is indicated below the tick labels. The explained variance of X-21441 by rs8187710 as estimated using plink (Methods) is indicated on the upper right corner of the panel. **c**, The levels of X-21441 versus the age of the participants (*x* axis) coloured by genotype of participants. Line and shaded colouring represent the fitting of a linear model and the 95% confidence interval. SE, standard error.

Extended Data Table 1 Basic characteristics and demographics of our main and validation cohorts

[Full size table](#)

Supplementary information

Supplementary Information

This file contains Supplementary Notes 1-4.

Reporting Summary

Supplementary Tables

This file contains Supplementary Tables 1-15.

Rights and permissions

Reprints and Permissions

About this article



Check for
updates

Cite this article

Bar, N., Korem, T., Weissbrod, O. *et al.* A reference map of potential determinants for the human serum metabolome. *Nature* **588**, 135–140 (2020). <https://doi.org/10.1038/s41586-020-2896-2>

Download citation

- Received: 23 January 2019

- Accepted: 29 September 2020
- Published: 11 November 2020
- Issue Date: 03 December 2020
- DOI: <https://doi.org/10.1038/s41586-020-2896-2>

Comments

By submitting a comment you agree to abide by our [Terms](#) and [Community Guidelines](#). If you find something abusive or that does not comply with our terms or guidelines please flag it as inappropriate.

[Access through your institution](#)

[Change institution](#)

[Buy or subscribe](#)

Associated Content

Nature | News & Views

[Building a chemical blueprint for human blood](#)

- Patrick H. Bradley
- & Katherine S. Pollard

This article was downloaded by **calibre** from <https://www.nature.com/articles/s41586-020-2896-2>

- Article
- [Published: 18 November 2020](#)

Widespread endogenization of giant viruses shapes genomes of green algae

- [Mohammad Moniruzzaman¹](#),
- [Alaina R. Weinheimer ORCID: orcid.org/0000-0002-6066-0591¹](#),
- [Carolina A. Martinez-Gutierrez¹](#) &
- [Frank O. Aylward ORCID: orcid.org/0000-0002-1279-4050¹](#)

Nature volume **588**, pages 141–145(2020) [Cite this article](#)

- 4135 Accesses
- 199 Altmetric
- [Metrics details](#)

Subjects

- [Eukaryote](#)
- [Evolutionary genetics](#)
- [Microbial ecology](#)
- [Molecular evolution](#)
- [Viral evolution](#)

Abstract

Endogenous viral elements (EVEs)—viruses that have integrated their genomes into those of their hosts—are prevalent in eukaryotes and have an important role in genome evolution^{1,2}. The vast majority of EVEs that have been identified to date are small genomic regions comprising a few genes², but recent evidence suggests that some large double-stranded DNA viruses may also endogenize into the genome of the host¹. Nucleocytoplasmic large DNA viruses (NCLDVs) have recently become of great interest owing to their large genomes and complex evolutionary origins^{3,4,5,6}, but it is not yet known whether they are a prominent component of eukaryotic EVEs. Here we report the widespread endogenization of NCLDVs in diverse green algae; these giant EVEs reached sizes greater than 1 million base pairs and contained as many as around 10% of the total open reading frames in some genomes, substantially increasing the scale of known viral genes in eukaryotic genomes. These endogenized elements often shared genes with host genomic loci and contained numerous spliceosomal introns and large duplications, suggesting tight assimilation into host genomes. NCLDVs contain large and mosaic genomes with genes derived from multiple sources, and their endogenization represents an underappreciated conduit of new genetic material into eukaryotic lineages that can substantially impact genome composition.

[Access through your institution](#)

[Change institution](#)

[Buy or subscribe](#)

Access options

Subscribe to Journal

Get full journal access for 1 year

185,98 €

only 3,58 € per issue

[Subscribe](#)

All prices are NET prices.
VAT will be added later in the checkout.

Rent or Buy article

Get time limited or full article access on ReadCube.

from \$8.99

[Rent or Buy](#)

All prices are NET prices.

Additional access options:

- [Log in](#)
- [Access through your institution](#)
- [Learn about institutional subscriptions](#)

Fig. 1: Distribution and general features of the GEVEs.



Fig. 2: Signatures of endogenization.

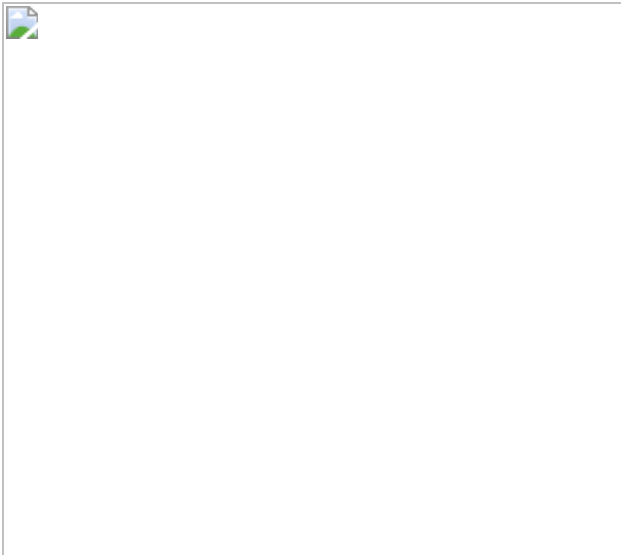
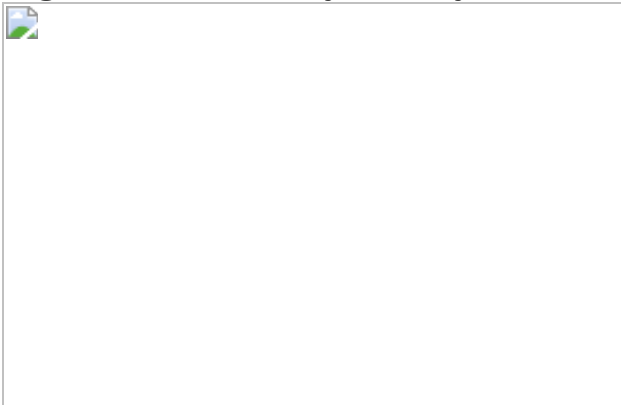


Fig. 3: Evolutionary history of the GEVEs.



Data availability

Nucleotide and protein sequences specific to each of the GEVEs, hallmark gene set used for phylogenetic analyses, alignments for all phylogenies presented, HMM profiles of the core genes and NCVOG families, and other data products are available at:

<https://zenodo.org/record/3975964#.XzFj0hl7mfZ>.

Code availability

A custom bioinformatic pipeline (ViralRecall) was developed in Python 3.5 for purposes of this study. This code is already publicly available on GitHub for the Aylward lab: <https://github.com/faylward/viralrecall>. For NCLDV

marker gene detection, we also used a custom Python script available on GitHub: https://github.com/faylward/ncldv_markersearch. Other bioinformatic analyses performed in this study were done using publicly available bioinformatic tools and are described in the Methods.

References

1. 1.

Feschotte, C. & Gilbert, C. Endogenous viruses: insights into viral evolution and impact on host biology. *Nat. Rev. Genet.* **13**, 283–296 (2012).

[CAS](#) [PubMed](#) [Google Scholar](#)

2. 2.

Holmes, E. C. The evolution of endogenous viral elements. *Cell Host Microbe* **10**, 368–377 (2011).

[CAS](#) [PubMed](#) [PubMed Central](#) [Google Scholar](#)

3. 3.

Fischer, M. G. Giant viruses come of age. *Curr. Opin. Microbiol.* **31**, 50–57 (2016).

[PubMed](#) [Google Scholar](#)

4. 4.

Wilhelm, S. W. et al. A student's guide to giant viruses infecting small eukaryotes: from *Acanthamoeba* to *zooxanthellae*. *Viruses* **9**, 46 (2017).

[Google Scholar](#)

5. 5.

Abergel, C., Legendre, M. & Claverie, J.-M. The rapidly expanding universe of giant viruses: *Mimivirus*, *Pandoravirus*, *Pithovirus* and *Mollivirus*. *FEMS Microbiol. Rev.* **39**, 779–796 (2015).

[CAS](#) [PubMed](#) [Google Scholar](#)

6. 6.

Weynberg, K. D., Allen, M. J. & Wilson, W. H. Marine prasinoviruses and their tiny plankton hosts: a review. *Viruses* **9**, 43 (2017).

[Google Scholar](#)

7. 7.

Bhattacharya, D. & Medlin, A. L. Algal phylogeny and the origin of land plants. *Plant Physiol.* **116**, 9–15 (1998).

[CAS](#) [Google Scholar](#)

8. 8.

Jeanniard, A. et al. Towards defining the chloroviruses: a genomic journey through a genus of large DNA viruses. *BMC Genomics* **14**, 158 (2013).

[CAS](#) [PubMed](#) [PubMed Central](#) [Google Scholar](#)

9. 9.

Moniruzzaman, M., Martinez-Gutierrez, C. A., Weinheimer, A. R. & Aylward, F. O. Dynamic genome evolution and complex virocell metabolism of globally-distributed giant viruses. *Nat. Commun.* **11**, 1710 (2020).

[ADS](#) [CAS](#) [PubMed](#) [PubMed Central](#) [Google Scholar](#)

10. 10.

Filée, J. Genomic comparison of closely related giant viruses supports an accordion-like model of evolution. *Front. Microbiol.* **6**, 593 (2015).

[PubMed](#) [PubMed Central](#) [Google Scholar](#)

11. 11.

Van Etten, J. L. et al. Chloroviruses have a sweet tooth. *Viruses* **9**, 88 (2017).

[Google Scholar](#)

12. 12.

Schvarcz, C. R. & Steward, G. F. A giant virus infecting green algae encodes key fermentation genes. *Virology* **518**, 423–433 (2018).

[CAS](#) [PubMed](#) [Google Scholar](#)

13. 13.

Sun, C., Feschotte, C., Wu, Z. & Mueller, R. L. DNA transposons have colonized the genome of the giant virus *Pandoravirus salinus*. *BMC Biol.* **13**, 38 (2015).

[PubMed](#) [PubMed Central](#) [Google Scholar](#)

14. 14.

Marcet-Houben, M. & Gabaldón, T. Acquisition of prokaryotic genes by fungal genomes. *Trends Genet.* **26**, 5–8 (2010).

[CAS](#) [PubMed](#) [Google Scholar](#)

15. 15.

Rossoni, A. W. et al. The genomes of polyextremophilic cyanidiales contain 1% horizontally transferred genes with diverse adaptive functions. *eLife* **8**, e45017 (2019).

[CAS](#) [PubMed](#) [PubMed Central](#) [Google Scholar](#)

16. 16.

Filée, J. Multiple occurrences of giant virus core genes acquired by eukaryotic genomes: the visible part of the iceberg? *Virology* **466–467**, 53–59 (2014).

[PubMed](#) [Google Scholar](#)

17. 17.

Maumus, F. & Blanc, G. Study of gene trafficking between *Acanthamoeba* and giant viruses suggests an undiscovered family of amoeba-infecting viruses. *Genome Biol. Evol.* **8**, 3351–3363 (2016).

[CAS](#) [PubMed](#) [PubMed Central](#) [Google Scholar](#)

18. 18.

Gallot-Lavallée, L. & Blanc, G. A glimpse of nucleo-cytoplasmic large DNA virus biodiversity through the eukaryotic genomics window. *Viruses* **9**, 17 (2017).

[Google Scholar](#)

19. 19.

Maumus, F., Epert, A., Nogué, F. & Blanc, G. Plant genomes enclose footprints of past infections by giant virus relatives. *Nat. Commun.* **5**, 4268 (2014).

[ADS](#) [CAS](#) [PubMed](#) [PubMed Central](#) [Google Scholar](#)

20. 20.

Guglielmini, J., Woo, A. C., Krupovic, M., Forterre, P. & Gaia, M. Diversification of giant and large eukaryotic dsDNA viruses predated

the origin of modern eukaryotes. *Proc. Natl Acad. Sci. USA* **116**, 19585–19592 (2019).

[CAS](#) [PubMed](#) [Google Scholar](#)

21. 21.

Forterre, P. & Gaïa, M. Giant viruses and the origin of modern eukaryotes. *Curr. Opin. Microbiol.* **31**, 44–49 (2016).

[PubMed](#) [Google Scholar](#)

22. 22.

Piacente, F., Gaglianone, M., Laugieri, M. E. & Tonetti, M. G. The autonomous glycosylation of large DNA viruses. *Int. J. Mol. Sci.* **16**, 29315–29328 (2015).

[CAS](#) [PubMed](#) [PubMed Central](#) [Google Scholar](#)

23. 23.

Schulz, F. et al. Giant virus diversity and host interactions through global metagenomics. *Nature* **578**, 432–436 (2020).

[ADS](#) [CAS](#) [PubMed](#) [PubMed Central](#) [Google Scholar](#)

24. 24.

Abrahão, J. et al. Tailed giant Tupanvirus possesses the most complete translational apparatus of the known virosphere. *Nat. Commun.* **9**, 749 (2018).

[ADS](#) [PubMed](#) [PubMed Central](#) [Google Scholar](#)

25. 25.

Wilson, W. H. et al. Complete genome sequence and lytic phase transcription profile of a *Coccolithovirus*. *Science* **309**, 1090–1092

(2005).

[ADS](#) [Google Scholar](#)

26. 26.

Roux, S. et al. Ecogenomics and potential biogeochemical impacts of globally abundant ocean viruses. *Nature* **537**, 689–693 (2016).

[Google Scholar](#)

27. 27.

Koonin, E. V. & Krupovic, M. The depths of virus exaptation. *Curr. Opin. Virol.* **31**, 1–8 (2018).

[CAS](#) [PubMed](#) [Google Scholar](#)

28. 28.

Ochman, H., Lawrence, J. G. & Groisman, E. A. Lateral gene transfer and the nature of bacterial innovation. *Nature* **405**, 299–304 (2000).

[ADS](#) [CAS](#) [PubMed](#) [Google Scholar](#)

29. 29.

Groisman, E. A. & Ochman, H. Pathogenicity islands: bacterial evolution in quantum leaps. *Cell* **87**, 791–794 (1996).

[CAS](#) [PubMed](#) [Google Scholar](#)

30. 30.

Martin, W. F. Too much eukaryote LGT. *BioEssays* **39**, 1700115 (2017).

[Google Scholar](#)

31. 31.

Keeling, P. J. & Palmer, J. D. Horizontal gene transfer in eukaryotic evolution. *Nat. Rev. Genet.* **9**, 605–618 (2008).

[CAS](#) [PubMed](#) [Google Scholar](#)

32. 32.

Cock, J. M. et al. The *Ectocarpus* genome and the independent evolution of multicellularity in brown algae. *Nature* **465**, 617–621 (2010).

[ADS](#) [CAS](#) [PubMed](#) [Google Scholar](#)

33. 33.

Delaroche, N., Maier, I., Knippers, R. & Müller, D. G. Persistent virus integration into the genome of its algal host, *Ectocarpus siliculosus* (Phaeophyceae). *J. Gen. Virol.* **80**, 1367–1370 (1999).

[CAS](#) [PubMed](#) [Google Scholar](#)

34. 34.

Delaroche, N. & Boland, W. The genome of the brown alga *Ectocarpus siliculosus* contains a series of viral DNA pieces, suggesting an ancient association with large dsDNA viruses. *BMC Evol. Biol.* **8**, 110 (2008).

[PubMed](#) [PubMed Central](#) [Google Scholar](#)

35. 35.

Hyatt, D. et al. Prodigal: prokaryotic gene recognition and translation initiation site identification. *BMC Bioinformatics* **11**, 119 (2010).

[PubMed](#) [PubMed Central](#) [Google Scholar](#)

36. 36.

Eddy, S. R. Accelerated profile HMM searches. *PLoS Comput. Biol.* **7**, e1002195 (2011).

[ADS](#) [MathSciNet](#) [CAS](#) [PubMed](#) [PubMed Central](#) [Google Scholar](#)

37. 37.

El-Gebali, S. et al. The Pfam protein families database in 2019. *Nucleic Acids Res.* **47**, D427–D432 (2019).

[CAS](#) [Google Scholar](#)

38. 38.

Yutin, N., Wolf, Y. I., Raoult, D. & Koonin, E. V. Eukaryotic large nucleo-cytoplasmic DNA viruses: clusters of orthologous genes and reconstruction of viral genome evolution. *Virol. J.* **6**, 223 (2009).

[PubMed](#) [PubMed Central](#) [Google Scholar](#)

39. 39.

Filée, J., Siguier, P. & Chandler, M. I am what I eat and I eat what I am: acquisition of bacterial genes by giant viruses. *Trends Genet.* **23**, 10–15 (2007).

[PubMed](#) [Google Scholar](#)

40. 40.

Filée, J., Pouget, N. & Chandler, M. Phylogenetic evidence for extensive lateral acquisition of cellular genes by nucleocytoplasmic large DNA viruses. *BMC Evol. Biol.* **8**, 320 (2008).

[PubMed](#) [PubMed Central](#) [Google Scholar](#)

41. 41.

Hoff, K. J. & Stanke, M. Predicting genes in single genomes with AUGUSTUS. *Curr. Protoc. Bioinformatics* **65**, e57 (2019).

[PubMed](#) [Google Scholar](#)

42. 42.

Stanke, M. & Morgenstern, B. AUGUSTUS: a web server for gene prediction in eukaryotes that allows user-defined constraints. *Nucleic Acids Res.* **33**, W465–W467 (2005).

[CAS](#) [PubMed](#) [PubMed Central](#) [Google Scholar](#)

43. 43.

Gu, Z., Gu, L., Eils, R., Schlesner, M. & Brors, B. circlize implements and enhances circular visualization in R. *Bioinformatics* **30**, 2811–2812 (2014).

[CAS](#) [PubMed](#) [Google Scholar](#)

44. 44.

O’Leary, N. A. et al. Reference sequence (RefSeq) database at NCBI: current status, taxonomic expansion, and functional annotation. *Nucleic Acids Res.* **44**, D733–D745 (2016).

[PubMed](#) [Google Scholar](#)

45. 45.

Kiełbasa, S. M., Wan, R., Sato, K., Horton, P. & Frith, M. C. Adaptive seeds tame genomic sequence comparison. *Genome Res.* **21**, 487–493 (2011).

[PubMed](#) [PubMed Central](#) [Google Scholar](#)

46. 46.

Federhen, S. The NCBI Taxonomy database. *Nucleic Acids Res.* **40**, D136–D143 (2012).

[CAS](#) [PubMed](#) [Google Scholar](#)

47. 47.

Huerta-Cepas, J., Serra, F. & Bork, P. ETE 3: reconstruction, analysis, and visualization of phylogenomic data. *Mol. Biol. Evol.* **33**, 1635–1638 (2016).

[CAS](#) [PubMed](#) [PubMed Central](#) [Google Scholar](#)

48. 48.

Pagès, H., Aboyoun, P., Gentleman, R. & DebRoy, S. Biostrings: efficient manipulation of biological strings. R package version 2.56.0 <https://bioconductor.org/packages/Biostrings> (2020).

49. 49.

Bao, Z. & Eddy, S. R. Automated de novo identification of repeat sequence families in sequenced genomes. *Genome Res.* **12**, 1269–1276 (2002).

[CAS](#) [PubMed](#) [PubMed Central](#) [Google Scholar](#)

50. 50.

Delcher, A. L., Phillippy, A., Carlton, J. & Salzberg, S. L. Fast algorithms for large-scale genome alignment and comparison. *Nucleic Acids Res.* **30**, 2478–2483 (2002).

[PubMed](#) [PubMed Central](#) [Google Scholar](#)

51. 51.

Tatusov, R. L., Galperin, M. Y., Natale, D. A. & Koonin, E. V. The COG database: a tool for genome-scale analysis of protein functions

and evolution. *Nucleic Acids Res.* **28**, 33–36 (2000).

[CAS](#) [PubMed](#) [PubMed Central](#) [Google Scholar](#)

52. 52.

Haft, D. H. et al. TIGRFAMs: a protein family resource for the functional identification of proteins. *Nucleic Acids Res.* **29**, 41–43 (2001).

[CAS](#) [PubMed](#) [PubMed Central](#) [Google Scholar](#)

53. 53.

Huerta-Cepas, J. et al. eggNOG 5.0: a hierarchical, functionally and phylogenetically annotated orthology resource based on 5090 organisms and 2502 viruses. *Nucleic Acids Res.* **47**, D309–D314 (2019).

[CAS](#) [PubMed](#) [Google Scholar](#)

54. 54.

Moniruzzaman, M. et al. Virus–host relationships of marine single-celled eukaryotes resolved from metatranscriptomics. *Nat. Commun.* **8**, 16054 (2017).

[ADS](#) [CAS](#) [PubMed](#) [PubMed Central](#) [Google Scholar](#)

55. 55.

Guindon, S. et al. New algorithms and methods to estimate maximum-likelihood phylogenies: assessing the performance of PhyML 3.0. *Syst. Biol.* **59**, 307–321 (2010).

[CAS](#) [Google Scholar](#)

56. 56.

Sievers, F. et al. Fast, scalable generation of high-quality protein multiple sequence alignments using Clustal Omega. *Mol. Syst. Biol.* **7**, 539 (2011).

[PubMed](#) [PubMed Central](#) [Google Scholar](#)

57. 57.

Capella-Gutiérrez, S., Silla-Martínez, J. M. & Gabaldón, T. trimAl: a tool for automated alignment trimming in large-scale phylogenetic analyses. *Bioinformatics* **25**, 1972–1973 (2009).

[PubMed](#) [PubMed Central](#) [Google Scholar](#)

58. 58.

Letunic, I. & Bork, P. Interactive Tree Of Life (iTOL) v4: recent updates and new developments. *Nucleic Acids Res.* **47**, W256–W259 (2019).

[CAS](#) [PubMed](#) [PubMed Central](#) [Google Scholar](#)

59. 59.

Lechner, M. et al. Proteinortho: detection of (co-)orthologs in large-scale analysis. *BMC Bioinformatics* **12**, 124 (2011).

[PubMed](#) [PubMed Central](#) [Google Scholar](#)

60. 60.

Csardi G, N. T. The igraph software package for complex network research. *InterJournal Complex Systems* **1695**, 1–9 (2006).

61. 61.

Burns, J. A., Paasch, A., Narechania, A. & Kim, E. Comparative genomics of a bacterivorous green algae reveals evolutionary

causalities and consequences of phago-mixotrophic mode of nutrition. *Genome Biol. Ecol.* **7**, 3047–3061 (2015).

[CAS](#) [Google Scholar](#)

62. 62.

Langmead, B. & Salzberg, S. L. Fast gapped-read alignment with Bowtie 2. *Nat. Methods* **9**, 357–359 (2012).

[CAS](#) [PubMed](#) [PubMed Central](#) [Google Scholar](#)

63. 63.

Quinlan, A. R. & Hall, I. M. BEDTools: a flexible suite of utilities for comparing genomic features. *Bioinformatics* **26**, 841–842 (2010).

[CAS](#) [PubMed](#) [PubMed Central](#) [Google Scholar](#)

64. 64.

Li, W. & Godzik, A. Cd-hit: a fast program for clustering and comparing large sets of protein or nucleotide sequences. *Bioinformatics* **22**, 1658–1659 (2006).

[CAS](#) [Google Scholar](#)

65. 65.

Yang, Z. PAML 4: phylogenetic analysis by maximum likelihood. *Mol. Biol. Evol.* **24**, 1586–1591 (2007).

[CAS](#) [PubMed](#) [Google Scholar](#)

66. 66.

Martinez-Gutierrez, C. A. & Aylward, F. O. Strong purifying selection is associated with genome streamlining in epipelagic Marinimicrobia. *Genome Biol. Evol.* **11**, 2887–2894 (2019).

[CAS](#) [PubMed](#) [PubMed Central](#) [Google Scholar](#)

67. 67.

Huerta-Cepas, J. et al. eggNOG 4.5: a hierarchical orthology framework with improved functional annotations for eukaryotic, prokaryotic and viral sequences. *Nucleic Acids Res.* **44**, D286–D293 (2016).

[CAS](#) [PubMed](#) [Google Scholar](#)

68. 68.

Nguyen, L.-T., Schmidt, H. A., von Haeseler, A. & Minh, B. Q. IQ-TREE: a fast and effective stochastic algorithm for estimating maximum-likelihood phylogenies. *Mol. Biol. Evol.* **32**, 268–274 (2015).

[CAS](#) [PubMed](#) [Google Scholar](#)

69. 69.

Kalyaanamoorthy, S., Minh, B. Q., Wong, T. K. F., von Haeseler, A. & Jermiin, L. S. ModelFinder: fast model selection for accurate phylogenetic estimates. *Nat. Methods* **14**, 587–589 (2017).

[CAS](#) [PubMed](#) [PubMed Central](#) [Google Scholar](#)

[Download references](#)

Acknowledgements

We thank J. Burns from the Bigelow Laboratory of Ocean Sciences and E. Kim from the American Museum of Natural History for providing access to the RNA sequencing data of *C. tetramitiformis*. We acknowledge use of the Virginia Tech Advanced Research Computing Center for bioinformatic analyses performed in this study. This work was supported by a Simons

Early Career Investigator Award in Marine Microbial Ecology and Evolution (grant no. 620443) and NSF grant IIBR-1918271 to F.O.A.

Author information

Affiliations

1. Department of Biological Sciences, Virginia Tech, Blacksburg, VA, USA

Mohammad Moniruzzaman, Alaina R. Weinheimer, Carolina A. Martinez-Gutierrez & Frank O. Aylward

Authors

1. Mohammad Moniruzzaman
[View author publications](#)

You can also search for this author in [PubMed](#) [Google Scholar](#)

2. Alaina R. Weinheimer
[View author publications](#)

You can also search for this author in [PubMed](#) [Google Scholar](#)

3. Carolina A. Martinez-Gutierrez
[View author publications](#)

You can also search for this author in [PubMed](#) [Google Scholar](#)

4. Frank O. Aylward
[View author publications](#)

You can also search for this author in [PubMed](#) [Google Scholar](#)

Contributions

F.O.A. and M.M. designed the project and wrote the paper. M.M. curated GEVEs, performed gene annotations and phylogenetic analysis. A.R.W. performed the GEVE protein annotations. C.A.M.-G. performed the dN/dS analysis.

Corresponding author

Correspondence to [Frank O. Aylward](#).

Ethics declarations

Competing interests

The authors declare no competing interests.

Additional information

Peer review information *Nature* thanks Chantal Abergel, Matthew Sullivan and the other, anonymous, reviewer(s) for their contribution to the peer review of this work.

Publisher's note Springer Nature remains neutral with regard to jurisdictional claims in published maps and institutional affiliations.

Extended data figures and tables

[Extended Data Fig. 1 Workflow for GEVE detection.](#)

Overview of the initial steps to identify virus-like regions in chlorophyte genomes and subsequent steps to curate Giant Endogenous Viral Elements (GEVEs). Steps in the grey box are implemented in the ViralRecall tool; steps outside this box represent additional analyses we performed to validate our findings and further analyse the GEVEs.

[Extended Data Fig. 2 General features of additional GEVEs.](#)

Circular genome plots of 6 additional GEVEs (apart from those shown in Fig. 1b) showing NCVOG HMM hits, spliceosomal intron locations, and best LAST hit matches. Black dots atop the outermost track mark the locations of the core genes, while the blue links inside the circles represent duplicated regions. The grey shading demarcates the location of integrated GEVE as determined by ViralRecall in case of *Chlorella* and *Tetradesmus obliquus*.

Extended Data Fig. 3 GEVEs have coding potential similar to known giant viruses.

a, Principal component analysis (PCA) of the coding potential of the GEVE genomes, corresponding host genomes and reference giant viruses based on the presence/absence of Nucleocytoplasmic virus orthologous group (NCVOG) specific proteins in these genomes. The plot demonstrates the similarity in coding content of GEVEs and reference giant viruses, whereas the eukaryotic hosts are distinct in terms of coding potential. Nonviral chlorophyte host chromosomes have a much more scattered distribution due to the sporadic occurrence and low abundance of some NCVOGs in these genomes (ankyrin repeat proteins and transposons are represented in NCVOGs and are present in the nonviral portion of host chromosomes, for example). Eukaryotic-specific proteins are not included in NCVOGs, and so the host chlorophyte genomes don't show tight clustering, since this aspect of their genomic repertoires is not captured by NCVOGs. The prcomp() function in R was used to calculate the values. **b**, Bipartite network of 18 GEVEs and 126 reference giant viruses based on shared gene content. The network is constructed by profiling the presence of NCVOGs across all the virus and GEVE genomes represented. Large nodes represent NCLDV or GEVE genomes, smaller nodes represent NCVOG protein families and edges denote gene families represented in different genomes.

Extended Data Fig. 4 Example of gene prediction approach within the GEVEs.

Genes predicted by AUGUSTUS (outer ring, brown) and non-overlapping Prodigal predicted genes (middle ring, green) in the GEVEs within

Chlamydomoans eustigma and *Tetraebaena socialis* are shown as examples. In most cases, Prodigal predicted many genes that were not detected by eukaryotic gene prediction algorithms. Many of the Prodigal predicted genes originally missed by AUGUSTUS have hits to NCVOGs (innermost right, purple) - including NCLDV core genes.

Extended Data Fig. 5 Level of duplications and core gene copy numbers in GEVE genomes versus reference giant virus genomes.

The left panel shows duplication level (repeated genomic regions at >90% nucleotide similarity) as estimated using RECON 1.08. The right panel shows copy numbers of NCLDV core genes in each of the GEVEs and reference genomes (see [Methods](#) for details).

Extended Data Fig. 6 Signature of relaxed selection in the GEVEs compared to free viruses.

Violin plot representing median dN/dS values of endogenized and free reference giant viruses. Statistical significance of differences between dN/dS values of the compared groups according to a non-paired, one-sided Mann–Whitney Wilcoxon test is denoted by: *** $P < 0.0001$. ‘W’ denotes the Wilcoxon test statistic. For this test 79 values were for GEVE-GEVE dN/dS values and 775 were for comparisons between free viruses. The IDs of the reference genomes used for calculating the dN/dS values are provided in Supplementary Data [6](#).

Extended Data Fig. 7 Expression profiles of GEVE genes.

Selected set of expressed genes in 6 of the GEVEs. For each GEVE, up to 15 genes with highest expressions are shown, with exception of *Tetraebaena socialis* GEVE_1, for which all genes having >1 expression coverage are presented. For a particular gene, expression is measured as the average read mapping coverage of the CDS(s) in that gene. Genes having putative functions (based on PFAM or COG annotations) are shown in red, while mobile elements are shown in blue.

[Extended Data Fig. 8 Functional potential coded by the GEVEs.](#)

Functional profiles (EggNOG) of the GEVEs normalized across all the NOG functional categories except category S (Function unknown). No gene was found to be in category R (General function prediction only). Number of genes having no hits or in category S (Function unknown) are shown in the table on the right.

Extended Data Table 1 NCLDV hallmark genes in diverse chlorophyte genomes without GEVEs

[Full size table](#)

Extended Data Table 2 GEVE feature summaries

[Full size table](#)

Supplementary information

[Supplementary Information](#)

This file contains the following: a) Supplementary results and discussion with references. b) Supplementary figures with captions describing each figure. c) Supplementary tables with captions describing each table.

[Reporting Summary](#)

[Supplementary Data](#)

Supplementary Data 1: Information on the genomes analysed in this study. FTP download link are provided for each of the genomes.

[Supplementary Data](#)

Supplementary Data 2: Summary statistics for individual contigs in each of the viral elements (GEVEs) analysed.

[Supplementary Data](#)

Supplementary Data 3: Average amino acid identities (AAI) between each pair of GEVEs.

Supplementary Data

Supplementary Data 4: Functional annotation for each of the GEVEs obtained using a number of protein family databases. Databases used are: COG, PFam, EggNOG, VOG, TIGR and EggVOG. See ‘Methods’ for references for all these databases.

Supplementary Data

Supplementary Data 5: Annotation and expression values of the expressed genes in six of the GEVEs. Annotations are only provided for the genes which had hits to different databases (as specified in Supplementary Data 4).

Supplementary Data

Supplementary Data 6: Genome IDs of the reference NCLDVs that were used to calculate dN/dS values in the *Phycodnaviridae* and *Mimiviridae* group. The reference genomes can be accessed from the study cited in the ‘Calculation of dN/dS ratios’ sub-section in the ‘Methods’.

Rights and permissions

Reprints and Permissions

About this article



Check for
updates

Cite this article

Moniruzzaman, M., Weinheimer, A.R., Martinez-Gutierrez, C.A. *et al.*
Widespread endogenization of giant viruses shapes genomes of green algae.
Nature **588**, 141–145 (2020). <https://doi.org/10.1038/s41586-020-2924-2>

[Download citation](#)

- Received: 07 June 2019
- Accepted: 01 September 2020
- Published: 18 November 2020
- Issue Date: 03 December 2020
- DOI: <https://doi.org/10.1038/s41586-020-2924-2>

Comments

By submitting a comment you agree to abide by our [Terms](#) and [Community Guidelines](#). If you find something abusive or that does not comply with our terms or guidelines please flag it as inappropriate.

[Access through your institution](#)

[Change institution](#)

[Buy or subscribe](#)

This article was downloaded by **calibre** from <https://www.nature.com/articles/s41586-020-2924-2>

Association of COVID-19 inflammation with activation of the C5a–C5aR1 axis
[Download PDF](#)

- Article
- [Published: 29 July 2020](#)

Association of COVID-19 inflammation with activation of the C5a–C5aR1 axis

- [Julien Carvelli](#)^{1,2 na1},
- [Olivier Demaria](#)^{3 na1},
- [Frédéric Vély](#)^{4,5 na1},
- [Luciana Batista](#)³,
- [Nassima Chouaki Benmansour](#)^{6,7},
- [Joanna Fares](#)³,
- [Sabrina Carpentier](#)³,
- [Marie-Laure Thibult](#)³,
- [Ariane Morel](#)³,
- [Romain Remark](#)³,
- [Pascale André](#)³,
- [Agnès Represa](#)³,
- [Christelle Piperoglou](#)^{4,5},
- [the Explore COVID-19 IPH group](#),
- [the Explore COVID-19 Marseille Immunopole group](#),
- [Pierre Yves Cordier](#)⁶,
- [Erwan Le Dault](#)⁶,
- [Christophe Guervilly](#)^{2,8},
- [Pierre Simeone](#) ORCID: orcid.org/0000-0002-0682-9405^{2,9},
- [Marc Gaiannier](#)^{1,2},
- [Yannis Morel](#)³,
- [Mikael Ebbo](#)^{4,10},
- [Nicolas Schleinitz](#)^{4,10} &
- [Eric Vivier](#) ORCID: orcid.org/0000-0001-7022-8287^{3,4,5}

[Nature](#) volume 588, pages 146–150 (2020) [Cite this article](#)

- 28k Accesses
- 21 Citations
- 326 Altmetric
- [Metrics details](#)

Subjects

- [Complement cascade](#)
- [Infectious diseases](#)
- [SARS-CoV-2](#)

Abstract

Coronavirus disease 2019 (COVID-19) is a disease caused by infection with severe acute respiratory syndrome coronavirus 2 (SARS-CoV-2) and has resulted in a pandemic¹. The C5a complement factor and its receptor C5aR1 (also known as CD88) have a key role in the initiation and maintenance of several inflammatory responses by recruiting and activating neutrophils and monocytes¹. Here we provide a longitudinal analysis of immune responses, including phenotypic analyses of immune cells and assessments of the soluble factors that are present in the blood and bronchoalveolar lavage fluid of patients at various stages of COVID-19 severity, including those who were paucisymptomatic or had pneumonia or acute respiratory distress syndrome. The levels of soluble C5a were increased in proportion to the severity of COVID-19 and high expression levels of C5aR1 receptors were found in blood and pulmonary myeloid cells, which supports a role for the C5a–C5aR1 axis in the pathophysiology of acute respiratory distress syndrome. Anti-C5aR1 therapeutic monoclonal antibodies prevented the C5a-mediated recruitment and activation of human myeloid cells, and inhibited acute lung injury in human C5aR1 knock-in mice. These results suggest that blockade of the C5a–C5aR1 axis could be used to limit the infiltration of myeloid cells in damaged organs and prevent the excessive lung inflammation and endothelialitis that are associated with acute respiratory distress syndrome in patients with COVID-19.

[Download PDF](#)

Main

Most patients with COVID-19 have only a few mild symptoms, but about 15% of patients progress to severe pneumonia, and about 5% develop acute respiratory distress syndrome (ARDS), for which effective therapeutic strategies are urgently required². The immune system has a dual role in the pathology of COVID-19, contributing to both virus elimination and the development of ARDS². A detailed characterization of the immune responses that occur during disease progression from mild to severe forms is therefore important for understanding the ways in which we can manipulate immunity to propose new therapies. In particular, given the urgent need for effective treatments for pneumonia in patients with COVID-19, the elucidation of the immune responses that occur during the course of COVID-19 could lead to the repurposing of approved immunomodulatory drugs and candidate drugs that have already been tested in clinical trials. We therefore monitored immune parameters in a cohort of 82 individuals: 10 healthy control individuals, 10 patients with COVID-19 who were paucisymptomatic, 34 patients with pneumonia and 28 patients with ARDS due to SARS-CoV-2 infection (Supplementary Table 1). We focused on molecular pathways that could block the overt inflammation associated with ARDS.

Disease severity was associated with an increase in the amounts of plasma C-reactive protein (CRP) and inflammatory cytokines—such as interleukin-6 (IL-6), and the chemokines CCL4 (macrophage inflammatory protein-1 β), CCL2 (monocyte chemoattractant protein 1) and CXCL9 (monokine induced by interferon- γ)—that are produced by and act on myeloid cells (Fig. 1a). These results confirmed previous observations of the ‘cytokine storm’ that develops in patients with severe COVID-19³. The ability of plasma from patients to neutralize the SARS-CoV-2 virus was also correlated with disease severity (Extended Data Fig. 1a), consistent with previous studies, which show higher titres of anti-SARS-CoV-2 antibodies in patients with severe COVID-19⁴.

Fig. 1: Inflammation is associated with a cytokine storm and C5a production in patients with COVID-19.

 **figure1**

a, Concentrations of CRP, IL-6, CCL4, CCL2 and CXCL9 in plasma from healthy control individuals (HC) and patients with COVID-19. **b**, Concentration of C5a desArg in plasma of HC and patients with COVID-19. Healthy control individuals, $n = 10$; patients who were paucisymptomatic (pauci), $n = 10$; patients with pneumonia (pneumo), $n = 31\text{--}34$; patients with ARDS, $n = 26\text{--}28$. For CRP (**a**) and **b**, P values were computed using two-tailed Wilcoxon rank-sum tests. For IL-6, CCL4, CCL2 and CXCL9 (**a**), a global comparison was first performed in which all values were classified into two categories: above or below the limit of quantification (P values for two-sided Fisher's exact tests show that there is an increase in the number of values above the limit of quantification with increasing severity); Fisher tests: $P = 5 \times 10^{-7}$ for IL-6, $P = 0.02$ for CCL4, $P = 0.001$ for CCL2, $P = 9 \times 10^{-6}$

for CXCL9. A comparison was then performed between patients with pneumonia and with ARDS, only for values above the limit of quantification (P values were computed using two-tailed Wilcoxon rank-sum tests). Each symbol represents a single donor. Box plots show the median and the 25th to 75th percentiles, and the whiskers denote the maximum and minimum values. The dotted lines for IL-6, CCL2 and CXCL9 (a) indicate the limit of quantification.

[Full size image](#)

We decided to focus on the complement factor C5a, which mediates strong chemoattraction and activation of myeloid cells⁵, and has well-documented roles specifically in lung inflammation and injury⁶. The complement cascade is important for the sensing and clearance of pathogens and inflammation⁷, and involves several components, including cell surface receptors and soluble regulators. In the final phase of the response, the membrane attack complex (MAC: C5b9) and the potent chemoattractants and inflammatory mediators C3a and C5a are generated. The MAC forms transmembrane channels on the surface of pathogen cells, disrupting the cell membrane and leading to cell death. The C3a and C5a proteins regulate inflammation by binding to their respective receptors, C3aR and C5aR1⁸. Exaggerated complement activation contributes to the pathogenesis of many inflammatory and immune diseases⁵. Numerous studies of the lung epithelium have reported depositions of complement components during inflammation and suggested that the systemic activation of complement leads, through C5a, to the recruitment, activation and adhesion of neutrophils to the pulmonary endothelium, which results in cell damage, and subsequent acute lung injury (ALI) and ARDS, which can be fatal^{1,6,9}. We observed an increase in plasma C5a levels that was proportional to COVID-19 severity (Fig. 1b). C5a levels increased in a few patients in the paucisymptomatic group, and were significantly higher in individuals with lung damage in the pneumonia and ARDS groups than in healthy controls (Fig. 1b). The longitudinal follow-up of patients with COVID-19 revealed that the upregulation of circulating C5a levels was maintained for at least 10 days after the inclusion of the patients in our cohort (Extended Data Fig. 1b). The higher level of C5a in the patients with the most-severe symptoms suggests a role for this anaphylatoxin in the inflammation that occurs in patients who develop ARDS. Increased systemic and local complement pathway activity was confirmed by transcriptomic analysis of peripheral blood from patients with COVID-19, which showed an upregulation of C1Q and C2 expression (Extended Data Fig. 1c) and by the presence of C5b9, as shown by immunostaining, in lung sections from patients with COVID-19 (Extended Data Fig. 1d). Consistent with these results, high levels of C5a in patients with COVID-19 have recently been reported to be a consequence of overt activation of the lectin pathway of the complement cascade by the N protein of SARS-CoV-

2¹⁰. Furthermore, anti-SARS-CoV-2 antibodies⁴ and CRP may also contribute to the activation of the classical and alternative pathways of complement during COVID-19. Thus, factors that trigger the activation of the complement pathways are upregulated in COVID-19 and may sustain the high levels of C5a that are detected in patients with severe COVID-19.

We found that COVID-19 was associated with peripheral blood neutrophilia (Fig. 2a), as reported in other cohorts¹¹. No major changes were observed in the total peripheral blood monocyte population (Fig. 2b), but the proportion of conventional CD14⁺CD16⁻ monocytes was increased, whereas the proportion of inflammatory CD14^{low}CD16⁺ monocytes was decreased in peripheral blood (Fig. 2c), consistent with the possibility that inflammatory monocytes leave the bloodstream and home to tissues. This hypothesis was supported by transcriptomic analyses of patients with COVID-19 who were symptomatic, which revealed not only an increase in the transcript levels of genes including *IRAK3*, *MS4A6A*, *CD33*, *CD300C*, *VCAN*, *CD1D*, *CCR1*, *OAS1*, *CD163* and *C3AR1* in peripheral blood mononuclear cells, but also an upregulation of macrophage and monocyte transcriptomic signatures in inflamed lungs (Extended Data Fig. 1c).

Fig. 2: C5aR1 is highly expressed on myeloid cells and promotes inflammation.

 **figure2**

a, Absolute numbers of circulating neutrophils per microlitre of peripheral blood from healthy control individuals and patients with COVID-19 at t_0 . **b**, Absolute numbers of circulating total monocytes per microlitre of peripheral blood from

healthy control individuals and patients with COVID-19 at t_0 . **c**, Percentages of CD14 $^+$ CD16 $^-$ conventional monocytes and CD14 $^{\text{low}}$ CD16 $^+$ inflammatory monocytes in the peripheral blood of healthy control individuals and patients with COVID-19 at t_0 . **d**, Percentage of C5aR1 $^+$ neutrophils and monocytes in peripheral blood from healthy control individuals and patients with COVID-19 at t_0 . **a–d**, Healthy control individuals, $n = 10$; patients who were paucisymptomatic, $n = 10$; patients with pneumonia, $n = 31$; patients with ARDS, $n = 26$. Each symbol represents a single donor. **e**, IL-6, TNF and CCL2 production by monocytes purified from peripheral blood mononuclear cells from patients with COVID-19. Peripheral blood mononuclear cells were activated overnight with LPS (0.5 ng ml $^{-1}$) or R848 (50 ng ml $^{-1}$) and recombinant human C5a (*HsC5a*) (1 $\mu\text{g ml}^{-1}$), as indicated. Each dot represents the mean value obtained from duplicate or triplicate analyses for a single patient ($n = 12$ patients). Box plots show the median and the 25th to 75th percentiles, and the whiskers denote the maximum and minimum values. The P values were obtained using two-tailed Wilcoxon rank-sum tests (**a–d**) and two-tailed Wilcoxon signed-rank tests (**e**). NS, no significant differences.

[Full size image](#)

Both circulating neutrophils and monocytes displayed strong C5aR1 expression in healthy individuals that was also observed in the various groups of patients with COVID-19 (Fig. 2d). Longitudinal immune-monitoring follow-up of patients with pneumonia and ARDS showed that the levels of C5aR1 molecules remained stable on circulating neutrophils and monocytes, or even increased during the course of the disease (Extended Data Fig. 2a). Consistent with the inflammatory function of C5a¹², and the expression of C5aR1 on monocytes, C5a increased the production of the inflammatory cytokines IL-6, TNF and CCL2 that is induced by lipopolysaccharide (LPS) on purified blood monocytes isolated from patients with COVID-19 (Fig. 2e). C5a also increased the production of cytokines by monocytes from patients with COVID-19 following stimulation with R848, which activates the TLR7 and/or TLR8 MyD88-dependent signalling pathway, mimicking the single-stranded RNA of SARS-CoV-2 (Fig. 2e).

Given that severe COVID-19 is associated with lung disease, we then focused on this organ. C5a was detected in the bronchoalveolar lavage fluid (BALF) of patients with COVID-19 who had ARDS (Fig. 3a). Inflammatory cytokines, such as CXCL8, CXCL9, CCL2 and—to a lesser extent—CCL4, IL-6, TNF and IL-1 β , were also detected in these samples (Fig. 3a). Large numbers of neutrophils and monocytes were found in the BALF of patients with COVID-19 who had ARDS and these cells expressed C5aR1 (Fig. 3b). In addition, the analysis of single-cell RNA-sequencing data from healthy control individuals and patients with COVID-19 who

had ARDS¹³ revealed major changes in the myeloid cell population that infiltrated the lungs during the course of the SARS-CoV-2 infection. Indeed, the major myeloid cell subset (subset A) in healthy control individuals and the major myeloid cell subset (subset B) in patients with COVID-19 who had ARDS were clearly different (Fig. 3c and Extended Data Fig. 3a, b). The cells of subset B were characterized by higher transcript levels of inflammatory cytokine genes, such as CXCL8, CCL2, CCL4, CXCL9, TNF and IL-6 (Fig. 3d). Both myeloid cell subsets expressed C5AR1, although a slight upregulation was observed in subset B (Fig. 3d). A multiplex immunohistochemistry analysis of lungs from patients with ARDS with COVID-19 who were deceased confirmed pulmonary infiltration of CD68⁺CD163⁺ macrophages, a substantial proportion of which expressed C5aR1 (Extended Data Fig. 3c (right)), relative to lung tissue from a control individual without COVID-19 (Extended Data Fig. 3c (left)). It is becoming increasingly clear that severe COVID-19 is associated with the spread of the virus through the epithelial barrier and with endothelialitis^{14,15,16}. We observed obliterating endarteritis that was associated with an accumulation of C5aR1⁺ macrophages around the arteries and in the thrombus (Extended Data Fig. 3d). Together with the high levels of C5a in patients with COVID-19 who were symptomatic, these data support the hypothesis that C5a production leads to the chemo-atraction and activation of myeloid cells in the lungs, and contributes to the overt release of inflammatory cytokines. As C5a can also promote the secretion of CCL2, a strong chemoattractant for monocytes, C5a could also indirectly promote the recruitment of inflammatory cells indirectly, through the induction of other chemokines. It is also possible that the vasculitis associated with severe COVID-19 is linked to the production of C5a, as other types of vasculitis, such as anti-neutrophil cytoplasmic antibody (ANCA)-associated vasculitis, are mediated by C5a¹⁷.

Fig. 3: C5aR1⁺ cells and C5a are detected in lung samples from patients with COVID-19.

 **figure3**

a, Concentration of C5a desArg and IL-6, CXCL9, CCL2, CCL4, CXCL8, TNF and IL-1 β in the BALF of patients with ARDS ($n = 4$). $^{\#}$ Values were above the detection limit of 52,200 pg ml $^{-1}$; $^{\$}$ values were below the detection limit of 29 pg ml $^{-1}$. Box plots show the median and the 25th to 75th percentiles, and the whiskers denote the maximum and minimum values. **b**, Left, CD45 $^{+}$ immune cell infiltration in BALF from patients with ARDS using flow cytometry. Right, C5aR1 expression (red) compared with negative control (fluorescence without antibody; black) staining on CD45 $^{+}$ CD14 $^{-}$ CD15 $^{+}$ CD16 $^{+}$ neutrophils and CD45 $^{+}$ CD33 $^{+}$ HLA-DR $^{+}$ CD14 $^{+}$ monocytes in BALF from patients with ARDS. The plots shown are representative of analyses performed on samples from three patients with ARDS. **c**, Uniform manifold approximation and projection (UMAP) analysis of myeloid cell clusters by patient group. Healthy control individuals, $n = 3$; patients with severe COVID-19, $n = 6$. **d**, Dot plot of pro-inflammatory cytokine expression in each of the subsets from **c**.

[Full size image](#)

On the basis of this hypothesis, we reasoned that blockade of the C5a–C5aR1 axis could be used as a potential therapeutic strategy for the treatment of severe COVID-19. Several molecules could be repurposed to this end, including anti-C5 monoclonal antibodies, anti-C5a monoclonal antibodies and C5aR1 antagonists. We focused on avdoralimab, a fully human Fc-silent monoclonal antibody against C5aR1 that prevents its binding to C5a. In vitro, C5aR1 blockade with avdoralimab inhibited C5a-induced activation of neutrophils, as shown by evaluation of the induction of CD11b expression at the cell surface (Fig. 4a). The C5a-mediated upregulation of CD11b was also inhibited by other C5aR1 antagonists or anti-C5a monoclonal antibodies (Extended Data Fig. 4a). Avdoralimab blocked the activation of neutrophils induced by very high concentrations of C5a (Fig. 4b). With regard to the infiltration of C5aR1⁺ myeloid cells in the inflamed lungs of patients with severe COVID-19, avdoralimab also inhibited the C5a-induced migration of neutrophils in vitro (Fig. 4c). We next investigated whether avdoralimab could block the development of ALI in a mouse model. As avdoralimab targets human C5aR1, we used mice with a knock-in gene of human C5aR1 (HsC5AR1 knock-in mice)¹⁸ that showed HsC5aR1 expression exclusively on CD11b⁺ myeloid cells (Extended Data Fig. 4b). HsC5AR1 knock-in mice that received an intranasal instillation of recombinant human C5a developed ALI and injury 18 h after injection, as shown by the infiltration of CD45⁺ immune cells including Ly6G⁺Ly6C⁺ neutrophils and Ly6G⁻Ly6C⁺ monocytes in the lung (Fig. 4d) and the release of albumin in BALF (Fig. 4e), a marker of alveolar-capillary permeability and lung injury. ALI was confirmed by histopathological analysis of lung sections that revealed massive inflammatory cell infiltration, alveolar haemorrhage and thickening of alveolar walls in lungs of C5a-treated mice (Extended Data Fig. 4c), as previously described⁹. Avdoralimab blocked the infiltration of both cell types (Fig. 4d), prevented albumin release in BALF (Fig. 4e) and limited C5a-induced ALI histopathological features (Extended Data Fig. 4c). Finally, avdoralimab also inhibited the increase in IL-6, TNF and CCL2 secretion induced in vitro by C5a in monocytes purified from patients with COVID-19 and activated with a single-strand RNA-virus-like stimulus (Fig. 4f). Therefore, avdoralimab seems to be suitable for blocking the C5a–C5aR1 axis, which is active during COVID-19. The high levels of C5a observed in patients with COVID-19 do not appear to be a passenger phenomenon, as preliminary efficacy data reported that two patients with COVID-19 recovered from ARDS after treatment with an anti-C5a blocking monoclonal antibody (IFX-1)¹⁰. Furthermore, four patients with severe COVID-19 treated with an anti-C5 monoclonal antibody (eculizumab) exhibited a drop in circulating inflammatory markers¹⁹. There are several advantages to blocking C5aR1 rather than other components of the complement cascade. First, blocking C5a or C5aR1 leaves C5b intact and preserves the MAC, which has a key role in controlling several infections. A loss of the MAC

would raise safety concerns for the treatment of COVID-19, as patients who are symptomatic often develop comorbid conditions, such as bacterial infections, for which the MAC is required. Second, C5aR1 blockade has the advantage over C5a blockade of having no effect on the second C5a receptor, C5L2. The function of C5L2 remains unclear, but it has been suggested that it can act as a decoy receptor, with anti-inflammatory roles²⁰.

Fig. 4: Targeting C5aR1 blocks the C5a-mediated activation and migration of myeloid cells.

 figure4

a, Representative flow cytometry histogram of the C5a-mediated upregulation of CD11b on whole-blood neutrophils, inhibited by avdoralimab. Grey, non-activated neutrophils; black, recombinant human C5a (*HsC5a*)-activated neutrophils; purple,

HsC5a-activated neutrophils treated with avdoralimab ($30 \mu\text{g ml}^{-1}$). **b**, CD11b induction through a dose-dependent response to *HsC5a* on untreated (grey) or $10 \mu\text{g ml}^{-1}$ avdoralimab-treated whole-blood neutrophils (purple). MFI, median fluorescence intensity. Data were obtained from two independent donors. **c**, Migrating neutrophils attracted by *HsC5a*. Neutrophils were treated with $10 \mu\text{g ml}^{-1}$ isotype control (IC) or avdoralimab (avdo) before the induction of migration by *HsC5a*. Data for neutrophils purified from four healthy control individuals are shown. **d, e**, BALF was collected from *HsC5AR1* knock-in mice 18 h after intranasal instillation of *HsC5a*. Mice were pretreated with avdoralimab or isotype control, as indicated. Each symbol represents data from a single mouse; $n = 5$ mice (PBS) and $n = 7$ mice (all other groups). Data are representative of two experiments. **d**, BALF cell analysis by flow cytometry of CD45 $^{+}$ immune cells, Ly6C $^{+}$ Ly6G $^{+}$ neutrophils and Ly6C $^{+}$ Ly6G $^{-}$ monocytes. **e**, Albumin concentration in BALF. **f**, Production of IL-6, TNF and CCL2 by monocytes purified from the peripheral blood mononuclear cells of patients with COVID-19 activated by overnight incubation with R848 (50 ng ml^{-1}) and *HsC5a* ($1 \mu\text{g ml}^{-1}$). Before activation, monocytes were incubated with $20 \mu\text{g ml}^{-1}$ avdoralimab or isotype control. Each dot represents the mean value obtained from duplicate or triplicate analyses of a single donor; $n = 10$ (IL-6) and $n = 12$ (TNF and CCL2). Box plots show the median and the 25th to 75th percentiles, and the whiskers denote the maximum and minimum values. The *P* values were computed using a paired one-way analysis of variance (ANOVA) (**c**), two-tailed Wilcoxon rank-sum tests (**d, e**) and two-tailed Wilcoxon signed-rank tests (**f**).

[Full size image](#)

Our data, which highlight the role of the C5a–C5aR1 axis in the pathogenesis of severe COVID-19, are consistent with several previous observations. Indeed, high C5a levels have also been described in various preclinical models of acute lung disease due to pathogenic viruses, such as SARS-CoV, H1N1, H5N1 and H7N9¹. High levels of C5a have also been found in the upper respiratory tract and in serum samples from patients infected with H1N1²¹. Furthermore, BALF from patients with ARDS was found to display robust C5a-dependent chemotactic activity²². In a mouse model of Middle East respiratory syndrome coronavirus (MERS-CoV) infection, C5a concentrations were high in serum samples and lung tissues²³, and anti-C5aR1 antibody treatment decreased viral replication in lung tissue²³. In a green monkey model of H7N9 infection, treatment with an anti-C5a antibody significantly decreased the levels of IL-6, interferon- γ , TNF and IL-1 β and neutrophil infiltration in the lungs²⁴. Overall, C5a inhibition markedly decreased the ALI and systemic inflammation induced by viral infection²⁵. Further evidence for

the involvement of the complement system in the pathogenesis of severe COVID-19 is provided by the existence of genetic variants of the complement cascade, which are associated with clinical outcome of SARS-CoV-2 infection, such as *CD55*²⁶.

In addition, the complement system links innate immunity to coagulation^{27,28}, and its overactivation could promote thrombotic events in patients with severe COVID-19²⁹. Complement blockade may, therefore, prevent thrombosis in affected individuals.

The data presented here support a role for the C5a–C5aR1 axis in the inflammatory mechanisms that underlie the development of ARDS in patients at early or late stages of infection with SARS-CoV-2, which is consistent with other reports^{10,30}. As described above, in addition to pneumonia and ARDS, there are data that suggest a role of C5a in other COVID-19-related symptoms, including heart, kidney or endothelial cell dysfunction¹⁴, providing support for the testing of the blockade of the C5a–C5aR1 axis in patients with COVID-19. We suggest that such a blockade may prevent the transition from a localized epithelial disease (non-severe COVID-19) to a diffuse endothelial disease (severe COVID-19) (Extended Data Fig. 4d).

Methods

Data reporting

No statistical methods were used to predetermine sample size. The experiments were not randomized and the investigators were not blinded to allocation during experiments and outcome assessment.

Study participants and clinical considerations

Over a period of one month (27 March 2020–24 April 2020), 82 participants were recruited from three hospitals (Timone and Nord University Hospitals, and Laveran Military Hospital, Marseille). Of the 82 participants, 28 were on mechanical ventilation for COVID-19-related-ARDS (*P/F* ratio < 300) (ARDS group), 34 patients required oxygen support at a rate of less than 5 l min⁻¹ for COVID-19-related pneumonia (pneumonia group) and 10 patients had a paucisymptomatic form of COVID-19 that was compatible with outpatient care (paucisymptomatic group). COVID-19 was diagnosed on the basis of positive SARS-CoV-2 real-time reverse-transcription PCR (RT-PCR) on nasopharyngeal samples and/or typical CT-scan findings³¹. We also included 10 healthy volunteers (control group), with no fever or symptoms on the days before sampling and negative for SARS-CoV-2 RT-PCR.

The characteristics of the patients are described in Supplementary Table 1. Biological samples were first collected within 3 days of diagnosis and the start of care (t_0 , <72 h, early time point). When possible, the next two time points for sample collection were located between days 5 and 10 (t_1 , intermediate time point) and after day 10 (t_2 , late time point). Flow cytometry analyses were performed on fresh blood samples (EDTA tubes) and BALFs, immediately after collection. Clinical progression was evaluated between the early and intermediate time points and between the intermediate and late time points. A favourable outcome was defined as weaning from mechanical ventilation (ARDS group) or oxygen support (pneumonia group). Death or multiple organ failure (ARDS group) and admission to the intensive care unit (pneumonia group) were considered unfavourable outcomes. In other cases, patients were considered to be stable.

Ethics approval statement

All of the patients (and/or initially their families) provided written informed consent before sampling and for the use of their clinical and biological data. The study protocol was approved on 27 March 2020 by the Committee for the Protection of Persons Ile-de-France III – France (2020-A00757-32). The pathological examination used in this study was performed secondary to a medical autopsy after COVID-19-related death, with agreement from the family and notification of the representative of the Commission on Data Processing and Freedom (MR003 research).

Animals

Female C57BL/6J mice were purchased at Janvier Labs and used between 8 and 12 weeks of age. HsC5AR1 knock-in mice were bred at Charles River Laboratories under specific-pathogen-free conditions. Female mice were used at 8–12 weeks of age and were allowed to acclimatize to the housing facility for at least one week. All animal experiments were performed in accordance with the rules of the Innate Pharma ethics committee and were approved by the Ministère de l'Enseignement Supérieur, de la Recherche et de l'Innovation – France (APAFIS#25418-2020051512242806 v2).

Reagent list

DPBS (1×) (14190-094, Gibco); RPMI medium 1640 (1×) (31870-025, Gibco); sodium pyruvate 100 mM (100×) (11360-039, Gibco); l-glutamine 200 mM (100×) (25030-024, Gibco); minimum essential medium non-essential amino acids solution

(11140-035, Gibco); trypan blue stain (0.4%) (15250-061, Gibco); Ficoll–Paque PLUS (17-1440-03, GE Healthcare); fetal calf serum (FCS; F7524, Sigma); dimethyl sulfoxide (DMSO; D2650-100ML, Sigma); CD14 microbeads human (130-050-201, Miltenyi Biotec); EasySep direct human neutrophil isolation kit (19666, StemCell Technologies); bovine serum albumin (BSA; A9418-100G, Sigma); UltraPure 0.5 M EDTA, pH 8.0 (15575-038, Invitrogen); LPS EK ultrapure (tlrl-peklps, Invivogen); R848 (tlrl-r848, Invivogen); C5a (IPH 1D9 batch 1A, Innate Pharma); C5a (2037-C5-025, R&D Systems); avdoralimab (Innate Pharma), isotype control (Fc-silent hIgG1) (Innate Pharma); CD33–PECF594 clone WM53 (562492, BD Biosciences); CD19–PECy7 clone SJ25C1(557835, BD Biosciences); CD3–BUV496 clone UCHT1 (564809/612940, BD Biosciences); CD15–BV510 clone W6D3 (563141, BD Biosciences); CD45–BV711 clone HI30 (564357, BD Biosciences); CD16–BUV395 clone 3G8 (563785, BD Biosciences); CD14–BUV737 clone M5E2 (564444/612763, BD Biosciences); HLA-DR–AF700 clone L243 (307626, BioLegend); LIVE/DEAD Near-IR (L34976, ThermoFisher); mouse serum (015-000-120, Jackson ImmunoResearch); CD88 C5aR PE clone S5/1 (344304, BioLegend); anti-CD16–FITC (556616, BD Biosciences); anti-CD11b–PE–Cy5 (555389, BD Biosciences); U-PLEX kit (N05235A-1, MSD); OptEIA *HsC5a* ELISA (557965, BD Biosciences); mouse albumin ELISA kit (E99-134, Bethyl Laboratories); Ficoll (11778538, Invitrogen); dextran (31382, Sigma); calcein AM (C3100MP, Invitrogen); fibrinogen (F3879, Sigma); Transwell Fluoroblok 3 µm insert (351151, Corning); EDTA (15575-038, Invitrogen); sodium azide (71290-100g, Sigma); Optilyse C solution (A11895, Beckman Coulter); CytoFix (554655, BD Bioscience); avacopan (HY-17627, Clinisciences); anti-C5a (Innate Pharma); anti-mouse Ly6C–BV510 clone HK1.4 (128033, BioLegend); anti-mouse Ly6G–BV786 clone 1A8 (740953, BD Biosciences); anti-mouse CD45–BUV395 clone 30F11 (564279, BD Biosciences), anti-mouse CD11b–BUV737 clone M1/70 (564443/612800, BD Biosciences); anti-mouse C5aR1–APC clone 20/70 (130-106-124, Miltenyi Biotec); anti-human CD88 clone S5/1 (HM2094-100UG, Hycult Biotech); anti-human CD68 clone KP1 (M0814, Agilent); anti-human CD163 clone EDHu-1 (MCA1853, BioRad).

SARS-CoV-2 detection by PCR

SARS-CoV-2 RNA was detected by RT–PCR, as previously described³².

Seroneutralization assay

Experiments were performed in BSL3 facilities with a clinical isolate of SARS-CoV-2. Virus-neutralization tests were performed as previously described³³. In brief, virus-neutralization tests were performed in a 96-well plate, with Vero E6 cells and a

SARS-CoV-2 strain (Ref-SKU:026V-03883 isolated at Charité University, Berlin, Germany; EVA-GLOBAL H2020 project; grant agreement 871029). Twofold serial dilutions of serum samples (final serum dilutions of 1:20 to 1:160) were mixed with a median tissue culture infective dose of 100 of SARS-CoV2 and dispensed on the confluent cell monolayer. The plates were incubated for 4 days and examined for the presence (no neutralization) or absence (neutralization) of cytopathogenic effects under an inverted microscope.

Preparation of peripheral blood mononuclear cells and plasma

Whole blood collected in EDTA tubes was pooled and diluted 1:2 in PBS. Peripheral blood mononuclear cells (PBMCs) were isolated by centrifugation on a Ficoll gradient, and 10^7 PBMCs per vial were frozen in freezing medium (90% FCS and 10% DMSO). Plasma was collected from the upper phase of the Ficoll gradient, aliquoted and used for the quantification of soluble factors.

Assessment of soluble factors

Human IL-6, CXCL9, CCL2, CCL4, CXCL8, TNF and IL-1 β levels were analysed with the U-PLEX kit supplied by MSD (U-PLEX 10-Assay, 96-Well SECTOR plate, N05235A-1), according to the manufacturer's instructions. The U-PLEX plate was loaded into an MSD instrument to measure the intensity of emitted light, which is proportional to the amount of analyte present in the sample. Circulating C5a desArg levels were analysed using a BD OptEIA HsC5a ELISA. Mouse albumin in BALF was analysed by ELISA (Bethyl). HRP-conjugated secondary antibodies were detected by incubation with a peroxidase substrate solution (TMB) and the reaction was stopped by acidification. Plates were read at 450 nm.

Flow cytometry

Blood collected into EDTA tubes was washed in PBS before staining with LIVE/DEAD (Thermo Fisher) according to the manufacturer's instructions. Cells were incubated with mouse serum to saturate the Fc receptors, and were then incubated with the appropriate antibody cocktail. Red blood cells were lysed in Optilyse C solution (Beckman Coulter), according to the manufacturer's instructions. Cells were fixed in CytoFix solution (BD Bioscience, 554655), according to the manufacturer's instructions. Data were acquired in an LSRII Fortessa X20 flow cytometer. The FCS3.0 files obtained were exported from BD FACSDiva software and imported into FlowJo v.10.5.2 (BD Biosciences). Automated compensation was calculated with FACSDiva software and single-antibody-stained compensation beads. This compensation matrix was analysed in

detail in FlowJo, by investigating the N-by-N view feature and the pairwise expression of all proteins stained in this study. Fluorescence minus one experiments were run before this study, to facilitate optimization of the compensation matrix. We then adjusted the compensation matrix where necessary due to over- or under-compensation by the automatic algorithm.

Immune cell counts

Absolute counts per microlitre of blood were determined with BD TBNK Trucount Tubes. Absolute counts for a particular cell population (A) were obtained by dividing the number of positive cell events (X) by the number of bead events (Y), and then multiplying by the BD Trucount bead concentration (N/V , where N is the number of beads per test and V is the test volume). $A = X/Y \times N/V$. The number of positive counts for neutrophils and monocytes was established with the $CD45^+SSC^{\text{high}}$ and $CD45^+SSC^{\text{int}}$ gating strategies, respectively.

C5a inhibitors

Avdoralimab is a fully human mutated Fc-silent IgG1 monoclonal antibody against C5aR1 (US 2020/0017599A1). Anti-C5a monoclonal antibody is a chimeric mutated Fc silent IgG1 isotype cloned from the sequences of mouse anti-*HsC5a* INab308 (WO2015/140304A1), and has the same variable sequences as IFX-1. The C5aR1 antagonist (avacopan) was purchased from Clinisciences (HY-17627).

Neutrophil migration

Neutrophils were isolated from fresh blood by sedimentation in 6% dextran to separate plasma and leukocytes, followed by centrifugation on a Ficoll density gradient. The pellet, containing neutrophils, was recovered, and the red blood cells were lysed by incubation in 0.2% NaCl. Osmotic balance was restored by adding an equal volume of 1.6% NaCl. Isolated neutrophils were loaded with 10 μM calcein AM. Cell density was adjusted before the addition of avdoralimab or its isotype control at a final concentration of 10 $\mu\text{g ml}^{-1}$. Neutrophils were dispensed into the top chamber of a fibrinogen- and BSA-coated Transwell Fluoroblok 3 μm insert. The lower chamber was filled with RPMI 1640 with or without 3 nM *HsC5a* (R&D Systems,) and the same antibody was added to the top chamber (avdoralimab, isotype control or PBS). After 30 min of incubation at $+37 \pm 1^\circ\text{C}$ under an atmosphere containing $5 \pm 1\%$ CO₂, images of the bottom side of the inserts were acquired on a Biotek Cytation 5 plate-reading microscope, and analysed with Halo

software (Indica Labs), using the CytoNuclear FL module to count the cells that had crossed the membrane.

Neutrophil activation

Various concentrations of avdoralimab were added to the blood samples in culture-treated 96-well U-bottom plates, and incubated for 20 min at 37 °C under an atmosphere containing 5% CO₂. We then added 18 nM *HsC5a* (R&D Systems) to the samples. Plates were incubated for 20 min at 37 °C under an atmosphere of 5% CO₂. Samples were then stained for flow cytometry analysis with anti-CD16–FITC and anti-CD11b–PE-Cy5 antibodies. Erythrocytes were lysed with Optilyse C solution (Beckman Coulter, A11895), according to the manufacturer's protocol, and resuspended in CytoFix (BD Bioscience 554655) for fixation. Cells were then analysed on a FACS Canto II flow cytometer (BD Biosciences) with FACS Diva software.

Monocyte activation

Monocytes were purified with the CD14⁺ selection kit (Miltenyi). We used 30,000 monocytes to seed 96-well U-bottom plates. Cells were activated by overnight incubation with R848 (50 ng ml⁻¹), LPS (0.5 ng ml⁻¹) and *HsC5a* (1 µg mL⁻¹; IPH). In some conditions, monocytes were incubated with avdoralimab (20 µg ml⁻¹; IPH) or its isotype control (20 µg ml⁻¹; IPH) for 30 min before stimulation. IL-6, TNF and CCL2 levels were quantified in the supernatant.

Mouse model of lung inflammation

Isoflurane-anaesthetized *HsC5AR1* knock-in mice received 3.1 µg of recombinant *HsC5a* (R&D) in 40 µl PBS, by intranasal instillation. After 18 h, mice were killed with a lethal dose of ketamine/xylazine cocktail (ketamine 300 mg kg⁻¹; xylazine 30 mg kg⁻¹). The lungs were flushed with 2 ml 2 mM EDTA in PBS to obtain BALF. After centrifugation (300g, 5 min, 4 °C), BALF cells were counted and stained for flow cytometry analysis with anti-CD45, anti-Ly6C, anti-Ly6G and anti-CD11b antibodies. For histology analysis, 18 h after intranasal instillation of *HsC5a*, lungs were fixed in formalin, dissected, embedded in paraffin and sectioned to 5 µm. Sections were dewaxed and stained with haematoxylin and eosin (H&E). Slides were scanned using a Nanozoomer S60 (Hamamatsu) and examined for evidence of lung damage.

Multiplex immunohistochemistry staining protocol, image acquisition and data analysis

Multiplexed immunohistochemistry (IHC) was performed with a Leica Bond Rx on 5- μm -thick formalin-fixed paraffin-embedded lung tissue sections from individuals with and without COVID-19. Consecutive staining was performed by heat-induced antigen retrieval followed by incubation with primary antibody (anti-C5aR1 clone S5/1 at 1 $\mu\text{g ml}^{-1}$). The signal was amplified and detected with Opal polymer horseradish peroxidase and Opal 520 (Akoya Biosciences). The sections were then subjected to heat-induced antibody stripping and incubated with the next antibody (anti-CD163 clone EDHu-1 at 1 $\mu\text{g ml}^{-1}$, detected with Opal 620, and, finally, anti-CD68 clone KP1 at 0.1 $\mu\text{g ml}^{-1}$, detected with Opal 690) and spectral DAPI. All Opal reagents were used at a dilution of 1:150. Slides were mounted in ProLong Diamond anti-fade mounting medium (Thermo Fisher) and scanned with a Vectra Polaris (Akoya Biosciences). H&E-stained slides were scanned with a Nanozoomer (Hamamatsu). After spectral deconvolution and whole-slide reconstruction of the multiplexed IHC stained sections, digital pathology methods were used to determine the density of positive cells. All analyses were performed with Halo (Indica Labs) and R.

Transcriptomic analysis

Transcriptomic analyses were performed on previously reported data^{13,34}. The RNA-sequencing (RNA-seq) data for two BALF samples from patients (each in duplicate), three PBMC samples from healthy control individuals and three PBMC samples from patients were downloaded from the National Genomics Data Center (<https://bigd.big.ac.cn/>; accession number PRJCA002326). The RNA-seq data for three BALF samples from healthy control individuals were downloaded from the SRA database (accession numbers, SRR10571724, SRR10571730 and SRR10571732).

RNA-seq pipeline

The reads were mapped to the human genome (hg38) release 96 from Ensembl with STAR³⁵. PCR replicates mapping to the human genome were removed with the Picard MarkDuplicates program (Broad Institute 2019, <http://broadinstitute.github.io/picard/>). Gene expression was calculated with featureCounts in the SubReads package (v.1.6.4)³⁶. Transcripts per million values were calculated from the raw counts and log₂-transformed. The depth of sequencing of the patient BALF samples was low (<1 million).

Batch effect correction

We corrected for the batch effect between the datasets for BALF samples from healthy control individuals and those from patients and PBMC samples with Combat³⁷, using the model: ~Batch + Status (Patient or Healthy) + Sample Type (PBMC or BALF). An analysis of differential expression between PBMC samples from healthy control individuals and patients was performed on raw counts with DESeq2³⁸. Significance was defined as an adjusted $P < 0.05$. The metagene *IRAK3*, *MS4A6A*, *CD33*, *CD300C*, *VCAN*, *CD1D*, *CCR1*, *OAS1*, *CD163*, *CD14*, *FCN1*, *AIF1* and *PLA2G7* was used to calculate the macrophage and monocyte transcriptomic signature. The significance of the difference between healthy control individuals and patients was evaluated using a Wilcoxon rank-sum test. The single-cell RNA-seq data for 12 BALF samples from three healthy control individuals, three patients with mild COVID-19 and six patients with severe COVID-19 were downloaded from the Gene Expression Omnibus (GEO) database (accession number GSE145926). Quality controls were applied to each cell, for all samples, with the same criteria as for the initial analysis (gene number between 200 and 6,000, UMI count $>1,000$ and mitochondrial gene percentage <0.1) with the Seurat package (v.3.1.0). After filtering, 63,740 cells were validated. As previously described¹³ the filtered gene–barcode matrix was first normalized with ‘LogNormalize’ methods in Seurat v.3, with default parameters. The top 2,000 variable genes were then identified by the ‘vst’ method with the Seurat FindVariableFeatures function. The variables ‘nCount_RNA’ and ‘percent.mito’ were regressed out in the scaling step and a principal component analysis was performed on the top 2,000 variable genes. For the reanalysis presented here, the batch effects across different donors were removed by Harmony³⁹ and UMAP was performed on the top 50 dimensions for visualizing the cells. Graph-based clustering was performed on the Harmony-corrected data, with a resolution of 1.2, and defined major clusters composed of epithelial cells, B and plasma cells, T and NK cells, dendritic cells, monocytes, macrophages and neutrophils. The 50,610 myeloid cells were reintegrated and reclustered.

Data analysis and statistics

All statistical analyses were performed with R (v.3.6.1). The ggpubr (v.0.2.5) and lmerTest (v.3.1.2) packages were used for statistical tests. The gtsummary package (v.1.3.0) was used for the table containing clinical information (Supplementary Table 1). The sva package (v.3.32.1) was used to correct the batch effect of RNA-seq. Packages ggplot2 (v.3.2.1) and pheatmap (v.1.0.12) were used for the graphical representations of RNA-seq analyses. The Seurat package (v.3.1.0) was used for all

analyses of single-cell RNA-seq. For the comparison of groups at time point t_0 , P values were obtained for two-tailed Wilcoxon rank-sum tests. For longitudinal analysis in the pneumonia group, the P values for comparisons of t_1 and t_0 were obtained using two-tailed Wilcoxon signed-rank tests. No statistical tests were performed for t_2 in this group. For the ARDS group, a mixed model was computed, with time point as a fixed effect (categorical variable) and patient as a random effect. Confidence intervals and P values were based on the t -distribution, with degrees of freedom according to the Kenward–Roger method, and the normality of residuals was verified. Plots were drawn with GraphPad Prism v.8.1.1. Box plots show the median (centre line) and 25th to 75th percentiles (box) and the whiskers denote the maximum and minimum values.

Reporting summary

Further information on research design is available in the [Nature Research Reporting Summary](#) linked to this paper.

Data availability

The RNA-seq data for two BALF samples from patients (each in duplicate), three PBMC samples from healthy control individuals and three PBMC samples from patients with COVID-19 were downloaded from the National Genomics Data Center (<https://bigd.big.ac.cn/>; accession number PRJCA002326). The RNA-seq data for three BALF samples from healthy control individuals were downloaded from the SRA database (accession numbers SRR10571724, SRR10571730 and SRR10571732). The single-cell RNA-seq data are available from the Gene Expression Omnibus (GEO) database (accession number [GSE145926](#)). Additional materials or data are available from the corresponding author upon reasonable request.

References

1. 1.

- Wang, R., Xiao, H., Guo, R., Li, Y. & Shen, B. The role of C5a in acute lung injury induced by highly pathogenic viral infections. *Emerg. Microbes Infect.* **4**, 1–7 (2015).

[Google Scholar](#)

2. 2.

Cao, X. COVID-19: immunopathology and its implications for therapy. *Nat. Rev. Immunol.* **20**, 269–270 (2020).

[CAS](#) [Article](#) [PubMed](#) [PubMed Central](#) [Google Scholar](#)

3. 3.

Mehta, P. et al. COVID-19: consider cytokine storm syndromes and immunosuppression. *Lancet* **395**, 1033–1034 (2020).

[CAS](#) [Article](#) [PubMed](#) [PubMed Central](#) [Google Scholar](#)

4. 4.

Long, Q. X. et al. Antibody responses to SARS-CoV-2 in patients with COVID-19. *Nat. Med.* **26**, 845–848 (2020).

[CAS](#) [Article](#) [PubMed](#) [Google Scholar](#)

5. 5.

Guo, R. F. & Ward, P. A. Role of C5a in inflammatory responses. *Annu. Rev. Immunol.* **23**, 821–852 (2005).

[CAS](#) [Article](#) [PubMed](#) [Google Scholar](#)

6. 6.

Bosmann, M. & Ward, P. A. Role of C3, C5 and anaphylatoxin receptors in acute lung injury and in sepsis. *Adv. Exp. Med. Biol.* **946**, 147–159 (2012).

[CAS](#) [Article](#) [PubMed](#) [PubMed Central](#) [Google Scholar](#)

7. 7.

Ricklin, D., Hajishengallis, G., Yang, K. & Lambris, J. D. Complement: a key system for immune surveillance and homeostasis. *Nat. Immunol.* **11**, 785–797 (2010).

[CAS](#) [Article](#) [PubMed](#) [PubMed Central](#) [Google Scholar](#)

8. 8.

Guo, R. F., Riedemann, N. C. & Ward, P. A. Role of C5a–C5aR interaction in sepsis. *Shock* **21**, 1–7 (2004).

[Article](#) [PubMed](#) [Google Scholar](#)

9. 9.

Russkamp, N. F. et al. Experimental design of complement component 5a-induced acute lung injury (C5a-ALI): a role of CC-chemokine receptor type 5 during immune activation by anaphylatoxin. *FASEB J.* **29**, 3762–3772 (2015).

[CAS](#) [Article](#) [PubMed](#) [PubMed Central](#) [Google Scholar](#)

10. 10.

Gao, T. et al. Highly pathogenic coronavirus N protein aggravates lung injury by MASP-2-mediated complement over-activation. Preprint at medRxiv
<https://doi.org/10.1101/2020.03.29.20041962> (2020).

11. 11.

Liu, J. et al. Neutrophil-to-lymphocyte ratio predicts critical illness patients with 2019 coronavirus disease in the early stage. *J. Transl. Med.* **18**, 206 (2020).

[CAS](#) [Article](#) [PubMed](#) [PubMed Central](#) [Google Scholar](#)

12. 12.

Riedemann, N. C. et al. Increased C5a receptor expression in sepsis. *J. Clin. Invest.* **110**, 101–108 (2002).

[CAS](#) [Article](#) [PubMed](#) [PubMed Central](#) [Google Scholar](#)

13. 13.

Liao, M. et al. Single-cell landscape of bronchoalveolar immune cells in patients with COVID-19. *Nat. Med.* **26**, 842–844 (2020).

[CAS](#) [Article](#) [PubMed](#) [Google Scholar](#)

14. 14.

Varga, Z. et al. Endothelial cell infection and endotheliitis in COVID-19. *Lancet* **395**, 1417–1418 (2020).

[CAS](#) [Article](#) [PubMed](#) [PubMed Central](#) [Google Scholar](#)

15. 15.

Teuwen, L.-A., Geldhof, V., Pasut, A. & Carmeliet, P. COVID-19: the vasculature unleashed. *Nat. Rev. Immunol.* **20**, 389–391 (2020).

[CAS](#) [Article](#) [PubMed](#) [Google Scholar](#)

16. 16.

Copin, M. C. et al. Time to consider histologic pattern of lung injury to treat critically ill patients with COVID-19 infection. *Intensive Care Med.* **46**, 1124–1126 (2020).

[CAS](#) [Article](#) [PubMed](#) [Google Scholar](#)

17. 17.

Jayne, D. R. W. et al. Randomized trial of C5a receptor inhibitor avacopan in ANCA-associated vasculitis. *J. Am. Soc. Nephrol.* **28**, 2756–2767 (2017).

[CAS](#) [Article](#) [PubMed](#) [PubMed Central](#) [Google Scholar](#)

18. 18.

Lee, H. et al. Human C5aR knock-in mice facilitate the production and assessment of anti-inflammatory monoclonal antibodies. *Nat. Biotechnol.* **24**, 1279–1284 (2006).

[CAS](#) [Article](#) [PubMed](#) [Google Scholar](#)

19. 19.

Diurno, F. et al. Eculizumab treatment in patients with COVID-19: preliminary results from real life ASL Napoli 2 Nord experience. *Eur. Rev. Med. Pharmacol. Sci.* **24**, 4040–4047 (2020).

[CAS](#) [PubMed](#) [Google Scholar](#)

20. 20.

Gerard, N. P. et al. An anti-inflammatory function for the complement anaphylatoxin C5a-binding protein, C5L2. *J. Biol. Chem.* **280**, 39677–39680 (2005).

[CAS](#) [Article](#) [PubMed](#) [Google Scholar](#)

21. 21.

Bjornson, A. B., Mellencamp, M. A. & Schiff, G. M. Complement is activated in the upper respiratory tract during influenza virus infection. *Am. Rev. Respir. Dis.* **143**, 1062–1066 (1991).

[CAS](#) [Article](#) [PubMed](#) [Google Scholar](#)

22. 22.

Trujillo, G. et al. Cofactor regulation of C5a chemotactic activity in physiological fluids. Requirement for the vitamin D binding protein, thrombospondin-1 and its receptors. *Mol. Immunol.* **49**, 495–503 (2011).

[CAS](#) [Article](#) [PubMed](#) [PubMed Central](#) [Google Scholar](#)

23. 23.

Jiang, Y. et al. Blockade of the C5a–C5aR axis alleviates lung damage in hDPP4-transgenic mice infected with MERS-CoV. *Emerg. Microbes Infect.* **7**, 1–12 (2018).

[Google Scholar](#)

24. 24.

Sun, S. et al. Treatment with anti-C5a antibody improves the outcome of H7N9 virus infection in African green monkeys. *Clin. Infect. Dis.* **60**, 586–595 (2015).

[CAS](#) [Article](#) [PubMed](#) [Google Scholar](#)

25. 25.

Sun, S. et al. Inhibition of complement activation alleviates acute lung injury induced by highly pathogenic avian influenza H5N1 virus infection. *Am. J. Respir. Cell Mol. Biol.* **49**, 221–230 (2013).

[CAS Article](#) [PubMed](#) [Google Scholar](#)

26. 26.

Ramlall, V. et al. Immune complement and coagulation dysfunction in adverse outcomes of SARS-CoV-2 infection. *Nat. Med.* <https://doi.org/10.1038/s41591-020-1021-2> (2020).

27. 27.

Foley, J. H. Examining coagulation-complement crosstalk: complement activation and thrombosis. *Thromb. Res.* **141**, S50–S54 (2016).

[CAS Article](#) [PubMed](#) [Google Scholar](#)

28. 28.

Thomson, T. M., Toscano, E., Casis, E. & Paciucci, R. C1 esterase inhibitor and the contact system in COVID-19. *Br J. Haematol.* **190**, 520–524 (2020).

[CAS Article](#) [Google Scholar](#)

29. 29.

Magro, C. et al. Complement associated microvascular injury and thrombosis in the pathogenesis of severe COVID-19 infection: a report of five cases. *Transl. Res.* **220**, 1–13 (2020).

[CAS Article](#) [PubMed](#) [PubMed Central](#) [Google Scholar](#)

30. 30.

Cugno, M. et al. Complement activation in patients with COVID-19: a novel therapeutic target. *J. Allergy Clin. Immunol.* **146**, 215–217 (2020).

[CAS Article](#) [PubMed](#) [PubMed Central](#) [Google Scholar](#)

31. 31.

Ai, T. et al. Correlation of chest CT and RT-PCR testing for coronavirus disease 2019 (COVID-19) in China: a report of 1014 cases. *Radiology* **296**, E32–E40 (2020).

[Article](#) [PubMed](#) [Google Scholar](#)

32. 32.

Amrane, S. et al. Rapid viral diagnosis and ambulatory management of suspected COVID-19 cases presenting at the infectious diseases referral hospital in Marseille, France, - January 31st to March 1st, 2020: a respiratory virus snapshot. *Travel Med. Infect. Dis.* <https://doi.org/10.1016/j.tmaid.2020.101632> (2020).

33. 33.

Nurtop, E. et al. Combination of ELISA screening and seroneutralisation tests to expedite Zika virus seroprevalence studies. *Virol. J.* **15**, 192 (2018).

[CAS](#) [Article](#) [PubMed](#) [PubMed Central](#) [Google Scholar](#)

34. 34.

Xiong, Y. et al. Transcriptomic characteristics of bronchoalveolar lavage fluid and peripheral blood mononuclear cells in COVID-19 patients. *Emerg. Microbes Infect.* **9**, 761–770 (2020).

[CAS](#) [Article](#) [PubMed](#) [PubMed Central](#) [Google Scholar](#)

35. 35.

Dobin, A. et al. STAR: ultrafast universal RNA-seq aligner. *Bioinformatics* **29**, 15–21 (2013).

[CAS](#) [Article](#) [PubMed](#) [PubMed Central](#) [Google Scholar](#)

36. 36.

Liao, Y., Smyth, G. K. & Shi, W. featureCounts: an efficient general purpose program for assigning sequence reads to genomic features. *Bioinformatics* **30**, 923–930 (2014).

[CAS](#) [Article](#) [PubMed](#) [PubMed Central](#) [Google Scholar](#)

37. 37.

Johnson, W. E., Li, C. & Rabinovic, A. Adjusting batch effects in microarray expression data using empirical Bayes methods. *Biostatistics* **8**, 118–127 (2007).

[Article](#) [PubMed](#) [Google Scholar](#)

38. 38.

Love, M. I., Huber, W. & Anders, S. Moderated estimation of fold change and dispersion for RNA-seq data with DESeq2. *Genome Biol.* **15**, 550 (2014).

[Article](#) [PubMed](#) [PubMed Central](#) [Google Scholar](#)

39. 39.

Korsunsky, I. et al. Fast, sensitive and accurate integration of single-cell data with Harmony. *Nat. Methods* **16**, 1289–1296 (2019).

[CAS](#) [Article](#) [PubMed](#) [PubMed Central](#) [Google Scholar](#)

[Download references](#)

Acknowledgements

We thank all of the healthcare workers involved in the analysis, diagnosis and treatment of patients at AP-HM and Hôpital Laveran, especially Elise Kaspi, Eric Garnotel, Corinne Surcouf, Francois Xavier Le Flem (Bataillon des Marins Pompiers Marseille). We thank all our patients, supporters and families for their confidence in our work. The E.V. laboratory at CIML and Assistance-Publique des Hôpitaux de Marseille is supported by funding from the European Research Council (ERC) under the European Union's Horizon 2020 research and innovation program (TILC, grant agreement number 694502 and MInfla-TILC, grant agreement number 875102 - MInfla-Tilc), the *Agence Nationale de la Recherche* including the PIONEER Project (ANR-17-RHUS-0007), MSDAvenir, Innate Pharma and institutional grants awarded to the CIML (INSERM, CNRS, and Aix-Marseille University) and Marseille Immunopole.

Author information

Author notes

1. These authors contributed equally: Julien Carvelli, Olivier Demaria, Frédéric Vély

Affiliations

1. Assistance Publique des Hôpitaux de Marseille, Hôpital de la Timone, Réanimation des Urgences, Marseilles, France

Julien Carvelli & Marc Gainnier

2. Aix Marseille Université, Marseilles, France

Julien Carvelli, Christophe Guervilly, Pierre Simeone & Marc Gainnier

3. Innate Pharma, Marseilles, France

Olivier Demaria, Luciana Batista, Joanna Fares, Sabrina Carpentier, Marie-Laure Thibult, Ariane Morel, Romain Remark, Pascale André, Agnès Represa, Laura Assante Miranda, William Baron, Nourhène Belaid, Clarisse Caillet, Flavien Caraguel, Barbara Carrette, Florent Carrette, Fabien Chanuc, Rachel Courtois, Aurore Fenis, Marilyn Giordano, Mathilde Girard-Madoux, Marc Giraudon-Paoli, Nicolas Gourdin, Gwendoline Grondin, Franceline Guillot, Guillaume Habif, Solène Jaubert, Julie Lopez, Mélanie Le Van, Naouel Lovera, Marine Mansuy, Elodie Bonnet, Audrey Sansaloni, Annick Reboul, Emmanuel Mitry, Camille Nekkar-Constant, Valentine Péri, Paul Ricaut, Léa Simon, Jean-Baptiste Vallier, Marie Vétizou, Robert Zerbib, Yannis Morel & Eric Vivier

4. Aix Marseille Université, CNRS, INSERM, CIML, Marseilles, France

Frédéric Vély, Christelle Piperoglou, Sophie Ugolini, Marion Etiennot, Justine Galluso, Mikael Ebbo, Nicolas Schleinitz & Eric Vivier

5. Assistance Publique des Hôpitaux de Marseille, Hôpital de la Timone, Immunology, Marseille Immunopole, Marseilles, France

Frédéric Vély, Christelle Piperoglou & Eric Vivier

6. Hôpital d'Instruction des Armées Laveran, Marseilles, France

Nassima Chouaki Benmansour, Jean-Paul Boudsocq, Axelle Clerc, Emmanuel Delmond, Pierre-Olivier Vidal, Hélène Savini, Pierre Yves Cordier & Erwan Le Dault

7. Assistance Publique des Hôpitaux de Marseille, Marseilles, France

Nassima Chouaki Benmansour, Luc Lyonnet, Jean-Marie Forel, Laurent Papazian, Lionel Velly, Baptiste André, Antoine Briantais, Benoit Faucher, Estelle Jean, Julie Seguier, Véronique Veit, Jean-Robert Harlé, Boris Pastorino, Clémence Delteil & Laurent Daniel

8. Assistance Publique des Hôpitaux de Marseille, Hôpital Nord,
Réanimation des Détresses Respiratoires et Infections Sévères, Aix-Marseille Université, Marseilles, France

Christophe Guervilly

9. Assistance Publique des Hôpitaux de Marseille, Hôpital de la Timone,
Réanimation Polyvalente, Aix-Marseille Université, Marseilles, France

Pierre Simeone

10. Assistance Publique des Hôpitaux de Marseille, Hôpital de la Timone,
Internal Medicine, Marseilles, France

Mikael Ebbo & Nicolas Schleinitz

11. Unité des Virus Émergents (UVE), Aix-Marseille Université, IRD 190,
Inserm 1207, IHU Méditerranée Infection, Marseilles, France

Bruno Coutard

Authors

1. Julien Carvelli

[View author publications](#)

You can also search for this author in [PubMed](#) [Google Scholar](#)

2. Olivier Demaria

[View author publications](#)

You can also search for this author in [PubMed](#) [Google Scholar](#)

3. Frédéric Vély

[View author publications](#)

You can also search for this author in [PubMed](#) [Google Scholar](#)

4. Luciana Batista

[View author publications](#)

You can also search for this author in [PubMed](#) [Google Scholar](#)

5. Nassima Chouaki Benmansour

[View author publications](#)

You can also search for this author in [PubMed](#) [Google Scholar](#)

6. Joanna Fares

[View author publications](#)

You can also search for this author in [PubMed](#) [Google Scholar](#)

7. Sabrina Carpentier

[View author publications](#)

You can also search for this author in [PubMed](#) [Google Scholar](#)

8. Marie-Laure Thibult

[View author publications](#)

You can also search for this author in [PubMed](#) [Google Scholar](#)

9. Ariane Morel

[View author publications](#)

You can also search for this author in [PubMed](#) [Google Scholar](#)

10. Romain Remark

[View author publications](#)

You can also search for this author in [PubMed](#) [Google Scholar](#)

11. Pascale André

[View author publications](#)

You can also search for this author in [PubMed](#) [Google Scholar](#)

12. Agnès Represa

[View author publications](#)

You can also search for this author in [PubMed](#) [Google Scholar](#)

13. Christelle Piperoglou

[View author publications](#)

You can also search for this author in [PubMed](#) [Google Scholar](#)

14. Pierre Yves Cordier

[View author publications](#)

You can also search for this author in [PubMed](#) [Google Scholar](#)

15. Erwan Le Dault

[View author publications](#)

You can also search for this author in [PubMed](#) [Google Scholar](#)

16. Christophe Guervilly

[View author publications](#)

You can also search for this author in [PubMed](#) [Google Scholar](#)

17. Pierre Simeone

[View author publications](#)

You can also search for this author in [PubMed](#) [Google Scholar](#)

18. Marc Gainnier

[View author publications](#)

You can also search for this author in [PubMed](#) [Google Scholar](#)

19. Yannis Morel

[View author publications](#)

You can also search for this author in [PubMed](#) [Google Scholar](#)

20. Mikael Ebbo

[View author publications](#)

You can also search for this author in [PubMed](#) [Google Scholar](#)

21. Nicolas Schleinitz

[View author publications](#)

You can also search for this author in [PubMed](#) [Google Scholar](#)

22. Eric Vivier

[View author publications](#)

You can also search for this author in [PubMed](#) [Google Scholar](#)

Consortia

the Explore COVID-19 IPH group

- Laura Assante Miranda
- , William Baron
- , Nourhène Belaid
- , Clarisse Caillet
- , Flavien Caraguel
- , Barbara Carrette
- , Florent Carrette
- , Fabien Chanuc
- , Rachel Courtois
- , Aurore Fenis
- , Marilyn Giordano
- , Mathilde Girard-Madoux
- , Marc Giraudon-Paoli
- , Nicolas Gourdin
- , Gwendoline Grondin
- , Franceline Guillot
- , Guillaume Habif
- , Solène Jaubert

- , Julie Lopez
- , Mélanie Le Van
- , Naouel Lovera
- , Marine Mansuy
- , Elodie Bonnet
- , Audrey Sansaloni
- , Annick Reboul
- , Emmanuel Mitry
- , Camille Nekkar-Constant
- , Valentine Péri
- , Paul Ricaut
- , Léa Simon
- , Jean-Baptiste Vallier
- , Marie Vétizou
- & Robert Zerbib

the Explore COVID-19 Marseille Immunopole group

- Sophie Ugolini
- , Marion Etiennot
- , Justine Galluso
- , Luc Lyonnet
- , Jean-Marie Forel
- , Laurent Papazian
- , Lionel Velly
- , Baptiste André
- , Antoine Briantais
- , Benoit Faucher
- , Estelle Jean
- , Julie Seguier
- , Veronique Veit
- , Jean-Robert Harlé
- , Boris Pastorino
- , Clémence Delteil
- , Laurent Daniel
- , Jean-Paul Boudsocq
- , Axelle Clerc

- , Emmanuel Delmond
- , Pierre-Olivier Vidal
- , Hélène Savini
- & Bruno Coutard

Contributions

J.C., F.V. and E.V. initiated and designed the research. O.D. and E.V. wrote the manuscript with the help of other co-authors. O.D., F.V., L.B., J.F., S.C., M.-L.T., A.M., R.R., P.A., A. Represa, C.P., L.A.M., W.B., N.B., C.C., F. Caraguel, B. Carrette, F. Carrette, F. Chanuc, R.C., A.F., M. Giordano, M.G.-M., M.G.-P., N.G., G.G., F.G., G.H., S.J., J.L., M.L.V., N.L., M.M., E.B., A.S., A. Reboul, E.M., C.N.-C., V.P., P.R., L.S., J.-B.V., M.V., Y.M., R.Z., L.L., J.G., M. Etiennot, S.U., B.P., B. Coutard, C.D. and L.D. performed the experiments and analysed and/or interpreted results. J.C., N.C.B., P.Y.C., E.L.D., C.G., P.S., M. Gainnier, M. Ebbo, N.S., J.-M.F., L.P., L.V., B.A., A.B., B.F., E.J., J.S., V.V., J.-R.H., B.P., C.D., L.D., J.-P.B., A.C., E.D., P.-O.V. and H.S. were in charge of patient care and contributed to the discussion of the results. L.B., N.C.B., J.F., S.C., M.-L.T. and A.M. contributed equally.

Corresponding author

Correspondence to [Eric Vivier](#).

Ethics declarations

Competing interests

O.D., L.B., J.F., S.C., M.-L.T., A.M., R.R., P.A., A.Represa, L.A.M., W.B., N.B., C.C., F. Caraguel, B.Carrette, F.Carrette, F.Chanuc, R.C., A.F., M.Giordano, M.G.-M., M.G.-P., N.G., G.G., F.G., G.H., S.J., J.L., M.L.V., N.L., M.M., E.B., A.S., A.Reboul, E.M., C.N.-C., V.P., P.R., L.S., J.-B.V., M.V., R.Z., Y.M. and E.V. are employees of Innate Pharma. The other authors declare no competing interests.

Additional information

Peer review information *Nature* thanks Bart Lambrecht and the other, anonymous, reviewer(s) for their contribution to the peer review of this work.

Publisher's note Springer Nature remains neutral with regard to jurisdictional claims in published maps and institutional affiliations.

Extended data figures and tables

[Extended Data Fig. 1 Immune activation in patients with COVID-19.](#)

a, Number of patients for each level of disease severity, classified according to SARS-CoV-2 seroneutralizing status. Biological samples were collected at t_0 (<72 h after the start of hospital care) and t_1 (between days 5 and 10).

b, Concentration of C5a desArg in plasma from patients with pneumonia (left; green) or ARDS (right; red) followed over time. t_0 , <72 h after the beginning of hospital care; t_1 , between days 5 and 10; t_2 , after day 10. P values for the comparison of t_1 ($n = 19$) and t_0 ($n = 34$) in the pneumonia group were obtained using two-tailed Wilcoxon signed-rank tests (not significant). No statistical tests were performed for t_2 ($n = 4$). For the ARDS group, a mixed model was computed with time point (categorical variable) as a fixed effect and patient as a random effect. $n = 28$ for t_0 , $n = 23$ for t_1 and $n = 18$ for t_2 . Confidence intervals and P values are based on the t -distribution, with degrees of freedom according to the Kenward–Roger method (not significant). Each symbol represents a single donor. **c**, Left, Heat map of genes that are differentially expressed (log-transformed fold change >2 and false-discovery rate $<5\%$) between PBMC samples from healthy control individuals and patients with COVID-19. Right, Heat map of monocyte and macrophage metagene expression in lung samples from healthy control individuals and patients with COVID-19. **d**, Three lung samples from patients who are deceased were obtained and were suitable for IHC analysis. Left, H&E staining of obliterating endarteritis lesions in

the lungs of a representative patient with COVID-19. Right, C5b9 IHC staining on lung sections of a representative patient with COVID-19, demonstrating complement pathway activation in the lung. Scale bars, 50 μ m.

Extended Data Fig. 2 C5aR1 expression remained stable on myeloid cells during the course of COVID-19.

The percentage of C5aR1-expressing neutrophils and monocytes in patients with pneumonia (green) and ARDS (red) followed over time. t_0 , <72 h after the start of hospital care; t_1 , between days 5 and 10; t_2 , after day 10. For the pneumonia group, $n = 34$ for t_0 , $n = 18$ (neutrophils) and 21 (monocytes) for t_1 and $n = 3$ for t_2 . For the ARDS group, $n = 28$ for t_0 , $n = 23$ for t_1 and $n = 22$ for t_2 . Each symbol represents a single donor.

Extended Data Fig. 3 Myeloid cell analysis in patients with COVID-19.

a, b, Integration of transcriptomic single-cell data with Harmony. **a**, UMAP projection of donors before integration. **b**, UMAP projection of major cell types and associated clusters after integration by Harmony. mDC, myeloid dendritic cells. **c**, Representative multiplexed IHC staining of C5aR (green), CD68 (red) and CD163 (orange) on lung sections from a control individual or patients with COVID-19 among three samples from patients with COVID-19 who are deceased and for whom tissue was available for IHC analyses. Scale bars, 100 μ m. Quantifications show the cell density per mm² of multiplexed IHC staining of C5aR1, CD68 and CD163. **d**, Three samples from patients who are deceased were obtained and were suitable for IHC analysis. Endoarteritis lesions were observed in two out of three patients, consistent with previous reports. The patient without endoarteritis lesions did not die from COVID-19. Left, representative H&E staining of obliterating endarteritis lesions in the lungs of patients with COVID-19. Right, representative multiplexed IHC staining of C5aR1 (green), CD68 (red) and CD163 (orange) showing that obliterating endarteritis was

frequently associated with C5aR1⁺ macrophages surrounding the arteries and in the thrombus (white dotted line). Scale bars, 100 µm.

Extended Data Fig. 4 Targeting C5aR1 to block C5a-mediated activation of myeloid cells.

a, Analysis of the efficacy of increasing doses of avdoralimab (purple), an anti-C5a monoclonal antibody (orange), a C5aR1 antagonist (avacopan, black) or isotype control (grey) to block C5a-induced upregulation of CD11b on human neutrophils. Each line represents the mean ± s.d. of the median fluorescence index from a single donor from experimental duplicates (isotype control) or triplicates (inhibitors). **b**, Comparative expression of mouse C5aR1 (moC5aR1) and human C5aR1 (huC5aR1) on CD11b⁻ non-myeloid cells, CD11b⁺ myeloid cells, including Ly6C⁺Ly6G⁺ neutrophils and Ly6C⁺Ly6G⁻ monocytes, from wild-type (blue) and HsC5AR1 knock-in (red) mice. **c**, H&E staining of lungs from HsC5AR1 knock-in mice treated intranasally with *HsC5a*. Mice were pretreated with avdralimab (avdo) or isotype control (IC), where indicated. Scale bar, 100 µm. Images are representative of two independent experiments. **d**, A model of C5a involvement in COVID-19: SARS-CoV-2 infects the human airway epithelium through the ACE2 receptors that are located predominantly on type-II pneumocytes. Left, in non-severe COVID-19, the infection remains confined to the epithelium (epithelial disease), because of the efficient action of the immune system. C5a enables the recruitment of myeloid cells without triggering an inflammatory storm and the virus is eliminated. Right, in severe COVID-19, SARS-CoV-2 escapes the immune system, crosses the epithelium and infect endothelial cells (endothelial disease). The myeloid cells recruited by C5a and endothelial cells release large amounts of inflammatory cytokines. COVID-19-related cytokine storm and endothelialitis-associated microthrombosis are triggered. The condition of the patient worsens and the virus can infect other organs.

Supplementary information

Supplementary Table 1

Clinical description of the COVID-19 cohort involved in the study.

Reporting Summary

Flow cytometry Gating Strategy

Rights and permissions

Reprints and Permissions

About this article



Check for
updates

Cite this article

Carvelli, J., Demaria, O., Vély, F. *et al.* Association of COVID-19 inflammation with activation of the C5a–C5aR1 axis. *Nature* **588**, 146–150 (2020). <https://doi.org/10.1038/s41586-020-2600-6>

Download citation

- Received: 29 April 2020
- Accepted: 23 July 2020
- Published: 29 July 2020
- Issue Date: 03 December 2020
- DOI: <https://doi.org/10.1038/s41586-020-2600-6>

Further reading

- [Increased Complement Receptor-3 levels in monocytes and granulocytes distinguish COVID-19 patients with pneumonia from those with mild symptoms](#)

- Rajeev Gupta
- , Vanya Alasdair Gant
- , Bryan Williams
- & Tariq Enver

International Journal of Infectious Diseases (2020)

- [Combining Antivirals and Immunomodulators to Fight COVID-19](#)

- Vincent Feuillet
- , Bruno Canard
- & Alain Trautmann

Trends in Immunology (2020)

- [The Complement C5a-C5aR1 GPCR Axis in COVID-19 Therapeutics](#)

- Trent M. Woodruff
- & Arun K. Shukla

Trends in Immunology (2020)

- [Biomimetic Nanoparticles Potentiate the Anti-Inflammatory Properties of Dexamethasone and Reduce the Cytokine Storm Syndrome: An Additional Weapon against COVID-19?](#)

- Roberto Molinaro
- , Anna Pasto
- , Francesca Taraballi

- , Federica Giordano
- , Jamil A. Azzi
- , Ennio Tasciotti
- & Claudia Corbo

Nanomaterials (2020)

- **Temporal changes in complement activation in haemodialysis patients with COVID-19 as a predictor of disease progression**

- Maria Prendecki
- , Candice Clarke
- , Nicholas Medjeral-Thomas
- , Stephen P McAdoo
- , Eleanor Sandhu
- , James E Peters
- , David C Thomas
- , Michelle Willicombe
- , Marina Botto
- & Matthew C Pickering

Clinical Kidney Journal (2020)

Comments

By submitting a comment you agree to abide by our [Terms](#) and [Community Guidelines](#). If you find something abusive or that does not comply with our terms or guidelines please flag it as inappropriate.

[Download PDF](#)

This article was downloaded by **calibre** from <https://www.nature.com/articles/s41586-020-2600-6>

- Article
- [Published: 04 November 2020](#)

Inhibition of LT β R signalling activates WNT-induced regeneration in lung

- [Thomas M. Conlon](#) [ORCID: orcid.org/0000-0002-4316-6612](#)^{1 na1},
- [Gerrit John-Schuster](#)^{1 na1},
- [Danijela Heide](#)²,
- [Dominik Pfister](#) [ORCID: orcid.org/0000-0002-0542-2638](#)²,
- [Mareike Lehmann](#)³,
- [Yan Hu](#)⁴,
- [Zeynep Ertüz](#)¹,
- [Martin A. Lopez](#)⁵,
- [Meshal Ansari](#) [ORCID: orcid.org/0000-0002-8819-7965](#)^{1,6},
- [Maximilian Strunz](#)¹,
- [Christoph Mayr](#)¹,
- [Chiara Ciminieri](#)^{4,7},
- [Rita Costa](#) [ORCID: orcid.org/0000-0003-0710-3611](#)³,
- [Marlene Sophia Kohlhepp](#)⁸,
- [Adrien Guillot](#) [ORCID: orcid.org/0000-0002-6002-9986](#)⁸,
- [Gizem Günes](#)¹,
- [Aicha Jeridi](#)¹,
- [Maja C. Funk](#) [ORCID: orcid.org/0000-0002-6007-1164](#)⁹,
- [Giorgi Beroshvili](#) [ORCID: orcid.org/0000-0002-8038-1493](#)¹,
- [Sandra Prokosch](#)²,
- [Jenny Hetzer](#)²,
- [Stijn E. Verleden](#)¹⁰,
- [Hani Alsafadi](#) [ORCID: orcid.org/0000-0002-1186-2517](#)^{3,11},

- [Michael Lindner](#)^{12,13},
- [Gerald Burgstaller](#) [ORCID: orcid.org/0000-0002-7121-2567](#)¹,
- [Lore Becker](#)¹⁴,
- [Martin Irmler](#) [ORCID: orcid.org/0000-0003-3169-479X](#)¹⁴,
- [Michael Dudek](#)¹⁵,
- [Jakob Janzen](#)^{2,16},
- [Eric Goffin](#)¹⁷,
- [Reinoud Gosens](#) [ORCID: orcid.org/0000-0002-5595-152X](#)⁷,
- [Percy Knolle](#) [ORCID: orcid.org/0000-0003-2983-0414](#)¹⁵,
- [Bernard Pirotte](#) [ORCID: orcid.org/0000-0001-8251-8257](#)¹⁷,
- [Tobias Stoeger](#) [ORCID: orcid.org/0000-0002-2790-0389](#)¹,
- [Johannes Beckers](#)^{14,18,19},
- [Darcy Wagner](#) [ORCID: orcid.org/0000-0003-3794-1309](#)^{3,11},
- [Indrabahadur Singh](#)^{2,19},
- [Fabian J. Theis](#) [ORCID: orcid.org/0000-0002-2419-1943](#)⁶,
- [Martin Hrabé de Angelis](#) [ORCID: orcid.org/0000-0002-7898-2353](#)^{14,17,18},
- [Tracy O'Connor](#)²,
- [Frank Tacke](#)⁸,
- [Michael Boutros](#)^{9,20},
- [Emmanuel Dejardin](#)⁵,
- [Oliver Eickelberg](#)⁴,
- [Herbert B. Schiller](#) [ORCID: orcid.org/0000-0001-9498-7034](#)¹,
- [Melanie Königshoff](#) [ORCID: orcid.org/0000-0001-9414-5128](#)^{3,4},
- [Mathias Heikenwalder](#) [ORCID: orcid.org/0000-0002-3135-2274](#)^{2 na2} &
- [Ali Önder Yildirim](#) [ORCID: orcid.org/0000-0003-1969-480X](#)^{1 na2}

[Nature](#) volume 588, pages 151–156 (2020) [Cite this article](#)

- 4998 Accesses
- 132 Altmetric
- [Metrics details](#)

Subjects

- [Cellular immunity](#)
- [Respiratory tract diseases](#)

Abstract

Lymphotoxin β -receptor (LT β R) signalling promotes lymphoid neogenesis and the development of tertiary lymphoid structures^{1,2}, which are associated with severe chronic inflammatory diseases that span several organ systems^{3,4,5,6}. How LT β R signalling drives chronic tissue damage particularly in the lung, the mechanism(s) that regulate this process, and whether LT β R blockade might be of therapeutic value have remained unclear. Here we demonstrate increased expression of LT β R ligands in adaptive and innate immune cells, enhanced non-canonical NF- κ B signalling, and enriched LT β R target gene expression in lung epithelial cells from patients with smoking-associated chronic obstructive pulmonary disease (COPD) and from mice chronically exposed to cigarette smoke. Therapeutic inhibition of LT β R signalling in young and aged mice disrupted smoking-related inducible bronchus-associated lymphoid tissue, induced regeneration of lung tissue, and reverted airway fibrosis and systemic muscle wasting. Mechanistically, blockade of LT β R signalling dampened epithelial non-canonical activation of NF- κ B, reduced TGF β signalling in airways, and induced regeneration by preventing epithelial cell death and activating WNT/ β -catenin signalling in alveolar epithelial progenitor cells. These findings suggest that inhibition of LT β R signalling represents a viable therapeutic option that combines prevention of tertiary lymphoid structures¹ and inhibition of apoptosis with tissue-regenerative strategies.

[Access through your institution](#)

[Change institution](#)

[Buy or subscribe](#)

Access options

Subscribe to Journal

Get full journal access for 1 year

185,98 €

only 3,58 € per issue

[Subscribe](#)

All prices are NET prices.

VAT will be added later in the checkout.

Rent or Buy article

Get time limited or full article access on ReadCube.

from \$8.99

[Rent or Buy](#)

All prices are NET prices.

Additional access options:

- [Log in](#)
- [Access through your institution](#)
- [Learn about institutional subscriptions](#)

Fig. 1: LT β R-signalling is activated in COPD and inhibition disrupts iBALT in the lungs of mice exposed to cigarette smoke.



Fig. 2: LT β R-Ig reverses emphysema in young and aged mice chronically exposed to cigarette smoke.



Fig. 3: Blocking LT β R induces WNT/ β -catenin signalling in alveolar epithelial cells.

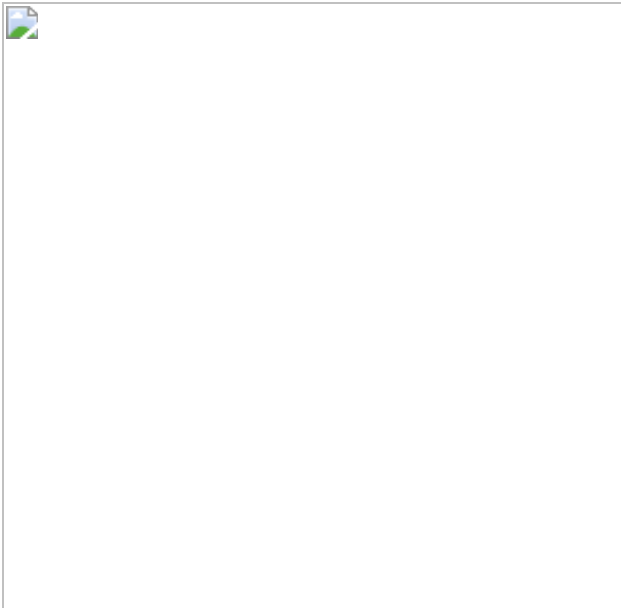
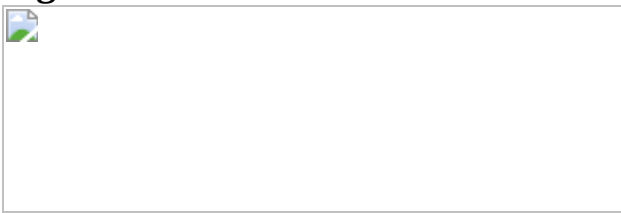


Fig. 4: Blocking WNT/β-catenin signalling reverses LTβR–Ig-induced regeneration.



Data availability

Microarray data were submitted to the NCBI Gene Expression Omnibus (GEO) database (<https://www.ncbi.nlm.nih.gov/geo/>) accession number [GSE125521](#). scRNA-seq data were submitted to the NCBI GEO database accession number [GSE151674](#). scRNA-seq metadata can be found in Supplementary Table 4. Proteomics data can be found in Supplementary Table 5. Series matrix files were also downloaded from the NCBI GEO databases: GSE47460–GPL14550, GSE37768, GSE56768 and GSE52509. Proteomic peak lists were searched against the mouse Uniprot FASTA database (version November 2016) <https://www.uniprot.org/proteomes/UP000000589>. All other data supporting the findings of this study are available within the Article and Supplementary Information. All data are available from the corresponding authors upon reasonable request. [Source data](#) are provided with this paper.

Code availability

All code used for data visualization of the scRNA-seq data can be found at https://github.com/theislab/2020_Inhibition_LTbetaR-signalling.

References

1. 1.

Kratz, A., Campos-Neto, A., Hanson, M. S. & Ruddle, N. H. Chronic inflammation caused by lymphotoxin is lymphoid neogenesis. *J. Exp. Med.* **183**, 1461–1472 (1996).

[CAS](#) [Google Scholar](#)

2. 2.

Drayton, D. L., Liao, S., Mounzer, R. H. & Ruddle, N. H. Lymphoid organ development: from ontogeny to neogenesis. *Nat. Immunol.* **7**, 344–353 (2006).

[CAS](#) [Google Scholar](#)

3. 3.

Hogg, J. C. et al. The nature of small-airway obstruction in chronic obstructive pulmonary disease. *N. Engl. J. Med.* **350**, 2645–2653 (2004).

[CAS](#) [Google Scholar](#)

4. 4.

Galkina, E. & Ley, K. Immune and inflammatory mechanisms of atherosclerosis*. *Annu. Rev. Immunol.* **27**, 165–197 (2009).

[CAS](#) [PubMed](#) [PubMed Central](#) [Google Scholar](#)

5. 5.

Pitzalis, C., Jones, G. W., Bombardieri, M. & Jones, S. A. Ectopic lymphoid-like structures in infection, cancer and autoimmunity. *Nat. Rev. Immunol.* **14**, 447–462 (2014).

[CAS](#) [Google Scholar](#)

6. 6.

Senda, T. et al. Microanatomical dissection of human intestinal T-cell immunity reveals site-specific changes in gut-associated lymphoid tissues over life. *Mucosal Immunol.* **12**, 378–389 (2019).

[CAS](#) [Google Scholar](#)

7. 7.

Lozano, R. et al. Global and regional mortality from 235 causes of death for 20 age groups in 1990 and 2010: a systematic analysis for the Global Burden of Disease Study 2010. *Lancet* **380**, 2095–2128 (2012).

[Google Scholar](#)

8. 8.

Vogelmeier, C. F. et al. Global Strategy for the Diagnosis, Management, and Prevention of Chronic Obstructive Lung Disease 2017 Report. GOLD Executive Summary. *Am. J. Respir. Crit. Care Med.* **195**, 557–582 (2017).

[CAS](#) [Google Scholar](#)

9. 9.

Baarsma, H. A. & Königshoff, M. ‘WNT-er is coming’: WNT signalling in chronic lung diseases. *Thorax* **72**, 746–759 (2017).

[CAS](#) [PubMed](#) [PubMed Central](#) [Google Scholar](#)

10. 10.

Polverino, F. et al. B cell-activating factor. An orchestrator of lymphoid follicles in severe chronic obstructive pulmonary disease. *Am. J. Respir. Crit. Care Med.* **192**, 695–705 (2015).

[CAS](#) [PubMed](#) [PubMed Central](#) [Google Scholar](#)

11. 11.

Faner, R. et al. Network analysis of lung transcriptomics reveals a distinct B-cell signature in emphysema. *Am. J. Respir. Crit. Care Med.* **193**, 1242–1253 (2016).

[CAS](#) [Google Scholar](#)

12. 12.

Sullivan, J. L. et al. B cell adaptive immune profile in emphysema-predominant COPD. *Am. J. Respir. Crit. Care Med.* **200**, 1434–1439 (2019).

13. 13.

Bracke, K. R. et al. Role of CXCL13 in cigarette smoke-induced lymphoid follicle formation and chronic obstructive pulmonary disease. *Am. J. Respir. Crit. Care Med.* **188**, 343–355 (2013).

[CAS](#) [Google Scholar](#)

14. 14.

Jia, J. et al. Cholesterol metabolism promotes B-cell positioning during immune pathogenesis of chronic obstructive pulmonary disease. *EMBO Mol. Med.* **10**, e8349 (2018).

[PubMed](#) [PubMed Central](#) [Google Scholar](#)

15. 15.

Wolf, M. J., Selezniak, G. M., Zeller, N. & Heikenwalder, M. The unexpected role of lymphotoxin beta receptor signaling in carcinogenesis: from lymphoid tissue formation to liver and prostate cancer development. *Oncogene* **29**, 5006–5018 (2010).

[CAS](#) [Google Scholar](#)

16. 16.

Finkin, S. et al. Ectopic lymphoid structures function as microniches for tumor progenitor cells in hepatocellular carcinoma. *Nat. Immunol.* **16**, 1235–1244 (2015).

[CAS](#) [PubMed](#) [PubMed Central](#) [Google Scholar](#)

17. 17.

Xiao, G., Harhaj, E. W. & Sun, S. C. NF-κB-inducing kinase regulates the processing of NF-κB2 p100. *Mol. Cell* **7**, 401–409 (2001).

[CAS](#) [Google Scholar](#)

18. 18.

Dejardin, E. et al. The lymphotoxin-β receptor induces different patterns of gene expression via two NF-κB pathways. *Immunity* **17**, 525–535 (2002).

[CAS](#) [Google Scholar](#)

19. 19.

Fava, R. A. et al. A role for the lymphotoxin/LIGHT axis in the pathogenesis of murine collagen-induced arthritis. *J. Immunol.* **171**, 115–126 (2003).

[CAS](#) [Google Scholar](#)

20. 20.

Haybaeck, J. et al. A lymphotoxin-driven pathway to hepatocellular carcinoma. *Cancer Cell* **16**, 295–308 (2009).

[CAS](#) [PubMed](#) [PubMed Central](#) [Google Scholar](#)

21. 21.

Uhl, F. E. et al. Preclinical validation and imaging of Wnt-induced repair in human 3D lung tissue cultures. *Eur. Respir. J.* **46**, 1150–1166 (2015).

[CAS](#) [Google Scholar](#)

22. 22.

Alsafadi, H. N. et al. Applications and approaches for 3D precision-cut lung slices: disease modeling and drug discovery. *Am. J. Respir. Cell Mol. Biol.* **62**, 681–691 (2020).

23. 23.

Verhamme, F. M., Bracke, K. R., Joos, G. F. & Brusselle, G. G. Transforming growth factor- β superfamily in obstructive lung diseases. more suspects than TGF- β alone. *Am. J. Respir. Cell Mol. Biol.* **52**, 653–662 (2015).

[CAS](#) [Google Scholar](#)

24. 24.

Rabe, K. F. & Watz, H. Chronic obstructive pulmonary disease. *Lancet* **389**, 1931–1940 (2017).

[Google Scholar](#)

25. 25.

Sandri, M. et al. PGC-1 α protects skeletal muscle from atrophy by suppressing FoxO3 action and atrophy-specific gene transcription.

Proc. Natl Acad. Sci. USA **103**, 16260–16265 (2006).

[ADS](#) [CAS](#) [Google Scholar](#)

26. 26.

Lee, H. Y. et al. Targeted expression of catalase to mitochondria prevents age-associated reductions in mitochondrial function and insulin resistance. *Cell Metab.* **12**, 668–674 (2010).

[CAS](#) [PubMed](#) [PubMed Central](#) [Google Scholar](#)

27. 27.

John-Schuster, G. et al. Inflammaging increases susceptibility to cigarette smoke-induced COPD. *Oncotarget* **7**, 30068–30083 (2016).

[Google Scholar](#)

28. 28.

Boutaffala, L. et al. NIK promotes tissue destruction independently of the alternative NF-κB pathway through TNFR1/RIP1-induced apoptosis. *Cell Death Differ.* **22**, 2020–2033 (2015).

[CAS](#) [PubMed](#) [PubMed Central](#) [Google Scholar](#)

29. 29.

Nabhan, A. N., Brownfield, D. G., Harbury, P. B., Krasnow, M. A. & Desai, T. J. Single-cell Wnt signaling niches maintain stemness of alveolar type 2 cells. *Science* **359**, 1118–1123 (2018).

[ADS](#) [CAS](#) [PubMed](#) [PubMed Central](#) [Google Scholar](#)

30. 30.

Zacharias, W. J. et al. Regeneration of the lung alveolus by an evolutionarily conserved epithelial progenitor. *Nature* **555**, 251–255

(2018).

[ADS](#) [CAS](#) [PubMed](#) [PubMed Central](#) [Google Scholar](#)

31. 31.

Kneidinger, N. et al. Activation of the WNT/β-catenin pathway attenuates experimental emphysema. *Am. J. Respir. Crit. Care Med.* **183**, 723–733 (2011).

[CAS](#) [Google Scholar](#)

32. 32.

de Leon-Boenig, G. et al. The crystal structure of the catalytic domain of the NF-κB inducing kinase reveals a narrow but flexible active site. *Structure* **20**, 1704–1714 (2012).

[Google Scholar](#)

33. 33.

Tokunaga, Y. et al. Selective inhibitor of Wnt/β-catenin/CBP signaling ameliorates hepatitis C virus-induced liver fibrosis in mouse model. *Sci. Rep.* **7**, 325 (2017).

[ADS](#) [PubMed](#) [PubMed Central](#) [Google Scholar](#)

34. 34.

Ying, Q. L. et al. The ground state of embryonic stem cell self-renewal. *Nature* **453**, 519–523 (2008).

[ADS](#) [CAS](#) [PubMed](#) [PubMed Central](#) [Google Scholar](#)

35. 35.

Hu, Y. et al. Wnt/β-catenin signaling is critical for regenerative potential of distal lung epithelial progenitor cells in homeostasis and

emphysema. *Stem Cells* <https://doi.org/10.1002/stem.3241> (2020).

36. 36.

Baarsma, H. A. et al. Noncanonical WNT-5A signaling impairs endogenous lung repair in COPD. *J. Exp. Med.* **214**, 143–163 (2017).

[PubMed](#) [PubMed Central](#) [Google Scholar](#)

37. 37.

Barkauskas, C. E. et al. Type 2 alveolar cells are stem cells in adult lung. *J. Clin. Invest.* **123**, 3025–3036 (2013).

[CAS](#) [PubMed](#) [PubMed Central](#) [Google Scholar](#)

38. 38.

Ng-Blichfeldt, J. P. et al. Retinoic acid signaling balances adult distal lung epithelial progenitor cell growth and differentiation. *EBioMedicine* **36**, 461–474 (2018).

[PubMed](#) [PubMed Central](#) [Google Scholar](#)

39. 39.

John, G. et al. The composition of cigarette smoke determines inflammatory cell recruitment to the lung in COPD mouse models. *Clin. Sci. (Lond.)* **126**, 207–221 (2014).

[CAS](#) [Google Scholar](#)

40. 40.

Yildirim, A. O. et al. Palifermin induces alveolar maintenance programs in emphysematous mice. *Am. J. Respir. Crit. Care Med.* **181**, 705–717 (2010).

[CAS](#) [Google Scholar](#)

41. 41.

Fuchs, H. et al. Mouse phenotyping. *Methods* **53**, 120–135 (2011).

[CAS](#) [PubMed](#) [Google Scholar](#)

42. 42.

Fallica, J., Das, S., Horton, M. & Mitzner, W. Application of carbon monoxide diffusing capacity in the mouse lung. *J. Appl. Physiol.* **110**, 1455–1459 (2011).

[PubMed](#) [PubMed Central](#) [Google Scholar](#)

43. 43.

Strunz, M. et al. Longitudinal single cell transcriptomics reveals Krt8⁺ alveolar epithelial progenitors in lung regeneration. Preprint at <https://doi.org/10.1101/705244> (2019).

44. 44.

Angelidis, I. et al. An atlas of the aging lung mapped by single cell transcriptomics and deep tissue proteomics. *Nat. Commun.* **10**, 963 (2019).

[ADS](#) [PubMed](#) [PubMed Central](#) [Google Scholar](#)

45. 45.

Macosko, E. Z. et al. Highly parallel genome-wide expression profiling of individual cells using nanoliter droplets. *Cell* **161**, 1202–1214 (2015).

[CAS](#) [PubMed](#) [PubMed Central](#) [Google Scholar](#)

46. 46.

Hughes, T. K. et al. Highly efficient, massively-parallel single-cell RNA-seq reveals cellular states and molecular features of human skin pathology. Preprint at <https://doi.org/10.1101/689273> (2019).

47. 47.

Wolf, F. A., Angerer, P. & Theis, F. J. SCANPY: large-scale single-cell gene expression data analysis. *Genome Biol.* **19**, 15 (2018).

[PubMed](#) [PubMed Central](#) [Google Scholar](#)

48. 48.

Luecken, M. D. & Theis, F. J. Current best practices in single-cell RNA-seq analysis: a tutorial. *Mol. Syst. Biol.* **15**, e8746 (2019).

[PubMed](#) [PubMed Central](#) [Google Scholar](#)

49. 49.

Lun, A. T., McCarthy, D. J. & Marioni, J. C. A step-by-step workflow for low-level analysis of single-cell RNA-seq data with Bioconductor. *F1000Res.* **5**, 2122 (2016).

[PubMed](#) [PubMed Central](#) [Google Scholar](#)

50. 50.

Shevchenko, A., Tomas, H., Havlis, J., Olsen, J. V. & Mann, M. In-gel digestion for mass spectrometric characterization of proteins and proteomes. *Nat. Protoc.* **1**, 2856–2860 (2006).

[CAS](#) [Google Scholar](#)

51. 51.

Cox, J. & Mann, M. MaxQuant enables high peptide identification rates, individualized p.p.b.-range mass accuracies and proteome-wide protein quantification. *Nat. Biotechnol.* **26**, 1367–1372 (2008).

[CAS](#) [Google Scholar](#)

52. 52.

Schiller, H. B. et al. Deep proteome profiling reveals common prevalence of MZB1-positive plasma B cells in human lung and skin fibrosis. *Am. J. Respir. Crit. Care Med.* **196**, 1298–1310 (2017).

[CAS](#) [PubMed](#) [PubMed Central](#) [Google Scholar](#)

53. 53.

Tyanova, S. et al. The Perseus computational platform for comprehensive analysis of (prote)omics data. *Nat. Methods* **13**, 731–740 (2016).

[CAS](#) [Google Scholar](#)

54. 54.

Rainer, J., Sanchez-Cabo, F., Stocker, G., Sturn, A. & Trajanoski, Z. CARMAweb: comprehensive R- and bioconductor-based web service for microarray data analysis. *Nucleic Acids Res.* **34**, W498–W503(2006).

[CAS](#) [PubMed](#) [PubMed Central](#) [Google Scholar](#)

55. 55.

Malehmir, M. et al. Platelet GPIbQ α is a mediator and potential interventional target for NASH and subsequent liver cancer. *Nat. Med.* **25**, 641–655 (2019).

[CAS](#) [Google Scholar](#)

56. 56.

Wang, X., Spandidos, A., Wang, H. & Seed, B. PrimerBank: a PCR primer database for quantitative gene expression analysis, 2012

update. *Nucleic Acids Res.* **40**, D1144–D1149 (2012).

[CAS](#) [Google Scholar](#)

57. 57.

Gendusa, R., Scalia, C. R., Buscone, S. & Cattoretti, G. Elution of high-affinity (>10⁻⁹ KD) antibodies from tissue sections: clues to the molecular mechanism and use in sequential immunostaining. *J. Histochem. Cytochem.* **62**, 519–531 (2014).

[PubMed](#) [PubMed Central](#) [Google Scholar](#)

58. 58.

Schindelin, J. et al. Fiji: an open-source platform for biological-image analysis. *Nat. Methods* **9**, 676–682 (2012).

[CAS](#) [Google Scholar](#)

59. 59.

Berg, S. et al. ilastik: interactive machine learning for (bio)image analysis. *Nat. Methods* **16**, 1226–1232 (2019).

[CAS](#) [Google Scholar](#)

60. 60.

Wählby, C. et al. An image analysis toolbox for high-throughput *C. elegans* assays. *Nat. Methods* **9**, 714–716 (2012).

[PubMed](#) [PubMed Central](#) [Google Scholar](#)

61. 61.

John-Schuster, G. et al. Cigarette smoke-induced iBALT mediates macrophage activation in a B cell-dependent manner in COPD. *Am. J. Physiol. Lung Cell. Mol. Physiol.* **307**, L692–L706 (2014).

[CAS](#) [Google Scholar](#)

62. 62.

Jenkins, R. G. et al. An official american thoracic society workshop report: use of animal models for the preclinical assessment of potential therapies for pulmonary fibrosis. *Am. J. Respir. Cell Mol. Biol.* **56**, 667–679 (2017).

[CAS](#) [PubMed](#) [PubMed Central](#) [Google Scholar](#)

63. 63.

Corti, M., Brody, A. R. & Harrison, J. H. Isolation and primary culture of murine alveolar type II cells. *Am. J. Respir. Cell Mol. Biol.* **14**, 309–315 (1996).

[CAS](#) [Google Scholar](#)

64. 64.

Königshoff, M. et al. WNT1-inducible signaling protein-1 mediates pulmonary fibrosis in mice and is upregulated in humans with idiopathic pulmonary fibrosis. *J. Clin. Invest.* **119**, 772–787 (2009).

[PubMed](#) [PubMed Central](#) [Google Scholar](#)

65. 65.

Mutze, K., Vierkotten, S., Milosevic, J., Eickelberg, O. & Königshoff, M. Enolase 1 (ENO1) and protein disulfide-isomerase associated 3 (PDIA3) regulate Wnt/β-catenin-driven trans-differentiation of murine alveolar epithelial cells. *Dis. Model. Mech.* **8**, 877–890 (2015).

[CAS](#) [PubMed](#) [PubMed Central](#) [Google Scholar](#)

66. 66.

Lehmann, M. et al. Senolytic drugs target alveolar epithelial cell function and attenuate experimental lung fibrosis *ex vivo*. *Eur. Respir. J.* **50**, 1602367 (2017).

[PubMed](#) [PubMed Central](#) [Google Scholar](#)

67. 67.

Caporale, A., Tartaggia, S., Castellin, A. & De Lucchi, O. Practical synthesis of aryl-2-methyl-3-butyn-2-ols from aryl bromides via conventional and decarboxylative copper-free Sonogashira coupling reactions. *Beilstein J. Org. Chem.* **10**, 384–393 (2014).

[PubMed](#) [PubMed Central](#) [Google Scholar](#)

68. 68.

Veeman, M. T., Slusarski, D. C., Kaykas, A., Louie, S. H. & Moon, R. T. Zebrafish prickle, a modulator of noncanonical Wnt/Fz signaling, regulates gastrulation movements. *Curr. Biol.* **13**, 680–685 (2003).

[CAS](#) [Google Scholar](#)

69. 69.

Mootha, V. K. et al. PGC-1 α -responsive genes involved in oxidative phosphorylation are coordinately downregulated in human diabetes. *Nat. Genet.* **34**, 267–273 (2003).

[CAS](#) [PubMed](#) [Google Scholar](#)

70. 70.

Subramanian, A. et al. Gene set enrichment analysis: a knowledge-based approach for interpreting genome-wide expression profiles. *Proc. Natl Acad. Sci. USA* **102**, 15545–15550 (2005).

[ADS](#) [CAS](#) [PubMed](#) [Google Scholar](#)

71. 71.

Kim, S. et al. Integrative phenotyping framework (iPF): integrative clustering of multiple omics data identifies novel lung disease subphenotypes. *BMC Genomics* **16**, 924 (2015).

[PubMed](#) [PubMed Central](#) [Google Scholar](#)

[Download references](#)

Acknowledgements

The authors acknowledge the help of C. Hollauer, M. Pankla, R. Pineda, M. Neumann and K. Hafner. We gratefully acknowledge the provision of human biomaterial and clinical data from the CPC-M bioArchive and its partners at the Asklepios Biobank Gauting, the Klinikum der Universität München and the Ludwig-Maximilians-Universität München. We would like to thank all the members of the Theis laboratory for valuable input and discussion regarding the analysis of single cell RNA-seq data. We thank J. Browning for providing LT β R-Ig. We thank the Flowcytometry Core facility of the TranslaTUM, TUM Munich for technical support. We thank the Mass Spectrometry-based Protein Analysis Unit of the DKFZ, Heidelberg for technical support. We are most thankful to Z. Ertuz for the art work and M. Gerckens for the precision cut lung image. M.H. was supported by the Deutsche Forschungsgemeinschaft (DFG, German Research Foundation) Project ID 272983813-SFBTR 179, project ID 360372040-SFB 1335 and project ID 314905040 -SFBTR 209, the ERC CoG (HepatoMetabopath), the ERC POC (Faith), the Helmholtz Future topic Inflammation and Immunology, an EOS grant from the FNRS (MODEL-IDI 30826052), the Rainer Hoenig foundation and the Horizon 2020 program HEPCAR. D.P. was supported by the Helmholtz Future topic Inflammation and Immunology. M.K. was funded by grant R01HL141380. M.K., R.G. and C.C. by a grant from Longfonds, project no. 5.1.17.166. Y.H. was funded by grant F32HL149290-01. M.A.L. is a Marie-Curie COFUND postdoctoral fellow at the University of Liege co-funded by the European Union. E.D. is supported by an EOS grant from the FNRS (MODEL-IDI 30826052). This work was supported by the Helmholtz

Alliance ‘Aging and Metabolic Programming, AMPro’ (J.B., M.C.F., M.B.). Work in the laboratory of M.B. was supported by the SFB 1324. M.H.dA. was supported by the German Federal Ministry of Education and Research (Infrafrontier grant 01KX1012). H.B.S. is supported by grants from the German Center for Lung Research (DZL) and the Helmholtz Association.

Author information

Author notes

1. These authors contributed equally: Thomas M. Conlon, Gerrit John-Schuster
2. These authors jointly supervised this work: Mathias Heikenwalder, Ali Önder Yildirim

Affiliations

1. Comprehensive Pneumology Center (CPC), Institute of Lung Biology and Disease, Helmholtz Zentrum München, Member of the German Center for Lung Research (DZL), Neuherberg, Germany

Thomas M. Conlon, Gerrit John-Schuster, Zeynep Ertüz, Meshal Ansari, Maximilian Strunz, Christoph Mayr, Gizem Günes, Aicha Jeridi, Giorgi Beroshvili, Gerald Burgstaller, Tobias Stoeger, Herbert B. Schiller & Ali Önder Yildirim

2. German Cancer Research Center (DKFZ), Division of Chronic Inflammation and Cancer, Heidelberg, Germany

Danijela Heide, Dominik Pfister, Sandra Prokosch, Jenny Hetzer, Jakob Janzen, Indrabahadur Singh, Tracy O’Connor & Mathias Heikenwalder

3. Comprehensive Pneumology Center (CPC), Lung Repair and Regeneration Research Unit, Helmholtz Zentrum München, Member

of the German Center for Lung Research (DZL), Munich, Germany

Mareike Lehmann, Rita Costa, Hani Alsafadi, Darcy
Wagner & Melanie Königshoff

4. Division of Pulmonary Sciences and Critical Care Medicine,
University of Colorado, Denver, CO, USA

Yan Hu, Chiara Ciminieri, Oliver Eickelberg & Melanie Königshoff

5. Laboratory of Molecular Immunology and Signal Transduction,
GIGA-Institute, University of Liège, Liège, Belgium

Martin A. Lopez & Emmanuel Dejardin

6. Institute of Computational Biology (ICB), Helmholtz Zentrum
München, Neuherberg, Germany

Meshal Ansari & Fabian J. Theis

7. Department of Molecular Pharmacology, Groningen Research Institute
for Asthma and COPD (GRIAC), University of Groningen, Groningen,
The Netherlands

Chiara Ciminieri & Reinoud Gosens

8. Department of Hepatology & Gastroenterology, Charité University
Medicine Berlin, Berlin, Germany

Marlene Sophia Kohlhepp, Adrien Guillot & Frank Tacke

9. German Cancer Research Center (DKFZ), Division of Signaling and
Functional Genomics, Heidelberg, Germany

Maja C. Funk & Michael Boutros

10. Division of Pneumology, KU Leuven, Leuven, Belgium

Stijn E. Verleden

11. Lung Bioengineering and Regeneration, Department of Experimental Medical Sciences, Lund University, Lund, Sweden

Hani Alsafadi & Darcy Wagner

12. Asklepios Fachkliniken Munich-Gauting, Member of the German Center for Lung Research (DZL), Munich, Germany

Michael Lindner

13. Translational Lung Research and CPC-M bioArchive, Comprehensive Pneumology Center, Helmholtz Zentrum München, Member of the German Center for Lung Research (DZL), Munich, Germany

Michael Lindner

14. Institute of Experimental Genetics, German Mouse Clinic, Helmholtz Zentrum München, Neuherberg, Germany

Lore Becker, Martin Irmler, Johannes Beckers & Martin Hrabé de Angelis

15. Institute of Molecular Immunology & Experimental Oncology, Klinikum rechts der Isar, Technical University of Munich, Munich, Germany

Michael Dudek & Percy Knolle

16. Emmy Noether Research Group Epigenetic Machineries and Cancer, Division of Chronic Inflammation and Cancer, German Cancer Research Center (DKFZ), Heidelberg, Germany

Jakob Janzen

17. Laboratory of Medicinal Chemistry, Center for Interdisciplinary Research on Medicines (CIRM), University of Liège, Liège, Belgium

Eric Goffin, Bernard Pirotte & Martin Hrabé de Angelis

18. Experimental Genetics, Technische Universität München, Freising, Germany

Johannes Beckers & Martin Hrabé de Angelis

19. German Center for Diabetes Research (DZD), Neuherberg, Germany

Johannes Beckers & Indrabahadur Singh

20. Medical Faculty Mannheim & BioQuant, Heidelberg University, Heidelberg, Germany

Michael Boutros

Authors

1. Thomas M. Conlon

[View author publications](#)

You can also search for this author in [PubMed](#) [Google Scholar](#)

2. Gerrit John-Schuster

[View author publications](#)

You can also search for this author in [PubMed](#) [Google Scholar](#)

3. Danijela Heide

[View author publications](#)

You can also search for this author in [PubMed](#) [Google Scholar](#)

4. Dominik Pfister

[View author publications](#)

You can also search for this author in [PubMed](#) [Google Scholar](#)

5. Mareike Lehmann

[View author publications](#)

You can also search for this author in [PubMed](#) [Google Scholar](#)

6. Yan Hu

[View author publications](#)

You can also search for this author in [PubMed](#) [Google Scholar](#)

7. Zeynep Ertüz

[View author publications](#)

You can also search for this author in [PubMed](#) [Google Scholar](#)

8. Martin A. Lopez

[View author publications](#)

You can also search for this author in [PubMed](#) [Google Scholar](#)

9. Meshal Ansari

[View author publications](#)

You can also search for this author in [PubMed](#) [Google Scholar](#)

10. Maximilian Strunz

[View author publications](#)

You can also search for this author in [PubMed](#) [Google Scholar](#)

11. Christoph Mayr

[View author publications](#)

You can also search for this author in [PubMed](#) [Google Scholar](#)

12. Chiara Ciminieri

[View author publications](#)

You can also search for this author in [PubMed](#) [Google Scholar](#)

13. Rita Costa

[View author publications](#)

You can also search for this author in [PubMed](#) [Google Scholar](#)

14. Marlene Sophia Kohlhepp
[View author publications](#)

You can also search for this author in [PubMed](#) [Google Scholar](#)

15. Adrien Guillot
[View author publications](#)

You can also search for this author in [PubMed](#) [Google Scholar](#)

16. Gizem Günes
[View author publications](#)

You can also search for this author in [PubMed](#) [Google Scholar](#)

17. Aicha Jeridi
[View author publications](#)

You can also search for this author in [PubMed](#) [Google Scholar](#)

18. Maja C. Funk
[View author publications](#)

You can also search for this author in [PubMed](#) [Google Scholar](#)

19. Giorgi Beroshvili
[View author publications](#)

You can also search for this author in [PubMed](#) [Google Scholar](#)

20. Sandra Prokosch
[View author publications](#)

You can also search for this author in [PubMed](#) [Google Scholar](#)

21. Jenny Hetzer
[View author publications](#)

You can also search for this author in [PubMed](#) [Google Scholar](#)

22. Stijn E. Verleden

[View author publications](#)

You can also search for this author in [PubMed](#) [Google Scholar](#)

23. Hani Alsafadi

[View author publications](#)

You can also search for this author in [PubMed](#) [Google Scholar](#)

24. Michael Lindner

[View author publications](#)

You can also search for this author in [PubMed](#) [Google Scholar](#)

25. Gerald Burgstaller

[View author publications](#)

You can also search for this author in [PubMed](#) [Google Scholar](#)

26. Lore Becker

[View author publications](#)

You can also search for this author in [PubMed](#) [Google Scholar](#)

27. Martin Irmler

[View author publications](#)

You can also search for this author in [PubMed](#) [Google Scholar](#)

28. Michael Dudek

[View author publications](#)

You can also search for this author in [PubMed](#) [Google Scholar](#)

29. Jakob Janzen

[View author publications](#)

You can also search for this author in [PubMed](#) [Google Scholar](#)

30. Eric Goffin

[View author publications](#)

You can also search for this author in [PubMed](#) [Google Scholar](#)

31. Reinoud Gosens

[View author publications](#)

You can also search for this author in [PubMed](#) [Google Scholar](#)

32. Percy Knolle

[View author publications](#)

You can also search for this author in [PubMed](#) [Google Scholar](#)

33. Bernard Pirotte

[View author publications](#)

You can also search for this author in [PubMed](#) [Google Scholar](#)

34. Tobias Stoeger

[View author publications](#)

You can also search for this author in [PubMed](#) [Google Scholar](#)

35. Johannes Beckers

[View author publications](#)

You can also search for this author in [PubMed](#) [Google Scholar](#)

36. Darcy Wagner

[View author publications](#)

You can also search for this author in [PubMed](#) [Google Scholar](#)

37. Indrabahadur Singh

[View author publications](#)

You can also search for this author in [PubMed](#) [Google Scholar](#)

38. Fabian J. Theis

[View author publications](#)

You can also search for this author in [PubMed](#) [Google Scholar](#)

39. Martin Hrabé de Angelis

[View author publications](#)

You can also search for this author in [PubMed](#) [Google Scholar](#)

40. Tracy O'Connor

[View author publications](#)

You can also search for this author in [PubMed](#) [Google Scholar](#)

41. Frank Tacke

[View author publications](#)

You can also search for this author in [PubMed](#) [Google Scholar](#)

42. Michael Boutros

[View author publications](#)

You can also search for this author in [PubMed](#) [Google Scholar](#)

43. Emmanuel Dejardin

[View author publications](#)

You can also search for this author in [PubMed](#) [Google Scholar](#)

44. Oliver Eickelberg

[View author publications](#)

You can also search for this author in [PubMed](#) [Google Scholar](#)

45. Herbert B. Schiller

[View author publications](#)

You can also search for this author in [PubMed](#) [Google Scholar](#)

46. Melanie Königshoff

[View author publications](#)

You can also search for this author in [PubMed](#) [Google Scholar](#)

47. Mathias Heikenwalder

[View author publications](#)

You can also search for this author in [PubMed](#) [Google Scholar](#)

48. Ali Önder Yıldırım

[View author publications](#)

You can also search for this author in [PubMed](#) [Google Scholar](#)

Contributions

T.M.C., G.J.S., O.E., M.K., M.H. and A.Ö.Y. conceived the study and experimental design. T.M.C., G.J.S., D.H., M.A.L., R.C., Y.H., Z.E., C.C., S.P., J.H., H.A., G.G., M.Z.J., L.B., D.P., M.S.K., A.G., A.J., G. Beroshvili, M.C.F., M.D., I.S., J.J. and D.W. performed experiments. M.H., F.T., D.P. and M.S.K. designed, undertook, and analysed flow cytometry experiments. A.G. designed, undertook, and analysed multiplex immunofluorescence, supervised by F.T. E.G. and B.P. prepared NIK inhibitor. S.E.V. prepared patient lung core samples. M.I. and J.B. contributed to microarray analysis. M.H., D.H. designed and executed the immunohistochemistry and RNA in situ hybridization analyses. M.H.dA. supervised microarray experiments. M.A. and M.S. designed, undertook, and analysed scRNA-seq experiments, supervised by H.B.S. and F.J.T. I.S. undertook proteomics analysis. C.M. analysed proteomic datasets. M. Lindner supplied human lung tissue for lung slices. D.W. and M.K. established the 3D human lung slice model. Y.H., C.C. and M.K. developed and undertook human lung organoid experiments. T.M.C., G.J.S., D.P., M. Lehmann, M.A., M.S., C.M., Y.H., T.S., P.K., C.C., G. Burgstaller, R.G., R.C., M.S.K., A.G., M.C.F., F.J.T., F.T., M.B., E.D., H.B.S., M.K., M.H. and A.Ö.Y. analysed and interpreted

data. T.M.C., G.J.S., T.O.C., M.H. and A.Ö.Y. wrote the manuscript. All authors read and edited the manuscript.

Corresponding authors

Correspondence to [Mathias Heikenwalder](#) or [Ali Önder Yildirim](#).

Ethics declarations

Competing interests

G.J.S. is currently employed as an editor at *Genome Medicine*, a Springer Nature journal. He joined the company after his participation in the study and was not involved in the editorial process at *Nature*. All other authors declare no competing interests.

Additional information

Peer review information *Nature* thanks the anonymous reviewers for their contribution to the peer review of this work.

Publisher's note Springer Nature remains neutral with regard to jurisdictional claims in published maps and institutional affiliations.

Extended data figures and tables

[Extended Data Fig. 1 Canonical and non-canonical NF-κB signalling pathways are activated in the lungs of patients with COPD and mice exposed to cigarette smoke.](#)

a, b, Representative images of immunohistochemical analysis for RELA (**a**) and RELB (**b**) (brown signal, indicated by arrows, nuclei counterstained with haematoxylin) in lung core biopsy sections from healthy participants ($n = 3$) patients with COPD ($n = 4$), with the quantification of RELA and RELB-positive alveolar epithelial nuclei shown as mean \pm s.d. Scale bar, 50 μm and 25 μm (inset). **c–e**, GSEA of the LT β R signalling, NF- κ B signalling (gene lists from IPA software, Qiagen), TNFR-mediated signalling (GO:0033209), positive regulation of I- κ B kinase NF- κ B signalling (GO:0043123) and NIK NF- κ B signalling (GO:0038061) pathways in publicly available array data from lung tissue (GSE47460–GPL14550) of healthy ($n = 91$) versus patients with COPD ($n = 145$) (**c**),

from lung tissue (GSE37768) of healthy ($n = 9$) versus patients with COPD ($n = 18$) (d) and from PBMCs (GSE56768) of healthy ($n = 5$) versus patients with COPD ($n = 49$) (e). f, mRNA expression levels of *Lta*, *Ltbr*, *Tnfsf14*, *Tnf*, *Ccl2* and *Cxcl13* determined by qPCR in whole lung from B6 mice exposed to filtered air ($n = 6$) or cigarette smoke ($n = 8$) for 6 months; individual mice are shown. g, GSEA of the pathways described in c–e in the publicly available array data (GSE52509) of lungs from our mice exposed to filtered air ($n = 3$) and cigarette smoke ($n = 6$) for 4 and 6 months. h, Western blot analysis for RELB, p100 and p52 in total lung homogenate from the mice described in f. Quantification relative to vinculin of individual mice shown ($n = 3$). For gel source data, see Supplementary Fig. 1. i, Schematic representation of the LT β R–Ig treatment protocol. j, Representative low and high magnification overlay images of Multiplex immunofluorescence staining to identify CD4 (red), CD8 (green), B220 (turquoise) and DAPI (blue) counterstained lung sections ($n = 4$) from B6 mice exposed to cigarette smoke for 6 months, plus LT β R–Ig fusion protein or control Ig (80 μ g intraperitoneally, weekly) therapeutically from 4 to 6 months, and analysed at 6 months. Scale bars, 100 μ m k, mRNA expression levels of *Cxcl13* and *Ccl19* determined by qPCR in whole lung from B6 mice exposed to filtered air or cigarette smoke for 4 and 6 months, plus LT β R–Ig fusion or control Ig (80 μ g intraperitoneally, weekly) prophylactically from 2 to 4 months and analysed at 4 months, and therapeutically from 4 to 6 months and analysed at 6m ($n = 4$ mice/group, repeated twice, pooled data shown). P values indicated, Mann–Whitney one-sided test (a, b), unpaired two-tailed Student’s *t*-test (f, h), one-way ANOVA multiple comparisons Bonferroni test (k). [Source data](#)

Extended Data Fig. 2 Immune response in lungs of mice exposed to cigarette smoke and treated with LT β R–Ig.

a–c, Flow cytometry analysis of single cell suspensions for adaptive immune cells from whole lung of B6 mice exposed to filtered air ($n = 6$) or cigarette smoke for 6 months, plus LT β R–Ig fusion ($n = 5$) or control Ig ($n = 5$) (80 μ g intraperitoneally, weekly) from 4 to 6 months and analysed at 6 months. a, t-SNE plots showing the distribution and composition of CD4 and CD8 T cells as central memory T cells (Tcm) (CD62L $^+$ CD44 $^+$), effector memory T cells (Tem) (CD62L $^-$ CD44 $^+$) and T memory stem cells (Tscm)

(CD62L⁺CD44⁻) (left) and *t*-SNE plots showing the distribution of the surface markers indicated (top right) and global changes in composition with treatment (bottom right). **b**, Abundance of the T cell populations indicated as a percentage of total CD45⁺ cells. **c**, Top, *t*-SNE plots showing the distribution of CD19-, IgG-, MHCII-, CD69- and GL7-positive cells. Bottom, the abundance of CD19⁺ B cells as a percentage of total CD45⁺ cells and the geometric mean fluorescence intensity of the expressed markers indicated on CD19⁺ B cells. **d–g**, B6 mice were exposed to filtered air or cigarette smoke for 4 and 6 months, plus LT β R–Ig fusion protein or control Ig (80 μ g i.p., weekly) prophylactically (Proph.) from 2 to 4 months and analysed at 4 months and therapeutically (Ther.) from 4 to 6 months, and analysed at 6 months. **d**, Representative images of immunohistochemical analysis for CD68 macrophages in lung sections from the mice ($n = 4$ mice per group, brown signal indicated by arrowheads, haematoxylin counter stained). Scale bar, 100 μ m. **e**, Quantification of CD68 positive macrophages across 20 random fields of view from lung sections stained in **d** ($n = 4$ mice per group). **f**, Representative low and high magnification overlay images of Multiplex immunofluorescence staining to identify IBA1 (red), iNOS (green), CD206 (turquoise) and DAPI (blue) counterstained lung sections from mice at 6 months ($n = 4$ mice per group). Scale bars, 100 μ m and 25 μ m, respectively. **g**, iNOS and IBA1 double-positive macrophages from Multiplex immunofluorescence staining on lung sections from mice treated both prophylactically and therapeutically was quantified using Ilastik and CellProfiler ($n = 4$ mice per group). **h–l**, Flow cytometry analysis of single cell suspensions for myeloid cells from whole lung of B6 mice exposed to filtered air ($n = 6$) or cigarette smoke for 6 months, plus LT β R–Ig fusion ($n = 5$) or control Ig ($n = 5$) (80 μ g intraperitoneally, weekly) from 4 to 6 months and analysed at 6 months. **h**, *t*-SNE plots showing the distribution and composition of myeloid cells and surface markers indicated. **i**, *t*-SNE plots showing global changes in composition with treatment. **j**, Composition of CD45⁺LY6G⁻F480⁺CD11c⁺ alveolar macrophages. **k**, Composition of CD45⁺LY6G⁻F480⁺CD11c⁻CD11b⁺ interstitial macrophages. **l**, Composition of CD45⁺LY6G⁻F480⁺CD11c⁻CD11b⁺LY6C^{high} infiltrating macrophages. Data are mean \pm s.d. *P* values determined by one-way ANOVA multiple comparisons Bonferroni test (**b**, **c**, **e**, **g**, **j–l**). [Source data](#)

Extended Data Fig. 3 scRNA-seq analysis of lungs from mice exposed to cigarette smoke and treated with LT β R–Ig.

Cells from whole lung suspensions of B6 mice exposed to filtered air ($n = 3$) or cigarette smoke for 6 months, plus LT β R–Ig fusion protein ($n = 5$) or control Ig ($n = 5$) therapeutically from 4 to 6 months, were analysed at 6 months by scRNA-seq (Drop-Seq). **a**, Heat map depicting the expression of key genes used in identifying the individual cell populations. **b**, UMAP of scRNA-seq profiles (dots) coloured by experimental group. **c**, UMAP plots showing expression of genes indicated in scRNA-seq profiles. **d**, Dot blot depicting the expression level (log-transformed, normalized UMI counts) and percentage of cells in a population positive for *Ltb*, *Lta*, *Tnf*, *Tnfsf14*, *Ltbr*, *Tnfrsf1a* and *Tnfrsf1b*. **e**, UMAP plot showing the relative intensity of the positive regulation of NIK (non-canonical) NF- κ B signalling pathway (GO:1901224) across the scRNA-seq profiles. **f**, UMAP plot of scRNA-seq profiles (dots) of lung epithelial cells coloured by experimental group (left) and the relative intensity of the positive regulation of NIK (non-canonical) NF- κ B signalling pathway (GO:1901224) (right). **g**, Box and whiskers plot (box representing 25th–75th percentile, median line indicated and Tukey whiskers representing $\pm 1.5 \times$ IQR) showing the relative score for the positive regulation of NIK (non-canonical) NF- κ B signalling pathway in the cell types indicated across the three groups. Statistical significance was assessed using Wilcoxon rank-sum two-sided test on normalized, log-transformed count values and corrected with Benjamini–Hochberg. [Source data](#)

Extended Data Fig. 4 Analysis of LTA and LTB expression in human and mouse lungs.

a, Representative images of in situ hybridization analysis for *LTA* and immunohistochemical analysis for *LTB* in lung sections from healthy participants and patients with COPD ($n = 4$, red signal indicated by arrowheads (*LTA*), brown signal (*LTB*) and nuclei counterstained with haematoxylin). Scale bar, 50 μ m. **b**, Representative images of in situ hybridization analysis for *Lta* and *Ltb* in lung sections from B6 mice exposed to cigarette smoke for 6 months with LT β R–Ig fusion protein or

control Ig (80 µg intraperitoneally, weekly) therapeutically for 4 to 6 months, and analysed at 6 months (brown positive staining (*Lta*) and red positive staining (*Ltb*) indicated by arrowheads, open arrowhead unstained cells, nuclei were counterstained with haematoxylin) ($n = 4$ mice per group, repeated twice). Scale bar, 20 µm. Non-staining with sense probe in cigarette smoke plus Ig sections shown as negative control. Representative images of immunohistochemical analysis identifying CD68-positive macrophages (brown staining indicated by arrowheads) also shown. **c**, Representative images of *in situ* hybridization analysis for *Tnfsf14* in lung sections from mice described in **b** (brown positive staining indicated by arrowheads, open arrowhead unstained cells, nuclei counterstained with haematoxylin) ($n = 4$ mice per group). Scale bars, 20 µm. Spleen section shown as a positive control. **d**, Representative images of *in situ* hybridization analysis for *Tnf* in lung sections from mice described in **b** (brown positive macrophage indicated by arrowheads, open arrowhead unstained macrophage, nuclei counterstained with haematoxylin). Scale bars, 20 µm. Representative immunohistochemical analysis identifying CD68-positive macrophages (brown staining indicated by arrowheads, haematoxylin counterstained) also shown. Scale bars, 20 µm. **e**, Quantification of *Tnf*-positive macrophages across 20 random fields of view per lung ($n = 4$). Data are mean ± s.d. *P* values determined by one-way ANOVA multiple comparisons Bonferroni test. [Source data](#)

Extended Data Fig. 5 Inhibition of LT β R signalling strongly reduces non-canonical but not canonical NF- κ B signalling in lung.

a, Principal component analysis of microarray data, using Mouse Ref-8 v2.0 Expression BeadChips (Illumina), performed on lung tissue from mice exposed to filtered air or cigarette smoke for 6 months, plus LT β R–Ig fusion or control Ig (80 µg intraperitoneally, weekly) therapeutically from 4 to 6 months ($n = 3$ mice per group). **b**, Principal component analysis of normalized z-scored mass spectrometry intensities from proteomics of whole lung lysates from mice exposed to filtered air ($n = 6$) or cigarette smoke for 6 months, plus LT β R–Ig fusion ($n = 7$) or control Ig ($n = 4$) (80 µg intraperitoneally, weekly) from 4 to 6 months. **c**, Heat map depicting the top 20 up and down LT β R–Ig regulated genes presented as fold change

(FDR < 10%) from the microarray data described in **a**. Left, expression in mice exposed to cigarette smoke plus Ig relative to mice exposed to filtered air. Right, expression in mice exposed to cigarette smoke plus LT β R–Ig relative to mice exposed to cigarette smoke plus Ig. **d**, GSEA of the NIK (non-canonical) NF- κ B signalling (GO:0038061) pathway of the microarray data from **a**. **e**, Heat map of significantly regulated proteins from the NIK (non-canonical) NF- κ B signalling (GO:0038061) pathway as determined by Student's *t*-test statistic from the proteomics data described in **b**. **f**, GSEA of the NIK (non-canonical) NF- κ B signalling (GO:0038061) pathway of the normalized proteome data described in **b**. **g**, Representative images of two independent experiments of immunohistochemical analysis for RELB in lung sections from B6 mice exposed to filtered air or cigarette smoke for 4 or 6 months, plus LT β R–Ig fusion or control Ig (80 μ g intraperitoneally, weekly) prophylactically from 2 to 4 months and analysed at 4 months, and therapeutically from 4 to 6 months and analysed at 6 months (brown signal indicated by arrowheads, nuclei counterstained with haematoxylin). Scale bar, 25 μ m. **h**, Quantification of RELB-positive alveolar epithelial nuclei from the immunohistochemistry sections in **g** ($n = 3$ mice per group). **i**, Representative images of two independent experiments of immunohistochemical analysis for RELA in lung sections from the mice described in **g** (brown signal indicated by arrowheads, nuclei counterstained with haematoxylin). Scale bar, 25 μ m. **j**, Quantification of RELA-positive alveolar epithelial nuclei from the immunohistochemistry sections in **i** ($n = 3$ mice per group). **k**, mRNA expression levels of *Ccl2*, *Ccl3*, *Cxcl1* and *Tnf* determined by qPCR in whole lung from the mice described in **g** ($n = 4$ mice per group, repeated twice, pooled data shown). **l**, mRNA expression levels of *Lta*, *CXCL13* and *TNF* determined by qPCR in ex vivo human precision-cut lung slices stimulated for 24 h with LPS (10 μ g ml $^{-1}$) in the presence or absence of human LT β R–Ig fusion protein (1 μ g ml $^{-1}$) ($n = 3$ independent experiments from three separate lungs). Left image shows a representative picture of preparing a lung slice from the three independent experiments. Data are mean \pm s.d. *P* values determined by one-way ANOVA multiple comparisons Bonferroni test. [Source data](#)

Extended Data Fig. 6 LT β R–Ig treatment reverses airway remodelling and comorbidities in mice chronically exposed to

cigarette smoke.

a, Representative images of Masson's Trichrome stained lung sections from B6 mice exposed to filtered air or cigarette smoke for 4 or 6 months, plus LT β R–Ig fusion protein or control Ig (80 μ g intraperitoneally, weekly) prophylactically from 2 to 4 months and analysed at 4 months, and therapeutically from 4 to 6 months and analysed at 6 months ($n = 4$ mice per group, repeated twice). Scale bar, 200 μ m. These are low-magnification images of the sections depicted and quantified in Fig. 2c,d. **b**, Representative images of immunohistochemical analysis for collagen I (red signal, nuclei counterstained with haematoxylin) in lung sections from B6 mice described in **a**. Scale bar, 100 μ m. **c**, Quantification of small airway collagen deposition normalized to the surface area of airway and vessel basement membrane from the sections in **b** ($n = 7$ mice FA, 7 mice CS+Ig, 7 mice CS+LT β R-Ig groups, from two independent experiments). **d**, Representative images of immunohistochemical analysis for phosphorylated SMAD2 in lung sections from mice described in **a** (red signal indicated by arrows, nuclei counterstained with haematoxylin) ($n = 4$ mice per group, repeated twice). Scale bar, 25 μ m. **e**, mRNA expression levels of *Ppargc1a* and *Mcat* determined by qPCR in gastrocnemius muscle from 6-month mice described in **a** ($n = 4$ mice per group, repeated twice, pooled data shown). **f**, Four-paw muscle strength test in mice at 6 months treated as described in **a** ($n = 8$ mice per group). **g**, Schematic representation of the LT β R–Ig treatment protocol in aged mice. **h**, Representative images of lung sections stained with H&E and Masson's Trichrome from 12-month-old B6 mice exposed to filtered air or cigarette smoke for 4 months, plus LT β R–Ig fusion protein or control Ig (80 μ g i.p., weekly) from 2 to 4 months and analysed at 4 months ($n = 5$ mice FA, 5 mice CS+Ig, 7/8 mice CS+LT β R-Ig groups, repeated twice). Scale bar, 50 μ m. These are low magnification images of the sections depicted and quantified in Fig. 2f,g.) Data are mean \pm s.d. *P* values determined by one-way ANOVA multiple comparisons Bonferroni test (**c**) or Student's two-tailed *t*-test (**e**, **f**). [Source data](#)

Extended Data Fig. 7 Disease development is not attenuated by LT β R–Ig treatment in iBALT independent emphysema.

a, Schematic representation of the LT β R–Ig treatment protocol in mice exposed to a single oropharyngeal application of PPE or PBS control. **b**, mRNA expression level fold changes (FC) of *Lta*, *Tnfsf14*, *Ltbr* and *Tnf* relative to *Hprt*, determined by qPCR in whole lung from B6 mice treated with a single oropharyngeal application of PBS ($n = 8$) or PPE (40 U kg $^{-1}$ body weight) and analysed after 3 months ($n = 7$) or 4 months of chronic exposure to cigarette smoke ($n = 8$ mice per group). **c**, Representative images of immunohistochemical analysis for B220-positive B cells and CD3-positive T cells (brown signal, indicated by arrowheads, nuclei counterstained with haematoxylin) in lung sections from mice treated with PBS or PPE as described in **b**, plus mice treated with PPE followed by LT β R–Ig fusion protein (80 μ g intraperitoneally, weekly) 28 days later for 2 months ($n = 8$ mice per group, repeated twice). Scale bar, 50 μ m. **d**, Lymphocyte counts in the BAL fluid from the mice described in **c** plus mice exposed to cigarette smoke for 4 months ($n = 8$ mice per group). **e**, Representative images of in situ hybridization analysis for *Lta* and *Ltb* in lung sections from mice described in **c**, plus splenic positive controls (brown staining, nuclei counterstained with haematoxylin) ($n = 4$ mice per group, repeated twice). Scale bar, 50 μ m. **f**, Representative images of immunohistochemical analysis for RELA and RELB in lung sections from B6 mice described in **c** (brown signal indicated by arrowheads, nuclei counterstained with haematoxylin) ($n = 4$ mice per group, repeated twice). Scale bar, 50 μ m. **g**, Representative images of H&E-stained lung sections from mice described in **c** ($n = 8$ mice per group, repeated twice). Scale bars, 200 μ m and 50 μ m (inset). **h**, Emphysema scoring (1–5; 5 most severe) of lung sections from **f** ($n = 5$ mice PBS, 5 mice PPE, 7 mice PPE+LT β R-Ig groups). **i**, Diffusing capacity of carbon monoxide (DF $_{CO}$) in the lungs of mice described in **c** ($n = 8$ mice PBS, 7 mice PPE, 8 mice PPE+LT β R-Ig groups). **j**, Dynamic compliance (Cdyn) pulmonary function data from the mice described in **c** ($n = 8$ mice PBS, 7 mice PPE, 8 mice PPE+LT β R-Ig groups). Data are mean \pm s.d. *P* values determined by one-way ANOVA multiple comparisons Bonferroni test. [Source data](#)

Extended Data Fig. 8 Inhibiting LT β R-signalling suppresses cigarette-smoke-induced apoptosis.

a, Representative images of immunohistochemical analysis for cleaved caspase-3 in lung sections from healthy participants and patients with COPD ($n = 5$, brown signal indicated by arrowheads, nuclei counterstained with haematoxylin). Scale bar, 50 μm . **b**, Quantification of alveolar epithelial cells positive for cleaved caspase-3 from the lung sections stained in **a**. Data are mean \pm s.d. ($n = 5$ patients per group). $P = 0.0079$, Mann–Whitney two-sided test. **c**, **d**, GSEA of apoptosis (Hallmark collection) in transcriptomic array data from publicly available array data of lung tissue (GSE47460–GPL14550) from healthy participants ($n = 91$) versus patients with COPD ($n = 145$) (**c**) and the lungs of B6 mice after exposure for 6 months to filtered air, cigarette smoke plus Ig, or cigarette smoke plus LT β R–Ig fusion protein therapeutically ($n = 3$ mice per group) (**d**). **e**, Box and whiskers plot (box representing 25th–75th percentile, median line indicated and Tukey whiskers representing $\pm 1.5 \times \text{IQR}$) showing the relative score for apoptosis (Hallmark collection) in AT2 cells after scRNA-seq analysis of lungs from B6 mice after exposure for 6 months to filtered air ($n = 3$ mice per group), cigarette smoke plus Ig ($n = 5$ mice per group) or cigarette smoke plus LT β R–Ig fusion protein ($n = 5$ mice per group) therapeutically. Statistical significance was determined by Wilcoxon rank-sum two-sided test on normalized, log-transformed count values and corrected with Benjamini–Hochberg. **f**, **g**, Proteome analysis of whole lung lysates from mice exposed to filtered air ($n = 6$) or cigarette smoke for 6 months, plus LT β R–Ig fusion ($n = 7$) or control Ig ($n = 4$) (80 μg intraperitoneally, weekly) from 4 to 6 months was undertaken. **f**, Heat map of the significantly regulated proteins from the Hallmark apoptosis list as determined by Student’s two-sided *t*-test. **g**, GSEA of the Hallmark apoptosis list on the normalized proteome data. **h**, Representative images of immunohistochemical analysis for cleaved caspase-3 in lung sections from B6 mice exposed to filtered air or cigarette smoke for 4 and 6 months, plus LT β R–Ig fusion protein or control Ig (80 μg intraperitoneally, weekly) prophylactically from 2 to 4 months and analysed at 4 months, and therapeutically from 4 to 6 months and analysed at 6 months ($n = 4$ mice per group, brown signal indicated by arrowheads, nuclei counterstained with haematoxylin). Scale bar, 50 μm . Quantification of cleaved caspase-3-positive alveolar epithelial cells from the immunohistochemistry sections also shown. **i**, Western blot analysis for cleaved caspase-3 (c-Cas-3) in total lung homogenate from mice described in **h**, quantification relative to β -

actin (prophylactic groups: FA $n = 7$, CS+Ig $n = 7$, CS+LT β R-Ig $n = 6$ mice per group, therapeutic groups: FA $n = 6$, CS+Ig $n = 5$, CS+LT β R-Ig $n = 6$ mice per group, pooled from two independent experiments), individual mice shown. For gel source data see Supplementary Fig. 1. **j–l**, The mouse AT2-like cell line LA4 was stimulated with LT β R-Ag ($2 \mu\text{g ml}^{-1}$), recombinant mouse TNF (1 ng ml^{-1}) or a combination of both, in the presence or absence of necrostatin-1 (Nec1, $50 \mu\text{M}$) (**j**) and (**k**) or Z-Val-Ala-DL-Asp-fluoromethylketone (z-VAD, $20 \mu\text{M}$) (**l**). Apoptosis was assessed at 6 h (**j–l**) and 24 h (**k, l**) by flow cytometric analysis of annexin V and propidium iodide (PI) staining ($n = 2–3$, repeated twice, pooled data shown in **k**). **m, n**, Wound-healing assay in LA4 cells grown to confluence, scratched and then incubated with LT β R-Ag ($2 \mu\text{g ml}^{-1}$), recombinant mouse TNF (1 ng ml^{-1}) or a combination of both, in the presence or absence of necrostatin-1 ($50 \mu\text{M}$). **m**, Representative images at 0 h and 56 h after scratch are shown ($n = 4$ from one experiment). Scale bar, $200 \mu\text{m}$. **n**, Degree of wound closure (100% representing fully closed) at 56 h ($n = 4$). Data are mean \pm s.d. P values determined by one-way ANOVA multiple comparisons Bonferroni test (**h, i, k, l, n**). [Source data](#)

[Extended Data Fig. 9 LT \$\beta\$ R stimulation regulates WNT/ \$\beta\$ -catenin-signalling.](#)

a, GSEA of canonical WNT signalling (GO: 0060070) and β -catenin/TCF transcription factor complex assembly (GO:1904837) in transcriptomic array data from the lungs of B6 mice after 6 months exposure to filtered air, cigarette smoke plus Ig, or cigarette smoke plus LT β R-Ig fusion protein therapeutically ($n = 3$ mice per group) and publicly available array data from lung tissue (GSE47460–GPL14550) of healthy participants ($n = 91$) versus patients with COPD ($n = 145$). **b**, Representative images of immunohistochemical analysis for AXIN2 in lung sections from healthy participants ($n = 6$) and patients with COPD ($n = 8$) (brown signal indicated by arrowheads, nuclei counterstained with haematoxylin). Scale bar, $50 \mu\text{m}$. **c**, mRNA expression levels of *Nkd1* and *Lgr5* relative to *Hprt* in primary mouse AT2 cells treated with LT β R-Ag ($2 \mu\text{g ml}^{-1}$) for 24 h, with or without mouse rWNT3A (100 ng ml^{-1}) ($n = 5$ individual experiments). **d**, mRNA expression levels of *Tcf4* relative to *Hprt* in the LA4 cells stimulated

with LT β R-Ag ($2 \mu\text{g ml}^{-1}$) or recombinant mouse TNF (1 ng ml^{-1}) ($n = 3$, repeated three times). **e**, mRNA expression levels of *Tcf4* relative to *Hprt* in LA4 cells stimulated with LT β R-Ag ($2 \mu\text{g ml}^{-1}$) plus recombinant mouse TNF (1 ng ml^{-1}) with or without necrostatin-1 ($50 \mu\text{M}$), and the IKK kinase inhibitors TPCA-1 ($10 \mu\text{M}$) or BAY 11-7082 ($10 \mu\text{M}$) ($n = 2$, repeated twice). **f**, mRNA expression levels of *AXIN2* relative to *HPRT* and normalized to vehicle, in human A549 cells treated with human LT β R-Ag ($0.5 \mu\text{g ml}^{-1}$) for 24 h with or without TPCA-1 ($5 \mu\text{M}$) ($n = 3$ independent experiments). **g**, WNT/ β -catenin luciferase reporter activity in mouse MLE12 cells, activated by GSK-3 β inhibitor (CHIR99021, $1 \mu\text{M}$) and treated with LT β R-Ag at the concentrations indicated for 24 h (activity relative to CHIR alone, $n = 2–9$). **h**, Western blot analysis for β -catenin in MLE12 cells treated with LT β R-Ag ($2 \mu\text{g ml}^{-1}$) for 24 h with or without mouse rWNT3A (100 ng ml^{-1}) plus bortezomib (10 nM). Quantification relative to actin shown ($n = 3$ independent experiments). For gel source data, see Supplementary Fig. 1. **i**, mRNA expression levels of *TCF4* relative to *HPRT* in ex vivo human precision-cut lung slices stimulated for 24 h with recombinant human TNF (20 ng ml^{-1}) or LT β R-Ag ($2 \mu\text{g ml}^{-1}$) for 24 h ($n = 5$ slices from individual lungs). **j**, Western blot analysis for β -catenin in MLE12 cells treated with mouse rWNT3A (200 ng ml^{-1}) and TNFSF14 (200 ng ml^{-1}) for 30 h. Quantification relative to vinculin shown ($n = 3$ independent experiments). For gel source data, see Supplementary Fig. 1. **k–m**, B6 mice were treated with a single oropharyngeal application of PBS ($n = 8$), PPE (40 U kg^{-1} body weight) ($n = 7$ mice per group) or PPE followed by LT β R-Ig fusion protein ($80 \mu\text{g}$ intraperitoneally, weekly) 28 days later for 2 months and all analysed after 3 months ($n = 8$ mice per group); see Extended Data Fig. 7a. **k**, mRNA expression levels of *Axin2*, *Bcl9l*, *Cdh1*, *Dvl1*, *Gsk3b*, *Rab5a*, *Tcf4*, *Wif1*, *Wnt2* and *Wnt4* relative to *Hprt*, determined by qPCR in whole lung. **l**, Representative images of immunohistochemical analysis for TCF and AXIN2 in lung sections from the mice described ($n = 4$ mice per group, brown signal indicated by arrowheads, nuclei counterstained with haematoxylin). Scale bar, $25 \mu\text{m}$. **m**, Quantification of alveolar epithelial cells positive for TCF4 and AXIN2 from **l**. Data shown as individual lungs (**c**, **i**) or mean \pm s.d. (**d–h**, **j**, **k** and **m**). *P* values determined by one-tailed (**c**) or two-tailed (**i**) paired Student's *t*-test, two-tailed unpaired Student's *t*-test (**h**, **j**) or one-way ANOVA

multiple comparisons Bonferroni test (**d–g** (compared to vehicle in **g**), **k**, **m**). [Source data](#)

Extended Data Fig. 10 LT β R-stimulation regulates lung repair and regeneration by modulating WNT/ β -catenin-signalling.

a, Schematic representation of the experiment in which B6 mice were exposed to filtered air ($n = 5$) or cigarette smoke for 6 months plus control Ig ($n = 5$), LT β R–Ig fusion protein (80 μ g intraperitoneally, weekly, $n = 5$), LT β R–Ig fusion protein plus β -catenin/CBP inhibitor PRI-724 (0.6 mg intraperitoneally, twice weekly, $n = 6$) or CHIR99021 (0.75 mg intraperitoneally, weekly, $n = 5$) from 4 to 6 months, and analysed at 6 months. **b**, mRNA expression levels of *Ltb*, *Tnfsf14* and *Ltbr* relative to *Hprt*, determined by qPCR in whole lung from the mice described in **a** (FA $n = 5$, CS plus control Ig $n = 5$, LT β R–Ig $n = 5$, LT β R–Ig + PRI-724 $n = 6$ and CHIR99021 $n = 5$ mice per group). **c**, Representative images of immunohistochemical analysis for CD3 $^{+}$ T cells and B220 $^{+}$ B cells (brown signal, nuclei counterstained with haematoxylin) in lung sections from the mice described in **a**. Scale bar, 100 μ m. **d**, mRNA expression levels of *Axin2* relative to *Hprt*, determined by qPCR in whole lung from the mice described in **a** (FA $n = 5$, CS plus control Ig $n = 5$, LT β R–Ig $n = 5$, LT β R–Ig + PRI-724 $n = 6$ and CHIR99021 $n = 5$ mice per group). **e**, Schematic representation of human lung organoid experiments. **f**, Representative images and quantification of lung organoids from primary human AT2 epithelial cells cultured for 14 days with or without human LT β R–Ag (2 μ g ml $^{-1}$) and LiCl (5 mM) ($n = 2$ replicates from 2 separate donors). Scale bar, 500 μ m. **g**, Schematic representation of the re-ignition of repair and regeneration pathways in AT2 lung cells after LT β R–Ig therapy in both young and aged mice chronically exposed to cigarette smoke. Data are mean \pm s.d. *P* values determined by two-tailed Student's *t*-test (**d**) or one-way ANOVA multiple comparisons Bonferroni test (**f**). [Source data](#)

Supplementary information

Supplementary Figure 1

This file contains gel source data, flow cytometry gating structure for Extended Data Fig 2 and the chemical structure of the NIK kinase inhibitor

CMP1.

Reporting Summary

Supplementary Tables 1-3

This file contains Supplementary Table 1: Demographics and clinical characteristics of healthy and COPD patients; Supplementary Table 2: Antibodies used for flow cytometry; and Supplementary Table 3: Primer sequences used for the quantitative real time RT-PCR.

Supplementary Table 4

This file contains metadata from the single cell RNA-Seq analysis of lungs from mice chronically exposed to cigarette smoke for 6 months and treated therapeutically with LT β R-Ig from 4 to 6 months and filtered air controls.

Supplementary Table 5

This file contains proteomics data from the lungs of mice mice chronically exposed to cigarette smoke for 6 months and treated therapeutically with LT β R-Ig from 4 to 6 months and filtered air controls.

Source data

Source Data Fig. 1

Source Data Fig. 2

Source Data Fig. 3

Source Data Fig. 4

Source Data Extended Data Fig. 1

[Source Data Extended Data Fig. 2](#)

[Source Data Extended Data Fig. 3](#)

[Source Data Extended Data Fig. 4](#)

[Source Data Extended Data Fig. 5](#)

[Source Data Extended Data Fig. 6](#)

[Source Data Extended Data Fig. 7](#)

[Source Data Extended Data Fig. 8](#)

[Source Data Extended Data Fig. 9](#)

[Source Data Extended Data Fig. 10](#)

Rights and permissions

[Reprints and Permissions](#)

About this article



Check for
updates

Cite this article

Conlon, T.M., John-Schuster, G., Heide, D. *et al.* Inhibition of LT β R signalling activates WNT-induced regeneration in lung. *Nature* **588**, 151–156 (2020). <https://doi.org/10.1038/s41586-020-2882-8>

Download citation

- Received: 01 October 2019
- Accepted: 19 August 2020
- Published: 04 November 2020
- Issue Date: 03 December 2020
- DOI: <https://doi.org/10.1038/s41586-020-2882-8>

Comments

By submitting a comment you agree to abide by our [Terms](#) and [Community Guidelines](#). If you find something abusive or that does not comply with our terms or guidelines please flag it as inappropriate.

[Access through your institution](#)

[Change institution](#)

[Buy or subscribe](#)

This article was downloaded by **calibre** from <https://www.nature.com/articles/s41586-020-2882-8>

- Article
- [Published: 25 November 2020](#)

Splicing factor YBX1 mediates persistence of *JAK2*-mutated neoplasms

- [Ashok Kumar Jayavelu](#)^{1 na1},
- [Tina M. Schnöder](#)^{2,3 na1},
- [Florian Perner](#)²,
- [Carolin Herzog](#)⁴,
- [Arno Meiler](#) [ORCID: orcid.org/0000-0003-0012-7952](#)¹,
- [Gurumoorthy Krishnamoorthy](#) [ORCID: orcid.org/0000-0002-7798-6707](#)¹,
- [Nicolas Huber](#)²,
- [Juliane Mohr](#)²,
- [Bärbel Edelmann-Stephan](#)⁴,
- [Rebecca Austin](#)^{5,6,7},
- [Sabine Brandt](#)⁸,
- [Francesca Palandri](#) [ORCID: orcid.org/0000-0001-8367-5668](#)⁹,
- [Nicolas Schröder](#)¹⁰,
- [Berend Isermann](#)¹¹,
- [Frank Edlich](#)^{12,13,14},
- [Amit U. Sinha](#)¹⁵,
- [Martin Ungelenk](#)¹⁶,
- [Christian A. Hübner](#)¹⁶,
- [Robert Zeiser](#) [ORCID: orcid.org/0000-0001-6565-3393](#)^{13,17},
- [Susann Rahmig](#)^{18,19},
- [Claudia Waskow](#) [ORCID: orcid.org/0000-0003-3261-0922](#)^{18,19,20},
- [Iain Coldham](#) [ORCID: orcid.org/0000-0003-4602-6292](#)²¹,

- [Thomas Ernst²](#),
- [Andreas Hochhaus²](#),
- [Stefanie Jilg²²](#),
- [Philipp J. Jost](#) ORCID: orcid.org/0000-0003-2454-0362^{22,23},
- [Ann Mullally²⁴](#),
- [Lars Bullinger²⁵](#),
- [Peter R. Mertens⁸](#),
- [Steven W. Lane](#) ORCID: orcid.org/0000-0002-8050-6209^{5,6,7},
- [Matthias Mann](#) ORCID: orcid.org/0000-0003-1292-4799^{1 na2} &
- [Florian H. Heidel](#) ORCID: orcid.org/0000-0003-2438-1955^{2,3,18 na2}

[Nature](#) volume **588**, pages 157–163(2020) [Cite this article](#)

- 3461 Accesses
- 66 Altmetric
- [Metrics details](#)

Subjects

- [Myeloproliferative disease](#)
- [Phosphorylation](#)
- [Proteomic analysis](#)
- [Proteomics](#)

Abstract

Janus kinases (JAKs) mediate responses to cytokines, hormones and growth factors in haematopoietic cells^{1,2}. The JAK gene *JAK2* is frequently mutated in the ageing haematopoietic system^{3,4} and in haematopoietic cancers⁵. *JAK2* mutations constitutively activate downstream signalling and are drivers of myeloproliferative neoplasm (MPN). In clinical use, JAK inhibitors have mixed effects on the overall disease burden of *JAK2*-mutated clones^{6,7}, prompting us to investigate the mechanism underlying disease persistence. Here, by in-depth phosphoproteome profiling, we

identify proteins involved in mRNA processing as targets of mutant JAK2. We found that inactivation of *YBX1*, a post-translationally modified target of JAK2, sensitizes cells that persist despite treatment with JAK inhibitors to apoptosis and results in RNA mis-splicing, enrichment for retained introns and disruption of the transcriptional control of extracellular signal-regulated kinase (ERK) signalling. In combination with pharmacological JAK inhibition, *YBX1* inactivation induces apoptosis in JAK2-dependent mouse and primary human cells, causing regression of the malignant clones *in vivo*, and inducing molecular remission. This identifies and validates a cell-intrinsic mechanism whereby differential protein phosphorylation causes splicing-dependent alterations of JAK2–ERK signalling and the maintenance of *JAK2*^{V617F} malignant clones. Therapeutic targeting of *YBX1*-dependent ERK signalling in combination with JAK2 inhibition could thus eradicate cells harbouring mutations in *JAK2*.

[Access through your institution](#)

[Change institution](#)

[Buy or subscribe](#)

Access options

Subscribe to Journal

Get full journal access for 1 year

185,98 €

only 3,58 € per issue

[Subscribe](#)

All prices are NET prices.

VAT will be added later in the checkout.

Rent or Buy article

Get time limited or full article access on ReadCube.

from \$8.99

[Rent or Buy](#)

All prices are NET prices.

Additional access options:

- [Log in](#)
- [Access through your institution](#)
- [Learn about institutional subscriptions](#)

Fig. 1: Functional phosphoproteomics screen identifies the mRNA splicing and processing factor YBX1 downstream of JAK2V617F.

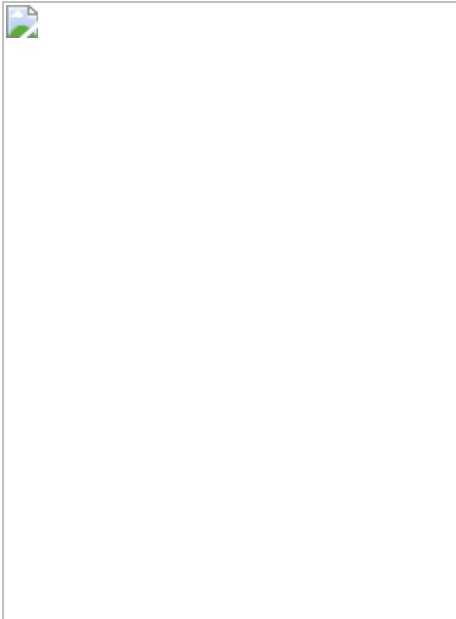


Fig. 2: Inactivation of YBX1 selectively sensitizes JAK2VF cells to apoptosis induced by JAK inhibitor.



Fig. 3: Targeting YBX1 in JAK2VF cells promotes intron retention.



Fig. 4: Jak2-mutated clones are selectively vulnerable to inhibition of ERK signalling.



Data availability

The MS raw data files and Maxquant output files reported in this manuscript are available at ProteomeXchange Consortium with the data identifier PXD006921. RNA-seq data have been deposited in the Gene expression Omnibus database with accession number GSE123417. ChIP-Seq data has been deposited to the Gene expression Omnibus database with the accession code GSE154025 for mouse and GSE146717 for human. All other data supporting the findings of this study are available from corresponding authors upon reasonable request. [Source data](#) are provided with this paper.

References

1. 1.

Darnell, J. E., Jr, Kerr, I. M. & Stark, G. R. Jak-STAT pathways and transcriptional activation in response to IFNs and other extracellular signaling proteins. *Science* **264**, 1415–1421 (1994).

[ADS](#) [CAS](#) [Article](#) [PubMed](#) [Google Scholar](#)

2. 2.

Perner, F., Perner, C., Ernst, T. & Heidel, F. H. Roles of JAK2 in aging, inflammation, hematopoiesis and malignant transformation. *Cells* **8**, 854 (2019).

[CAS](#) [Article](#) [PubMed Central](#) [Google Scholar](#)

3. 3.

Genovese, G. et al. Clonal hematopoiesis and blood-cancer risk inferred from blood DNA sequence. *N. Engl. J. Med.* **371**, 2477–2487 (2014).

[Article](#) [PubMed](#) [PubMed Central](#) [Google Scholar](#)

4. 4.

Jaiswal, S. et al. Age-related clonal hematopoiesis associated with adverse outcomes. *N. Engl. J. Med.* **371**, 2488–2498 (2014).

[Article](#) [PubMed](#) [PubMed Central](#) [Google Scholar](#)

5. 5.

Forbes, S. A. et al. COSMIC: somatic cancer genetics at high-resolution. *Nucleic Acids Res.* **45** (D1), D777–D783 (2017).

[CAS](#) [Article](#) [PubMed](#) [Google Scholar](#)

6. 6.

Deininger, M. et al. The effect of long-term ruxolitinib treatment on JAK2p.V617F allele burden in patients with myelofibrosis. *Blood* **126**, 1551–1554 (2015).

[CAS](#) [Article](#) [PubMed](#) [PubMed Central](#) [Google Scholar](#)

7. 7.

Harrison, C. N. et al. Long-term findings from COMFORT-II, a phase 3 study of ruxolitinib vs best available therapy for myelofibrosis. *Leukemia* **30**, 1701–1707 (2016).

[CAS](#) [Article](#) [PubMed](#) [PubMed Central](#) [Google Scholar](#)

8. 8.

Humphrey, S. J., Azimifar, S. B. & Mann, M. High-throughput phosphoproteomics reveals in vivo insulin signaling dynamics. *Nat. Biotechnol.* **33**, 990–995 (2015).

[CAS](#) [Article](#) [PubMed](#) [Google Scholar](#)

9. 9.

Hsu, T. Y. et al. The spliceosome is a therapeutic vulnerability in MYC-driven cancer. *Nature* **525**, 384–388 (2015).

[ADS](#) [CAS](#) [Article](#) [PubMed](#) [PubMed Central](#) [Google Scholar](#)

10. 10.

Climente-González, H., Porta-Pardo, E., Godzik, A. & Eyras, E. The functional impact of alternative splicing in cancer. *Cell Rep.* **20**, 2215–2226 (2017).

[Article](#) [PubMed](#) [Google Scholar](#)

11. 11.

Dolfini, D. & Mantovani, R. YB-1 (YBX1) does not bind to Y/CCAAT boxes in vivo. *Oncogene* **32**, 4189–4190 (2013).

[CAS](#) [Article](#) [PubMed](#) [Google Scholar](#)

12. 12.

Stickeler, E. et al. The RNA binding protein YB-1 binds A/C-rich exon enhancers and stimulates splicing of the CD44 alternative exon v4. *EMBO J.* **20**, 3821–3830 (2001).

[CAS](#) [Article](#) [PubMed](#) [PubMed Central](#) [Google Scholar](#)

13. 13.

Wei, W. J. et al. YB-1 binds to CAUC motifs and stimulates exon inclusion by enhancing the recruitment of U2AF to weak polypyrimidine tracts. *Nucleic Acids Res.* **40**, 8622–8636 (2012).

[CAS](#) [Article](#) [PubMed](#) [PubMed Central](#) [Google Scholar](#)

14. 14.

Kaelin, W. G., Jr. The concept of synthetic lethality in the context of anticancer therapy. *Nat. Rev. Cancer* **5**, 689–698 (2005).

[CAS](#) [Article](#) [PubMed](#) [Google Scholar](#)

15. 15.

McCubrey, J. A. et al. Involvement of p53 and Raf/MEK/ERK pathways in hematopoietic drug resistance. *Leukemia* **22**, 2080–2090 (2008).

[CAS](#) [Article](#) [PubMed](#) [Google Scholar](#)

16. 16.

Meyer, S. C. Mechanisms of resistance to JAK2 inhibitors in myeloproliferative neoplasms. *Hematol. Oncol. Clin. North Am.* **31**, 627–642 (2017).

[Article](#) [PubMed](#) [Google Scholar](#)

17. 17.

Stivala, S. et al. Targeting compensatory MEK/ERK activation increases JAK inhibitor efficacy in myeloproliferative neoplasms. *J. Clin. Invest.* **129**, 1596–1611 (2019).

[Article](#) [PubMed](#) [PubMed Central](#) [Google Scholar](#)

18. 18.

Humphrey, S. J., Karayel, O., James, D. E. & Mann, M. High-throughput and high-sensitivity phosphoproteomics with the EasyPhos platform. *Nat. Protocols* **13**, 1897–1916 (2018).

[CAS](#) [Article](#) [PubMed](#) [Google Scholar](#)

19. 19.

Kulak, N. A., Pichler, G., Paron, I., Nagaraj, N. & Mann, M. Minimal, encapsulated proteomic-sample processing applied to copy-number estimation in eukaryotic cells. *Nat. Methods* **11**, 319–324 (2014).

[CAS](#) [Article](#) [PubMed](#) [PubMed Central](#) [Google Scholar](#)

20. 20.

Cox, J. & Mann, M. MaxQuant enables high peptide identification rates, individualized p.p.b.-range mass accuracies and proteome-wide protein quantification. *Nat. Biotechnol.* **26**, 1367–1372 (2008).

[CAS](#) [Article](#) [Google Scholar](#)

21. 21.

Tyanova, S. & Cox, J. Perseus: a bioinformatics platform for integrative analysis of proteomics data in cancer research. *Methods Mol. Biol.* **1711**, 133–148 (2018).

[CAS](#) [Article](#) [PubMed](#) [Google Scholar](#)

22. 22.

Dobin, A. et al. STAR: ultrafast universal RNA-seq aligner. *Bioinformatics* **29**, 15–21 (2013).

[CAS](#) [Article](#) [PubMed](#) [PubMed Central](#) [Google Scholar](#)

23. 23.

Liao, Y., Smyth, G. K. & Shi, W. featureCounts: an efficient general purpose program for assigning sequence reads to genomic features. *Bioinformatics* **30**, 923–930 (2014).

[CAS](#) [Article](#) [PubMed](#) [PubMed Central](#) [Google Scholar](#)

24. 24.

Ritchie, M. E. et al. limma powers differential expression analyses for RNA-sequencing and microarray studies. *Nucleic Acids Res.* **43**, e47 (2015).

[Article](#) [PubMed](#) [PubMed Central](#) [Google Scholar](#)

25. 25.

Romero, J. P. et al. EventPointer: an effective identification of alternative splicing events using junction arrays. *BMC Genomics* **17**, 467 (2016).

[Article](#) [PubMed](#) [PubMed Central](#) [Google Scholar](#)

26. 26.

Schnöder, T. M. et al. Cell autonomous expression of CXCL-10 in JAK2V617F-mutated MPN. *J. Cancer Res. Clin. Oncol.* **143**, 807–820 (2017).

[PubMed](#) [Google Scholar](#)

27. 27.

Webb, C. H. & Hertel, K. J. Preparation of splicing competent nuclear extracts. *Methods Mol. Biol.* **1126**, 117–121 (2014).

[Article](#) [PubMed](#) [PubMed Central](#) [Google Scholar](#)

28. 28.

Uckelmann, H. J. et al. Therapeutic targeting of preleukemia cells in a mouse model of *NPM1* mutant acute myeloid leukemia. *Science* **367**, 586–590 (2020).

[ADS](#) [CAS](#) [Article](#) [PubMed](#) [Google Scholar](#)

29. 29.

Lu, Z. H., Books, J. T. & Ley, T. J. YB-1 is important for late-stage embryonic development, optimal cellular stress responses, and the prevention of premature senescence. *Mol. Cell. Biol.* **25**, 4625–4637 (2005).

[CAS](#) [Article](#) [PubMed](#) [PubMed Central](#) [Google Scholar](#)

30. 30.

Mullally, A. et al. Physiological Jak2V617F expression causes a lethal myeloproliferative neoplasm with differential effects on hematopoietic stem and progenitor cells. *Cancer Cell* **17**, 584–596 (2010).

[CAS](#) [Article](#) [PubMed](#) [PubMed Central](#) [Google Scholar](#)

31. 31.

Cosgun, K. N. et al. Kit regulates HSC engraftment across the human-mouse species barrier. *Cell Stem Cell* **15**, 227–238 (2014).

[CAS](#) [Article](#) [PubMed](#) [Google Scholar](#)

32. 32.

Schnöder, T. M. et al. Epo-induced erythroid maturation is dependent on Plcy1 signaling. *Cell Death Differ.* **22**, 974–985 (2015).

[ADS](#) [Article](#) [PubMed](#) [Google Scholar](#)

33. 33.

Till, J. E. & McCULLOCH, E. A. A direct measurement of the radiation sensitivity of normal mouse bone marrow cells. *Radiat. Res.* **14**, 213–222 (1961).

[ADS](#) [CAS](#) [Article](#) [PubMed](#) [Google Scholar](#)

34. 34.

Quintás-Cardama, A. et al. Preclinical characterization of the selective JAK1/2 inhibitor INCB018424: therapeutic implications for the treatment of myeloproliferative neoplasms. *Blood* **115**, 3109–3117 (2010).

[Article](#) [PubMed](#) [PubMed Central](#) [Google Scholar](#)

35. 35.

Heidel, F. H. et al. The cell fate determinant Llgl1 influences HSC fitness and prognosis in AML. *J. Exp. Med.* **210**, 15–22 (2013).

[CAS](#) [Article](#) [PubMed](#) [PubMed Central](#) [Google Scholar](#)

36. 36.

Heidel, F. H. et al. Genetic and pharmacologic inhibition of β-catenin targets imatinib-resistant leukemia stem cells in CML. *Cell Stem Cell* **10**, 412–424 (2012).

[CAS](#) [Article](#) [PubMed](#) [PubMed Central](#) [Google Scholar](#)

37. 37.

Arreba-Tutusaus, P. et al. Impact of FLT3-ITD location on sensitivity to TKI-therapy in vitro and in vivo. *Leukemia* **30**, 1220–1225 (2016).

[CAS Article](#) [PubMed](#) [Google Scholar](#)

[Download references](#)

Acknowledgements

We thank A. Fenske (Central Animal Facility, OvGU Magdeburg) and M. van der Wall (Central Animal Facility, University Hospital Jena) for support with animal care; the Animal Facility of the Leibniz Institute on Aging Jena for providing NSGW41 animals; R. Hartig (FACS Core Facility, Medical Faculty, and CRC854, OvGU Magdeburg) and K. Schubert (FACS Core Facility, Leibniz-Institute on Aging, Jena) for support with cell sorting, M. Milsom (DKFZ, Heidelberg) for providing constructs; S. Frey, A. Sammt and C. Kathner-Schaffert for technical assistance; K. Mayr, I. Paron and G. Sowa for their assistance and support in the mass spectrometry analysis (MPI Biochemistry); M. Driessen for RNA sequencing and S.-H. Yu for ChIP sequencing analysis (Bioinformatics Core Facility, MPI Biochemistry); and Th. Fischer (Magdeburg), K.L. Rudolph (Jena) and C. Müller-Tidow (Heidelberg) for helpful comments and discussions.

Author information

Author notes

1. These authors contributed equally: Ashok Kumar Jayavelu, Tina M. Schnöder
2. These authors jointly supervised this work: Matthias Mann, Florian H. Heidel

Affiliations

1. Max Planck Institute of Biochemistry, Munich, Germany

Ashok Kumar Jayavelu, Arno Meiler, Gurumoorthy Krishnamoorthy & Matthias Mann

2. Innere Medizin II, Hämatologie und Onkologie, Universitätsklinikum Jena, Jena, Germany

Tina M. Schnöder, Florian Perner, Nicolas Huber, Juliane Mohr, Thomas Ernst, Andreas Hochhaus & Florian H. Heidel

3. Innere Medizin C, Universitätsmedizin Greifswald, Greifswald, Germany

Tina M. Schnöder & Florian H. Heidel

4. Department of Haematology and Oncology, Center of Internal Medicine, Otto von Guericke University Medical Center, Magdeburg, Germany

Carolin Herzog & Bärbel Edelmann-Stephan

5. QIMR Berghofer Medical Research Institute, Brisbane, Queensland, Australia

Rebecca Austin & Steven W. Lane

6. Cancer Care Services, Royal Brisbane and Women's Hospital, Brisbane, Queensland, Australia

Rebecca Austin & Steven W. Lane

7. University of Queensland, Brisbane, Queensland, Australia

Rebecca Austin & Steven W. Lane

8. Department of Nephrology and Endocrinology, Center of Internal Medicine, Otto von Guericke University Medical Center, Magdeburg, Germany

Sabine Brandt & Peter R. Mertens

9. Azienda Ospedaliero–Universitaria di Bologna, Bologna, Italy

Francesca Palandri

10. Pathology, Klinikum Ernst-von-Bergmann, Potsdam, Germany

Nicolas Schröder

11. Institute for Clinical Chemistry and Pathobiochemistry, Center of Internal Medicine, Otto von Guericke University Medical Center, Magdeburg, Germany

Berend Isermann

12. Institute for Biochemistry and Molecular Biology, University of Freiburg, Freiburg, Germany

Frank Edlich

13. Faculty of Biology, University of Freiburg, Freiburg, Germany

Frank Edlich & Robert Zeiser

14. BIOSS, Centre for Biological Signaling Studies, Freiburg, Germany

Frank Edlich

15. Basepair Technology Inc, New York, NY, USA

Amit U. Sinha

16. Institut für Humangenetik, Universitätsklinikum Jena, Jena, Germany

Martin Ungelenk & Christian A. Hübner

17. Department of Hematology and Oncology, Medical Center, Faculty of Medicine, University of Freiburg, Freiburg, Germany

Robert Zeiser

18. Leibniz Institute on Aging, Fritz Lipmann Institute, Jena, Germany

Susann Rahmig, Claudia Waskow & Florian H. Heidel

19. Immunology of Aging, Leibniz Institute on Aging, Fritz Lipmann Institute, Jena, Germany

Susann Rahmig & Claudia Waskow

20. Faculty of Biological Sciences, Friedrich Schiller University Jena, Jena, Germany

Claudia Waskow

21. Department of Chemistry, University of Sheffield, Sheffield, UK

Iain Coldham

22. Medical Department III for Haematology and Oncology, Klinikum rechts der Isar, Technische Universität München, Munich, Germany

Stefanie Jilg & Philipp J. Jost

23. Division of Oncology, Department of Internal Medicine, Medical University of Graz (MUG), Graz, Austria

Philipp J. Jost

24. Division of Hematology, Department of Medicine, Brigham and Women's Hospital and Harvard Medical School, Boston, MA, USA

Ann Mullally

25. Clinic for Hematology, Oncology and Tumor Immunology, Charite University, Berlin, Germany

Lars Bullinger

Authors

1. Ashok Kumar Jayavelu
[View author publications](#)

You can also search for this author in [PubMed](#) [Google Scholar](#)

2. Tina M. Schnöder
[View author publications](#)

You can also search for this author in [PubMed](#) [Google Scholar](#)

3. Florian Perner
[View author publications](#)

You can also search for this author in [PubMed](#) [Google Scholar](#)

4. Carolin Herzog
[View author publications](#)

You can also search for this author in [PubMed](#) [Google Scholar](#)

5. Arno Meiler
[View author publications](#)

You can also search for this author in [PubMed](#) [Google Scholar](#)

6. Gurumoorthy Krishnamoorthy
[View author publications](#)

You can also search for this author in [PubMed](#) [Google Scholar](#)

7. Nicolas Huber
[View author publications](#)

You can also search for this author in [PubMed](#) [Google Scholar](#)

8. Juliane Mohr
[View author publications](#)

You can also search for this author in [PubMed](#) [Google Scholar](#)

9. Bärbel Edelmann-Stephan

[View author publications](#)

You can also search for this author in [PubMed](#) [Google Scholar](#)

10. Rebecca Austin

[View author publications](#)

You can also search for this author in [PubMed](#) [Google Scholar](#)

11. Sabine Brandt

[View author publications](#)

You can also search for this author in [PubMed](#) [Google Scholar](#)

12. Francesca Palandri

[View author publications](#)

You can also search for this author in [PubMed](#) [Google Scholar](#)

13. Nicolas Schröder

[View author publications](#)

You can also search for this author in [PubMed](#) [Google Scholar](#)

14. Berend Isermann

[View author publications](#)

You can also search for this author in [PubMed](#) [Google Scholar](#)

15. Frank Edlich

[View author publications](#)

You can also search for this author in [PubMed](#) [Google Scholar](#)

16. Amit U. Sinha

[View author publications](#)

You can also search for this author in [PubMed](#) [Google Scholar](#)

17. Martin Ungelenk

[View author publications](#)

You can also search for this author in [PubMed](#) [Google Scholar](#)

18. Christian A. Hübner

[View author publications](#)

You can also search for this author in [PubMed](#) [Google Scholar](#)

19. Robert Zeiser

[View author publications](#)

You can also search for this author in [PubMed](#) [Google Scholar](#)

20. Susann Rahmig

[View author publications](#)

You can also search for this author in [PubMed](#) [Google Scholar](#)

21. Claudia Waskow

[View author publications](#)

You can also search for this author in [PubMed](#) [Google Scholar](#)

22. Iain Coldham

[View author publications](#)

You can also search for this author in [PubMed](#) [Google Scholar](#)

23. Thomas Ernst

[View author publications](#)

You can also search for this author in [PubMed](#) [Google Scholar](#)

24. Andreas Hochhaus

[View author publications](#)

You can also search for this author in [PubMed](#) [Google Scholar](#)

25. Stefanie Jilg

[View author publications](#)

You can also search for this author in [PubMed](#) [Google Scholar](#)

26. Philipp J. Jost

[View author publications](#)

You can also search for this author in [PubMed](#) [Google Scholar](#)

27. Ann Mullally

[View author publications](#)

You can also search for this author in [PubMed](#) [Google Scholar](#)

28. Lars Bullinger

[View author publications](#)

You can also search for this author in [PubMed](#) [Google Scholar](#)

29. Peter R. Mertens

[View author publications](#)

You can also search for this author in [PubMed](#) [Google Scholar](#)

30. Steven W. Lane

[View author publications](#)

You can also search for this author in [PubMed](#) [Google Scholar](#)

31. Matthias Mann

[View author publications](#)

You can also search for this author in [PubMed](#) [Google Scholar](#)

32. Florian H. Heidel

[View author publications](#)

You can also search for this author in [PubMed](#) [Google Scholar](#)

Contributions

Conception and design: A.K.J., T.M.S., S.W.L., F.H.H. Development of methodology: A.K.J., T.M.S., C.H., M.M., F.H.H. Acquisition of data (provided animals, acquired and managed patients, provided facilities etc.): T.M.S., A.K.J., G.K., C.H., F. Perner., J.M., B.E.-S., N.S., T.E., A.M., B.I., P.R.M., S.W.L., M.M., F.H.H. Analysis and interpretation of data (e.g., computational analysis, statistical analysis): A.K.J., C.H., T.M.S., A.M., N.H., S.J., A.S., F.E., M.U., T.E., C.A.H., A.H., L.B., S.W.L., F.H. Writing, review and/or revision of the manuscript: A.K.J., T.M.S., F. Palandri, F. Perner., L.B., S.W.L., P.J.J., R.Z., A.M., P.R.M., C.W., B.I., M.M., F.H.H.. Administrative, technical or material support: A.K.J., C.H., T.M.S., J.M., B.E.-S., F. Palandri, G.K., R.A., S.B., N.S., S.J., I.C., A.M., S.R., C.W., M.M., A.H., B.I., P.R.M. Study supervision: M.M., F.H.H. This work was supported by grants of the German Research Council (DFG; HE6233/4-1 and 4-2 to F.H.H.), by the DFG-Collaborative Research Center (CRC854/2) to P.R.M. (Project A1), B.I. (Project B26N) and F.H.H. (Project A20) and by the Thuringian state program ProExzellenz (RegenerAging–FSU-I-03/14) of the Thuringian Ministry for Economics, Science and Digital Society (TMWWWDG; to F.H.H.). A.K.J. and M.M. were supported by the Max Planck Society for the Advancement of Science and by the German Research Foundation (DFG/Gottfried Wilhelm Leibniz Prize). P.J.J. by DFG (SFB1335) and F. Perner was supported by a DFG fellowship grant (PE-3217/1-1). G.K. was supported by ERC starting grant 635617 and the DFG (SFB-TR128-A1). C.W. was supported by FOR2033-A03, TRR127-A5, WA2837/6-1 and WA2837/7-1. R.Z. was supported by the Deutsche Krebshilfe grant #70113473 and the ERC Consolidator grant (681012 GvHDCure). S.W.L. has received research funding support from the Australian National Health and Medical Research Council (NHMRC).

Corresponding authors

Correspondence to [Matthias Mann](#) or [Florian H. Heidel](#).

Ethics declarations

Competing interests

F.H.H. has served as an advisory board member for and received research funding from Novartis, Celgene and CTI. S.W.L. has served on an advisory board for Novartis Australia. A.H. received research support by Novartis, BMS, Pfizer, Incyte. A.M. has received honoraria from Blueprint Medicines, Roche and Incyte and receives research support from Janssen and Actuate Therapeutics. No potential conflicts of interest were disclosed by the other authors.

Additional information

Peer review information *Nature* thanks Fabienne Meier-Abt, Michael Yaffe and the other, anonymous, reviewer(s) for their contribution to the peer review of this work.

Publisher's note Springer Nature remains neutral with regard to jurisdictional claims in published maps and institutional affiliations.

Extended data figures and tables

[Extended Data Fig. 1 Phosphoproteomic analysis uncovers differential regulation of splicing factors in Jak2-mutated cells.](#)

a, Schematic of the phosphoproteome workflow. Following sample collection, phosphopeptides were enriched using EasyPhos work flow⁸ and analysed in single-run LC-MS/MS. Data were analysed in Maxquant and Perseus. **b**, Quantified phosphosite depth per sample. Samples were measured as biological quadruplicates. **c**, Heatmap of sample correlation matrix of all measured samples (in **b**) based on Pearson correlation values. The reproducibility between the phosphoproteome sample is highlighted. **d**, Summary of identified and quantified class-I phosphosites (localization probability of >0.75) corresponding to number of proteins of this experiment. **e**, Principal component analysis of the samples. **f**, Network map of significantly enriched GO terms (*P* value <0.05) of differentially phosphorylated proteins in JAK2V617F. Phosphorylated proteins

significantly regulated in Jak2V617F were subsequently used as an input for *Cytoscape* to obtain the network. The highlighted sub-network was obtained with P value <0.01 and kappa score >0.6 . Two-sided hypergeometric test, P value correction–Bonferroni stepdown (**g, h**), western blot validation of shRNA library targets. **g**, Pcbp1 protein and **h**, YBX1 protein in mouse JAK2VF cells. $n = 3$ with comparable results. **i**, Pearson correlation profile of the independent shRNA experiments.

Extended Data Fig. 2 Functional consequences of YBX1 depletion in Jak2-mutated cells.

a, In vitro shRNA validation of selected top 15 targets essential for JAK2VF cell survival and growth in the presence (green) and absence (grey) of JAK inhibitor (RUX, 0.5 μ M) measured by proliferation assays (16 technical replicates measured in 2 plates independently, mean). **b**, Immunofluorescence analysis of YBX1 and JAK2 localization in JAKVF positive Ba/F3 cells (left) and mouse JAK2^{VF} positive stem- and progenitor cells (lineage-negative cells) (right panel) (representative image of $n = 3$). **c**, Immunoprecipitation of JAK2 receptor from mouse JAK2VF cells showing binding of YBX1 to mutated JAK2 receptor ($n = 3$ with similar results). **d**, **e**, Percentages of cell growth in JAK2WT (**d**) and JAK2VF cells (**e**) following lentiviral infection with shRNAs targeting *Ybx1* or non-targeting control (shNT) measured by MTS assay. **f**, Representative histogram and bar plot showing ROS levels measured in JAK2VF cells with shRNAs targeting *Ybx1* or control. **g**, Representative histogram and bar plot showing proliferative marker PCNA levels in JAK2VF cells with shRNAs targeting *Ybx1* or control. **h**, Cell cycle analysis after YBX1 inactivation in JAK2VF cells. **d–h**, $n = 4$ independent experiments, mean \pm s.d., two-tailed *t*-test with equal variance. **i**, Representative confocal images of DNA damage marker yH2AX pS139 in JAK2VF cells with shRNAs targeting *Ybx1* or non-targeting control. Cells exposed to UV light for 20 min were used as positive controls ($n = 4$ independent experiments). **j**, FACS plots showing percentage of apoptotic cells in *Jak2*^{+/+} and *Jak2*^{VF/+} mouse BM cells after JAK inhibitor treatment (RUX, 0.5 μ M) after lentiviral knockdown of *Ybx1* (sh1 and sh2) compared to non-targeting control (shNT).

Extended Data Fig. 3 Functional consequences of *Ybx1* deletion in vivo.

a, Schematic representation of the wild-type *Ybx1* allele (Genomic Locus), the targeting vector (Targeting Vector), the desired targeted allele (Targeted Allele), the desired conditional allele flanked by LoxP sequences (Conditional Allele) and the null recombined allele (Recombined Allele) after Cre-mediated recombination of the conditional allele. Triangles indicate *loxP* sequences. **b**, Excision control by genomic PCR on whole bone marrow cells at week 16 following genetic inactivation of *Ybx1* in conditional knockout mice. Representative micrograph of $n = 5$ animals from a total of $n = 9$ controls (+/+) and $n = 9$ knockout (-/-) replicates. **c**, Schematic as in Fig. 2j. FACS plots showing percentage of *Jak2*^{V617F} (CD45.2) cells of *Ybx1*^{+/+} or *Ybx1*^{-/-} recipients. **d**, Histology of liver, spleen and lung of *Jak2*^{V617F}-*Ybx1*^{+/+} and *Jak2*^{V617F}-*Ybx1*^{-/-} recipient mice at week 20 after BMT. Representative micrographs of $n = 9$ individual mouse replicates. Haematoxylin and eosin stain (H&E) at $\times 10$ magnification. Focal leukocyte infiltration (arrows) and haemorrhage (stars) of liver, spleen and lung, respectively. Scale bar: 200 μ m. **e**, Peripheral blood chimerism of lethally irradiated (12 Gy) recipient mice. FACS plots showing abundance of CD45.2 myeloid cells in *Jak2*^{V617F}-*Ybx1*^{+/+} and *Jak2*^{V617F}-*Ybx1*^{-/-} recipient mice at week 20 after BMT. **f**, Design for assessment of steady state haematopoiesis. **g**, White blood count (WBC), Gr-1 positive cells ($\text{Gr}1^+$), haemoglobin (HGB) and platelets (PLT) following genetic inactivation of *Ybx1* (*Ybx1*^{-/-} mice, $n = 10$) compared to *Ybx1*^{+/+} controls ($n = 10$). Data represented as mean \pm s.e.m. **h**, FACS plots showing comparable percentages of LSK cells and HSCs (SLAM⁺CD34⁻L⁻S⁺K⁺ cells) following genetic inactivation of *Ybx1* in conditional knockout mice (compared to wildtype littermate controls). **i**, stem- and progenitor cell numbers per 1×10^6 whole bone marrow cells at week 16 after genetic inactivation of *Ybx1* ($n = 6$; mean \pm s.d.). **j**, FACS plot showing comparable abundance of mature myeloid and erythroid cells following genetic deletion of *Ybx1*. **k**, Total numbers of mature blood cells of the myeloid ($\text{Gr}1^+$), erythroid (TER119⁺), B-lymphoid (CD19) and T-lymphoid (CD3) lineages at week 16 after genetic inactivation of *Ybx1* ($n = 6$; mean \pm s.d.). **l**, Experimental protocol for investigation of haematopoietic progenitor cell

function. **m**, Colony numbers of $Ybx1^{+/+}$ versus $Ybx1^{-/-}$ mouse stem/progenitor cells. Colonies were counted at day 8 after plating (each sample plated in duplicate, $n = 3$ independent experiments, mean \pm s.d.). **n**, Spleen colony numbers counted on day 12 after injection of $Ybx1^{+/+}$ or $Ybx1^{-/-}$ LSK cells into lethally irradiated (12Gy) recipient mice (CFU-S12) ($n = 12$ $Ybx1^{+/+}$; $n = 12$ $Ybx1^{-/-}$ independent biological mouse replicates in $n = 3$ independent cohorts). **o**, BM chimerism of primary recipient mice ($n = 10$ individual biological replicates) at week 20 after BMT. Whole bone marrow chimerism (WBMC) and chimerism of myeloid cells (Gr1⁺ BMC) (left panel). HSPC chimerism (LSK) and HSC chimerism (CD34⁻ LSK) (right panel). Data shown as mean \pm s.d. **p**, BM chimerism of secondary recipient mice ($n = 5$ individual biological replicates) at week 20 after BMT. Whole BM chimerism (WBMC) and chimerism of myeloid cells (Gr1⁺ BMC) (left panel). HSPC chimerism (LSK) and HSC chimerism (CD34⁻ LSK) (right panel). Data shown as mean \pm s.d.

Extended Data Fig. 4 Regulation of YBX1 phosphorylation dynamics in JAK2VF cells.

a, Profile plot showing significantly regulated individual phosphorylated residues of YBX1 in JAK2WT and JAK2VF. Each data point is the averaged median of biological quadruplicate and significance was tested using two-sample test. **b**, Profile plot showing individual phosphorylated residues of YBX1 that are significantly regulated in JAK2WT when unstimulated (control) or stimulated with erythropoietin or erythropoietin + JAK inhibitor. **c**, Profile plot showing significantly regulated individual phosphorylated residues of YBX1 in JAK2VF when unstimulated or stimulated with EPO or EPO + JAK inhibitor. **b**, **c**, Each data point is the averaged median of biological quadruplicate, z-scored (\log_2 phosphosite intensity), and significance was tested using multiple sample test. **d**, Experimental design for phosphoproteome analysis of short-term JAK2 downstream effector kinase inhibitor treatment in JAK2VF cells. $n = 4$ per group, phosphopeptides were enriched using EasyPhos workflow and analysed in single-run LC-MS/MS. **e**, Dot plot showing the successful inhibition of respective targets of the corresponding kinase inhibitor used in this study (ANOVA test with permutation-based FDR < 0.01). **f**, Dot plot

showing changes in quantified YBX1 phosphosites after various kinase inhibitor treatment (ANOVA test, permutation-based FDR < 0.01). The highlighted YBX1 pS30 phosphosite is the only site highly significantly downregulated upon MEK/ERK inhibitor treatment compared to controls.

e, f, Size and colour of the dots are proportional to the phosphosite intensity, z-scored (\log_2 intensity). **g**, Amino acid sequence alignment of YBX1 across different species shows that mouse YBX1 Ser30 and Ser34 are conserved. [Source data](#)

Extended Data Fig. 5 YBX1 interaction with spliceosome components and validation of YBX1-MAPK1 partnership.

a, Study design of mouse YBX1 interactome. $n = 4$ biological replicates and YBX1 interactome analysed in LC-MS/MS. Using *Perseus*, samples were filtered for a minimum of three valid values in at least one group. In total 614 high confident interactors of YBX1 were identified (*t*-test with permutation-based FDR < 0.05) with 260 JAK2VF-specific interactors. **b**, Network representation of YBX1 interacting spliceosomal proteins in JAK2VF cells. The size and colour of the node indicates the abundance of the corresponding proteins (z-scored protein intensity) and the edges are connected by STRING database interactions. **c**, List of significant YBX1-interacting spliceosomal proteins presented according to their spliceosome complex. **d**, Spliceosome proteins interacting with YBX1 participate in spliceosome assembly reaction in a stepwise manner to excise intronic sequences from immature mRNA to form a mature mRNA. **e**, Network representation of YBX1 interactome (regulated in both JAK2WT and JAK2VF) based on annotation keywords. The keywords are highlighted in colours according to the protein function. $n = 4$ biological replicates, *t*-test with permutation-based FDR < 0.05. **f**, Scatter plot of YBX1 interactome in JAK2VF vs control. YBX1 interactome is enriched for GO term mRNA splicing factor (green) and Ribonucleoproteins (blue) assessed by Fisher's exact test. Fold enrichment of YBX1 and MAPK1 in JAK2VF cells compared to IgG control plotted against $-\log_{10}$ Student *t*-test *P* value. **g**, Scatter plot of YBX1 interactome in DMSO vs JAK inhibitor (RUX 0.5 μ M, 4 h)-treated JAK2VF cells. Fold enrichment of MAPK1 in DMSO vs JAK inhibitor plotted against $-\log_{10}$ Student's *t*-test *P* value. **h**,

Immunoprecipitation of YBX1 from mouse JAK2VF cells ± RUX, 0.5 – μ M for 4 h and analysed for interaction with MAPK1 by western blot analysis using ERK1/2 antibody. Representative images from $n = 3$ biological experiments. [Source data](#)

Extended Data Fig. 6 YBX1 phospho-null mutants display impaired nuclear localization and increased sensitivity to JAK inhibitor.

a, Western blot showing the expression of YBX1 phosphomutants in Ba/F3 JAK2VF cells as indicated. **b**, Confocal images of YBX1 localization (Red) in YBX1 phosphomutants expressing Ba/F3 JAK2VF cells. Cells were counterstained with DAPI and GFP confirms the phosphomutant expression. **a b**, Representative images from $n = 3$ biological experiments. **c**, Bar plot showing quantification of nuclear YBX1 expression in YBX1 phosphomutants expressing Ba/F3 JAK2VF cells; P values were determined by two-tailed t -test. Control ($n = 67$): min = 15.39; max = 33.01; whisker = [15.39–33.01]; median = [24.74], S1($n = 70$): min = 4.14; max = 9.75; whisker = [4.14–9.75]; median = [7.0053], S2($n = 64$): min = 5.32; max = 14.11; whisker = [5.32–14.11]; median = [7.9], S3($n = 57$): min = 4.44; max = 17.6; whisker = [4.44–17.6]; median = [11.4], S4($n = 72$): min = 13.32; max = 23.82; whisker = [13.32–23.82]; median = [19.3], S5($n = 61$): min = 13.08; max = 27.97; whisker = [13.08–27.97]; median = [22.05], S6($n = 57$): min = 18.89; max = 30.04; whisker = [18.89–30.04]; median = [22.92], S7($n = 60$): min = 16.69; max = 32.53; whisker = [16.69–32.53]; median = [24.65]. **d**, Cell growth curve of YBX1 phosphomutants expressing Ba/F3 JAK2VF cells following treatment with increase doses of JAK inhibitor (1 nM–10 μ M RUX) measured by MTS assay. $n = 4$ independent experiments each with 8 technical replicates. **e**, FACS plots showing induction of apoptosis in Ba/F3 JAK2VF cells expressing YBX1 phosphomutants following JAK inhibitor treatment (RUX, 0.5 μ M) compared to untreated YBX1 wild-type Ba/F3 JAK2VF cells. **f**, Bar plot shows quantification of the percentages of apoptotic (annexin V- and 7-AAD-positive) cells. $n = 6$ independent experiments since YBX1 phosphomutants endogenously express GFP, $n = 3$ for annexin V–APC staining and $n = 3$ for 7-AAD–APC staining (error bars represent mean \pm s.d.).

Extended Data Fig. 7 MEK-inhibition prevents YBX1 nuclear localization in Jak2-mutated cells.

a, Confocal images of YBX1 localization (Red) in Ba/F3 JAK2VF cells after treatment for 2 h with RUX (0.5 μ M), MEK inhibitor (2 μ M), the ERK inhibitor trametinib (Tram; 100 and 200 nM), RUX + Tram or DMSO (control). Cells were counterstained with DAPI. **b**, Bar plot shows quantification of nuclear YBX1 expression in Ba/F3 JAK2VF cells ($n \geq 3$ independent imaging experiments, P value determined by Student's t -test). DMSO ($n = 67$): min = 7.05; max = 27.27; whisker = [7.05–27.27]; median = [15.01], RUX ($n = 77$): min = 6.6; max = 35.8; whisker = [6.6–35.8]; median = [16.39], CGP57380 ($n = 89$): min = 3.2; max = 16.35; whisker = [3.2–16.35]; median = [8.35], Tram ($n = 67$): min = 2.44; max = 14.18; whisker = [2.44–14.18]; median = [12.01], Tram ($n = 62$): min = 2.5; max = 17.96; whisker = [2.5–17.96]; median = [12.01], Tram + RUX ($n = 64$): min = 3.44; max = 19.23; whisker = [3.44–19.23]; median = [13.04], MEK inhibitor + RUX ($n = 68$): min = 4.06 max = 14.68; whisker = [4.06–14.68]; median = [13.01]. **c**, Bubble plot showing the regulation of human YBX1 pS32 and pS36 phosphorylation in HEL cells treated with RUX (0.5 μ M), CGP57380 (10 μ M), Tram (500 nM and 2 μ M) or DMSO (control) for 4 h in vitro. Phosphorylation status of MAPK and JAK2 is shown as successful inhibition of respective targets of the corresponding kinase inhibitors. $n = 4$ biological samples per group. Size and colour of bubbles are proportional to the z-scored \log_2 phosphosite intensity; significance assessed using multiple sample test. **d**, Confocal images of YBX1 localization (red) in HEL cells treated with inhibitors or DMSO for 2 h. Cells were counterstained with DAPI. $n = 3$ biological experiments. **e**, Bar plot shows quantification of nuclear YBX1 expression in HEL cells; P values were determined by Student's t -test. DMSO ($n = 44$): min = 17.51; max = 34.56; whisker = [17.51–34.56]; median = [24.30], RUX ($n = 44$): min = 13.04; max = 36.92; whisker = [13.04–36.92]; median = [23.9], MEK inhibitor ($n = 41$): min = 7.62; max = 15.36; whisker = [7.62–15.36]; median = [11.89], Tram ($n = 48$): min = 6.38; max = 19.03; whisker = [6.38–19.03]; median = [12.01], Tram + RUX ($n = 55$): min = 3.31; max = 19.19; whisker = [3.31–19.19]; median = [13.04], MEK inhibitor + RUX ($n = 49$): min = 4.32; max = 19.46; whisker = [4.32–19.46]; median = [13.01]. **f**,

Immunoprecipitation of YBX1 from Ba/F3 JAK2VF cells expressing YBX1 phosphomutants. $n = 3$ independent experiments. [Source data](#)

Extended Data Fig. 8 Nuclear YBX1 regulates *Mknk1* mRNA splicing in JAK2VF cells.

a, Experimental design of RNA sequencing and data analysis. **b**, Bars represent number of retained intron events significantly upregulated in YBX1-depleted cells with two-tailed test P value < 0.05 (1,064 RI events), then filtered for P value < 0.01 and ΔPSI 0.1, reducing the number to 472 highly significant RI events. **c**, Network map displaying enrichment of gene sets in the 472 highly significant RI events. Each node represents significantly enriched gene sets. Clusters of functionally related gene sets are circled, and labels are highlighted. Two-sided hypergeometric test, P value correction–Bonferroni step down. **d**, Visualization of spliced *Mknk1* mRNA product after in vitro splicing assay. Nuclear extracts with and without YBX1 knockdown and with and without ATP were incubated for 2 h with biotin-labelled *Mknk1* pre-mRNA (exon 12–exon 13). mRNA was isolated and reverse transcribed, PCR was performed using the primers at the indicated arrow, and products were agarose gel resolved and visualized using gel-red stain. Representative images from $n = 3$ biological experiments. **e, f**, Flow cytometric analysis of MKNK1 protein expression rescue experiment in CRISPR–Cas9-induced YBX1 knockout mouse JAK2VF cells upon nonsense-mediated decay (NMD) inhibition. Representative flow cytometry histogram and violin plot showing quantification of MKNK1–DyLight 649 mean fluorescence intensity (MFI) upon **e**, compound C treatment (NMD inhibitor (dorsomorphin), termed CC, 10 μM , for 24 h), and **f**, VG-1 treatment (5 μM and 10 μM , for 20 h) ($n = 3$, two-sided t -test; mean \pm s.d.). **g**, Genomic track profile of human *MKNK1*, *ARAF* and *BRAF* loci in HEL cells from YBX1 ChIP sequence data set ($n = 2$). **h**, Genomic track profile of mouse *Mknk1*, *Araf* and *Braf* loci in Ba/F3 JAK2VF cells from YBX1 ChIP sequence data set. $n = 3$ biological experiments. Genomic track profile of human and mouse *Prkcb* shown as positive control from the YBX1 ChIP-seq data set compared to IgG controls. **i**, Western blot showing the regulation of MKNK1 protein abundance in YBX1 phosphomutants expressing Ba/F3 JAK2VF cells as indicated. $n = 3$ independent experiments. [Source data](#)

Extended Data Fig. 9 Targeting *Mknk1* deregulates ERK signalling in *Jak2*-mutated cells.

a, Unsupervised hierarchical clustering of significantly down regulated phosphosites ($n = 2,390$ sites) in human HEL cells following inactivation of *YBX1* by two independent shRNAs compared to non-targeting control. $n = 4$ biological replicates. Heatmap represents z-scored and averaged \log_2 phosphosite intensity, significance by ANOVA test with permutation-based FDR < 0.01 . **b**, Kinase-substrate motifs significantly downregulated in *YBX1*-targeted HEL cells are shown including Benjamini–Hochberg FDR value ($-\log_{10}$). **c**, ERK substrate motifs significantly downregulated and shared between *Ybx1*-targeted mouse and human JAK2VF cells. **d**, Western blot analysis of total protein abundance and phosphorylation of JAK2 downstream targets upon treatment with JAK inhibitor and/or genetic inactivation of *YBX1* by RNAi. GAPDH used as loading control. Representative images from $n = 3$ independent experiments. **e**, **f**, Bar plots show the mean fluorescence intensity of pERK levels measured in human HEL (**e**; $n = 3$) and in patient *JAK2*-mutated cells (**f**; $n = 4$ independent biological replicates from 4 individual patients) following genetic inactivation of *YBX1* by RNAi with or without drug treatment as indicated. Representative FACS plots shown in Fig. 4d. Data shown as mean \pm s.d. and P value determined by two-tailed Student's *t*-test. **g**, Western blot validation of *Mknk1*-targeting shRNAs in mouse Ba/F3 JAK2VF cells. **h**, Representative western blot analysis of pERK upon genetic inactivation of *Mknk1* in Ba/F3 JAK2VF cells. $n = 4$ with comparable results. **i**, Growth curve of JAK2VF cells following lentiviral infection with shRNAs targeting *Mknk1* or non-targeting control and treatment with increase doses of JAK inhibitor (1nM–10 μ M RUX) measured by MTS assay. $n = 4$, each with 8 technical replicates. **j**, Percentage of apoptotic JAK2VF cells following lentiviral knockdown of *Mknk1* (sh2, sh3 \pm RUX 0.5 μ M) or infection with non-targeting control (shSCR) ($n = 4$, two-tailed Student *t*-test, mean \pm s.d.). [Source data](#)

Extended Data Fig. 10 MCL-1 rescue of *Ybx1*-targeted cells and phosphoproteome analysis of primary *Jak2*-mutated cells upon JAK inhibitor treatment.

a, Proteome analysis of mouse *Jak2*-mutated cells following inactivation of *Ybx1* by two shRNAs compared to non-targeting control. Heatmap representation of significantly enriched GO term biological processes in YBX1-depleted JAK2VF cells assessed by Fisher's exact test (P ($-\log_{10}$) shown). **b**, Quantification of MCL-1 phosphosite pT144 in sh1Ybx1, sh2Ybx1 and shNT control in mouse JAK2VF cells. The y axis is the \log_2 intensity of the phosphopeptide ($n = 4$ biological replicates, two-tailed Student *t*-test). shNT: min = 23.8; max = 24.7; whisker = [23.8–24.7]; box = [24–24.2], sh1Ybx1: min = 19.8; max = 22; whisker = [19.8–22]; box = [21.3–21.6], sh2Ybx1: min = 19.2; max = 22.4; whisker = [19.2–22.4]; box = [21.8–22.4]. **c**, Scatter dot plot of MCL-1 phosphosite pT144 after respective kinase inhibitor treatment ($n = 3$, biological replicates, P values using two-tailed Student *t*-test, error bars represent \pm s.d.). The y axis is the z-scored, \log_2 phosphopeptide intensity. DMSO: min = -0.09; max = 1.02; whisker = [-0.09 to 1.02], RUX: min = -0.554; max = 0.135; whisker = [-0.55 to 0.135], AKT inhibitor: min = 1.071; max = 1.263; whisker = [1.07–1.2634], PI3Ki: min = -1.008; max = -0.89; whisker = [-1.008 to 0.89], MEK inhibitor: min = -1.266; max = -0.699; whisker = [-1.266 to 0.699]. **d**, Western blot analysis of MCL-1, YBX1, BIM and BCL-XL following genetic inactivation of *Ybx1* with four different shRNA constructs, compared to non-targeting control. $n = 3$ independent experiments. **e**, Measurement of apoptosis (annexin V- and Sytox-positive cells) after genetic inactivation of *Ybx1* and concomitant JAK inhibitor treatment (RUX, 100 nM, 500 nM). Rescue by ectopic overexpression of MCL-1 ($n = 4$ independent experiments, two-tailed *t*-test). **f**, Western blot analysis of Ba/F3 JAK2VF cells showing downregulation of MKN1 protein abundance following overnight combination treatment with RUX and Tram. $n = 3$ biological independent experiments. **g**, Peripheral blood cell analysis of human cell chimerism in NSG-W41 humanized mice at week 4 and 20 ($n = 5$ per cohort). **h**, Heatmap shows unsupervised hierarchical clustering of significantly regulated (*t*-test with permutation-based FDR < 0.01) phosphosites with ($n = 24$) and without ($n = 24$) JAK inhibitor treatment in *Jak2*-mutated primary patient samples. Phosphoproteome analysis of *Jak2*-mutated primary patient samples (total $n = 48$) samples following in vitro ($n = 18$, JAK inhibitor treatment for 2 h) or in vivo ($n = 6$, 2 h post dosing of RUX samples) exposure to ruxolitinib. **i**, Network map of significantly enriched GO terms (P value <0.01) of

dephosphorylated proteins upon JAK inhibitor treatment. Two-sided hypergeometric test, *P* value correction–Bonferroni step down. **j**, Box plot shows no significant changes in the MAPK1 and MAPK3 phosphorylation in control (*n* = 24) vs JAK inhibitor treated (*n* = 24) patient samples. MAPK1pT185 (DMSO): min = 19.61; max = 24.82; whisker = [19.61–24.82]; box = [21.34–23.11], MAPK1pT185 (RUX): min = 19.5; max = 24.81; whisker = [19.5–24.81]; box = [21.64–23.72], MAPK1pY187 (DMSO): min = 21.04; max = 26.45; whisker = [21.04–26.45]; box = [23.22–25.46], MAPK1pY187(RUX): min = 21.09; max = 25.89; whisker = [21.09–25.89]; box = [22.63–24.77], MAPK3pT202(DMSO): min = 19.72; max = 26.06; whisker = [19.72–26.06]; box = [21.46–24.78], MAPK3pT202 (RUX): min = 20.41; max = 26.93; whisker = [20.41–26.93]; box = [22.05–23.88], MAPK3pY204 (DMSO): min = 20.70; max = 26.51; whisker = [20.70–26.51]; box = [22.02–24.99], MAPK3pY204 (RUX): min = 20.31; max = 25.76; whisker = [20.31–25.76]; box = [22.72–24.42]. **k**, Box plot shows significant changes in IKBKB, STAT3 and STAT5 phosphorylation in control (*n* = 24) vs JAK inhibitor treated (*n* = 24) patient samples. *P* values as determined by Mann–Whitney test. IKBKBpS697 (DMSO): min = 20.66; max = 25.79; whisker = [20.66–25.79]; box = [22.89–24.40], IKBKBpS697 (RUX): min = 20.66; max = 25.04; whisker = [20.66–25.04]; box = [21.88–23.88], IKBKBpS672 (DMSO): min = 20.71; max = 26.30; whisker = [20.71–26.30]; box = [22.5–23.86], IKBKBpS672 (RUX): min = 18.85; max = 24.73; whisker = [18.85–24.73]; box = [21.44–23.24], STAT5pY699 (DMSO): min = 22.02; max = 25.33; whisker = [22.02–25.33]; box = [22.73–23.63], STAT5pY699 (RUX): min = 19.90; max = 24.83; whisker = [19.90–24.83]; box = [21.8–23.2], STAT3pY705 (DMSO): min = 21.87; max = 26.66; whisker = [21.87–26.66]; box = [22.41–25.62], STAT3pY705 (RUX): min = 20.07; max = 26.17; whisker = [20.07–26.17]; box = [21.22–23.26]. **l**, Schematic depicting the mechanism of YBX1-mediated JAK inhibitor persistence. [Source data](#)

Supplementary information

[Supplementary Figures](#)

This file contains Supplementary Figures 1-7: FACS gating strategy.

Reporting Summary

Supplementary Figures

This file contains Supplementary Figures 8-15: Uncropped western blot images.

Supplementary Table

This file contains Supplementary Table 9.

Source data

Source Data Fig. 1

Source Data Fig. 2

Source Data Extended Data Fig. 4

Source Data Extended Data Fig. 5

Source Data Extended Data Fig. 7

Source Data Extended Data Fig. 8

Source Data Extended Data Fig. 9

Source Data Extended Data Fig. 10

Rights and permissions

Reprints and Permissions

About this article



Check for
updates

Cite this article

Jayavelu, A.K., Schnöder, T.M., Perner, F. *et al.* Splicing factor YBX1 mediates persistence of JAK2-mutated neoplasms. *Nature* **588**, 157–163 (2020). <https://doi.org/10.1038/s41586-020-2968-3>

[Download citation](#)

- Received: 11 December 2018
- Accepted: 15 September 2020
- Published: 25 November 2020
- Issue Date: 03 December 2020
- DOI: <https://doi.org/10.1038/s41586-020-2968-3>

Comments

By submitting a comment you agree to abide by our [Terms](#) and [Community Guidelines](#). If you find something abusive or that does not comply with our terms or guidelines please flag it as inappropriate.

[Access through your institution](#)

[Change institution](#)

[Buy or subscribe](#)

| [Section menu](#) | [Main menu](#) |

- Article
- [Published: 18 November 2020](#)

Small-molecule-induced polymerization triggers degradation of BCL6

- [Mikołaj Ślabicki](#) ORCID: [orcid.org/0000-0001-6317-9296^{1,2,3 na1}](https://orcid.org/0000-0001-6317-9296),
- [Hojong Yoon](#) ORCID: [orcid.org/0000-0002-6062-5489^{4,5 na1}](https://orcid.org/0000-0002-6062-5489),
- [Jonas Koeppel](#) ORCID: [orcid.org/0000-0003-1306-3994^{1,2,3 na1}](https://orcid.org/0000-0003-1306-3994),
- [Lena Nitsch](#)^{1,2,3},
- [Shourya S. Roy Burman](#) ORCID: [orcid.org/0000-0001-9274-9104^{4,5}](https://orcid.org/0000-0001-9274-9104),
- [Cristina Di Genua](#)^{1,2},
- [Katherine A. Donovan](#) ORCID: [orcid.org/0000-0002-8539-5106^{4,5}](https://orcid.org/0000-0002-8539-5106),
- [Adam S. Sperling](#)^{1,2},
- [Moritz Hunkeler](#) ORCID: [orcid.org/0000-0003-0246-1188^{4,5}](https://orcid.org/0000-0003-0246-1188),
- [Jonathan M. Tsai](#)^{1,2},
- [Rohan Sharma](#)²,
- [Andrew Guirguis](#) ORCID: [orcid.org/0000-0003-3134-0596^{1,2}](https://orcid.org/0000-0003-3134-0596),
- [Charles Zou](#)²,
- [Priya Chudasama](#)⁶,
- [Jessica A. Gasser](#)^{1,2},
- [Peter G. Miller](#)^{1,2},
- [Claudia Scholl](#) ORCID: [orcid.org/0000-0001-6768-322X⁷](https://orcid.org/0000-0001-6768-322X),
- [Stefan Fröhling](#) ORCID: [orcid.org/0000-0001-7907-4595^{3,8}](https://orcid.org/0000-0001-7907-4595),
- [Radosław P. Nowak](#) ORCID: [orcid.org/0000-0002-0605-0071^{4,5}](https://orcid.org/0000-0002-0605-0071),
- [Eric S. Fischer](#) ORCID: [orcid.org/0000-0001-7337-6306^{4,5}](https://orcid.org/0000-0001-7337-6306) &
- [Benjamin L. Ebert](#) ORCID: [orcid.org/0000-0003-0197-5451^{1,2,9}](https://orcid.org/0000-0003-0197-5451)

- 8434 Accesses
- 151 Altmetric
- [Metrics details](#)

Subjects

- [Drug discovery](#)
- [Electron microscopy](#)
- [Haematological cancer](#)
- [Mechanism of action](#)
- [Ubiquitin ligases](#)

Abstract

Effective and sustained inhibition of non-enzymatic oncogenic driver proteins is a major pharmacological challenge. The clinical success of thalidomide analogues demonstrates the therapeutic efficacy of drug-induced degradation of transcription factors and other cancer targets^{1,2,3}, but a substantial subset of proteins are resistant to targeted degradation using existing approaches^{4,5}. Here we report an alternative mechanism of targeted protein degradation, in which a small molecule induces the highly specific, reversible polymerization of a target protein, followed by its sequestration into cellular foci and subsequent degradation. BI-3802 is a small molecule that binds to the Broad-complex, Tramtrack and Bric-à-brac (BTB) domain of the oncogenic transcription factor B cell lymphoma 6 (BCL6) and leads to the proteasomal degradation of BCL6⁶. We use cryo-electron microscopy to reveal how the solvent-exposed moiety of a BCL6-binding molecule contributes to a composite ligand–protein surface that engages BCL6 homodimers to form a supramolecular structure. Drug-induced formation of BCL6 filaments facilitates ubiquitination by the SIAH1 E3 ubiquitin ligase. Our findings demonstrate that a small molecule such as BI-3802 can induce polymerization coupled to highly specific protein degradation, which in the case of BCL6 leads to increased pharmacological activity compared to the

effects induced by other BCL6 inhibitors. These findings open new avenues for the development of therapeutic agents and synthetic biology.

[Access through your institution](#)

[Change institution](#)

[Buy or subscribe](#)

Access options

Subscribe to Journal

Get full journal access for 1 year

185,98 €

only 3,58 € per issue

[Subscribe](#)

All prices are NET prices.

VAT will be added later in the checkout.

Rent or Buy article

Get time limited or full article access on ReadCube.

from \$8.99

[Rent or Buy](#)

All prices are NET prices.

Additional access options:

- [Log in](#)
- [Access through your institution](#)
- [Learn about institutional subscriptions](#)

Fig. 1: Treatment with BI-3802 induces reversible formation of BCL6 cellular foci.

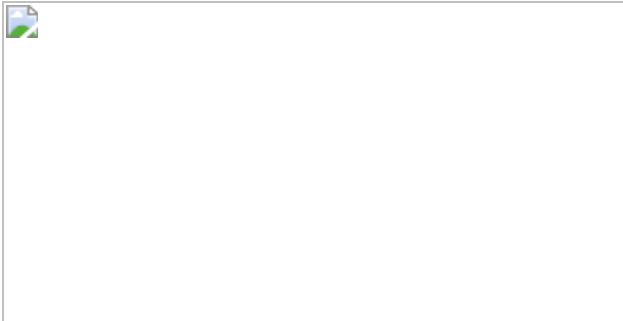


Fig. 2: BI-3802 induces the formation of helical filaments of BCL6 in vitro.

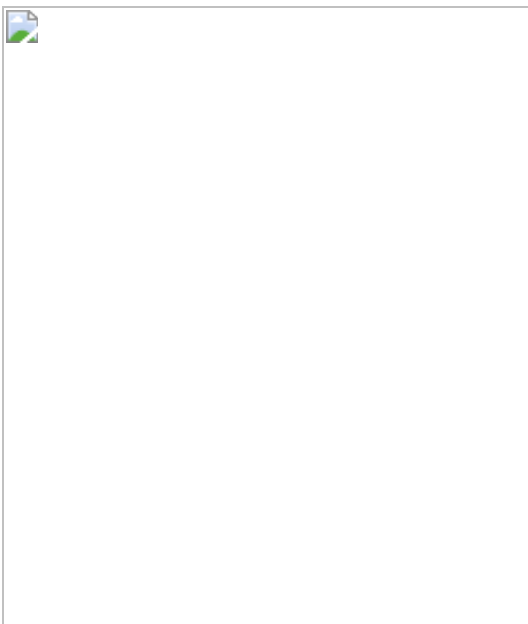
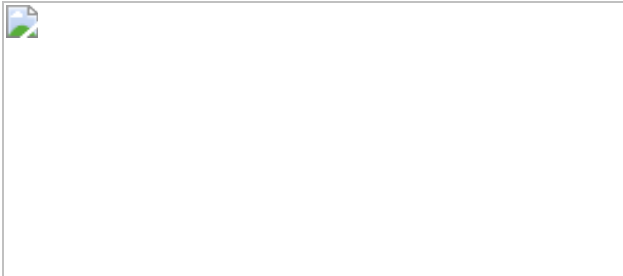


Fig. 3: BCL6 polymerization enhances SIAH1 interaction and ubiquitination.



Data availability

Structural data have been deposited to the Electron Microscopy Data Bank (EMDB; [EMD-22265](#)) and the RCSB PDB ([6XMX](#)). Proteome quantification data are available in the PRIDE repository (<https://www.ebi.ac.uk/pride/archive>; PXD016185). Uncropped gel and western blot data are shown in Supplementary Fig. [1](#), and the flow cytometry gating strategy is shown in Supplementary Fig. [2](#).

Code availability

The scripts used for modelling and analysis in this study are available on Github (https://github.com/fischerlab/scripts-publications/tree/master/2020_BCL6_polymerization).

References

1. 1.

Krönke, J. et al. Lenalidomide causes selective degradation of IKZF1 and IKZF3 in multiple myeloma cells. *Science* **343**, 301–305 (2014).

[ADS](#) [Google Scholar](#)

2. 2.

Lu, G. et al. The myeloma drug lenalidomide promotes the cereblon-dependent destruction of Ikaros proteins. *Science* **343**, 305–309 (2014).

[ADS](#) [CAS](#) [Google Scholar](#)

3. 3.

Krönke, J. et al. Lenalidomide induces ubiquitination and degradation of CK1 α in del(5q) MDS. *Nature* **523**, 183–188 (2015).

[ADS](#) [PubMed](#) [PubMed Central](#) [Google Scholar](#)

4. 4.

Huang, H.-T. et al. A chemoproteomic approach to query the degradable kinome using a multi-kinase degrader. *Cell Chem. Biol.* **25**, 88–99 (2018).

[CAS](#) [Google Scholar](#)

5. 5.

McCoull, W. et al. Development of a novel B-cell lymphoma 6 (BCL6) PROTAC to provide insight into small molecule targeting of BCL6. *ACS Chem. Biol.* **13**, 3131–3141 (2018).

[CAS](#) [Google Scholar](#)

6. 6.

Kerres, N. et al. Chemically induced degradation of the oncogenic transcription factor BCL6. *Cell Rep.* **20**, 2860–2875 (2017).

[CAS](#) [Google Scholar](#)

7. 7.

Toure, M. & Crews, C. M. Small-molecule PROTACS: new approaches to protein degradation. *Angew. Chem. Int. Edn Engl.* **55**, 1966–1973 (2016).

[CAS](#) [Google Scholar](#)

8. 8.

Bondeson, D. P. et al. Catalytic in vivo protein knockdown by small-molecule PROTACs. *Nat. Chem. Biol.* **11**, 611–617 (2015).

[CAS](#) [PubMed](#) [PubMed Central](#) [Google Scholar](#)

9. 9.

Winter, G. E. et al. Phthalimide conjugation as a strategy for in vivo target protein degradation. *Science* **348**, 1376–1381 (2015).

[ADS](#) [CAS](#) [PubMed](#) [PubMed Central](#) [Google Scholar](#)

10. 10.

Nowak, R. P. et al. Plasticity in binding confers selectivity in ligand-induced protein degradation. *Nat. Chem. Biol.* **14**, 706–714 (2018).

[CAS](#) [PubMed](#) [PubMed Central](#) [Google Scholar](#)

11. 11.

Petzold, G., Fischer, E. S. & Thomä, N. H. Structural basis of lenalidomide-induced CK1 α degradation by the CRL4^{CRBN} ubiquitin ligase. *Nature* **532**, 127–130 (2016).

[ADS](#) [CAS](#) [Google Scholar](#)

12. 12.

Sievers, Q. L. et al. Defining the human C2H2 zinc finger degrome targeted by thalidomide analogs through CRBN. *Science* **362**, eaat0572 (2018).

[ADS](#) [PubMed](#) [PubMed Central](#) [Google Scholar](#)

13. 13.

Cerchietti, L. C. et al. A small-molecule inhibitor of BCL6 kills DLBCL cells in vitro and in vivo. *Cancer Cell* **17**, 400–411 (2010).

[CAS](#) [PubMed](#) [PubMed Central](#) [Google Scholar](#)

14. 14.

Cardenas, M. G. et al. Rationally designed BCL6 inhibitors target activated B cell diffuse large B cell lymphoma. *J. Clin. Invest.* **126**,

3351–3362 (2016).

[PubMed](#) [PubMed Central](#) [Google Scholar](#)

15. 15.

Bosga-Bouwer, A. G. et al. BCL6 alternative translocation breakpoint cluster region associated with follicular lymphoma grade 3B. *Genes Chromosom. Cancer* **44**, 301–304 (2005).

[ADS](#) [CAS](#) [Google Scholar](#)

16. 16.

Hatzi, K. & Melnick, A. Breaking bad in the germinal center: how deregulation of BCL6 contributes to lymphomagenesis. *Trends Mol. Med.* **20**, 343–352 (2014).

[CAS](#) [PubMed](#) [PubMed Central](#) [Google Scholar](#)

17. 17.

Cattoretti, G. et al. Deregulated BCL6 expression recapitulates the pathogenesis of human diffuse large B cell lymphomas in mice. *Cancer Cell* **7**, 445–455 (2005).

[CAS](#) [Google Scholar](#)

18. 18.

Ranuncolo, S. M., Polo, J. M. & Melnick, A. BCL6 represses CHEK1 and suppresses DNA damage pathways in normal and malignant B-cells. *Blood Cells Mol. Dis.* **41**, 95–99 (2008).

[CAS](#) [PubMed](#) [PubMed Central](#) [Google Scholar](#)

19. 19.

Tunyaplin, C. et al. Direct repression of *prdm1* by Bcl-6 inhibits plasmacytic differentiation. *J. Immunol.* **173**, 1158–1165 (2004).

[CAS](#) [Google Scholar](#)

20. 20.

Phan, R. T., Saito, M., Basso, K., Niu, H. & Dalla-Favera, R. BCL6 interacts with the transcription factor Miz-1 to suppress the cyclin-dependent kinase inhibitor p21 and cell cycle arrest in germinal center B cells. *Nat. Immunol.* **6**, 1054–1060 (2005).

[CAS](#) [Google Scholar](#)

21. 21.

Schlager, S. et al. Inducible knock-out of BCL6 in lymphoma cells results in tumor stasis. *Oncotarget* **11**, 875–890 (2020).

[PubMed](#) [PubMed Central](#) [Google Scholar](#)

22. 22.

Ghetu, A. F. et al. Structure of a BCOR corepressor peptide in complex with the BCL6 BTB domain dimer. *Mol. Cell* **29**, 384–391 (2008).

[CAS](#) [PubMed](#) [PubMed Central](#) [Google Scholar](#)

23. 23.

Sievers, Q. L., Gasser, J. A., Cowley, G. S., Fischer, E. S. & Ebert, B. L. Genome-wide screen identifies cullin-RING ligase machinery required for lenalidomide-dependent CRL4^{CRBN} activity. *Blood* **132**, 1293–1303 (2018).

[CAS](#) [PubMed](#) [PubMed Central](#) [Google Scholar](#)

24. 24.

Hunkeler, M. et al. Structural basis for regulation of human acetyl-CoA carboxylase. *Nature* **558**, 470–474 (2018).

[ADS](#) [CAS](#) [Google Scholar](#)

25. 25.

House, C. M. et al. A binding motif for Siah ubiquitin ligase. *Proc. Natl Acad. Sci. USA* **100**, 3101–3106 (2003).

[ADS](#) [CAS](#) [Google Scholar](#)

26. 26.

Ji, L. et al. The SIAH E3 ubiquitin ligases promote Wnt/β-catenin signaling through mediating Wnt-induced Axin degradation. *Genes Dev.* **31**, 904–915 (2017).

[CAS](#) [PubMed](#) [PubMed Central](#) [Google Scholar](#)

27. 27.

Garcia-Seisdedos, H., Empereur-Mot, C., Elad, N. & Levy, E. D. Proteins evolve on the edge of supramolecular self-assembly. *Nature* **548**, 244–247 (2017).

[ADS](#) [CAS](#) [Google Scholar](#)

28. 28.

Słabicki, M. et al. The CDK inhibitor CR8 acts as a molecular glue degrader that depletes cyclin K. *Nature* **585**, 293–297 (2020).

[Google Scholar](#)

29. 29.

Bellenie, B. R. et al. Achieving in vivo target depletion through the discovery and optimization of benzimidazolone BCL6 degraders. *J.*

Med. Chem. **63**, 4047–4068 (2020).

[CAS](#) [PubMed](#) [PubMed Central](#) [Google Scholar](#)

30. 30.

Meyers, R. M. et al. Computational correction of copy number effect improves specificity of CRISPR–Cas9 essentiality screens in cancer cells. *Nat. Genet.* **49**, 1779–1784 (2017).

[CAS](#) [PubMed](#) [PubMed Central](#) [Google Scholar](#)

31. 31.

Donovan, K. A. et al. Thalidomide promotes degradation of SALL4, a transcription factor implicated in Duane Radial Ray syndrome. *eLife* **7**, e38430 (2018).

[PubMed](#) [PubMed Central](#) [Google Scholar](#)

32. 32.

Abdulrahman, W. et al. A set of baculovirus transfer vectors for screening of affinity tags and parallel expression strategies. *Anal. Biochem.* **385**, 383–385 (2009).

[CAS](#) [Google Scholar](#)

33. 33.

Faust, T. B. et al. Structural complementarity facilitates E7820-mediated degradation of RBM39 by DCAF15. *Nat. Chem. Biol.* **16**, 7–14 (2020).

[CAS](#) [Google Scholar](#)

34. 34.

Marze, N. A., Roy Burman, S. S., Sheffler, W. & Gray, J. J. Efficient flexible backbone protein-protein docking for challenging targets. *Bioinformatics* **34**, 3461–3469 (2018).

[CAS](#) [PubMed](#) [PubMed Central](#) [Google Scholar](#)

35. 35.

Enkhbayar, P., Damdinsuren, S., Osaki, M. & Matsushima, N. HELFIT: helix fitting by a total least squares method. *Comput. Biol. Chem.* **32**, 307–310 (2008).

[CAS](#) [MATH](#) [Google Scholar](#)

36. 36.

Zheng, S. Q. et al. MotionCor2: anisotropic correction of beam-induced motion for improved cryo-electron microscopy. *Nat. Methods* **14**, 331–332 (2017).

[CAS](#) [PubMed](#) [PubMed Central](#) [Google Scholar](#)

37. 37.

Rohou, A. & Grigorieff, N. CTFFIND4: fast and accurate defocus estimation from electron micrographs. *J. Struct. Biol.* **192**, 216–221 (2015).

[PubMed](#) [PubMed Central](#) [Google Scholar](#)

38. 38.

Wagner, T. et al. SPHIRE-crYOLO is a fast and accurate fully automated particle picker for cryo-EM. *Commun. Biol.* **2**, 218 (2019).

[Google Scholar](#)

39. 39.

Zivanov, J. et al. New tools for automated high-resolution cryo-EM structure determination in RELION-3. *eLife* **7**, e42166 (2018).

[PubMed](#) [PubMed Central](#) [Google Scholar](#)

40. 40.

Tan, Y. Z. et al. Addressing preferred specimen orientation in single-particle cryo-EM through tilting. *Nat. Methods* **14**, 793–796 (2017).

[CAS](#) [PubMed](#) [PubMed Central](#) [Google Scholar](#)

41. 41.

Emsley, P., Lohkamp, B., Scott, W. G. & Cowtan, K. Features and development of Coot. *Acta Crystallogr. D* **66**, 486–501 (2010).

[CAS](#) [PubMed](#) [PubMed Central](#) [Google Scholar](#)

42. 42.

Adams, P. D. et al. PHENIX: a comprehensive Python-based system for macromolecular structure solution. *Acta Crystallogr. D* **66**, 213–221 (2010).

[CAS](#) [PubMed](#) [PubMed Central](#) [Google Scholar](#)

43. 43.

Doench, J. G. et al. Optimized sgRNA design to maximize activity and minimize off-target effects of CRISPR–Cas9. *Nat. Biotechnol.* **34**, 184–191 (2016).

[CAS](#) [PubMed](#) [PubMed Central](#) [Google Scholar](#)

44. 44.

Sanjana, N. E., Shalem, O. & Zhang, F. Improved vectors and genome-wide libraries for CRISPR screening. *Nat. Methods* **11**, 783–784

(2014).

[CAS](#) [PubMed](#) [PubMed Central](#) [Google Scholar](#)

45. 45.

Sperling, A. S. et al. Patterns of substrate affinity, competition, and degradation kinetics underlie biological activity of thalidomide analogs. *Blood* **134**, 160–170 (2019).

[CAS](#) [PubMed](#) [PubMed Central](#) [Google Scholar](#)

[Download references](#)

Acknowledgements

We thank the Broad Institute Flow Facility (particularly P. Rogers), the Broad Institute Walk-Up Sequencing Team (particularly T. Mason) and the Broad Institute Genetic Perturbation Platform and Whitehead Institute Microscopy Facility (particularly W. Salmon) for technical assistance. Cryo-EM data were collected at the Harvard Cryo-Electron Microscopy Center for Structural Biology. We acknowledge the Research Computing Group at Harvard Medical School for computational modeling, and the SBGrid suite for structural biology software packages. We thank S. Sterling and R. Walsh for microscopy support; S. Rawson for comments and computing support; H.-S. Seo for help with the isothermal calorimetry experiment; and J. Kennedy for providing the sgRNA.SFFV.tBFP backbone. We are grateful to all members of the Ebert and Fischer laboratories for discussion, particularly B. Liddicoat, R. Belizaire, S. Koochaki, Q. L. Sievers, R. S. Sellar, M. Jan, P. M.C. Park, D. Levin and T. B. Faust, as well as N. H. Thomä, G. Petzold, Z. Kozicka, K. Mulvaney, D. Pal, and J. Schmid-Burgk. M.S. has received funding from the European Union’s Horizon 2020 Research and Innovation Program under the Marie Skłodowska-Curie grant agreement no. 702642; H.Y. was supported by a Chleck Foundation fellowship and is a recipient of the NCI Predoctoral to Postdoctoral Fellow Transition (F99/K00) Award (F99CA253754); S.S.R.B. is the recipient of a Cancer Research Institute Irvington

Postdoctoral Fellowship (CRI 3442); A.S.S. is supported by a DF/HCC K12 grant, a Conquer Cancer Foundation Young Investigator Award and an award from the Wong Family Foundation; and M.H. is supported by a Swiss National Science Foundation Fellowship 174331. This work was supported by the National Institutes of Health (NIH) grants R01HL082945, P01CA108631 and P50CA206963 (to B.L.E.), the Howard Hughes Medical Institute, the Edward P. Evans Foundation and the Leukemia and Lymphoma Society (to B.L.E.), NIH grant NCI R01CA214608 (to E.S.F.) and a Mark Foundation Emerging Leader Award 19-001-ELA (grant to E.S.F.).

Author information

Author notes

1. These authors contributed equally: Mikołaj Ślabicki, Hojong Yoon, Jonas Koeppel

Affiliations

1. Broad Institute of MIT and Harvard, Cambridge, MA, USA

Mikołaj Ślabicki, Jonas Koeppel, Lena Nitsch, Cristina Di Genua, Adam S. Sperling, Jonathan M. Tsai, Andrew Guirguis, Jessica A. Gasser, Peter G. Miller & Benjamin L. Ebert

2. Department of Medical Oncology, Dana-Farber Cancer Institute, Boston, MA, USA

Mikołaj Ślabicki, Jonas Koeppel, Lena Nitsch, Cristina Di Genua, Adam S. Sperling, Jonathan M. Tsai, Rohan Sharma, Andrew Guirguis, Charles Zou, Jessica A. Gasser, Peter G. Miller & Benjamin L. Ebert

3. Division of Translational Medical Oncology, German Cancer Research Center (DKFZ) and National Center for Tumor Diseases (NCT), Heidelberg, Germany

Mikołaj Ślabicki, Jonas Koeppel, Lena Nitsch & Stefan Fröhling

4. Department of Cancer Biology, Dana-Farber Cancer Institute, Boston, MA, USA

Hojong Yoon, Shourya S. Roy Burman, Katherine A. Donovan, Moritz Hunkeler, Radosław P. Nowak & Eric S. Fischer

5. Department of Biological Chemistry and Molecular Pharmacology, Harvard Medical School, Boston, MA, USA

Hojong Yoon, Shourya S. Roy Burman, Katherine A. Donovan, Moritz Hunkeler, Radosław P. Nowak & Eric S. Fischer

6. Precision Sarcoma Research Group, German Cancer Research Center (DKFZ) and National Center for Tumor Diseases (NCT), Heidelberg, Germany

Priya Chudasama

7. Division of Applied Functional Genomics, German Cancer Research Center (DKFZ) and National Center for Tumor Diseases (NCT), Heidelberg, Germany

Claudia Scholl

8. German Cancer Consortium (DKTK), Heidelberg, Germany

Stefan Fröhling

9. Howard Hughes Medical Institute, Boston, MA, USA

Benjamin L. Ebert

Authors

1. Mikołaj Ślabicki

[View author publications](#)

You can also search for this author in [PubMed](#) [Google Scholar](#)

2. Hojong Yoon

[View author publications](#)

You can also search for this author in [PubMed](#) [Google Scholar](#)

3. Jonas Koeppel

[View author publications](#)

You can also search for this author in [PubMed](#) [Google Scholar](#)

4. Lena Nitsch

[View author publications](#)

You can also search for this author in [PubMed](#) [Google Scholar](#)

5. Shourya S. Roy Burman

[View author publications](#)

You can also search for this author in [PubMed](#) [Google Scholar](#)

6. Cristina Di Genua

[View author publications](#)

You can also search for this author in [PubMed](#) [Google Scholar](#)

7. Katherine A. Donovan

[View author publications](#)

You can also search for this author in [PubMed](#) [Google Scholar](#)

8. Adam S. Sperling

[View author publications](#)

You can also search for this author in [PubMed](#) [Google Scholar](#)

9. Moritz Hunkeler

[View author publications](#)

You can also search for this author in [PubMed](#) [Google Scholar](#)

10. Jonathan M. Tsai

[View author publications](#)

You can also search for this author in [PubMed](#) [Google Scholar](#)

11. Rohan Sharma

[View author publications](#)

You can also search for this author in [PubMed](#) [Google Scholar](#)

12. Andrew Guirguis

[View author publications](#)

You can also search for this author in [PubMed](#) [Google Scholar](#)

13. Charles Zou

[View author publications](#)

You can also search for this author in [PubMed](#) [Google Scholar](#)

14. Priya Chudasama

[View author publications](#)

You can also search for this author in [PubMed](#) [Google Scholar](#)

15. Jessica A. Gasser

[View author publications](#)

You can also search for this author in [PubMed](#) [Google Scholar](#)

16. Peter G. Miller

[View author publications](#)

You can also search for this author in [PubMed](#) [Google Scholar](#)

17. Claudia Scholl

[View author publications](#)

You can also search for this author in [PubMed](#) [Google Scholar](#)

18. Stefan Fröhling

[View author publications](#)

You can also search for this author in [PubMed](#) [Google Scholar](#)

19. Radosław P. Nowak

[View author publications](#)

You can also search for this author in [PubMed](#) [Google Scholar](#)

20. Eric S. Fischer

[View author publications](#)

You can also search for this author in [PubMed](#) [Google Scholar](#)

21. Benjamin L. Ebert

[View author publications](#)

You can also search for this author in [PubMed](#) [Google Scholar](#)

Contributions

M.S., H.Y., J.K., R.P.N., E.S.F. and B.L.E conceptualized and initiated the study; M.S., J.K., L.N. and A.S.S. designed and performed molecular and cellular biology experiments with the help of C.D.G., J.M.T., C.Z., R.S., A.G., P.C., P.G.M. and J.A.G.; H.Y. designed and carried out biochemical studies and structural analyses with the help of M.H. and R.P.N.; S.S.R.B. conducted computational modelling; K.A.D. performed the mass spectrometry experiments; C.S., S.F., R.P.N., E.S.F. and B.L.E supervised the project.; M.S., H.Y., J.K., E.S.F. and B.L.E. wrote the manuscript with input from all authors.

Corresponding authors

Correspondence to [Eric S. Fischer](#) or [Benjamin L. Ebert](#).

Ethics declarations

Competing interests

B.L.E. has received research funding from Celgene and Deerfield. He has received consulting fees from GRAIL, and he serves on the scientific advisory boards for and holds equity in Skyhawk Therapeutics and Exo Therapeutics. He is a founder, member of the scientific advisory board and equity holder of Neomorph. E.S.F. is a founder, member of the scientific advisory board and equity holder of Civetta Therapeutics, Jengu Therapeutics (board member) and Neomorph, holds equity in C4 Therapeutics and is a consultant to Astellas and EcoR1 capital. The Fischer laboratory receives or has received research funding from Novartis, Deerfield, Ajax and Astellas. S.F. has had a consulting or advisory role, received honoraria, research funding and/or funding for travel or accommodation expenses from the following for-profit companies: Bayer, Roche, Amgen, Eli Lilly, PharmaMar, AstraZeneca and Pfizer. M.S., H.Y., J.K., E.S.F. and B.L.E are named as inventors on pending US Provisional Application Nos. 62/938,736 and 63/074,279, filed by The Broad Institute, Inc and Dana Farber Cancer Institute related to this work. The remaining authors declare no competing interests.

Additional information

Peer review information *Nature* thanks Ivan Dikic, Frank Sicheri and the other, anonymous, reviewer(s) for their contribution to the peer review of this work.

Publisher's note Springer Nature remains neutral with regard to jurisdictional claims in published maps and institutional affiliations.

Extended data figures and tables

[Extended Data Fig. 1 Characterization of BI-3802-induced BCL6 degradation.](#)

a, Immunoblots of BCL6 levels in cytoplasmic, nuclear or chromatin-bound fractions of SuDHL4_{Cas9} cells after treatment with DMSO or 1 μM BI-3802 for 24 h ($n = 2$). **b**, mRNA levels quantified by qPCR in SuDHL4_{Cas9} cells after treatment with 1 μM BI-3802 or DMSO for 1 h (bars represent mean and s.d., $n = 3$). **c**, Whole-proteome quantification of SuDHL4_{Cas9} cells treated with 1 μM BI-3812 ($n = 1$) or DMSO ($n = 3$) for 4 h (two-sided moderated *t*-test, $n = 3$). **d**, Immunoblots of BCL6 levels in SuDHL4_{Cas9} cells treated with 10 μM MG132 (26S proteasome inhibitor) for 1 h, 1 μM BI-3802 for 45 min or 10 μM BI-3812 for 10 min. A subset of the polymerized BCL6 was insoluble and lost during the western blot sample preparation, however, treatment with an excess of BI-3812 shortly before protein collection reverted polymerization, solubilized BCL6 and allowed for reliable quantification ($n = 2$). **e**, Immunoblots of BCL6 levels in SuDHL4_{Cas9} cells treated with DMSO, 10 μM MLN7243 (ubiquitin activating enzyme inhibitor), 10 μM MG132 (26S proteasome inhibitor), 10 μM chloroquine (lysosomal inhibitor) or 5 μM MLN4924 (neddylation inhibitor) for 15 min; then, for indicated samples, 1 μM BI-3802 was added and 35 min later, 10 μM BI-3812 was added for the final 10 min, resulting in a total of 1 h treatment with MLN7243, MG132, chloroquine or MLN4924, 45 min with BI-3802 and 10 min with BI-3812 ($n = 2$). **f**, Cytospin immunofluorescence images of SuDHL4_{Cas9} cells treated with DMSO (left) or 0.5 μM MLN7243 for 2 h and 1 μM BI-3802 (right) for 1 h. Scale bar, 5 μm ($n = 2$). **g**, Flow cytometry analysis of HEK293T_{Cas9} cells expressing eGFP–BCL6(1–275) that were exposed simultaneously to the indicated concentrations of BI-3802 and BI-3812 for 24 h. Lines represent standard four-parameter log-logistic curve fit ($n = 3$).

Extended Data Fig. 2 Computational docking of BCL6 helical filament models with distinct binding modes.

Visualization of top-scoring BCL6 BTB domain filament model from three different binding modes: end-to-end (E2E), face-to-end (F2E) and face-to-face (F2F). Each BTB monomer used for building the tetramer model is labelled in a distinct colour. BI-3802 is visualized as a sphere. The interface score is an estimate of the binding energy between the dimers. The helical pitch was calculated by extending the tetramer. Sub-angstrom variations in

the F2F binding mode have a profound effect on helical pitch (more than 10 nm).

Extended Data Fig. 3 Structure determination of BCL6 filaments by cryo-EM.

a, Representative cryo-EM micrograph at $-2\text{ }\mu\text{m}$ defocus. Micrograph was low-pass-filtered. Scale bar, 100 nm. **b**, Local-resolution map of the final reconstruction with a threshold of 0.0154 (Chimera) calculated using RELION v.3.0. **c**, Data-processing scheme for the BCL6 filaments. Iterative 2D classifications resulted in 274,999 particles. Multiple subsequent rounds of 3D classification, refinement, and polishing improved map resolution to a final overall resolution of 3.7 Å. Percentages refer to the particles in each class. Red density maps indicate the classes that were used for the next round of processing, and blue density maps are from 3D refinements. **d**, FSC plots for unmasked and masked maps. Overall resolution is indicated at $\text{FSC} = 0.143$. **e**, Histogram and directional FSC plot for BCL6 cryo-EM map. **f**, **g**, Regions of the cryo-EM model for the BCL6 filament fit into the density map, demonstrating side-chain density for multiple residues. Each density is shown at a threshold of 0.0178 (from Chimera).

Extended Data Fig. 4 Structural details of BI-3802-induced BCL6 filaments.

a, Density for BI-3802 in the 3.7-Å cryo-EM reconstruction. The crystal structure of BCL6 bound to BI-3802 (PDB 5MW2) was docked into the cryo-EM map and refined using phenix.real_space_refine. The cryo-EM density is shown in grey at a threshold of 0.0178 (from Chimera). **b**, Density of BI-3802 and key interacting residues (Arg28, Glu41, Tyr58, Cys84) for BCL6 polymerization. Each density in mesh is shown at a threshold of 0.0178 (from Chimera). **c**, **d**, Comparison of the cryo-EM model of polymerized BCL6 (white) with the BCL6 crystallographic lattice (yellow, PDB 5MW2) for dimer–dimer (**c**), and filament (**d**). **e**, Superimposed structures of BI-3802 (yellow) and BI-3812 (orange) bound to the BCL6 filament. BI-3812 was docked to the crystal structure of BCL6 BTB (PDB 5MW2), which was then aligned to the BI-3802-mediated

BCL6 filament model. The solvent-exposed moiety of the inhibitor is clashing with the adjacent BCL6 dimer (grey). **f**, Preassembled 0.1 μ M FITC-labelled BCOR peptide and 0.1 μ M biotinylated BCL6(5–129) variants were treated with an increasing concentration of BI-3802, and the signal was measured by TR-FRET. The interaction of BCL6 with the BCOR co-repressor peptide was used to quantitatively determine drug binding. Lines represent standard four-parameter log-logistic curve fit ($n = 3$).

Extended Data Fig. 5 Analysis of BCL6 BTB variants in vivo.

a, Schematic of alanine mutagenesis resistance screen of the BCL6 BTB domain in SuDHL4_{Cas9} cells. **b**, Schematic of alanine mutagenesis reporter screen of the BCL6 BTB domain in HEK293T_{Cas9} cells. **c**, Alanine mutagenesis screen of the BCL6 BTB domain for impaired BI-3802 induced degradation at 1 μ M BI-3802 in HEK293T_{Cas9} cells. Mutations that confer resistance are labelled. Four different codons were collapsed to each unique amino acid position (greater than threefold enrichment, $P < 10^{-4}$; $n = 2$; four codons per position; two-sided empirical rank-sum test-statistics). **d**, Correlation of *BCL6* mRNA expression (transcripts per million (TPM)) and *BCL6* dependency (CERES score) in a set of 559 cancer cell lines from the Dependency Map Project. Cell lines chosen for experiments are labelled. **e**, SuDHL4_{Cas9}, Raji_{Cas9} (both BCL6-dependent) and DEL_{Cas9} (BCL6-independent) cells were infected with the indicated BCL6 variants and treated with 1 μ M BI-3802 or DMSO over 21 days. Lines represent measurement from each replicate ($n = 2$). **f**, BI-3802 in the polymerization interface. Residues identified in the alanine scan are highlighted, with the following colour code: orange, Gly55, Tyr58 (residues involved in drug binding); magenta, Glu41, Cys84 (residues involved in polymerization). Hydrogen atoms in Gly55 are depicted as spheres.

Extended Data Fig. 6 Genome-wide CRISPR–Cas9 screens to identify the molecular machinery involved in BI-3802-induced degradation of BCL6.

a, Schematic of the BCL6 stability reporter-based sorting screen. **b, c**, Genome-wide CRISPR–Cas9 knockout screen for eGFP–BCL6 stability in HEK293T_{Cas9} cells after 16 h of treatment with 1 μM BI-3802 or DMSO. Results for SIAH1 and FBXO11 (a previously reported E3 ligase involved in BCL6 endogenous degradation) are labelled. Guides were collapsed to gene level ($n = 3$; four guides per gene; two-sided empirical rank-sum test-statistics). **d**, Normalized read counts in each sorted gate for 4 sgRNAs targeting *SIAH1* and 4,000 non-targeting controls (NTC). Symbols indicate the mean normalized read numbers for each sgRNA ($n = 3$). **e**, Flow cytometry analysis of HEK293T_{Cas9} cells expressing the full-length eGFP–BCL6 reporter and individual sgRNAs after 4 h treatment with DMSO or 1 μM BI-3802. Bars represent mean ($n = 3$). **f**, Schematic of the genome-wide CRISPR–Cas9 resistance screen. **g**, Genome-wide CRISPR–Cas9 knockout screen for resistance to BI-3802. Guides were collapsed to gene level ($n = 3$; four guides per gene; two-sided empirical rank-sum test-statistics). **h**, Flow cytometry analysis of SuDHL4_{Cas9} cells expressing sgRNAs and blue fluorescent protein (marker) treated with DMSO or 1 μM BI-3802. Lines represent measurement from each replicate ($n = 3$).

Extended Data Fig. 7 SIAH1 induces degradation of BCL6 through the VxP motif.

a, Flow cytometry analysis of HEK293T_{Cas9} cells expressing full-length eGFP–BCL6 stability reporter and vectors expressing no-insert control, SIAH1 or SIAH1(C44S), treated with DMSO or BI-3802 for 2 h. Bars represent the mean ($n = 3$). **b**, Alignment of the BCL6 SIAH1-recognition site with previously published peptide sequences recognized by SIAH1 with inferred consensus SIAH1-binding site. **c**, CRISPR–Cas9 knockout screen with the Bison library for eGFP–BCL6(1–129 + 241–260) stability in HEK293T_{Cas9} cells after 16 h of treatment with 1 μM BI-3802 or DMSO. Guides were collapsed to gene level ($n = 1$; four guides per gene; two-sided empirical rank-sum test-statistics). **d**, Flow cytometry analysis of HEK293T_{Cas9} cells expressing eGFP–BCL6(FL) or eGFP–BCL6(FL;VSP>GSA) treated with DMSO or 1 μM BI-3802 for 7 h (bars represent mean, $n = 3$).

Extended Data Fig. 8 Characterization of SIAH1-mediated degradation of polymerized BCL6.

a, SDS-PAGE gel analysis of the in vitro pull-down between recombinant SIAH1(SBD) and recombinant Strep-BCL6 in the presence of BI-3802 or DMSO. Strep, strep•Tag II ($n = 2$). **b**, Titration of BCL6(241–260) peptide binding to SIAH1(SBD) using isothermal calorimetry ($n = 1$). **c**, Titration of SIAH1(SBD) binding to BCL6(5–360) using isothermal calorimetry ($n = 1$). **d**, Recombinant strep•Tag II–BCL6(5–360) was combined with full length SIAH1 and a panel of E2 enzymes (Boston Biochem) and screened for ubiquitination activity in vitro. Samples were analysed by western blot and visualized by strep•Tag II antibody–HRP conjugate ($n = 1$). **e**, Bodipy-labelled BCL6(5–360) variants (WT, E41A, Y58A) were titrated to 0.2 μ M biotinylated SIAH1(SBD) in the presence of 2 μ M BI-3802, and the signal was measured by TR-FRET. Dots represent mean. Lines represent standard four-parameter log-logistic curve fit ($n = 3$). **f**, Preassembled 0.2 μ M Bodipy-labelled BCL6(5–360) and 0.2 μ M biotinylated SIAH1(SBD) were treated with an increasing concentration of BI-3802 or BI-3812, and the signal was measured by TR-FRET. Dots represent mean. Lines represent standard four-parameter log-logistic curve fit ($n = 3$). **g**, HEK293T cells transiently transfected with nano-luciferase-tagged SIAH1(C44S) and HaloTag-labelled BCL6 constructs were treated with DMSO, 1 μ M BI-3802 or 1 μ M BI-3812 for 2 h and the mBRET signal was measured. Bars represent mean ($n = 3$). One-sided *t*-test. **h**, Preassembled 0.1 μ M FITC-labelled BCoR peptide and 0.1 μ M biotinylated BCL6(5–129) were treated with an increasing concentration of BI-3802 or BI-3812, and the signal was measured by TR-FRET. Lines represent standard four-parameter log-logistic curve fit ($n = 3$). **i**, HEK293T_{Cas9} cells expressing the eGFP–BCL6(1–250) stability reporter and V5–SIAH1 were treated with 0.5 μ M MLN7243 for 2 h and 1 μ M BI-3802 for 1 h. Cells were imaged by indirect immunofluorescence as indicated. Scale bar, 5 μ m ($n = 2$).

Extended Data Table 1 Cryo-EM data collection, refinement and validation statistics

[Full size table](#)

Supplementary information

Supplementary Figures

This file contains Supplementary Figure 1: Uncropped Western blots and SDS-PAGE gels, and Supplementary Figure 2: Gating strategy for flow cytometry.

Reporting Summary

Supplementary Data

Supplementary Data 1: Proteome quantification using tandem mass tag spectrometry data.

Supplementary Data

Supplementary Data 2: Functional genomics data.

Supplementary Table 1

Oligonucleotides used in this study.

Supplementary Data

Scripts used to analyze the proteomics, computational modeling, and functional genomic data: https://github.com/fischerlab/scripts-publications/tree/master/2020_BCL6_polymerization.

Video 1

HEK293T_{Cas9} cells expressing the eGFPBCL6^{1–250} reporter were imaged after treatment with 1 μM BI-3802.

Video 2

HEK293T_{Cas9} cells expressing the eGFPBCL6^{1–250} reporter were imaged after treatment with DMSO.

[Video 3](#)

HEK293T_{Cas9} cells expressing the eGFPBCL6^{1–275} reporter were imaged after treatment with 1 μM BI-3802.

[Video 4](#)

HEK293T_{Cas9} cells expressing the eGFPBCL6^{1–275} reporter were imaged after treatment with DMSO.

[Video 5](#)

HEK293T_{Cas9} cells expressing the eGFPBCL6^{FL} reporter were imaged after treatment with 1 μM BI-3802.

[Video 6](#)

HEK293T_{Cas9} cells expressing the eGFPBCL6^{FL} reporter were imaged after treatment with DMSO.

[Video 7](#)

HEK293T_{Cas9} cells expressing the eGFPBCL6^{1–250} reporter were imaged after treatment with 1 μM BI-3802 and after 75 minutes, 10 μM BI-3812 was spiked in.

Rights and permissions

[Reprints and Permissions](#)

About this article



Check for
updates

Cite this article

Słabicki, M., Yoon, H., Koeppel, J. *et al.* Small-molecule-induced polymerization triggers degradation of BCL6. *Nature* **588**, 164–168 (2020). <https://doi.org/10.1038/s41586-020-2925-1>

[Download citation](#)

- Received: 09 November 2019
- Accepted: 03 September 2020
- Published: 18 November 2020
- Issue Date: 03 December 2020
- DOI: <https://doi.org/10.1038/s41586-020-2925-1>

Comments

By submitting a comment you agree to abide by our [Terms](#) and [Community Guidelines](#). If you find something abusive or that does not comply with our terms or guidelines please flag it as inappropriate.

[Access through your institution](#)

[Change institution](#)

[Buy or subscribe](#)

This article was downloaded by **calibre** from <https://www.nature.com/articles/s41586-020-2925-1>

- Article
- [Published: 09 September 2020](#)

SLC25A51 is a mammalian mitochondrial NAD⁺ transporter

- [Timothy S. Luongo](#) ORCID: orcid.org/0000-0001-7621-7992¹,
- [Jared M. Eller](#)²,
- [Mu-Jie Lu](#)²,
- [Marc Niere](#)³,
- [Fabio Raith](#)^{4,5},
- [Caroline Perry](#)¹,
- [Marc R. Bornstein](#)¹,
- [Paul Oiphint](#)²,
- [Lin Wang](#)⁶,
- [Melanie R. McReynolds](#) ORCID: orcid.org/0000-0001-5427-2739⁶,
- [Marie E. Migaud](#)⁷,
- [Joshua D. Rabinowitz](#) ORCID: orcid.org/0000-0002-1247-4727⁶,
- [F. Brad Johnson](#) ORCID: orcid.org/0000-0002-7443-7227⁸,
- [Kai Johnsson](#)^{4,9},
- [Mathias Ziegler](#) ORCID: orcid.org/0000-0001-6961-2396³,
- [Xiaolu A. Cambronne](#) ORCID: orcid.org/0000-0002-3547-448X² &
- [Joseph A. Baur](#) ORCID: orcid.org/0000-0001-8262-6549¹

[Nature](#) volume 588, pages174–179(2020) [Cite this article](#)

- 18k Accesses
- 307 Altmetric
- [Metrics details](#)

Subjects

- [Energy metabolism](#)

Abstract

Mitochondria require nicotinamide adenine dinucleotide (NAD^+) to carry out the fundamental processes that fuel respiration and mediate cellular energy transduction. Mitochondrial NAD^+ transporters have been identified in yeast and plants^{1,2}, but their existence in mammals remains controversial^{3,4,5}. Here we demonstrate that mammalian mitochondria can take up intact NAD^+ , and identify SLC25A51 (also known as MCART1)—an essential^{6,7} mitochondrial protein of previously unknown function—as a mammalian mitochondrial NAD^+ transporter. Loss of SLC25A51 decreases mitochondrial—but not whole-cell— NAD^+ content, impairs mitochondrial respiration, and blocks the uptake of NAD^+ into isolated mitochondria. Conversely, overexpression of SLC25A51 or SLC25A52 (a nearly identical parologue of SLC25A51) increases mitochondrial NAD^+ levels and restores NAD^+ uptake into yeast mitochondria lacking endogenous NAD^+ transporters. Together, these findings identify SLC25A51 as a mammalian transporter capable of importing NAD^+ into mitochondria.

[Access through your institution](#)

[Change institution](#)

[Buy or subscribe](#)

Access options

Subscribe to Journal

Get full journal access for 1 year

185,98 €

only 3,58 € per issue

Subscribe

All prices are NET prices.
VAT will be added later in the checkout.

Rent or Buy article

Get time limited or full article access on ReadCube.

from \$8.99

Rent or Buy

All prices are NET prices.

Additional access options:

- [Log in](#)
- [Access through your institution](#)
- [Learn about institutional subscriptions](#)

Fig. 1: SLC25A51 and SLC25A52 expression dictates mitochondrial NAD⁺ concentration.

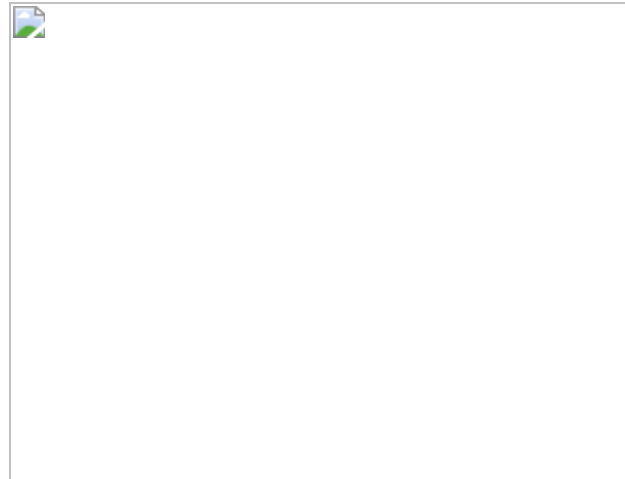


Fig. 2: SLC25A51 modulates mitochondrial respiratory capacity.



Fig. 3: SLC25A51 expression is required for NAD⁺ uptake in isolated mitochondria.



Fig. 4: SLC25A51 is sufficient for transport of NAD⁺ into yeast mitochondria lacking the endogenous transporters NDT1 and NDT2.



Data availability

The authors declare that the data supporting the findings of this study are available within the paper and its [supplementary information files](#). [Source data](#) are provided with this paper.

Code availability

No custom codes were used during this study. Mathematical calculations are described in the materials and methods section or by cited works.

References

1. 1.

Palmieri, F. et al. Molecular identification and functional characterization of *Arabidopsis thaliana* mitochondrial and chloroplastic NAD⁺ carrier proteins. *J. Biol. Chem.* **284**, 31249–31259 (2009).

[CAS](#) [PubMed](#) [PubMed Central](#) [Google Scholar](#)

2. 2.

Todisco, S., Agrimi, G., Castegna, A. & Palmieri, F. Identification of the mitochondrial NAD⁺ transporter in *Saccharomyces cerevisiae*. *J. Biol. Chem.* **281**, 1524–1531 (2006).

[CAS](#) [Google Scholar](#)

3. 3.

Berger, F., Ramírez-Hernández, M. H. & Ziegler, M. The new life of a centenarian: signalling functions of NAD(P). *Trends Biochem. Sci.* **29**, 111–118 (2004).

[CAS](#) [Google Scholar](#)

4. 4.

Yang, H. et al. Nutrient-sensitive mitochondrial NAD⁺ levels dictate cell survival. *Cell* **130**, 1095–1107 (2007).

[CAS](#) [PubMed](#) [PubMed Central](#) [Google Scholar](#)

5. 5.

VanLinden, M. R. et al. Subcellular distribution of NAD⁺ between cytosol and mitochondria determines the metabolic profile of human cells. *J. Biol. Chem.* **290**, 27644–27659 (2015).

[CAS](#) [PubMed](#) [PubMed Central](#) [Google Scholar](#)

6. 6.

Wang, T. et al. Identification and characterization of essential genes in the human genome. *Science* **350**, 1096–1101 (2015).

[ADS](#) [CAS](#) [PubMed](#) [PubMed Central](#) [Google Scholar](#)

7. 7.

Bertomeu, T. et al. A high-resolution genome-wide CRISPR/Cas9 viability screen reveals structural features and contextual diversity of the human cell-essential proteome. *Mol. Cell. Biol.* **38**, e00302-17 (2017).

[PubMed](#) [PubMed Central](#) [Google Scholar](#)

8. 8.

Yoshino, J., Baur, J. A. & Imai, S. I. NAD⁺ intermediates: the biology and therapeutic potential of NMN and NR. *Cell Metab.* **27**, 513–528 (2018).

[CAS](#) [Google Scholar](#)

9. 9.

Cambronne, X. A. et al. Biosensor reveals multiple sources for mitochondrial NAD⁺. *Science* **352**, 1474–1477 (2016).

[ADS](#) [CAS](#) [PubMed](#) [PubMed Central](#) [Google Scholar](#)

10. 10.

Pittelli, M. et al. Inhibition of nicotinamide phosphoribosyltransferase: cellular bioenergetics reveals a mitochondrial insensitive NAD pool. *J. Biol. Chem.* **285**, 34106–34114 (2010).

[CAS](#) [PubMed](#) [PubMed Central](#) [Google Scholar](#)

11. 11.

Sims, C. A. et al. Nicotinamide mononucleotide preserves mitochondrial function and increases survival in hemorrhagic shock. *JCI Insight* **3**, 120182 (2018).

[Google Scholar](#)

12. 12.

Titus, S. A. & Moran, R. G. Retrovirally mediated complementation of the glyB phenotype. Cloning of a human gene encoding the carrier for entry of folates into mitochondria. *J. Biol. Chem.* **275**, 36811–36817 (2000).

[CAS](#) [Google Scholar](#)

13. 13.

Spaan, A. N. et al. Identification of the human mitochondrial FAD transporter and its potential role in multiple acyl-CoA dehydrogenase deficiency. *Mol. Genet. Metab.* **86**, 441–447 (2005).

[CAS](#) [Google Scholar](#)

14. 14.

Berger, F., Lau, C., Dahlmann, M. & Ziegler, M. Subcellular compartmentation and differential catalytic properties of the three

human nicotinamide mononucleotide adenylyltransferase isoforms. *J. Biol. Chem.* **280**, 36334–36341 (2005).

[CAS](#) [Google Scholar](#)

15. 15.

Davila, A. et al. Nicotinamide adenine dinucleotide is transported into mammalian mitochondria. *eLife* **7**, e33246 (2018).

[PubMed](#) [PubMed Central](#) [Google Scholar](#)

16. 16.

Fletcher, R. S. et al. Nicotinamide riboside kinases display redundancy in mediating nicotinamide mononucleotide and nicotinamide riboside metabolism in skeletal muscle cells. *Mol. Metab.* **6**, 819–832 (2017).

[CAS](#) [PubMed](#) [PubMed Central](#) [Google Scholar](#)

17. 17.

Nikiforov, A., Dölle, C., Niere, M. & Ziegler, M. Pathways and subcellular compartmentation of NAD biosynthesis in human cells: from entry of extracellular precursors to mitochondrial NAD generation. *J. Biol. Chem.* **286**, 21767–21778 (2011).

[CAS](#) [PubMed](#) [PubMed Central](#) [Google Scholar](#)

18. 18.

Hikosaka, K. et al. Deficiency of nicotinamide mononucleotide adenylyltransferase 3 (nmnAT3) causes hemolytic anemia by altering the glycolytic flow in mature erythrocytes. *J. Biol. Chem.* **289**, 14796–14811 (2014).

[CAS](#) [PubMed](#) [PubMed Central](#) [Google Scholar](#)

19. 19.

Yamamoto, M. et al. Nmnat3 is dispensable in mitochondrial NAD⁺ level maintenance in vivo. *PLoS ONE* **11**, e0147037 (2016).

[PubMed](#) [PubMed Central](#) [Google Scholar](#)

20. 20.

Uhlén, M. et al. Proteomics. Tissue-based map of the human proteome. *Science* **347**, 1260419 (2015).

[Google Scholar](#)

21. 21.

Sallin, O. et al. Semisynthetic biosensors for mapping cellular concentrations of nicotinamide adenine dinucleotides. *eLife* **7**, e32638 (2018).

[PubMed](#) [PubMed Central](#) [Google Scholar](#)

22. 22.

Blomen, V. A. et al. Gene essentiality and synthetic lethality in haploid human cells. *Science* **350**, 1092–1096 (2015).

[ADS](#) [CAS](#) [Google Scholar](#)

23. 23.

Hart, T. et al. High-resolution CRISPR screens reveal fitness genes and genotype-specific cancer liabilities. *Cell* **163**, 1515–1526 (2015).

[CAS](#) [PubMed](#) [Google Scholar](#)

24. 24.

Agerholm, M. et al. Perturbations of NAD⁺ salvage systems impact mitochondrial function and energy homeostasis in mouse myoblasts

and intact skeletal muscle. *Am. J. Physiol. Endocrinol. Metab.* **314**, E377–E395 (2018).

[CAS](#) [Google Scholar](#)

25. 25.

Frederick, D. W. et al. Loss of NAD homeostasis leads to progressive and reversible degeneration of skeletal muscle. *Cell Metab.* **24**, 269–282 (2016).

[MathSciNet](#) [CAS](#) [PubMed](#) [PubMed Central](#) [Google Scholar](#)

26. 26.

Rustin, P. et al. Fluxes of nicotinamide adenine dinucleotides through mitochondrial membranes in human cultured cells. *J. Biol. Chem.* **271**, 14785–14790 (1996).

[CAS](#) [Google Scholar](#)

27. 27.

Agrimi, G. et al. Deletion or overexpression of mitochondrial NAD⁺ carriers in *Saccharomyces cerevisiae* alters cellular NAD and ATP contents and affects mitochondrial metabolism and the rate of glycolysis. *Appl. Environ. Microbiol.* **77**, 2239–2246 (2011).

[CAS](#) [PubMed](#) [PubMed Central](#) [Google Scholar](#)

28. 28.

Floyd, B. J. et al. Mitochondrial protein interaction mapping identifies regulators of respiratory chain function. *Mol. Cell* **63**, 621–632 (2016).

[CAS](#) [PubMed](#) [PubMed Central](#) [Google Scholar](#)

29. 29.

Dölle, C., Niere, M., Lohndal, E. & Ziegler, M. Visualization of subcellular NAD pools and intra-organellar protein localization by poly-ADP-ribose formation. *Cell. Mol. Life Sci.* **67**, 433–443 (2010).

[Google Scholar](#)

30. 30.

Trammell, S. A. & Brenner, C. Targeted, LCMS-based metabolomics for quantitative measurement of NAD⁺ metabolites. *Comput. Struct. Biotechnol. J.* **4**, e201301012 (2013).

[PubMed](#) [PubMed Central](#) [Google Scholar](#)

31. 31.

Zhang, Q., Piston, D. W. & Goodman, R. H. Regulation of corepressor function by nuclear NADH. *Science* **295**, 1895–1897 (2002).

[ADS](#) [CAS](#) [Google Scholar](#)

32. 32.

Zhao, Y. et al. SoNar, a highly responsive NAD⁺/NADH sensor, allows high-throughput metabolic screening of anti-tumor agents. *Cell Metab.* **21**, 777–789 (2015).

[CAS](#) [PubMed](#) [PubMed Central](#) [Google Scholar](#)

33. 33.

Ho, B., Baryshnikova, A. & Brown, G. W. Unification of protein abundance datasets yields a quantitative *Saccharomyces cerevisiae* proteome. *Cell Syst.* **6**, 192–205 (2018).

[CAS](#) [Google Scholar](#)

34. 34.

Malecki, M. J. et al. Leukemia-associated mutations within the NOTCH1 heterodimerization domain fall into at least two distinct mechanistic classes. *Mol. Cell. Biol.* **26**, 4642–4651 (2006).

[CAS](#) [PubMed](#) [PubMed Central](#) [Google Scholar](#)

35. 35.

Eller, J. M. et al. Flow cytometry analysis of free intracellular NAD⁺ using a targeted biosensor. *Curr. Protoc. Cytom.* **88**, e54 (2019).

[Google Scholar](#)

36. 36.

Wang, L. et al. Peak annotation and verification engine for untargeted LC–MS metabolomics. *Anal. Chem.* **91**, 1838–1846 (2019).

[CAS](#) [PubMed](#) [PubMed Central](#) [Google Scholar](#)

37. 37.

Adusumilli, R. & Mallick, P. Data conversion with ProteoWizard msConvert. *Methods Mol. Biol.* **1550**, 339–368 (2017).

[CAS](#) [Google Scholar](#)

38. 38.

Su, X., Lu, W. & Rabinowitz, J. D. Metabolite spectral accuracy on orbitraps. *Anal. Chem.* **89**, 5940–5948 (2017).

[CAS](#) [PubMed](#) [PubMed Central](#) [Google Scholar](#)

39. 39.

Chong, J., Wishart, D. S. & Xia, J. Using MetaboAnalyst 4.0 for comprehensive and integrative metabolomics data analysis. *Curr. Protoc. Bioinformatics* **68**, e86 (2019).

[PubMed](#) [PubMed Central](#) [Google Scholar](#)

40. 40.

Amberg, D. C., Burke, D. J. & Strathern, J. N. High-efficiency transformation of yeast. *CSH Protoc* **2006**, pdb.prot4145 (2006).

[Google Scholar](#)

41. 41.

Meisinger, C., Pfanner, N. & Truscott, K. N. Isolation of yeast mitochondria. *Methods Mol. Biol.* **313**, 33–39 (2006).

[CAS](#) [Google Scholar](#)

42. 42.

Izawa, T. & Unger, A. K. Isolation of mitochondria from *Saccharomyces cerevisiae*. *Methods Mol. Biol.* **1567**, 33–42 (2017).

[CAS](#) [Google Scholar](#)

43. 43.

Bricker, D. K. et al. A mitochondrial pyruvate carrier required for pyruvate uptake in yeast, *Drosophila*, and humans. *Science* **337**, 96–100 (2012).

[ADS](#) [CAS](#) [PubMed](#) [PubMed Central](#) [Google Scholar](#)

[Download references](#)

Acknowledgements

We thank all members of the Baur and Cambronne laboratories, V. Moiseenkova-Bell, A. Ellington, E. Marcotte, R. Goodman, I. Heiland, M. Whorton, E. Gouaux and J. Dixon for constructive discussions and

suggestions; and M. Blair, Q. Chen, V. Annamalai, X. Yu, A. Slepian and CBRS UT Austin Proteomics Facility for technical support. This work was supported by grants from the National Institutes of Health (R01DK098656 to J.A.B., DP2GM126897 to X.A.C., TL1TR001880, T32AR53461 and F32HL145923 to T.S.L.) and the Norwegian Research Council (250395/F20 to M.Z.).

Author information

Affiliations

1. Department of Physiology and Institute for Diabetes, Obesity, and Metabolism, Perelman School of Medicine, University of Pennsylvania, Philadelphia, PA, USA

Timothy S. Luongo, Caroline Perry, Marc R. Bornstein & Joseph A. Baur

2. Department of Molecular Biosciences, University of Texas at Austin, Austin, TX, USA

Jared M. Eller, Mu-Jie Lu, Paul Oliiphint & Xiaolu A. Cambronne

3. Department of Biomedicine, University of Bergen, Bergen, Norway

Marc Niere & Mathias Ziegler

4. Department of Chemical Biology, Max Planck Institute for Medical Research, Heidelberg, Germany

Fabio Raith & Kai Johnsson

5. Faculty of Chemistry and Earth Sciences, University of Heidelberg, Heidelberg, Germany

Fabio Raith

6. Lewis-Sigler Institute for Integrative Genomics, Department of Chemistry, Princeton University, Princeton, NJ, USA

Lin Wang, Melanie R. McReynolds & Joshua D. Rabinowitz
 7. Mitchell Cancer Institute, University of South Alabama, Mobile, AL, USA

Marie E. Migaud
 8. Department of Pathology and Laboratory Medicine, Perlman School of Medicine, University of Pennsylvania, Philadelphia, PA, USA

F. Brad Johnson
 9. Institute of Chemical Sciences and Engineering, École Polytechnique Fédérale de Lausanne (EPFL), Lausanne, Switzerland

Kai Johnsson
- Authors
1. Timothy S. Luongo
[View author publications](#)

You can also search for this author in [PubMed](#) [Google Scholar](#)
 2. Jared M. Eller
[View author publications](#)

You can also search for this author in [PubMed](#) [Google Scholar](#)
 3. Mu-Jie Lu
[View author publications](#)

You can also search for this author in [PubMed](#) [Google Scholar](#)
 4. Marc Niere
[View author publications](#)

You can also search for this author in [PubMed](#) [Google Scholar](#)

5. Fabio Raith

[View author publications](#)

You can also search for this author in [PubMed](#) [Google Scholar](#)

6. Caroline Perry

[View author publications](#)

You can also search for this author in [PubMed](#) [Google Scholar](#)

7. Marc R. Bornstein

[View author publications](#)

You can also search for this author in [PubMed](#) [Google Scholar](#)

8. Paul Oliphint

[View author publications](#)

You can also search for this author in [PubMed](#) [Google Scholar](#)

9. Lin Wang

[View author publications](#)

You can also search for this author in [PubMed](#) [Google Scholar](#)

10. Melanie R. McReynolds

[View author publications](#)

You can also search for this author in [PubMed](#) [Google Scholar](#)

11. Marie E. Migaud

[View author publications](#)

You can also search for this author in [PubMed](#) [Google Scholar](#)

12. Joshua D. Rabinowitz

[View author publications](#)

You can also search for this author in [PubMed](#) [Google Scholar](#)

13. F. Brad Johnson

[View author publications](#)

You can also search for this author in [PubMed](#) [Google Scholar](#)

14. Kai Johnsson

[View author publications](#)

You can also search for this author in [PubMed](#) [Google Scholar](#)

15. Mathias Ziegler

[View author publications](#)

You can also search for this author in [PubMed](#) [Google Scholar](#)

16. Xiaolu A. Cambronne

[View author publications](#)

You can also search for this author in [PubMed](#) [Google Scholar](#)

17. Joseph A. Baur

[View author publications](#)

You can also search for this author in [PubMed](#) [Google Scholar](#)

Contributions

T.S.L., X.A.C. and J.A.B. conceived and designed the overall study. T.S.L., J.M.E., M.-J.L., M.E.M., J.D.R., F.B.J., X.A.C. and J.A.B. contributed to the development of the hypotheses and experimental approaches. T.S.L., J.M.E., M.-J.L., M.N., F.R., M.R.M, C.P., M.R.B. and P.O. performed and analysed experiments. All authors contributed to the interpretation of experiments. T.S.L., X.A.C. and J.A.B. wrote the manuscript. J.M.E., M.-J.L., K.J. and M.Z. edited, and all authors reviewed the manuscript.

Corresponding authors

Correspondence to [Xiaolu A. Cambronne](#) or [Joseph A. Baur](#).

Ethics declarations

Competing interests

J.D.R. is a co-founder of Toran Therapeutics. The remaining authors declare no competing interests.

Additional information

Peer review information *Nature* thanks Ferdinando Palmieri and the other, anonymous, reviewer(s) for their contribution to the peer review of this work.

Publisher's note Springer Nature remains neutral with regard to jurisdictional claims in published maps and institutional affiliations.

Extended data figures and tables

[Extended Data Fig. 1 SLC25A51 is a mitochondrial protein that affects cellular NAD⁺ distribution, proliferation, and metabolome profiles.](#)

a, b, qPCR quantification of *SLC25A51* mRNA expression in HEK 293T ($n = 3$) (**a**) and HeLa cells ($n = 3$) (**b**) expressing shRNA targeting *SLC25A51*. **c, d,** NAD⁺ content of isolated mitochondria ($n = 3$) (**c**) and whole cell lysates ($n = 3$) (**d**) from HeLa cells with stable shRNA knockdown of *SLC25A51* (KD) and non-targeting control (Ctrl). **e,** Western blot confirming shRNA targeting murine *Slc25a51* reduces SLC25A51 protein expression in cells transfected with cDNA encoding SLC25A51-FLAG. **f,** Mitochondrial free NAD⁺ levels in mouse embryonic stem cells expressing shRNA against *Slc25a51* and non-targeting shRNA (shFF2), as measured with the mitochondrial cpVenus NAD⁺ biosensor ($n = 3$). **g,** qPCR quantification of *SLC25A51* mRNA expression in HeLa cells

transfected with siRNA targeting *SLC25A51* ($n = 3$). **h**, Western blot confirming protein expression of Flag-tagged mitochondrial carriers. Controls include stable expression of the NAD⁺ biosensor (sensor) and anti-Tubulin for loading. **i**, Immunofluorescent detection of *SLC25A51* and *SLC25A52* subcellular localization. Cells were transiently transfected with cDNA encoding Flag-HA-tagged *SLC25A51* or *SLC25A52* and probed with anti-Flag and the mitochondrial marker, anti-MTC02. Scale bar: 10 μM, 2 μM on inset. Inset represents zoomed view of Flag localization and mitochondria. **j–l**, Proliferation of HAP1 *SLC25A51*-KO ($n = 8$) (**j**), HEK 293T *SLC25A51* shRNA-knockdown ($n = 8$) (**k**), HeLa *SLC25A51* shRNA-knockdown cells ($n = 8$) (**l**) and their respective controls. Proliferation was measured by CyQuant, a fluorescent DNA dye, at 0h and 96h after plating and expressed as fold change. **m–o**, qPCR quantification of *SLC25A52* mRNA expression in HAP1 *SLC25A51*-KO (**m**), HEK 293T *SLC25A51* shRNA-knockdown (**n**) and HeLa *SLC25A51* shRNA-knockdown cells ($n = 3$) (**o**). **p**, Western blot of whole cell protein lysates from HAP1 wild type (WT) and *SLC25A51* knockout (KO) cells confirming *SLC25A51* loss. Loading control is total protein measured by Revert 700 Total Protein. **q, r**, Heat map of top 30 mitochondrial (**q**) and whole cell metabolites (**r**) that differ between HAP1 wild type and *SLC25A51*-KO cells ($n = 3$). Data represented as mean ± SEM. *P* values were determined by unpaired, two-tailed Student's *t*-test (for two groups) or one-way ANOVA with multiple comparisons analysis using Dunnett's method (for groups of three or more). **P* < 0.05, and ****P* < 0.001 vs control or WT (exact *P* values are provided in the source data). [Source data](#)

Extended Data Fig. 2 NAD⁺ and *SLC25A51* affect oxidative phosphorylation.

a, Respiration of isolated mitochondria from HEK 293T cells treated with either vehicle (Veh) or the NAMPT inhibitor FK866 to deplete mitochondrial NAD⁺. Mitochondria were treated with pyruvate and malate (state 2), then ADP was added to induce state 3 respiration. 1 mM NAD⁺ was added to test the ability of exogenous NAD⁺ to rescue respiration in the setting of mitochondria NAD⁺ depletion (Trace is representative of $n = 4$ independent experiments). *P* values were determined by two-way ANOVA

with multiple comparisons analysis using the Sidak method. **b**, Oxygen consumption rate (OCR) was measured in *SLC25A51* shRNA knockdown (KD) and control (Ctrl) HeLa cells using a Seahorse XF96e. Basal OCR was measured before the addition of treatments and maximal respiration was measured after the sequential addition of oligomycin (Oligo, ATP synthase inhibitor) and FCCP (uncoupler). Rotenone (Rot) and Antimycin A (AA) were added as a control to completely block mitochondrial oxygen consumption ($n = 6$). **c**, Respiration of isolated mitochondria from *SLC25A51* knockdown HEK 293T cells. Mitochondria were treated with pyruvate/malate (state 2), and then ADP was added to induce state 3 respiration. Oligomycin was added to block ATP synthase-mediated respiration ($n = 3$ independent experiments). **d**, Mitochondria were isolated from HEK 293T control, *SLC25A51* shRNA knockdown cells, and controls treated with FK866 to deplete mitochondrial NAD⁺. Mitochondrial oxygen consumption rate was measured after treatment with pyruvate/malate (state 2), ADP (state 3), and 1 mM NAD⁺ ($n = 4$ independent experiments). **e, f**, Mean volume per mitochondrial unit (**e**) and number of distinct mitochondria per cell (**f**) quantified from confocal image reconstructions of mitochondrial voxels in *SLC25A51* shRNA knockdown ($n = 31$ cells) and control ($n = 32$ cells) HeLa cells. Data represented as mean \pm SEM. *P* values were determined by unpaired, two-tailed Student's *t*-test. **P* < 0.05, ***P* < 0.01, and ****P* < 0.001 vs vehicle or control; ###*P* < 0.001 vs state 3 (exact *P* values are provided in the source data). [Source data](#)

Extended Data Fig. 3 Intact NAD⁺, but not nicotinamide or nicotinamide mononucleotide contributes to the mitochondrial NAD[±] pool.

a, Mitochondrial NAD⁺ content was measured in isolated mitochondria from HeLa control (Ctrl) cells, control cells treated with FK866 (Ctrl+FK), and *SLC25A51* shRNA-knockdown (KD) cells. NAD⁺ content of isolated mitochondria was determined before (untreated) and after a 40-min incubation with 1 mM NAD⁺ ($n = 3$ independent experiments). **b**, NAD⁺ levels in HEK 293T mitochondria incubated with 1 mM nicotinamide (NAM), 1 mM nicotinamide mononucleotide (NMN), or 1 mM NAD⁺

($n = 3$ independent experiments). **c**, NAD⁺ uptake in NAD⁺-depleted mitochondria isolated from HEK 293T cells incubated with NAD⁺ ± 2 mM NAM or 2mM NMN ($n = 4$ independent experiments). **d**, Fractional labelling of mitochondrial NAD⁺ in HAP1 cells treated with isotopically double labelled NaR ($n = 3$ biological independent replicates). Data represented as mean ± SEM. P values were determined by unpaired, two-tailed Student's *t*-test (for two groups) or one-way ANOVA with multiple comparisons analysis using Dunnett's or Tukey's method (for groups of three or more). * $P < 0.05$ and *** $P < 0.001$ vs untreated, vehicle, and wild-type M+0; # $P < 0.05$ vs wild-type M+1. [Source data](#)

Extended Data Fig. 4 Generation and validation of yeast strains for testing mitochondrial NAD⁺ transport.

a, PCR genotyping to confirm double knockout gene deletion in BY4727 *S. cerevisiae* via antibiotic-resistance cassette replacement at the *NDT1* and *NDT2* loci. **b, c**, Deletion of the mitochondrial NAD⁺ carriers *NDT1* and *NDT2* in DKO strain phenocopied previously described growth defects on non-fermentative media (YP, 3% glycerol media)², which was rescued by plasmid expression of NDT1. **d**, Western blot confirmed enrichment of mitochondrial markers (MTC02 and COXIV) and absence of cytoplasmic proteins (actin) or ER (SC2) in isolated mitochondria from yeast. **e**, RT-PCR confirmed ectopic expression from pRS415-SLC25A51 and pRS415-SLC25A52 in DKO strains.

Extended Data Fig. 5 Kinetics and selectivity of NAD⁺ transport by human SLC25A51 expressed in yeast mitochondria.

a–c, Co-incubation with excess unlabelled NAD⁺ ($n = 5$ independent experiments for 1 mM NAD⁺) (a), supraphysiological levels of NMN (100 μM, $n = 4$ independent experiments; 500 μM, $n = 5$ independent experiments) (b), NADH ($n = 3$ independent experiments) with ³H-NAD⁺ to measure uptake competition in mitochondria from DKO yeast expressing SLC25A51 (c). **d**, Proportional relationship between integrated peak

intensities from mass spectrometry of mitochondrial samples compared to a known meta data set of absolute protein abundances; used to quantitate SLC25A51 abundance in yeast samples. **e**, Uptake measured with indicated NAD⁺ concentrations; calculated from specific activity ($n = 3$ independent experiments, mean \pm SEM). **f**, Lineweaver-Burk plot based on a nonlinear fit with datapoints overlaid ($n = 3$ independent experiments). P values were determined by two-way ANOVA with multiple comparisons analysis using Sidak's method. * $P < 0.05$ and ** $P < 0.01$ vs 100 μM cold NAD⁺. [Source data](#)

Extended Data Table 1 Essential mitochondrial solute carrier family 25 genes determined by genome-wide CRISPR/Cas9 screens examining cellular viability

[Full size table](#)

Extended Data Table 2 Initial NAD⁺ uptake rates calculated from specific activity in isolated mitochondria

[Full size table](#)

Supplementary information

[Supplementary Figures](#)

This file contains Supplementary Figure 1: the uncropped scan images of western blot membranes and DNA gels, and Supplementary Figure 2: the gating strategy for flow cytometry analysis.

[Reporting Summary](#)

Source data

[Source Data Fig. 1](#)

[Source Data Fig. 2](#)

[Source Data Fig. 3](#)

[Source Data Fig. 4](#)

[Source Data Extended Data Fig. 1](#)

[Source Data Extended Data Fig. 2](#)

[Source Data Extended Data Fig. 3](#)

[Source Data Extended Data Fig. 5](#)

Rights and permissions

[Reprints and Permissions](#)

About this article



Check for
updates

Cite this article

Luongo, T.S., Eller, J.M., Lu, M.J. *et al.* SLC25A51 is a mammalian mitochondrial NAD⁺ transporter. *Nature* **588**, 174–179 (2020).
<https://doi.org/10.1038/s41586-020-2741-7>

[Download citation](#)

- Received: 22 December 2019
- Accepted: 01 September 2020
- Published: 09 September 2020
- Issue Date: 03 December 2020

- DOI: <https://doi.org/10.1038/s41586-020-2741-7>

Comments

By submitting a comment you agree to abide by our [Terms](#) and [Community Guidelines](#). If you find something abusive or that does not comply with our terms or guidelines please flag it as inappropriate.

[Access through your institution](#)

[Change institution](#)

[Buy or subscribe](#)

This article was downloaded by **calibre** from <https://www.nature.com/articles/s41586-020-2741-7>

| [Section menu](#) | [Main menu](#) |

Amendments & Corrections

- [**Author Correction: Insulin resistance in cavefish as an adaptation to a nutrient-limited environment**](#) [13 November 2020]
Author Correction •
- [**Author Correction: Relatives of rubella virus in diverse mammals**](#) [17 November 2020]
Author Correction •
- [**Publisher Correction: Exuberant fibroblast activity compromises lung function via ADAMTS4**](#) [18 November 2020]
Publisher Correction •
- [**Addendum: A pneumonia outbreak associated with a new coronavirus of probable bat origin**](#) [17 November 2020]
Addendum •
- [**Retraction Note: Living annulative \$\pi\$ -extension polymerization for graphene nanoribbon synthesis**](#) [25 November 2020]
Retraction •
- [**Publisher Correction: Butterfly effect and a self-modulating El Niño response to global warming**](#) [17 November 2020]
Publisher Correction •

Author Correction: Insulin resistance in cavefish as an adaptation to a nutrient-limited environment

[Download PDF](#)

- Author Correction
- [Published: 13 November 2020](#)

Author Correction: Insulin resistance in cavefish as an adaptation to a nutrient-limited environment

- [Misty R. Riddle](#)^{1 na1},
- [Ariel C. Aspiras](#)^{1 na1},
- [Karin Gaudenz](#)²,
- [Robert Peuß](#)²,
- [Jenny Y. Sung](#)²,
- [Brian Martineau](#)¹,
- [Megan Peavey](#)¹,
- [Andrew C. Box](#)²,
- [Julius A. Tabin](#)¹,
- [Suzanne McGaugh](#)³,
- [Richard Borowsky](#)⁴,
- [Clifford J. Tabin](#)¹ &
- [Nicolas Rohner](#)^{2,5}

[Nature](#) volume 588, page E1 (2020) [Cite this article](#)

- 1035 Accesses

- 3 Altmetric
- [Metrics details](#)

Subjects

- [Ecophysiology](#)
- [Evolutionary genetics](#)

The [Original Article](#) was published on 21 March 2018

[Download PDF](#)

Correction to: *Nature* <https://doi.org/10.1038/nature26136> Published online
21 March 2018

Cave-adapted populations of the Mexican tetra, *Astyanax mexicanus*, have dysregulated blood glucose homeostasis and are insulin-resistant compared to river-adapted ('surface') populations. We found that multiple cave populations, including those inhabiting the Tinaja and Pachón caves, carry a mutation in the insulin receptor that leads to decreased insulin binding in vitro and contributes to hyperglycaemia. As part of the analysis that led to this conclusion, we measured fasting blood glucose levels in F₂ fish derived from a cross between a surface fish homozygous for the ancestral insulin receptor allele and a cavefish homozygous for the derived allele, allowing us to correlate inheritance of the mutation with inheritance of glucose dysregulation. In this Article, we inadvertently indicated that the cavefish grandparent used in this cross was descended from the Tinaja population. However, subsequent analysis has definitively indicated that this individual actually belongs to the Pachón population. However, as both the Tinaja and Pachón populations carry the same P211L mutation in the insulin receptor, the logic of the experiment, the genotype–phenotype correlation we observed, and the conclusions of the study remain unchanged. Everything in the manuscript is still accurate, other than the name of the cave in the second and third paragraphs on page 649 of the PDF version of the original

Article and in Fig. 3b and its legend. This error has not been corrected online.

Author information

Author notes

1. These authors contributed equally: Misty R. Riddle, Ariel C. Aspiras

Affiliations

1. Department of Genetics, Harvard Medical School, Boston, Massachusetts, 02115, USA

Misty R. Riddle, Ariel C. Aspiras, Brian Martineau, Megan Peavey, Julius A. Tabin & Clifford J. Tabin

2. Stowers Institute for Medical Research, Kansas City, Missouri, 64110, USA

Karin Gaudenz, Robert Peuß, Jenny Y. Sung, Andrew C. Box & Nicolas Rohner

3. College of Biomedical Sciences, University of Minnesota, St. Paul, Minnesota, 55108, USA

Suzanne McGaugh

4. Department of Biology, New York University, New York, New York, 10003, USA

Richard Borowsky

5. Department of Molecular and Integrative Physiology, University of Kansas Medical Center, Kansas City, Kansas, 66160, USA

Nicolas Rohner

Authors

1. Misty R. Riddle

[View author publications](#)

You can also search for this author in [PubMed](#) [Google Scholar](#)

2. Ariel C. Aspiras

[View author publications](#)

You can also search for this author in [PubMed](#) [Google Scholar](#)

3. Karin Gaudenz

[View author publications](#)

You can also search for this author in [PubMed](#) [Google Scholar](#)

4. Robert Peuß

[View author publications](#)

You can also search for this author in [PubMed](#) [Google Scholar](#)

5. Jenny Y. Sung

[View author publications](#)

You can also search for this author in [PubMed](#) [Google Scholar](#)

6. Brian Martineau

[View author publications](#)

You can also search for this author in [PubMed](#) [Google Scholar](#)

7. Megan Peavey

[View author publications](#)

You can also search for this author in [PubMed](#) [Google Scholar](#)

8. Andrew C. Box

[View author publications](#)

You can also search for this author in [PubMed](#) [Google Scholar](#)

9. Julius A. Tabin

[View author publications](#)

You can also search for this author in [PubMed](#) [Google Scholar](#)

10. Suzanne McGaugh

[View author publications](#)

You can also search for this author in [PubMed](#) [Google Scholar](#)

11. Richard Borowsky

[View author publications](#)

You can also search for this author in [PubMed](#) [Google Scholar](#)

12. Clifford J. Tabin

[View author publications](#)

You can also search for this author in [PubMed](#) [Google Scholar](#)

13. Nicolas Rohner

[View author publications](#)

You can also search for this author in [PubMed](#) [Google Scholar](#)

Corresponding author

Correspondence to [Clifford J. Tabin](#).

Rights and permissions

[Reprints and Permissions](#)

About this article



Check for
updates

Cite this article

Riddle, M.R., Aspiras, A.C., Gaudenz, K. *et al.* Author Correction: Insulin resistance in cavefish as an adaptation to a nutrient-limited environment. *Nature* **588**, E1 (2020). <https://doi.org/10.1038/s41586-020-2953-x>

[Download citation](#)

- Published: 13 November 2020
- Issue Date: 03 December 2020
- DOI: <https://doi.org/10.1038/s41586-020-2953-x>

Comments

By submitting a comment you agree to abide by our [Terms](#) and [Community Guidelines](#). If you find something abusive or that does not comply with our terms or guidelines please flag it as inappropriate.

[Download PDF](#)

This article was downloaded by **calibre** from <https://www.nature.com/articles/s41586-020-2953-x>

Author Correction: Relatives of rubella virus in diverse mammals

[Download PDF](#)

- Author Correction
- [Published: 17 November 2020](#)

Author Correction: Relatives of rubella virus in diverse mammals

- [Andrew J. Bennett^{1 na1}](#),
- [Adrian C. Paskey^{2,3,4 na1}](#),
- [Arnt Ebinger^{5 na1}](#),
- [Florian Pfaff](#) [ORCID: orcid.org/0000-0003-0178-6183⁵](#),
- [Grit Priemer⁶](#),
- [Dirk Höper⁵](#),
- [Angele Breithaupt](#) [ORCID: orcid.org/0000-0002-6373-5923⁷](#),
- [Elisa Heuser^{8,9}](#),
- [Rainer G. Ulrich^{8,9}](#),
- [Jens H. Kuhn](#) [ORCID: orcid.org/0000-0002-7800-6045¹⁰](#),
- [Kimberly A. Bishop-Lilly^{2,4}](#),
- [Martin Beer](#) [ORCID: orcid.org/0000-0002-0598-5254⁵](#) &
- [Tony L. Goldberg](#) [ORCID: orcid.org/0000-0003-3962-4913^{1,11}](#)

[Nature](#) volume 588, page E2(2020) [Cite this article](#)

- 317 Accesses
- 2 Altmetric
- [Metrics details](#)

Subjects

- [Microbial ecology](#)
- [Viral infection](#)

The [Original Article](#) was published on 07 October 2020

[Download PDF](#)

Correction to: *Nature* <https://doi.org/10.1038/s41586-020-2812-9> Published online 07 October 2020

In the main text of this Article, ‘a Bennett’s tree-kangaroo (*Dendrolagus bennettianus* De Vis, 1886)’ should have stated ‘a red-necked wallaby (*Macropus rufogriseus* Desmarest, 1817)’, and all occurrences of ‘Bennett’s tree-kangaroo’ in the text should have been ‘red-necked wallaby’. This error resulted from a mistranslation from German to English of ‘Bennettkänguru’ (red-necked wallaby) as ‘Bennett-Baumkänguru’ (Bennett’s tree-kangaroo). No molecular data were included in the paper from this animal, so no changes are necessary to any data deposited in online databases. The original Article has been corrected online.

Author information

Author notes

1. These authors contributed equally: Andrew J. Bennett, Adrian C. Paskey, Arnt Ebinger

Affiliations

1. Department of Pathobiological Sciences, University of Wisconsin-Madison, Madison, WI, USA

Andrew J. Bennett & Tony L. Goldberg

2. Department of Microbiology and Immunology, Uniformed Services University of the Health Sciences, Bethesda, MD, USA

Adrian C. Paskey & Kimberly A. Bishop-Lilly

3. Leidos, Reston, VA, USA

Adrian C. Paskey

4. Genomics and Bioinformatics Department, Biological Defense Research Directorate, Naval Medical Research Center–Frederick, Fort Detrick, Frederick, MD, USA

Adrian C. Paskey & Kimberly A. Bishop-Lilly

5. Institute of Diagnostic Virology, Friedrich-Loeffler-Institut, Greifswald-Insel Riems, Germany

Arnt Ebinger, Florian Pfaff, Dirk Höper & Martin Beer

6. State Office for Agriculture, Food Safety and Fisheries, Rostock, Germany

Grit Priemer

7. Department of Experimental Animal Facilities and Biorisk Management, Friedrich-Loeffler-Institut, Greifswald-Insel Riems, Germany

Angele Breithaupt

8. Institute of Novel and Emerging Infectious Diseases, Friedrich-Loeffler-Institut, Greifswald-Insel Riems, Germany

Elisa Heuser & Rainer G. Ulrich

9. German Center for Infection Research (DZIF), Hamburg-Lübeck-Borstel-Insel Riems, Greifswald-Insel Riems, Germany

Elisa Heuser & Rainer G. Ulrich

10. Integrated Research Facility at Fort Detrick, National Institute of Allergy and Infectious Diseases, National Institutes of Health, Fort Detrick, Frederick, MD, USA

Jens H. Kuhn

11. Global Health Institute, University of Wisconsin-Madison, Madison, WI, USA

Tony L. Goldberg

Authors

1. Andrew J. Bennett

[View author publications](#)

You can also search for this author in [PubMed](#) [Google Scholar](#)

2. Adrian C. Paskey

[View author publications](#)

You can also search for this author in [PubMed](#) [Google Scholar](#)

3. Arnt Ebinger

[View author publications](#)

You can also search for this author in [PubMed](#) [Google Scholar](#)

4. Florian Pfaff

[View author publications](#)

You can also search for this author in [PubMed](#) [Google Scholar](#)

5. Grit Priemer

[View author publications](#)

You can also search for this author in [PubMed](#) [Google Scholar](#)

6. Dirk Höper

[View author publications](#)

You can also search for this author in [PubMed](#) [Google Scholar](#)

7. Angele Breithaupt

[View author publications](#)

You can also search for this author in [PubMed](#) [Google Scholar](#)

8. Elisa Heuser

[View author publications](#)

You can also search for this author in [PubMed](#) [Google Scholar](#)

9. Rainer G. Ulrich

[View author publications](#)

You can also search for this author in [PubMed](#) [Google Scholar](#)

10. Jens H. Kuhn

[View author publications](#)

You can also search for this author in [PubMed](#) [Google Scholar](#)

11. Kimberly A. Bishop-Lilly

[View author publications](#)

You can also search for this author in [PubMed](#) [Google Scholar](#)

12. Martin Beer

[View author publications](#)

You can also search for this author in [PubMed](#) [Google Scholar](#)

13. Tony L. Goldberg

[View author publications](#)

You can also search for this author in [PubMed](#) [Google Scholar](#)

Corresponding authors

Correspondence to [Martin Beer](#) or [Tony L. Goldberg](#).

Rights and permissions

[Reprints and Permissions](#)

About this article



Check for
updates

Cite this article

Bennett, A.J., Paskey, A.C., Ebinger, A. *et al.* Author Correction: Relatives of rubella virus in diverse mammals. *Nature* **588**, E2 (2020).
<https://doi.org/10.1038/s41586-020-2897-1>

[Download citation](#)

- Published: 17 November 2020
- Issue Date: 03 December 2020
- DOI: <https://doi.org/10.1038/s41586-020-2897-1>

Comments

By submitting a comment you agree to abide by our [Terms](#) and [Community Guidelines](#). If you find something abusive or that does not comply with our terms or guidelines please flag it as inappropriate.

[Download PDF](#)

This article was downloaded by **calibre** from <https://www.nature.com/articles/s41586-020-2897-1>

| [Section menu](#) | [Main menu](#) |

Publisher Correction: Exuberant fibroblast activity compromises lung function via ADAMTS4

[Download PDF](#)

- Publisher Correction
- [Published: 18 November 2020](#)

Publisher Correction: Exuberant fibroblast activity compromises lung function via ADAMTS4

- [David F. Boyd¹,](#)
- [E. Kaitlynn Allen¹,](#)
- [Adrienne G. Randolph^{2,3},](#)
- [Xi-zhi J. Guo¹,](#)
- [Yunceng Weng⁴,](#)
- [Catherine J. Sanders¹,](#)
- [Resha Bajracharya¹,](#)
- [Natalie K. Lee⁵,](#)
- [Clifford S. Guy¹,](#)
- [Peter Vogel ORCID: orcid.org/0000-0002-7535-0545⁶,](#)
- [Wenda Guan⁴,](#)
- [Yimin Li ORCID: orcid.org/0000-0003-0810-5256⁴,](#)
- [Xiaoqing Liu⁴,](#)
- [Tanya Novak ORCID: orcid.org/0000-0002-7115-7545^{2,3},](#)
- [Margaret M. Newhams²,](#)
- [Thomas P. Fabrizio ORCID: orcid.org/0000-0002-8960-0728⁵,](#)
- [Nicholas Wohlgemuth ORCID: orcid.org/0000-0002-6450-6452⁵,](#)
- [Peter M. Mourani⁷,](#)
- [PALISI Pediatric Intensive Care Influenza \(PICFLU\) Investigators,](#)
- [Thomas N. Wight⁸,](#)

- [Stacey Schultz-Cherry](#) ORCID: [orcid.org/0000-0002-2021-727X⁵](https://orcid.org/0000-0002-2021-727X),
- [Stephanie A. Cormier^{9,10}](#),
- [Kathryn Shaw-Saliba¹¹](#),
- [Andrew Pekosz¹²](#),
- [Richard E. Rothman¹¹](#),
- [Kuan-Fu Chen^{13,14}](#),
- [Zifeng Yang⁴](#),
- [Richard J. Webby⁵](#),
- [Nanshan Zhong⁴](#),
- [Jeremy Chase Crawford](#) ORCID: [orcid.org/0000-0003-4096-6048¹](https://orcid.org/0000-0003-4096-6048) &
- [Paul G. Thomas](#) ORCID: [orcid.org/0000-0001-7955-0256¹](https://orcid.org/0000-0001-7955-0256)

[Nature](#) volume 588, pageE5(2020)[Cite this article](#)

- 513 Accesses
- 3 Altmetric
- [Metrics details](#)

Subjects

- [Acute inflammation](#)
- [Viral infection](#)

The [Original Article](#) was published on 28 October 2020

[Download PDF](#)

Correction to: *Nature* <https://doi.org/10.1038/s41586-020-2877-5> Published online 28 October 2020

In the Abstract of this Article, owing to an error during the production process, the start of the third sentence erroneously read ‘Although th influenza A/Puerto Rico/8/34 e host inflammatory response limits spread of

and eventually clears the pathogen,...' instead of 'Although the host inflammatory response limits spread of and eventually clears the pathogen, ...'. The original Article has been corrected online.

Author information

Affiliations

1. Department of Immunology, St Jude Children's Research Hospital, Memphis, TN, USA

David F. Boyd, E. Kaitlynn Allen, Xi-zhi J. Guo, Catherine J. Sanders, Resha Bajracharya, Clifford S. Guy, Jeremy Chase Crawford & Paul G. Thomas

2. Boston Children's Hospital, Department of Anesthesiology, Critical Care and Pain Medicine, Boston, MA, USA

Adrienne G. Randolph, Tanya Novak & Margaret M. Newhams

3. Department of Anesthesia, Harvard Medical School, Boston, MA, USA

Adrienne G. Randolph & Tanya Novak

4. State Key Laboratory of Respiratory Diseases, National Clinical Research Center for Respiratory Disease, Guangzhou Institute of Respiratory Health, The First Affiliated Hospital of Guangzhou Medical University, Guangzhou, China

Yunceng Weng, Wenda Guan, Yimin Li, Xiaoqing Liu, Zifeng Yang & Nanshan Zhong

5. Department of Infectious Diseases, St Jude Children's Research Hospital, Memphis, TN, USA

Natalie K. Lee, Thomas P. Fabrizio, Nicholas Wohlgemuth, Stacey Schultz-Cherry & Richard J. Webby

6. Veterinary Pathology Core, St Jude Children's Research Hospital,
Memphis, TN, USA

Peter Vogel

7. Section of Critical Care Medicine, Department of Pediatrics,
University of Colorado School of Medicine and Children's Hospital
Colorado, Aurora, CO, USA

Peter M. Mourani

8. Matrix Biology Program, Benaroya Research Institute, Seattle, WA,
USA

Thomas N. Wight

9. Department of Biological Sciences, Louisiana State University, Baton
Rouge, LA, USA

Stephania A. Cormier

10. Pennington Biomedical Research Center, Baton Rouge, LA, USA

Stephania A. Cormier

11. Department of Emergency Medicine and Medicine, Infectious
Diseases, Johns Hopkins University School of Medicine, Baltimore,
MD, USA

Kathryn Shaw-Saliba & Richard E. Rothman

12. Department of Molecular Microbiology and Immunology, Johns
Hopkins Bloomberg School of Public Health, Baltimore, MD, USA

Andrew Pekosz

13. Department of Emergency Medicine of Chang Gung Memorial
Hospital at Keelung, Keelung City, Taiwan

Kuan-Fu Chen

14. Clinical Informatics and Medical Statistics Research Center of Chang Gung University, Taoyuan, Taiwan

Kuan-Fu Chen

15. Children's of Alabama, Birmingham, AL, USA

Michele Kong

16. Arkansas Children's Hospital, Little Rock, AR, USA

Ronald C. Sanders Jr & Katherine Irby

17. Diamond Children's Medical Center, Tucson, AZ, USA

Katri Typpo

18. Children's Hospital Los Angeles, Los Angeles, CA, USA

Barry Markovitz

19. UCSF Benioff Children's Hospital Oakland, Oakland, CA, USA

Natalie Cvijanovich & Heidi Flori

20. Children's Hospital of Orange County, Orange, CA, USA

Adam Schwarz & Nick Anas

21. Children's Hospital Colorado, Aurora, CO, USA

Peter Mourani & Angela Czaja

22. Holtz Children's Hospital, Miami, FL, USA

Gwenn McLaughlin

23. Children's Healthcare of Atlanta at Egleston, Atlanta, GA, USA

Matthew Paden & Keiko Tarquinio

24. Ann & Robert H. Lurie Children's Hospital of Chicago, Chicago, IL, USA

Bria M. Coates

25. The University of Chicago Medicine Comer Children's Hospital, Chicago, IL, USA

Neethi Pinto & Juliane Bubeck Wardenburg

26. Boston Children's Hospital, Boston, MA, USA

Adrienne G. Randolph, Anna A. Agan, Tanya Novak & Margaret M. Newhams

27. Children's Hospital and Clinics of Minnesota, Minneapolis, MN, USA

Stephen C. Kuracheck

28. St Louis Children's Hospital, St Louis, MO, USA

Mary E. Hartman & Allan Doctor

29. Children's Hospital of Nebraska, Omaha, NE, USA

Edward J. Truemper & Sidharth Mahapatra

30. Golisano Children's Hospital, Rochester, NY, USA

Kate G. Ackerman & L. Eugene Daugherty

31. Nationwide Children's Hospital, Columbus, OH, USA

Mark W. Hall

32. Penn State Hershey's Children's Hospital, Hershey, PA, USA

Neal Thomas

33. The Children's Hospital of Philadelphia, Philadelphia, PA, USA

Scott L. Weiss & Julie Fitzgerald

34. Dell Children's Medical Center of Central Texas, Austin, TX, USA

Renee Higgerson

35. Texas Children's Hospital, Houston, TX, USA

Laura L. Loftis

36. Children's Hospital of Wisconsin, Milwaukee, WI, USA

Rainer G. Gedeit

37. Centre Hospitalier de l'Université Laval, Quebec, Quebec, Canada

Marc-André Dugas

Authors

1. David F. Boyd

[View author publications](#)

You can also search for this author in [PubMed](#) [Google Scholar](#)

2. E. Kaitlynn Allen

[View author publications](#)

You can also search for this author in [PubMed](#) [Google Scholar](#)

3. Adrienne G. Randolph

[View author publications](#)

You can also search for this author in [PubMed](#) [Google Scholar](#)

4. Xi-zhi J. Guo

[View author publications](#)

You can also search for this author in [PubMed](#) [Google Scholar](#)

5. Yunceng Weng

[View author publications](#)

You can also search for this author in [PubMed](#) [Google Scholar](#)

6. Catherine J. Sanders

[View author publications](#)

You can also search for this author in [PubMed](#) [Google Scholar](#)

7. Resha Bajracharya

[View author publications](#)

You can also search for this author in [PubMed](#) [Google Scholar](#)

8. Natalie K. Lee

[View author publications](#)

You can also search for this author in [PubMed](#) [Google Scholar](#)

9. Clifford S. Guy

[View author publications](#)

You can also search for this author in [PubMed](#) [Google Scholar](#)

10. Peter Vogel

[View author publications](#)

You can also search for this author in [PubMed](#) [Google Scholar](#)

11. Wenda Guan

[View author publications](#)

You can also search for this author in [PubMed](#) [Google Scholar](#)

12. Yimin Li

[View author publications](#)

You can also search for this author in [PubMed](#) [Google Scholar](#)

13. Xiaoqing Liu

[View author publications](#)

You can also search for this author in [PubMed](#) [Google Scholar](#)

14. Tanya Novak

[View author publications](#)

You can also search for this author in [PubMed](#) [Google Scholar](#)

15. Margaret M. Newhams

[View author publications](#)

You can also search for this author in [PubMed](#) [Google Scholar](#)

16. Thomas P. Fabrizio

[View author publications](#)

You can also search for this author in [PubMed](#) [Google Scholar](#)

17. Nicholas Wohlgemuth

[View author publications](#)

You can also search for this author in [PubMed](#) [Google Scholar](#)

18. Peter M. Mourani

[View author publications](#)

You can also search for this author in [PubMed](#) [Google Scholar](#)

19. Thomas N. Wight

[View author publications](#)

You can also search for this author in [PubMed](#) [Google Scholar](#)

20. Stacey Schultz-Cherry
[View author publications](#)

You can also search for this author in [PubMed](#) [Google Scholar](#)

21. Stephanie A. Cormier
[View author publications](#)

You can also search for this author in [PubMed](#) [Google Scholar](#)

22. Kathryn Shaw-Saliba
[View author publications](#)

You can also search for this author in [PubMed](#) [Google Scholar](#)

23. Andrew Pekosz
[View author publications](#)

You can also search for this author in [PubMed](#) [Google Scholar](#)

24. Richard E. Rothman
[View author publications](#)

You can also search for this author in [PubMed](#) [Google Scholar](#)

25. Kuan-Fu Chen
[View author publications](#)

You can also search for this author in [PubMed](#) [Google Scholar](#)

26. Zifeng Yang
[View author publications](#)

You can also search for this author in [PubMed](#) [Google Scholar](#)

27. Richard J. Webby
[View author publications](#)

You can also search for this author in [PubMed](#) [Google Scholar](#)

28. Nanshan Zhong

[View author publications](#)

You can also search for this author in [PubMed](#) [Google Scholar](#)

29. Jeremy Chase Crawford

[View author publications](#)

You can also search for this author in [PubMed](#) [Google Scholar](#)

30. Paul G. Thomas

[View author publications](#)

You can also search for this author in [PubMed](#) [Google Scholar](#)

Consortia

PALISI Pediatric Intensive Care Influenza (PICFLU) Investigators

- Michele Kong
- , Ronald C. Sanders Jr
- , Katherine Irby
- , Katri Typpo
- , Barry Markovitz
- , Natalie Cvijanovich
- , Heidi Flori
- , Adam Schwarz
- , Nick Anas
- , Peter Mourani
- , Angela Czaja
- , Gwenn McLaughlin
- , Matthew Paden
- , Keiko Tarquinio
- , Bria M. Coates
- , Neethi Pinto
- , Juliane Bubeck Wardenburg

- , Adrienne G. Randolph
- , Anna A. Agan
- , Tanya Novak
- , Margaret M. Newhams
- , Stephen C. Kuracheck
- , Mary E. Hartman
- , Allan Doctor
- , Edward J. Truemper
- , Sidharth Mahapatra
- , Kate G. Ackerman
- , L. Eugene Daugherty
- , Mark W. Hall
- , Neal Thomas
- , Scott L. Weiss
- , Julie Fitzgerald
- , Renee Higgerson
- , Laura L. Loftis
- , Rainer G. Gedeit
- & Marc-André Dugas

Corresponding author

Correspondence to [Paul G. Thomas](#).

Rights and permissions

[Reprints and Permissions](#)

About this article



Check for
updates

Cite this article

Boyd, D.F., Allen, E.K., Randolph, A.G. *et al.* Publisher Correction: Exuberant fibroblast activity compromises lung function via ADAMTS4. *Nature* **588**, E5 (2020). <https://doi.org/10.1038/s41586-020-2987-0>

[Download citation](#)

- Published: 18 November 2020
- Issue Date: 03 December 2020
- DOI: <https://doi.org/10.1038/s41586-020-2987-0>

Comments

By submitting a comment you agree to abide by our [Terms](#) and [Community Guidelines](#). If you find something abusive or that does not comply with our terms or guidelines please flag it as inappropriate.

[Download PDF](#)

This article was downloaded by **calibre** from <https://www.nature.com/articles/s41586-020-2987-0>

| [Section menu](#) | [Main menu](#) |

Addendum: A pneumonia outbreak associated with a new coronavirus of probable bat origin

[Download PDF](#)

- Addendum
- [Published: 17 November 2020](#)

Addendum: A pneumonia outbreak associated with a new coronavirus of probable bat origin

- [Peng Zhou^{1 na1},](#)
- [Xing-Lou Yang^{1 na1},](#)
- [Xian-Guang Wang^{2 na1},](#)
- [Ben Hu¹,](#)
- [Lei Zhang¹,](#)
- [Wei Zhang¹,](#)
- [Hao-Rui Si^{1,3},](#)
- [Yan Zhu¹,](#)
- [Bei Li¹,](#)
- [Chao-Lin Huang²,](#)
- [Hui-Dong Chen²,](#)
- [Jing Chen^{1,3},](#)
- [Yun Luo^{1,3},](#)
- [Hua Guo^{1,3},](#)
- [Ren-Di Jiang^{1,3},](#)
- [Mei-Qin Liu^{1,3},](#)
- [Ying Chen^{1,3},](#)
- [Xu-Rui Shen^{1,3},](#)
- [Xi Wang^{1,3},](#)
- [Xiao-Shuang Zheng^{1,3},](#)

- [Kai Zhao^{1,3}](#),
- [Quan-Jiao Chen¹](#),
- [Fei Deng¹](#),
- [Lin-Lin Liu⁴](#),
- [Bing Yan¹](#),
- [Fa-Xian Zhan⁴](#),
- [Yan-Yi Wang¹](#),
- [Geng-Fu Xiao¹](#) &
- [Zheng-Li Shi](#) [ORCID: orcid.org/0000-0001-8089-163X¹](#)

[Nature volume 588](#), page E6(2020) [Cite this article](#)

- 8113 Accesses
- 10 Citations
- 245 Altmetric
- [Metrics details](#)

Subjects

- [Pathogens](#)
- [SARS-CoV-2](#)
- [Virology](#)

The [Original Article](#) was published on 03 February 2020

[Download PDF](#)

Addendum to: *Nature* <https://doi.org/10.1038/s41586-020-2012-7> Published online 03 February 2020

Here we provide further information about the bat SARS-related coronavirus (SARSr-CoV) strain RaTG13 reported in our Article. Between 1 July and 1 October 2012, we received 13 serum samples collected from 4

patients (one of whom was deceased) who showed severe respiratory disease. These patients had visited a mine cave in Tongguan town, Mojjiang County, Yunnan Province, China, to clean bat faeces in order to mine copper before being admitted to the First Affiliated Hospital of Kunming Medical University on 26–27 April 2012. The samples we received were collected by the hospital staff in June, July, August and September 2012. To investigate the cause of the respiratory disease, we tested the samples using PCR methods developed in our laboratory targeting the RNA-dependent RNA polymerases (RdRp) of Ebola virus, Nipah virus and bat SARSr-CoV Rp3, and all of the samples were negative for the presence of these viruses. We also tested the serum samples for the presence of antibodies against the nucleocapsid proteins of these three viruses, and none of the samples gave a positive result. Recently, we retested the samples with our validated enzyme-linked immunosorbent assay (ELISA) against the SARS coronavirus 2 (SARS-CoV-2) nucleocapsid protein—which has greater than 90% amino acid sequence identity with bat SARSr-CoV Rp3—and confirmed that these patients were not infected by SARS-CoV-2.

We suspected that the patients had been infected by an unknown virus. Therefore, we and other groups sampled animals including bats, rats and musk shrews in or around the cave, and found some alphacoronaviruses¹ and paramyxoviruses². Between 2012 and 2015, our group sampled bats once or twice a year in this cave and collected a total of 1,322 samples. From these samples, we detected 293 highly diverse coronaviruses, of which 284 were designated alphacoronaviruses and 9 were designated betacoronaviruses on the basis of partial RdRp sequences. All of the nine betacoronaviruses are SARSr-CoVs, one of which (sample ID4991; renamed RaTG13 in our Article to reflect the bat species, the location and the sampling year) was described in a 2016 publication¹. The partial RdRp sequence (370 bp) of ID4991 was deposited in GenBank in 2016 under accession number KP876546. All of the identified bat SARSr-CoVs are distantly related to SARS-CoV based on partial RdRp sequences. In 2018, as the next-generation sequencing technology and capability in our laboratory had improved, we performed further sequencing of these bat viruses and obtained almost the full-length genome sequence (without the 5' and 3' ends) of RaTG13. In 2020, we compared the sequence of SARS-

CoV-2 with our unpublished bat coronavirus sequences and found that it shared a 96.2% identity with RaTG13.

References

1. 1.

Ge, X. Y. et al. Coexistence of multiple coronaviruses in several bat colonies in an abandoned mineshaft. *Virol. Sin.* **31**, 31–40 (2016).

[CAS Article](#) [PubMed](#) [PubMed Central](#) [Google Scholar](#)

2. 2.

Wu, Z. et al. Novel Henipa-like virus, Mojiang paramyxovirus, in rats, China, 2012. *Emerg. Infect. Dis.* **20**, 1064–1066 (2014).

[PubMed](#) [PubMed Central](#) [Google Scholar](#)

[Download references](#)

Author information

Author notes

1. These authors contributed equally: Peng Zhou, Xing-Lou Yang, Xian-Guang Wang

Affiliations

1. CAS Key Laboratory of Special Pathogens, Wuhan Institute of Virology, Center for Biosafety Mega-Science, Chinese Academy of Sciences, Wuhan, China

Peng Zhou, Xing-Lou Yang, Ben Hu, Lei Zhang, Wei Zhang, Hao-Rui Si, Yan Zhu, Bei Li, Jing Chen, Yun Luo, Hua Guo, Ren-Di Jiang, Mei-Qin Liu, Ying Chen, Xu-Rui Shen, Xi Wang, Xiao-Shuang

Zheng, Kai Zhao, Quan-Jiao Chen, Fei Deng, Bing Yan, Yan-Yi Wang, Geng-Fu Xiao & Zheng-Li Shi

2. Wuhan Jin Yin-Tan Hospital, Wuhan, China

Xian-Guang Wang, Chao-Lin Huang & Hui-Dong Chen

3. University of Chinese Academy of Sciences, Beijing, China

Hao-Rui Si, Jing Chen, Yun Luo, Hua Guo, Ren-Di Jiang, Mei-Qin Liu, Ying Chen, Xu-Rui Shen, Xi Wang, Xiao-Shuang Zheng & Kai Zhao

4. Hubei Provincial Center for Disease Control and Prevention, Wuhan, China

Lin-Lin Liu & Fa-Xian Zhan

Authors

1. Peng Zhou

[View author publications](#)

You can also search for this author in [PubMed](#) [Google Scholar](#)

2. Xing-Lou Yang

[View author publications](#)

You can also search for this author in [PubMed](#) [Google Scholar](#)

3. Xian-Guang Wang

[View author publications](#)

You can also search for this author in [PubMed](#) [Google Scholar](#)

4. Ben Hu

[View author publications](#)

You can also search for this author in [PubMed](#) [Google Scholar](#)

5. Lei Zhang

[View author publications](#)

You can also search for this author in [PubMed](#) [Google Scholar](#)

6. Wei Zhang

[View author publications](#)

You can also search for this author in [PubMed](#) [Google Scholar](#)

7. Hao-Rui Si

[View author publications](#)

You can also search for this author in [PubMed](#) [Google Scholar](#)

8. Yan Zhu

[View author publications](#)

You can also search for this author in [PubMed](#) [Google Scholar](#)

9. Bei Li

[View author publications](#)

You can also search for this author in [PubMed](#) [Google Scholar](#)

10. Chao-Lin Huang

[View author publications](#)

You can also search for this author in [PubMed](#) [Google Scholar](#)

11. Hui-Dong Chen

[View author publications](#)

You can also search for this author in [PubMed](#) [Google Scholar](#)

12. Jing Chen

[View author publications](#)

You can also search for this author in [PubMed](#) [Google Scholar](#)

13. Yun Luo

[View author publications](#)

You can also search for this author in [PubMed](#) [Google Scholar](#)

14. Hua Guo

[View author publications](#)

You can also search for this author in [PubMed](#) [Google Scholar](#)

15. Ren-Di Jiang

[View author publications](#)

You can also search for this author in [PubMed](#) [Google Scholar](#)

16. Mei-Qin Liu

[View author publications](#)

You can also search for this author in [PubMed](#) [Google Scholar](#)

17. Ying Chen

[View author publications](#)

You can also search for this author in [PubMed](#) [Google Scholar](#)

18. Xu-Rui Shen

[View author publications](#)

You can also search for this author in [PubMed](#) [Google Scholar](#)

19. Xi Wang

[View author publications](#)

You can also search for this author in [PubMed](#) [Google Scholar](#)

20. Xiao-Shuang Zheng

[View author publications](#)

You can also search for this author in [PubMed](#) [Google Scholar](#)

21. Kai Zhao

[View author publications](#)

You can also search for this author in [PubMed](#) [Google Scholar](#)

22. Quan-Jiao Chen

[View author publications](#)

You can also search for this author in [PubMed](#) [Google Scholar](#)

23. Fei Deng

[View author publications](#)

You can also search for this author in [PubMed](#) [Google Scholar](#)

24. Lin-Lin Liu

[View author publications](#)

You can also search for this author in [PubMed](#) [Google Scholar](#)

25. Bing Yan

[View author publications](#)

You can also search for this author in [PubMed](#) [Google Scholar](#)

26. Fa-Xian Zhan

[View author publications](#)

You can also search for this author in [PubMed](#) [Google Scholar](#)

27. Yan-Yi Wang

[View author publications](#)

You can also search for this author in [PubMed](#) [Google Scholar](#)

28. Geng-Fu Xiao

[View author publications](#)

You can also search for this author in [PubMed](#) [Google Scholar](#)

29. Zheng-Li Shi

[View author publications](#)

You can also search for this author in [PubMed](#) [Google Scholar](#)

Corresponding author

Correspondence to [Zheng-Li Shi](#).

Rights and permissions

[Reprints and Permissions](#)

About this article



Check for
updates

Cite this article

Zhou, P., Yang, XL., Wang, XG. *et al.* Addendum: A pneumonia outbreak associated with a new coronavirus of probable bat origin. *Nature* **588**, E6 (2020). <https://doi.org/10.1038/s41586-020-2951-z>

[Download citation](#)

- Published: 17 November 2020
- Issue Date: 03 December 2020
- DOI: <https://doi.org/10.1038/s41586-020-2951-z>

Further reading

- Could SARS-CoV-2-induced lung injury be attenuated by vitamin D?

- Dongqiong Xiao
- , Xihong Li
- , Xiaojuan Su
- , Dezhi Mu
- & Yi Qu

International Journal of Infectious Diseases (2021)

- LPD-12: a promising lipopeptide to control COVID-19

- Trinath Chowdhury
- , Piyush Baindara
- & Santi M. Mandal

International Journal of Antimicrobial Agents (2020)

- Hock-a-loogie saliva as a diagnostic specimen for SARS-CoV-2 by a PCR-based assay: A diagnostic validity study

- Jian Fan
- , Fei Yu
- , Xiang Wang
- , Qianda Zou
- , Bin Lou
- , Guoliang Xie
- , Xianzhi Yang
- , Weizhen Chen
- , Qi Wang
- , Dan Zhang
- , Ruonan Wang
- , Baihuan Feng
- , Yuejiao Dong
- , Li Huang
- , Yun Teng

- , Zhenzhen Deng
- , Ling Yu
- , Kaijin Xu
- , Jifang Sheng
- , Shufa Zheng
- & Yu Chen

Clinica Chimica Acta (2020)

- **The main protease and RNA-dependent RNA polymerase are two prime targets for SARS-CoV-2**

- Zhenming Jin
- , Haofeng Wang
- , Yinkai Duan
- & Haitao Yang

Biochemical and Biophysical Research Communications (2020)

- **Gastrointestinal coronavirus disease 2019: epidemiology, clinical features, pathogenesis, prevention, and management**

- Simona Deidda
- , Lorena Tora
- , Davide Firinu
- , Stefano Del Giacco
- , Marcello Campagna
- , Federico Meloni
- , Germano Orrù
- , Luchino Chessa
- , Mauro Giovanni Carta
- , Alessandra Melis
- , Gaya Spolverato
- , Roberto Littera
- , Andrea Perra
- , Simona Onali

- , Luigi Zorcolo
- & Angelo Restivo

Expert Review of Gastroenterology & Hepatology (2020)

Comments

By submitting a comment you agree to abide by our [Terms](#) and [Community Guidelines](#). If you find something abusive or that does not comply with our terms or guidelines please flag it as inappropriate.

[Download PDF](#)

This article was downloaded by **calibre** from <https://www.nature.com/articles/s41586-020-2951-z>

| [Section menu](#) | [Main menu](#) |

Retraction Note: Living annulative π -extension polymerization for graphene nanoribbon synthesis

[Download PDF](#)

- Retraction Note
- [Published: 25 November 2020](#)

Retraction Note: Living annulative π -extension polymerization for graphene nanoribbon synthesis

- [Yuuta Yano¹](#),
- [Nobuhiko Mitoma^{1,2}](#),
- [Kaho Matsushima¹](#),
- [Feijiu Wang^{1,2}](#),
- [Keisuke Matsui^{1,2}](#),
- [Akira Takakura^{1,2}](#),
- [Yuhei Miyauchi^{1,2,3}](#),
- [Hideto Ito^{1,2}](#) &
- [Kenichiro Itami^{1,2,4}](#)

[Nature](#) volume 588, page 180 (2020) [Cite this article](#)

- 8649 Accesses
- 36 Altmetric
- [Metrics details](#)

Subjects

- [Nanoscale materials](#)

- [Organic chemistry](#)
- [Polymer synthesis](#)

The [Original Article](#) was published on 26 June 2019

[Download PDF](#)

Retraction to: *Nature* <https://doi.org/10.1038/s41586-019-1331-z> Published online 26 June 2019

We would like to retract this Letter. *Nature* previously issued an Editorial Expression of Concern (<https://doi.org/10.1038/s41586-020-2756-0>) after we, the authors, alerted the journal to potential problems with the matrix-assisted laser desorption/ionization time-of-flight (MALDI–TOF) mass spectrometry data. These issues undermine our confidence in the integrity of the study as a whole and we therefore now wish to retract the Letter. Our group continues to explore the synthesis of graphene nanoribbons (GNRs), but we have been unable to reproduce some of the results presented in this Letter. Careful scrutiny of the source data has identified potential problems with the manner in which the MALDI–TOF mass spectrometry data in this Letter were originally generated and processed. Specifically, the exact molecular weights (m/z calculated for $[M]^+$ and $[M + Ag]^+$) of GNRs **2** (Extended Data Fig. 1), **7** (Extended Data Fig. 6) and **8** (Extended Data Fig. 7) were calculated wrongly on the basis of the assumption that all carbon atoms in these GNRs were ^{12}C (monoisotopic). In all GNRs, the exact mass peaks should appear approximately 6 to 9 mass units higher. Thus, the observed mass spectra do not match the proposed GNR structures. The isotopic patterns of some GNRs (for example, Extended Data Fig. 7c, d for GNR **8**) do not match the (correct) calculated spectra. These also do not support the formation of the proposed GNR structures. The baselines (noise) of the mass spectra of GNRs **2** and **8** appear to be identical, which calls into question the integrity of the mass data. The original MALDI-TOF mass spectrometry data are unavailable and only editable secondary data exist, which also raises concerns regarding the integrity of the mass data. We regret any confusion and apologize to the scientific community.

Author information

Affiliations

1. Graduate School of Science, Nagoya University, Nagoya, Japan

Yuuta Yano, Nobuhiko Mitoma, Kaho Matsushima, Feijiu Wang, Keisuke Matsui, Akira Takakura, Yuhei Miyauchi, Hideto Ito & Kenichiro Itami

2. JST-ERATO, Itami Molecular Nanocarbon Project, Nagoya, Japan

Nobuhiko Mitoma, Feijiu Wang, Keisuke Matsui, Akira Takakura, Yuhei Miyauchi, Hideto Ito & Kenichiro Itami

3. Institute of Advanced Energy, Kyoto University, Kyoto, Japan

Yuhei Miyauchi

4. Institute of Transformative Bio-Molecules (WPI-ITbM), Nagoya University, Nagoya, Japan

Kenichiro Itami

Authors

1. Yuuta Yano

[View author publications](#)

You can also search for this author in [PubMed](#) [Google Scholar](#)

2. Nobuhiko Mitoma

[View author publications](#)

You can also search for this author in [PubMed](#) [Google Scholar](#)

3. Kaho Matsushima

[View author publications](#)

You can also search for this author in [PubMed](#) [Google Scholar](#)

4. Feijiu Wang

[View author publications](#)

You can also search for this author in [PubMed](#) [Google Scholar](#)

5. Keisuke Matsui

[View author publications](#)

You can also search for this author in [PubMed](#) [Google Scholar](#)

6. Akira Takakura

[View author publications](#)

You can also search for this author in [PubMed](#) [Google Scholar](#)

7. Yuhei Miyauchi

[View author publications](#)

You can also search for this author in [PubMed](#) [Google Scholar](#)

8. Hideto Ito

[View author publications](#)

You can also search for this author in [PubMed](#) [Google Scholar](#)

9. Kenichiro Itami

[View author publications](#)

You can also search for this author in [PubMed](#) [Google Scholar](#)

Corresponding authors

Correspondence to [Hideto Ito](#) or [Kenichiro Itami](#).

Rights and permissions

[Reprints and Permissions](#)

About this article



Check for
updates

Cite this article

Yano, Y., Mitoma, N., Matsushima, K. *et al.* Retraction Note: Living annulative π -extension polymerization for graphene nanoribbon synthesis. *Nature* **588**, 180 (2020). <https://doi.org/10.1038/s41586-020-2950-0>

[Download citation](#)

- Published: 25 November 2020
- Issue Date: 03 December 2020
- DOI: <https://doi.org/10.1038/s41586-020-2950-0>

Comments

By submitting a comment you agree to abide by our [Terms](#) and [Community Guidelines](#). If you find something abusive or that does not comply with our terms or guidelines please flag it as inappropriate.

[Download PDF](#)

This article was downloaded by **calibre** from <https://www.nature.com/articles/s41586-020-2950-0>

Publisher Correction: Butterfly effect and a self-modulating El Niño response to global warming

[Download PDF](#)

- Publisher Correction
- [Published: 17 November 2020](#)

Publisher Correction: Butterfly effect and a self-modulating El Niño response to global warming

- [Wenju Cai](#) [ORCID: orcid.org/0000-0001-6520-0829^{1,2}](#),
- [Benjamin Ng](#) [ORCID: orcid.org/0000-0002-4458-4592²](#),
- [Tao Geng](#) [ORCID: orcid.org/0000-0002-3385-7110^{1,2}](#),
- [Lixin Wu](#) [ORCID: orcid.org/0000-0002-4694-5531¹](#),
- [Agus Santoso](#) [ORCID: orcid.org/0000-0001-7749-8124^{2,3}](#) &
- [Michael J. McPhaden](#) [ORCID: orcid.org/0000-0002-8423-5805⁴](#)

[Nature](#) volume 588, page E3 (2020) [Cite this article](#)

- 465 Accesses
- 2 Altmetric
- [Metrics details](#)

Subjects

- [Atmospheric dynamics](#)
- [Climate and Earth system modelling](#)
- [Physical oceanography](#)
- [Projection and prediction](#)

The [Original Article](#) was published on 02 September 2020

[Download PDF](#)

Correction to: *Nature* <https://doi.org/10.1038/s41586-020-2641-x> Published online 2 September 2020

In this Article, owing to an error in the production process, the R value stated in Fig. 5b should be 0.914 instead of -0.914 . In addition, in Extended Data Fig. 4a, b, the y axis should range from -4.0 to 4.0 , rather than from -0.4 to 0.4 . Finally, a minor typographical error was corrected in the Abstract. The Article has been corrected online.

Author information

Affiliations

1. Key Laboratory of Physical Oceanography—Institute for Advanced Ocean Studies, Ocean University of China and Qingdao National Laboratory for Marine Science and Technology, Qingdao, China

Wenju Cai, Tao Geng & Lixin Wu

2. Centre for Southern Hemisphere Oceans Research (CSHOR), CSIRO Oceans and Atmosphere, Hobart, Tasmania, Australia

Wenju Cai, Benjamin Ng, Tao Geng & Agus Santoso

3. Australian Research Council (ARC) Centre of Excellence for Climate Extremes, The University of New South Wales, Sydney, New South Wales, Australia

Agus Santoso

4. NOAA/Pacific Marine Environmental Laboratory, Seattle, WA, USA

Michael J. McPhaden

Authors

1. Wenju Cai

[View author publications](#)

You can also search for this author in [PubMed](#) [Google Scholar](#)

2. Benjamin Ng

[View author publications](#)

You can also search for this author in [PubMed](#) [Google Scholar](#)

3. Tao Geng

[View author publications](#)

You can also search for this author in [PubMed](#) [Google Scholar](#)

4. Lixin Wu

[View author publications](#)

You can also search for this author in [PubMed](#) [Google Scholar](#)

5. Agus Santoso

[View author publications](#)

You can also search for this author in [PubMed](#) [Google Scholar](#)

6. Michael J. McPhaden

[View author publications](#)

You can also search for this author in [PubMed](#) [Google Scholar](#)

Corresponding authors

Correspondence to [Wenju Cai](#) or [Lixin Wu](#).

Rights and permissions

[Reprints and Permissions](#)

About this article



Check for
updates

Cite this article

Cai, W., Ng, B., Geng, T. *et al.* Publisher Correction: Butterfly effect and a self-modulating El Niño response to global warming. *Nature* **588**, E3 (2020). <https://doi.org/10.1038/s41586-020-2958-5>

[Download citation](#)

- Published: 17 November 2020
- Issue Date: 03 December 2020
- DOI: <https://doi.org/10.1038/s41586-020-2958-5>

Comments

By submitting a comment you agree to abide by our [Terms](#) and [Community Guidelines](#). If you find something abusive or that does not comply with our terms or guidelines please flag it as inappropriate.

[Download PDF](#)

This article was downloaded by **calibre** from <https://www.nature.com/articles/s41586-020-2958-5>

Collections